UNIVERSITY OF OKLAHOMA

GRADUATE COLLEGE

OBSERVATIONS OF EVOLVING LIGHTNING, MICROPHYSICS, AND KINEMATICS FOR A SUPERCELL, A MULTICELL, AND A MESOSCALE CONVECTIVE SYSTEM

A DISSERTATION

SUBMITTED TO THE GRADUATE FACULTY

in partial fulfillment of the requirements for the

Degree of

DOCTOR OF PHILOSOPHY

By

ELIZABETH DIGANGI
Norman, Oklahoma
2019

OBSERVATIONS OF EVOLVING LIGHTNING, MICROPHYSICS, AND KINEMATICS FOR A SUPERCELL, A MULTICELL, AND A MESOSCALE CONVECTIVE SYSTEM

A DISSERTATION APPROVED FOR THE
SCHOOL OF METEOROLOGY

BY

Dr. Michael Biggerstaff, Chair

Dr. Donald MacGorman

Dr. Conrad Ziegler

Dr. Alan Shapiro

Dr. Guifu Zhang

Dr. Kieran Mullen

This dissertation is dedicated to Michael Smith.

Acknowledgements

The research presented in this dissertation is the culmination of over six years of collaborative work with scientists in both CIMMS/NSSL and the School of Meteorology. The project was sponsored by NSF grants AGS-1063945 and AGS-1063537 and by a NASA Earth and Space Sciences Fellowship. Although I have valued all the feedback, assistance, and suggestions received from my entire committee, I would like to especially acknowledge Dr. MacGorman, Dr. Biggerstaff, and Dr. Ziegler for their exemplary mentorship throughout my tenure as a graduate student. Under your tutelage, I have learned more about being a scientist than I thought was possible. I would also like to acknowledge Dr. Ted Mansell, Dr. Kristin Calhoun, Dr. Eric Bruning, Dr. Vanna Chmielewski, Dr. Kim Elmore, Dr. Gerry Creager, and Dr. Daniel Betten for the help, guidance, and mentorship they have been able to provide as well.

This journey has been about more than learning how to be a scientist, though, and so I must also acknowledge some of the people who kept me sane and encouraged me through the most difficult times, and who celebrated with me during the best times. To Rachel Miller, Addison Alford, Maddy Clark Frank, Ash Amos, Yuuki Crowley, Chris Allen, Will Bramall, Josh King, Erik Wittrock, Chris Dalby, my parents, my siblings, and any others I may have forgotten to name, because the list was long: thank you.

Most of all, however, I would like to thank Michael Smith. You uprooted your life to follow me halfway across the country as I pursued my dream of becoming a scientist, and have been there with me through every light and dark moment of the experience. I love you, and I really, truly could not have done this without you.

Table of Contents

List of Figures

Abstract

The Deep Convective Clouds and Chemistry (DC3) field experiment collected data on a variety of storms to investigate the relationships between lightning and other storm processes. This study focuses on the relationships between lightning and storm microphysics and kinematics for a supercell storm, a multicell storm, and a mesoscale convective system. All three storms occurred in Oklahoma, in range of the 3-D Oklahoma Lightning Mapping Array (LMA), and were sampled by ground-based mobile radars. 3-D wind fields derived from the mobile radar data and the results of a C-band hydrometeor classification algorithm are compared with gridded lightning parameters, including flash extent density, flash initiation density, mean flash size, and charge distribution for each storm. A series of horizontal and vertical cross-sections is shown for each of the three cases, along with bulk analyses of the microphysical and updraft characteristics compared with the gridded lightning parameters. The relationships between all these datasets and the implications these results have on the electrification of thunderstorms will be discussed. In general, evidence of the noninductive charging mechanism generating the most charge was present in all three cases, and many of the lightning-storm intensity relationships investigated by past studies apply to all three of the storms studied here.

Chapter 1: Introduction

The relationships between storm-scale motions and other processes has been an ongoing subject of study for decades. Given the difficulties in measuring in-situ storm kinematics and microphysics, lightning characteristics have been proposed as potential proxies for storm intensity, including temporal trends in parameters such as total flash rate to spatial trends in parameters such as the distribution of flash area within storms. Lightning also contributes to atmospheric chemistry processes, such as the production of nitrogen oxides. Field campaigns over the years have collected data specifically seeking to understand various relationships, and case studies have incrementally added to our understanding over time. This study will synthesize multiple observational datasets from the Deep Convective Clouds and Chemistry field experiment (DC3, Barth et al. 2015) to enable a detailed spatial and temporal analysis of three storms with very different morphologies to compare how their variations in microphysical and kinematic parameters influence the lightning and charge structures they produce.

1.1 Background

1.1.1 Electrification and Lightning

Charge separation within convective storms is a complex process, intrinsically dependent on the microphysical and kinematic structure of a given storm, and thus highly variable from case to case. However, there are certain charging mechanisms which are generally accepted in the community to be prevalent in convective storms. Results from laboratory experiments (e.g., Takahashi 1978; Jayaratne et al., 1983; Emersic and Saunders, 2013) led to the most widely accepted theory for the microscopic separation of storm charge, which is known as the noninductive charge mechanism: rebounding collisions between riming graupel particles and ice crystals result in the exchange of electrons between the hydrometeors. Under certain conditions

(i.e., supercooled cloud water content (CWC) is ~1-2 g m^{-3}), the graupel and ice particles exchange enough charge to create lightning in storms, although the polarity of the graupel after the collision depends on the ambient temperature. For $0 > T > -10^{o}C$ in Takahashi's (1978) experiments, graupel will become positively charged, whereas for $T < -10^{o}C$ graupel will become negatively charged; in both cases, the corresponding ice crystals then gain the opposite polarity of the graupel. The polarity of charge gained by graupel during a collision reverses as the ambient temperature in which the graupel is located changes. Takahashi and Miyawaki (2002) confirmed their results with further experiments in a wind tunnel. The specific temperature thresholds differed in other studies and were influenced by other microphysical characteristics, such as the riming rate of graupel and the effective cloud liquid water content (e.g., Jayaratne et al. 1983; Emersic and Saunders 2013). Laboratory experiments have also substantiated the potential for charge separation between colliding ice crystals when they are either growing by vapor deposition or shrinking by sublimation (e.g. Gaskell and Illingworth 1980). Although the differences from laboratory to laboratory can have large effects on the resulting charge distributions in numerical storm simulations, all simulation studies since 1990 have found that noninductive charge exchange during rebounding ice particle collisions can produce charge distributions similar to those observed in storms and can produce enough charge to cause lightning (e.g., Ziegler et al. 1991; Helsdon et al. 2001; Mansell et al. 2005, 2010).

Though the noninductive mechanism is considered to account for most storm electrification, other processes are almost certainly at work as well. Saunders (1993) reviewed the thunderstorm electrification processes accepted as viable by the community. After noninductive charging, inductive charging processes are considered to have a substantial impact on storm electrification. Inductive processes require an existing vertical electric field which

causes hydrometeors to become polarized. When they are vertically polarized and a smaller particle bounces off the underside of a large particle, the two particles carry opposite charge when they separate. In numerical storm simulations in which both inductive and noninductive processes are included, noninductive processes are responsible for electrifying the storms, although inductive processes appear to be responsible for some subsequent smaller charge regions that typically form in storms, such as the charge often observed near and below the melting level in downdrafts. Saunders also noted the convective charging process: electric fields at the ground beneath thunderstorms are often strong enough to produce weak currents from the ground, and the charge from these currents is captured on aerosols and hydrometeors beneath clouds (e.g., Chauzy and Raizonville, 1982). A similar mechanism had been suggested for electrifying thunderstorms, but has been found to be too weak to actually cause thunderstorm electrification (e.g., Helson et al. 2002).

One other process resulting in thunderstorm charge regions is the charge resulting from the divergence in electric current due to the change in electric conductivity occurring at the boundaries of clouds. The charge forms in response to the electric field driving the current and reaches equilibrium when the currents just above and below the cloud are equal. These charge regions are referred to as screening layers.

Once particles have become charged by microphysical processes, differential sedimentation and advection can move the different sized particles apart macroscopically to produce regions of net charge. Vertical motion in updrafts and downdrafts causes particles to rise or descend, and divergence and detrainment of air from updrafts will advect particles horizontally into less convectively active portions of a storm. The principle motion that is usually considered is differential sedimentation causing smaller ice particles to rise faster or fall more

slowly than graupel particles, which usually creates a large upper positive charge region on small ice particles and a small lower positive charge on graupel, and creates midlevel negative charge from graupel particles falling from above and small ice particles rising from below. The large electric fields that initiate lightning typically occur between adjacent regions of opposite charge, not in the charge regions themselves.

The traditional basic conceptual model for the charge distribution in a thunderstorm is known as the "tripole" model, consisting of a central negative charge region with a comparable positive charge region above it and a smaller positive region below it (e.g. Simpson and Scrace 1937; Simpson and Robinson 1941; Williams 1989). However, Marshall et al. (1989) and Marshall and Rust (1991), among others, have pointed out various shortcomings of the tripole paradigm for representing thunderstorm charge structure. The complexity of a given storm's charge structure will depend on its updraft characteristics; a supercell with a large, persistent updraft may have a more complicated charge structure than an airmass thunderstorm with a small, pulsing updraft (e.g. Marshall and Rust 1991; Stolzenburg et al. 1998a; Wiens et al. 2005; Weiss et al. 2008; Bruning et al. 2010). To better illustrate the complex nature of thunderstorm charge structures, Stolzenburg et al. (1998a) synthesized the balloon data from almost 50 electric field soundings through convection of various modes and found that convective storms have an average of four charge layers within the updraft and at least six outside of it. This conceptual model is shown in Figure 1.

Many storms have also been observed to have vertically stacked layers of charge of opposite polarity to that in the "normal" tripole paradigm; such storms, which have charge structures characterized by a central positive charge region and upper negative charge region, are often referred to as "inverted" polarity storms (e.g. Rust and MacGorman 2002; MacGorman et

al. 2005; Wiens et al. 2005; Tessendorf et al. 2007a,b). However, Bruning et al. (2012) noted that the terms “normal” and “inverted” charge structure are adequate only to describe the distribution of charge in a thunderstorm in the most basic sense, and that those terms do not demonstrate charge structure complexity any better than the tripole paradigm.

Brothers et al. (2018) simulated charge regions in both a multicell and a supercell thunderstorm using the COMMAS model, which can resolve large eddies and the resultant turbulent air flows. They demonstrated that the net charge structure of a given storm is highly complex, with many regions of charge that are impossible to analyze with data from an LMA because lightning channels don’t traverse them. Charge advection via overturning eddies in the turbulent region around the main updraft results in small pockets of charge; such a complicated charge structure is conducive to frequent small flashes observed in supercell case studies in the past (e.g. Bruning and MacGorman 2013; Calhoun et al. 2013; DiGangi et al. 2016). These regions were also collocated with higher charge density values and adjacent to actively charging regions. Though Brothers et al. is limited by their selected resolution for the lightning modeling scheme of Mansell (2002) and the single charge generation mechanism implemented (the noninductive mechanism), it nevertheless supports many existing theories regarding the real texture of net storm charge and the mechanisms by which that charge is distributed.

If the electric field reaches the dielectric breakdown threshold, then flash initiation will occur (MacGorman and Rust 1998). From the initiation point, stepped leaders branch out into the different charge regions (Kasemir 1960; MacGorman et al. 1981; Mazur 1989; MacGorman and Rust 1998); a negatively charged leader traverses the positive charge, and a positively charged leader traverses the negative charge. This process dissipates the charge regions that caused the dielectric breakdown to begin with (MacGorman et al. 1981), and the storm may have to

recharge before another lightning flash can occur. If breakdown and flash initiation occurs between the lowest layer of charge and the central layer of charge in the tripole paradigm, the flash can be either an intra-cloud flash (IC) or a cloud-to-ground flash (CG). Typically, a flash will continue to ground as a CG if the negatively charged leader propagating downward toward the lower positive charge does not encounter enough charge to balance the charge the positive leader encounters in the negative region (Kasemir 1960; Mazur 1989; Rison et al. 1999). Investigators have confirmed this conceptual model of lightning, suggesting that the lower charge region is not a sufficient condition, but is a necessary condition, for initiating CG flashes in many situations (e.g. Livingston and Krider 1978; Wiens et al. 2005; Kuhlman et al. 2006; Tessendorf et al. 2007a, b).

A multitude of past studies have investigated the links between storm updraft characteristics, microphysical characteristics, and lightning (e.g. Carey and Rutledge 1996; Lang and Rutledge 2002; Wiens et al. 2005; Kuhlman et al. 2006; Bruning et al. 2007; Tessendorf et al. 2007a, b; Deierling and Petersen 2008; Bruning et al. 2010; Calhoun et al. 2013; Mecikalski et al. 2015; Schultz et al. 2015; DiGangi et al. 2016; Schultz et al. 2017). These studies found that updraft intensity and graupel content are positively correlated with total flash rate. Quantities such as the lightning jump (e.g. Schultz et al. 2009) can be used to diagnose a storm's severe weather potential by acting as a proxy for updraft intensity. In a study of 39 storms, Schultz et al. (2017) found that most large increases in flash rate lagged the growth of updraft volume, graupel mass, and/or peak updraft speed by ~4-13 minutes. They also found that the maximum updraft speed was more representative of short time scale changes in total flash rate, whereas changes in updraft volume > 10 m s^{-1} were more representative of changes in total flash rate across a storm's entire lifetime.

Total flash rate is not the only lightning quantity with a demonstrated relationship to storm kinematics and microphysics. Bruning and MacGorman (2013) hypothesized and showed that flash area is inversely related to updraft intensity. Other literature (e.g., Wiens et al. 2005; Payne et al. 2010; Emersic et al. 2011; Calhoun et al. 2013; Kozlowski and Carey 2014) shows that lightning typically propagates around regions of peak updraft intensity, where hydrometeor concentrations and thus the charge density were low. Regions of hydrometeors with a history of wet growth also tend to support less charge generation than regions of hydrometeors with a history of dry growth (e.g. Bruning et al. 2007; Emersic et al. 2011). Recent work by Rison et al. (2016) tentatively concluded that lightning is initiated by fast positive dielectric breakdown, and positive streamers initiated by hydrometeors can locally enhance electric field until breakdown occurs (e.g. Peterson et al. 2008). This breakdown takes place over relatively small spatial scales, and a strong ambient electric field is required to initiate streamers; thus microphysical and kinematic properties of storms directly affect lightning initiation.

1.1.2 Supercells

The main vertical wind features in the conceptual model for supercell structure from Lemon and Doswell (1979) include an intense rotating updraft and two downdrafts: the forward flank downdraft (FFD), embedded in the main precipitation region downwind of the updraft, and the rear flank downdraft (RFD), immediately upwind of the updraft. Supercells generally begin their life cycle as multicell storms which organize and develop one strong, quasi-steady rotating updraft. Supercell updrafts usually begin to rotate as a result of tilting of low-level streamwise horizontal vorticity associated with strong environmental vertical wind shear (Klemp, 1987; Wakimoto et al., 1988). Within ~30 min of convective initiation (CI) in suitable environments, the developing updraft splits, with one segment rotating cyclonically and the other rotating

anticyclonically. An environment characterized by a clockwise-curving hodograph will favor the intensification of the cyclonic updraft (the mesocyclone) and inhibit the development of the anticyclonic updraft (Klemp et al., 1981).

The appearance of a bounded weak echo region (BWER) in the storm's reflectivity structure signals strong updraft intensification and the development of mid-level rotation in the updraft (i.e., mesocyclone formation). Several factors contribute to the formation of the BWER, including the short residence time for particle growth within very fast updrafts, the centrifuging of precipitation to the periphery of a rotating updraft, and a descending fountain of precipitation from the diverging updraft at higher altitudes (e.g., Lemon and Doswell 1979, Doswell and Burgess 1993, Payne et al. 2010).

The BWER dissipates as the updraft weakens and growing precipitation begins filling the reflectivity vault, a reflection of the weakening mid-level mesocyclone. As precipitation grows to the point of beginning to fall, downdrafts form and begin strengthening and lowering and can lead to downbursts at the ground. Convergence of the vertical vorticity from the RFD with the axis of rotation in the low-level mesocyclone and stretching of vorticity in the updraft appear to be crucial to the formation of strong tornadoes (e.g., Marquis et al. 2016). The mesocyclone typically separates from the main updraft/BWER region prior to the BWER's collapse (Burgess et al., 1977; Lemon et al. 1978), and during this period, strong tornadoes are most likely to occur (Lemon and Doswell 1979). In the classic scenario presented by these last three papers, the RFD spreads outward after reaching the ground and eventually cuts off the storm's inflow, which hastens the storm's decay.

As discussed in the previous section, the intensity and size of supercell updrafts is conducive to high flash rates and complicated charge structures. Stolzenburg et al. (1998a) found

the average height of the center of the main negative charge region in supercells is approximately 9.12 km (-22^{o}C), and a stronger updraft typically means the altitude of the center of this mid-level charge region tends to be higher, as inferred by MacGorman et al. (1989). Ray et al. (1987) studied one supercell case over central Oklahoma and found that its VHF source density was unimodal in the vertical, and most of its observed lightning tended to occur outside the main updraft/reflectivity core. In a study of LMA data and electric field soundings for two supercell storms observed during the Severe Thunderstorm Electrification and Precipitation Study (STEPS), MacGorman et al. (2005) found that charge structures in supercell updrafts were consistent with the noninductive charging mechanism dominating the electrification of the two storms. They concluded that inductive charging mechanisms and charge deposition by lightning were likely responsible for the generation of extra charge layers outside the updraft in the low levels, and hypothesized that the inverted polarity charge structure of the observed storms could be due to a larger than usual graupel rime accretion rate in the presence of a strong updraft. Wiens et al. (2005) further analyzed one of the same storms using LMA data and the three-dimensional winds synthesized from triple-Doppler radar data and found that increased complexity in the storm's charge structure followed surges in updraft intensity, and that at least one positive charge layer that was elevated in the main updraft region sloped downward into the forward flank. More charge regions were inferred from LMA data outside the updraft than within it. Both studies found that minima in lightning activity known as lightning holes were collocated horizontally with BWERs, although at a slightly higher altitude.

Calhoun et al. (2013) found that flashes near the updraft of the 29-30 May 2004 Geary supercell storm during the Thunderstorm Electrification and Lightning Experiment (TELEX) tended to be frequent but small in horizontal extent and of short duration, while flashes closer to

the edges of the storm were less frequent but tended to be much larger, sometimes propagating into the anvil in roughly horizontal layers, consistent with the findings of Bruning and MacGorman (2013). They hypothesized that the charge regions in the storm core consisted of small pockets of charge rather than the broad layers of charge found in the anvil. Like other documented supercell cases, the storm had extremely high flash rates, which were the result of a consistently strong updraft and large concentrations of hydrometeors. The strong updraft consistently produced a lightning hole that was roughly collocated with the updraft and BWER. They also noted continual VHF discharges in the overshooting top unconnected to organized flashes; these discharges were generally associated with the 18 dBZ echo top ascending above a storm's level of neutral buoyancy (e.g. MacGorman et al. 2017), and thus tended to indicate a strong updraft.

1.1.3 Multicells

Multicell storms are typically comprised of multiple convective cells merged together into one storm complex. Their convective intensity and structure can vary widely from case to case, with updrafts either growing and decaying at different times from one another or merging together to form a more unified updraft region. As such, the distribution of VHF sources and lightning relative to storm features is also highly variable (e.g. Taylor et al. 1984; Ray et al. 1987). Ray et al. (1987) observed a severe multicell storm in addition to the supercell storm mentioned in section 1.1.2. Overall, it had weaker horizontal and vertical winds, as well as weaker reflectivity, than the supercell, and its maximum reflectivities and lightning activity tended to align with updraft cores. At any given time, there was more lightning occurring near the most active convective cells in this multicell complex. The vertical distribution of VHF source density was bimodal in the multicell, much simpler than observed in the supercell.

Carey and Rutledge (1996) studied a multicell storm with relatively weak maximum updrafts (Doppler-inferred updrafts of 11-16 m s^{-1}), and low to moderate flash rates peaking around 10 flashes min^{-1}. They found that increasing in-cloud flash rates were well correlated with the increasing volume of small graupel/hail particles suspended in the upper portion of the storm's updraft region, although lagging graupel/hail by roughly 10 min, and that the decay in IC flash rate over the last 30 min of the observed period occurred as the volume of graupel/hail above the melting level decreased by an order of magnitude. Bruning et al. (2007) observed similar phenomena in a multicell sampled during TELEX: it had weak updrafts and low flash rates, but there were relatively high graupel concentrations aloft, where those particles were suspended by the main updraft. The storm's charge structure agreed in polarity and vertical distribution with the Stolzenburg et al. (1998a) conceptual model. Differential sedimentation created the low and middle level charge regions in/around a vigorous updraft pulse and created an upper-level charge region as the updraft reached upper levels but was starting to weaken.

Tessendorf et al. (2007a) studied two multicell storms with different charge structures: the polarity of the overall charge structure of one storm was "normal" and the that of the other was "inverted". The inverted polarity storm had more vigorous updrafts and total flash rates up to 500 flashes min^{-1}, while the normal polarity storm had weaker convective properties and peak flash rates of 80-120 flashes min^{-1}. In the normal polarity storm, the volumes of updraft >10 m s^{-1} were two orders of magnitude smaller than in the inverted polarity storm and the maximum updraft speed was half. The overall charge structure of the inverted polarity storm clarified and stabilized after developing a broad, strong updraft, which could have been conducive to positive graupel charging (i.e. Williams et al. 2005). However, the storm retained its original charge structure outside the updraft core.

Weiss et al. (2008) also observed a multicell storm with charge structures that varied from one embedded cell to another; that storm was divisible into four different sections, with charge regions in each section ranging from 2-6 vertically stacked layers, and the most complex charge structures were associated with the strongest convective cores. They observed that almost all of the storm's IC flashes propagated through areas of high reflectivity, sometimes through multiple reflectivity cores, traversing regions of positive charge at very different altitudes connected via vertical channels. Some flashes occurring next to each other in different cells at the same altitudes indicated regions of positive and negative charge located side by side. They attributed the charge structure's complexity compared to some past studies of multicell storms to the fact that it contained multiple cells in various stages of development, and that enhanced convergence along an outflow boundary from a different storm produced new cells that merged with the main storm. However, consistent with other past studies, they observed that the IC flash rate decreased and the CG flash rate increased in each cell as its updraft weakened and its reflectivity core descended.

1.1.4 Mesoscale Convective Systems

A typical mesoscale convective system (MCS) begins as a contiguous line of thunderstorms with merged cold pools and anvil clouds, often referred to as a squall line. As the squall line intensifies, ice particles generated in the convective updrafts are transported rearward relative to storm motion, where they contribute to the growth and expansion of the anvil cloud into a region of stratiform precipitation (e.g. Houze et al. 1989). Modeling studies such as Rutledge and Houze (1987) have shown that the fallout pattern of ice particles transported out of the convective region determines the width and location of the stratiform precipitation region; the most common configuration for a mature MCS in the contiguous United States is to have a

leading convective line and a trailing stratiform region (TS), though leading stratiform/trailing line (LS) and parallel stratiform (PS) MCSs are not rare (the mode of an MCS is determined primarily by the mid-level storm-relative flow; Parker and Johnson 2000). The classic description of the stratiform region by Biggerstaff and Houze (1991) is that it is maintained by a mesoscale updraft-downdraft couplet, where the updraft's (downdraft's) horizontal extent is on the order of the stratiform cloud (stratiform precipitation); the updraft is generally in the upper levels and the downdraft is in the lower levels. A mature MCS with trailing stratiform also generally has a transition zone, or a band of weak reflectivity in the presence of deep descent which is stronger than the mesoscale downdraft in the stratiform region, located between the convective and stratiform regions. Hydrometeors in the transition zone are generally advected from a lower source region of the convective line and have undergone less aggregation than hydrometeors in the stratiform region. The overall smaller sizes of particles in the transition zone cause the observed reflectivity minimum (Biggerstaff and Houze 1993).

The average electrical structure of TS MCSs is also generally well known. Early studies of the electrical properties of MCSs noted that, although the charge structure of the convective region was consistent with that observed in isolated thunderstorms, the stratiform region had different electrical characteristics, including frequent +CG lightning (CGs which deposit positive charge at the ground), as opposed to the -CG lightning (which deposit negative charge at the ground) typically occurring in the convective line. This prompted many observational studies using in-situ electric field meter (EFM) soundings through MCSs, eventually including field programs such as MEaPRS, STEPS, and TELEX.

These studies (e.g. Schuur et al. 1991; Hunter et al. 1992; Marshall and Rust 1993; Stolzenburg et al. 1994; Stolzenburg 1996; Stolzenburg et al. 1998b; Schuur and Rutledge 2000;

Winger 2000; Stolzenburg et al. 2001, and Biermann 2010) have ultimately resulted in the formation of a conceptual model for the charge distribution in TS MCSs (Figure 2) consisting of 4-5 vertically separated charge layers with alternating polarities which are horizontally stratified such that a vertical cross section normal to the convective line in a TS MCS can be approximated as representative of the entire storm.

The consistency of kinematic and microphysical properties of MCSs naturally leads to the assumption of consistency in MCS electrical properties (Marshall and Rust 1993), because storm kinematics and microphysics drive storm charging. Biermann (2010) and several other studies have noted that most flashes observed in the stratiform region actually began in the convective line and propagated rearward through the system; those flashes tended to be very large in extent. Flashes observed to begin in the stratiform region tended to be far smaller than those which began in the convective line, suggesting that some of the charge layers in the stratiform region were not as horizontally extensive as those represented by the conceptual model. However, several aspects of the conceptual model are still uncertain. For example, questions remain regarding the evolution of MCS charge structure, as most studies have sampled MCSs with EFMs at one time. Stolzenburg et al. (2001) is a noteworthy case in which a single MCS was sampled multiple times at different locations from its convective line through the stratiform region, and the stratiform region EFM soundings in particular did not conform to the conceptual models from Marshall and Rust (1993), Stolzenburg et al. (1994), or Stolzenburg (1996). Similarly, the charge structure inferred by Ely et al. (2008) from a LMA differed in some respects from the conceptual model.

1.2 DC3 Case Profiles

The DC3 field campaign in 2012 sampled thunderstorms in three domains across the United States: northern Alabama, eastern Colorado, and Oklahoma/West Texas. Three cases from the Oklahoma/West Texas domain are considered here due to the availability of dual-Doppler measurements from mobile radars for those cases in addition to LMA coverage. The three cases selected for intensive study are: 1) the 29 May "Kingfisher" supercell; 2) the 16 June "Eakly" multicell; and 3) the 6 June MCS.

1.2.1 The 29 May 2012 Supercell Storm

The Kingfisher supercell was the right-mover following a storm splitting northwest of Oklahoma City and was within three-dimensional LMA coverage for its entire lifetime. One hour and nine minutes of dual-Doppler coverage from mobile radars enabled a time-evolving analysis of the bulk storm kinematics, as discussed initially by DiGangi (2014) and DiGangi et al. (2016). However, at the time of the original study, the only gridded lightning analysis routine available was 2-D (e.g. Bruning and MacGorman 2013). The subsequent development of the 3-D gridded lightning analysis methodology (e.g. Fuchs et al. 2016) has made detailed spatial analysis of lightning parameters vs. radar parameters much more feasible. Additionally, DiGangi (2014) and DiGangi et al. (2016) only utilized a diabatic Lagrangian analysis (Ziegler et al. 2013a,b) for examining the storm's microphysical evolution. The availability of a C-band HCA which can be applied to the mobile radar data now provides another point of view of the storm's microphysical structure and evolution. As such, the spatial analyses performed in DiGangi (2014) and DiGangi et al. (2016) will be expanded upon in this study to examine vertical distributions of electrical, kinematic, and microphysical quantities measured during the dual-Doppler analysis time.

1.2.2 The 16 June 2012 Multicell Storm

The multicell case was a storm complex consisting of a few small multicells, which either dissipated or merged together into a larger multicell cluster. It formed and propagated slowly east-southeast in west-central Oklahoma, in range of the three-dimensional LMA. In-storm ballooning, mobile radar, and environmental sounding teams operated in the vicinity of the complex at different stages of its overall lifetime. Unfortunately, the continual development of new cells and collapse of existing cells in and around the complex rendered it impossible to obtain long periods of dual-Doppler radar coverage. This study will thus address temporal and spatial trends in lightning, microphysics, and kinematics for one of the multicell storms the mobile radars were able to sample early in the complex's lifetime, referred to hereafter as the Eakly storm.

1.2.3 The 6 June 2012 MCS

The 6 June MCS formed in southern Oklahoma and northern Texas. Its northernmost section, extending almost to Oklahoma City, was sampled by mobile radars and balloon crews and was within three-dimensional mapping range of the OK LMA. Because most of the MCS was outside of the OK LMA's coverage for three-dimensional mapping, a bulk analysis of the MCS's lightning characteristics (e.g. total flash rate) is not feasible. However, the mobile radars collected over an hour of triple-Doppler data, including a period in which the MCS developed a stratiform region on its northern flank. The triple-Doppler data were not ideal, and issues with the wind retrievals performed for this case are discussed in Chapter 2. This study will examine how the system's electrical, microphysical, and kinematic characteristics interacted in this part of the MCS as it evolved.

Chapter 2: Data and Methods

2.1 Lightning

The Oklahoma Lightning Mapping Array (OK LMA) supplied the lightning data for this study. An LMA (Rison et al. 1999; Krehbiel et al. 2000; Thomas et al. 2004) is a ground-based network of stations that detect very high frequency (VHF) radiation from lightning channel segments, hereafter referred to as VHF sources, as a flash develops (MacGorman et al. 2008). The system uses a time-of-arrival (TOA) technique to map lightning leaders in three spatial dimensions and time. VHF source locations within ~150 km of the network center are considered within the LMA's 3-D range, and sources in that range are located within a few tens of meters of spatial accuracy and ~40-50 ns accuracy in time (Thomas et al. 2004). The high spatiotemporal resolution of 3-D LMA data enables very accurate, detailed analyses of lightning activity on a sub-storm scale.

Noise points detected by the LMA were filtered by applying a few basic constraints to the dataset for each case: sources detected by fewer than seven stations, above 20 km altitude, and with a reduced χ^2 value greater than 2 were removed from our analysis (e.g. MacGorman et al. 2008; Lund et al. 2009; Weiss et al. 2012; Calhoun et al. 2013). VHF sources not associated with the storms of interest were also removed. The MCS examined in this study stretched from central Oklahoma nearly to Dallas, so for that case, VHF sources outside the 3-D LMA range were not considered.

The evolution of total flash rates for the multicell case was determined by passing the LMA data satisfying the above criteria through a flash sorting algorithm based on the McCaul (2009) technique to obtain one-minute total-storm flash counts. This analysis was not applied to the MCS case, as most of the MCS was outside the range of the 3-D LMA. Total flash rate was

calculated previously for the Kingfisher case and presented in DiGangi et al. (2016). The criteria for adding a VHF source to a flash were based on the elapsed time (<150 ms) and distance (<3 km) from previous sources in the flash, and flashes were required to have a horizontal dimension of at least 0.15 km (e.g. DiGangi et al. 2016). Time series of the vertical distribution of VHF sources were also generated for the Kingfisher and Eakly cases by counting sources in 500 m vertical bins from the ground to 20 km. These results for the Kingfisher case were presented in DiGangi et al. (2016).

The spatial distribution of lightning in each case was quantified via a lightning gridding algorithm, "lmatools", published initially by Bruning and MacGorman (2013), which has since been updated to include 3-D gridding capabilities (e.g. Fuchs et al. 2016). The gridded lightning characteristics considered in this study are: flash extent density (FED), the number of flashes which pass through a given grid cell; flash initiation density (FID), the number of flashes initiations in a given grid cell; and flash footprint (FP), the average area of the convex hulls of all flashes which pass through a given grid cell. Source density (SD), or the number of VHF sources within a given grid cell, was calculated separately to include sources not grouped into flashes in the analysis. These parameters were gridded to a 500 m x 500 m x 500 m grid corresponding to each case's radar analysis grid (further described in section 2.2). 500 m grid spacing was the highest resolution possible consistent with uncertainties expected in the objective analysis applied to the radar volume scans.

The space charge distribution within each storm was inferred by manual analysis of the OK LMA data. Individual flashes recorded by an LMA can be used to infer space charge based on the timing, signal amplitude, and other characteristics of the mapped VHF sources. Negative leaders are more impulsive than positive leaders and tend to emit a stronger VHF signal; thus,

each leader type has a different appearance in the context of VHF sources. Bruning et al. (2010) described three criteria one can use to infer space charge: 1) leaders that develop quickly and steadily with a relatively high concentration of VHF sources are considered negative leaders, and propagate through positive space charge, while leaders that develop slowly and with more intermittent VHF source signatures are considered positive, and propagate through negative space charge; 2) the first leaders generally observed by the LMA for a given flash are normally negative leaders propagating into positive space charge; and 3) recoil streamers, or k-changes (Mazur 2002), propagate rapidly in the vertical from negative charge toward positive charge. Natural limitations of this charge identification method include that positive storm charge is preferentially identified over negative space charge because a larger proportion of signals are above each station's receiver threshold. Furthermore, space charge cannot be identified where lightning does not propagate, and it provides no quantitative information about the magnitude of storm charge (Bruning et al. 2010). In spite of its limitations, however, this method still provides insight into the spatiotemporal evolution of a storm's charge distribution.

Once storm charge was inferred, and an identifier (+/- 3, or 0 if on a channel that either connected charge regions or otherwise could not have its polarity determined) was assigned to each VHF source within analyzed flashes. The charge-analyzed data were then run through a simple gridding routine using the same Cartesian grids as the radar analyses. In each grid cell, the qualitative net space charge was determined by summing the charge IDs of each VHF source in the cell during the time period being analyzed.

2.2 Radar

Three mobile radars were deployed in the OK-TX domain during DC3: The Shared Mobile Atmospheric Research and Teaching Radars (SMART-Rs; SR1 and SR2, Biggerstaff et

al. 2005) and the NOAA X-POL radar (NOXP). SR1 and SR2 both operate at a wavelength of 5 cm (C-band), and NOXP operates at a wavelength of 3 cm (X-band). Their shorter wavelengths allow C- and X-band radars to use smaller dishes than used by 10-cm radars (S-band) to achieve the same solid-angle beamwidth and so are used on mobile platforms. The Weather Surveillance Radars, 1988 Doppler (WSR-88Ds, Crum and Alberty 1993) used by the National Weather Service are S-band radars. Data from the KTLX WSR-88D radar located in Oklahoma City were used to identify trends in reflectivity during a storm's entire lifetime for all three cases. For the MCS case, these data were also included in the 3-D wind retrievals.

Mounting C- and X-band radars on mobile platforms allows them to be consistently closer to the storms they observe and so to collect data with higher spatial resolution than can be collected by S-band radars, whose antennas are too large to be mobile. However, the choice of operating wavelengths also involves other tradeoffs. For example, if there are enough large hydrometeors (e.g. big drops, graupel, or hail) in a given storm, they will attenuate a C- or X-band radar beam before it can penetrate the whole storm, and X-band radars are impacted more by attenuation more than C-band radars are (e.g. Hildebrand et al. 1981). However, X-band radars detect smaller cloud particles than detected by C and S band radars and so provide more information about regions of clouds in which there are no larger particles. Furthermore, radars with larger wavelengths tend to have a higher Nyquist velocity, and so are less affected by velocity ambiguities.

SR1 was a single-pol radar, operating only with horizontally polarized waves. SR2 and NOXP are both dual-pol radars, transmitting and receiving both horizontally and vertically polarized waves. Dual-polarization radars provide information on the shape and orientation of the scatterer, which enables the diagnosis of scatterer types, i.e. through the use of a hydrometeor

classification algorithm (HCA; see section 2.2.3). The variables used in this study from all three radars were reflectivity (Z) and radial velocity (VR). SR2 and NOXP also measured differential reflectivity (Z_{DR}), correlation coefficient (ρ_{hv}), differential phase (Φ_{DP}), and specific differential phase (K_{DP}). The HCA results in this study were determined using dual-polarimetric data only from SR2.

For the duration of DC3, all three mobile radars collected data synchronously in overlapping sector scans, with each volume collected over the radars' full range of elevations in 3 minutes. The range of elevation angles scanned by each radar was: 0.8^o to 57.5^o for SR1, 0.6^o to 20.6^o for SR2, 1.0^o to 28.0^o for NOXP, and 0.5^o to 19.5^o for KTLX. Volume scans by KTLX were completed in ~4 minutes. For the MCS radar synthesis, KTLX volume scans were sorted to align as well as possible in time with the mobile radar volume scans.

The mobile radar data required extensive pre-processing, detailed in section 2.2.1. Once the data were clear of noise and velocity errors, multi-Doppler analyses were performed for each 3 minute analysis time (e.g. section 2.2.2). Additional pre-processing was performed on the dual-pol radar variables from SR2 before they could be analyzed with a hydrometeor classification algorithm.

2.2.1 Radar Pre-processing

The first stage in pre-processing the mobile radar data was to remove errors with a combination of manual hand-editing with SOLO3 (Oye et al. 1995) and automated editing via Py-ART (Helmus and Collins 2016). The Kingfisher storm's data were entirely hand-edited. SR1 and SR2 data from the Eakly and MCS cases were processed with the standard Py-ART dealiasing procedure and then hand-edited to remove noise and side-lobe errors. Since NOXP generally had more errors and more velocity aliasing in its data than SR1 or SR2, NOXP data

from the Eakly and MCS cases were processed with a new 4-D dealiasing and editing software (A. Alford, 2017, personal communication) which uses a Py-ART framework but only requires hand-editing of the first volume of radar data for each sector scanned.

The above editing procedures focused primarily on Z and VR for all three radars; however, the dual-pol variables for SR2 were also hand-edited, since they were used for Hydrometeor classification (section 2.2.3). Preparing the SR2 dual-pol data for the HCA required three more stages of pre-processing: first, the ρ_{hv} field was corrected for bias following the procedure in Schuur et al. (2003); then, the Z and Z_{DR} fields were corrected for attenuation in a Py-ART framework using the Gu et al. (2011) method; and finally, in order to mitigate the effects of resonance, Φ_{DP} was smoothed with a least squares filter designed to remove the backscatter component of the phase shift, and a new K_{DP} field was calculated from the smoothed Φ_{DP} (A. Alford, 2017, personal comm.).

2.2.2 Multi-Doppler Analysis

Because storms typically moved during periods they were observed and one or more radar trucks sometimes moved or changed the sector they were scanning, long-term multi-Doppler analysis of mobile radar data was not always possible. The full volume of data from each 3-minute mobile radar scan in a given case was interpolated with a natural neighbor scheme (e.g. Alford et al. 2019; Sibson 1981) to a three-dimensional Cartesian grid. The interpolation procedure included a correction for advection due to storm motion: the u and v components of storm motion for each case were calculated via manual inspection in SOLO and then assigned in the interpolation procedure using the same method as Alford et al. (2019). In all three cases, the storms were advected to the time at the beginning of the volume scan. For the MCS case, the manually selected KTLX volumes were interpolated with the same scheme to the same grid.

For the Kingfisher case, the dual-Doppler analysis of each volume scan used the pair of mobile radars providing the most favorable dual-Doppler lobes covering the storm at that time (e.g. DiGangi et al. 2016). The Eakly case had consistently good dual-Doppler coverage from SR1 and SR2. For the MCS study, the sector scanned by the mobile radars changed with time to follow the MCS, so the position of the radars did not always provide optimal geometry for pure triple- or dual-Doppler analysis. Data from the mobile radars were therefore supplemented with KTLX data. The final wind fields presented for the MCS case consisted of a mix of triple- and dual-Doppler, and the radar pairs or triplets were selected automatically based on which triplet or pair had the best geometry and coverage at a given point in the analysis domain.

The 3-D wind field was retrieved from the interpolated data using the "MultiDop" 3DVAR analysis procedure (e.g., a modified version of the Potvin et al. 2012 method; code available at https://github.com/nasa/MultiDop). As discussed by Potvin et al., the 3DVAR method offers several advantages over traditional 3-D wind retrievals (e.g. Gao et al. 2009). The most prominent advantage is that, because it does not explicitly integrate the equation of mass continuity in the vertical, it is more flexible than traditional methods and less susceptible to the errors inherent in them. The 3DVAR wind synthesis method was updated after the publication of Potvin et al. (2012) to include a function which takes initial nondimensional coefficients (e.g. Potvin et al. 2011) for the mass conservation equation and horizontal and vertical smoothing (which were set to 5, 100, and 100, respectfully) and optimizes them based on the error in each iteration of the wind synthesis calculation: after 10 iterations, if the observation error is low and the mass conservation error is greater than a normalized threshold for mass conservation error, then the coefficients are increased by 20%; after 100 iterations, if the maximum observation error has increased substantially and if the mass conservation error is less than the mass

conservation normalized threshold, the coefficients are decreased by 10%. The mass conservation normalized threshold is set as 0.3. This procedure continues until the coefficients converge to an optimal solution. A two-step Leise filter (Leise 1982) option was also included in MultiDop, and it was implemented in this study to minimize the introduction of artifacts into the wind analyses (e.g. Betten 2018). Other recent studies (e.g. Betten et al. 2018; Alford et al. 2019; Fernandez-Caban et al. 2019) utilized the techniques described here to produce robust, smoothly transitioning vertical wind fields with dual-Doppler datasets. 200 iterations of the 3DVAR calculations were used for the Kingfisher and Eakly cases with the Leise filter applied every 50 iterations, and 300 iterations were used for the MCS with the Leise filter applied every 20 iterations.

Attempting to perform triple-Doppler on the MCS case resulted in a problematic set of wind fields. Although updrafts identified in the convective line seemed reasonably realistic, there were large, weak updrafts analyzed in the low levels, particularly in the developing stratiform region. These “updrafts” were consistently triangular and generally located where triple-Doppler coverage was expected. As such, they are considered in this study to be artifacts rather than physical phenomena. The exact source of these errors is unclear at this time.

Finally, for the Kingfisher case, the radar-derived wind syntheses all employed a nearby environmental sounding to provide the background field for each synthesis, which was then blended smoothly with in-storm winds using a low-pass spatial filter (DiGangi et al. 2016). This smoothing routine did not affect the wind analysis in the Kingfisher storm itself, and the ambient flow field was used to calculate and initialize trajectories for the DLA.

2.2.3 Hydrometeor Classification

The hydrometeor classification algorithm (HCA) used to determine the distribution of particle types observed in all three cases included in this study was the scheme developed by Dolan et al. (2013) for C-Band radar data. It is a fuzzy logic algorithm which uses the horizontal component of reflectivity (Z_h), Z_{DR}, ρ_{hv}, and K_{DP} from a polarimetric C-band radar along with temperature (T) from an environmental sounding to calculate a score for each potential hydrometeor class. Equation 14 of Dolan and Rutledge (2009) is used to calculate the membership beta functions (MBFs) for each of the radar variables and T:

$$\beta = \frac{1}{1+\left[\left(\frac{x-m}{a}\right)^2\right]^b}$$

where *a* is the width of the membership function, *m* is the midpoint, *b* is the slope, and *x* is the observed data point. Values for *a*, *b*, and *m* for a C-band dataset were taken from Table A2 of Dolan and Rutledge (2013).

The algorithm calculates the MBFs of Z_h, Z_{DR}, ρ_{hv}, K_{DP}, and T for 10 different classes, then calculates a score for a given class *i* using Eq. 8 from Dolan and Rutledge (2013):

$$\mu_i = \left[\frac{W_{Z_{DR}}\beta_{Z_{DR},i} + W_{K_{DP}}\beta_{K_{DP},i} + W_{\rho_{hv}}\beta_{\rho_{hv},i}}{W_{Z_{DR}} + W_{K_{DP}} + W_{\rho_{hv}}}\right]\beta_{T,i}\beta_{Z_h,i}$$

where W is the weight of a given variable. For this study, W was set to 1.0 for all three polarimetric radar variables.

Once scores are calculated for each class, the class associated with the maximum μ at a given data point is considered the dominant class for that point. The ten possible hydrometeor classes are: rain (RA), drizzle (DR), wet snow (WS), dry snow (DS), ice crystals (CR), high density graupel (GR_{HD}), low density graupel (GR_{LD}), hail (HA), big drops (BD), and vertically aligned ice (VI).

2.3 Diabatic Lagrangian Analysis

A diabatic Lagrangian analysis (DLA, Ziegler 2013a,b) was used to diagnose mixing ratios and other parameters for the Kingfisher supercell from the three dimensional wind field. The DLA calculates upstream parcel trajectories using the time-dependent 3-D wind field calculated in section 2.2.2 to trace parcels backward in time to their environmental values outside the storm, where the environment is constrained by a sounding. At the origin of a parcel outside the storm, the environmental sounding parameters at that location are used to calculate the initial water vapor mixing ratio (q_v, g kg^{-1}), potential temperature (θ, K), and ambient pressure (P, mb). The algorithm then integrates a system of first-order ordinary differential equations forward in time along the parcel trajectories to their end points within the DLA domain (Ziegler 2013a, DiGangi et al. 2016). Gridded reflectivity data are interpolated to every point along these trajectories, and the algorithm then diagnoses the time-varying Lagrangian values of rain water mixing ratio (q_r, g kg^{-1}), graupel/hail mixing ratio (q_g, g kg^{-1}), and snow mixing ratio (q_s, g kg^{-1}), which are subsequently used to predict cloud ice mixing ratio (q_x, g kg^{-1}), cloud water mixing ratio (q_c, g kg^{-1}), θ, and q_v within the storm (DiGangi et al. 2016). Further details on the original DLA algorithm can be found in Ziegler (2013a,b). Details for the addition of diagnosed q_s and an

updated prediction of q_x can be found in the appendix of DiGangi et al. (2016). Note that q_s was constrained to a maximum possible value of 1.0 g kg^{-1} while the other microphysical mixing ratios could be much larger (i.e. > 10.0 g kg^{-1}).

The Kingfisher case had a long enough period of continuous multi-Doppler coverage that it was viable for running the DLA. The DLA analysis was also extended because supercell thunderstorms can safely be assumed to be steady-state during certain portions of their lifetime. Given the focus on mixed-phase microphysics in this study, the DLA variables shown in figures for the Kingfisher case include q_c, q_g, and a composite of q_s, and q_x, referred to hereafter as q_{xs}. Unfortunately, dual-Doppler coverage for the Eakly case was available for too short a period to calculate the trajectories of parcels in regions of interest backward to their environmental origins, and multicell systems cannot be considered steady-state, so the DLA was not run on that storm. Problems which arose during the synthesis of the MCS wind fields precluded the inclusion of the DLA for that case as well. Thus, the only particle classification data available for the Eakly and MCS cases were the HCA results.

Chapter 3: 29 May 2012

During the ~1 hour of dual-Doppler observations, the Kingfisher supercell storm steadily intensified in terms of both kinematic structure and lightning. Six times spanning the majority of the radar analysis period were selected for investigation: 23:09 UTC, 23:21 UTC, 23:33 UTC, 23:42 UTC, 23:51 UTC, and 00:00 UTC. Five horizontal and five vertical cross sections through the storm were generated to give a 3-D view of the storm's electrical, microphysical, and kinematic structure above the freezing level (e.g., where most collision-based electrification takes place) at each time. The altitudes selected for horizontal cross sections were: 6.2 km, 7.2 km, 8.2 km, 9.2 km, and 10.2 km. Figure 3 shows the 6.2 km reflectivity (Z), wind fields, and locations of vertical cross sections taken through the storm at each time. Figures 4-63 depict these cross sections: color-filled Z, flash extent density, flash footprint, source density, HCA, and net charge are overlaid with contours of w, q_g, q_c, q_{xs} (a composite of q_x and q_s), w, and w, respectively, along with wind vectors and X's to represent flash initiation locations. The two different types of contours in the q_{xs} figures indicate where the composite mixing ratios were dominated by snow (dashed contours; 0 – 1.0 g kg^{-1}) or cloud ice (solid contours; > 1.0 g kg^{-1}).

3.1: 3-D Storm Structure and Evolution with Time

3.1.1: 23:09 UTC

At 23:09 UTC, the Kingfisher storm was well-organized, with a total flash rate of ~27 flashes min^{-1} (e.g. DiGangi et al. 2016). A BWER was present in the mid-level reflectivity (e.g. Figures 4a-7a, 11a) and hail up to 3 inches in diameter had already been reported at the ground (e.g. DiGangi et al. 2016). The updraft was located in the northwestern portion of the storm, which included two regions of w_{max} ~40-45 m s^{-1} embedded in the broader updraft region, and weak adjacent downdrafts (e.g. Figures 4a-8a). The BWER was collocated with the eastern w_{max}

core, which was located approximately between 8.2-10.2 km (e.g. Figures 6a-8a, 11a). The deeper region of w_{max} was beneath an elevated maximum in Z and q_g (e.g. Figures 11a,b), where the HCA indicated that there was a mixture of graupel and hail being suspended aloft (e.g. Figure 11e). Updrafts and downdrafts both increased in breadth around 9.2 km compared with the lower levels (e.g. Figure 7a). The maxima in q_g and q_c were generally in and around the updraft region through the midlevels, where the HCA identified mixtures of hail and graupel between 6.2 and 10.2 km (e.g. Figures 4e-8e). Below 9.2 km, the q_{xs} field was dominated by snow, and above 9.2 km there were greater mixing ratios of cloud ice (e.g. Figures 4d-12d). The cloud water mixing ratio in the updraft region decreased with altitude until just below 9.2 km (e.g. Figures 4c-12c), indicating that at approximately this altitude in the updraft core, any liquid water in the cloud was freezing. Southeast of the updraft region into the forward flank of the storm, there were pockets of hail and graupel identified at different levels mixed in with dry snow, and no substantial vertical motion aside from a couple of small ~5 m s^{-1} downdrafts (e.g. Figures 4e-8e).

Most of the lightning at this time occurred in the forward flank and around the updraft, with secondary maxima in flash extent density and source density on the northern flank of the updraft at 8.2 and 9.2 km (e.g. Figures 6b,d-7b,d). At 8.2 km, there was a lightning hole collocated with the BWER and q_c maximum (e.g. Figure 7a,b,c). The lightning activity in the updraft region was characterized by generally smaller flashes (flash footprints < 25 km^2) than most of those occurring in the forward flank (e.g. Figures 11c-12c). The very high source densities coupled with small flash footprints around the updraft indicates that the flashes there likely had more tortuous propagation than those outside the updraft. There were also multiple flash initiations noted among these small flashes, which tended to occur outside of regions of w_{max} and where the HCA and DLA combined indicated graupel in varying concentrations, and

the DLA also indicated a strong gradient in cloud water and snow mixing ratios. There were more small flashes and flash initiations located north of the primary updraft region, where there were alternating regions of weak ascent and descent through the depth of the storm (e.g. Figure 13a) along with a mixture of particle types (e.g. Figures 13b-e). In the forward flank SE of the updraft region, flashes tended to be much larger than in the updraft region, particularly below 9 km (e.g. Figures 4c-6c, 9c-13c). Only a few flashes were initiated below 8 km in the forward flank at this time, and the charge distribution between 6.2-8.2 km was primarily positive, with more negative charge inferred above 9 km (e.g. Figures 4f-8f). Most of the flash initiations in the forward flank captured by these cross sections occurred at 9.2 and 10.2 km, where there was a switch in the dominant space charge, a decrease in flash footprints, and where flash activity shifted further to the south, closer to the upper level reflectivity edge (e.g. Figures 7b-8b). The HCA and DLA identified mostly cloud ice and snow at these upper levels, although the HCA also indicates that at 9.2 and 10.2 km there were pockets of low-density graupel in the same region where most of the storm's flash initiations were located. This region of mixed hydrometeors is also characterized by smaller flash footprints than the portion of the forward flank dominated by either snow or graupel.

3.1.2: 23:21 UTC

By 23:21 UTC, the storm's maximum updraft had increased to ~48 m s^{-1}, it had grown broader in size, and the total flash rate had increased to ~38 flashes min^{-1}. The downdraft in the forward flank southeast of the updraft also strengthened from -5 m s^{-1} to -15 m s^{-1} in the midlevels, and there was deeper descent on the northwest side of the updraft which reached -25 m s^{-1} (e.g. Figures 14a, 20a). The BWER was broader and offset from the location of the maximum updraft, and Figures 14a-18a show that it was slightly more tilted towards the

northeast in the vertical than at 23:09. A lightning hole was collocated with the BWER in the horizontal cross sections between 7.2-9.2 km (e.g. Figures 15a,b-17a,b). The vertical cross section through w_{max} shows that no organized flashes passed through the BWER (e.g. Figure 21b,c). The maximum q_c was still collocated with the updraft, BWER, and lightning hole (e.g. Figures 15c-17c). Overall, q_g increased in the region southeast of the updraft by this time, where the HCA indicated substantially more hail as its primary classification than at 23:09 (e.g. Figures 14b,e-18b,e). The maxima in q_{xs} were still primarily located above and around the q_c maximum, though there were pockets detected downstream of the updraft as well; the q_{xs} field was still dominated by snow in lower levels and cloud ice in upper levels (e.g. Figures 15d-17d).

Most of the lightning in the storm at this time occurred between 6.2 and 9.2 km in altitude, and was still located in and around the updraft as well as into the southeastern forward flank. In the western portion of the updraft, there were flashes detected between 6.7 and 13.7 km with most flash footprints < 50 km^2 (e.g. Figures 19c-22c). These flashes were also associated with an elevated source density maximum and multiple flash initiations (e.g. Figure 19d) in a region dominated by hail according to the HCA; the DLA indicated very high q_g in this region, but also q_c and q_{xs}, suggesting that the mixture of particle types required for noninductive charging were present and the radar signal was simply dominated by hail. In general, however, most of the lightning activity in the storm occurred in the forward flank southeast of the updraft and on the north-northeastern side of the updraft, as it did at 23:09. Flash extent densities and source densities tended to peak in these regions, particularly above 7 km. The region of lightning activity NNE of the main updraft was associated with a mixture of graupel, hail, and dry snow primarily identified by the HCA and corroborated by the q_g and q_{xs} DLA fields, along with q_c values of 0-2 g kg^{-1}, at 7.2 and 8.2 km, indicating that that region likely had active noninductive

charging present. The presence of alternating regions of weak ascent and descent probably enabled this mixture of hydrometeors and thus the charging process. Flash footprints in that region were variable, but generally > 25 km^2. In the forward flank, flash activity shifted further south with altitude, and as with the lightning at 23:09, flash footprints were larger in the lower levels and smaller in the upper levels; at 9.2 km, as with 23:09 at the same level, flash footprints increased with distance from the edge of the reflectivity signature in that region. Flash initiations continued to be concentrated in the forward flank area and in the upper levels, although there were also flash initiations within the updraft and in the electrically active area NNE of it. The inferred space charge distribution in the storm did not change drastically between 23:09 and 23:21, although at 23:21 a lower positive and upper negative charge region were inferred within the updraft region (but outside the core of the updraft) at approximately the same altitudes as the corresponding charge outside the updraft. The analyzed charge in Figure 19f also indicates some potentially complex charge structures, given the pocket of negative charge analyzed amid some of the positive charge.

3.1.3: 23:33 UTC

Total flash rate increased to 48 flashes min^{-1} by 23:33 UTC, continuing the upward trend seen between the first two analysis times. The overall size of the primary updraft region was maintained between 23:21 and 23:33, and w_{max} had increased to ~52 m s^{-1}. The BWER was still present but Figures 24a-28a show that between 7.2-9.2 km, it contained Z > 25 dBZ, which is higher than the minimum Z within it at previous analysis times. Figure 30a depicts a highly tilted BWER, along with a deep downdraft immediately adjacent to the primary updraft. The HCA identified a comparable amount of hail and graupel in the horizontal cross sections shown in Figures 24e-28e as at 23:21, but, unlike at 23:21, it was visibly mixed with dry snow on the

northern and eastern sides of the BWER. A secondary maximum in q_c appeared on the eastern side of the BWER (e.g. Figures 26c and 27c), approximately collocated with another area of high reflectivity (e.g. Figures 26a and 27a) and q_g (e.g. Figures 26b and 27b), but the primary HCA identification in this region was dry snow. The q_{xs} field differed from the HCA output in this region, as cloud ice and snow mixing ratios were highest at the top of that reflectivity core and closer to 0 within it (e.g. Figures 24d-28d, 30d-31d). The vertical cross section taken through this feature reveals that there was hail beneath the secondary updraft maximum (Figure 31e). A region of weak ascent (~5 m s^{-1}) developed between 23:21 and 23:33 in the forward flank southeast of the main updraft core, as depicted in Figures 24a-28a. A greater volume of hail and graupel than at earlier times extended southeastward into the forward flank, captured both by the HCA and q_g fields, and was roughly collocated with the aforementioned weak ascent. The DLA indicated a local maximum in q_s from 6.2-8.2 km in that weak ascent region as well (e.g. Figures 24d-26d).

Lightning activity continued in the same regions as at previous times, although there were more small flashes detected within the primary updraft region, apparent as a distinct maximum in flash extent density and source density and a minimum in flash footprint at ~11.2 km (e.g. Figures 30b,c,d), along with multiple flash initiations (e.g. Figures 29-31). The nature of these flashes (i.e., small size, large source densities, and tortuous propagation) rendered charge analysis difficult, as with previous analysis times, but there were indications of negative charge above the flash initiations associated with the flash extent density/source density maximum (e.g. Figure 30f). Microphysically, this flash extent density/source density maximum was characterized primarily by hail and low-density graupel identified by the HCA, and by moderate q_g and q_c and variable q_{xs} values; the latter field was dominated by q_s in the regions of highest

FED/SD. Dry snow was also indicated by the HCA adjacent to the low-density graupel and the lightning maximum; together with the aforementioned mixing ratios, this suggests that there was a mixture of particles present there. The southernmost vertical cross section also contains elevated secondary maxima in source density above 11.2 km (e.g. Figure 29d), which could have been an early indication of the updraft intensifying in that region.

The rest of the lightning was primarily located on the ENE side of the updraft region and in the forward flank SE of it. Both regions were characterized by larger flashes than those in the updraft core, although flash footprints in both regions decreased with altitude. Most of the flash initiations captured by the cross sections occurred in the SE forward flank, where the HCA and DLA both indicated relatively high graupel/hail content mixed with some snow and the wind analysis indicated weak ascent. Flash footprints in this region were overall smaller than at previous times and decreased with altitude. The charge structure of these regions was more complicated than at previous times. ENE of the updraft, horizontal cross sections of net space charge (Figures 24f-28f) indicate regions of opposite charge adjacent to each other in the horizontal, with negative charge closer to the updraft and positive charge further from it at 6.2 km giving way to primarily positive charge at 7.2 km. Above that, there was positive charge closer to the updraft and negative charge further downstream. However, the 9.2-10.2 km layer was primarily characterized by negative charge. Figures 29f-30f also have alternating positive and negative charge in the horizontal east of the updraft region. Most of the lightning in the forward flank SE of the updraft was elevated higher than the lightning ENE of the updraft, and Figures 24f-28f indicate that there were pockets of negative charge embedded in a broader region of positive charge at 8.2 and 9.2 km which shifted to primarily negative charge at 10.2 km.

3.1.4: 23:42 UTC

By 23:42, the total flash rate of the Kingfisher storm had increased to 79 flashes min^{-1} and w_{max} had increased slightly to ~56 m s^{-1}.The size of the updraft region did not change substantially, but the region of weak ascent in the near forward flank was maintained, and appeared to connect with the main updraft at some horizontal levels (e.g. Figures 34a-36a). The downdraft immediately east of the updraft core remained present through most of the depth of the storm and maintained its maximum intensity of -15 m s^{-1} (e.g. Figure 41a). Another weak updraft (~5 m s^{-1}) became consistently present between 6.2 and 10.2 km NNE of the primary updraft (e.g. Figures 34a-38a). The BWER became more vertically erect, but also filled in further with higher reflectivity (e.g. Figures 34a-38a, 41a), a trend which was first hinted at 23:33 UTC. High values of q_g surrounded the updraft region between 6.2 and 9.2 km, and at 10.2 km the q_g maximum was located on the western side of the updraft, through its primary core (e.g. Figures 34b-38b). The HCA identified a broad region of hail, and graupel in the same area, and the graupel signatures expanded into the northern and southeastern flanks of the storm, including pockets of graupel embedded in what was otherwise diagnosed as dry snow well downstream of the updraft (e.g. Figures 34e-38e). The q_c maximum in the mid-to-upper levels continued to be collocated with the updraft (e.g. Figures 34c-38c), and streams of small q_c were present following the easterly flow exiting the updraft region above 8 km (e.g. Figures 35c-38c). The q_{xs} maxima were scattered across the storm core: at lower levels, snow mixing ratios surrounded the cloud water maximum with some overlap in both mixing ratio gradients and extended eastward (e.g. Figures 34c,d-36c,d), and at upper levels, a plume of cloud ice was visible in horizontal cross sections in between plumes of cloud water east of the storm core (e.g. Figures 37c,d-38c,d). Vertical cross sections of q_c and q_{xs} (e.g. Figures 39c,d-43c,d) reveal that, as observed at

previous times, q_x peaked above regions of high q_c, where there was enhanced freezing of cloud droplets at the top of the updraft, and outside of the updraft core in the mid-levels the storm's cloud ice/snow mixing ratios were dominated by snow.

Lightning activity continued to be focused in the same general regions as at previous times: in/above the western (i.e. the strongest) portion of the main updraft; ENE of the main updraft region; and southeast of the updraft region in the forward flank. In the main updraft, the lightning signature was similar to that seen at 23:33: the maximum flash extent density and source density was found in the upper half of the updraft, just above where the peak updraft speed was reached, in a region of mixed phase particles (e.g. Figure 41b,c,d,e). The footprints associated with these flashes were small (Figure 41c), there were several flash initiations in the area (Figure 41a-f), and the inferred charge appeared to include small, horizontally adjacent positive and negative charge regions (Figure 41f). In addition to this particular maximum, Figure 40d reveals the continued presence of the source density maximum associated with the storm's overshooting top originally noted at 23:33. Note that the updraft beneath the OT source density maximum increased from 15 m s^{-1} at 23:33 to 25 m s^{-1} at 23:42.

At 6.2 km there was more lightning due east of the updraft than ENE or SE of it, although flash extent densities and source densities were not high and flash footprints were overall large (e.g. Figure 34b,c,d). This area of lightning was mostly associated with some pockets of q_s and q_g, as well alternating regions of dry snow and graupel identified by the HCA (e.g. Figure 34b,c,d,e). Positive charge was mostly identified in the northern half of the storm's forward flank, where the HCA and DLA identified more dry snow/q_{xs} than other particle types, and there were indications of negative charge at the same horizontal level further south, where there was more graupel present (e.g. Figure 34f). At 7.2 km, there was primarily positive charge identified

where the source density was greatest in a region dominated by dry snow/q_s, although there were potentially pockets of negative charge scattered through it (e.g. Figure 35d,e,f); flash initiations in this level were in the updraft region though outside of w_{max} (e.g. Figure 35). Above 7.2 km, flash sizes in the forward flank region decreased in size (Figures 36c-37c) and the number of flash initiations increased; the charge associated with this region of flashes was primarily positive, with some negative charge inferred on its NE and SW edges (Figures 36f-37f). Flash initiations ESE of the updraft were generally associated with regions of mixed inferred charge and low-density graupel and dry snow. At 10.2 km, the storm's charge was identified primarily as negative with pockets of positive, with scattered flash initiations through it, especially where there was graupel identified by the HCA and DLA (e.g. Figure 38b, e, f). Flashes this high up tended to be small (< 25 km^2).

ENE of the updraft, the flash size distribution was comparable with that SE of the updraft: flash footprints were larger lower in the storm and smaller higher up. There were only a couple flash initiations in the vertical cross section through this region. More flashes were initiated close to the northern boundary of the storm in the upper levels (e.g. 9.2-10.2 km, Figures 37-38). That region of the storm was characterized by regions of low-density graupel and dry snow identified by both the HCA and DLA (e.g. Figure 43d,e). The charge distribution here was not truly horizontally uniform at any level, although it was more clearly dominated by positive charge at lower levels (e.g. Figures 34f-35f).

3.1.5: 23:51 UTC

By 23:51 UTC, the region of weak ascent initially observed at 23:33 had fully merged with the primary updraft and intensified. Whereas at 23:09 the updraft was relatively compact and somewhat round and symmetric in shape, by 23:51 it had become more elongated as the

region of peak updraft speed (>35 m s^{-1}, where w_{max} ~ 44 m s^{-1}) stretched from the northwest portion of the storm a few tens of kilometers to the southeast; a broader region of weaker ascent (~5-10 m s^{-1}) extended ENE around the storm's central downdraft (e.g. Figures 44a-48a). A BWER was visible at 6.2 km (Figure 44a), but was unbounded on its NE side above that, and tilted towards the NE (e.g. Figures 45a-48a). As with previous times, the BWER was not directly collocated with the updraft maximum, but rather was situated between the region of w_{max} and the storm's central downdraft. The elongated updraft region was associated with hail and graupel identified by both the HCA (Figures 44e-48e) and DLA (Figures 44b-48b) from 6.2 to 10.2 km. The storm's central downdraft was also associated with hail in both these fields, which was particularly visible in the cross sections shown in Figure 52b,e. The structure of the q_c field was not substantially changed from 23:42, but the distribution of q_{xs} across the storm's forward flank east of the updraft between 6.2-7.2 km was wider than at 23:42.

Flash extent densities were relatively low across most of the northern portion of the storm below 9.2 km (e.g. Figures 44b-46b). At 9.2 km, there was a noticeable flash extent density maximum well northeast of the updraft region (e.g. Figure 47b), near the edge of its northern reflectivity signature. That portion of the Kingfisher storm was beginning to interact with the cell to its north, as evinced by the mingling reflectivity signatures and region of apparently deep but weak (~5 m s^{-1}) ascent between the two cells (e.g. Figures 44a-48a). Flash footprints in this region were smaller overall through the depth of the storm than at previous times, and the source density distribution was generally similar to the flash extent density field. Most of the inferred charge in this region was positive (e.g. Figures 44f-46f), with some negative charge inferred at 9.2-10.2 km (e.g. Figures 47f-48f). Only a few flash initiations were evident in the vertical cross sections closest to this region (e.g. Figures 52-53) because, like at 23:42, most of the initiations

were close to the storm's edge (e.g. Figures 44-48). Figure 53d depicts an interesting trend which is easiest to recognize in the source density distribution: the vertical distribution of lightning discharges in this part of the storm tended to follow the air flow in the mid-to-upper levels, which rose and fell in a wave-like pattern.

The greatest increase in lightning activity in the domain at this time was in the maximum updraft region. Figures 51b-d show a relative maximum in flash extent density within a graupel/hail core in the upper portion of the updraft, above 11 km; these flashes had small footprints and large source densities, indicating that there were several small but highly tortuous flashes propagating through the same compact region. There were also a few flash initiations analyzed around the edges of this flash activity. A secondary maximum in source density was visible above 15 km (Figure 51d), which is a continuation of the overshooting top signature noted at previous times. In general, all the vertical cross sections through this primary updraft region had similar characteristics; although the overshooting top source density signature was only really visible in Figure 51, Figures 50 and 52 also depicted a concentration of lightning within the upper half of the updraft, including several flash initiations, local maxima in source density and flash extent density, and small flash footprints. Figure 49 shows the southern edge of the storm and did not intersect the strongest updraft region, but it did capture some ascent, and also had a cluster of very small flashes occurring in between the lower region of updraft and a weak upper-level region of descent representing air being entrained into the storm. The charge structure throughout the updraft region was difficult to infer, but in general there appeared to be positive charge through a deep layer, with small pockets of negative charge at ~10.2 km (e.g. Figures 48f, 52f). The regions outside of the main updraft in these vertical cross sections were characterized overall by larger flashes and the channels involved mostly positive charge.

By 23:51, the portion of the forward flank southeast of the updraft region had moved outside the analysis domain as the storm propagated southeast. The edge of that electrically active region visible in the 23:51 horizontal cross sections reveals smaller flashes than at previous times with flash footprints generally < 50 km^2 and values of flash extent density and source density similar to those in the northern and western portions of the storm (e.g. Figures 44b,c,d-48b,c,d). This region also appeared to have mostly positive charge, possibly with a few small pockets of negative charge from 6.2-9.2 km (Figures 44f-47f), switching at 10.2 km to primarily negative charge with a few pockets of positive charge (Figure 48f).

3.1.6: 00:00 UTC

As of 00:00 UTC, the Kingfisher storm's updraft had reintensified to $w_{max} \sim 52$ m s^{-1} and had regained its relatively cylindrical shape (e.g. Figures 54a-58a) as it reorganized during the 27 minutes between the 23:33 analysis time and this one. The total flash rate at 00:00 UTC had increased to ~125 flashes min^{-1}, which was the largest increase in total flash rate between analysis times in this study. This increase coupled with the more organized updraft appearance and the reformation of a BWER (e.g. Figure 59a) indicates that the storm was intensifying more rapidly than at previous times. The storm's increase in intensity was also represented by the expansion of the graupel and hail volume in the storm core: the HCA and DLA identified a broadened region of hail and graupel in the storm's northern flank, ENE of the updraft region, through all five horizontal levels examined here (e.g. Figures 54b,e-58b,e, 61b,e-63b,e). a region of weak ascent also spread from the primary updraft past this region even further into the forward flank, past the region of expanded graupel/hail (e.g. Figures 54e-58e, 61e-63e). Downdrafts persisted on the ENE side of the primary updraft, between it and the aforementioned weak ascent, as well as on the north and west sides of the storm. The volume of hail, graupel,

and q_g also expanded southeast of the updraft region, and the former three were the primary classification of the HCA through most of the storm's depth in this area (e.g. Figures 58e-59e). In the 15 minutes following this analysis time, there were four more reports of 1-3 inch hail reaching the ground (e.g. DiGangi et al. 2016). The q_c and q_{xs} maxima remained in the same relative locations in the storm, but they appeared to expand slightly in volume, particularly into the E and ENE forward flank.

Lightning activity continued to be concentrated in the same three regions as during previous times, although the storm's continued propagation to the southeast limited analysis of the far SE forward flank. Immediately southeast of the updraft region, a local maximum in source density at 6.2 and 7.2 km (e.g. Figures 54d-55d) was just outside the q_c maximum at those levels and associated with a local q_{xs} maximum, as well as large amounts of hail and graupel. Flash footprints in this region were generally < 50 km^2 (e.g. Figures 54c-58c), and there were several flash initiations in the upper levels (e.g. Figure 57). ENE of the primary updraft region, in the same general vicinity of the aforementioned area of weak ascent, flash footprints had decreased in general again between 6.2-8.2 km compared to 23:51 UTC (e.g. Figures 54c-56c), though the overall distribution of flash extent density and source density was not much different than before. The same collocated maxima in flash extent density and source density were visible in the upper levels of the updraft core again (e.g. Figures 57b,d), and were associated with very small flash footprints (< 10 km^2) and multiple flash initiations. The overshooting top signature in source density was visible in Figure 59d.

Inferred charge across all three of these regions tended to be positive through the midlevels with upper negative charge (e.g. Figures 59f-63f). In some places, there appeared to be possible pockets of negative charge amid the positive (e.g. Figure 54f); however, most of the

negative charge visible below 10 km was located in the far forward flank, at the eastern analysis domain boundary. The updraft region was, as usual, more complicated, with hints of negative charge amid the positive charge in midlevels (e.g. Figure 59f), but as flashes grew smaller and more complex there, space charge inference became less feasible. Another flash characteristic at this time, which appeared ubiquitous across the storm core and near forward flank, was the general elevation of flash initiations: in all the cross sections shown for 00:00 UTC, most flash initiations shown in the cross sections occurred above 8 km; flashes initiation locations below 8 km were well outside of the storm core, into the forward flank where the primary HCA class was dry snow. Flash initiations which occurred in the updraft core were above the regions of w_{max}, and across all cross sections, flash initiations were concentrated near the boundaries of different regions of dominant particle types identified by the HCA. The apparent trend of source density following the flow of air currents leaving the storm core, which was initially noted at 23:51, continued at this time as well, and is particularly evident in Figures 61d-63d. Source density closer to the updraft core (e.g. Figures 59d-60d) exhibited some of this trend as well, but the regions of enhanced source density could be attributed to the presence of large q_g and extensive hail and graupel.

3.2: Bulk Relationships between Lightning, Microphysics, and Kinematics

The detailed analysis in the previous section provides important context for which areas of the storm contained lightning activity, updrafts and downdrafts, and the spatial distributions of different mixing ratios from the DLA and dominant hydrometeor types identified by the HCA. In this section, a bulk view of relationships between the previously discussed lightning attributes and both the HCA and w fields will be described. At each horizontal grid level, the sum of all values for flash extent density, flash initiation density, source density, and inferred charge

associated with each hydrometeor class and 5 m s^{-1} bins of w, as well as the mean of all flash footprints associated with each hydrometeor class and 5 m s^{-1} bins of w, were recorded for each analysis time to enable a more direct analysis of relationships between the storm's lightning attributes and its microphysical and kinematic attributes. Figures 64-69 show the lightning distributions with respect to hydrometeor class, and Figures 70-75 show the lightning distributions with respect to w. Each polarity of gridded inferred charge was plotted separately in Figures 64-75 to avoid assumptions about horizontal homogeneity of charge layers. The figures are all overlaid with horizontal lines denoting the locations of the 0°, -20°, and -40°C isotherms from a nearby environmental sounding launched as part of DC3 operations and the one used in the HCA.

At all analysis times, flash extent density peaked between -20° and -40°, and flashes propagated preferentially through regions of dry snow and high-density graupel. Flash initiation density peaked around the -40°C level, at slightly higher altitudes than the maximum flash extent density. Most flash initiations were associated with dry snow and high-density graupel. Flashes also initiated and propagated in regions of hail and low-density graupel, but less frequently. Flashes sometimes propagated through grid cells classified as vertically aligned ice, but none were initiated in those regions. Flash footprint at each horizontal level did not seem associated with any particular hydrometeor type, except that there were larger flashes associated with vertically aligned ice. Source density followed the same general trends as flash extent density in terms of hydrometeor association, except that they occurred over a greater depth of the storm, including below the freezing level; at 23:21, 23:33, 23:42, and 00:00 UTC, a small number of sources were associated with rain.

The distribution of positive and negative charge with respect to hydrometeor class lends interesting insight into the storm's overall charge structure. Figures 64-69 show that positive and negative charge were often associated with the same types of particles, but at different altitudes and thus different temperatures: the largest concentrations of inferred positive charge associated with dry snow, low- and high-density graupel, hail, and vertically aligned ice were generally identified between -20^{o} and -40^{o}, whereas the largest concentrations of inferred negative charge associated with these same particle types were generally higher, closer to -40^{o}C. The variety in hydrometeor types associated with both signs of charge could be due to mixtures of hydrometeors carrying the same charge, mixtures of hydrometeors carrying opposite signs of charge where one sign/hydrometeor type was clearly dominant over the other(s), or it could simply be due to the aggregation of these datasets in the horizontal. The boundary in altitude between the locations of maxima in charge density also tended to align with the altitudes of the highest flash initiation density, which is consistent with flashes being initiated in regions of charge density minima/electric field maxima.

Figures 70-75 depict the same lightning parameters as Figures 64-69, but relate them to 5 m s^{-1} bins of w. Overall, most lightning activity occurred in regions where $-5 < w < 5$ m s^{-1}: flash extent density, flash initiation density, and source density peaked in this range of w and between -20^{o} and -40^{o} at all analysis times. As time progressed, more lightning activity spread to the higher bins of w, although the frequency of lightning in these bins was never very large. Average flash footprint varied noticeably with respect to w: at all times, the flash size decreased as |w| increased. The trend of flash sizes decreasing with height noted in section 3.1 was reflected somewhat here, particularly at 23:21, 23:33, and 23:42 UTC. At 23:51 and 00:00 most of the storm's forward flank, which had contained most of the largest footprint values, had exited the

analysis domain, so there were fewer flashes, especially fewer large flashes, in the dataset at these times. However, there were still slightly larger mean flash footprints in regions of smaller |w|.

Interestingly, although much of the analyzed charge overlapped with the flash extent density and flash footprint maxima with respect to |w| described above, there was also a fair amount of charge analyzed in the $20 < w < 25$ m s^{-1} range. This is likely a reflection of the types of flashes found in regions of strong w: the previous section noted that regions of larger flash extent density contained within regions of stronger w were characterized by small flash footprints and high source densities, and propagated more in the vertical than the horizontal. These flashes likely spanned no more than a few grid cells even in the vertical and only one or two grid cells in the horizontal, and therefore only a few flashes would contribute to the horizontal aggregation of flash extent density or source density at each grid level analyzed in this section. However, these small flashes were certainly propagating through small pockets of charge generated within the updraft, and that signal does appear in this analysis. The relationship of charge to variations in w is much weaker than its relationship to temperature; most of the negative charge was analyzed close to -40°C, and most of the positive charge was analyzed between -20°C and -40°C.

Chapter 4: 16 June 2012

The small multicell storm that is analyzed in this section was one of several multicell storms that formed in central Oklahoma on 16 June 2012 shortly after passage of a mesoscale convective system (MCS). Although the MCS was the principle target of DC3 aircraft, it quickly moved too far south for the mobile in-storm ballooning team and radars to position themselves for data collection. However, enough instability and outflow boundaries were behind the squall line to trigger the formation of scattered short-lived, multicell storms in central Oklahoma, and the OKLMA and multi-Doppler radar provided data on two of them. The earlier of the two, and the one studied here, occurred over the town of Eakly, Oklahoma, approximately 30 km south of I-40 on State Highway 58. That storm dissipated before a balloon could be launched into it, but dual-Doppler radar analyses were available for most of the storm following its peak in lightning flash rates. The second storm occurred over the town of Hydro, Oklahoma as the previous storm dissipated. Although an electric field meter and particle imager were launched into that storm, dual-Doppler radar data were available only for a part of the storm that produced no lightning, so we did not select it for study.

The Eakly storm began around 22:00 UTC, and the evolution of total flash rates for its entire lifetime, a period of roughly 1 hour, is shown in Figure 76. Following its first flash at 22:05 UTC, flash rates increased rapidly to a peak >130 flashes min^{-1}at 22:16 UTC, before reaching their maximum of 146 flashes min^{-1}at 22:24 UTC and then declining steadily until lightning ended at 23:09 UTC. Most of the mapped lightning was elevated: vertical VHF source density peaked at ≥9 km MSL throughout the storm's lifetime (Figure 77). The peak in both total flash rates and vertical source density occurred shortly before the period of dual-Doppler radar data indicated in Figure 76.

The mobile radars collected dual-Doppler data on this cell between 22:36-23:06 UTC, during its decay phase. The following analysis times will be discussed in detail below: 22:36 UTC, 22:42 UTC, 22:48 UTC, 22:54 UTC, and 23:00 UTC. Figure 78 shows the storm's reflectivity at 6.2 km AGL at each of these analysis times and the locations of the vertical cross sections taken at each time.

4.1: 3-D Storm Structure and Evolution with Time

4.1.1: 22:36 UTC

At 22:36 UTC, the Eakly storm's total flash rate was 47 flashes min^{-1}, and w_{max} was 52 m s^{-1}. The storm had three distinct updrafts at this time: two of them were adjacent to downdrafts centered on the storm's reflectivity maxima, and one was on the east side of the main reflectivity core and thus likely was the remnants of an older decayed cell (e.g. Figures 79a-83a). The HCA identified two regions of hail at this time, both of which were associated with the two stronger updraft/downdraft couplets and the storm's two reflectivity maxima (e.g. Figures 79e-83e).

Most of the lightning was concentrated between 8.2 and 11.2 km (e.g. Figures 81-88b,d), reflecting the trend observed in Figure 77. Flash extent density and source density both peaked just outside of the two regions of w_{max}, and flash footprints collocated with these relative maxima were generally < 10 km^2. The footprints observed at this time were almost all < 50 km^2, with a few exceptions in the 7.2-8.2 km levels (e.g. Figures 79-80c). The regions of the densest flash propagation (i.e., where there were local maxima in flash extent density and source density) were generally characterized by either graupel or snow identified by the HCA. Flash initiations primarily occurred between 8.2 and 10.2 km, and most of them were associated with reflectivity cores (e.g. Figures 85a-87a); there were no flash initiations found in the vertical cross section taken through the outer edges of the storm (Figure 88). Initiations tended to be clustered along

gradients of w and reflectivity, on the edges of inferred charge regions, and near boundaries between particle types in the HCA output, especially the boundaries between graupel and snow (e.g. Figures 84e-87e). The western cell had a distinctly dipolar inferred charge structure, with a layer of negative charge between ~6-8 km AGL and a positive charge layer above it (e.g. Figures 84f-86f), while the cell to the northeast had a more complicated inferred charge structure (e.g. Figures 87f-88f); overall, however, positive (negative) charge was inferred where the HCA identified low density graupel (high density graupel).

4.1.2: 22:42 UTC

By 22:42 UTC, the storm's morphology had changed somewhat: the western cell became the primary strong cell in the storm and the cell to the northeast began to decay. The storm's total flash rate reached a secondary maximum of 59 flashes min^{-1} at 22:41 before beginning to decrease again. This increase in total flash rate reflects the observed increase in w_{max} to almost 70 m s^{-1} in the western cell. The downdraft coupled with this strong updraft had increased in intensity to -35 m s^{-1} from 22:36 to 22:42. The western reflectivity maximum at 22:36 UTC became the only reflectivity maximum by 22:42 UTC (e.g. Figures 89a-93a). The decrease in reflectivity of the cell to the northeast of it, which had been the middle of the three cells, was likely a reflection of the hail that had been in the updraft/downdraft couplet falling out, as the HCA identified some graupel but no hail there at 22:42 (e.g. Figures 89e-93e, 97e).

The flash extent density and source density maxima at this time overlapped with and extended east of w_{max} (e.g. Figures 89b,d-93b,d, 95b,d). The eastward extensions, with some branching downwind of the updraft, occurred in two distinct layers, one at roughly 10-11 km AGL and one at roughly 6 km AGL (e.g. Figure 95b,d). These branches tended to follow the horizontal wind flow as it detrained from or flowed around the updraft at different levels. The

distribution of flash footprint did not change greatly from 22:36 to 22:42, with footprints remaining quite small in and around the main core of the cell, although there were some larger flashes identified outside the storm core in the midlevels (e.g. Figures 89c-91c, 94c-97c). Flash initiations were much more tightly clustered inside the primary cell's updraft; they were not associated with any particular hydrometeor types or gradients at this time compared with 22:36, and most of them were associated with inferred positive charge. The dipolar charge structure and its hydrometeor affiliations noted in this cell at 22:36 remained approximately the same at 22:42 (e.g. Figures 94e,f-97e,f).

4.1.3: 22:48 UTC

The Eakly storm had weakened substantially by 22:48 UTC. The total flash rate at this time was 26 flashes min^{-1}, and w_{max} had decreased to 37 m s^{-1}. Although there were still small pockets of updraft in the decaying cells on the northeast side of the storm, the larger reflectivities were still associated with w_{max} (e.g. 98a-102a). The reflectivity maximum was also weaker than at 22:42. The volume of downdrafts in the storm was at least equal to, if not greater than, that of updrafts by this point, another sign pointing to the storm's overall decay, with the downdraft strength peaking at -25 m s^{-1} in the upper levels (e.g. Figure 101). Almost all the hail in the storm had fallen out by this point, except for a narrow column adjacent to the primary updraft/downdraft couplet (e.g. Figures 98e-100e, 103e).

The lightning in the storm was still generally elevated except for a few large flashes propagating through the mid-levels (e.g. Figures 98c-99c). The flash extent density and source density maxima, as well as the majority of the flash initiations, were still clustered in and around the primary updraft/reflectivity core of the storm, where flash footprints were quite small. The flashes in the storm at this time continued to indicate a dipolar charge distribution, where the

lower (upper) layer of lightning propagation was characterized primarily by negative (positive) charge (e.g. Figures 103f-105f). The positive charge layer was associated mostly with snow and the negative charge layer mostly with graupel.

4.1.4: 22:54 UTC

By 22:54, the westernmost cell had decayed even further. The total flash rate was 9 flashes min^{-1} and the maximum vertical wind speed in both the storm's primary updraft and downdraft was $5 < |w_{max}| < 15$ m s^{-1} (e.g. Figures 107-110). The actual w_{max} at this time was 29 m s^{-1}, but that maximum was most likely in the updraft persisting on the edge of the storm which was not associated with substantial reflectivity or any lightning activity. There was lightning associated with the remaining reflectivity, which was dominated by a downdraft (e.g. Figures 113a-114a). The only hail still identified by the HCA was close to the ground, where it was finishing falling out (e.g. Figures 111e-114e). The flashes that occurred at this analysis time were almost entirely concentrated in the remaining reflectivity core, which was dominated by graupel (e.g. Figures 107e-110e), with one flash initiation observed outside the central region of relatively high reflectivity (e.g. Figure 108a). Flash footprints were highly variable, with some small flashes located in the core of the primary dying cell and some larger flashes propagating outside of it (e.g. Figures 107c-114c). The dipolar charge structure remained the same as at previous times (e.g. Figures 111f-113f).

4.1.5: 23:00 UTC

At 23:00, the storm was almost completely dead; the total flash rate was at or near 0 for the duration of the six-minute period of LMA data shown in Figures 115-121. Reflectivity did not exceed 40 dBZ above the freezing level (e.g. Figures 115a-121a) and vertical motion in the storm's reflectivity core was almost entirely comprised of weak downdrafts. The HCA identified

a small region of graupel (e.g. Figures 115e, 128e), but otherwise the storm's hydrometeor composition was simply snow above the melting level and rain below it (e.g. Figures 115e-120e). Flash footprints at this time were larger overall than previously (e.g. Figures 115c-120e), and the two flash initiations observed in the selected cross sections were located near the top edge of the dissipating reflectivity maximum (e.g. Figures 117a, 120a). As observed at 22:54, the weak elevated downdraft observed at 23:00 (e.g. Figures 120a-121a) might have been an error in the wind analysis. The few flashes observed during this time highlighted the same charge structure as at previous times (e.g. Figure 119f-121f); the negative charge was associated with the remnants of graupel in some cross sections (e.g. Figure 119e,f).

4.2: Bulk Relationships between Lightning, Microphysics, and Kinematics

As in section 3.2, a summary of the lightning data as it relates to HCA and dual-Doppler output for the Eakly storm will be shown in this section. Figures 122-126 show the vertical distribution of the frequency of flash extent density, flash initiation density, source density, and positive and negative charge, as well as the average flash footprints, associated with all instances of hydrometeor classes across the entire grid domain at each time. The dark grey horizontal lines on the figures depict the 0^{o}C, -20^{o}C, and -40^{o}C levels from the environmental sounding used in the HCA.

Flashes were initiated preferentially in regions of hail, graupel, and snow, and most flashes propagated through either graupel or snow. There were several discharges identified well above the -40^{o}C level, but flash extent density, flash initiation density, and source density were largest between -20^{o}C and -40^{o}C. The clustering of flash initiations in grid cells identified primarily as hail (e.g. Figure 122b) is likely related to the fact that initiations tended to occur in the region of maximum updraft in this storm, which contained hail at the first three analysis

times. In general, there was lightning activity through a great depth of the storm at the earlier analysis times, which tapered to a narrower vertical distribution toward the end of the storm's lifetime. Flash footprint did not appear directly related to any specific hydrometeor class. However, at early times, the average flash footprint tended to be larger at lower levels and smaller at upper levels. As time progressed the average flash footprint increased throughout the depth of the storm, which accurately reflects the results shown in section 4.1.

The charge distribution with respect to altitude and hydrometeor type reveals a similar result as that discussed in section 3.2. In general, positive charge was affiliated with all observed ice particle types above the -20^{o}C level, and negative charge was affiliated with all observed ice particle types at or below the -20^{o}C level. Most of the ice particles carrying charge were categorized as either dry snow, high density graupel, or low density graupel, though positive charge was also associated with vertically aligned ice.

The distribution of lightning activity with respect to 5 m s^{-1} bins of w is shown in Figures 127-131. Early in the analysis period, the Eakly storm had lightning associated with a wide range of w values, with lightning propagating and being initiated in updrafts, downdrafts, and regions of very weak vertical motion (-5 m s^{-1} < w < 5 m s^{-1}). As time progressed, lightning tended to initiate and propagate in a narrower distribution of w, reflecting the storm's decay. Charge distribution was more closely related to temperature/altitude than w. Both positive and negative charge were analyzed in regions with -25 m s^{-1} < w < 25 m s^{-1}, but positive charge tended to be above the -20^{o}C level and negative charge tended to be at or below the negative 20^{o}C level. Overall, when compared with both the storm's hydrometeor content and vertical motion, the distributions of lightning propagation and inferred charge were more dependent on temperature than on either hydrometeor types or w.

Chapter 5: 6 June 2012

The 6 June 2012 storm was a weakly forced mesoscale convective system (MCS) which formed in north-central Texas and propagated north-northeast into central Oklahoma. Because a large portion of the storm extended into north-central Texas and was, therefore, outside the range of the OK LMA, it was not feasible to determine a total flash count for the entire system, so this analysis focuses on the northern segment of the line which was within range of the 3-D OK LMA and sampled by the mobile DC3 ground facilities. The data collected by the mobile radars and LMA were sufficient for performing spatial analysis over a one hour period. Six times were selected for detailed analysis from the triple-Doppler dataset: 20:51 UTC, 21:03 UTC, 21:15 UTC, 21:27 UTC, 21:39 UTC, and 21:51 UTC. The horizontal levels selected for analysis are: 4.7 km, 5.7 km, 6.7 km, 7.7 km, and 8.7 km AGL. Figure 132 shows the 4.7 km AGL reflectivity at all six analysis times, with dashed lines representing the locations and orientations of the vertical cross sections generated at each time. The southernmost cells were outside the coverage by one of the mobile radars, so vertical velocity estimates in the following sections are less reliable in that region.

5.1: 3-D Storm Structure and Evolution with Time

5.1.1: 20:51 UTC

At 20:51 UTC, the MCS was still in its early stages of development, lacking a well-established stratiform region and transition zone. Figures 133a-137a show the shallow convective line with the beginnings of a stratiform region west-southwest of it. The strongest updrafts were around 15-20 m s^{-1} and were adjacent to reflectivity cores in the leading line. The HCA identified primarily graupel associated with these reflectivity cores through 5.7 km and dry snow above that, with regions of vertically aligned ice primarily west of the convective line (e.g.

Figures 133e-137e). Vertical cross sections in the southern part of the domain show that the line was maintained by front and rear inflow, where inflow from the east-southeast occurred through all levels but the rear inflow was low-level (e.g. Figures 138a-139a). Further north, the strongest updrafts were often above 40-dBZ reflectivity cores; the low-level ascent ($w \sim 5$ m s^{-1}) immediately behind the leading line beneath elevated descent ($w \sim -5$ m s^{-1}) were both the result of errors in the wind synthesis (e.g. Figures 140a-142a).

Overall, flash extent density and source density increased with altitude in the storm; most of the flashes were propagating around and above the updrafts in the convective line (e.g. Figures 135b,d-142b,d). Flash initiations tended to occur in the convective line as well, but below 8 km AGL and outside of the updrafts and outside of the regions of appreciable flash extent density and source density. The very large flash footprints dominating the analysis domain (e.g. Figures 133c-142c) coupled with the flash initiations being located outside of flash extent density maxima (Figures 133b-136b) and the sloping of lightning from the front of the convective line to the rear of it (e.g. Figures 139-141) suggests that lightning activity was characterized by very large flashes which were initiated in the leading line and propagated rearward through spatially extensive and sloped charge layers. Charge in the low levels of the storm was primarily negative and transitioned to positive with increasing altitude (e.g. Figures 133f-142f; remember that VHF mapping tends to detect fewer points in negative charge). The most elevated negative charge was detected near regions of the stronger updrafts in the convective line (e.g. Figure 140f), where the stronger updrafts was lofting hydrometeors higher and thus elevating the locations of charge generation and lightning. In general, negative charge was identified in regions dominated by graupel, and positive charge was identified in layers dominated by snow and vertically aligned ice.

5.1.2: 21:03 UTC

Horizontal cross sections of the storm at 21:03 are shown in Figures 143-147. By 21:03, the basic morphology of the section of MCS in the analysis domain had not changed substantially, although the area of updrafts ≥ 5 m s^{-1} and of ≥ 40 dBZ well behind the line at 4.7 km AGL had both decreased (Figures 132a,b). Reflectivity ≥30 dBZ extended to 8.7 km in a greater area of the storm than previously, but the updraft intensity and size did not increase noticeably (compare Figures 137a and 147a). The volume of graupel in the line appeared to decrease in northern reflectivity cores but increase slightly in the one closest to the radar from 20:51 to 21:03 in the horizontal cross sections, and the locations of pockets of vertically aligned ice shifted but the volume of VI appeared comparable to that at 20:51 (compare Figures 133e-137e with 143e-147e). The basic vertical structure of the reflectivity and wind fields of the MCS did not substantially change from 20:51 to 21:03, either (compare Figures 138a-142a with 148a-152a): Along the leading line, there were still relatively strong elevated updrafts above the highest reflectivity maxima, sustained by a combination of front and rear inflow. Behind the leading line, much of the region above 5.2 km AGL had weak updrafts; updrafts identified below 3.7 km in this region were most likely artifacts still, but it is unclear whether or not the aforementioned more elevated updrafts were real.

As at 20:51, most of the lightning activity in the storm at 21:03 was elevated, although flash extent density did not define the leading line as clearly and spread more behind the line at 21:03 (compare Figures 133b-137b with 143b-147b). Relative maxima of flash extent and source densities were generally adjacent to convective cores to their rear, but there were relative minima in these lightning fields collocated with updrafts, especially at higher altitudes (e.g. Figures 143b,d-147b,d). The one exception to this was on the far southern edge of the domain, where

there was a peak in lightning frequency associated with high reflectivity and vertical velocity magnitudes were <5 m s^{-1} at all the levels that are shown (Figures 146a,b-147a,b). Flash initiations were scattered across the storm in the horizontal cross sections, with the largest concentration associated with the southernmost reflectivity maximum near x = 29 and y = 7. Some were associated with relative minima in flash extent and source densities, but others were associated with higher flash densities. Flash footprints at 21:03 were still overall very large, but there were more grid points with smaller average flash sizes (i.e., < 100 km^2; see Figures 143c-152c). Some vertical cross sections show that flashes with small sizes were lower in the storm, and close enough to possibly be cloud-to-ground flashes (e.g. Figure 149c). The charge distribution at this time was similar to that at 20:51, with inferred negative charge in the lower levels and positive charge in the upper levels (e.g. Figures 143f-152f), and with more complicated charge structures near updrafts (e.g. Figure 150f). Inferred positive charge was most often associated with dry snow and vertically aligned ice. Near convective cores, negative charge was associated with graupel, but in regions of weak or no ascent, negative charge tended to be inferred near the melting level, and there it was associated with graupel and wet and dry snow.

5.1.3: 21:15 UTC

The MCS had propagated farther NNE by 21:15, and the beginnings of a transition zone and stratiform region were visible in the western section of the analysis domain (e.g. Figures 153a-157a). The cell in the leading line that had the strongest observed updraft at previous times strengthened to w_{max} = 25 m s^{-1} (e.g. at approximately x = 39, y = 30 in Figure 153a). The area of reflectivity above 30 dBZ at higher altitudes increased again (e.g. compare Figures 147a and 157a), and the cell in the southern portion of the domain appeared to intensify as well. Unfortunately, that cell was outside the area of ideal multi-Doppler coverage, so no information

on its updraft is available. The HCA retrieval in the cell with the strongest measured updraft indicated slightly increased graupel volume there from 21:03, although cells farther north which had previously contained graupel either weakened or moved out of the analysis domain (e.g. Figures 153e-157e). The volume of vertically aligned ice in the developing stratiform region increased more substantially than the graupel content between 21:03 and 21:15 (compare Figures 153e-157e with Figures 143e-147e). Behind the leading line, there were still artifacts in the vertical wind field which made the true nature of the flow there difficult to diagnose (e.g. Figures 158a-159a).

Lightning activity appeared to increase again by 21:15, as indicated by larger regions of greater flash extent density and source density, especially in the upper levels (compare Figures 146b,d-147b,d and 156b,d-157b,d), and by a larger number of flash initiations in the analyzed region (compare Figures 143-147 and 153-157). Once again, lightning activity peaked outside of and above updrafts and downdrafts (Figures 153-157). In vertical cross sections reliably depicting updrafts aligned with relatively deep reflectivity cores relative maxima in flash extent and source density tending to be located above or in the upper part of updrafts in the leading line (e.g. Figures 160b,d-161b,d). Additionally, flash extent density and source density fields tended to follow the storm-relative flow downstream from relative maxima (e.g. Figures 158b,d-162b,d). Flash footprint was much more varied than at previous times in the southern cell (e.g. Figures 153c-157c), indicating many more small flashes occurring there than in the central cell. The vertical cross sections revealed flash size characteristics similar to those at previous times, with smaller flashes occurring in the leading line and at low levels (e.g. Figures 158c-162c). The storm's charge structure was essentially the same as at previous times (compare Figures 153f-162f with Figures 133f-142r and 143f-152f).

5.1.4: 21:27 UTC

The horizontal cross sections at 21:27 UTC (Figures 163-167) show that the leading line had weakened, as the area of reflectivity >50 dBZ in the southernmost cell had decreased (compare, for example, Figures 163a and 153a) and the maximum updraft in the middle cells had decreased to $w < 25$ m s^{-1}. The reflectivity field indicates that the MCS was maturing, however, as the area of reflectivity ≥ 30 dBZ aloft increased substantially in the developing stratiform region from 21:15 to 21:27 (compare Figures 165a-167a with 155a-157a). There was also a relative minimum in reflectivity between the leading line and the developing trailing stratiform regions (e.g. Figures 163a-167a). The amount of graupel identified by the HCA had also decreased again by this time, with the bulk of the MCS which was sampled by SR2 dominated by dry snow and vertically aligned ice above the freezing level, wet snow at the freezing level, and rain below it (e.g. Figures 163e-172e). The artifacts in the wind analysis manifesting as broad, weak, low-level updrafts and downdrafts were still visible in some vertical cross sections (e.g. Figures 171a-172a).

The number of flash initiations in the selected cross sections at 21:27 was only 56% of the number at 21:15, a substantial decrease reflecting the weakening of the storm's convective updrafts. Flash extent and source density relative maxima were located in roughly the same storm-relative locations (compare Figures 163b,d-167b,d with 153b,d-157b,d), but the proportion of flashes and sources in the upper levels (7.7-9.7 km AGL), which had previously contained maxima, was smaller and flashes tended to be distributed somewhat lower in altitude (compare, for example, Figures 171b,d and 161b,d) . In general, most of the lightning in the storm was still elevated relative to regions of ascent, but unlike at previous times, it did not slope noticeably downward into the developing stratiform region (e.g. Figures 168b,d-172b,d). Flash initiations

had transitioned from being located mostly outside of flash extent and source density maxima to being mostly collocated with them (e.g. Figures 163b,d-168b,d, 171b,d). The variety in flash footprint observed at 21:15 compared with the two earlier times was also observed at 21:27, and as with 21:15, the smaller flash footprints tended to be observed near stronger updrafts and downdrafts in the convective line (e.g. Figures 163c-172c). The charge structure did not change substantially between 21:15 and 21:27, although Figure 163(f) shows that inferred negative charge at 4.7 km was associated with the convective line and that there was positive charge inferred in the developing transition zone and stratiform region behind it.

5.1.5: 21:39 UTC

The MCS's stratiform region appeared better developed by 21:39 (compare Figures 173a-176a with 163a-166a), but overall, the intensity of the convective line continued diminishing. Updrafts had weakened further in the convective line, as only one cell (near the northern edge of the domain) contained an elevated updraft with $w_{max} \geq 15$ m s^{-1} (e.g. Figures 176a-177a). There was almost no reflectivity ≥ 30 dBZ above 7.7 km (e.g. Figure 177a). The volume of graupel in the storm had decreased as well, where the only substantial hail signature in the HCA horizontal cross sections was at 4.7 km (e.g. Figures 173e-182e). The HCA also identified almost entirely dry snow outside of the hail cores, with very little in the way of vertically aligned ice, particularly compared with earlier times. The reflectivity data in Figures 173a-180a suggest that there still were relatively weak convective cells in the southern part of the analysis domain, which was outside of the region observed by SR2 by this time. Although the w field in the stratiform region and transition zones was still contaminated by artifacts, the reflectivity structure of the storm was continuing to develop towards the Houze et al. (1989) conceptual model.

Flash extent density and source density both continued to decrease in the selected cross sections as the observed portion of the convective line weakened (e.g. Figures 173b,d-182b,d). Lightning propagated through a greater depth of the storm at this time, though the relative maxima in observed flash extent and source density were still elevated higher in the northernmost cell in the convective line (e.g. Figure 182b,d). At 21:39, the analysis region had almost the same number of flash initiations as at 21:27, and again flash initiations tended to cluster near the relative maxima in flash extent density and source density in most of the cross sections; initiations in the northern cell, where there still were regions with $w \geq 5$ m s^{-1}, clustered around, but not inside, 5 m s^{-1} contours (Figures 173b,d-177b,d). Flash footprints continued to be very large overall, with smaller flashes mixed in, particularly in the southern half of the analysis domain (e.g. Figures 174c-176c, 177c). There were fewer VHF sources detected in inferred negative charge regions at this time than previously (remember that LMAs tend to detect a much smaller percentage of radiation sources in negative charge than in positive charge), but most of those detected in negative charge were collocated primarily with graupel and wet and dry snow in and just above the melting layer. Positive charge was inferred through most of the depth of the storm above the melting layer, where most hydrometeors were classified as dry snow or vertically aligned ice (e.g. Figures 178f-182f). There was also a small amount of negative charge above the relatively deep layer of positive charge (e.g. Figures 178f-182f). That upper negative charge was likely part of a screening layer at the cloud top.

5.1.6: 21:51 UTC

At 21:51 UTC, the MCS had continued moving farther northeast, so more of the southern part of the convective line and stratiform region had moved out of the area covered by SR2, thereby degrading the reliability of vertical velocity estimates and eliminating HCA estimates

there. Within the region of best mobile radar coverage, the region of $w \geq 5$ m s^{-1} had broadened further (compare, for example, Figure 173a with 183a). The reflectivity structure of the storm was similar to the structure at the 21:39 analysis time, although the whole system was generally shallower, with substantial reflectivity at lower levels but less reflectivity ≥ 30 dBZ in the upper levels (compare Figures 183a-192a with 173a-182a). A region of $w_{max} \geq 15$ m s^{-1} was observed both in the northern segment of the convective line up to the highest horizontal level shown (e.g. Figures 183a-187a, 192a) and in one analyzed altitude of the stratiform region (e.g. Figure 185a), although the w field in the stratiform region was still questionable due to issues with the wind synthesis. The HCA still detected graupel associated with a few reflectivity cores in the leading line between 3.2-5.7 km (e.g. Figures 183e-184e, 190e-192e), but there was very little of it present compared with earlier times. There was also slightly more vertically aligned ice identified by the HCA at 7.7-8.7 km at 21:51 compared with 21:39, but a similar lack of it in the lower levels as at 21:39 (compare Figures 183e-187e with Figures 173e-177e).

At heights below 6.7 km, the flash extent density and source density relative maxima were just behind (west) of the reflectivity maxima in the convective line and behind the updraft closest to the convective line (Figures 183a,b,d-184a,b,d). This also was mostly true at altitudes ≥ 6.7 km, but lightning also overlapped regions of reflectivity relative maxima and updraft in the convective line at roughly y = 40 km (Figures 185a,b,d-187a,b,d). Lightning was also west of the reflectivity maxima at all altitudes in a new cell that formed ahead of the line in the southeast corner of the domain. Flash footprints were still very large, with most of the domain characterized by flashes ≥ 200 km^2. The relative maxima in flash extent and source density were characterized more by flash footprints between 100-200 km^2 (e.g. Figures 185c-187c), and several flash initiations were noted there. The smallest flashes were south of this region (e.g.

Figures 183c-189c), and, given the groundward extent of the gridded lightning signatures in Figures 188-189, it is possible that those small flashes were cloud-to-ground flashes. The charge structure of the storm at 21:51 was effectively the same as at 21:39, including the apparent negative screening layer aloft (e.g. Figures 188f-192f). The lower regions of inferred negative charge were still generally associated with snow and small pockets of graupel in the melting layer, while the more elevated regions of inferred positive charge were still associated with dry snow and vertically aligned ice.

5.2: Bulk Relationships between Lightning, Microphysics, and Kinematics

Figures 193-198 show the vertical distribution of flash extent density, flash initiation density, source density, mean flash footprint, and inferred positive and negative charge with respect to each hydrometeor class identified by the HCA for each analysis time discussed in section 5.1. As is typical, most of the lightning propagated between the 0^{o}C and -40^{o}C levels at all times (e.g. Figures 193a,d-198a,d). The clear maxima in flash extent and source density associated with dry snow, as well as the secondary maxima associated with vertically aligned ice and graupel, reflects the observations in Section 5.1, where it was shown that most of the MCS above the freezing level was dominated by dry snow and vertically aligned ice and that the convective cores in the leading line contained substantial graupel. Flash initiations were primarily located in regions of dry snow and graupel; unlike the other two storms analyzed in this study, however, initiations in the MCS were located almost entirely between 0^{o}C and -20^{o}C (e.g. Figures 193b-198b). At early analysis times, average flash footprints were generally very large above the melting level, with smaller flashes identified below it (e.g. Figures 193c, 197c-198c). Most of the small flashes at early times were likely cloud-to-ground flashes, given that

they were associated with rain, graupel, and hail below the melting level and frequently occurred near the ground.

The charge distribution with height relative to hydrometeor class also reflects the results discussed in section 5.1: earlier in the analysis period, positive charge was inferred through most of the 0°C to -40°C layer, while negative charge was lower in the storm, closer to the melting level (e.g. Figures 193e,f-196e,f). Both polarities of charge were associated with a variety of hydrometeor types at all levels, although positive charge was preferentially found in grid cells identified as dry snow and vertically aligned ice, and negative charge was preferentially found in cells identified as graupel, wet snow, and dry snow. However, after the MCS had matured more, negative charge was also associated with dry snow and vertically aligned ice high up in the storm, above the -20°C level, while the layer of positive charge became slightly shallower and descended closer to the melting level, and there was still negative charge at and below the melting level (e.g. Figures 197e,f-198e,f). As noted in sections 5.1.5-5.1.6, this upper negative charge layer was located near the top of the MCS reflectivity signature and thus was likely a screening layer which formed near the cloud top.

Figures 199-204 depict the same lightning characteristics as Figures 193-198, but relative to 5 m s^{-1} bins of w. Most of the lightning occurred in regions of $-5 < w < 5$ m s^{-1}, which is consistent with the results shown in section 5.1, where most lightning was observed outside of updraft cores. The same altitude-related trends noted in the previous discussion of lightning activity relative to hydrometeor classes are observed relative to w: while lightning propagation extended through most of the 0°C to -40°C layer and toward the ground, flash initiations were primarily concentrated between 0°C and -20°C (e.g. Figures 199a,b,d-204a,b,d). Mean flash footprint was still characterized by the smaller flashes occurring at and below the melting level at

early times, and more frequently above the melting level at later times (e.g. Figures 199c-204c). The small flashes observed at higher altitudes at all analysis times were associated with regions of stronger updraft or downdraft, whereas the small flashes below the melting level were associated with the $-5 < w < 5$ m s^{-1} bins.

Most of the inferred charge throughout the analysis period was associated with the $-5 < w < 5$ m s^{-1} bins (e.g. Figures 199e,f-204e,f). The development of an upper negative charge layer and slight descent of the positive charge layer in the latter half of the analysis period, noted in both the previous HCA-relative analysis and in the vertical cross sections in sections 5.1.5-5.1.6, is also evident in the w-relative analysis, since that development was more dependent on altitude than any specific storm characteristic. Relative to both HCA and w, the charge structure of the storm is more complex between 0^{o}C and -20^{o}C than at other levels, because both positive and negative charge were inferred in regions of similar kinematic microphysical characteristics.

Chapter 6: Discussion and Conclusions

Chapters 3-5 presented highly detailed spatial analyses for three storms of very different morphologies: a supercell, a multicell, and an MCS. As discussed in Chapter 1, the literature is full of past case studies from different storms sampled during various field experiments and from modeling studies, all with the aim of furthering the field's understanding of the relationships between lightning and other storm characteristics. Because of the nature of the observations necessary to achieve these research goals, the process of developing and confirming hypotheses regarding these relationships has been long and slow, relying heavily on the gradual accumulation of individual case studies. This study not only adds to the body of literature supporting several hypotheses about the nature of storm charge and lightning generation and distribution as they relate to a storm's microphysical and updraft characteristics, but also presents relatively new or under-utilized ways of studying them, particularly with respect to storm microphysics. Few past studies have implemented hydrometeor classification algorithm results as they compare to lightning and charge in storms (e.g. Tessendorf et al. 2007b), and none have presented multiple methods of diagnosing storm microphysics, as this study was able to do for the Kingfisher storm. Furthermore, only a few studies have focused on how the relationships between lightning, microphysics, and updraft characteristics vary across different storm modes.

6.1 Lightning distribution relative to storm morphology

6.1.1: Relationships of lightning with updrafts

Each storm studied herein had lightning characteristics which were consistent with past observational and modeling studies that examined the distribution of lightning and the relationships between lightning and updraft characteristics of different storms. It is generally understood that the updraft intensity of a storm partially controls its lightning frequency (e.g.

Carey and Rutledge 1996; Lang and Rutledge 2002; Wiens et al. 2005; Kuhlman et al. 2006; Bruning et al. 2007; Tessendorf et al. 2007a, b; Deierling and Petersen 2008; Bruning et al. 2010; Calhoun et al. 2013; Mecikalski et al. 2015; Schultz et al. 2015; DiGangi et al. 2016; Schultz et al. 2017). Figures 205-206 show the time series of total flash rate and maximum updraft for the Kingfisher and Eakly storms. The total flash rate for the Kingfisher supercell increased when the updraft intensified and sometimes decreased when the updraft weakened; the mobile radars sampled that storm during its intensification phase, and its intensification was reflected in both w_{max} and total flash rate. Although radars observed the Eakly storm during its decay phase, it similarly showed that the total flash rate generally decreased as the updraft dissipated. Figures 207-208 show the simple linear regressions calculated for w_{max} versus total flash rate for the Kingfisher and Eakly storms: in both cases, w_{max} and total flash rate were positively correlated ($R = 0.63052$ and $R = 0.7468$, respectively). The observations of these two storms are insufficient in themselves to draw a more general conclusion, but the result is similar to observed relationships in the many storms referenced above and so adds to support for the relationship between updrafts and lightning flash rates.

Such an analysis was not feasible for the MCS; because only the northern end of a long convective line was analyzed, no total flash rate was calculated for the system. Furthermore, the errors in the wind field make quantities like maximum updraft speed or updraft mass flux unreliable from that case. However, many of the observed cross sections had more initiations and greater flash extent densities in the leading convective line, which contains the strongest updrafts in MCSs (see, for example, Figures 153a,b-157a,b).

A similar trend was also reflected by the overshooting top (OT) signature in the vertical VHF source density for the Kingfisher storm, according to DiGangi et al. (2016). The OT

signature is a relative maximum in VHF source density observed in a storm's overshooting top (MacGorman et al. 2017). Since overshooting tops are the result of strong updrafts penetrating the level of neutral buoyancy, this source density signature can be used to infer strong updrafts in a storm with better temporal and spatial resolution than provided by the WSR-88D network (e.g. Calhoun et al. 2013, DiGangi et al. 2016, MacGorman et al. 2017). The OT signature was observed in the spatial analyses of the Kingfisher storm presented in this study, where secondary maxima in source density were evident in some vertical cross sections at ~15-16 km beginning at 2333 UTC (e.g. Figure 29d), which accurately reflects the time series shown in DiGangi et al. (2016). The Eakly storm also exhibited the overshooting top signature (e.g. Figure 85d), particularly in the time series of vertical VHF source density (Figure 77). However, the Eakly storm's OT signature was much less consistent than the OT signature observed in the Kingfisher storm, as it had the smaller, more transient updrafts characteristic of multicellular storms rather than the quasi-steady updraft of the supercell storm. The MCS did not exhibit an OT signature, likely because updrafts were shallower and not as vigorous. The differences in the OT signature across these three storms is a result of the differences in their updraft characteristics: the Kingfisher storm was intensifying and had a persistent, very strong updraft; the Eakly storm was decaying and had a more transient, pulsing updraft; and the MCS updrafts were consistently much weaker than the updrafts in the other two storms.

Besides updraft strength and overshoot affecting lightning rates, strong rotation of the updraft also has a unique, repeatable effect on the distribution of lightning. Payne et al. (2010), in their detailed investigation of a lightning "ring" around the mesocyclonic updraft of a supercell storm observed during TELEX, concluded that the vorticity maximum in the updraft appeared to have more control over the lightning distribution around the updraft than the updraft speed itself.

Specifically, the lightning ring developed a clear structure when the vorticity peaked and then dissipated as the storm occluded and its mesocyclone weakened. Other studies (e.g. Calhoun et al. 2013) have referred to the minimum in lightning activity collocated with a vertical vorticity maximum in the updraft as a lightning hole surrounded by a lightning ring.

This feature also appears to be caused in part by the cores of supercell updrafts being so strong that they provide little time for precipitation growth and charging at levels where precipitation and charge typically are seen in weaker storms. The implied intense vertical advection shifts reflectivity and charge separation higher in the storm, as suggested by MacGorman et al. (1989) and Marshall et al. (1995). The lightning hole thus appears to have been caused by a combination of effects: (1) There is some charge separation at lower altitudes in weaker vertical speeds along the periphery of the updraft, and the mesocyclone circulation sweeps charged particles in the periphery around the updraft; (2) Charged particles at altitudes where the stronger updrafts begin diverging form a precipitation and charge cascade and are swept around the updraft core as they fall. These kinematic effects are very similar to those causing the bounded weak echo region (BWER) in the reflectivity structure associated with supercell updrafts, although the lightning ring and overhang tend to be displaced slightly higher in altitude than the BWER.

Of the three storms analyzed in this study, only the Kingfisher storm had a lightning ring surrounding a lightning hole, and the lightning hole was horizontally collocated with and slightly above a persistent BWER (e.g. Figure 6b,d; Figure 15 b,d; Figure 20 b,d). Although the Eakly storm exhibited updraft speeds comparable to Kingfisher's at some analysis times, it lacked a mesocyclone. The updrafts observed in the MCS were relatively weak and most likely were not rotating, so there were no lightning holes/rings associated with them, either. The need for an

organized mesocyclone to support the development of a lightning ring/hole identified in this study thus supports the findings of Payne et al. (2010).

However, even without possessing any organized lightning hole, the Eakly storm had relative maxima in flash initiation density and VHF source density above and around its primary updraft (e.g. Figures 85b,d; 95b,d; 104b,d), which aligns with the conclusions of past studies that distinguished this region as favorable for charge generation and separation across multiple storm modes (e.g. Calhoun et al. 2013; Kuhlmann et al. 2006; Dye et al. 1986). The errors in the MCS wind fields render it difficult to determine the exact location of lightning relative to updrafts, but it had high flash extent densities near and above reflectivity cores (e.g. Figures 136b, 137b, 140b). By contrast, many of the flash initiation locations in the MCS were in the lower levels and outside of the reflectivity cores (e.g. Figures 143a, 144a, 163a, 164a). The strong, persistent charge regions at and immediately above the melting level likely contributed to skewing the average altitude of flash initiations to lower levels in the MCS.

This study's most interesting divergence from the results of past literature regarding the location of spatially small flashes is the characterization of lightning in the forward flank of the Kingfisher supercell storm. Previous studies (e.g., Calhoun et al. 2013, Bruning and MacGorman, 2013) have reported the flash size distribution with respect to storm morphology in a supercell is for small flashes to be concentrated in a storm's updraft region, while updraft flashes increase in size farther from updrafts. This was true in the lower-level cross sections observed in the 2-D integrated flash footprints for the Kingfisher storm shown in DiGangi et al. (2016). However, the flashes in the Kingfisher storm's southeastern forward flank decreased in size with increasing altitude and with increasing proximity to the edge of the storm cloud (e.g. Figures 14c-18c). This trend was also observed in the 2004 Geary supercell's flash size and

initiation distribution analyzed in Bruning and MacGorman (2013); however, Bruning and MacGorman noted only that late in the storm's lifetime the storm's updraft had propagated in that direction and thus that region contained many small flashes. Subsequent work by Brothers et al. (2018) investigated the simulated texture of charge regions in a supercell and a multicell with the COMMAS model, which can resolve turbulent eddies in the storm's flow field. They demonstrated that complex charge structures associated with turbulent convective flow can exist downstream of the updraft, especially at high altitudes. The advection and generation of charge by turbulent eddies in the air detraining from the Kingfisher storm's primary updraft appears, therefore, to be a viable explanation for the small flash sizes in the storm's forward flank.

6.1.2: Relationships of lightning with reflectivity structure and microphysics

Many studies have also identified relationships between mixed-phase ice mass and total flash rate (e.g. Goodman et al. 1988; Dye et al. 1989; Carey and Rutledge 1996; Lang and Rutledge 2002; Wiens et al. 2005; Deierling and Petersen 2008; Schultz et al. 2017). Although no mixed phase ice mass or volume calculation was performed in this study, the bulk distribution of lightning provided by the HCA from polarimetric radar observations supports this theory. The exact range of temperatures in which lightning was primarily located varied from storm to storm: lightning activity in both the Kingfisher and Eakly storms was elevated, occurring primarily between the environmental -20^{o}C and -40^{o}C levels. However, lightning in the northern part we analyzed of the long north-south MCS initially occurred throughout the 0^{o}C to -40^{o}C layer and then became more concentrated between 0^{o}C and -20^{o}C as the transition zone and stratiform region developed in the analysis domain and the part of the convective line in our analysis domain weakened.

The MCS was the only storm with a discernable relationship specifically between flash size and hydrometeor class: most of the storm's smallest flash sizes were associated with graupel, hail, and rain (e.g. Figures 193c, 197c). Some vertical cross sections in section 5.1 also revealed relatively small flashes located near, but not inside, updrafts in the MCS's convective line, where the HCA identified graupel mixed with the snow (e.g. Figure 161c,e). Low-altitude flashes possibly went to ground through rain, although the location of lightning ground strikes in the MCS was not analyzed, as the ground strikes were not a focus of this study. Flash extent density extended into the stratiform region as the MCS matured and the stratiform region grew, consistent with very large flashes beginning in the convective line and propagating rearward into the stratiform region, as observed, for example, by Ely et al. (2008) and Biermann (2010).

The HCA categorized some sections of the stratiform region of the MCS as having vertically aligned ice at all analysis times, although the amount and distribution of vertically aligned ice identified varied from time to time (e.g., compare Figures 163e-167e with Figures 173e-177e). Past studies (e.g. Weinheimer and Few 1987; Saunders and Rimmer 1999; Foster and Hallett 2008) have shown that small ice particles will become vertically aligned in the presence of electric fields on the order of 10-50 kV m^{-1}, and electric fields up to ~100 kV m^{-1} can force larger particles to align. Historically, this phenomenon has been diagnosed by studies using the polarimetric radar variables, as discussed in Biggerstaff et al. (2017); furthermore, Biggerstaff et al. demonstrated that large flashes in an MCS tended to propagate along the 0-K_{DP} boundaries surrounding a region of negative K_{DP} in the stratiform region. The negative KDP was associated with ice particles aligned by a strong electric field, and the flashes analyzed in that study were propagating through the regions of highest charge density around the electric field maximum.

The regions of vertically aligned ice in the present case analyzed were associated with flash extent densities, but these FEDs consistently indicated smaller densities of lightning than the FEDs associated with the dry snow category (e.g. Figures 193a-198a). It is possible that the vertically aligned ice signature was simply overshadowed in places by a stronger signature of the dry snow category. However, these vertically aligned ice observations appear consistent with those of Biggerstaff et al. (2017), because lightning channels tend to propagate through the relatively small electric field magnitudes that are within charge regions, while the VI signature indicates regions of large electric field magnitudes, Regardless of its relationship with lightning, the presence of strong transient VI signatures in the stratiform region of this MCS indicates that there were regions of strong electric field that formed and dissipated outside the MCS's convective line.

The peak in the vertical distribution of lightning might be expected to be influenced by the height of storms, which varied considerably from case to case in this study. The reflectivity signature of the MCS topped at ~10-11 km at highest in the MCS (e.g. Figure 171a), while the Kingfisher and Eakly storms topped at ~16.2 km (e.g. Figures 30a, 60a) and ~13-14 km (e.g. Figures 85a, 86a), respectively. Because the MCS thus had the shallowest convection, it makes sense that most of the lightning in the MCS occurred at lower altitudes than in the other two cases. Furthermore, peak lightning activity shifted downward, much closer to the freezing level, during some periods as the convective line weakened, behavior that was not observed in either of the other two cases. It is possible that the height of the majority of charge generation shifted to lower altitudes as later cells formed as weaker convection, similar to initial charging inferred in a weak multicell by Bruning et al. (2007). In the Bruning et al. case, lightning initially involved only the lower dipole charges in what eventually became a tripole; infrequent lightning involving

the upper dipole began later, as the storm finally grew high enough to produce sufficient precipitation growth and charge at the upper altitudes.

The influence of storm height was not as strong in the other two cases, as their lightning activity peaked at a similar altitude and environmental temperature range, even though the Eakly storm was shallower than the Kingfisher storm. The result was a much different relationship with storm structure, as lightning in the Kingfisher supercell storm surrounded the core of the mesocyclonic updraft while lightning in the Eakly storm was concentrated near the top of the updraft, as discussed previously.

Although the rough relationship with environmental temperature in the Eakly and Kingfisher storms is suggestive of the temperature dependence of microphysical charge exchange during rebounding collisions of ice particles, the kinematic details complicate the relationship with temperature. For one thing, being above the level of free convection means that an air parcel in an updraft is warmer than environmental air until it reaches its level of neutral buoyancy. Furthermore, water vapor condensing and liquid freezing release latent heat, which makes ascending air parcels even warmer. These combined effects can mean that isotherms can be a kilometer or more higher in strong updrafts than in the near-storm environment. Even after particles exchange charge in a given temperature range, they continue to rise in strong updrafts as they separate macroscopically, a process essential to producing regions of net charge. Thus, lightning at the top of the updraft in the Eakly storm probably was due to a combination of the temperature at which hydrometeors exchanged charge plus the altitude at which charged graupel began to collect due to convergence from below as the updraft weakened, a process described previously by Ziegler et al. (1991) based on a scenario from Kessler (1969). In the Kingfisher supercell, on the other hand, the peak altitude range of lightning was probably due to a

combination of the same process as for the Eakly storm in the weaker updraft regions of the supercell plus the altitude range at which particles settled after cascading from the strong updraft core.

The relative contributions of these processes to the altitude of lightning may have been weighted somewhat more by the process outside the updraft core, although Payne et al. (2010) showed the cascading process does contribute to lightning. However, Dye et al. (1986) found from *in situ* aircraft measurements that precipitation growth, and presumably charge exchange, was greater in regions of weaker updrafts surrounding the updraft core of a small Montana thunderstorm. Thus, it is possible that the electrification process in weaker updrafts, which more directly relates the temperature dependence of charge exchange to the altitude of charge regions, may dominate the altitude at which lightning peaks in these two storms.

6.2 Charge generation and distribution relative to storm morphology

The inferred charge structures of the three storms presented in this study conform in some ways to the conceptual models of charge generation and distribution in storms depicted in the literature. At a glance, the charge structure of the Kingfisher supercell fits the "inverted polarity" tripole paradigm: the dominant middle charge region was positive and flanked by upper and lower negative charge regions (i.e., as depicted in some vertical cross sections like Figure 10f). However, the cross sections and the bulk analyses indicate more complexity than can be captured by that description. The updraft region contained small pockets of opposing charge adjacent to each other in both the horizontal and the vertical cross sections (e.g. Figures 36f, 41f). Although at some analysis times there was negative charge at two distinct levels, positive and negative charge were frequently observed at the same altitude (e.g. Figures 4f, 14f, 19f, 24f, etc.). In those figures, grid cells with positive charge observed at the same altitude as nearby negative charge

sometimes had a different updraft speed than the grid cells with negative charge, thereby supporting the notion of small pockets of opposing charge polarities separated horizontally across updraft gradients at the same level. At 23:33 and 23:42 UTC, before most of the forward flank moved out of the analysis domain, charge of both polarities was inferred in the same deep layer in varying concentrations in regions characterized by $-5 < w < 5$ m s^{-1} (e.g. Figures 24f-27f, 29f-30f, 34f-38f, 41f, 43f). The horizontal inhomogeneity in updrafts and inferred charge polarity in the forward flank of the storm is consistent with the observation of small lightning sizes noted in the previous section.

Overall, the Kingfisher storm's charge distribution with respect to particle type is in line with noninductive charge generation. In this process ice crystals and riming graupel exchange charge during rebounding collisions in the mixed phase region; the sign of the particles after charge exchange depends on the storm's supercooled liquid water content and on the temperature range in which the collisions occur (e.g. Takahashi 1978; Takahashi and Miyawaki 2002). Macroscopic separation of charge occurs when convective currents transport the charged hydrometeors having different charge polarities and different fall speeds into different parts of the storm. Differential sedimentation causes larger, denser particles to descend faster than smaller, less dense particles. As discussed already, much of the complexity of the observed charge structures in the Kingfisher storm was likely the result of (1) turbulent mixing in the strong gradients in vertical speed along the periphery of the intense updraft and (2) the complex structure of air detrained from the updraft and of air flowing nearby around the updraft. As noted previously, how these features enhanced charge generation in some regions and advected particles to create a lightning ring right around a lightning hole is too complex to determine from the available observations. Microphysically, the region of the lightning ring in the Kingfisher

storm was characterized by mixtures of ice particles identified by both the HCA and DLA, as well as supercooled liquid cloud water identified by the DLA (e.g. Figures 50b,c,d,e). Such combinations of particle types would be conducive to microphysical charge exchange by the noninductive mechanism.

The Eakly storm's inferred charge structure was much closer to the dipole/tripole paradigm than the Kingfisher storm's. The distribution of charge with respect to both hydrometeor class and vertical velocity indicated an upper positive charge region and a lower negative charge region (e.g. Figures 122e,f-131e,f); however, around the -20°C level, there was some overlap between the two polarities of charge which coincided with the highest FED values. The distribution of charge with respect to updraft speed had greater variability in the Eakly storm than in the Kingfisher storm, in part because most of the Eakly storm's lightning occurred in and near its updraft core and most of the Kingfisher storm's lightning occurred farther from its updraft core. In both storms, some of the observed complexity of charge structures could have been influenced by charge deposition by lightning (e.g. Ziegler and MacGorman 1994; Coleman et al. 2003; Kuhlman et al. 2006). Although the Eakly storm did not have the benefit of the DLA dataset, so no supercooled liquid water could be identified in it, the HCA generally classified the region with the most lightning as containing dry snow, graupel, and some hail (e.g. Figures 79b,e-83b,e). The presence of graupel and hail implies the presence of water content, since both of those hydrometeor types grow by riming and accretion of supercooled liquid water. Thus, the Eakly storm also had inferred charge signatures consistent with noninductive charge generation and macroscopic charge separation by differential sedimentation and charge advection.

Although the distribution of charge relative to updraft speed had greater variability in the Eakly storm than in the Kingfisher storm, the Eakly storm's overall charge structure was simpler

than that of the Kingfisher storm's, even though they had comparable maxima in w. This is likely caused by the simpler streamlines in and around the updraft of the Eakly storm due to its shorter lifetime, smaller size, and the absence of a rotating updraft. Updraft rotation is important for producing the series of interactions that keep most of the rainfall away from inflow and allow some of the downdraft or rainfall to enhance convergence with the inflow to produce a rapid series of new updraft cores that together form what is sometimes called quasi-steady updraft structure (e.g., Lemon and Doswell 1979; Betten et al. 2018).

Taylor et al. (1984) was the first to show that lightning was concentrated in a mushroom shape around and above the updraft of a strong storm that was not a supercell and to contrast that distribution with the much more spatially extensive distribution of lightning in a supercell. In a multicell storm, charge is produced in the updraft of each cell and then spreads outward in the upper part of the storm as the updraft diverges, with some eventually descending to somewhat lower levels as precipitation falls. The falling precipitation eventually cuts off inflow to the updraft as the cell begins dissipating. Although the lightning of adjoining cells can interact with multiple cells that are in different stages of evolution, the basic charge structure of each cell typically follows this relatively simple evolution (see, for example, Bruning et al. 2007).

In a supercell, rotating updrafts and strong downdrafts occur simultaneously, wrapped around each other in a complex structure, with additional precipitation falling outside this interlocked structure. As discussed in the previous section, the charge and lightning close to the rotating updraft tend to form a ring around the periphery of the updraft at upper levels (e.g., Payne et al. 2010; Calhoun et al. 2013). Furthermore, updrafts persist much longer, for hours in some cases, than the individual updrafts in a multicell storm and tend to advect much more mass from the persistent diverging updraft into upper levels of the storm, where further charging has

been inferred to occur in gravity waves or in the secondary convection that forms from descending precipitation in anvils (e.g., Kuhlman et al. 2009; Weiss et al. 2012). Some kind of interaction in the outflow probably was responsible for the small flashes initiated in the forward flank of the Kingfisher storm. Although there is no known link between lightning and tornadoes, Stough et al. (2017) observed lightning jumps associated with the increasing strength of mid-level mesocyclones in several supercell thunderstorms.

The charge structure of MCSs has been observed to be similar in the convective line to that of multicell storms, but has the added complexity of charge advected into and forming within the stratiform region (Stolzenburg et al. 1998b, Ely et al. 2008, Lund et al. 2009), where it often descends slowly to the melting level. This made the inferred charge structure of the MCS very different from that of the other two cases. Positive charge existed through the whole depth of the storm above the 0^{o}C level at early analysis times when positive charge was descending in the stratiform region from the upper part of the convective line and collapsed to a lower level, around mid-levels of the system (e.g., between 4 and 8 km AGL, or 0^{o}C and -20^{o}C; see Figures 199e-204e) by later analysis times as the analyzed part of the convective line weakened. Most of the storm's negative charge was located at lower levels compared with positive charge. At earlier times, negative charge was inferred between 0^{o}C and -20^{o}C; by the end of the period, negative charge was concentrated below the melting level, at the melting level, and at the top of the storm's reflectivity signature (e.g. Figures 199f-204f). This upper level was inferred to be screening layer charge, similar to the screening layer inferred by Stolzenburg et al. (1998b).

Like the other two storms in this study, both polarities of charge were found on all identified hydrometeor classes. However, positive charge was preferentially associated with the

dry snow and vertically aligned ice categories, while negative charge was preferentially associated with graupel, dry snow, wet snow, and rain (e.g. Figures 193e,f-198e,f).

The positive charge in the storm's mid-levels was most likely generated via the noninductive mechanism and advected rearward, where it may have been enhanced by further in-situ charge generation, consistent with the findings of past studies (e.g., Carey et al. 2005; Lang and Rutledge 2008; Silveira 2016). The flashes traversing predominantly positive charge in the MCS generally were initiated near the convective line and propagated west into the developing transition zone and stratiform region, as described in section 6.1. The presence of large sections of vertically aligned ice identified by the HCA in the stratiform region at different times suggests locally strong electric fields forcing the alignment of the ice particles there, a phenomenon documented in past studies such as Biggerstaff et al. (2017), which was also discussed in section 6.1. The very large sizes of flashes exhibiting this behavior implies some continuity between the positive charge in the convective line and the developing transition zone, indicating that charge advection from the convective line was at work, although it probably was also enhanced by some in-situ charge generation through this region due to the weak vertical motions of decaying cells advected rearward into the developing stratiform region (e.g. Biermann 2010). The upper negative charge region observed at later times in the analysis period was probably a screening layer which developed as the transition zone and stratiform region did, since it was located at the top of the storm's reflectivity signature and had a weaker signal than other charge regions. The negative charge identified around the melting level, especially at later times, was most likely generated by multiple mechanisms. Negative charge in the low levels of the leading convective line was most likely generated by noninductive charging. Negative charge identified in the developing transition zone was likely advected from the leading convective line and then

possibly enhanced by the inductive melting charge generation mechanism (e.g. Stolzenburg and Marshall 2008; Silveira 2016). The negative charge below the melting level was likely due to charged aggregates and graupel melting, although there could have also been charge deposition by horizontally extensive lightning propagating inside the cloud near the melting level.

The discussion of charge distribution across these three storms would be remiss without reviewing upon of the limitations of the charge analysis procedure. Inferring charge from LMA data was described in section 2.1. As mentioned there, this method relies on the existence of lightning channels to detect space charge and is biased in favor of positive charge identified from the propagation of highly impulsive negative leaders. Lightning is initiated when electric fields in a storm enhance locally to magnitudes high enough to achieve dielectric breakdown, and that breakdown is bidirectional. A negative leader propagates into positive charge, and a positive leader propagates into negative charge. These leaders tend to propagate toward charge regions to maximize the electrical potential difference between the positive and negative ends of the flash. Brothers et al. (2018), in addition to simulating the charge distribution of a supercell and a multicell storm, also simulated their electrical potential distribution. Their cross-sections showed the distribution of potential was much smoother and more uniform than the distribution of charge, and the potential distribution was almost identical to the standard results of charge inferred from LMA data, without the higher order details of the charge distribution itself. Comparing the charge analysis shown in this study with the results of Brothers et al., the true charge distribution in all three storms observed herein was undoubtedly more complicated than what was inferred from the LMA data. The Kingfisher storm exhibited the most complex inferred charge distribution because the greater variety of flash shapes and sizes in that storm enabled a more detailed charge analysis than could be performed on the other two storms.

Ultimately, the charge distribution in all three storms perhaps should be expressed in terms of *potential* rather than charge, because the charge inferred from LMA data is more representative of the potential distribution than the charge distribution of storms, although the two are obviously related.

6.3 Concluding Remarks

This study presented a set of spatiotemporal analyses of three storms having much different morphologies, all of which were sampled during the Deep Convective Clouds and Chemistry experiment. The availability of multi-Doppler and dual-polarimetric mobile radar data coupled with data from the Oklahoma Lightning Mapping Array enabled a highly detailed study of the observed relationships between lightning and storm structure, with a focus on the microphysical and kinematic characteristics of storms.

Relationships between lightning characteristics and storm structure observed in this study which support the findings of past studies include:

- Total flash rate increased during periods of updraft intensification and decreased during periods of updraft decay in the supercell and multicell storms.
- Total flash rate also tended to increase with increasing estimated graupel content and to decrease with decreasing graupel content in the supercell and multicell storms.
- Flashes in and around storm updrafts decreased in size with increasing updraft intensity and increased in size with decreasing updraft intensity.
- The supercell was the only storm with a lightning hole because it was the only storm with a mesocyclonic updraft. The lightning hole was aligned with and extended slightly above the storm's BWER.

- An overshooting top VHF signature was observed in both the supercell storm and the multicell storm. The OT signature in the supercell first appeared when the updraft increased in intensity and was consistently present for the rest of the analysis period. The OT signature in the multicell storm appeared more transient but was still related to increases in updraft intensity.
- The MCS was dominated by very large flashes, several of which propagated from the convective line rearward into the developing transition zone and stratiform region.
- Inferred charge distributions for all three storms relative to the distribution of different hydrometeor classes and updrafts supports the hypothesis that the noninductive mechanism is the primary source of charge generation in thunderstorms.

Further conclusions which have been related back to a few past studies but which are less certain, based on the evidence provided, include:

- Flashes were initiated preferentially in gradients of w and on boundaries between regions dominated by different hydrometeor classes (and thus tending to carry opposing polarities of charge) in the supercell and multicell storms.
- Flashes in the supercell also were initiated frequently tens of kilometers downstream from the mesocyclone updraft, in a region of lightning activity in the supercell storm's forward flank that was characterized by small, high-altitude flashes in both regions of graupel and regions of dry snow that were identified by the HCA.
- Flashes were initiated at much lower elevations in the MCS than in the supercell or in the multicell storms, probably because convection in the leading line was much weaker and

shallower than convection in the other two cases and possibly because the majority of charge was produced at lower altitudes of the mixed phase region rather than throughout the region as a consequence of precipitation growth in upper regions being later and of shorter duration than usual in the evolution of stronger cells.

- Charge advection in the turbulent flow due to large gradients in vertical velocity likely contributed to the frequency of small flashes in active convective regions in all three storms, although small flashes were less prevalent in the MCS.
- The charge regions near the melting level in the MCS support the hypothesis that some inductive process involving melting contributes substantially to charge generation in the transition zones and stratiform regions of MCSs.
- LMA-inferred charge distributions represent the distribution of electrical potential in storms better than the detailed structure of their charge.

Even with the expansive analysis shown here, there are still unanswered questions and unexplored topics related to the analyses discussed. Some of these include: further details concerning the generation and maintenance of charge in storms, especially in the stratiform regions of MCSs; how much graupel is required to generate charge in a storm via the noninductive mechanism; the exact conditions required to initiate flashes; and quantitative relationships between flash size distribution and storm intensity. Answering these questions and others relating lightning and meteorology will take an extensive aggregation of observational and modeling case studies, with larger-scale statistical studies where possible. Modeling studies are essential, because the current state of observational technology is not advanced enough to measure the full temporal and spatial scales of processes that control lightning inside storms.

Future work with the data presented in this study should include: more quantitative bulk relationships between lightning attributes, hydrometeor types, and the three-dimensional wind fields; comparing the DLA and HCA results more directly; and modeling studies based on our present understanding of hydrometeor electrification processes to compare how variations in microphysics and kinematics affect the distribution of charge and lightning across these three storm morphologies.

References

Alford, A. A., M. I. Biggerstaff, G. D. Carrie, J. L. Schroeder, B. D. Hirth, and S. M. Waugh, 2019: Near-Surface Maximum Winds During the Landfall of Hurricane Harvey. *Geophys. Res. Lett.*, **46**, 973–982, doi:10.1029/2018GL080013. https://doi.org/10.1029/2018GL080013.

Barth, M. C., and Coauthors, 2015: The deep convective clouds and chemistry (DC3) field campaign. *Bull. Am. Meteorol. Soc.*, **96**, 1281–1310, doi:10.1175/BAMS-D-13-00290.1. http://dx.doi.org/10.1175/BAMS-D-13-00290.1.

Betten, D., 2018: A Lagrangian perspective of mesocyclones and downdrafts in observed and numerically simulated supercells. Dissertation (Ph.D. in Metr.)—University of Oklahoma, 278 pp. https://shareok.org/handle/11244/299851

Betten, D. P., M. I. Biggerstaff, and C. L. Ziegler, 2018: Three-dimensional storm structure and low level boundaries at different stages of cyclic mesocyclone evolution in a high-precipitation tornadic supercell, *Advances in Meteorology*, **2018**, 9432670, 24 pp, doi: 10.1155/2018/9432670

Biermann, N. S., 2010: Lightning characteristics, kinematic structure, and mesoscale evolution of the 19 June 2004 TELEX MCS. Thesis (M.S. in Metr.)—University of Oklahoma.

Biggerstaff, M. I., and R. A. Houze, 1991: Midlevel Vorticity Structure of the 10–11 June 1985 Squall Line. *Mon. Weather Rev.*, **119**, 3066–3079, doi:10.1175/1520-0493(1991)119<3066:MVSOTJ>2.0.CO;2. http://dx.doi.org/10.1175/1520-0493(1991)119%3C3034:KAPSOT%3E2.0.CO.

Biggerstaff, M. I., and R. A. Houze, 1993: Kinematics and Microphysics of the Transition Zone of the 10–11 June 1985 Squall Line. *J. Atmos. Sci.*, **50**, 3091–3110, doi:10.1175/1520-0469(1993)050<3091:KAMOTT>2.0.CO;2. http://dx.doi.org/10.1175/1520-0469(1993)050%3C3091:KAMOTT%3E2.0.CO.

Biggerstaff, M. I., and Coauthors, 2005: The Shared Mobile Atmospheric Research and Teaching Radar: A Collaboration to Enhance Research and Teaching. *Bull. Am. Meteorol. Soc.*, **86**, 1263–1274, doi:10.1175/BAMS-86-9-1263. http://dx.doi.org/10.1175/BAMS-86-9-1263.

Brothers, M. D., E. C. Bruning, and E. R. Mansell, 2018: Investigating the Relative Contributions of Charge Deposition and Turbulence in Organizing Charge within a Thunderstorm. *J. Atmos. Sci.*, **75**, 3265–3284, doi:10.1175/JAS-D-18-0007.1. https://doi.org/10.1175/JAS-D-18-0007.1.

Bruning, E. C., 2012: The West Texas LMA. *GLM Science Team Meeting*, Huntsville, AL.

Bruning, E. C., and D. R. MacGorman, 2013: Theory and Observations of Controls on Lightning Flash Size Spectra. *J. Atmos. Sci.*, **70**, 4012–4029, doi:10.1175/JAS-D-12-0289.1. http://dx.doi.org/10.1175/JAS-D-12-0289.1.

Bruning, E. C., W. D. Rust, D. R. MacGorman, M. I. Biggerstaff, and T. J. Schuur, 2010: Formation of Charge Structures in a Supercell. *Mon. Weather Rev.*, **138**, 3740–3761, doi:10.1175/2010MWR3160.1. http://dx.doi.org/10.1175/2010MWR3160.1.

Bruning, E. C., W. D. Rust, T. J. Schuur, D. R. MacGorman, P. R. Krehbiel, and W. Rison, 2007: Electrical and Polarimetric Radar Observations of a Multicell Storm in TELEX. *Mon. Weather Rev.*, **135**, 2525–2544, doi:10.1175/MWR3421.1. http://dx.doi.org/10.1175/MWR3421.1.

Calhoun, K. M., D. R. MacGorman, C. L. Ziegler, and M. I. Biggerstaff, 2013: Evolution of Lightning Activity and Storm Charge Relative to Dual-Doppler Analysis of a High-Precipitation Supercell Storm. *Mon. Weather Rev.*, **141**, 2199–2223, doi:10.1175/MWR-D-12-00258.1. http://dx.doi.org/10.1175/MWR-D-12-00258.1.

Carey, L., and S. Rutledge, 1996: A multiparameter radar case study of the microphysical and kinematic evolution of a lightning producing storm. *Meteorol. Atmos. Phys.*, **59**, 33–64. http://link.springer.com/article/10.1007/BF01032000 (Accessed October 24, 2014).

Chauzy, S., and P. Raizonville, 1982: Space charge layers created by coronae at ground level below thunderclouds: Measurements and modeling. *J. Geophys. Res. Ocean.*, **87**, 3143–3148, doi:10.1029/JC087iC04p03143. https://doi.org/10.1029/JC087iC04p03143.

Coleman, L. M., T. C. Marshall, M. Stolzenburg, T. Hamlin, P. R. Krehbiel, W. Rison, and R. J. Thomas, 2003: Effects of charge and electrostatic potential on lightning propagation. *J. Geophys. Res. Atmos.*, **108**, doi:10.1029/2002JD002718. https://doi.org/10.1029/2002JD002718.

Crum, T. D., and R. L. Alberty, 1993: The WSR-88D and the WSR-88D Operational Support Facility. *Bull. Am. Meteorol. Soc.*, **74**, 1669–1687, doi:10.1175/1520-0477(1993)074<1669:TWATWO>2.0.CO;2. http://dx.doi.org/10.1175/1520-0477(1993)074%3C1669:TWATWO%3E2.0.CO.

Deierling, W., and W. A. Petersen, 2008: Total lightning activity as an indicator of updraft characteristics. *J. Geophys. Res. Atmos.*, **113**, n/a-n/a, doi:10.1029/2007JD009598. http://dx.doi.org/10.1029/2007JD009598.

DiGangi, E. A., D. R. MacGorman, C. L. Ziegler, D. Betten, M. Biggerstaff, M. Bowlan, and C. K. Potvin, 2016: An overview of the 29 May 2012 Kingfisher supercell during DC3. *J. Geophys. Res. Atmos.*, **121**, 14,314-316,343, doi:10.1002/2016JD025690. http://dx.doi.org/10.1002/2016JD025690.

DiGangi, E. A., 2014: A Study Of The Electrical, Microphysical, And Kinematic Properties Of The 29 May 2012 Kingfisher Supercell. Thesis (M.S. in Metr.)—University of Oklahoma, 106 pp. https://shareok.org/handle/11244/14246.

Dolan, B., and S. A. Rutledge, 2009: A Theory-Based Hydrometeor Identification Algorithm for X-Band Polarimetric Radars. *J. Atmos. Ocean. Technol.*, **26**, 2071–2088, doi:10.1175/2009JTECHA1208.1. http://dx.doi.org/10.1175/2009JTECHA1208.1.

Dolan, B., S. A. Rutledge, S. Lim, V. Chandrasekar, and M. Thurai, 2013: A Robust C-Band Hydrometeor Identification Algorithm and Application to a Long-Term Polarimetric Radar Dataset. *J. Appl. Meteorol. Climatol.*, **52**, 2162–2186, doi:10.1175/JAMC-D-12-0275.1. http://dx.doi.org/10.1175/JAMC-D-12-0275.1.

Doswell III, C. A., and D. W. Burgess, 1993: Tornadoes and Toraadic Storms: a Review of Conceptual Models. *Tornado Its Struct. Dyn. Predict. Hazards*, doi:doi:10.1029/GM079p0161. https://doi.org/10.1029/GM079p0161.

Dye, J. E., W. P. Winn, J. J. Jones, and D. W. Breed, 1989: The electrification of New Mexico thunderstorms: 1. Relationship between precipitation development and the onset of electrification. *J. Geophys. Res. Atmos.*, **94**, 8643–8656, doi:10.1029/JD094iD06p08643. https://doi.org/10.1029/JD094iD06p08643.

Dye, J. E., J.J. Jones, W.P. Winn, T.A. Cerni, B. Gardiner, D. Lamb, R.L. Pitter, J. Hallet, and C.P.R. Saunders, 1986: Early electrification and precipitation development in a small, isolated Montana cumulonimbus. *J. Geophys. Res. Atmos.*, **91**, 1231–1247, doi:10.1029/JD091iD01p01231. https://doi.org/10.1029/JD091iD01p01231.

Emersic, C., P. L. Heinselman, D. R. MacGorman, and E. C. Bruning, 2011: Lightning Activity in a Hail-Producing Storm Observed with Phased-Array Radar. *Mon. Weather Rev.*, **139**, 1809–1825, doi:10.1175/2010MWR3574.1. http://dx.doi.org/10.1175/2010MWR3574.1.

Ely, B. L., R. E. Orville, L. D. Carey, and C. L. Hodapp, 2008: Evolution of the total lightning structure in a leading-line, trailing-stratiform mesoscale convective system over Houston, Texas. *J. Geophys. Res.*, **113,** D008113, doi: 10.1029/2007JD008445.Fernández-Cabán, P. L., and Coauthors, 2018: Observing Hurricane Harvey's Eyewall at Landfall. *Bull. Am. Meteorol. Soc.*, doi:10.1175/BAMS-D-17-0237.1. https://doi.org/10.1175/BAMS-D-17-0237.1.

Fuchs, B. R., E. C. Bruning, S. A. Rutledge, L. D. Carey, P. R. Krehbiel, and W. Rison, 2016: Climatological analyses of LMA data with an open-source lightning flash-clustering algorithm. *J. Geophys. Res. Atmos.*, **121**, 8625–8648, doi:10.1002/2015JD024663. https://doi.org/10.1002/2015JD024663.

Gao, J., M. Xue, A. Shapiro, and K. K. Droegemeier, 1999: A Variational Method for the Analysis of Three-Dimensional Wind Fields from Two Doppler Radars. *Mon. Weather*

Rev., **127**, 2128–2142, doi:10.1175/1520-0493(1999)127<2128:AVMFTA>2.0.CO;2. https://doi.org/10.1175/1520-0493(1999)127%3C2128:AVMFTA%3E2.0.CO.

Gaskell, W., and A. J. Illingworth, 1980: Charge transfer accompanying individual collisions between ice particles and its role in thunderstorm electrification. *Q. J. R. Meteorol. Soc.*, **106**, 841–854, doi:10.1002/qj.49710645013. http://dx.doi.org/10.1002/qj.49710645013.

Goodman, S. J., D. E. Buechler, P. D. Wright, and W. D. Rust, 1988: Lightning and precipitation history of a microburst-producing storm. *Geophys. Res. Lett.*, **15**, 1185–1188, doi:10.1029/GL015i011p01185. https://doi.org/10.1029/GL015i011p01185.

Gu, J.-Y., A. Ryzhkov, P. Zhang, P. Neilley, M. Knight, B. Wolf, and D.-I. Lee, 2011: Polarimetric Attenuation Correction in Heavy Rain at C Band. *J. Appl. Meteorol. Climatol.*, **50**, 39–58, doi:10.1175/2010JAMC2258.1. http://dx.doi.org/10.1175/2010JAMC2258.1.

Helsdon Jr., J. H., W. A. Wojcik, and R. D. Farley, 2001: An examination of thunderstorm-charging mechanisms using a two-dimensional storm electrification model. *J. Geophys. Res. Atmos.*, **106**, 1165–1192, doi:10.1029/2000JD900532. https://doi.org/10.1029/2000JD900532.

Helsdon Jr., J. H., S. Gattaleeradapan, R. D. Farley, and C. C. Waits, 2002: An examination of the convective charging hypothesis: Charge structure, electric fields, and Maxwell currents. *J. Geophys. Res. Atmos.*, **107**, ACL 9-1-ACL 9-26, doi:10.1029/2001JD001495. https://doi.org/10.1029/2001JD001495.

Hildebrand, P. H., R. A. Oye, and R. E. Carbone, 1981: X-hand vs C-band Aircraft Radar: The Relative Effects of Beamwidth and Attenuation in Severe Storm Situations. *J. Appl. Meteorol.*, **20**, 1353–1361, doi:10.1175/1520-0450(1981)020<1353:XHVCBA>2.0.CO;2. https://doi.org/10.1175/1520-0450(1981)020%3C1353:XHVCBA%3E2.0.CO.

Houze, R. A., M. I. Biggerstaff, S. A. Rutledge, and B. F. Smull, 1989: Interpretation of Doppler Weather Radar Displays of Midlatitude Mesoscale Convective Systems. *Bull. Am. Meteorol. Soc.*, **70**, 608–619, doi:10.1175/1520-0477(1989)070<0608:IODWRD>2.0.CO;2. http://dx.doi.org/10.1175/1520-0477(1989)070%3C0608:IODWRD%3E2.0.CO.

Hunter, S. M., T. J. Schuur, T. C. Mapshall, and W. D. Rust, 1992: Electric and Kinematic Structure of the Oklahoma Mesoscale Convective System of 7 June 1989. *Mon. Weather Rev.*, **120**, 2226–2239, doi:10.1175/1520-0493(1992)120<2226:EAKSOT>2.0.CO;2. http://dx.doi.org/10.1175/1520-0493(1992)120%3C2226:EAKSOT%3E2.0.CO.

Kasemir, H. W., 1960: A contribution to the electrostatic theory of a lightning discharge. *J. Geophys. Res.*, **65**, 1873–1878, doi:10.1029/JZ065i007p01873. http://dx.doi.org/10.1029/JZ065i007p01873.

Kessler, E., 1969: *On the Distribution and Continuity of Water Substance in Atmospheric Circulations, Meteorol. Monogr., vol. 10,* American Meteorological Society, Boston, Mass., 84 pp.

Klemp, J. B., R. B. Wilhelmson, and P. S. Ray, 1981: Observed and Numerically Simulated Structure of a Mature Supercell Thunderstorm. *J. Atmos. Sci.,* **38**, 1558–1580, doi:10.1175/1520-0469(1981)038<1558:OANSSO>2.0.CO;2. https://doi.org/10.1175/1520-0469(1981)038%3C1558:OANSSO%3E2.0.CO.

Kozlowski, D. M., and L. D. Carey, 2014: An analysis of lightning holes in northern Alabama severe storms using a lightning mapping array and dual-polarization radar. *Fifth Int. Lightning Meteorology Conf.,* Tucson, AZ, Vaisala http://www.vaisala.com/Vaisala Documents/Scientific papers/2014 ILDC ILMC/ILMC-Thursday/Kozlowski and Carey-An Analysis of Lightning Holes in Northern Alabama-2014-ILDC-ILMC.pdf.

Krehbiel, P. R., R. J. Thomas, W. Rison, T. Hamlin, J. Harlin, and M. Davis, 2000: GPS-based mapping system reveals lightning inside storms. *Eos, Trans. Am. Geophys. Union*, **81**, 21–25, doi:10.1029/00EO00014. http://dx.doi.org/10.1029/00EO00014.

Kuhlman, K. M., C. L. Ziegler, E. R. Mansell, D. R. MacGorman, and J. M. Straka, 2006: Numerically Simulated Electrification and Lightning of the 29 June 2000 STEPS Supercell Storm. *Mon. Weather Rev.*, **134**, 2734–2757, doi:10.1175/MWR3217.1. http://dx.doi.org/10.1175/MWR3217.1.

Kuhlman, K. M., D. R. MacGorman, M. I. Biggerstaff, and P. R. Krehbiel, 2009: Lightning initiation in the anvil of supercell storms. *Geophys. Res. Lttr.*, **36**, L07802, doi: 10.1029/2008GL036650.

Lang, T. J., and Coauthors, 2004: The Severe Thunderstorm Electrification and Precipitation Study. *Bull. Am. Meteorol. Soc.*, **85**, 1107–1125, doi:10.1175/BAMS-85-8-1107. http://dx.doi.org/10.1175/BAMS-85-8-1107.

Lang, T. J., and S. A. Rutledge, 2002: Relationships between Convective Storm Kinematics, Precipitation, and Lightning. *Mon. Weather Rev.*, **130**, 2492–2506, doi:10.1175/1520-0493(2002)130<2492:RBCSKP>2.0.CO;2. https://doi.org/10.1175/1520-0493(2002)130%3C2492:RBCSKP%3E2.0.CO.

Leise, J. A., 1981: A multidimensional scale-telescoped filter and data extension package. NOAA Tech. Memo. ERL WPL-82, 18 pp. [NTIS PB82-164104.].

Lemon, L. R., D. W. Burgess, and R. A. Brown, 1978: Tornadic Storm Airflow and Morphology Derived from Single-Doppler Radar Measurements. *Mon. Weather Rev.,* **106**, 48–61, doi:10.1175/1520-0493(1978)106<0048:TSAAMD>2.0.CO;2. https://doi.org/10.1175/1520-0493(1978)106%3C0048:TSAAMD%3E2.0.CO.

Lemon, L. R., and C. A. Doswell, 1979: Severe Thunderstorm Evolution and Mesocyclone Structure as Related to Tornadogenesis. *Mon. Weather Rev.*, **107**, 1184–1197, doi:10.1175/1520-0493(1979)107<1184:STEAMS>2.0.CO;2. http://dx.doi.org/10.1175/1520-0493(1979)107%3C1184:STEAMS%3E2.0.CO.

Livingston, J. M., and E. P. Krider, 1978: Electric fields produced by Florida thunderstorms. *J. Geophys. Res. Ocean.*, **83**, 385–401, doi:10.1029/JC083iC01p00385. https://doi.org/10.1029/JC083iC01p00385.

Lund, N. R., D. R. MacGorman, T. J. Schuur, M. I. Biggerstaff, and W. D. Rust, 2009: Relationships between Lightning Location and Polarimetric Radar Signatures in a Small Mesoscale Convective System. *Mon. Weather Rev.*, **137**, 4151–4170, doi:10.1175/2009MWR2860.1. http://dx.doi.org/10.1175/2009MWR2860.1.

MacGorman, D. R., and W. D. Rust, 1998: *The Electrical Nature of Storms*. Oxford University Press, https://books.google.com/books?id=_NbHNj7KJecC.

MacGorman, D. R., A. A. Few, and T. L. Teer, 1981: Layered Lightning Activity. *J. Geophys. Res.*, **86**, 9900–9910.

MacGorman, D. R., M. S. Elliott, and E. DiGangi, 2017: Electrical discharges in the overshooting tops of thunderstorms. *J. Geophys. Res. Atmos.*, **122**, 2929–2957, doi:10.1002/2016JD025933. https://doi.org/10.1002/2016JD025933.

MacGorman, D. R., D. W. Burgess, V. Mazur, W. D. Rust, W. L. Taylor, and B. C. Johnson, 1989: Lightning Rates Relative to Tornadic Storm Evolution on 22 May 1981. *J. Atmos. Sci.*, **46**, 221–251, doi:10.1175/1520-0469(1989)046<0221:LRRTTS>2.0.CO;2. http://dx.doi.org/10.1175/1520-0469(1989)046%3C0221:LRRTTS%3E2.0.CO.

MacGorman, D. R., W. D. Rust, P. Krehbiel, W. Rison, E. Bruning, and K. Wiens, 2005: The Electrical Structure of Two Supercell Storms during STEPS. *Mon. Weather Rev.*, **133**, 2583–2607, doi:10.1175/MWR2994.1. http://dx.doi.org/10.1175/MWR2994.1.

MacGorman, D. R., and Coauthors, 2008: TELEX The Thunderstorm Electrification and Lightning Experiment. *Bull. Am. Meteorol. Soc.*, **89**, 997–1013, doi:10.1175/2007BAMS2352.1. http://dx.doi.org/10.1175/2007BAMS2352.1.

Mansell, E. R., D. R. MacGorman, C. L. Ziegler, and J. M. Straka, 2002: Simulated three-dimensional branched lightning in a numerical thunderstorm model. *J. Geophys. Res. Atmos.*, **107**, ACL 2-1-ACL 2-12, doi:10.1029/2000JD000244. http://dx.doi.org/10.1029/2000JD000244.

Mansell, E. R., D. R. MacGorman, C. L. Ziegler, and J. M. Straka, 2005: Charge structure and lightning sensitivity in a simulated multicell thunderstorm. *J. Geophys. Res. Atmos.*, **110**, n/a-n/a, doi:10.1029/2004JD005287. http://dx.doi.org/10.1029/2004JD005287.

Mansell, E. R., C. L. Ziegler, and E. C. Bruning, 2010: Simulated Electrification of a Small Thunderstorm with Two-Moment Bulk Microphysics. *J. Atmos. Sci.*, **67**, 171–194, doi:10.1175/2009JAS2965.1. http://dx.doi.org/10.1175/2009JAS2965.1.

Marquis, J., Y. Richardson, P. Markowski, J. Wurman, K. Kosiba, and P. Robinson, 2016: An Investigation of the Goshen County, Wyoming, Tornadic Supercell of 5 June 2009 Using EnKF Assimilation of Mobile Mesonet and Radar Observations Collected during VORTEX2. Part II: Mesocyclone-Scale Processes Affecting Tornado Formation, Maintenance, and Decay. *Mon. Weather Rev.*, **144**, 3441–3463, doi:10.1175/MWR-D-15-0411.1. https://doi.org/10.1175/MWR-D-15-0411.1.

Marshall, T. C., and W. D. Rust, 1993: Two Types of Vertical Electrical Structures in Stratiform Precipitation Regions of Mesoscale Convective Systems. *Bull. Am. Meteorol. Soc.*, **74**, 2159–2170, doi:10.1175/1520-0477(1993)074<2159:TTOVES>2.0.CO;2. http://dx.doi.org/10.1175/1520-0477(1993)074%3C2159:TTOVES%3E2.0.CO.

Marshall, T. C., and W. D. Rust, 1991: Electric field soundings through thunderstorms. *J. Geophys. Res. Atmos.*, **96**, 22297–22306, doi:10.1029/91JD02486. http://dx.doi.org/10.1029/91JD02486.

Marshall, T. C., W. D. Rust, W. P. Winn, and K. E. Gilbert, 1989: Electrical structure in two thunderstorm anvil clouds. *J. Geophys. Res. Atmos.*, **94**, 2171–2181, doi:10.1029/JD094iD02p02171. http://dx.doi.org/10.1029/JD094iD02p02171.

Marshall, T.C., W.D. Rust, and M. Stolzenburg, 1995: Electrical structure and updraft speeds in thunderstorms over the southern Great Plains. *J. Geophys. Res.*, **100**, 1001-1015.

Mazur, V., 1989: A physical model of lightning initiation on aircraft in thunderstorms. *J. Geophys. Res. Atmos.*, **94**, 3326–3340, doi:10.1029/JD094iD03p03326. http://dx.doi.org/10.1029/JD094iD03p03326.

Mazur, V., 2002: Physical processes during development of lightning flashes. *Comptes Rendus Phys.*, **3**, 1393–1409, doi:https://doi.org/10.1016/S1631-0705(02)01412-3. http://www.sciencedirect.com/science/article/pii/S1631070502014123.

McCaul, E. W., S. J. Goodman, K. M. LaCasse, and D. J. Cecil, 2009: Forecasting Lightning Threat Using Cloud-Resolving Model Simulations. *Weather Forecast.*, **24**, 709–729, doi:10.1175/2008WAF2222152.1. https://doi.org/10.1175/2008WAF2222152.1.

Mecikalski, R. M., A. L. Bain, and L. D. Carey, 2015: Radar and Lightning Observations of Deep Moist Convection across Northern Alabama during DC3: 21 May 2012. *Mon. Weather Rev.*, doi:10.1175/MWR-D-14-00250.1.

Oye, R. A., C. Mueller, and S. Smith, 1995: Software for the radar translation, visualization, editing, and interpolation. *27th Conf. on Radar Meteorology*, Vail, CO, Amer. Meteor. Soc., 359–361.

Parker, M. D., and R. H. Johnson, 2000: Organizational Modes of Midlatitude Mesoscale Convective Systems. *Mon. Weather Rev.*, **128**, 3413–3436, doi:10.1175/1520-0493(2001)129<3413:OMOMMC>2.0.CO;2. http://dx.doi.org/10.1175/1520-0493(2001)129%3C3413:OMOMMC%3E2.0.CO.

Payne, C. D., T. J. Schuur, D. R. MacGorman, M. I. Biggerstaff, K. M. Kuhlman, and W. D. Rust, 2010: Polarimetric and Electrical Characteristics of a Lightning Ring in a Supercell Storm. *Mon. Weather Rev.*, **138**, 2405–2425, doi:10.1175/2009MWR3210.1. http://dx.doi.org/10.1175/2009MWR3210.1.

Petersen, D., M. Bailey, W. H. Beasley, and J. Hallett, 2008: A brief review of the problem of lightning initiation and a hypothesis of initial lightning leader formation. *J. Geophys. Res. Atmos.*, **113**, n/a-n/a, doi:10.1029/2007JD009036. http://dx.doi.org/10.1029/2007JD009036.

Potvin, C. K., D. Betten, L. J. Wicker, K. L. Elmore, and M. I. Biggerstaff, 2012: 3DVAR versus Traditional Dual-Doppler Wind Retrievals of a Simulated Supercell Thunderstorm. *Mon. Weather Rev.*, **140**, 3487–3494, doi:10.1175/MWR-D-12-00063.1. https://doi.org/10.1175/MWR-D-12-00063.1.

Potvin, C. K., A. Shapiro, and M. Xue, 2011: Impact of a Vertical Vorticity Constraint in Variational Dual-Doppler Wind Analysis: Tests with Real and Simulated Supercell Data. *J. Atmos. Ocean. Technol.*, **29**, 32–49, doi:10.1175/JTECH-D-11-00019.1. https://doi.org/10.1175/JTECH-D-11-00019.1.

Ray, P. S., D. R. Macgorman, W. D. Rust, W. L. Taylor, and L. W. Rasmussen, 1987: Lightning location relative to storm structure in a supercell storm and a multicell storm. *J. Geophys. Res. Atmos.*, **92**, 5713–5724, doi:10.1029/JD092iD05p05713. http://dx.doi.org/10.1029/JD092iD05p05713.

Rison, W., R. J. Thomas, P. R. Krehbiel, T. Hamlin, and J. Harlin, 1999: A GPS-based three-dimensional lightning mapping system: Initial observations in central New Mexico. *Geophys. Res. Lett.*, **26**, 3573–3576, doi:10.1029/1999GL010856. http://dx.doi.org/10.1029/1999GL010856.

Rison, W., P. R. Krehbiel, M. G. Stock, H. E. Edens, X.-M. Shao, R. J. Thomas, M. A. Stanley, and Y. Zhang, 2016: Observations of narrow bipolar events reveal how lightning is initiated in thunderstorms. *Nat. Commun.*, **7**, 10721. http://dx.doi.org/10.1038/ncomms10721.

Rust, W. D., and D. R. MacGorman, 2002: Possibly inverted-polarity electrical structures in thunderstorms during STEPS. *Geophys. Res. Lett.*, **29**, 12–13, doi:10.1029/2001GL014303. http://dx.doi.org/10.1029/2001GL014303.

Rutledge, S. A., and R. A. Houze, 1987: A Diagnostic Modelling Study of the Trailing Stratiform Region of a Midlatitude Squall Line. *J. Atmos. Sci.*, **44**, 2640–2656, doi:10.1175/1520-0469(1987)044<2640:ADMSOT>2.0.CO;2. http://dx.doi.org/10.1175/1520-0469(1987)044%3C2640:ADMSOT%3E2.0.CO.

Saunders, C. P. R., 1993: A Review of Thunderstorm Electrification Processes. *J. Appl. Meteorol.*, **32**, 642–655, doi:10.1175/1520-0450(1993)032<0642:AROTEP>2.0.CO;2. http://dx.doi.org/10.1175/1520-0450(1993)032%3C0642:AROTEP%3E2.0.CO.

Schultz, C. J., L. D. Carey, E. V Schultz, and R. J. Blakeslee, 2015: Insight into the Kinematic and Microphysical Processes that Control Lightning Jumps. *Weather Forecast.*, **30**, 1591–1621, doi:10.1175/WAF-D-14-00147.1. http://dx.doi.org/10.1175/WAF-D-14-00147.1.

Schultz, C. J., L. D. Carey, E. V Schultz, and R. J. Blakeslee, 2017: Kinematic and Microphysical Significance of Lightning Jumps versus Nonjump Increases in Total Flash Rate. *Weather Forecast.*, **32**, 275–288, doi:10.1175/WAF-D-15-0175.1. https://doi.org/10.1175/WAF-D-15-0175.1.

Schultz, C. J., W. A. Petersen, and L. D. Carey, 2009: Preliminary Development and Evaluation of Lightning Jump Algorithms for the Real-Time Detection of Severe Weather. *J. Appl. Meteorol. Climatol.*, **48**, 2543–2563, doi:10.1175/2009JAMC2237.1. http://dx.doi.org/10.1175/2009JAMC2237.1.

Schuur, T. J., W. D. Rust, B. F. Smull, and T. C. Marshall, 1991: Electrical and Kinematic Structure of the Stratiform Precipitation Region Trailing an Oklahoma Squall Line. *J. Atmos. Sci.*, **48**, 825–842, doi:10.1175/1520-0469(1991)048<0825:EAKSOT>2.0.CO;2. http://dx.doi.org/10.1175/1520-0469(1991)048%3C0825:EAKSOT%3E2.0.CO.

Schuur, T. J., and S. A. Rutledge, 2000: Electrification of Stratiform Regions in Mesoscale Convective Systems. Part I: An Observational Comparison of Symmetric and Asymmetric MCSs. *J. Atmos. Sci.*, **57**, 1961–1982, doi:10.1175/1520-0469(2000)057<1961:EOSRIM>2.0.CO;2. http://dx.doi.org/10.1175/1520-0469(2000)057%3C1961:EOSRIM%3E2.0.CO.

Sibson, R., 1981: A brief description of natural neighbor interpolation. *Interpreting multivariate data*, pp. 21–36. New York: John Wiley & Sons.

Simpson, S. G., and G. D. Robinson, 1941: The distribution of electricity in thunderclouds, II. *Proc. R. Soc. London. Ser. A. Math. Phys. Sci.*, **177**, 281 LP-329. http://rspa.royalsocietypublishing.org/content/177/970/281.abstract.

Simpson, S. G., and F. J. Scrase, 1937: The distribution of electricity in thunderclouds. *Proc. R. Soc. London. Ser. A - Math. Phys. Sci.*, **161**, 309 LP-352. http://rspa.royalsocietypublishing.org/content/161/906/309.abstract.

Stolzenburg, M., W. D. Rust, and T. C. Marshall, 1998a: Electrical structure in thunderstorm convective regions: 3. Synthesis. *J. Geophys. Res. Atmos.*, **103**, 14097–14108, doi:10.1029/97JD03545. http://dx.doi.org/10.1029/97JD03545.

Stolzenburg, M., W. D. Rust, B. F. Smull, and T. C. Marshall, 1998b: Electrical structure in thunderstorm convective regions: 1. Mesoscale convective systems. *J. Geophys. Res. Atmos.*, **103**, 14059–14078, doi:10.1029/97JD03546. http://dx.doi.org/10.1029/97JD03546.

Stolzenburg, M., 1996: An observational study of electrical structure in convective regions of mesoscale convective systems.

Stolzenburg, M., T. C. Marshall, and W. D. Rust, 2001: Serial soundings of electric field through a mesoscale convective system. *J. Geophys. Res. Atmos.*, **106**, 12371–12380, doi:10.1029/2001JD900074. http://dx.doi.org/10.1029/2001JD900074.

Stolzenburg, M., T. C. Marshall, W. D. Rust, and B. F. Smull, 1994: Horizontal Distribution of Electrical and Meteorological Conditions across the Stratiform Region of a Mesoscale Convective System. *Mon. Weather Rev.*, **122**, 1777–1797, doi:10.1175/1520-0493(1994)122<1777:HDOEAM>2.0.CO;2. http://dx.doi.org/10.1175/1520-0493(1994)122%3C1777:HDOEAM%3E2.0.CO.

Stolzenburg, M., and T. C. Marshall, 2008: Charge Structure and Dynamics in Thunderstorms. *Space Science Reviews - SPACE SCI REV*, Vol. 137 of, 355–372.

Takahashi, T., 1978: Riming Electrification as a Charge Generation Mechanism in Thunderstorms. *J. Atmos. Sci.*, **35**, 1536–1548, doi:10.1175/1520-0469(1978)035<1536:REAACG>2.0.CO;2. http://dx.doi.org/10.1175/1520-0469(1978)035%3C1536:REAACG%3E2.0.CO.

Takahashi, T., and K. Miyawaki, 2002: Reexamination of Riming Electrification in a Wind Tunnel. *J. Atmos. Sci.*, **59**, 1018–1025, doi:10.1175/1520-0469(2002)059<1018:ROREIA>2.0.CO;2. http://dx.doi.org/10.1175/1520-0469(2002)059%3C1018:ROREIA%3E2.0.CO.

Taylor, W. L., E. A. Brandes, W. D. Rust, and D. R. MacGorman, 1984: Lightning activity and severe storm structure. *Geophys. Res. Lett.*, **11**, 545–548, doi:10.1029/GL011i005p00545. https://doi.org/10.1029/GL011i005p00545.

Tessendorf, S. A., S. A. Rutledge, and K. C. Wiens, 2007: Radar and Lightning Observations of Normal and Inverted Polarity Multicellular Storms from STEPS. *Mon. Weather Rev.*, **135**, 3682–3706, doi:10.1175/2007MWR1954.1. http://dx.doi.org/10.1175/2007MWR1954.1.

Tessendorf, S. A., K. C. Wiens, and S. A. Rutledge, 2007: Radar and Lightning Observations of the 3 June 2000 Electrically Inverted Storm from STEPS. *Mon. Weather Rev.*, **135**, 3665–3681, doi:10.1175/2006MWR1953.1. http://dx.doi.org/10.1175/2006MWR1953.1.

Thomas, R. J., P. R. Krehbiel, W. Rison, S. J. Hunyady, W. P. Winn, T. Hamlin, and J. Harlin, 2004: Accuracy of the Lightning Mapping Array. *J. Geophys. Res. Atmos.*, **109**, D14207, doi:10.1029/2004JD004549. http://dx.doi.org/10.1029/2004JD004549.

Wakimoto, R. M., C. Liu, and H. Cai, 1998: The Garden City, Kansas, Storm during VORTEX 95. Part I: Overview of the Storm's Life Cycle and Mesocyclogenesis. *Mon. Weather Rev.*, **126**, 372–392, doi:10.1175/1520-0493(1998)126<0372:TGCKSD>2.0.CO;2. https://doi.org/10.1175/1520-0493(1998)126%3C0372:TGCKSD%3E2.0.CO.

Waugh, S. M., 2016: A BALLOON-BORNE PARTICLE SIZE, IMAGING, AND VELOCITY PROBE FOR IN SITU MICROPHYSICAL MEASUREMENTS. University of Oklahoma, https://shareok.org/handle/11244/45407.

Waugh, S. M., C. L. Ziegler, D. R. MacGorman, S. E. Fredrickson, D. W. Kennedy, and W. D. Rust, 2015: A Balloonborne Particle Size, Imaging, and Velocity Probe for in Situ Microphysical Measurements. *J. Atmos. Ocean. Technol.*, **32**, 1562–1580, doi:10.1175/JTECH-D-14-00216.1. http://dx.doi.org/10.1175/JTECH-D-14-00216.1.

Weiss, S. A., D. R. MacGorman, and K. M. Calhoun, 2012: Lightning in the Anvils of Supercell Thunderstorms. *Mon. Weather Rev.*, **140**, 2064–2079, doi:10.1175/MWR-D-11-00312.1. http://dx.doi.org/10.1175/MWR-D-11-00312.1.

Weiss, S. A., W. D. Rust, D. R. MacGorman, E. C. Bruning, and P. R. Krehbiel, 2008: Evolving Complex Electrical Structures of the STEPS 25 June 2000 Multicell Storm. *Mon. Weather Rev.*, **136**, 741–756, doi:10.1175/2007MWR2023.1. http://dx.doi.org/10.1175/2007MWR2023.1.

Wiens, K. C., S. A. Rutledge, and S. A. Tessendorf, 2005: The 29 June 2000 Supercell Observed during STEPS. Part II: Lightning and Charge Structure. *J. Atmos. Sci.*, **62**, 4151–4177, doi:10.1175/JAS3615.1. http://dx.doi.org/10.1175/JAS3615.1.

Williams, E., V. Mushtak, D. Rosenfeld, S. Goodman, and D. Boccippio, 2005: Thermodynamic conditions favorable to superlative thunderstorm updraft, mixed phase microphysics and lightning flash rate. *Atmos. Res.*, **76**, 288–306, doi:10.1016/J.ATMOSRES.2004.11.009. https://www.sciencedirect.com/science/article/pii/S0169809505000554?via%3Dihub (Accessed October 29, 2018).

Williams, E. R., 1989: The tripole structure of thunderstorms. *J. Geophys. Res. Atmos.*, **94**, 13151–13167, doi:10.1029/JD094iD11p13151. http://dx.doi.org/10.1029/JD094iD11p13151.

Winger, I. R., 2000: Microphysical and electrical properties of a Mesoscale convective system on June 5, 1998. Thesis (M.S.)--University of Oklahoma, 2000., .

Ziegler, C. L., 2013: A Diabatic Lagrangian Technique for the Analysis of Convective Storms. Part I: Description and Validation via an Observing System Simulation Experiment. *J. Atmos. Ocean. Technol.*, **30**, 2248–2265, doi:10.1175/JTECH-D-12-00194.1. http://dx.doi.org/10.1175/JTECH-D-12-00194.1.

Ziegler, C. L., 2013: A Diabatic Lagrangian Technique for the Analysis of Convective Storms. Part II: Application to a Radar-Observed Storm. *J. Atmos. Ocean. Technol.*, **30**, 2266–2280, doi:10.1175/JTECH-D-13-00036.1. http://dx.doi.org/10.1175/JTECH-D-13-00036.1.

Ziegler, C. L., D. R. MacGorman, J. E. Dye, and P. S. Ray, 1991: A model evaluation of noninductive graupel-ice charging in the early electrification of a mountain thunderstorm. *J. Geophys. Res. Atmos.*, **96**, 12833–12855, doi:10.1029/91JD01246. https://doi.org/10.1029/91JD01246.

Ziegler, C.L., and D.R. MacGorman, 1994: Observed lightning morphology relative to modeled space charge and electric field distributions in a tornadic storm. *J. Atmos. Sci.*, **51**, 833-851.

Appendix A: Figures

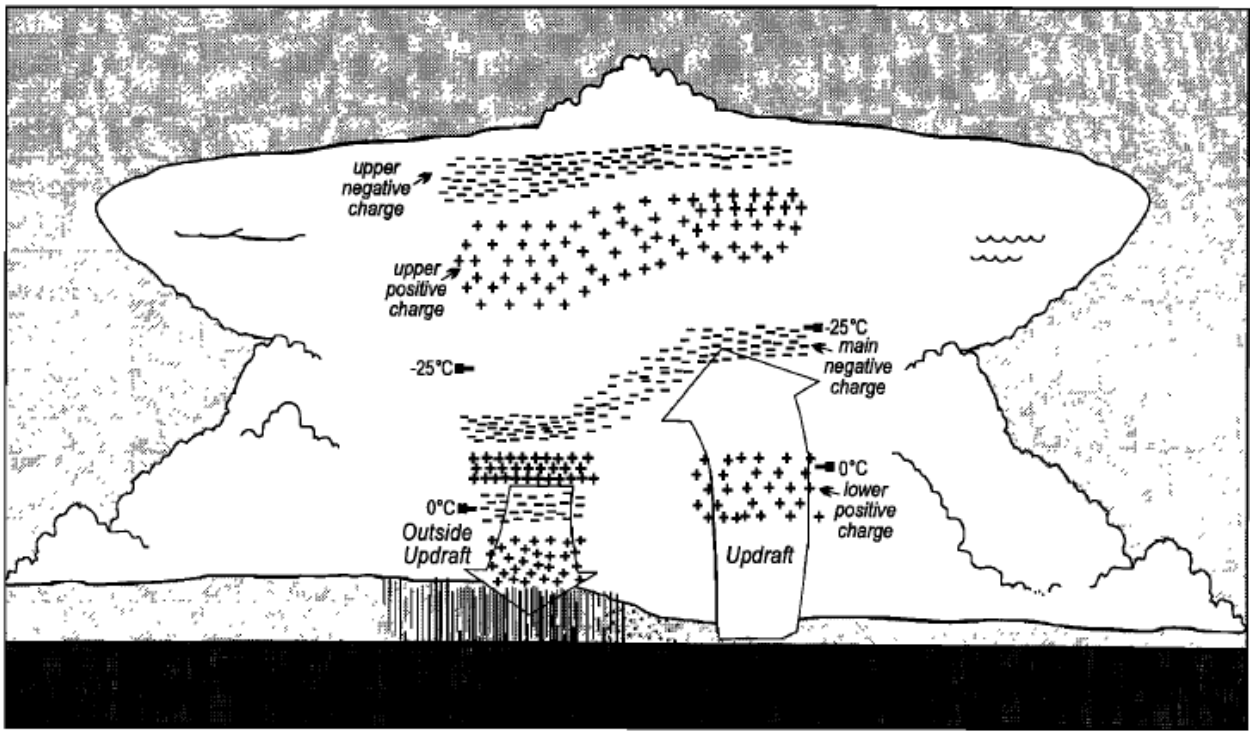

Figure 1: Conceptual model for thunderstorm charge distribution from Stolzenburg et al. (1998a).

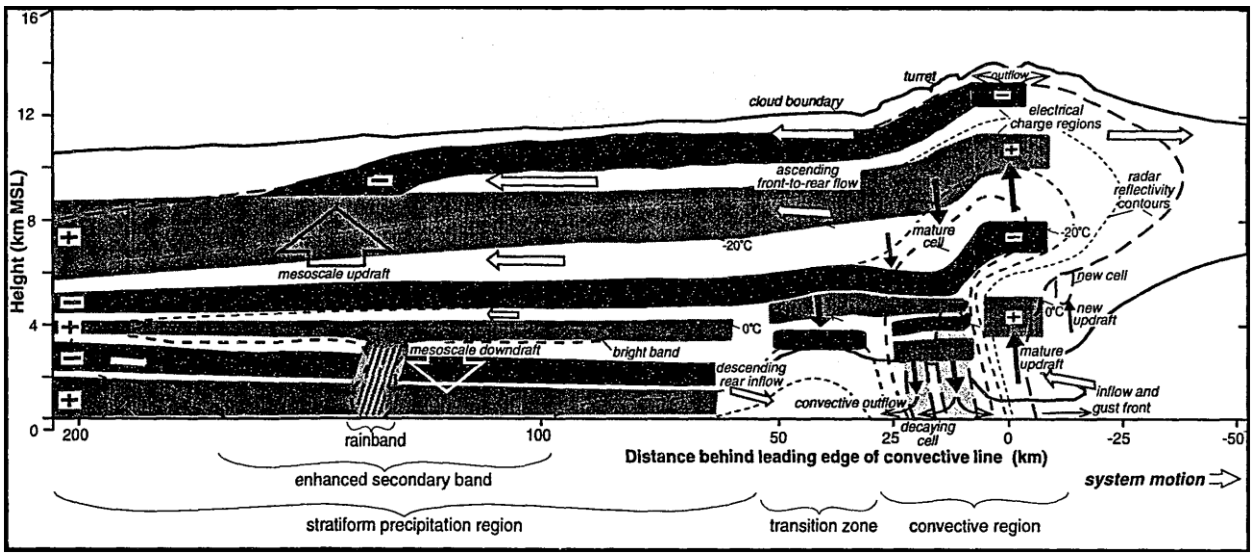

Figure 2: Conceptual model of MCS charge distribution from Stolzenburg (1996).

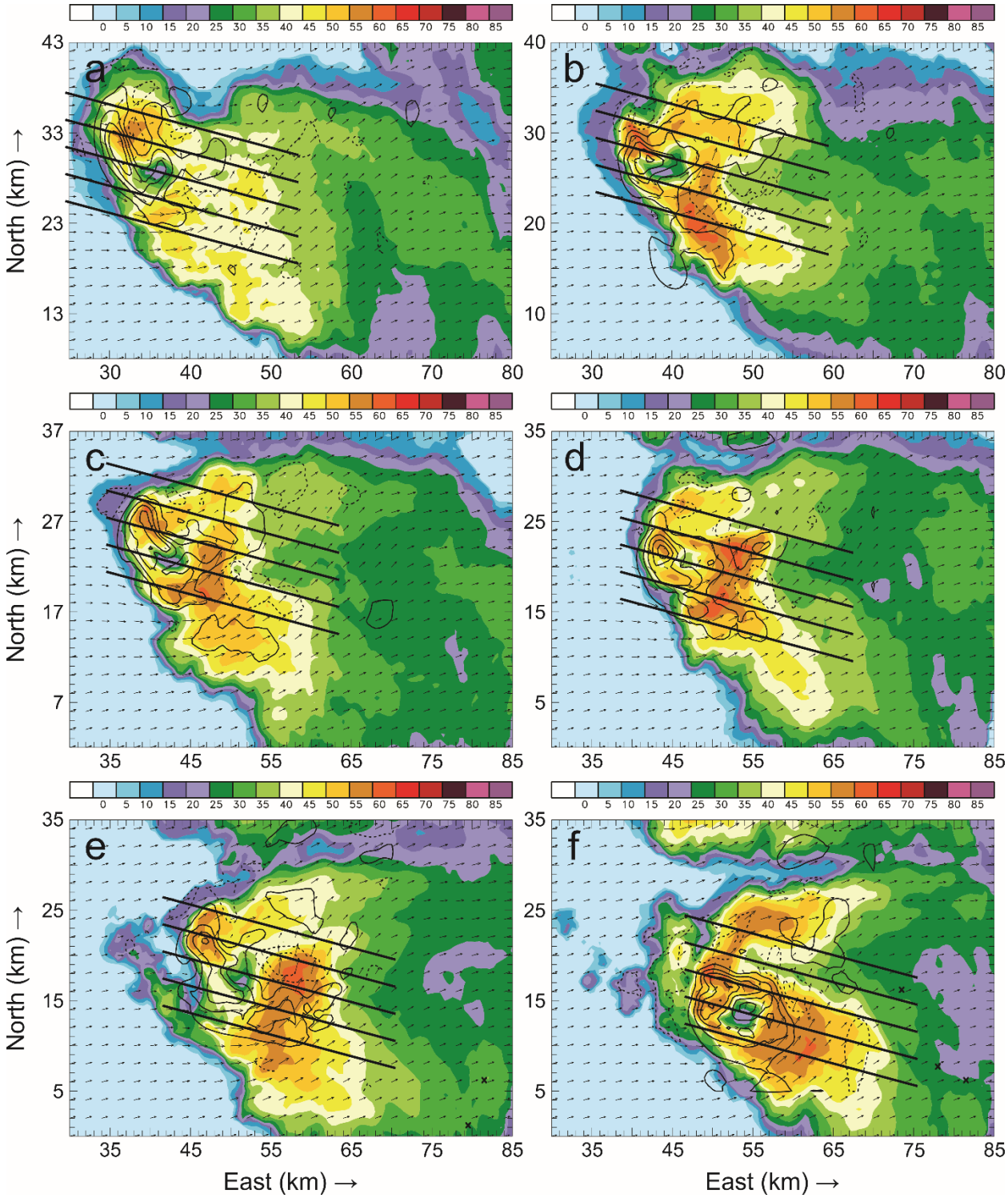

Figure 3: Horizontal cross-sections of color-filled Z, w contours (every 10 m s^{-1} starting at 5 m s^{-1}), and horizontal storm-relative wind vectors at 6.2 km AGL for a) 23:09 UTC, b) 23:21 UTC, c) 23:33 UTC, d) 23:42 UTC, e) 23:51 UTC, and f) 00:00 UTC. The diagonal black lines on each figure indicate the locations of the vertical cross sections generated for each analysis time.

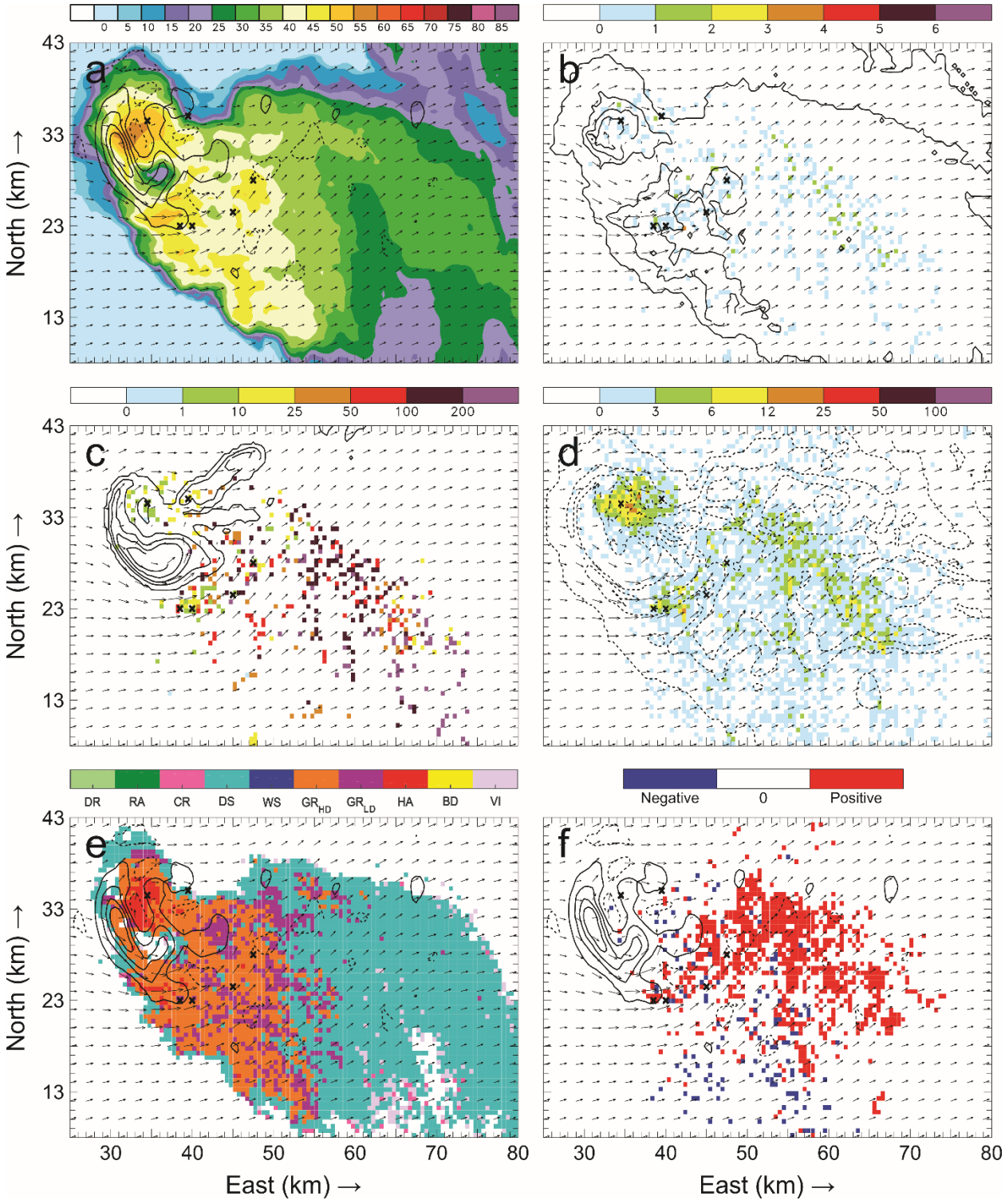

Figure 4: Horizontal cross-sections for 29 May 23:09 UTC taken at 6.2 km AGL of: a) color-filled Z and w contours (every 10 m s^{-1} starting at 5 m s^{-1}); b) color-filled FED and q_g contours (every 1.0 g kg^{-1} starting at 0 g kg^{-1}); c) color-filled FP and q_c contours (every 2.0 g kg -1 starting at 0 g kg^{-1}); d) color-filled SD and q_{xs} contours (dashed contours are every 0.25 g kg^{-1} starting at 0 g kg^{-1}, solid contours are every 1.0 g kg^{-1} starting at 1.0 g kg^{-1}); e) color-filled HCA and w contours (every 10 m s^{-1} starting at 5 m s^{-1}); and f) color-filled net inferred space charge and w contours (every 10 m s^{-1} starting at 5 m s^{-1}). All figures have the same horizontal storm-relative wind vectors, and black X's denote grid cells with FID > 0.

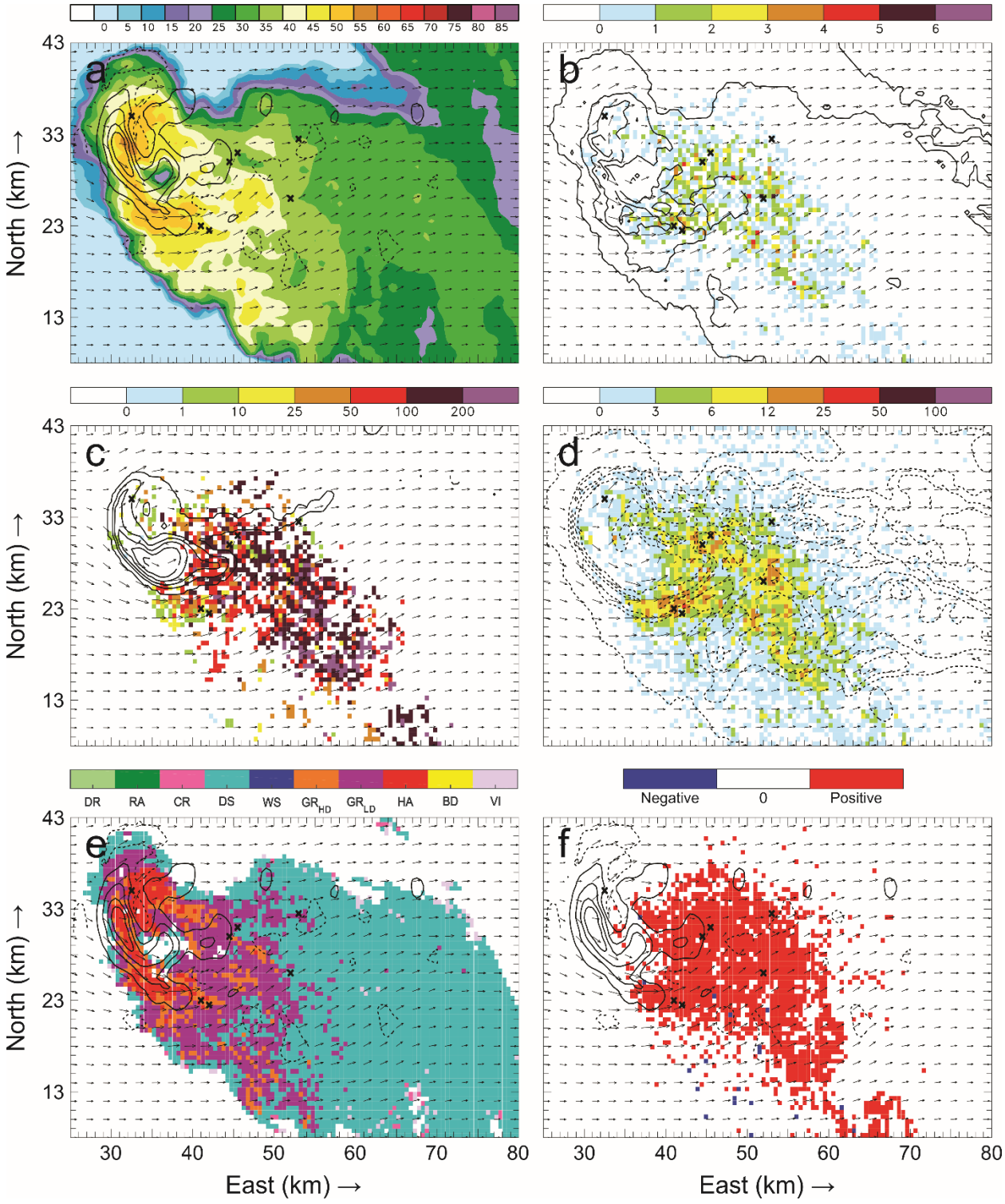

Figure 5: Horizontal cross-sections for 29 May 23:09 UTC. As in Figure 4, but at 7.2 km AGL.

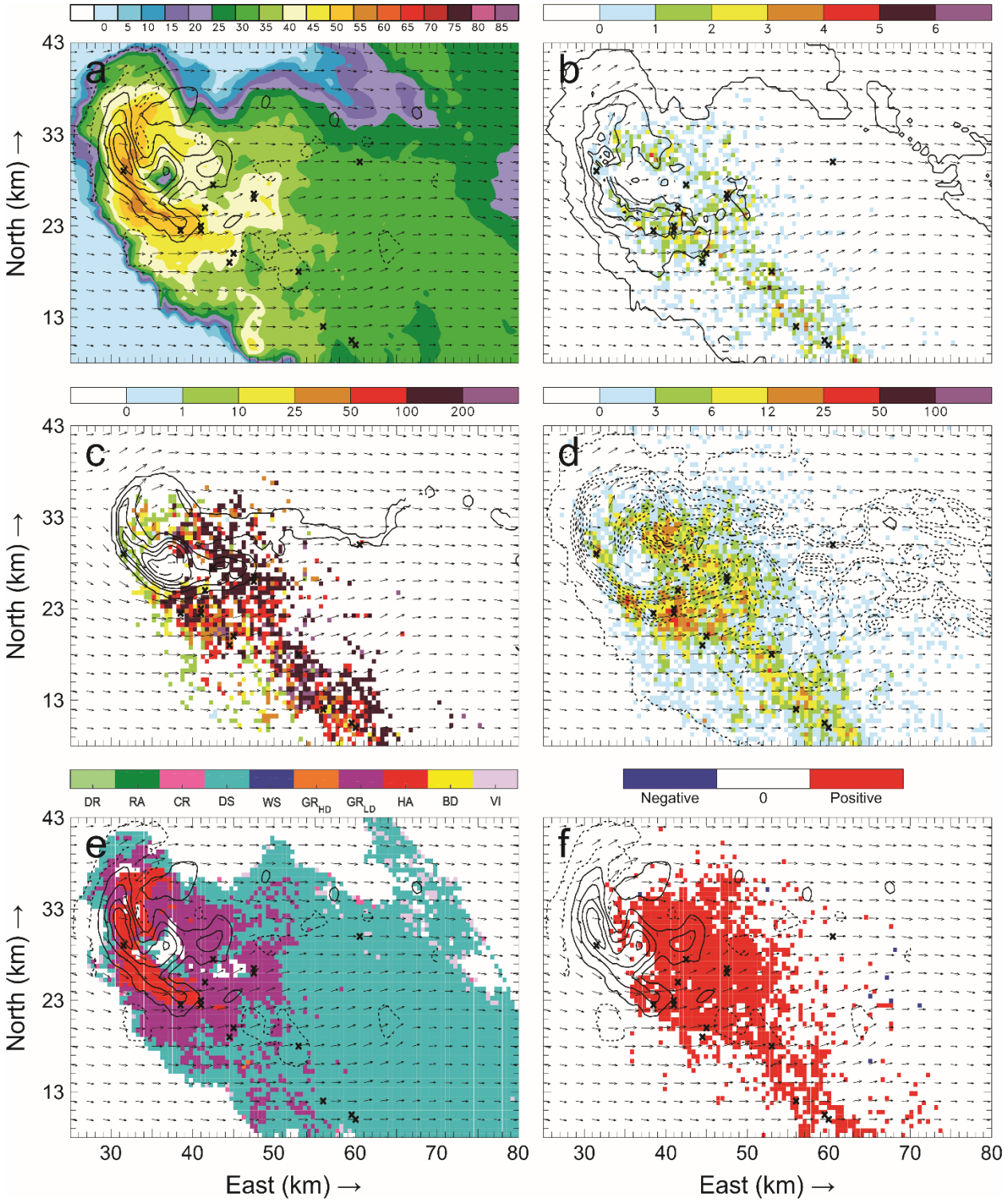

Figure 6: Horizontal cross-sections for 29 May 23:09 UTC. As in Figure 4, but at 8.2 km AGL.

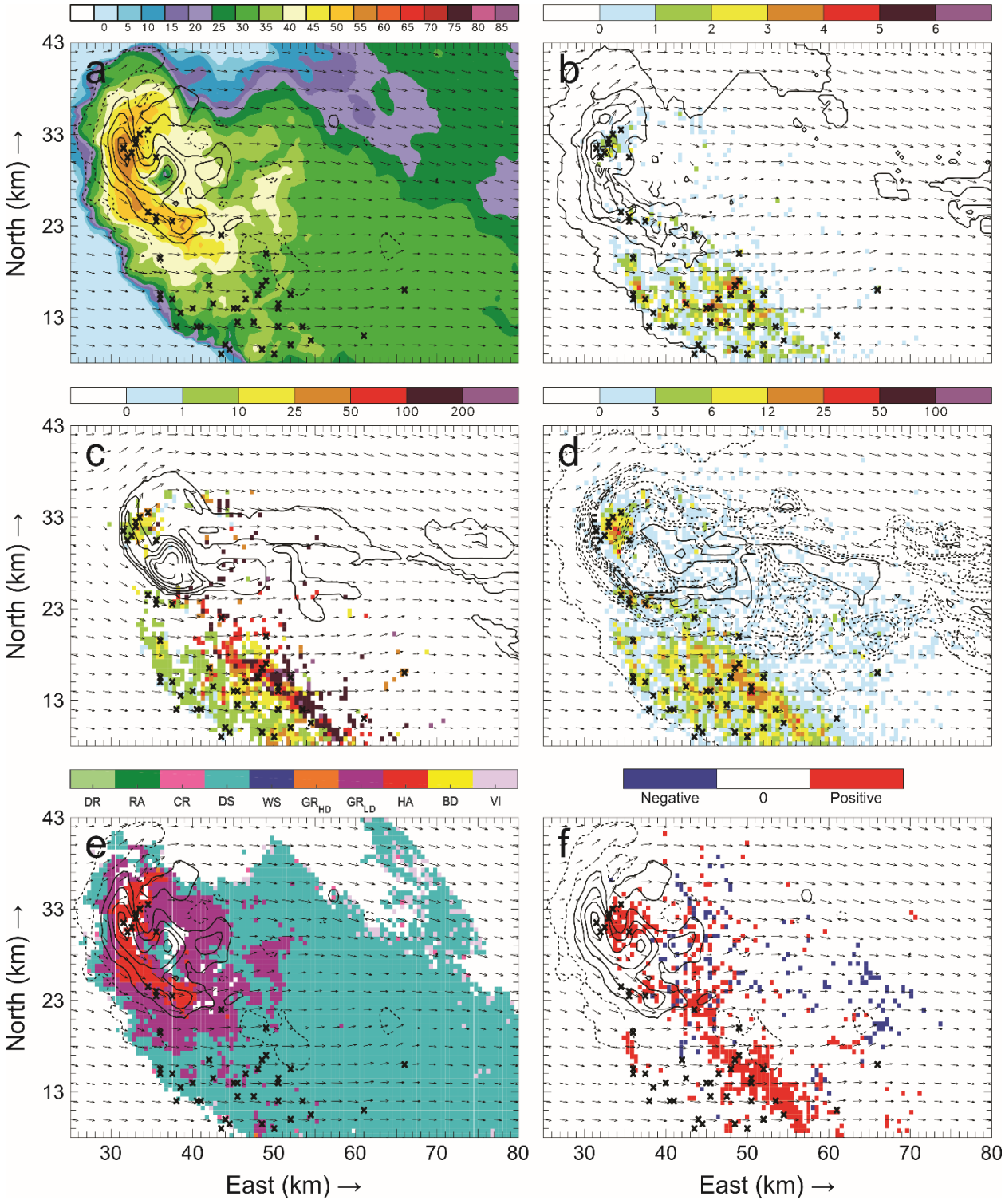

Figure 7: Horizontal cross-sections for 29 May 23:09 UTC. As in Figure 4, but at 9.2 km AGL.

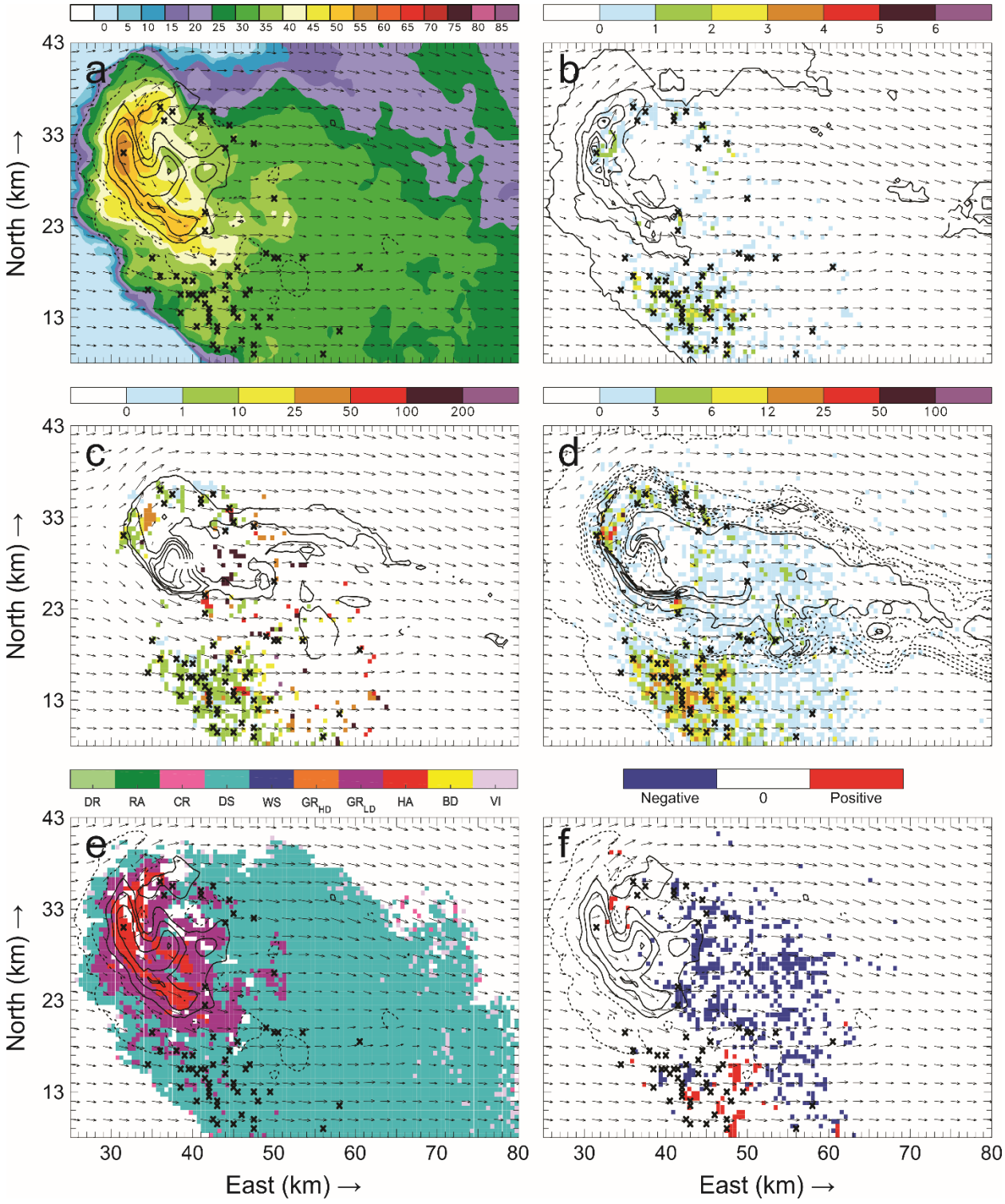

Figure 8: Horizontal cross-sections for 29 May 23:09 UTC. As in Figure 4, but at 10.2 km AGL.

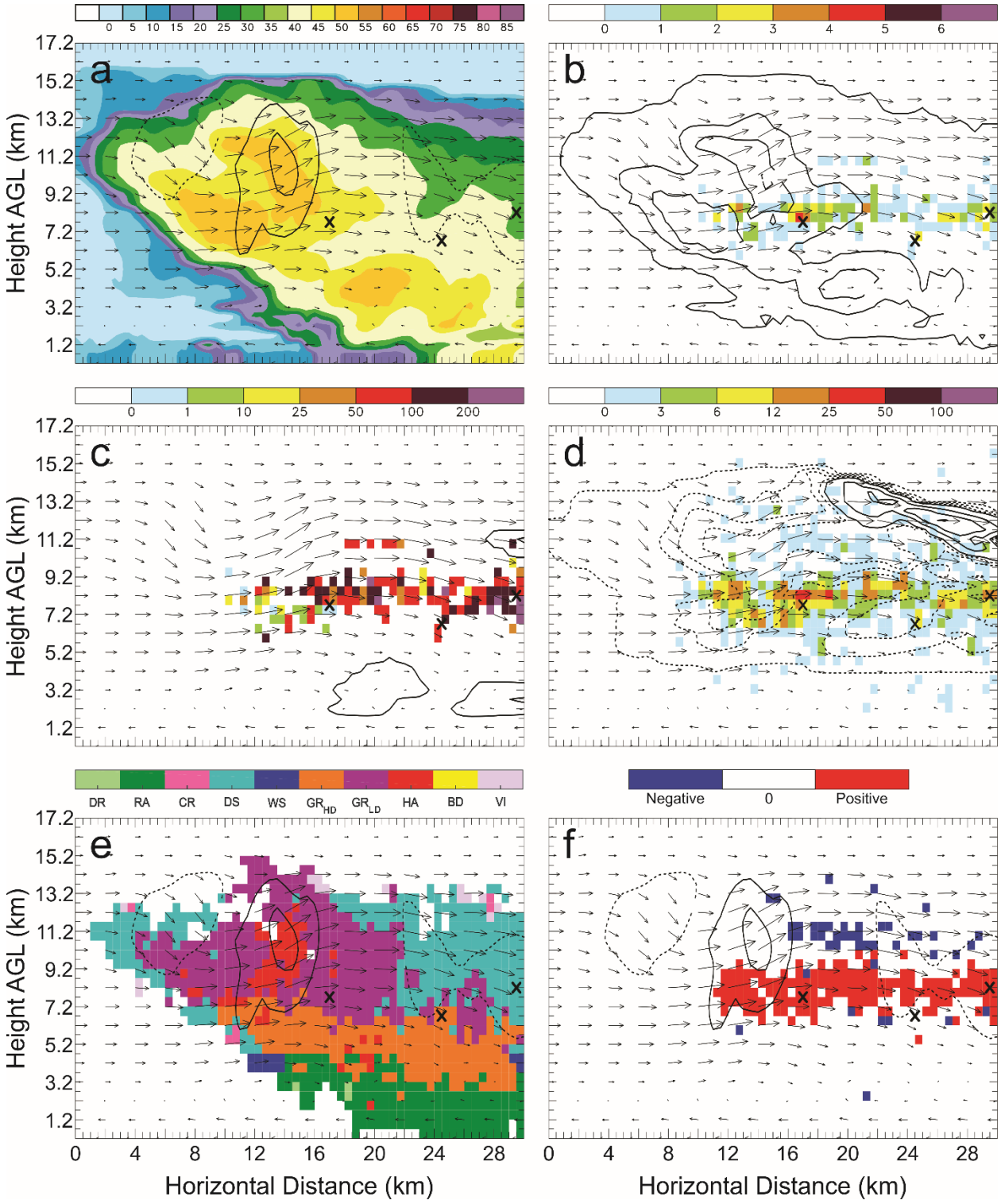

Figure 9: Vertical cross-sections for 29 May 23:09 UTC taken along the southernmost line in Figure 3(a) of: a) color-filled Z and w contours (every 10 m s^{-1} starting at 5 m s^{-1}); b) color-filled FED and q_g contours (every 1.0 g kg^{-1} starting at 0 g kg^{-1}); c) color-filled FP and q_c contours (every 2.0 g kg -1 starting at 0 g kg^{-1}); d) color-filled SD and q_{xs} contours (dashed contours are every 0.25 g kg^{-1} starting at 0 g kg^{-1}, solid contours are every 1.0 g kg^{-1} starting at 1.0 g kg^{-1}); e) color-filled HCA and w contours (every 10 m s^{-1} starting at 5 m s^{-1}); and f) color-filled net inferred space charge and w contours (every 10 m s^{-1} starting at 5 m s^{-1}). All figures have the same horizontal storm-relative wind vectors, and black X's denote grid cells with FID > 0.

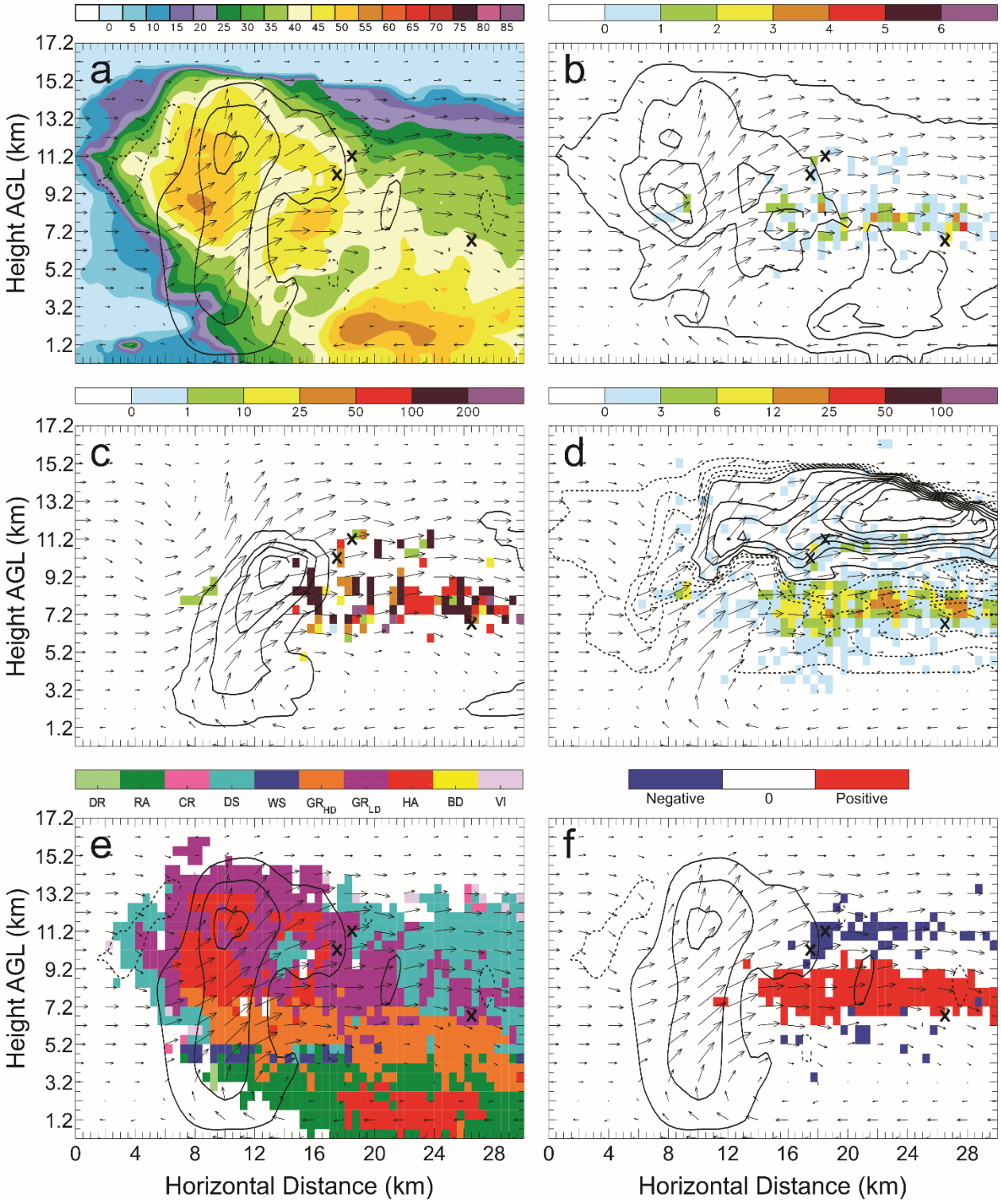

Figure 10: Vertical cross-sections for 29 May 23:09 UTC. As in Figure 9, but taken along the second line from the south in Figure 3(a).

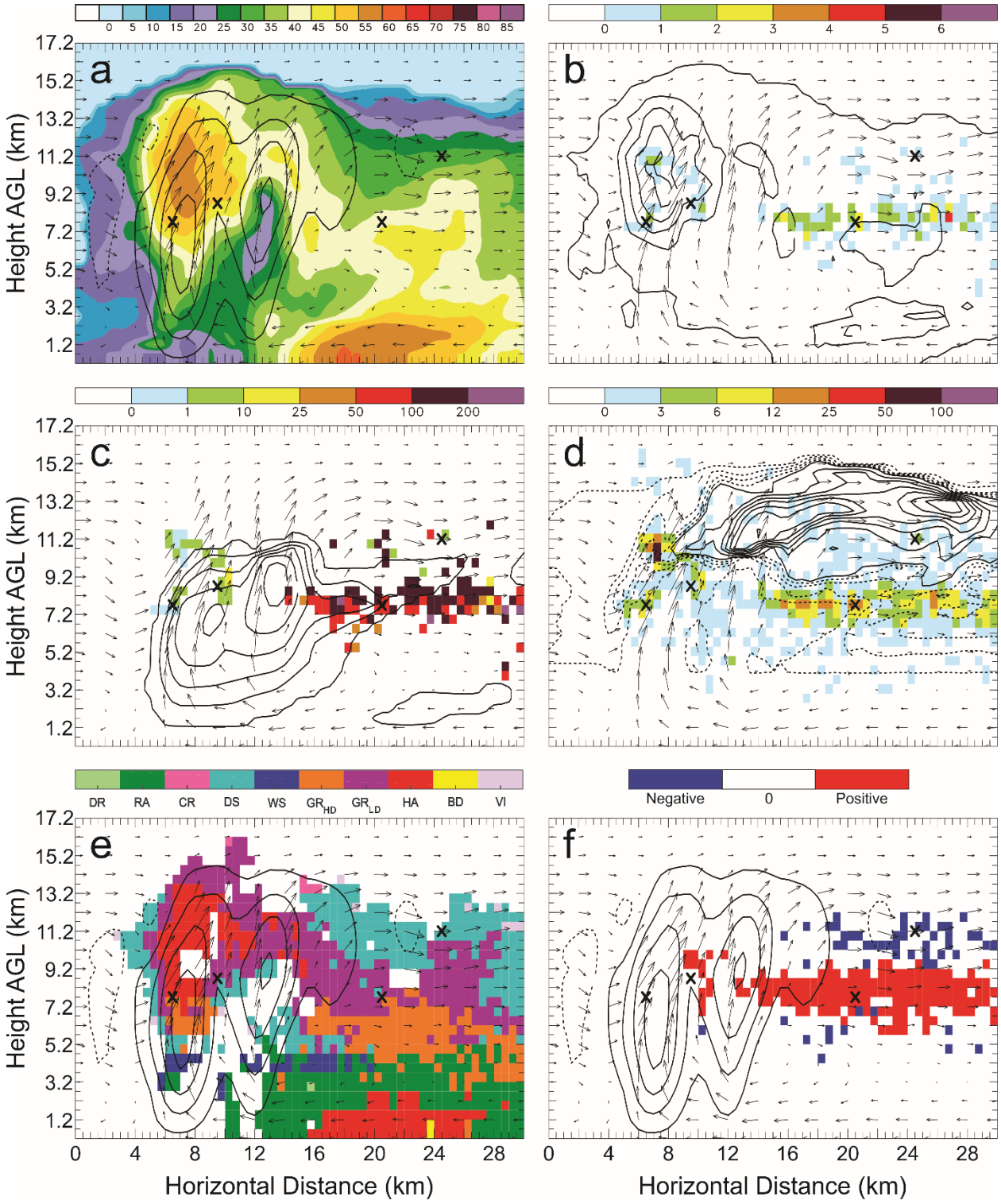

Figure 11: Vertical cross-sections for 29 May 23:09 UTC. As in Figure 9, but taken along the central line in Figure 3(a).

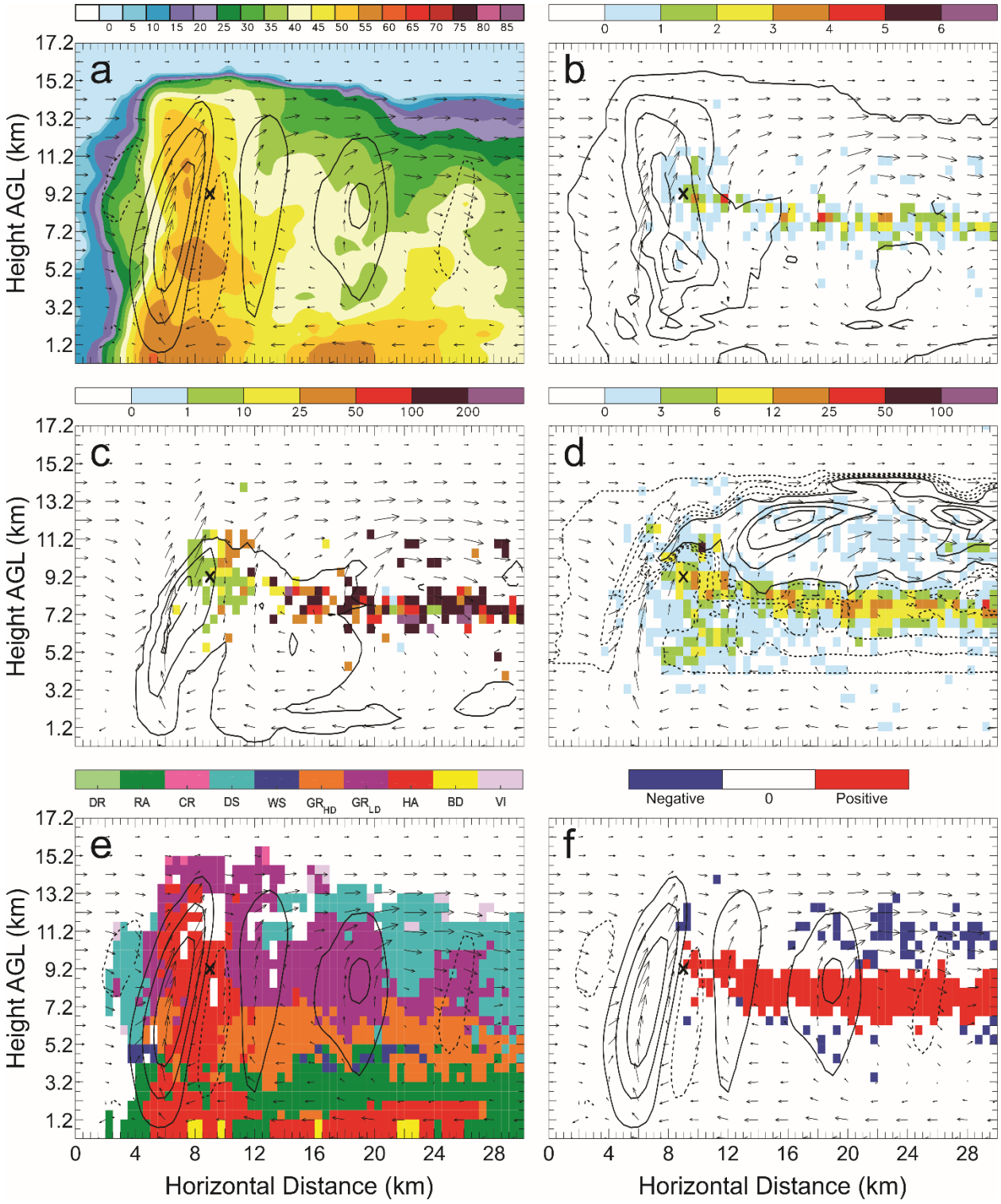

Figure 12: Vertical cross-sections for 29 May 23:09 UTC. As in Figure 9, but taken along the second line from the north in Figure 3(a).

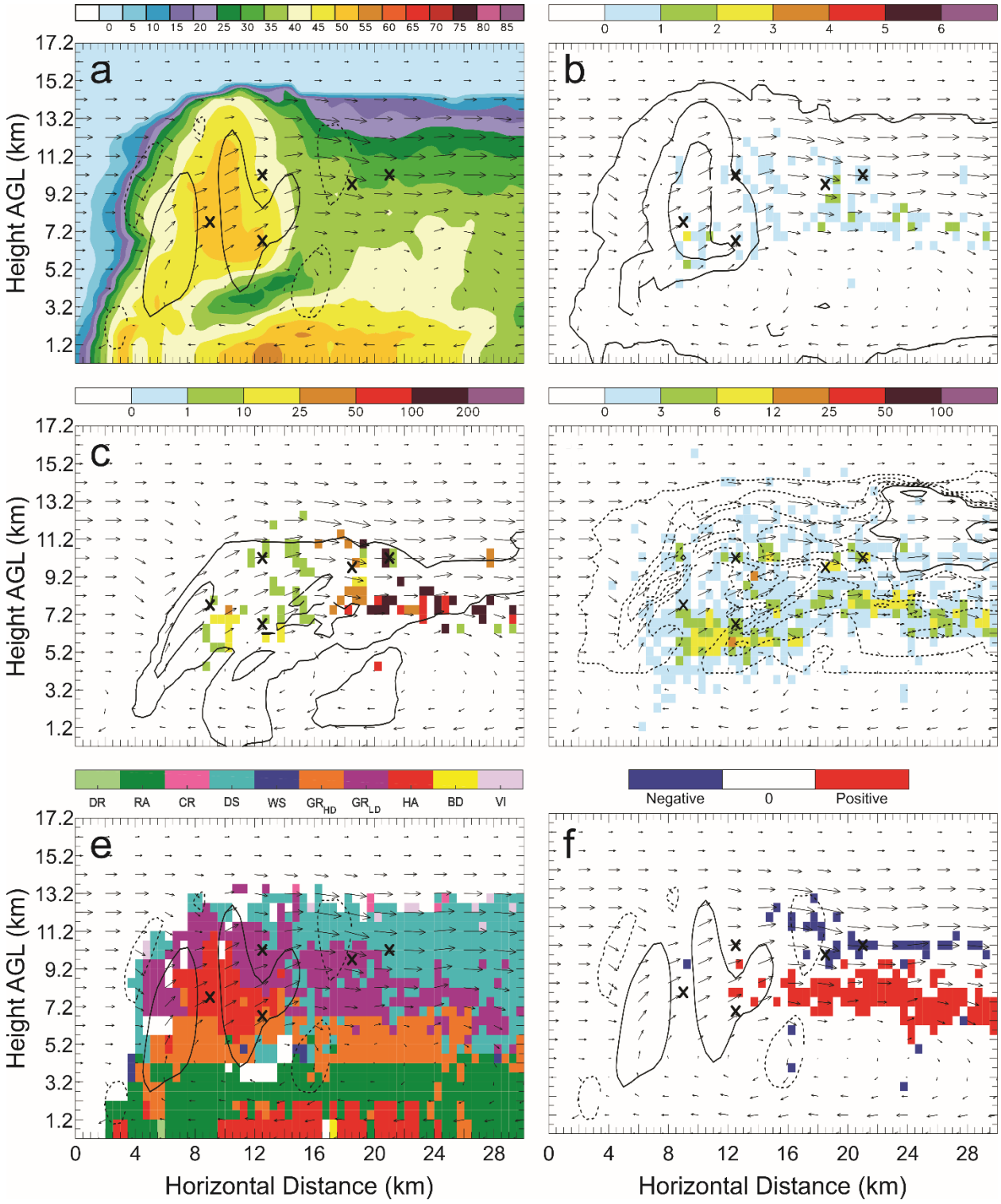

Figure 13: Vertical cross-sections for 29 May 23:09 UTC. As in Figure 9, but taken along the northernmost line in Figure 3(a).

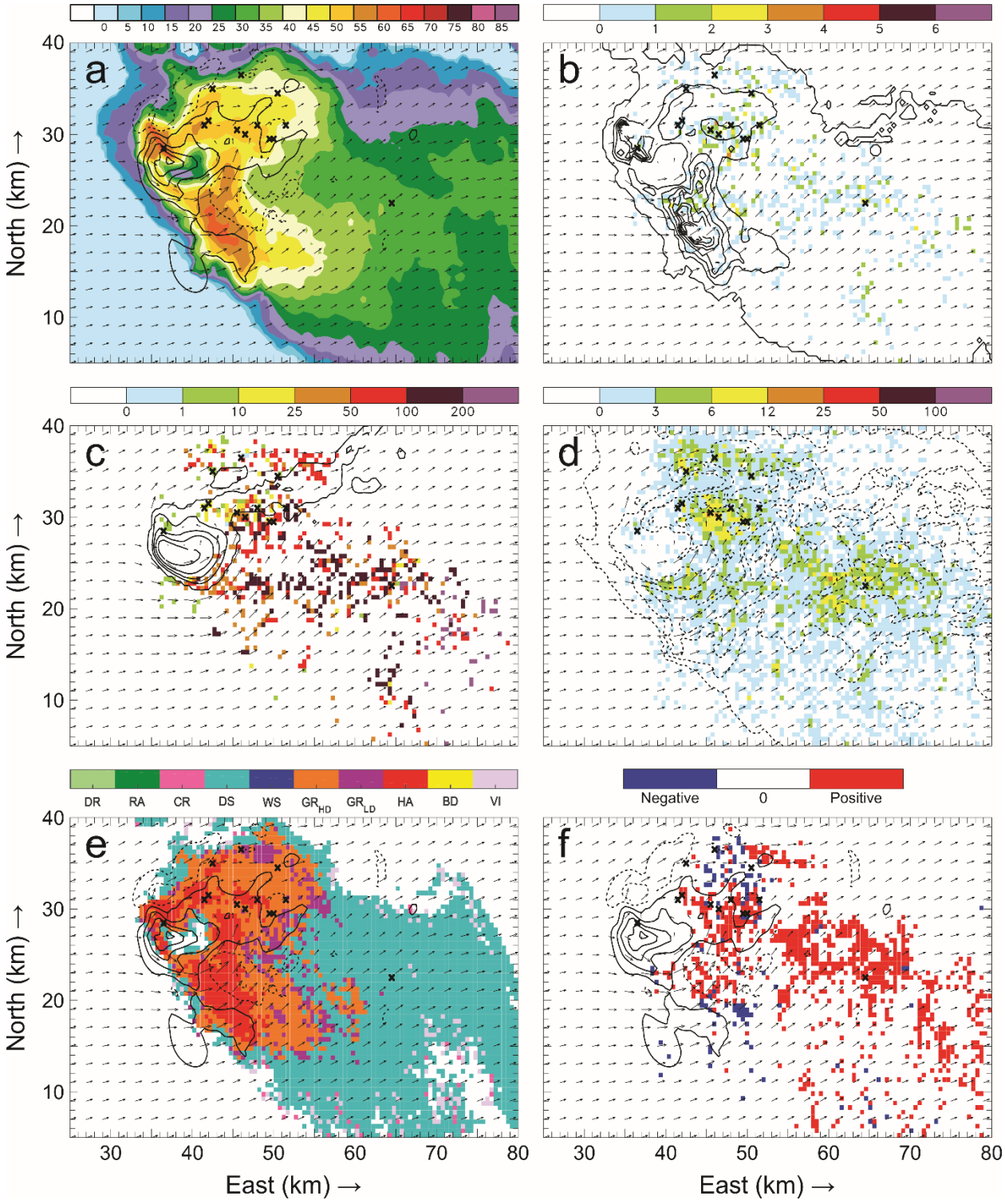

Figure 14: Horizontal cross-sections for 29 May 23:21 UTC taken at 6.2 km AGL of: a) color-filled Z and w contours (every 10 m s^{-1} starting at 5 m s^{-1}); b) color-filled FED and q_g contours (every 1.0 g kg^{-1} starting at 0 g kg^{-1}); c) color-filled FP and q_c contours (every 2.0 g kg -1 starting at 0 g kg^{-1}); d) color-filled SD and q_{xs} contours (dashed contours are every 0.25 g kg^{-1} starting at 0 g kg^{-1}, solid contours are every 1.0 g kg^{-1} starting at 1.0 g kg^{-1}); e) color-filled HCA and w contours (every 10 m s^{-1} starting at 5 m s^{-1}); and f) color-filled net inferred space charge and w contours (every 10 m s^{-1} starting at 5 m s^{-1}). All figures have the same horizontal storm-relative wind vectors, and black X's denote grid cells with FID > 0.

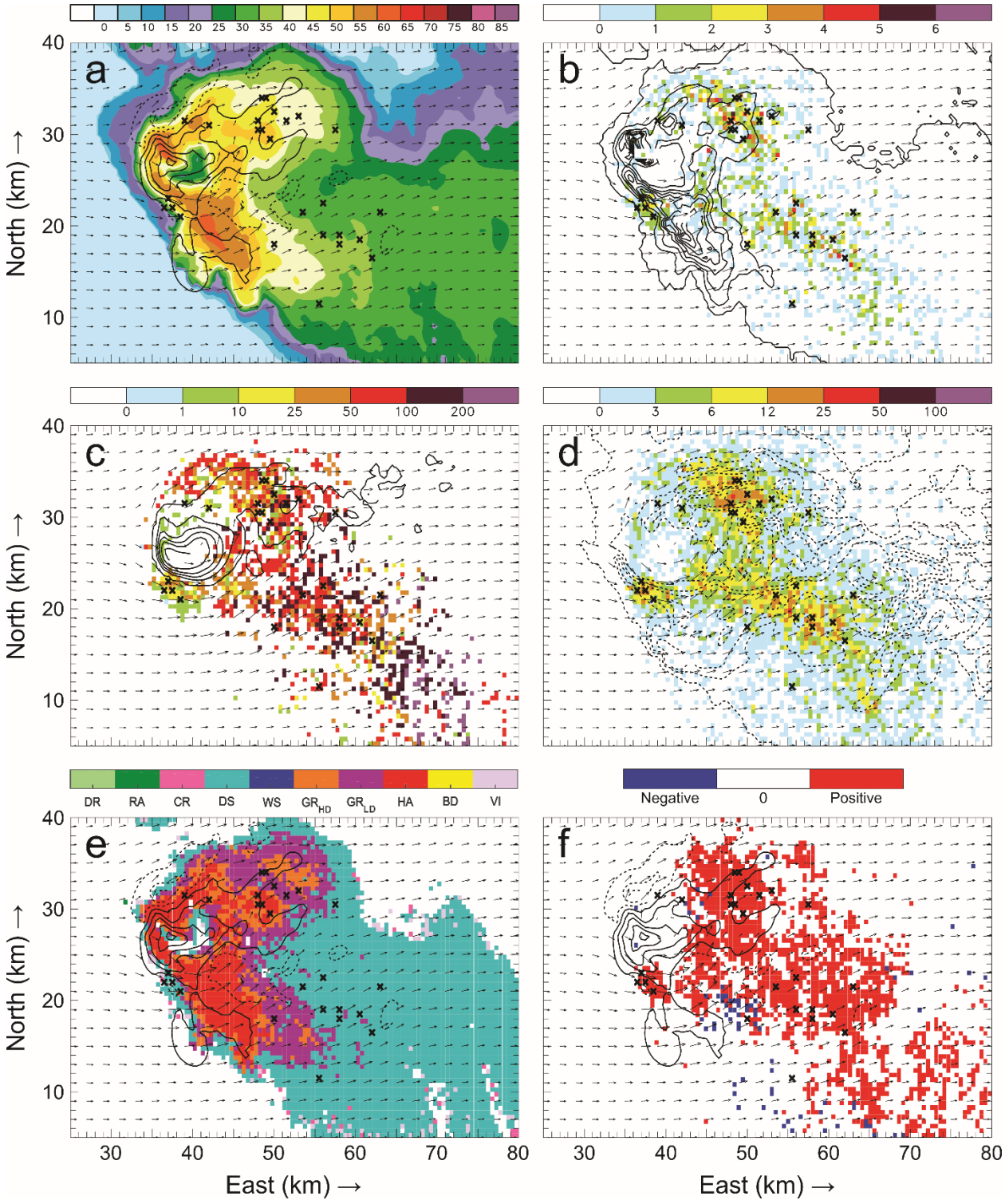

Figure 15: Horizontal cross-sections for 29 May 23:21 UTC. As in Figure 14, but taken at 7.2 km AGL.

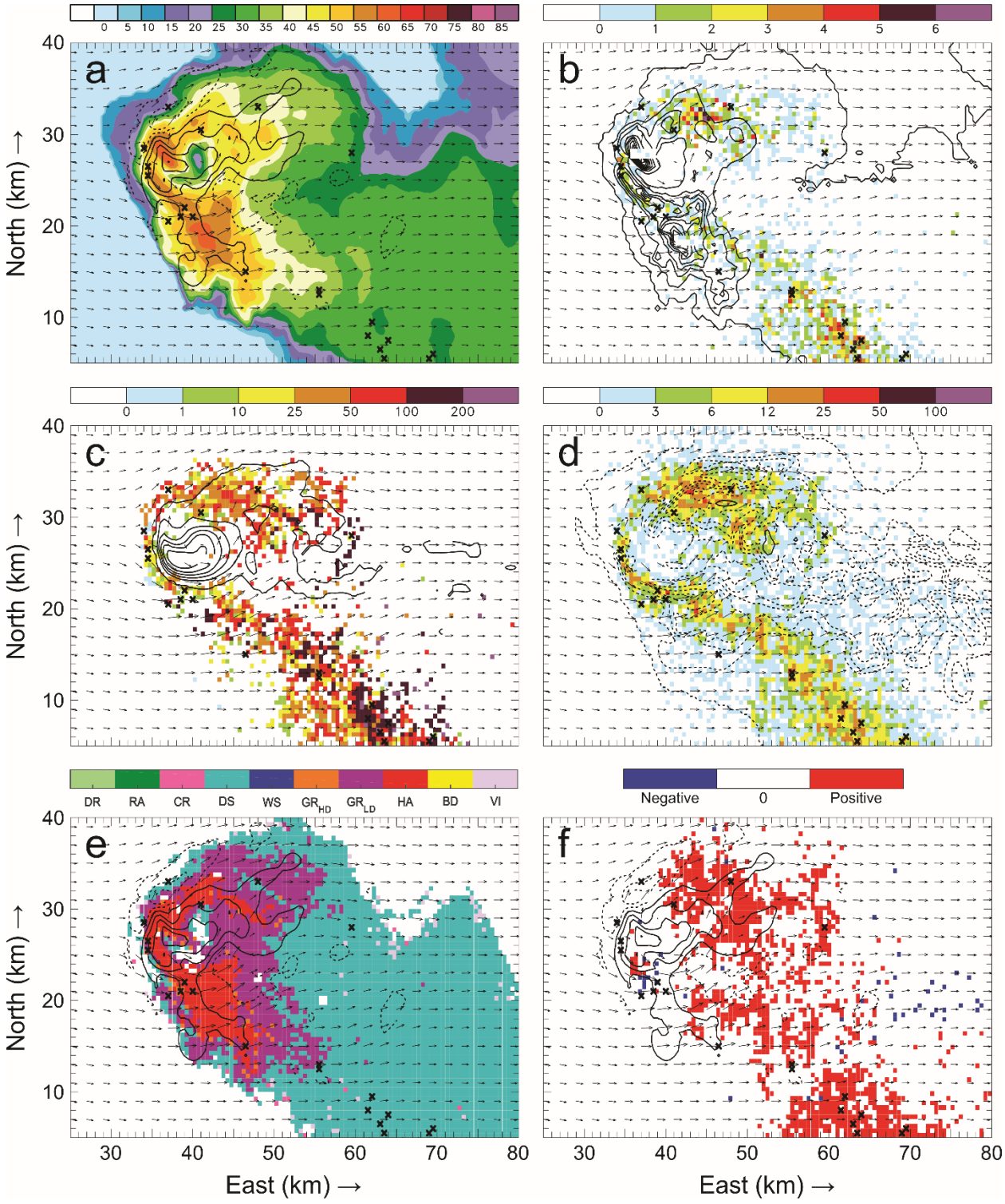

Figure 16: Horizontal cross-sections for 29 May 23:21 UTC. As in Figure 14, but taken at 8.2 km AGL.

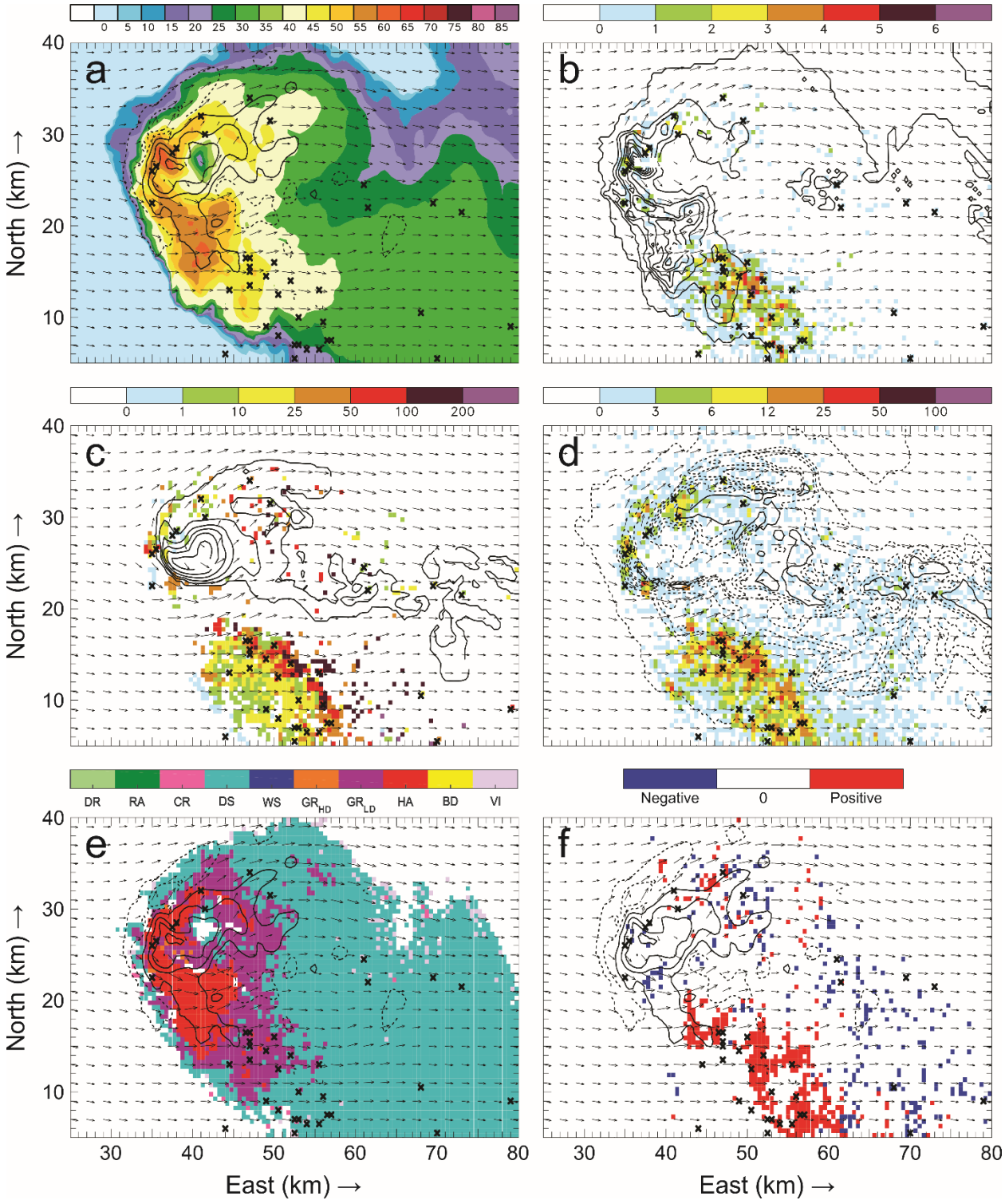

Figure 17: Horizontal cross-sections for 29 May 23:21 UTC. As in Figure 14, but taken at 9.2 km AGL.

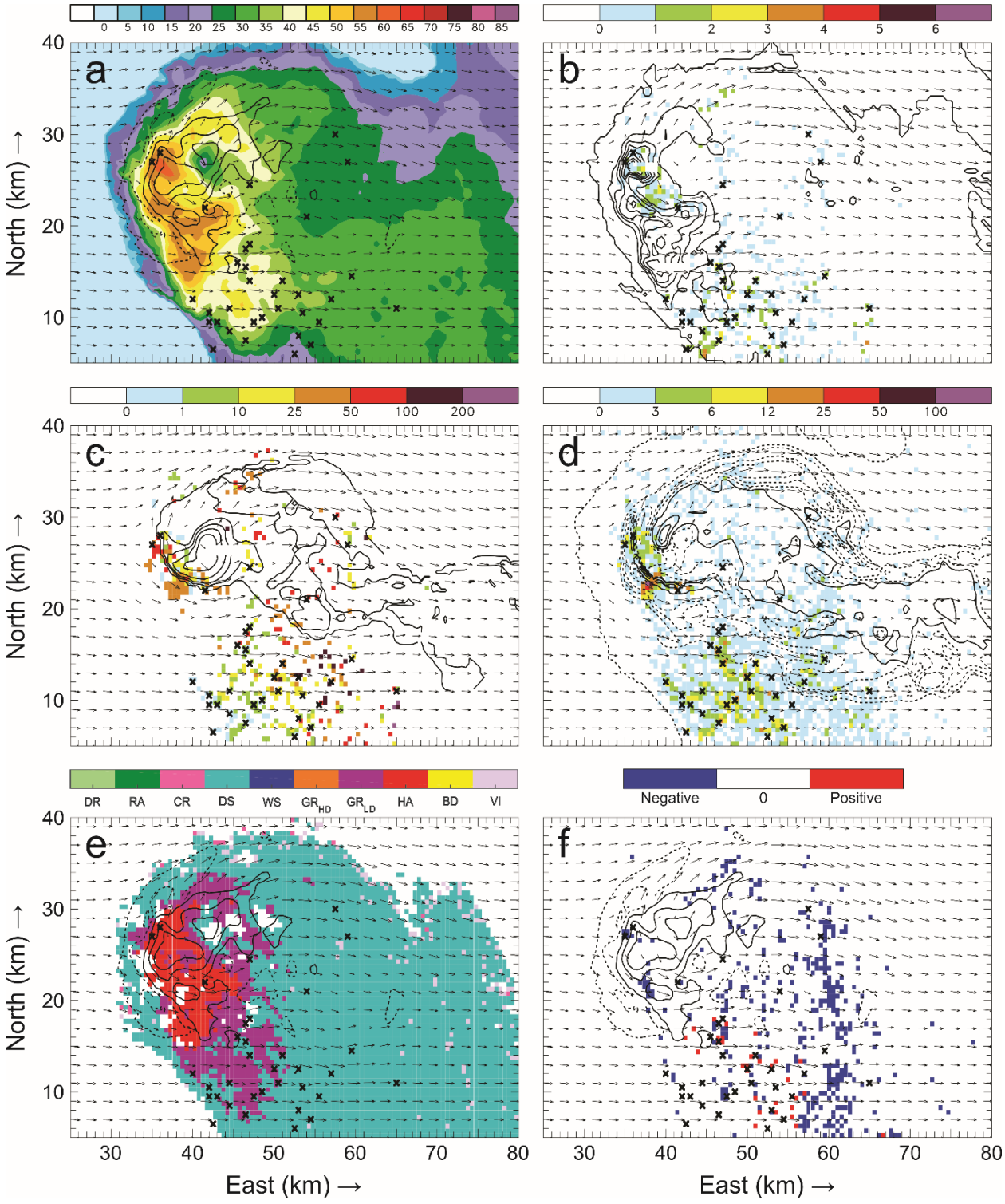

Figure 18: Horizontal cross-sections for 29 May 23:21 UTC. As in Figure 14, but taken at 10.2 km AGL.

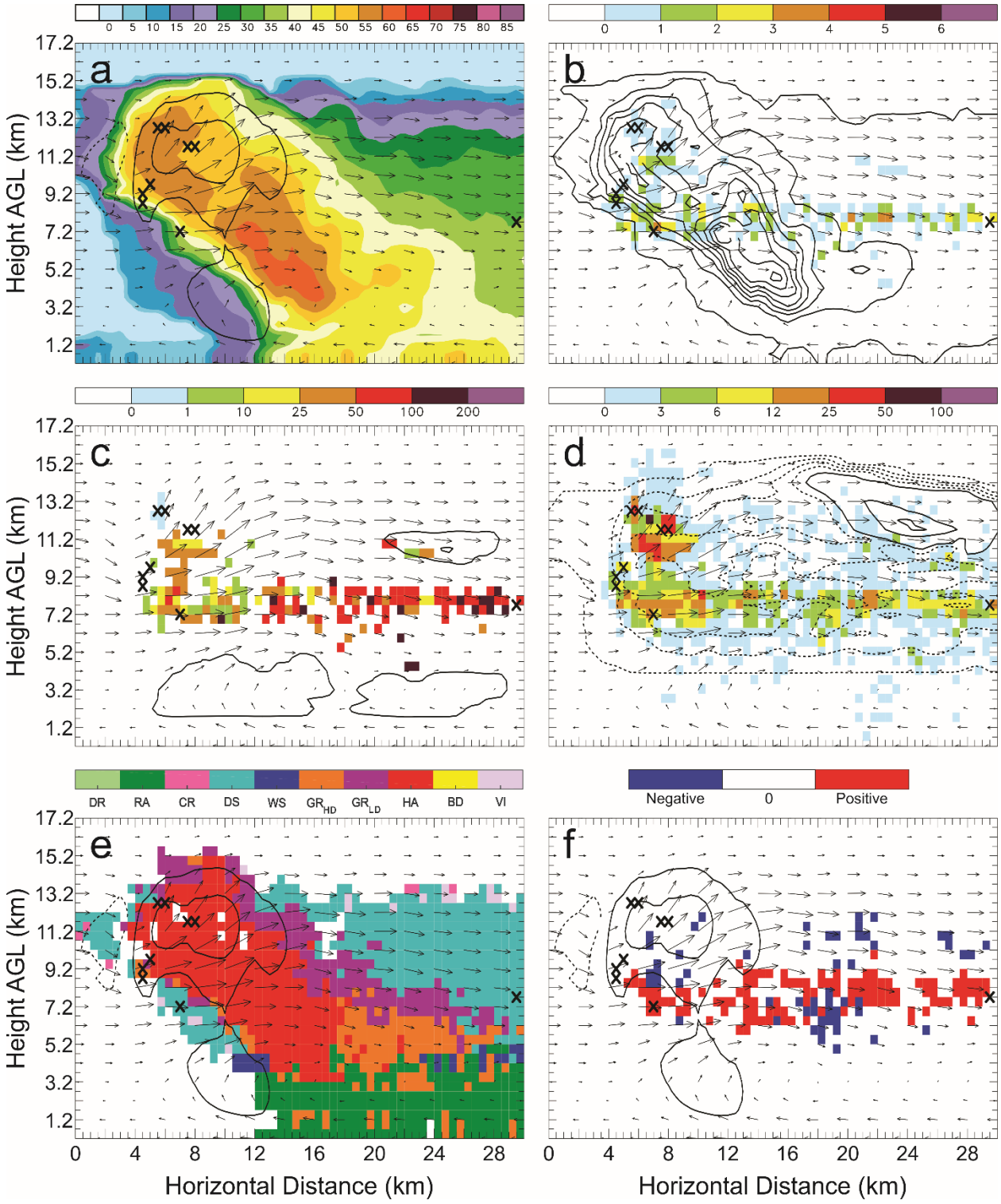

Figure 19: Vertical cross-sections for 29 May 23:21 UTC taken along the southernmost line in Figure 3(b) of: a) color-filled Z and w contours (every 10 m s^{-1} starting at 5 m s^{-1}); b) color-filled FED and q_g contours (every 1.0 g kg^{-1} starting at 0 g kg^{-1}); c) color-filled FP and q_c contours (every 2.0 g kg -1 starting at 0 g kg^{-1}); d) color-filled SD and q_{xs} contours (dashed contours are every 0.25 g kg^{-1} starting at 0 g kg^{-1}, solid contours are every 1.0 g kg^{-1} starting at 1.0 g kg^{-1}); e) color-filled HCA and w contours (every 10 m s^{-1} starting at 5 m s^{-1}); and f) color-filled net inferred space charge and w contours (every 10 m s^{-1} starting at 5 m s^{-1}). All figures have the same horizontal storm-relative wind vectors, and black X's denote grid cells with FID > 0.

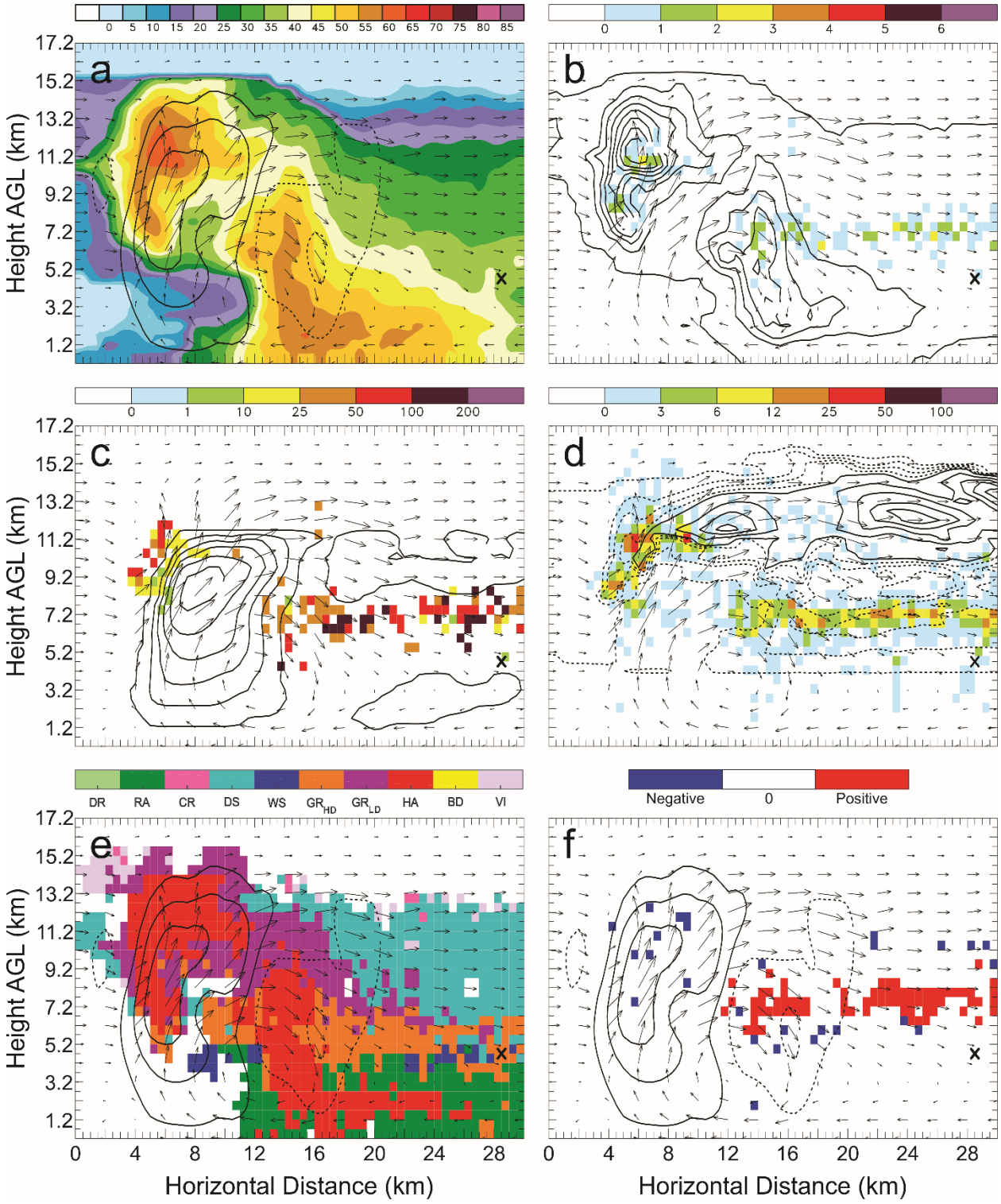

Figure 20: Vertical cross-sections for 29 May 23:21 UTC. As in Figure 19, but taken along the second line from the south in Figure 3(b).

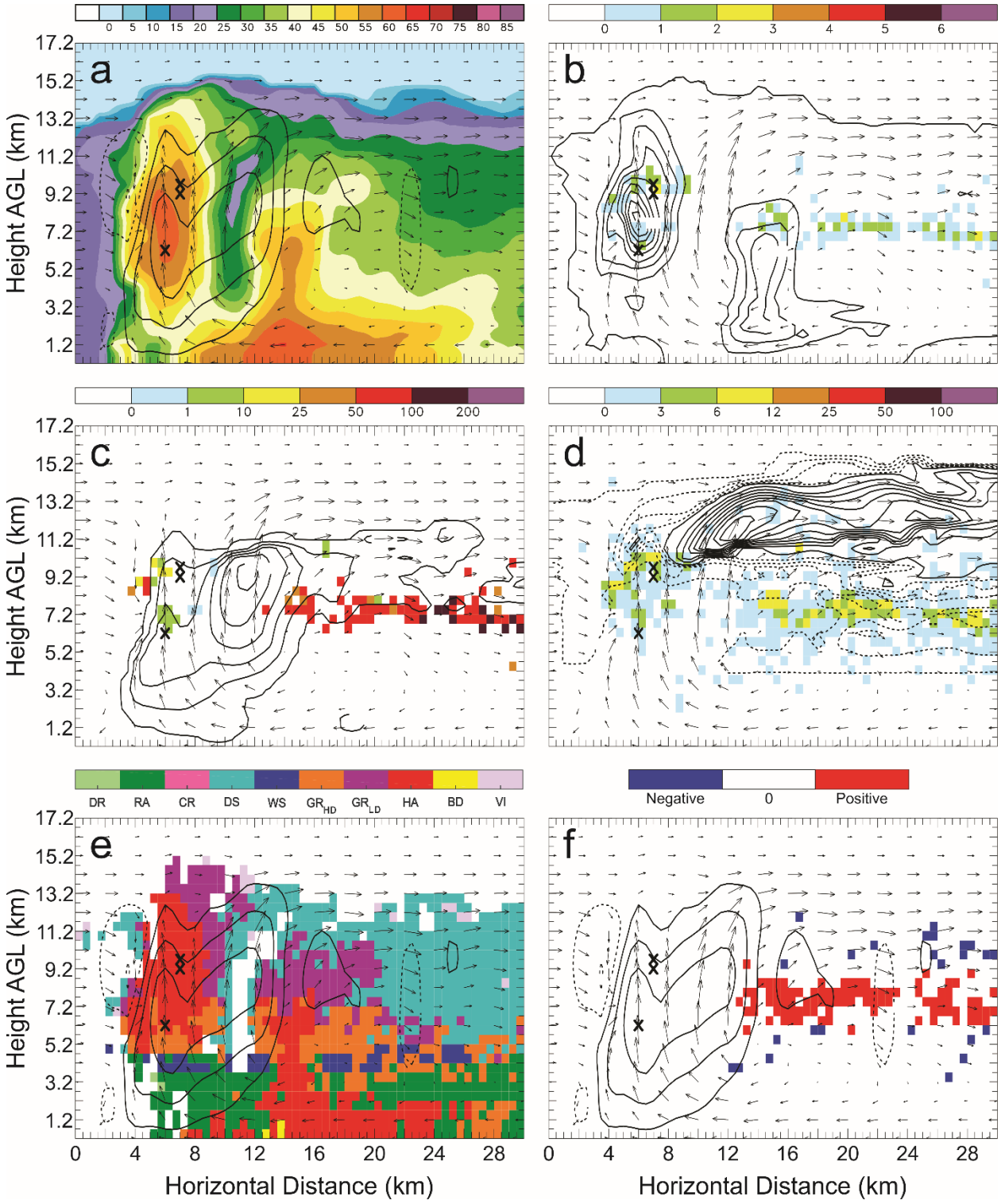

Figure 21: Vertical cross-sections for 29 May 23:21 UTC. As in Figure 19, but taken along the central line in FIgure 3(b).

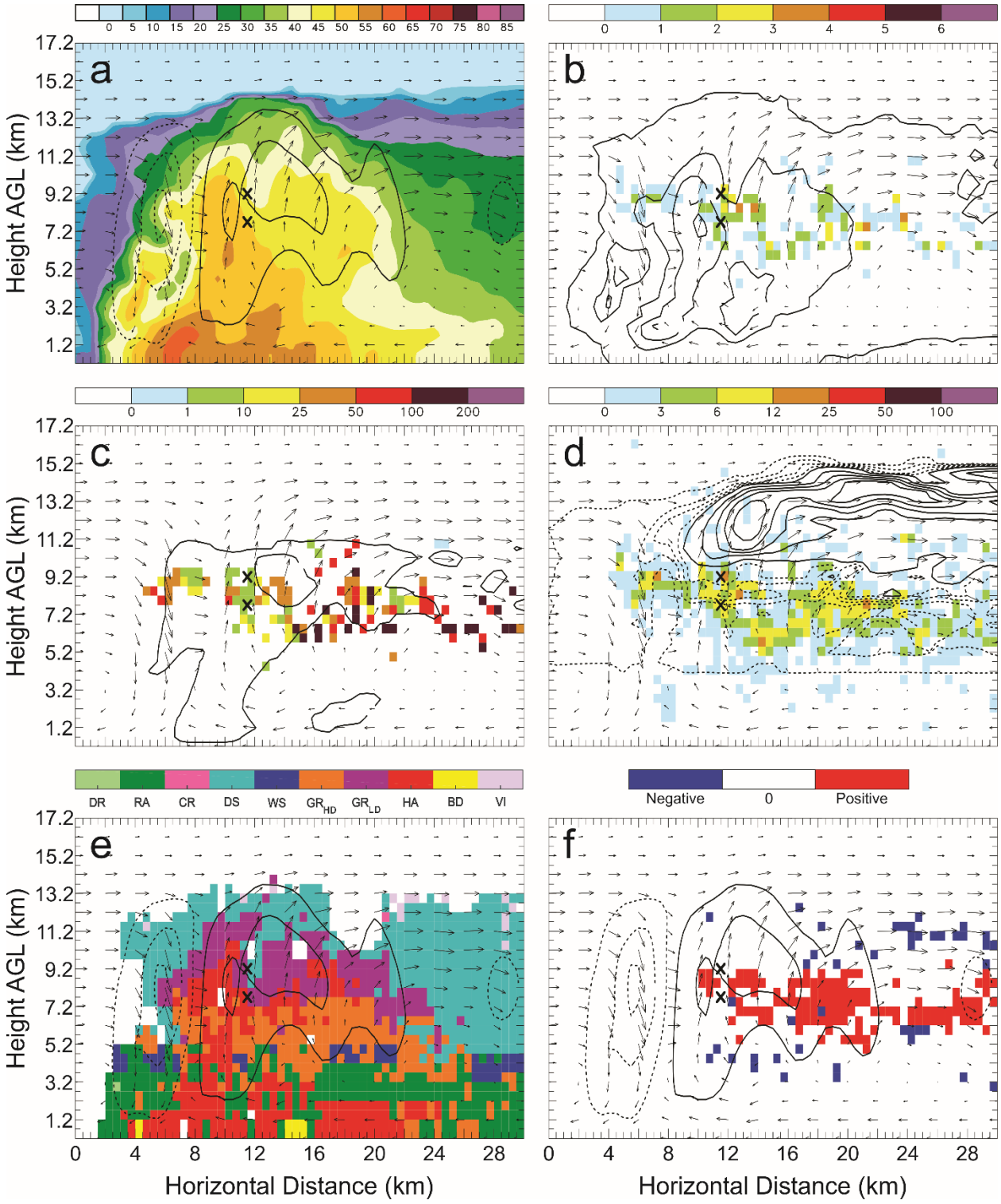

Figure 22: Vertical cross-sections for 29 May 23:21 UTC. As in Figure 19, but taken along the second line from the north in Figure 3(b).

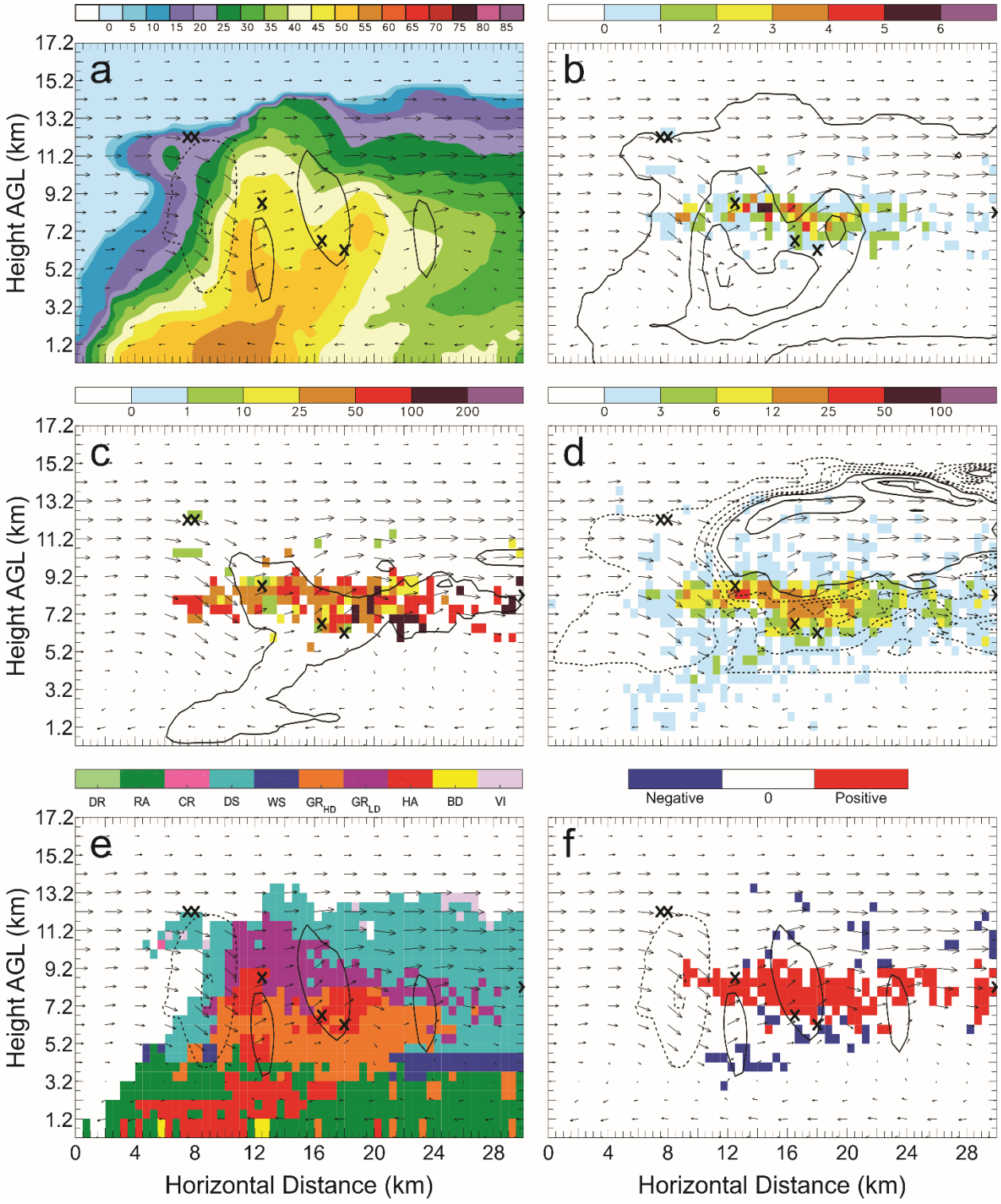

Figure 23: Vertical cross-sections for 29 May 23:21 UTC. As in Figure 19, but taken along the northernmost line in Figure 3(b).

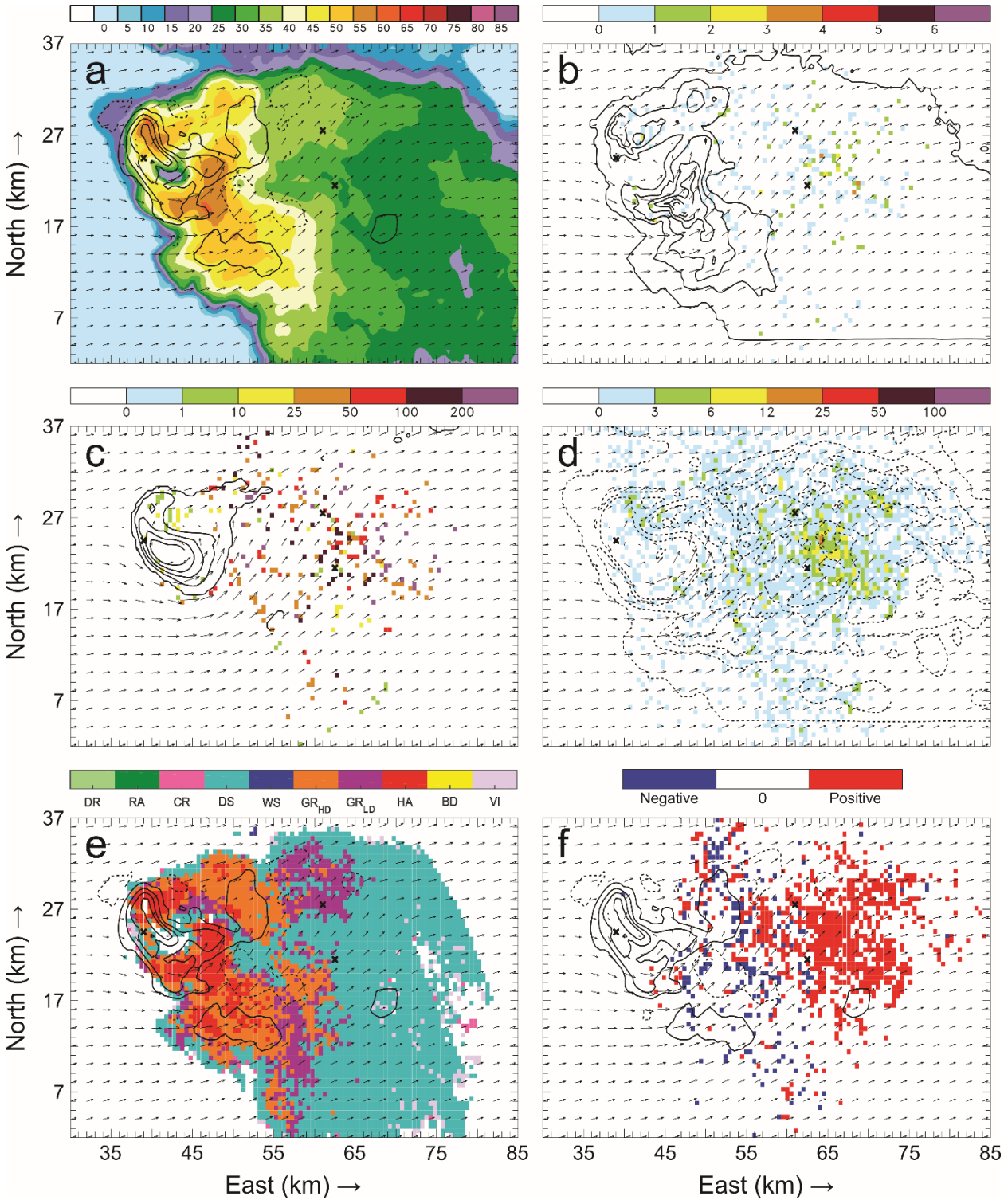

Figure 24: Horizontal cross-sections for 29 May 23:33 UTC taken at 6.2 km AGL of: a) color-filled Z and w contours (every 10 m s^{-1} starting at 5 m s^{-1}); b) color-filled FED and q_g contours (every 1.0 g kg^{-1} starting at 0 g kg^{-1}); c) color-filled FP and q_c contours (every 2.0 g kg -1 starting at 0 g kg^{-1}); d) color-filled SD and q_{xs} contours (dashed contours are every 0.25 g kg^{-1} starting at 0 g kg^{-1}, solid contours are every 1.0 g kg^{-1} starting at 1.0 g kg^{-1}); e) color-filled HCA and w contours (every 10 m s^{-1} starting at 5 m s^{-1}); and f) color-filled net inferred space charge and w contours (every 10 m s^{-1} starting at 5 m s^{-1}). All figures have the same horizontal storm-relative wind vectors, and black X's denote grid cells with FID > 0.

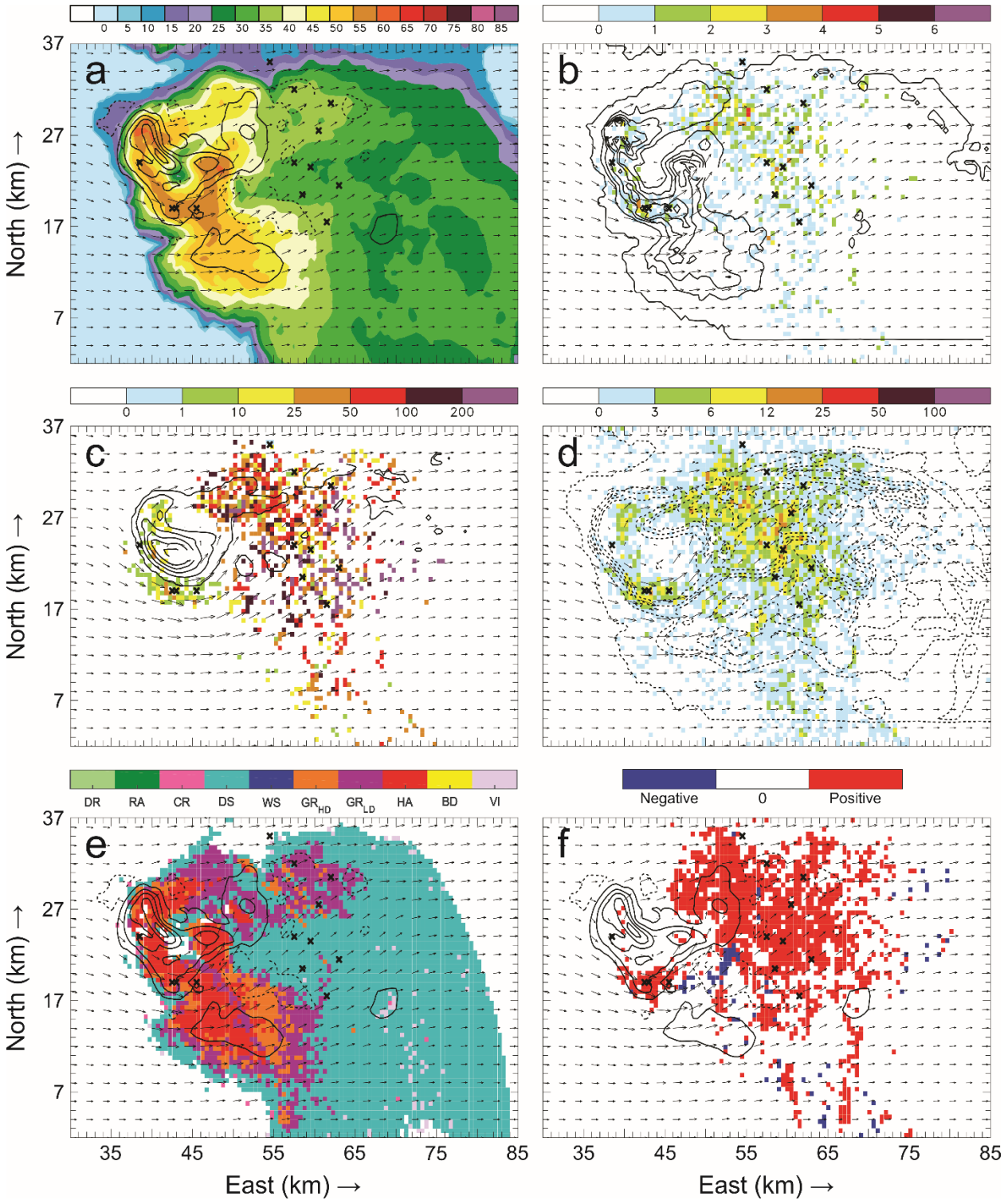

Figure 25: Horizontal cross-sections for 29 May 23:33 UTC. As in Figure 24, but taken at 7.2 km AGL.

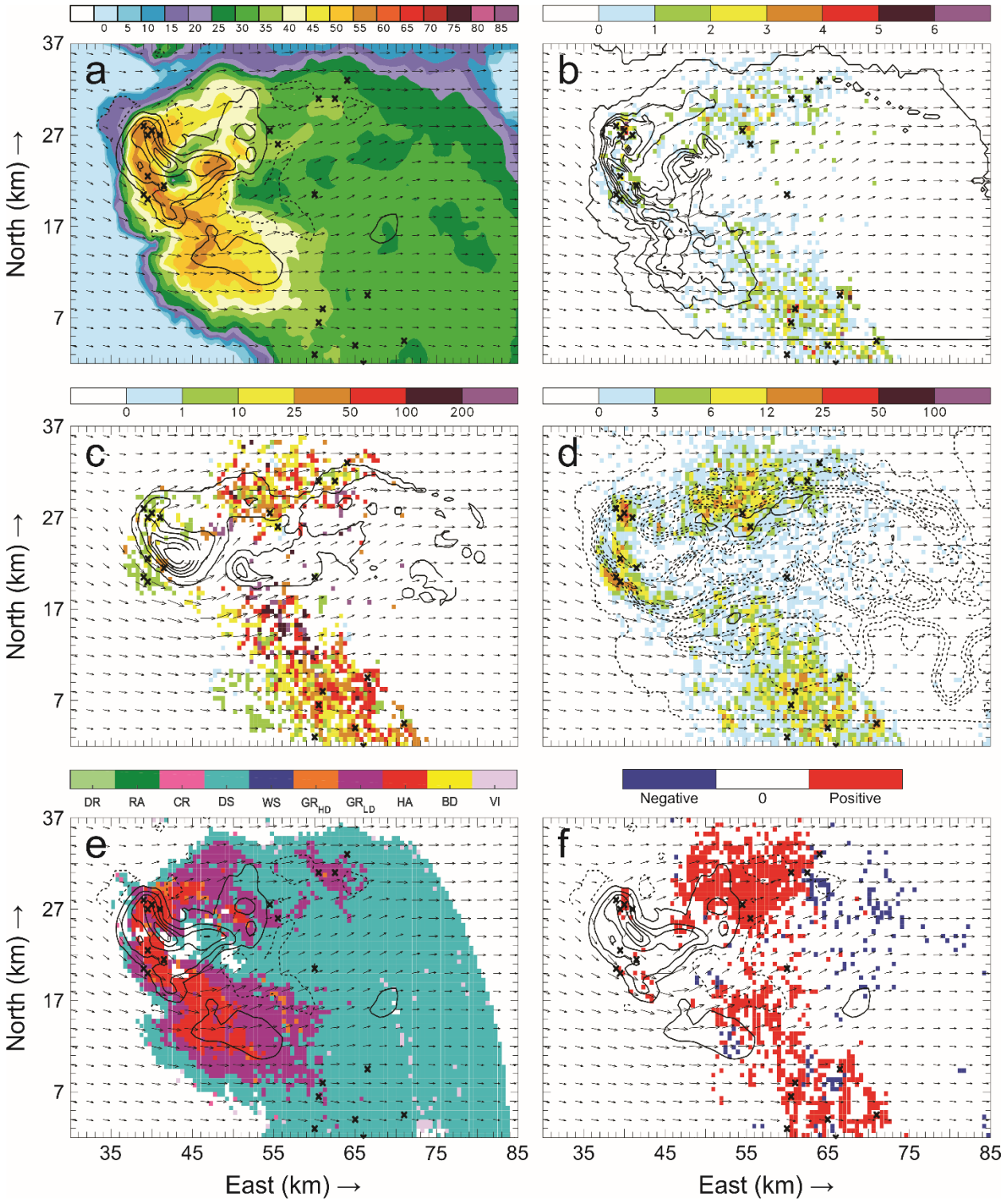

Figure 26: Horizontal cross-sections for 29 May 23:33 UTC. As in Figure 24, but taken at 8.2 km AGL.

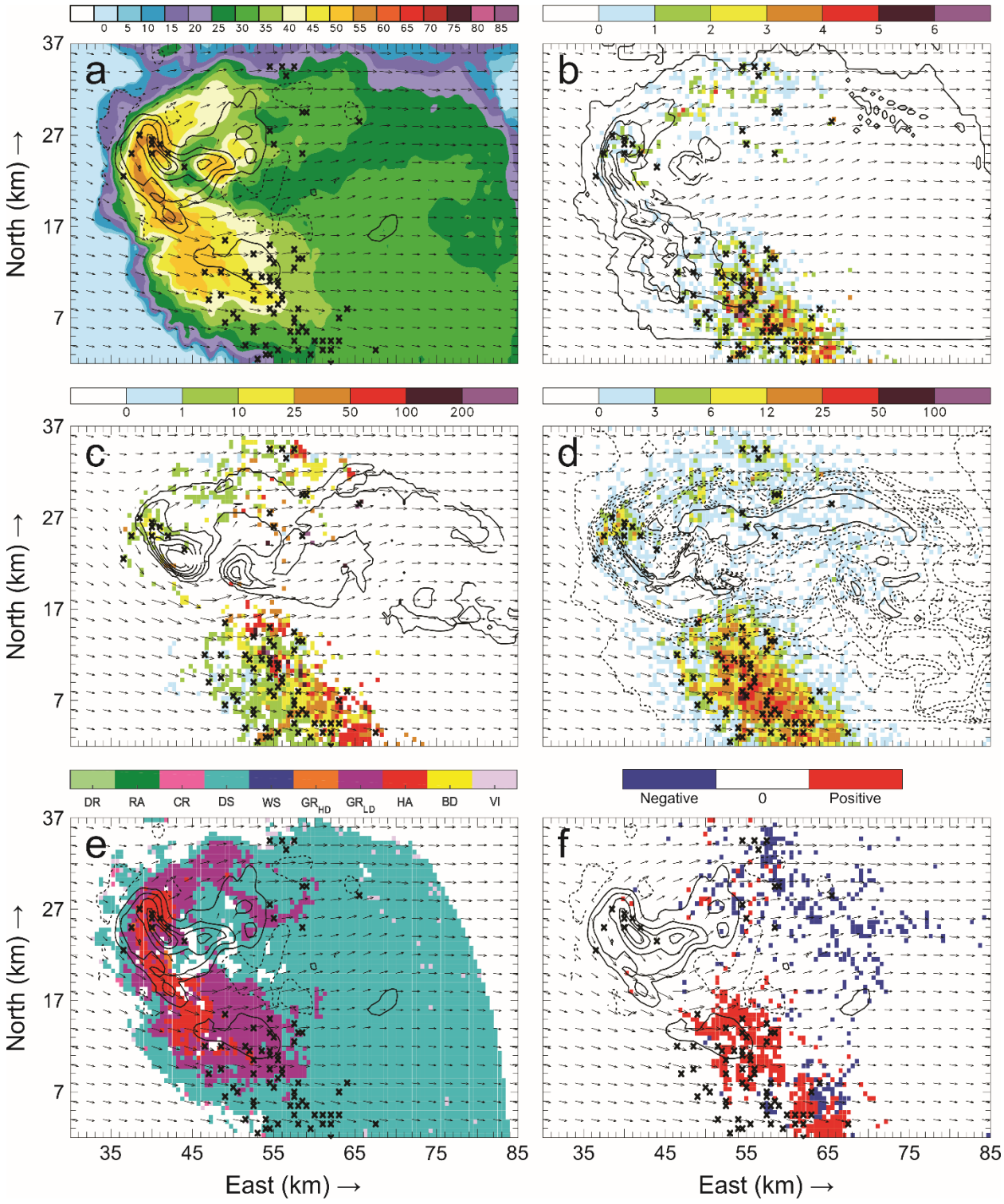

Figure 27: Horizontal cross-sections for 29 May 23:33 UTC. As in Figure 24, but taken at 9.2 km AGL.

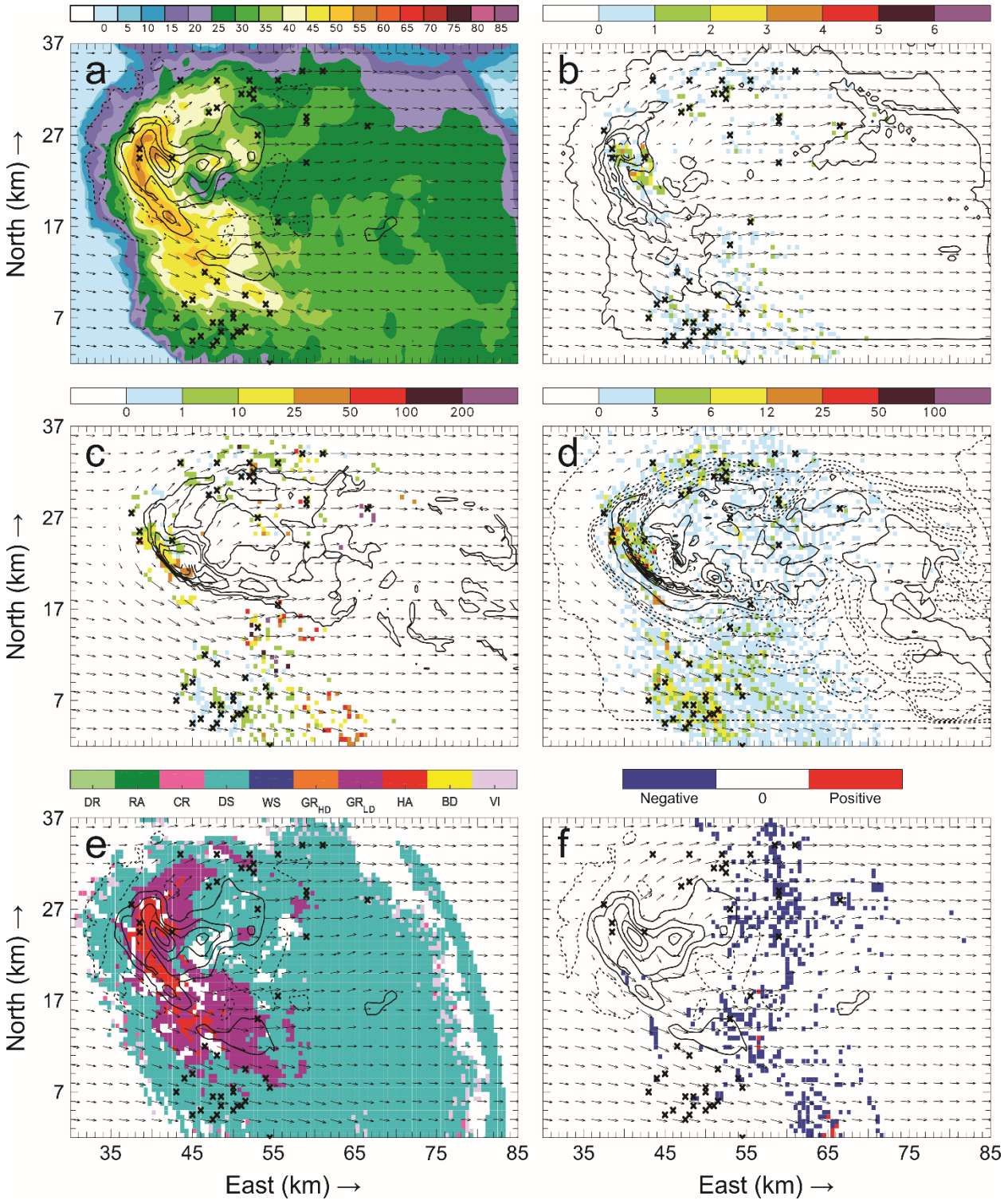

Figure 28: Horizontal cross-sections for 29 May 23:33 UTC. As in Figure 24, but taken at 10.2 km AGL.

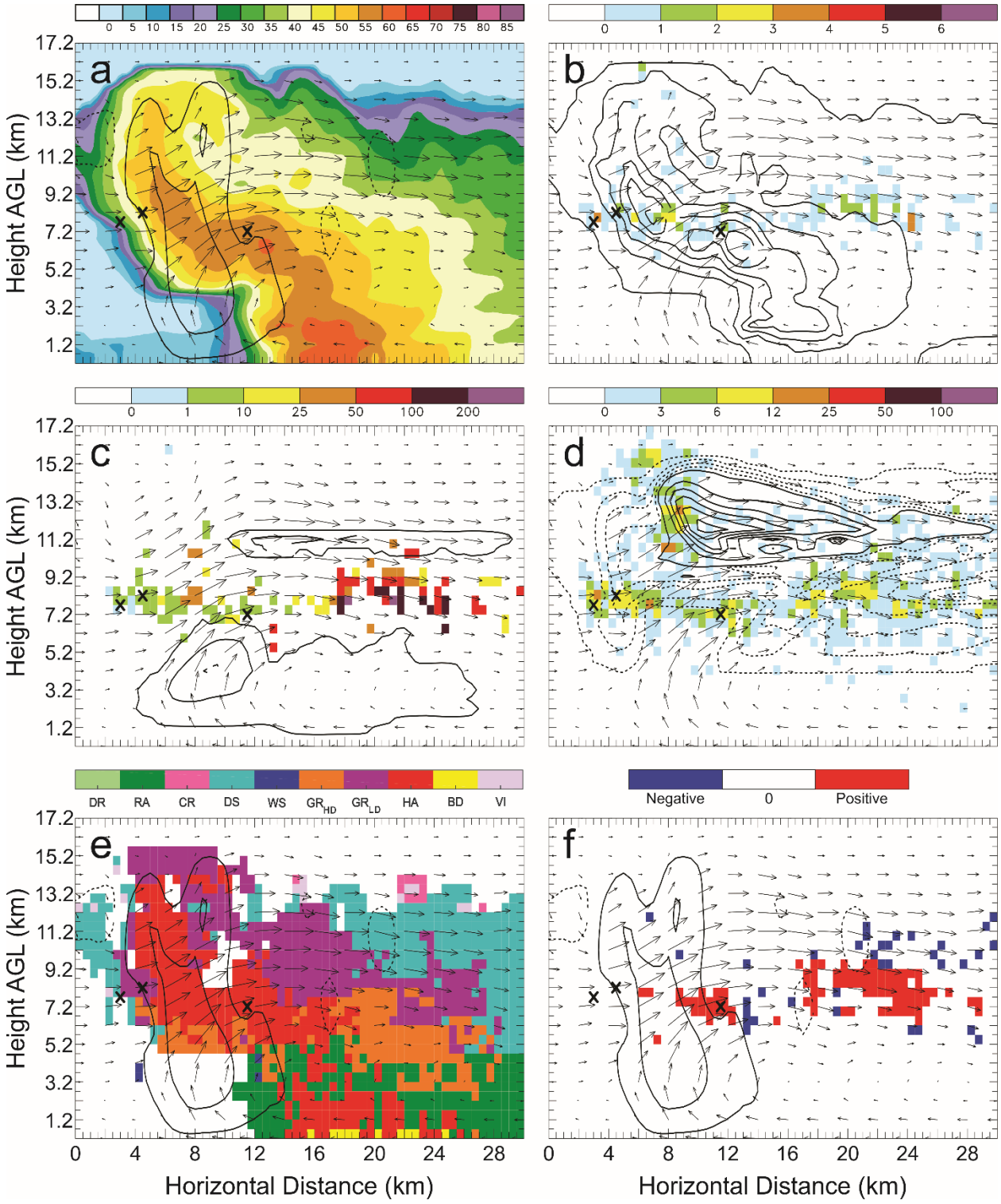

Figure 29: Vertical cross-sections for 29 May 23:33 UTC taken along the southernmost line in Figure 3(c) of: a) color-filled Z and w contours (every 10 m s^{-1} starting at 5 m s^{-1}); b) color-filled FED and q_g contours (every 1.0 g kg^{-1} starting at 0 g kg^{-1}); c) color-filled FP and q_c contours (every 2.0 g kg -1 starting at 0 g kg^{-1}); d) color-filled SD and q_{xs} contours (dashed contours are every 0.25 g kg^{-1} starting at 0 g kg^{-1}, solid contours are every 1.0 g kg^{-1} starting at 1.0 g kg^{-1}); e) color-filled HCA and w contours (every 10 m s^{-1} starting at 5 m s^{-1}); and f) color-filled net inferred space charge and w contours (every 10 m s^{-1} starting at 5 m s^{-1}). All figures have the same horizontal storm-relative wind vectors, and black X's denote grid cells with FID > 0.

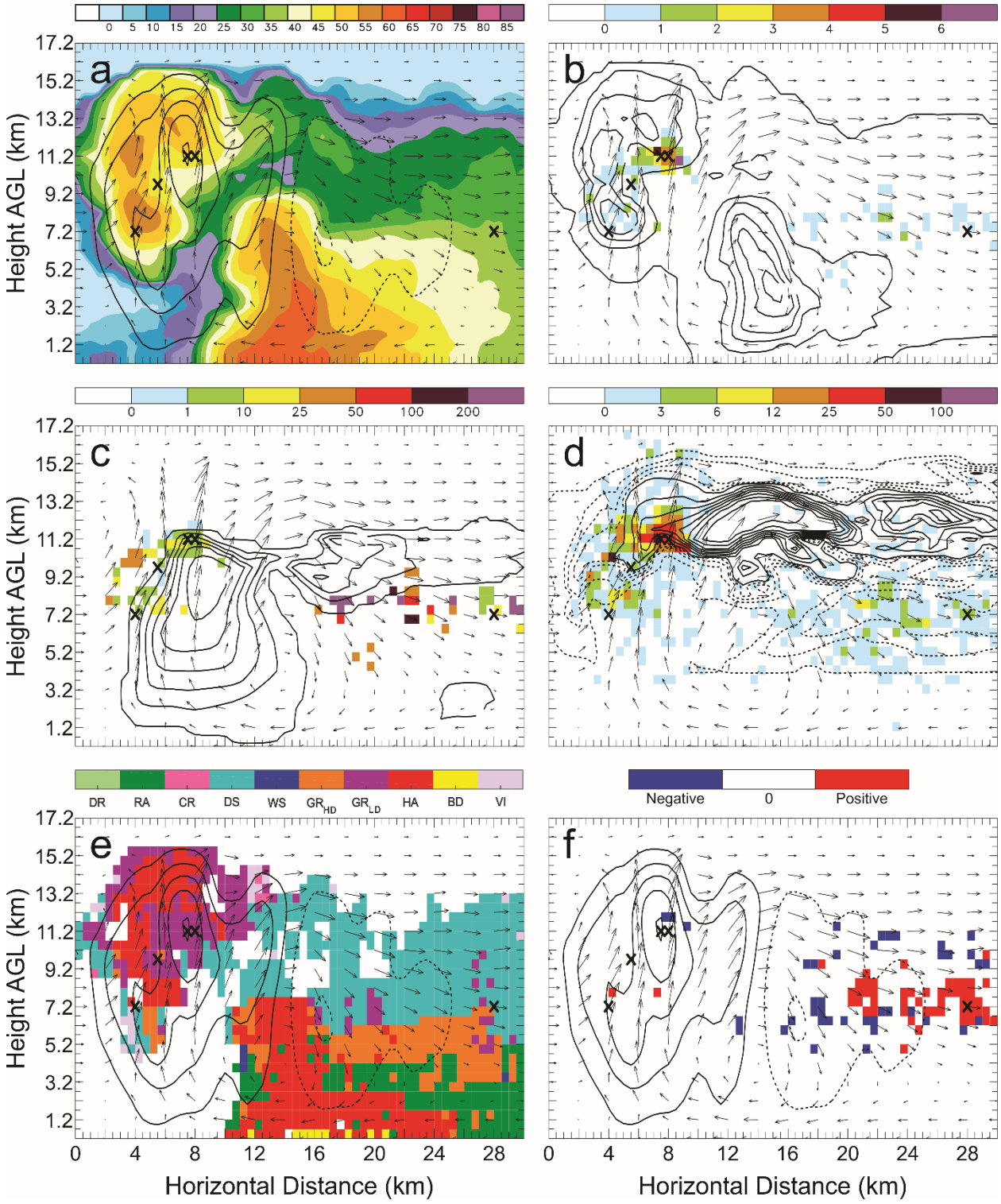

Figure 30: Vertical cross-sections for 29 May 23:33 UTC. As in Figure 29, but taken along the second line from the south in Figure 3(c).

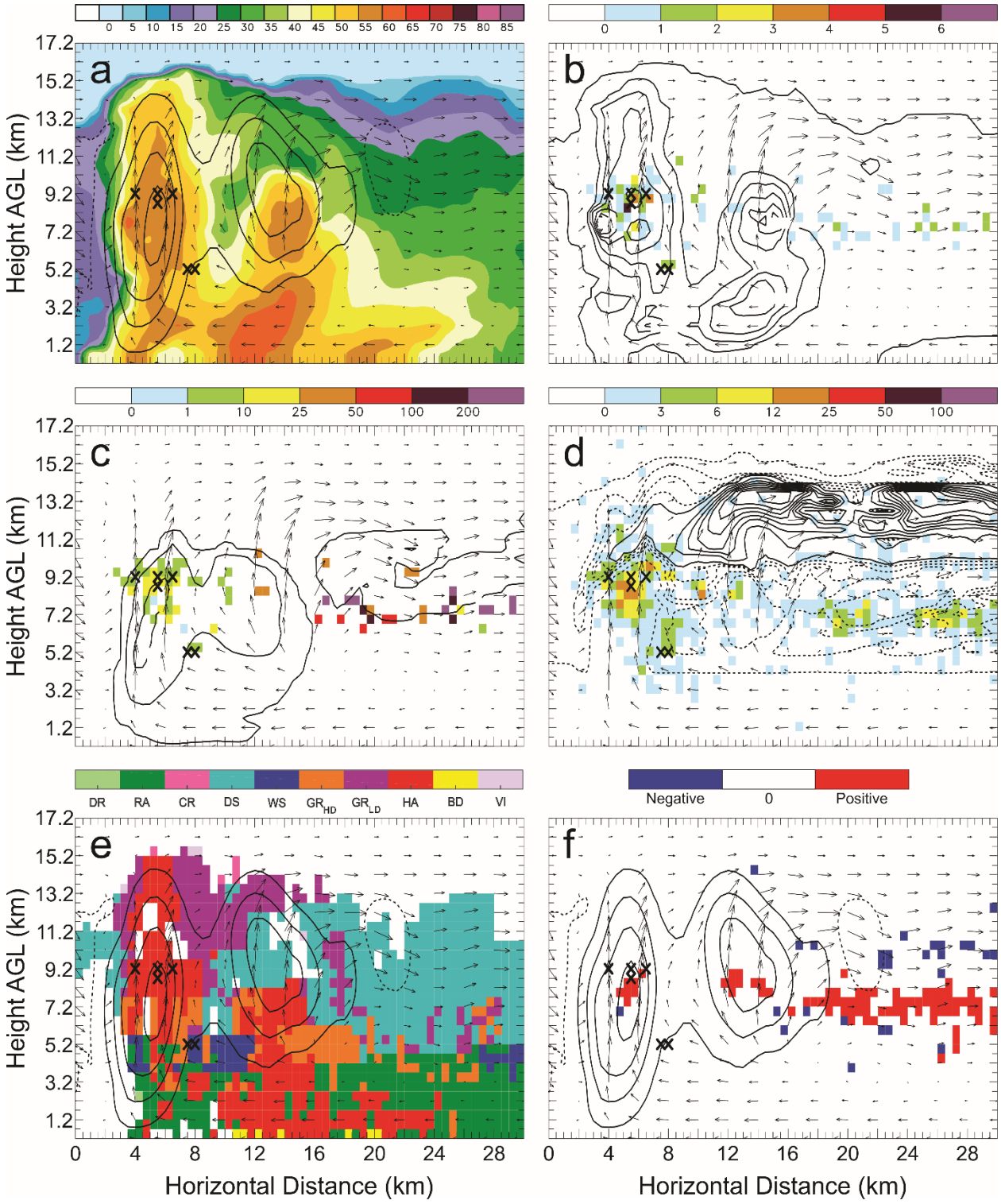

Figure 31: Vertical cross-sections for 29 May 23:33 UTC. As in Figure 29, but taken along the central line in Figure 3(c).

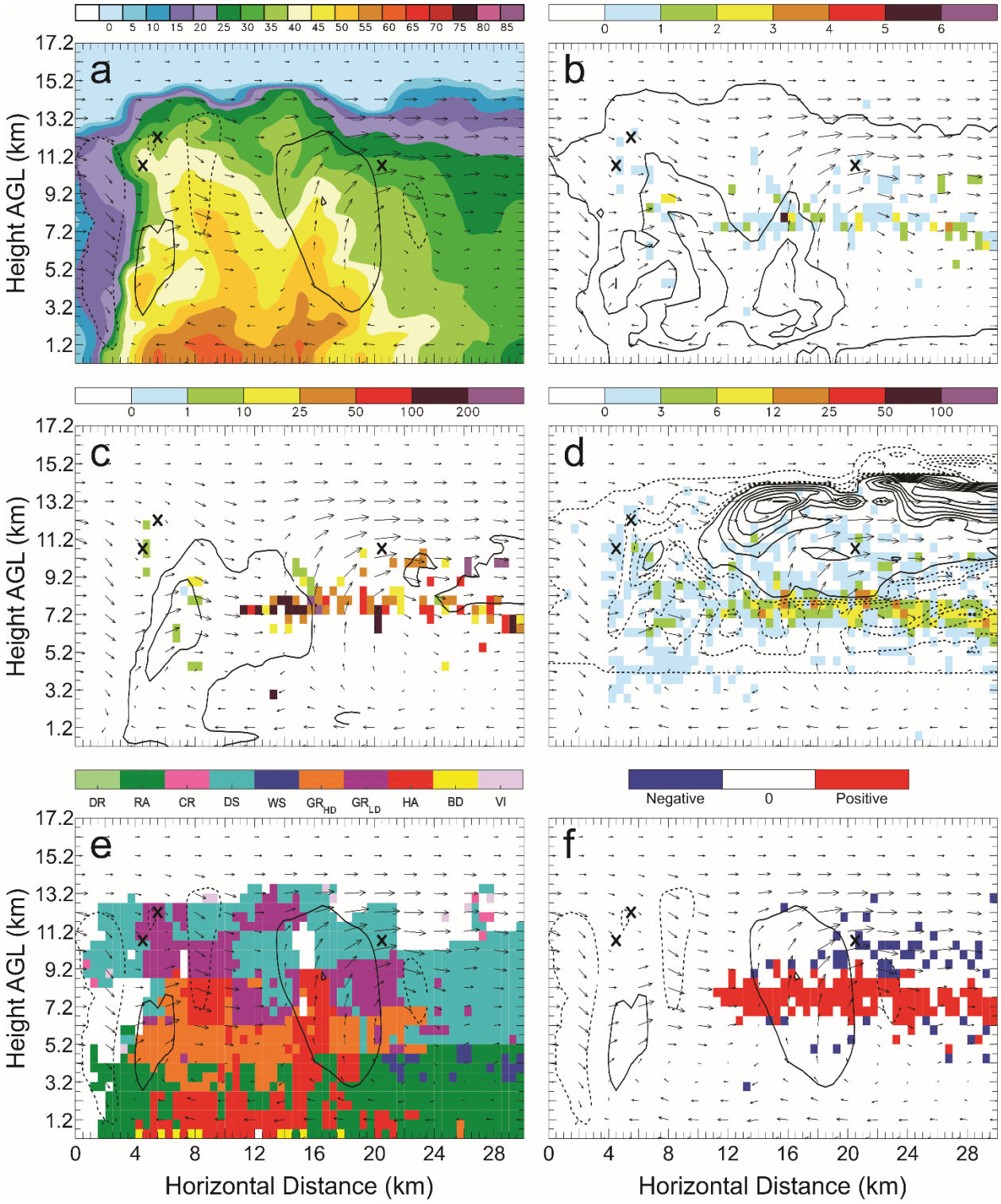

Figure 32: Vertical cross-sections for 29 May 23:33 UTC. As in Figure 29, but taken along the second line from the north in Figure 3(c).

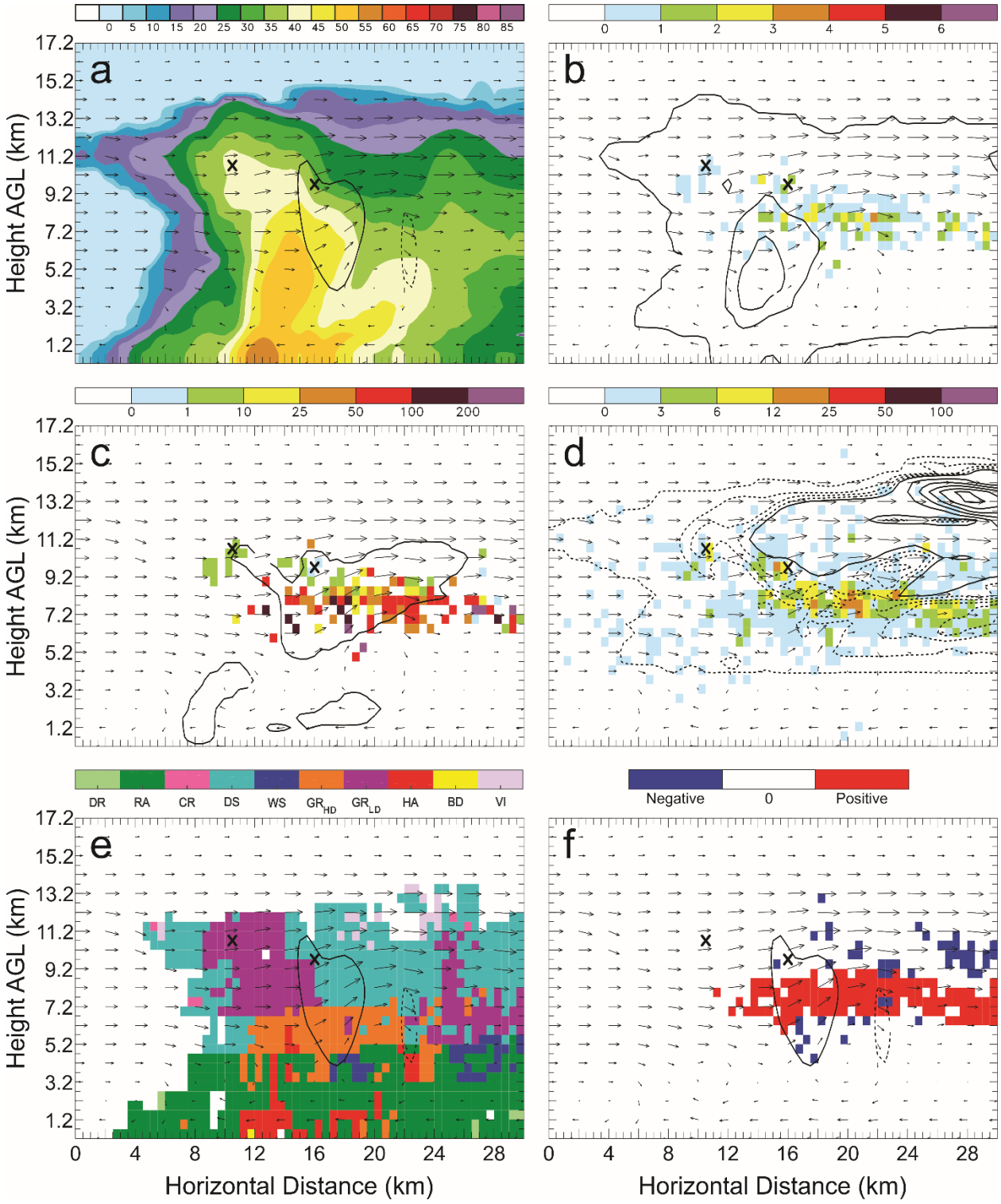

Figure 33: Vertical cross-sections for 29 May 23:33 UTC. As in Figure 29, but taken along the northernmost line in Figure 3(c).

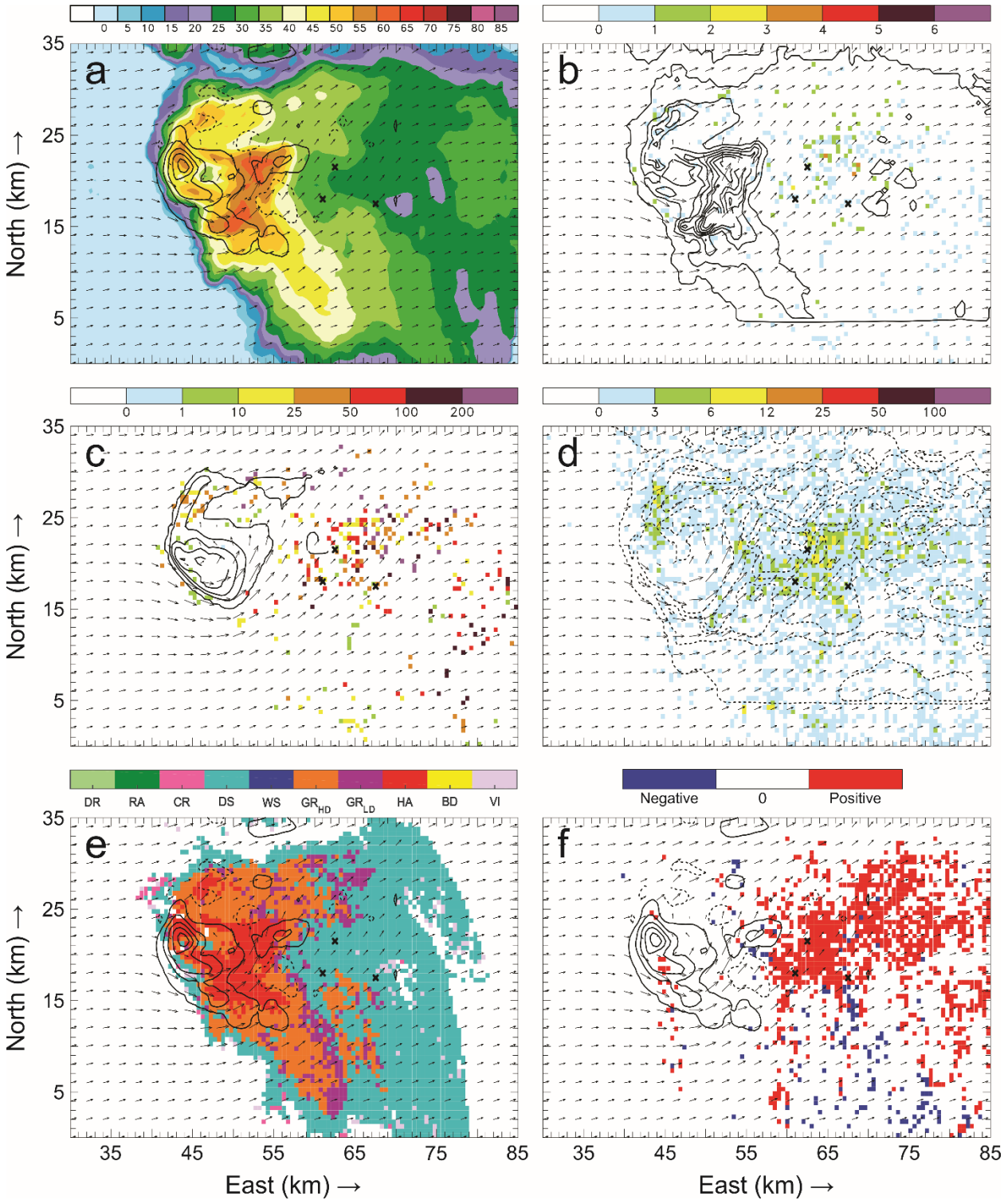

Figure 34: Horizontal cross-sections for 29 May 23:42 UTC taken at 6.2 km AGL of: a) color-filled Z and w contours (every 10 m s^{-1} starting at 5 m s^{-1}); b) color-filled FED and q_g contours (every 1.0 g kg^{-1} starting at 0 g kg^{-1}); c) color-filled FP and q_c contours (every 2.0 g kg -1 starting at 0 g kg^{-1}); d) color-filled SD and q_{xs} contours (dashed contours are every 0.25 g kg^{-1} starting at 0 g kg^{-1}, solid contours are every 1.0 g kg^{-1} starting at 1.0 g kg^{-1}); e) color-filled HCA and w contours (every 10 m s^{-1} starting at 5 m s^{-1}); and f) color-filled net inferred space charge and w contours (every 10 m s^{-1} starting at 5 m s^{-1}). All figures have the same horizontal storm-relative wind vectors, and black X's denote grid cells with FID > 0.

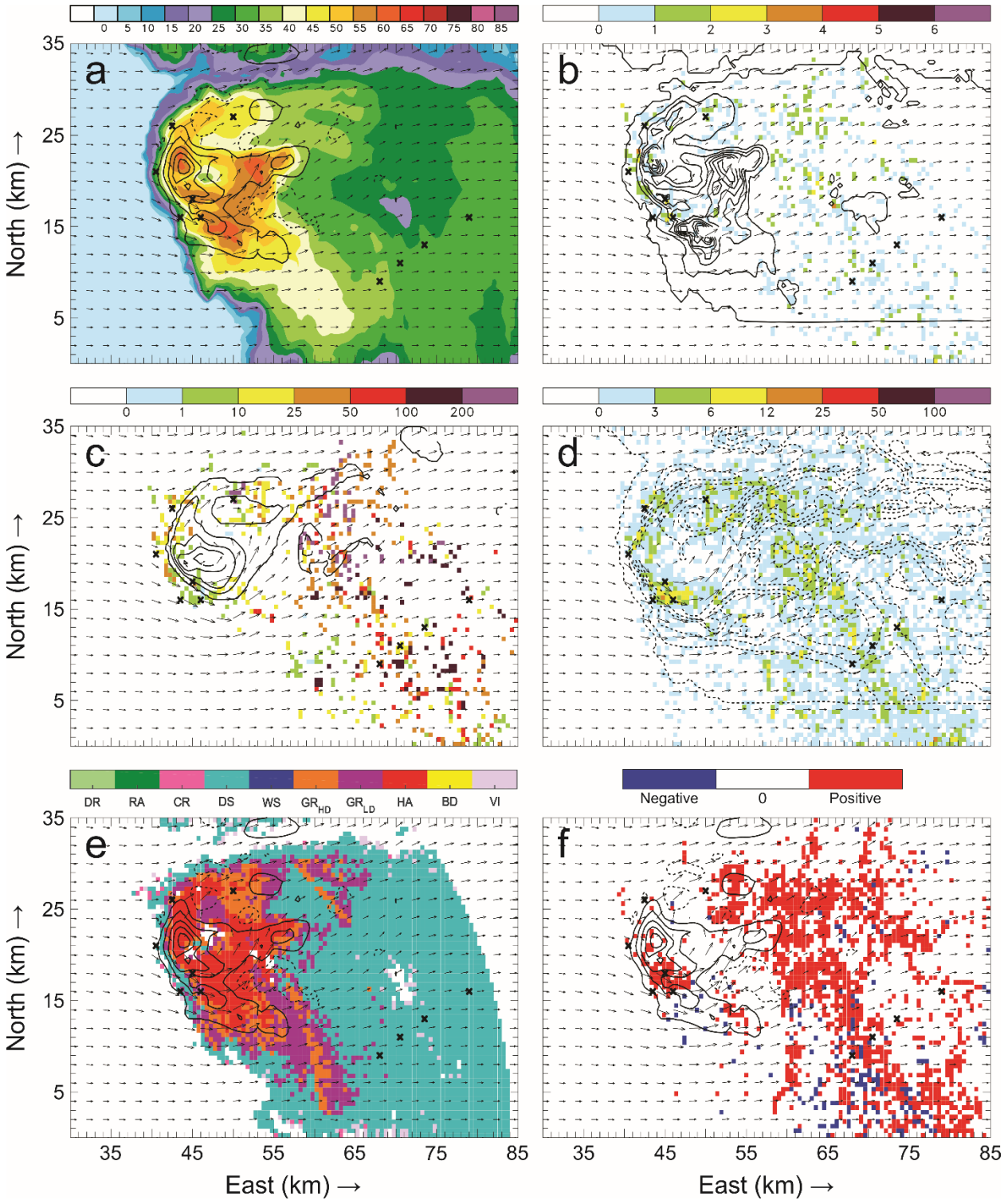

Figure 35: Horizontal cross-sections for 29 May 23:42 UTC. As in Figure 34, but taken at 7.2 km AGL.

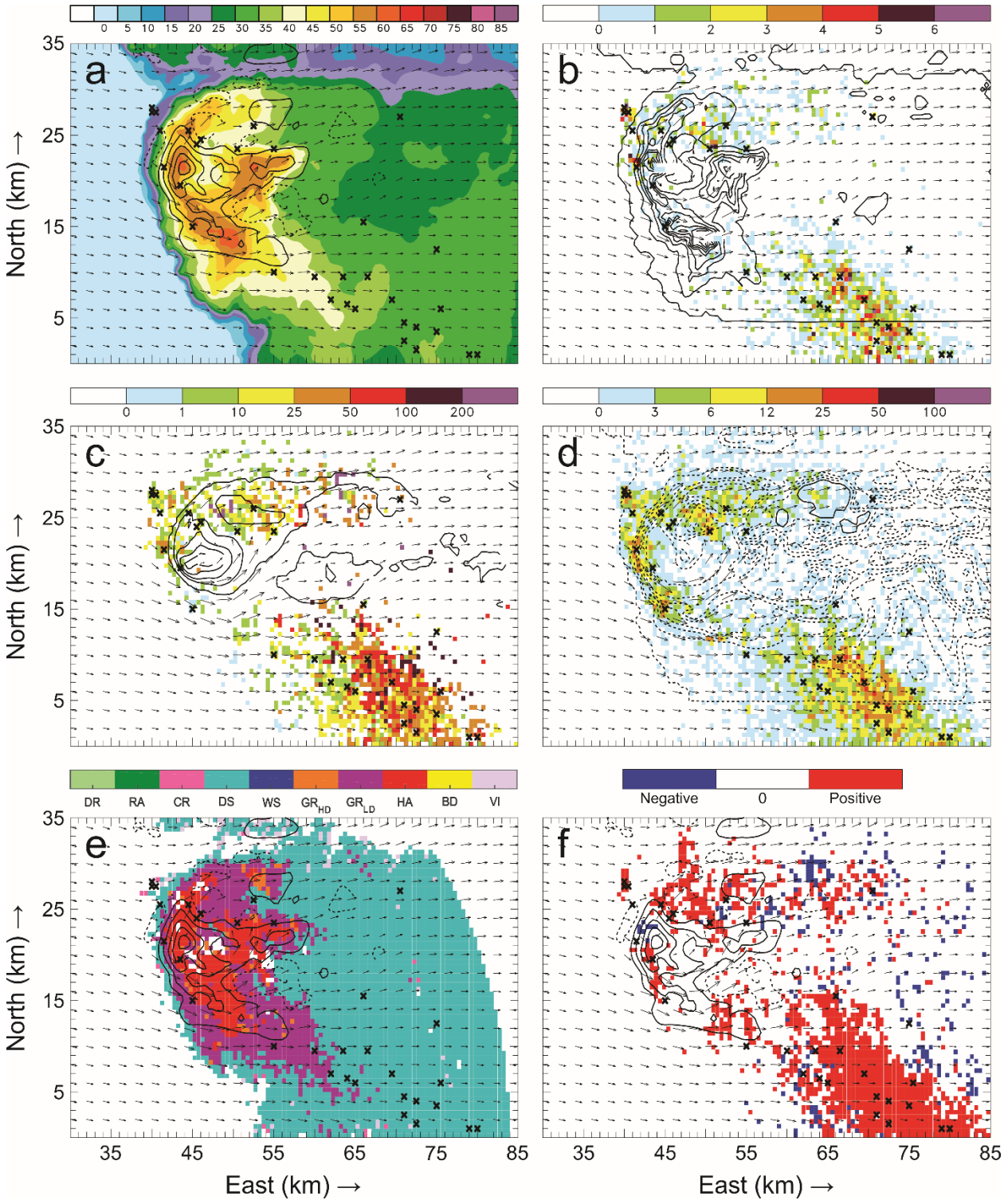

Figure 36: Horizontal cross-sections for 29 May 23:42 UTC. As in Figure 34, but taken at 8.2 km AGL.

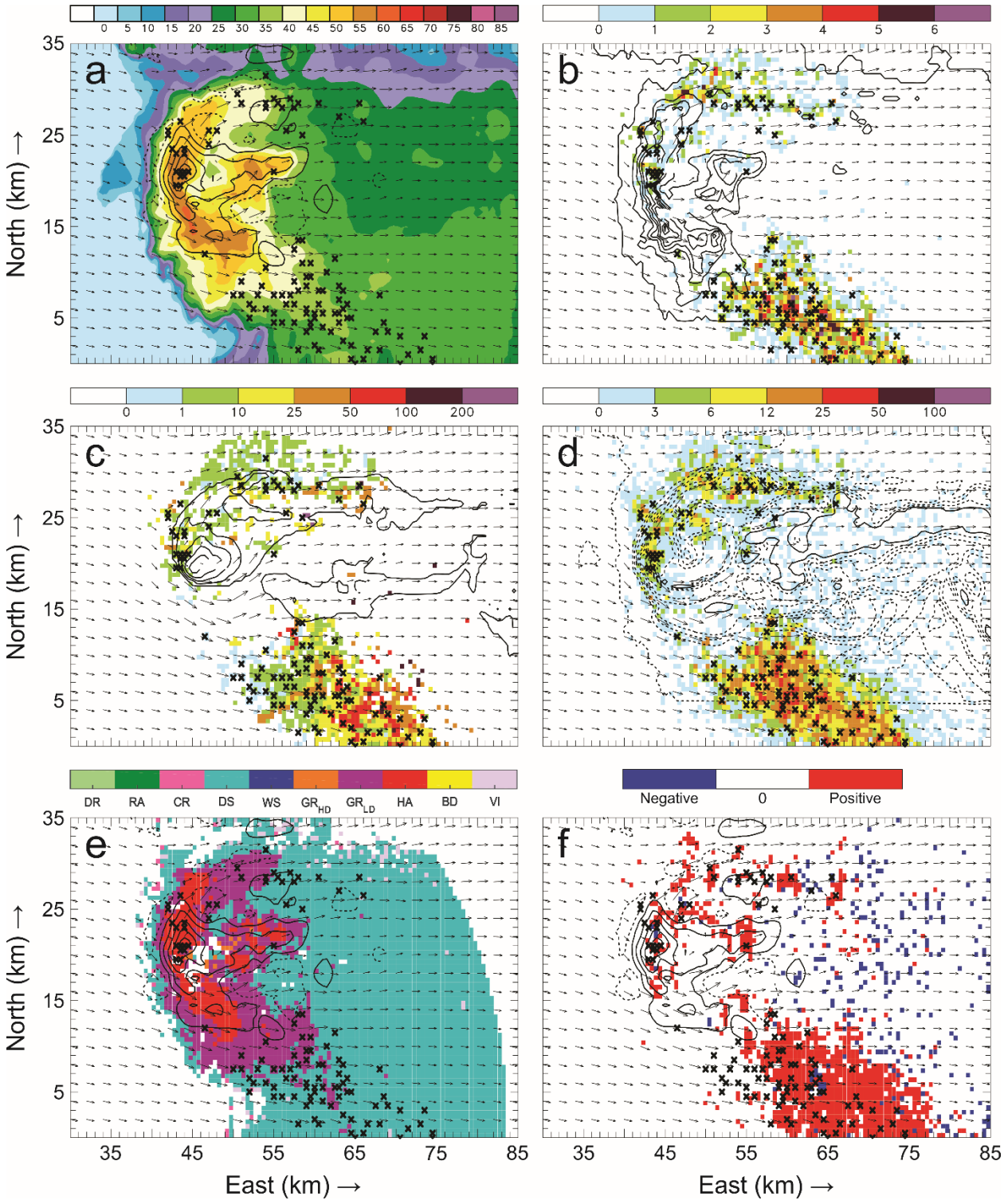

Figure 37: Horizontal cross-sections for 29 May 23:42 UTC. As in Figure 34, but taken at 9.2 km AGL.

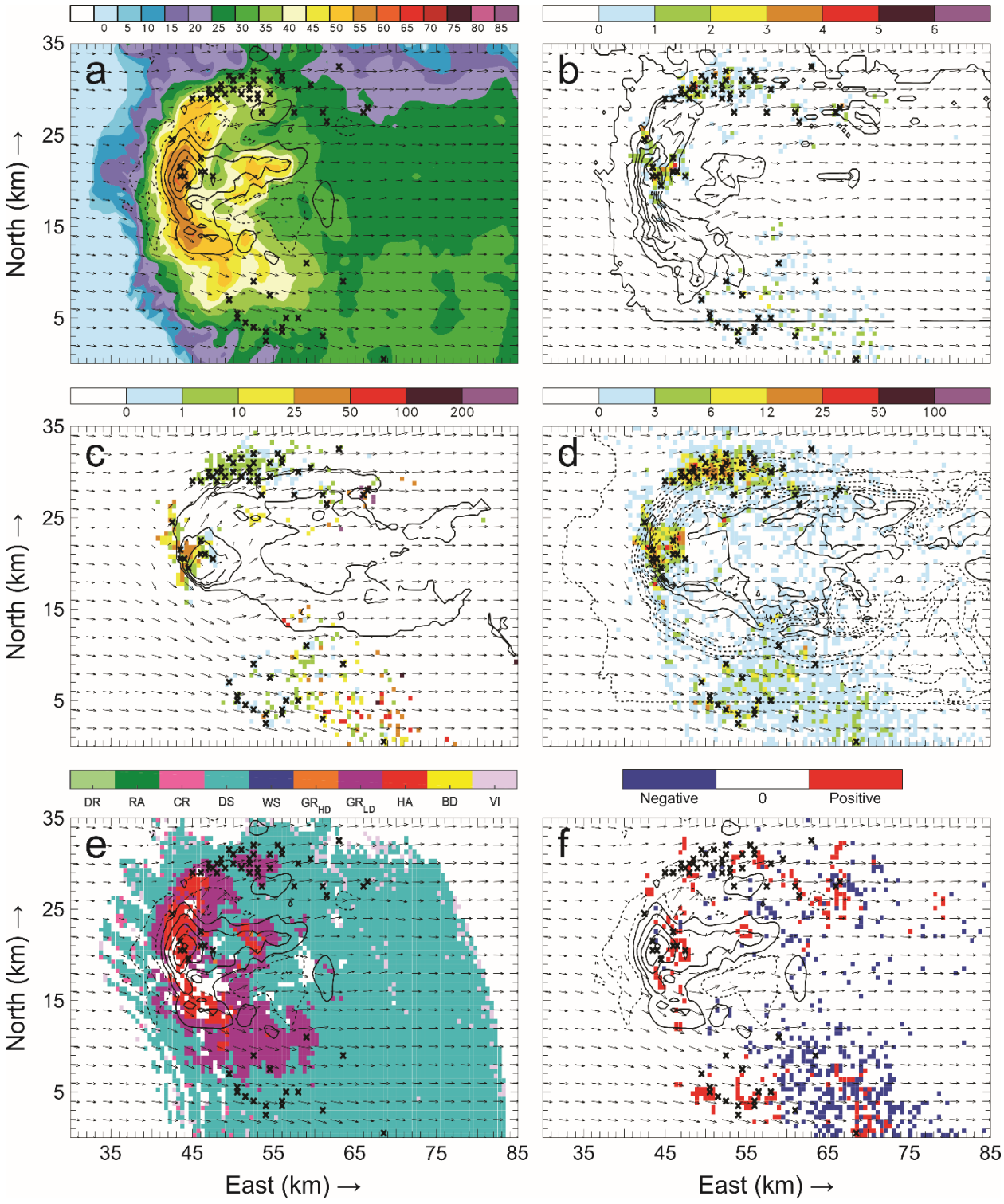

Figure 38: Horizontal cross-sections for 29 May 23:42 UTC. As in Figure 34, but taken at 10.2 km AGL.

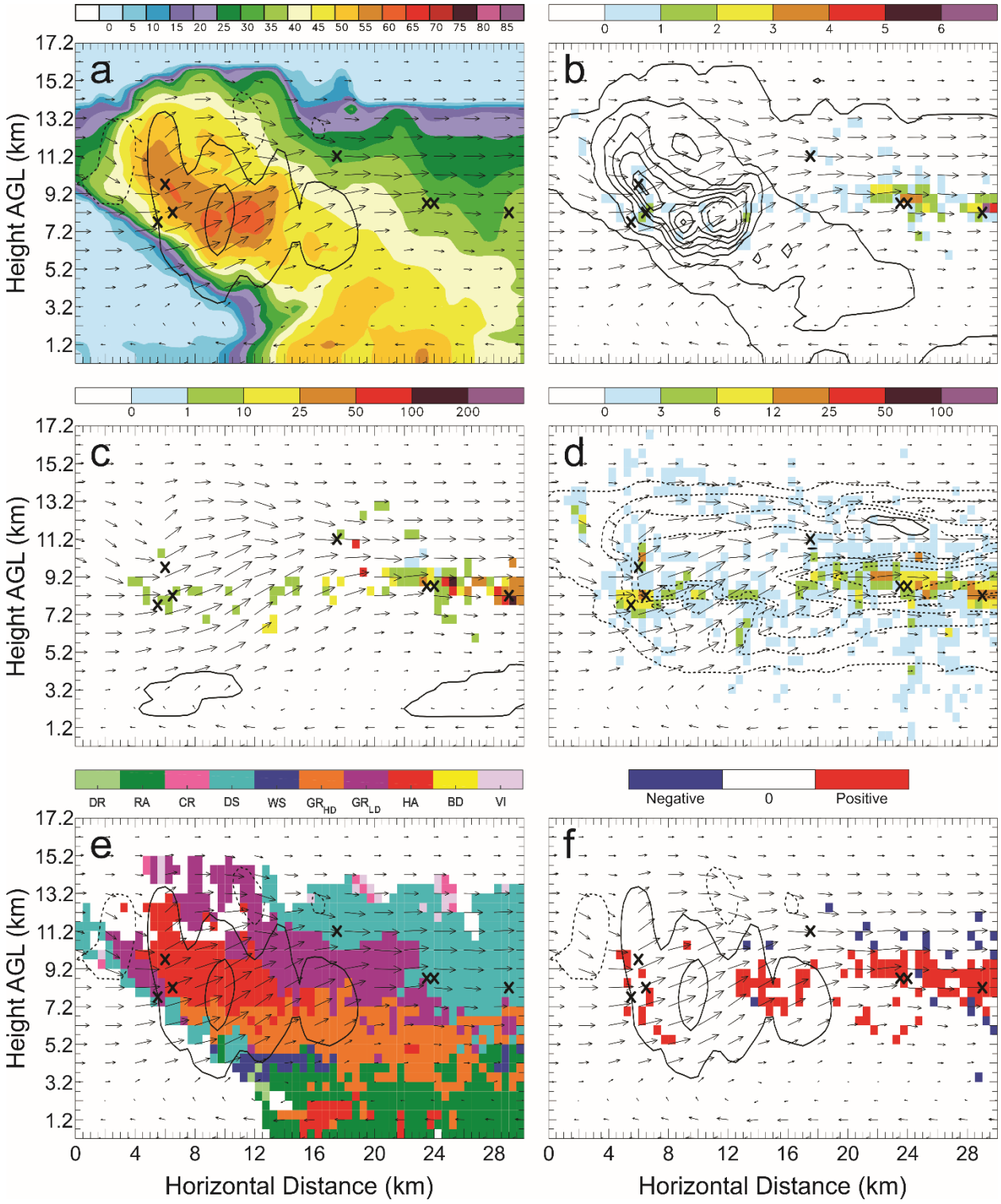

Figure 39: Vertical cross-sections for 29 May 23:42 UTC taken along the southernmost line in Figure 3(d) of: a) color-filled Z and w contours (every 10 m s^{-1} starting at 5 m s^{-1}); b) color-filled FED and q_g contours (every 1.0 g kg^{-1} starting at 0 g kg^{-1}); c) color-filled FP and q_c contours (every 2.0 g kg -1 starting at 0 g kg^{-1}); d) color-filled SD and q_{xs} contours (dashed contours are every 0.25 g kg^{-1} starting at 0 g kg^{-1}, solid contours are every 1.0 g kg^{-1} starting at 1.0 g kg^{-1}); e) color-filled HCA and w contours (every 10 m s^{-1} starting at 5 m s^{-1}); and f) color-filled net inferred space charge and w contours (every 10 m s^{-1} starting at 5 m s^{-1}). All figures have the same horizontal storm-relative wind vectors, and black X's denote grid cells with FID > 0.

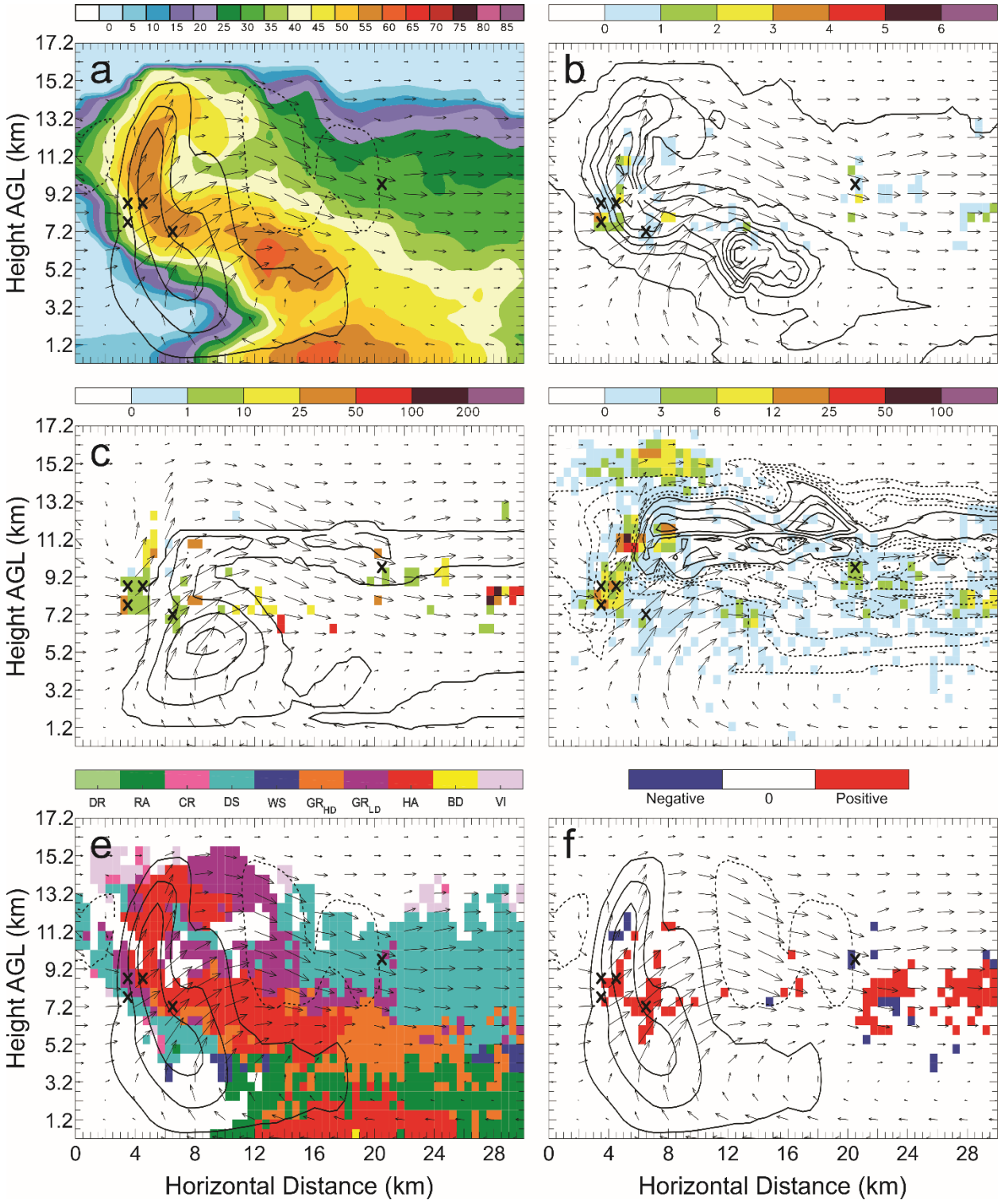

Figure 40: Vertical cross-sections for 29 May 23:42 UTC. As in Figure 39, but taken along the second line from the south in Figure 3(d).

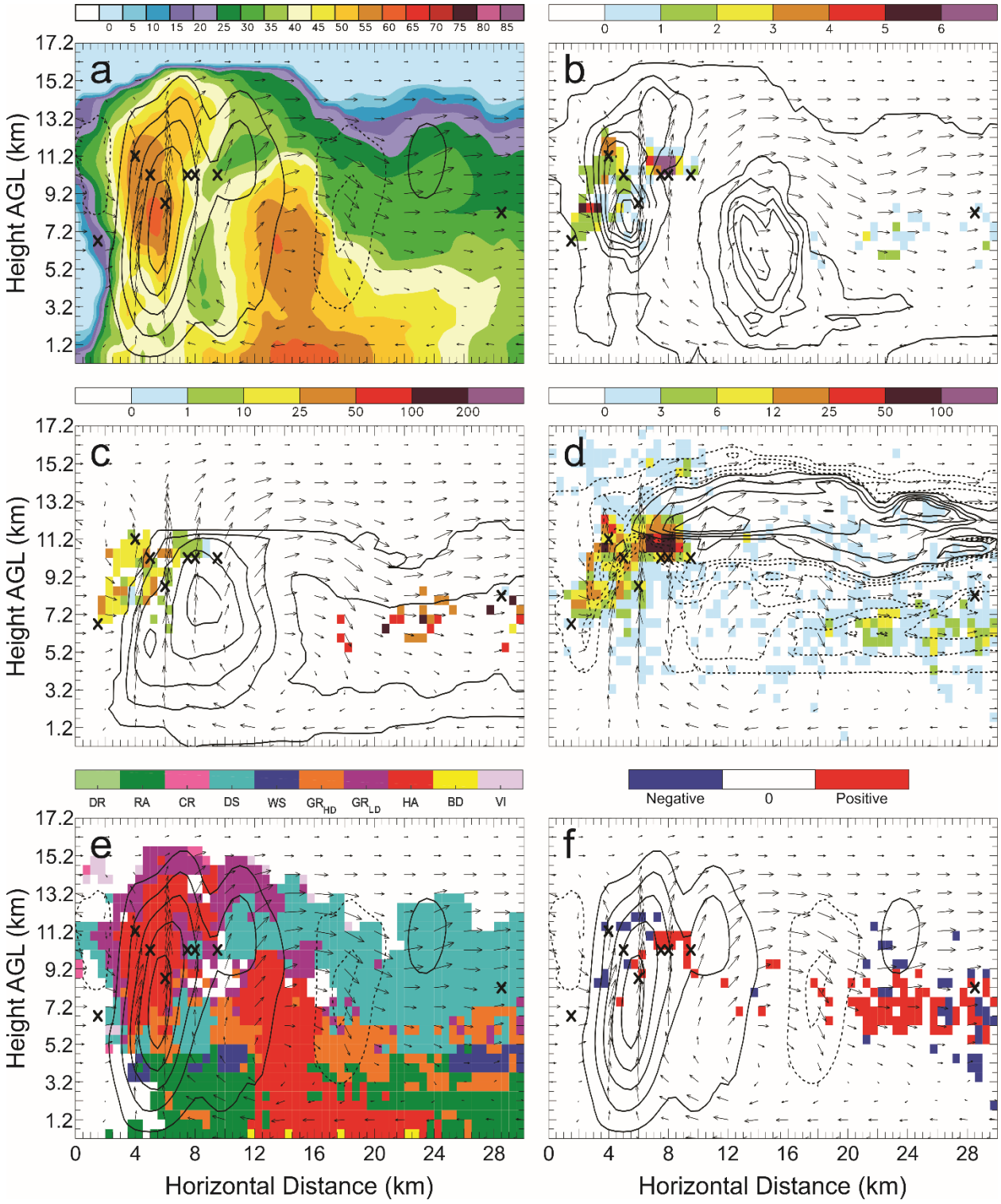

Figure 41: Vertical cross-sections for 29 May 23:42 UTC. As in Figure 39, but taken along the central line in Figure 3(d).

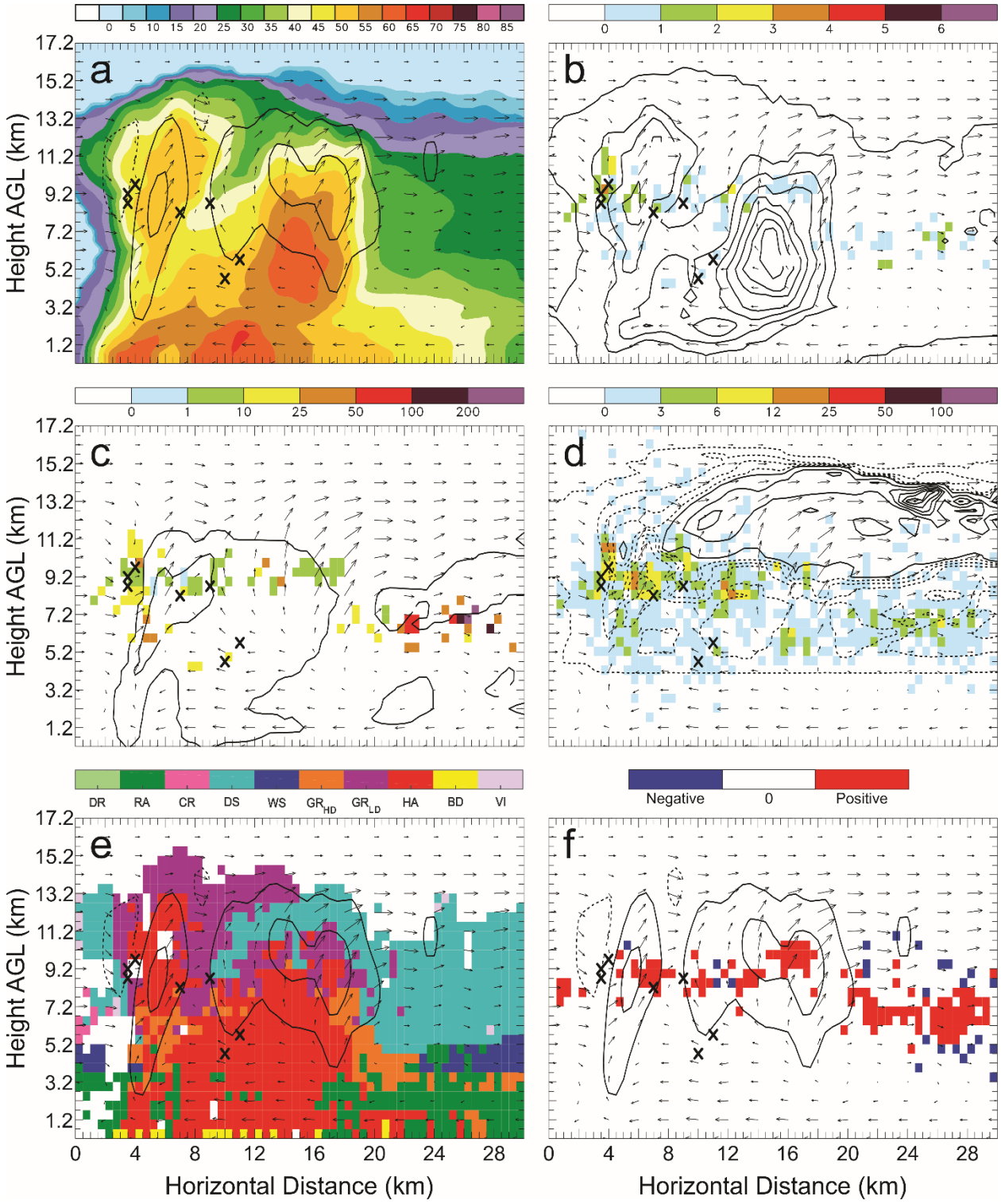

Figure 42: Vertical cross-sections for 29 May 23:42 UTC. As in Figure 39, but taken along the second line from the north in Figure 3(d).

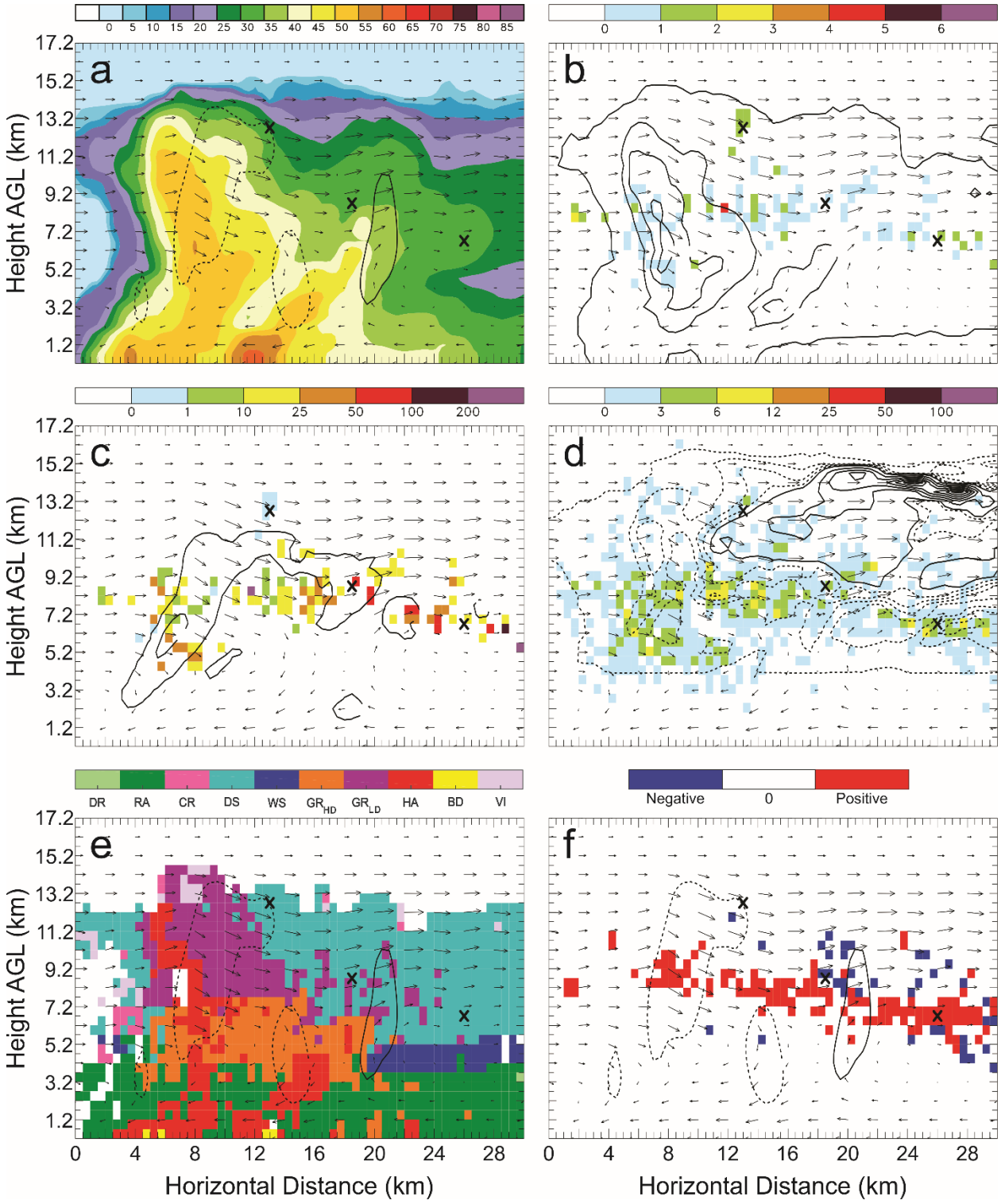

Figure 43: Vertical cross-sections for 29 May 23:42 UTC. As in Figure 39, but taken along the northernmost line in Figure 3(d).

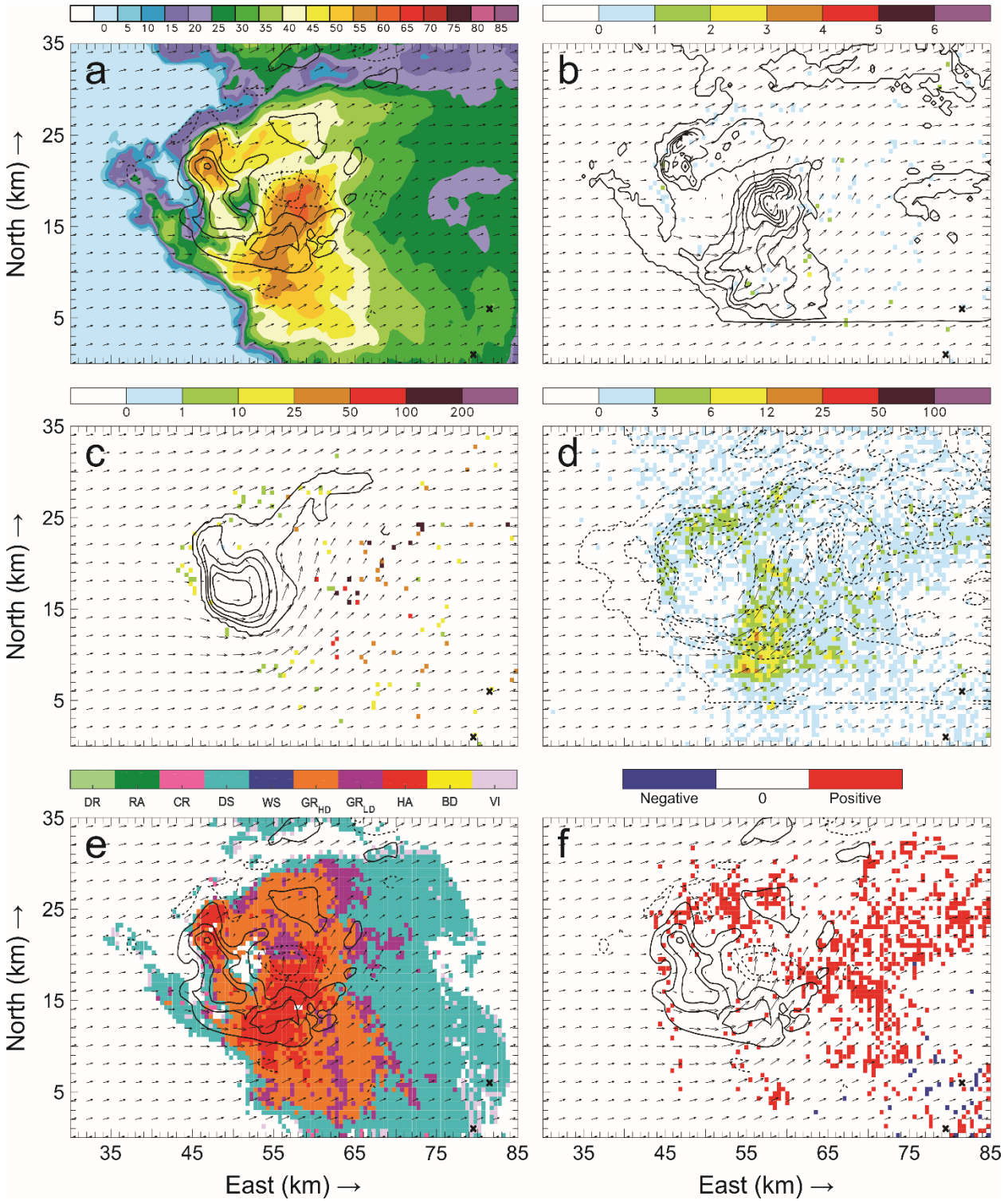

Figure 44: Horizontal cross-sections for 29 May 23:51 UTC taken at 6.2 km AGL of: a) color-filled Z and w contours (every 10 m s^{-1} starting at 5 m s^{-1}); b) color-filled FED and q_g contours (every 1.0 g kg^{-1} starting at 0 g kg^{-1}); c) color-filled FP and q_c contours (every 2.0 g kg -1 starting at 0 g kg^{-1}); d) color-filled SD and q_{xs} contours (dashed contours are every 0.25 g kg^{-1} starting at 0 g kg^{-1}, solid contours are every 1.0 g kg^{-1} starting at 1.0 g kg^{-1}); e) color-filled HCA and w contours (every 10 m s^{-1} starting at 5 m s^{-1}); and f) color-filled net inferred space charge and w contours (every 10 m s^{-1} starting at 5 m s^{-1}). All figures have the same horizontal storm-relative wind vectors, and black X's denote grid cells with FID > 0.

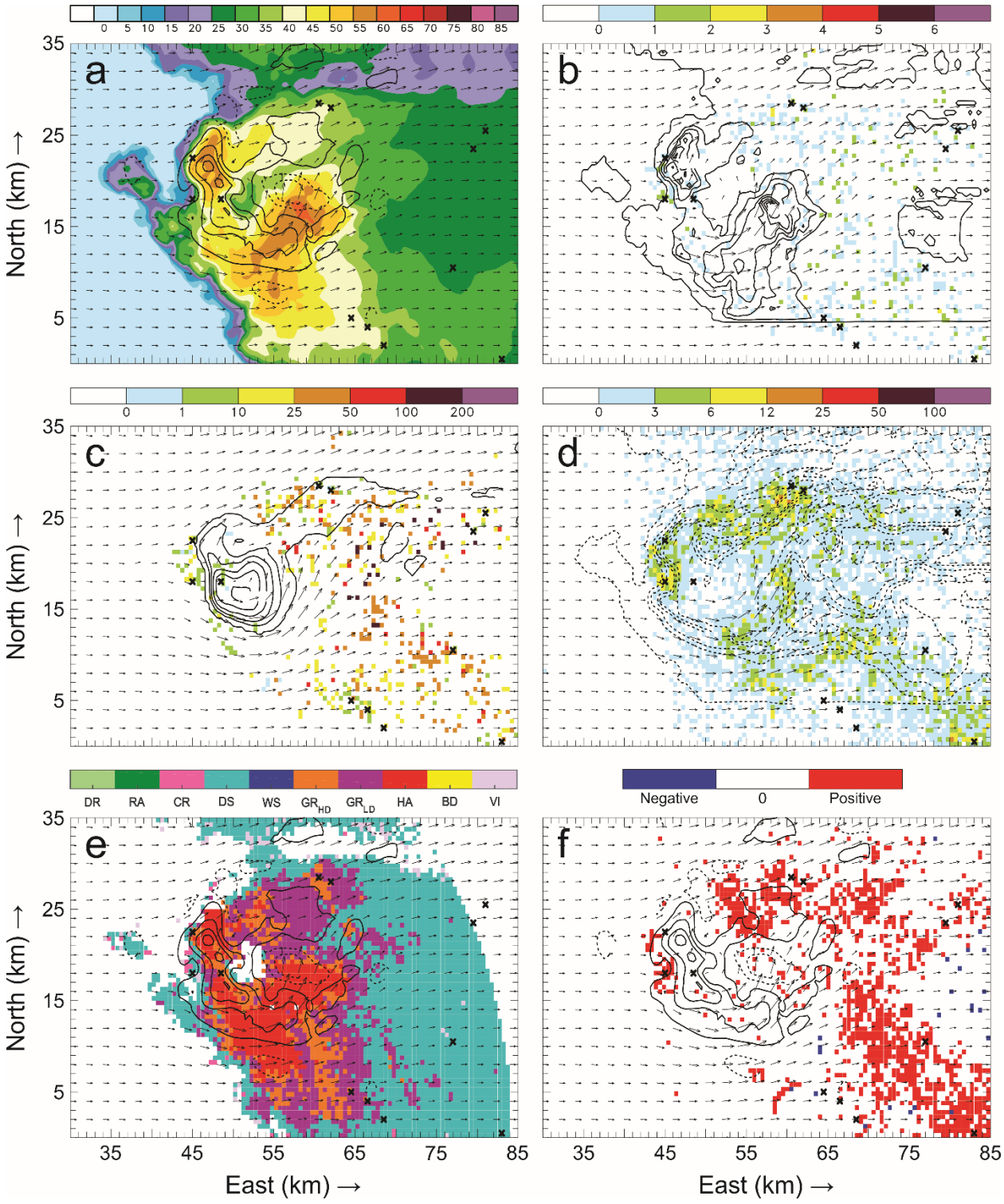

Figure 45: Horizontal cross-sections for 29 May 23:51 UTC. As in Figure 44, but taken at 7.2 km AGL.

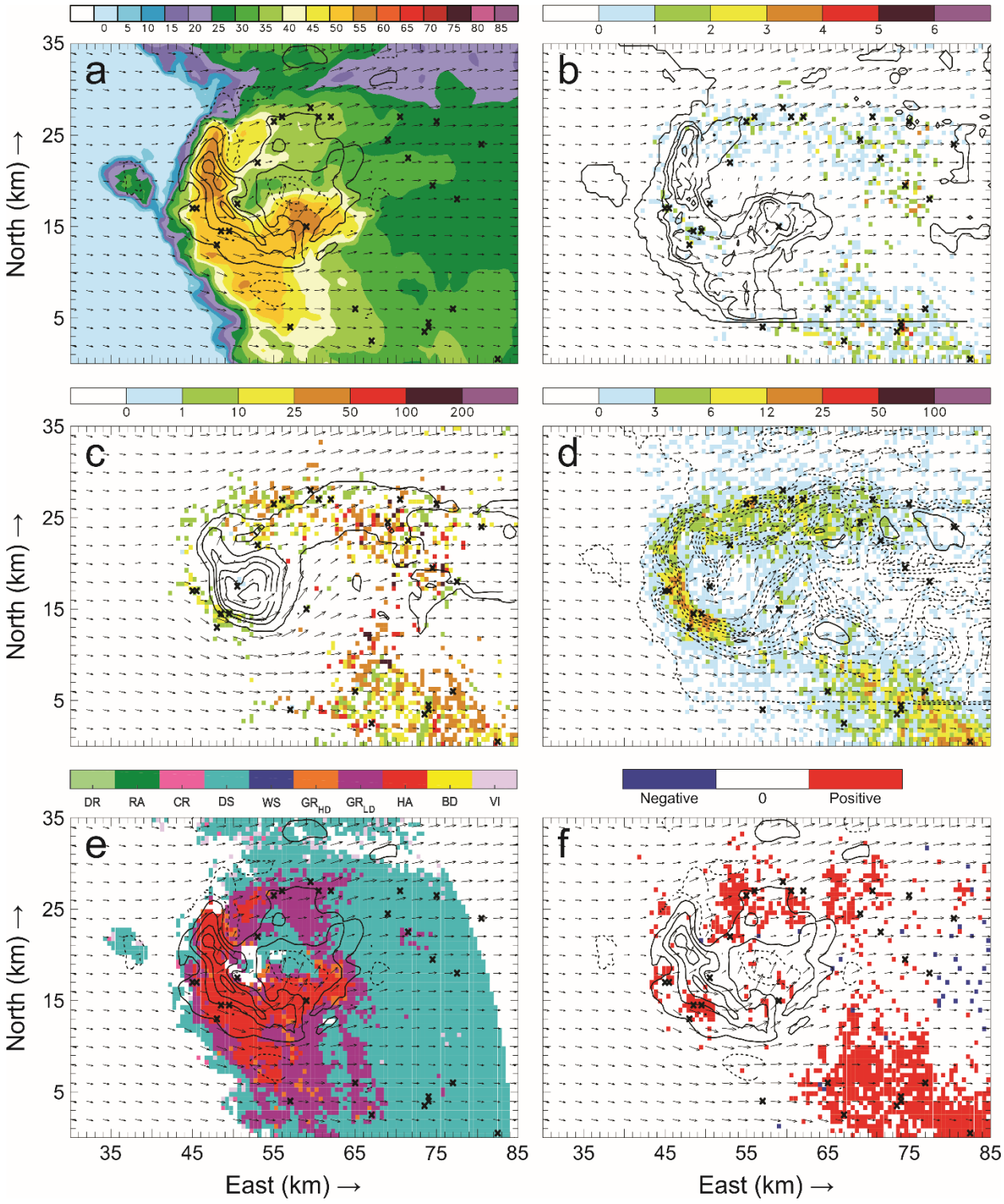

Figure 46: Horizontal cross-sections for 29 May 23:51 UTC. As in Figure 44, but taken at 8.2 km AGL.

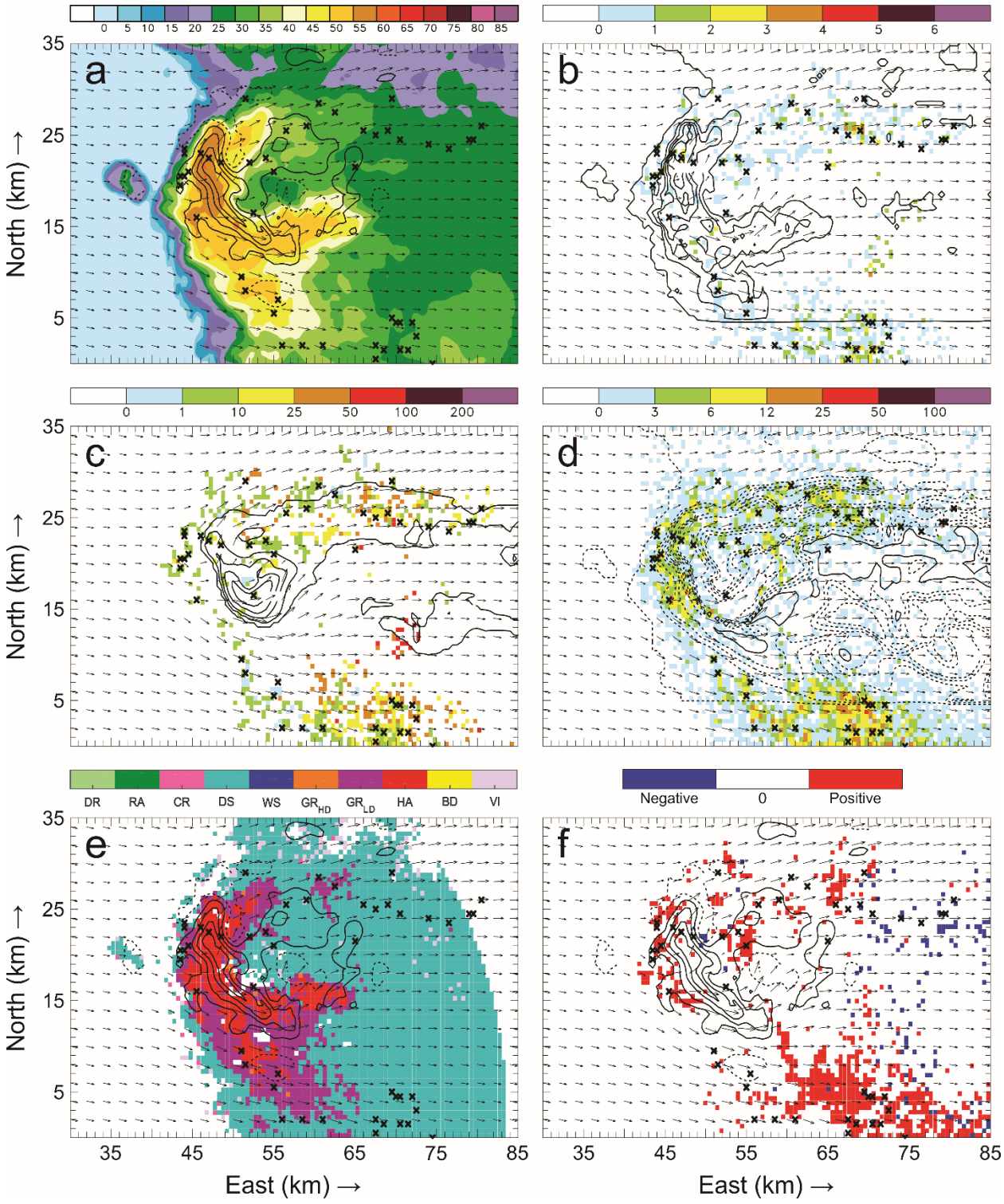

Figure 47: Horizontal cross-sections for 29 May 23:51 UTC. As in Figure 44, but taken at 9.2 km AGL.

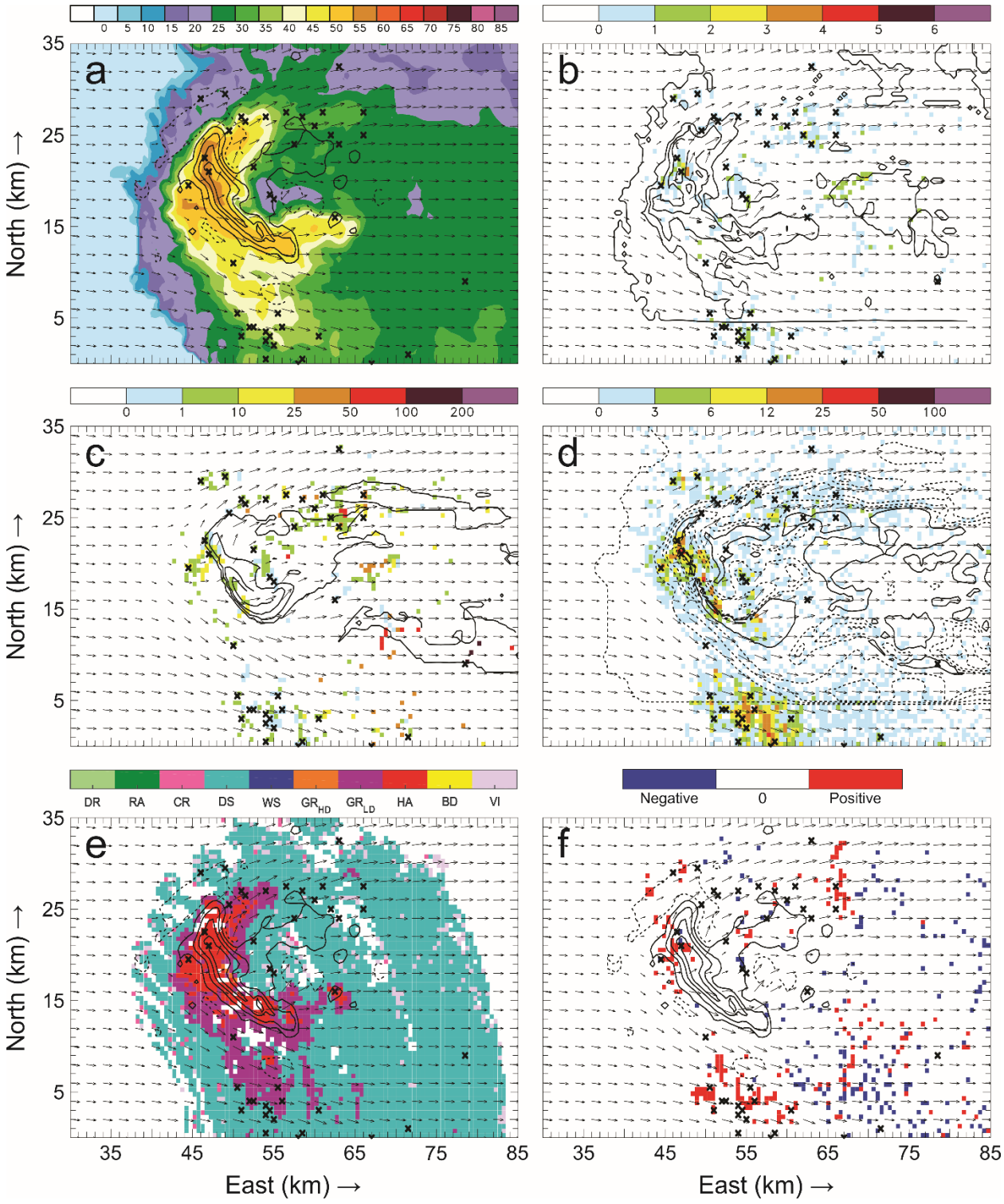

Figure 48: Horizontal cross-sections for 29 May 23:51 UTC. As in Figure 44, but taken at 10.2 km AGL.

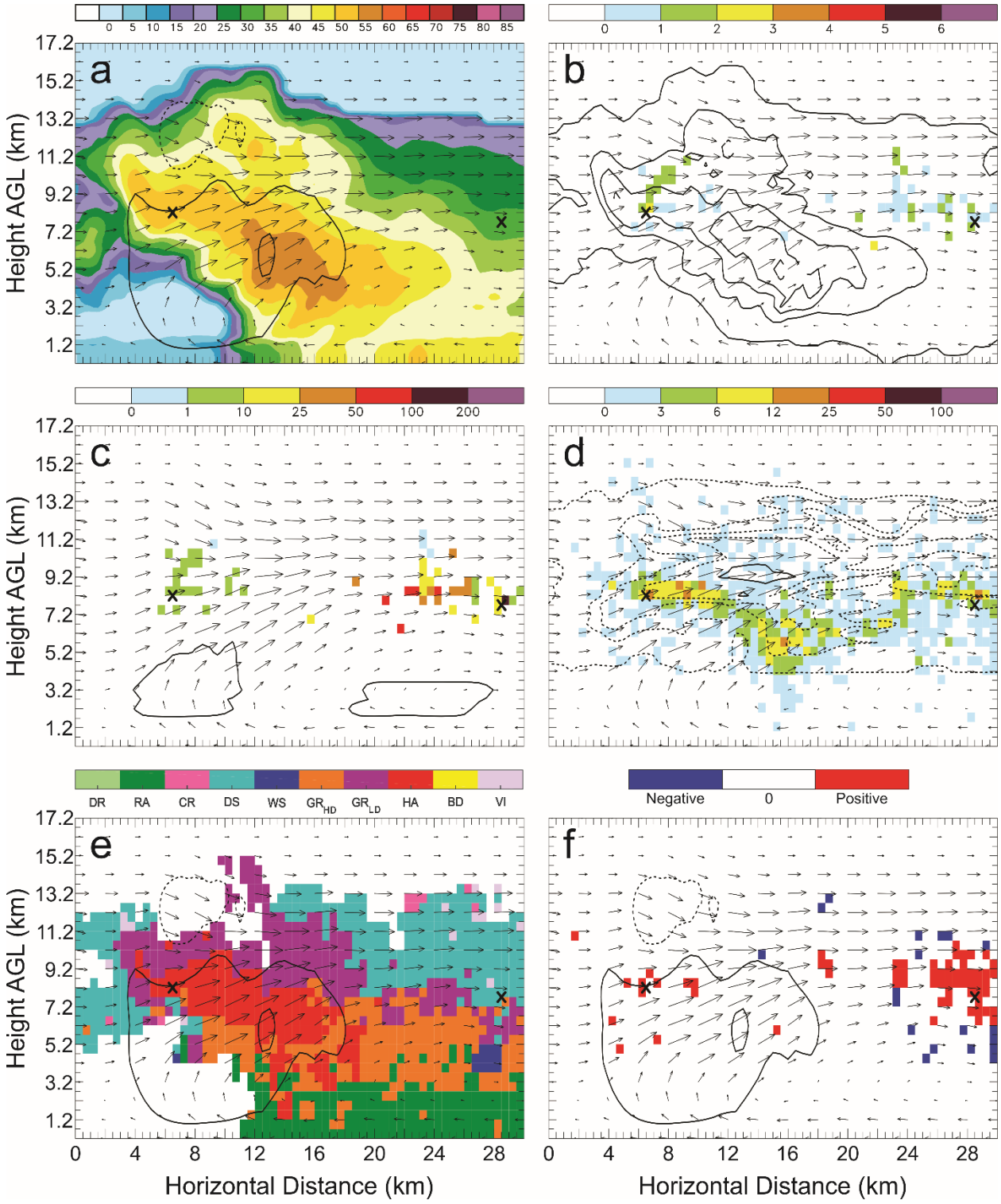

Figure 49: Vertical cross-sections taken for 29 May 23:51 UTC along the southernmost line in Figure 3(e) of: a) color-filled Z and w contours (every 10 m s^{-1} starting at 5 m s^{-1}); b) color-filled FED and q_g contours (every 1.0 g kg^{-1} starting at 0 g kg^{-1}); c) color-filled FP and q_c contours (every 2.0 g kg -1 starting at 0 g kg^{-1}); d) color-filled SD and q_{xs} contours (dashed contours are every 0.25 g kg^{-1} starting at 0 g kg^{-1}, solid contours are every 1.0 g kg^{-1} starting at 1.0 g kg^{-1}); e) color-filled HCA and w contours (every 10 m s^{-1} starting at 5 m s^{-1}); and f) color-filled net inferred space charge and w contours (every 10 m s^{-1} starting at 5 m s^{-1}). All figures have the same horizontal storm-relative wind vectors, and black X's denote grid cells with FID > 0.

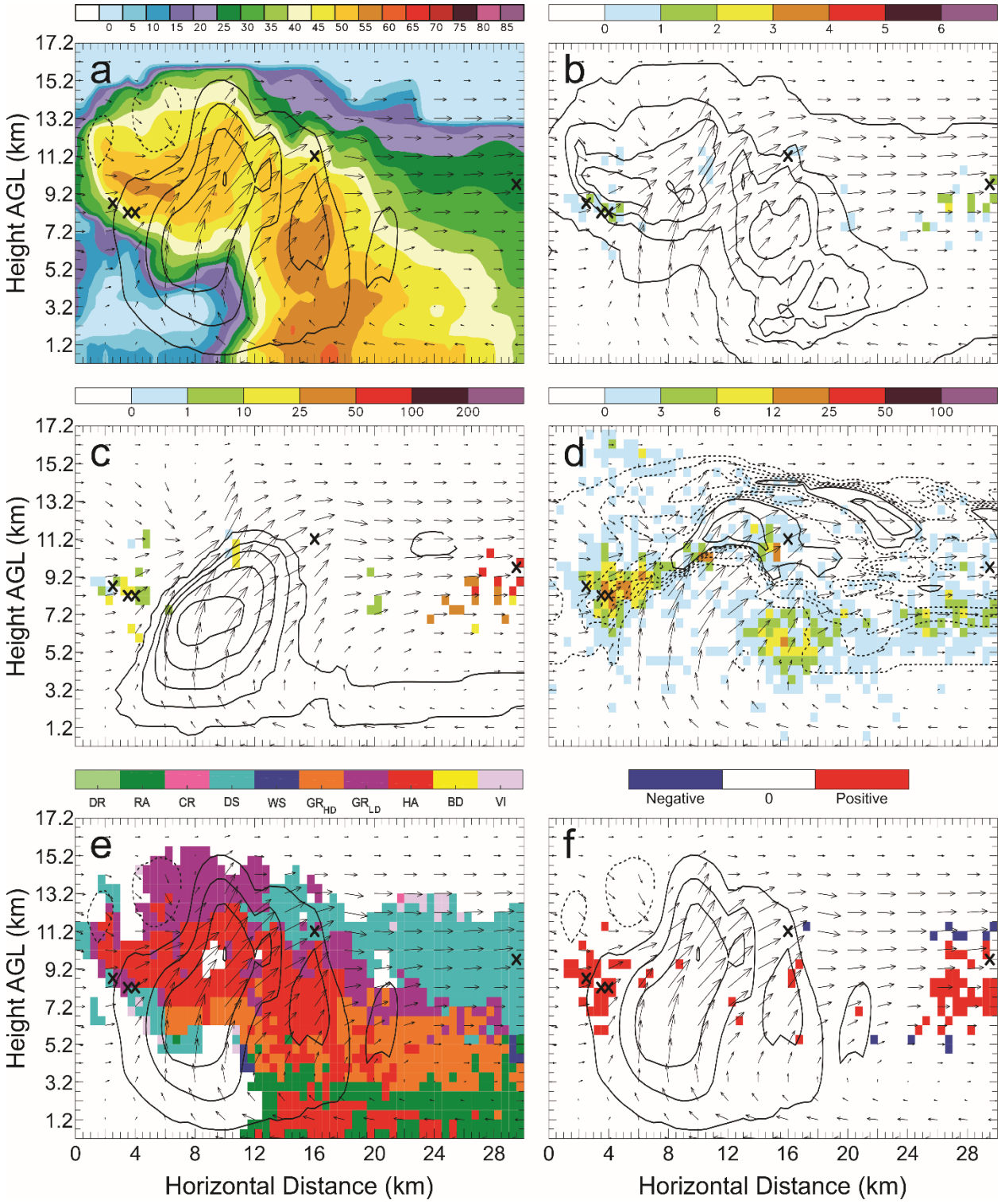

Figure 50: Vertical cross-sections taken for 29 May 23:51 UTC. As in Figure 49, but taken along the second line from the south in Figure 3(e).

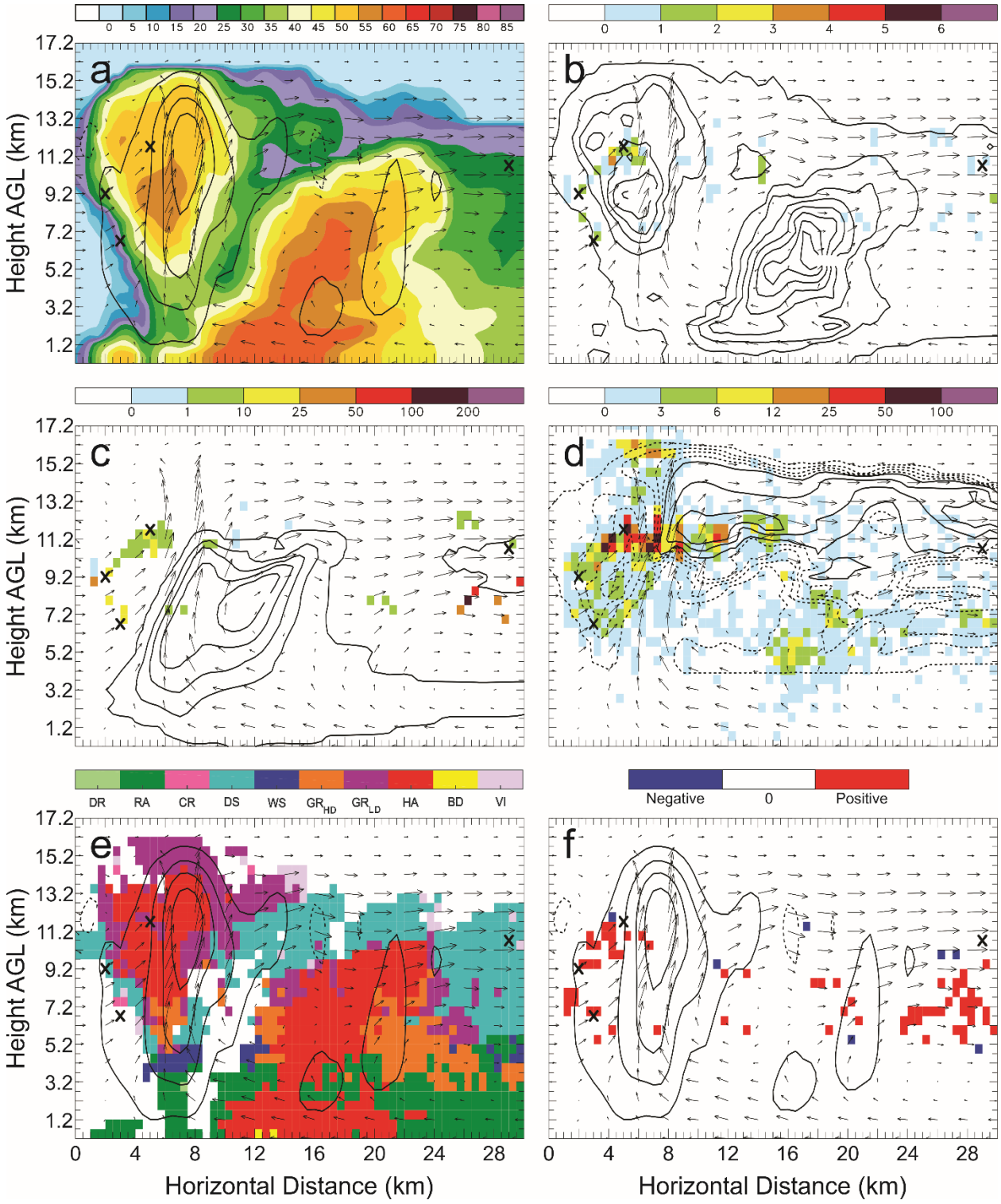

Figure 51: Vertical cross-sections taken for 29 May 23:51 UTC. As in Figure 49, but taken along the central line in Figure 3(e).

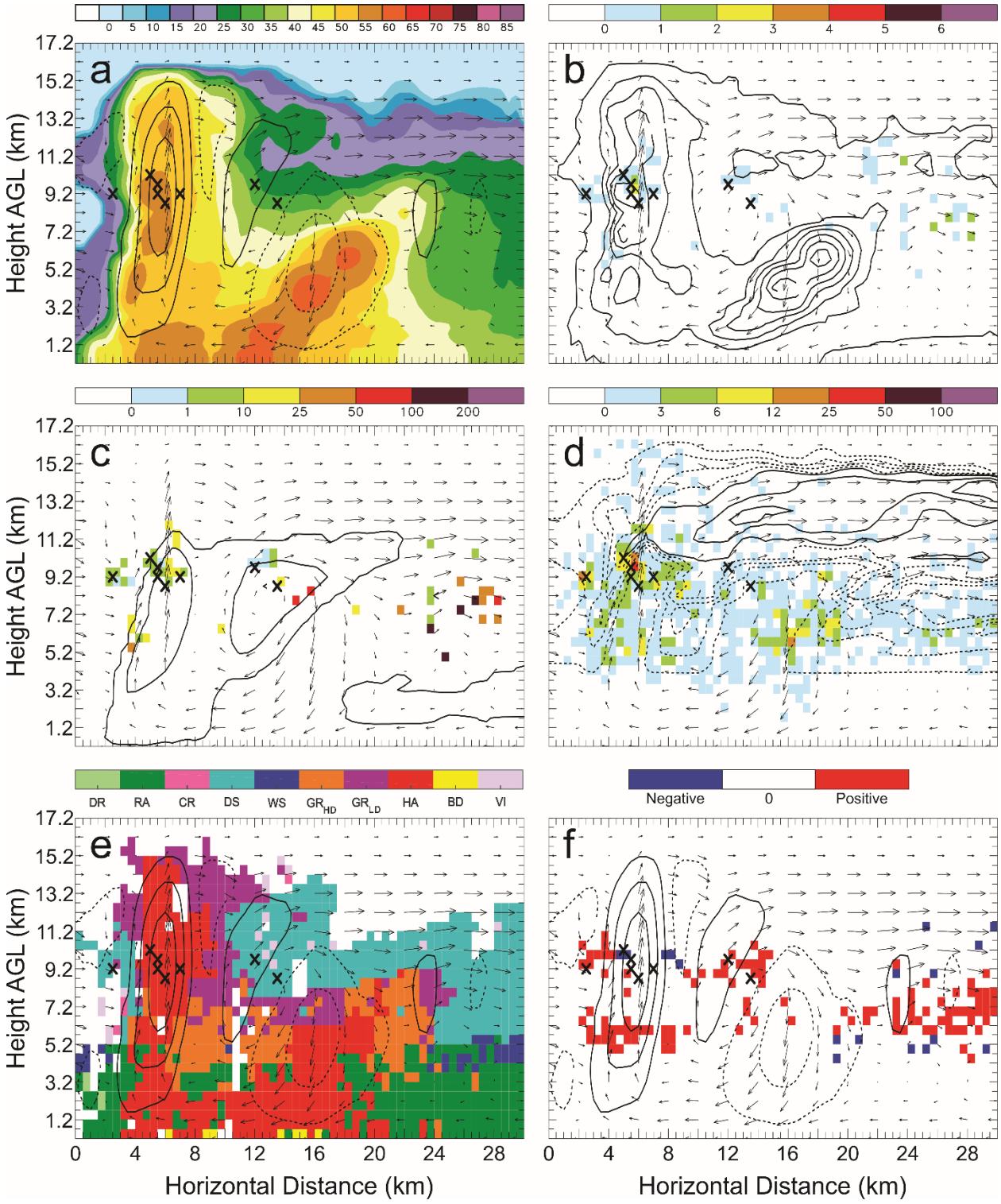

Figure 52: Vertical cross-sections taken for 29 May 23:51 UTC. As in Figure 49, but taken along the second line from the north in Figure 3(e).

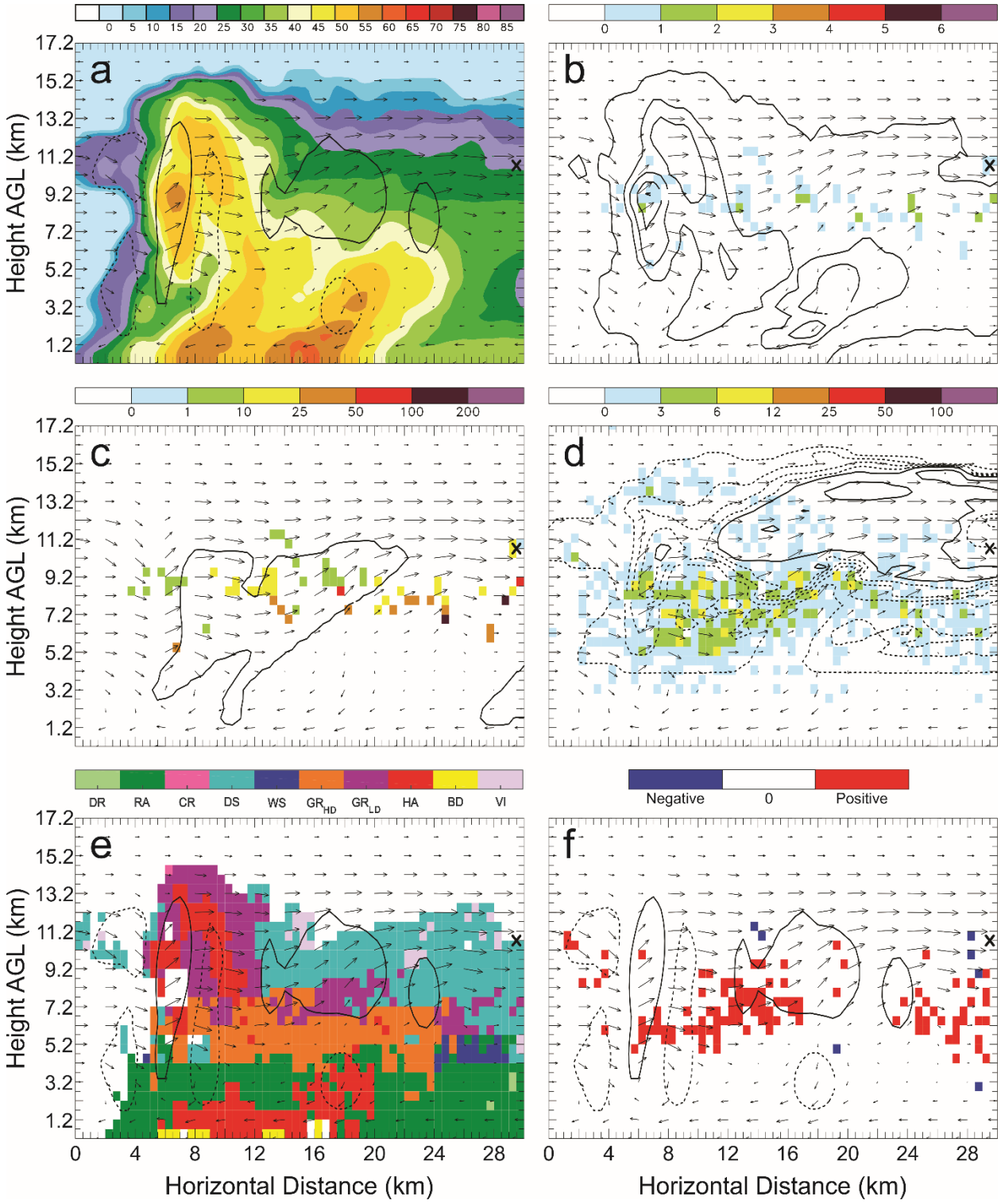

Figure 53: Vertical cross-sections taken for 29 May 23:51 UTC. As in Figure 49, but taken along the northernmost line in Figure 3(e).

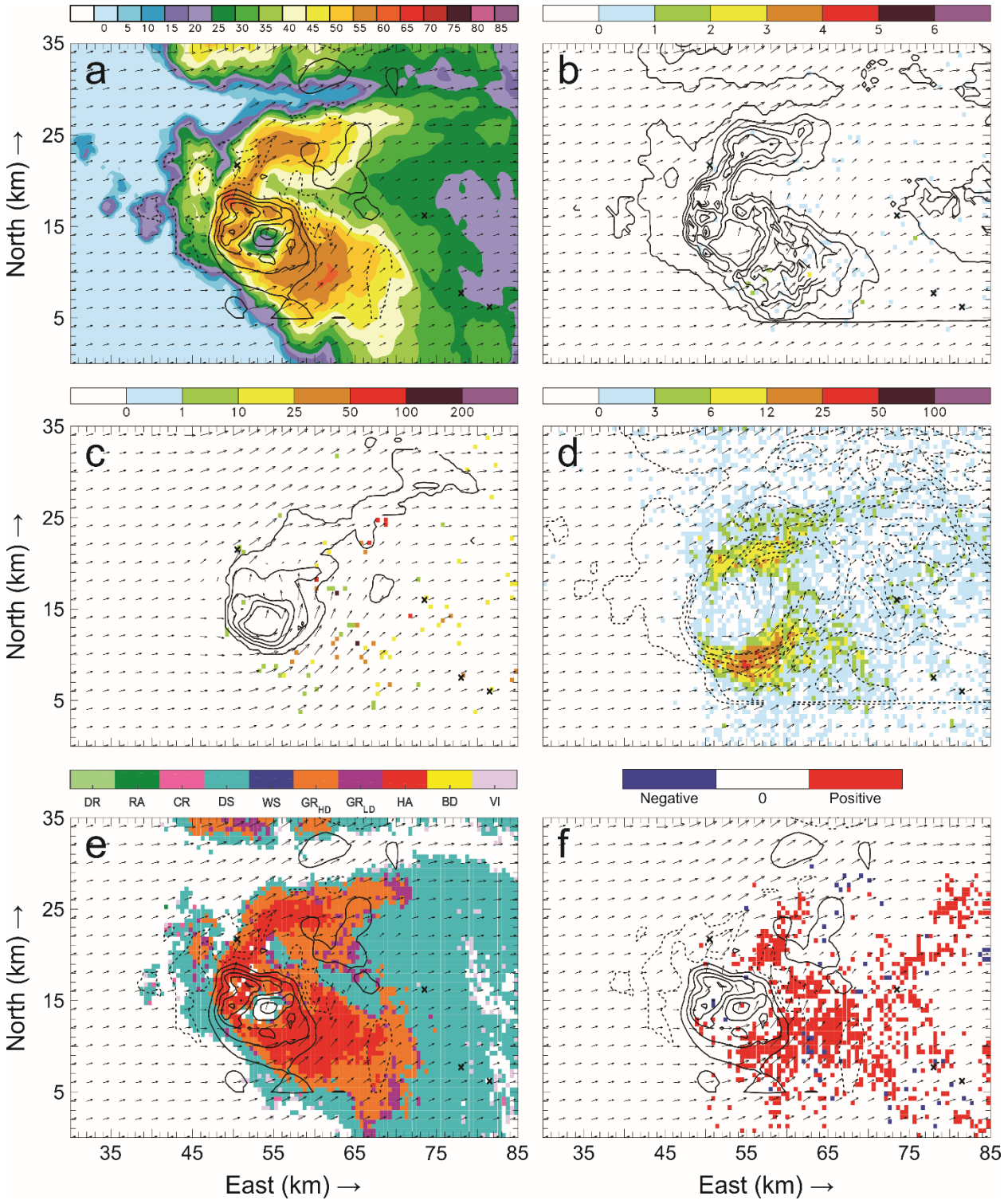

Figure 54: Horizontal cross-sections for 29 May 00:00 UTC taken at 6.2 km AGL of: a) color-filled Z and w contours (every 10 m s^{-1} starting at 5 m s^{-1}); b) color-filled FED and q_g contours (every 1.0 g kg^{-1} starting at 0 g kg^{-1}); c) color-filled FP and q_c contours (every 2.0 g kg -1 starting at 0 g kg^{-1}); d) color-filled SD and q_{xs} contours (dashed contours are every 0.25 g kg^{-1} starting at 0 g kg^{-1}, solid contours are every 1.0 g kg^{-1} starting at 1.0 g kg^{-1}); e) color-filled HCA and w contours (every 10 m s^{-1} starting at 5 m s^{-1}); and f) color-filled net inferred space charge and w contours (every 10 m s^{-1} starting at 5 m s^{-1}). All figures have the same horizontal storm-relative wind vectors, and black X's denote grid cells with FID > 0.

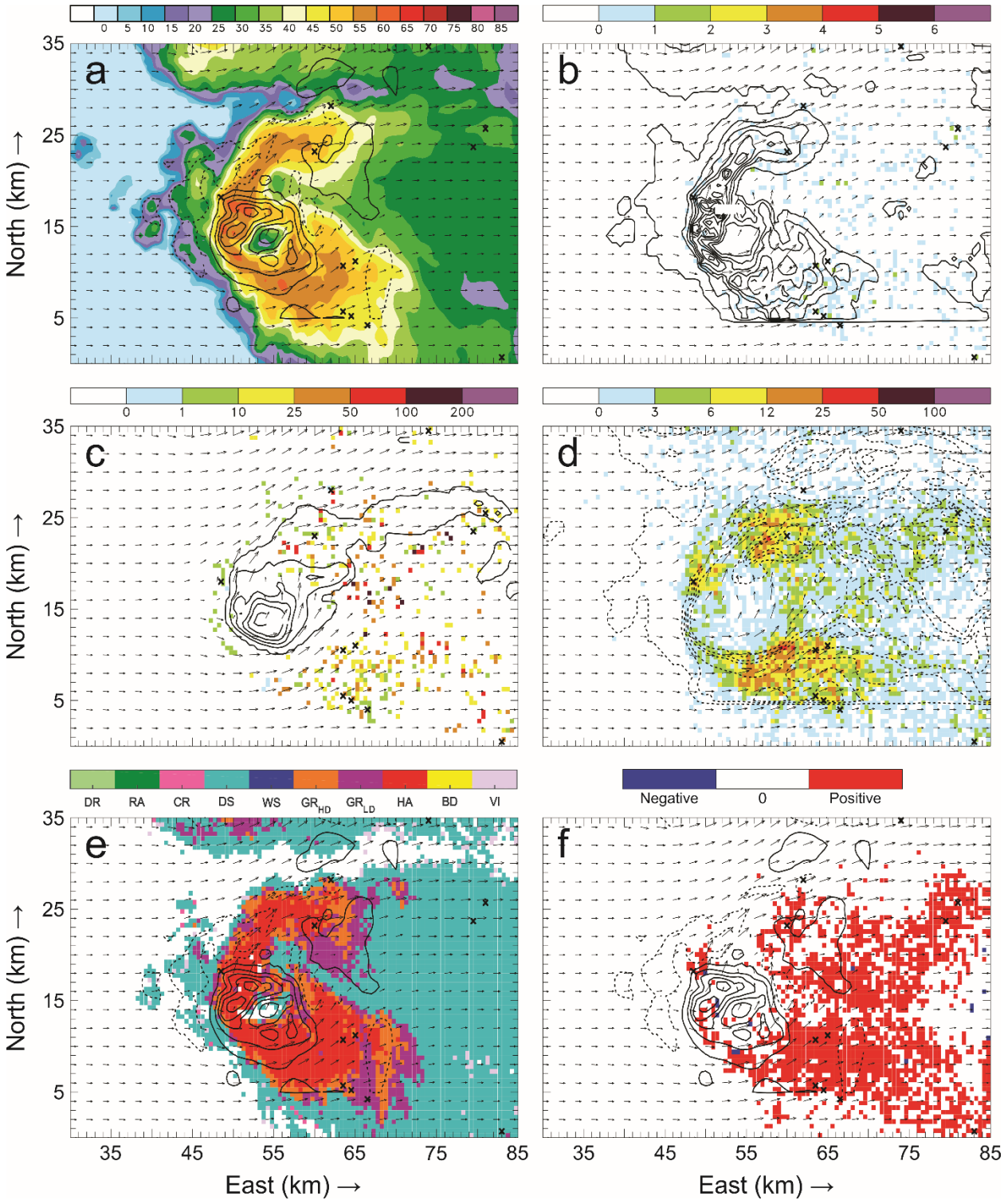

Figure 55: Horizontal cross-sections for 29 May 00:00 UTC. As in Figure 54, but taken at 7.2 km AGL.

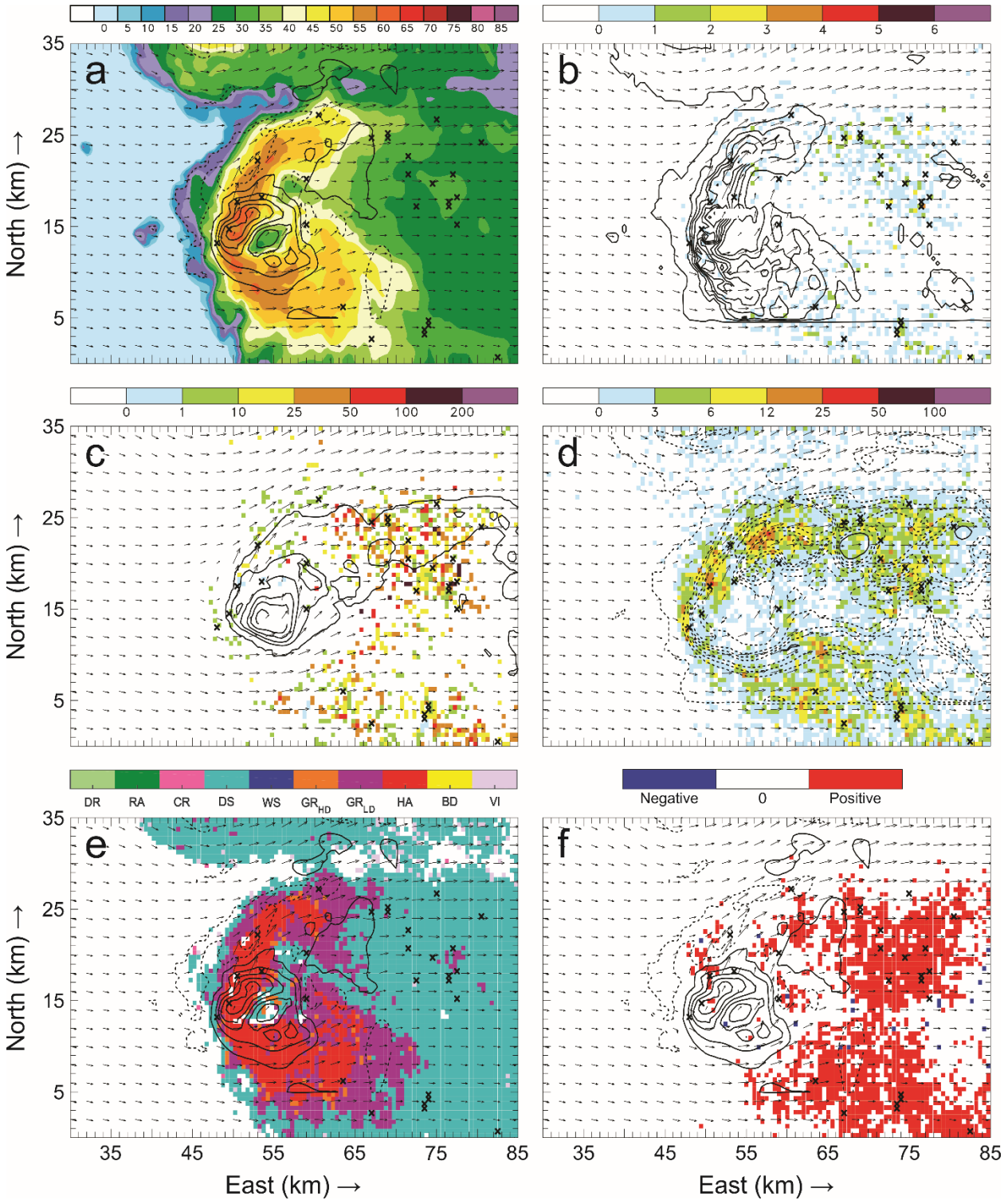

Figure 56: Horizontal cross-sections for 29 May 00:00 UTC. As in Figure 54, but taken at 8.2 km AGL.

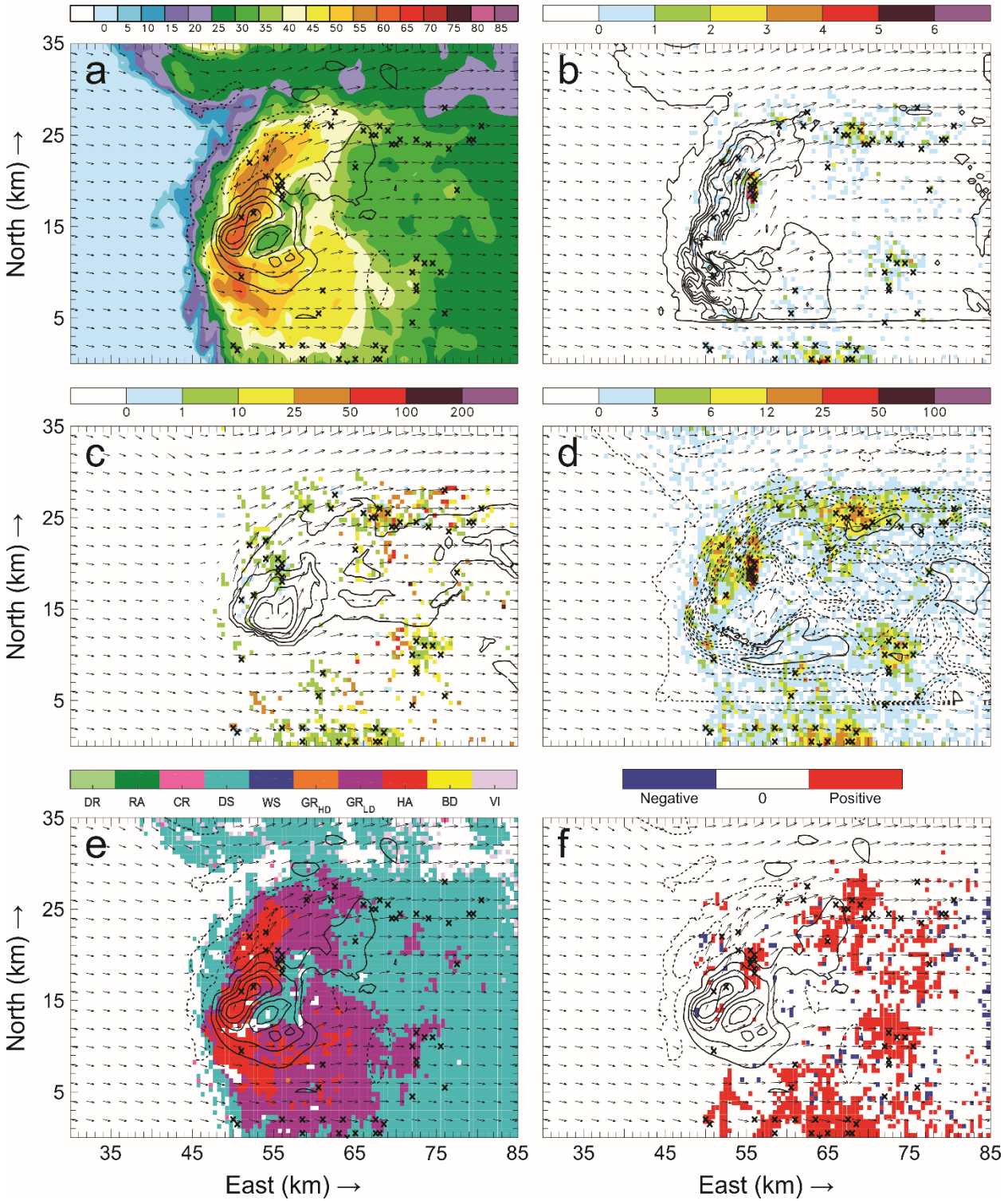

Figure 57: Horizontal cross-sections for 29 May 00:00 UTC. As in Figure 54, but taken at 9.2 km AGL.

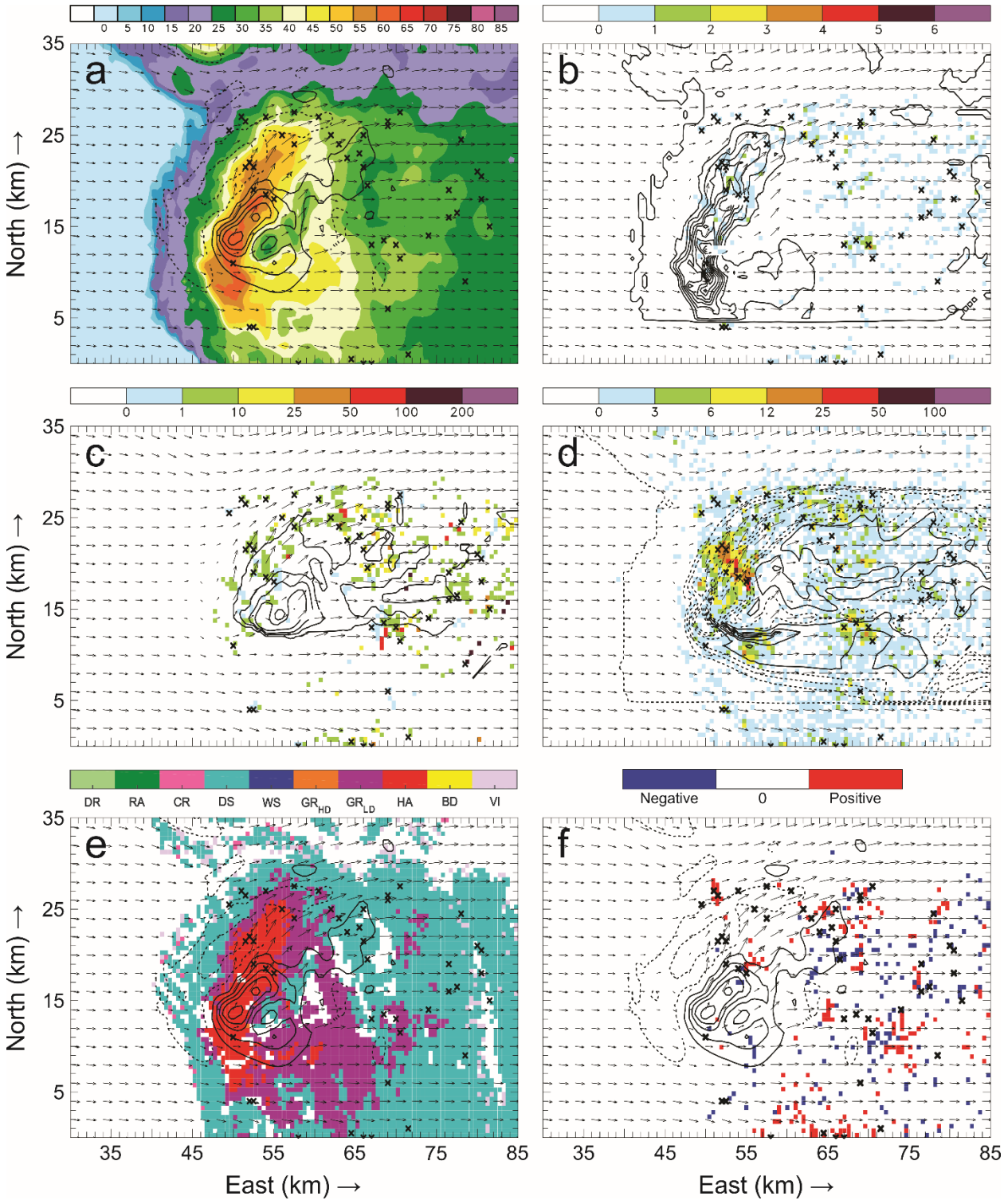

Figure 58: Horizontal cross-sections for 29 May 00:00 UTC. As in Figure 54, but taken at 10.2 km AGL.

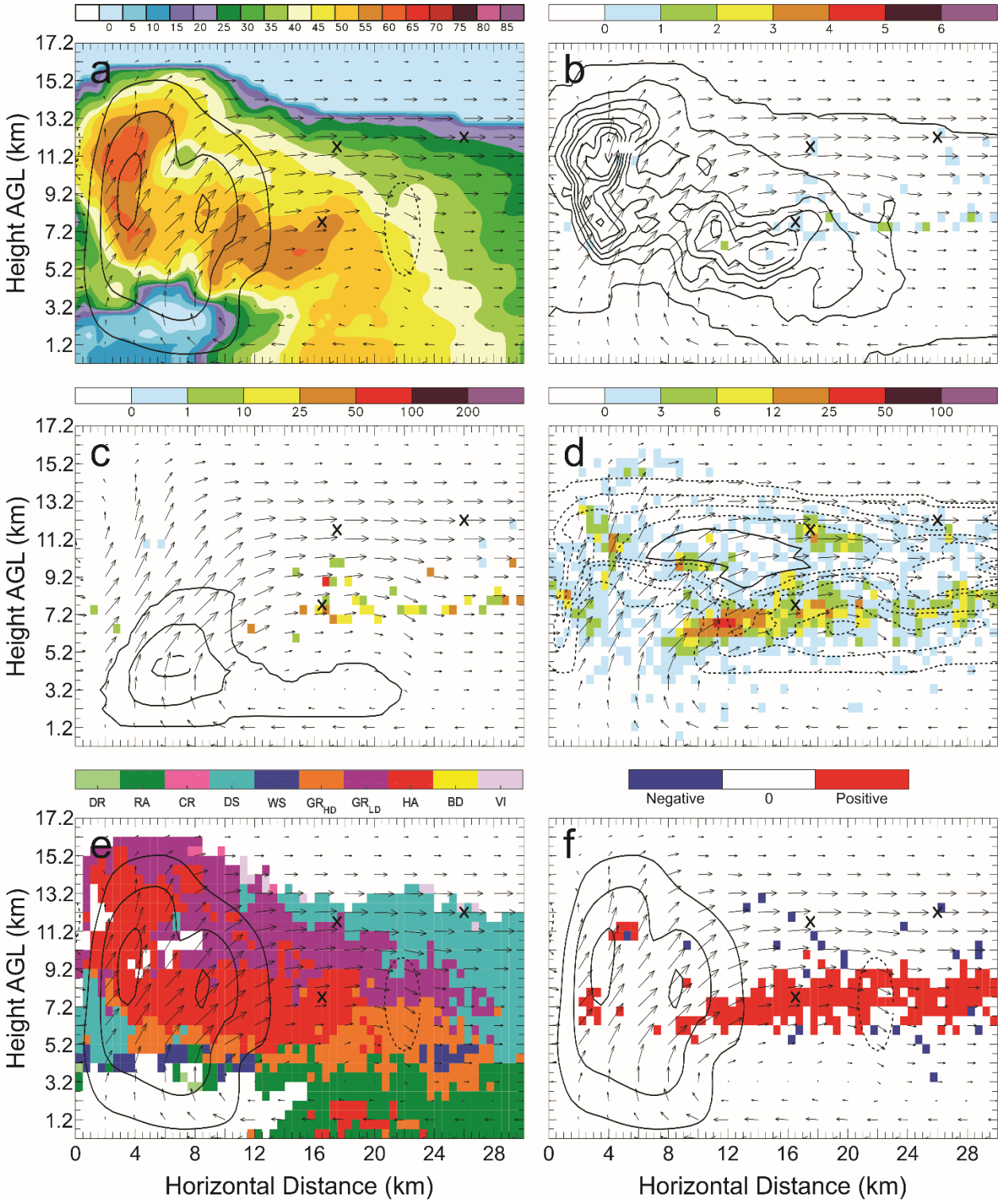

Figure 59: Vertical cross-sections for 29 May 00:00 UTC taken along the southernmost line in Figure 3(f) of: a) color-filled Z and w contours (every 10 m s^{-1} starting at 5 m s^{-1}); b) color-filled FED and q_g contours (every 1.0 g kg^{-1} starting at 0 g kg^{-1}); c) color-filled FP and q_c contours (every 2.0 g kg -1 starting at 0 g kg^{-1}); d) color-filled SD and q_{xs} contours (dashed contours are every 0.25 g kg^{-1} starting at 0 g kg^{-1}, solid contours are every 1.0 g kg^{-1} starting at 1.0 g kg^{-1}); e) color-filled HCA and w contours (every 10 m s^{-1} starting at 5 m s^{-1}); and f) color-filled net inferred space charge and w contours (every 10 m s^{-1} starting at 5 m s^{-1}). All figures have the same horizontal storm-relative wind vectors, and black X's denote grid cells with FID > 0.

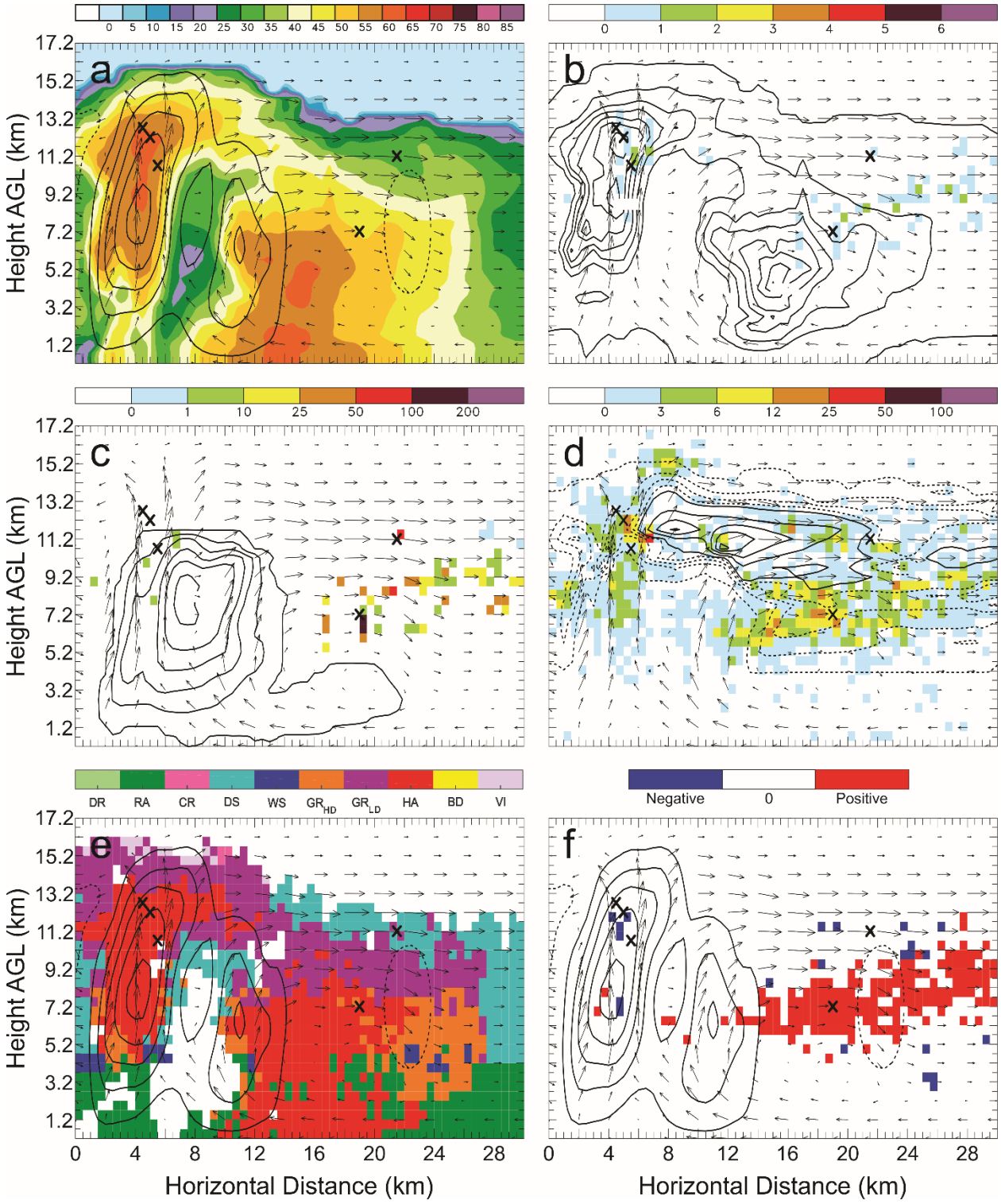

Figure 60: Vertical cross-sections for 29 May 00:00 UTC. As in Figure 59, but taken along the second line from the south in Figure 3(f).

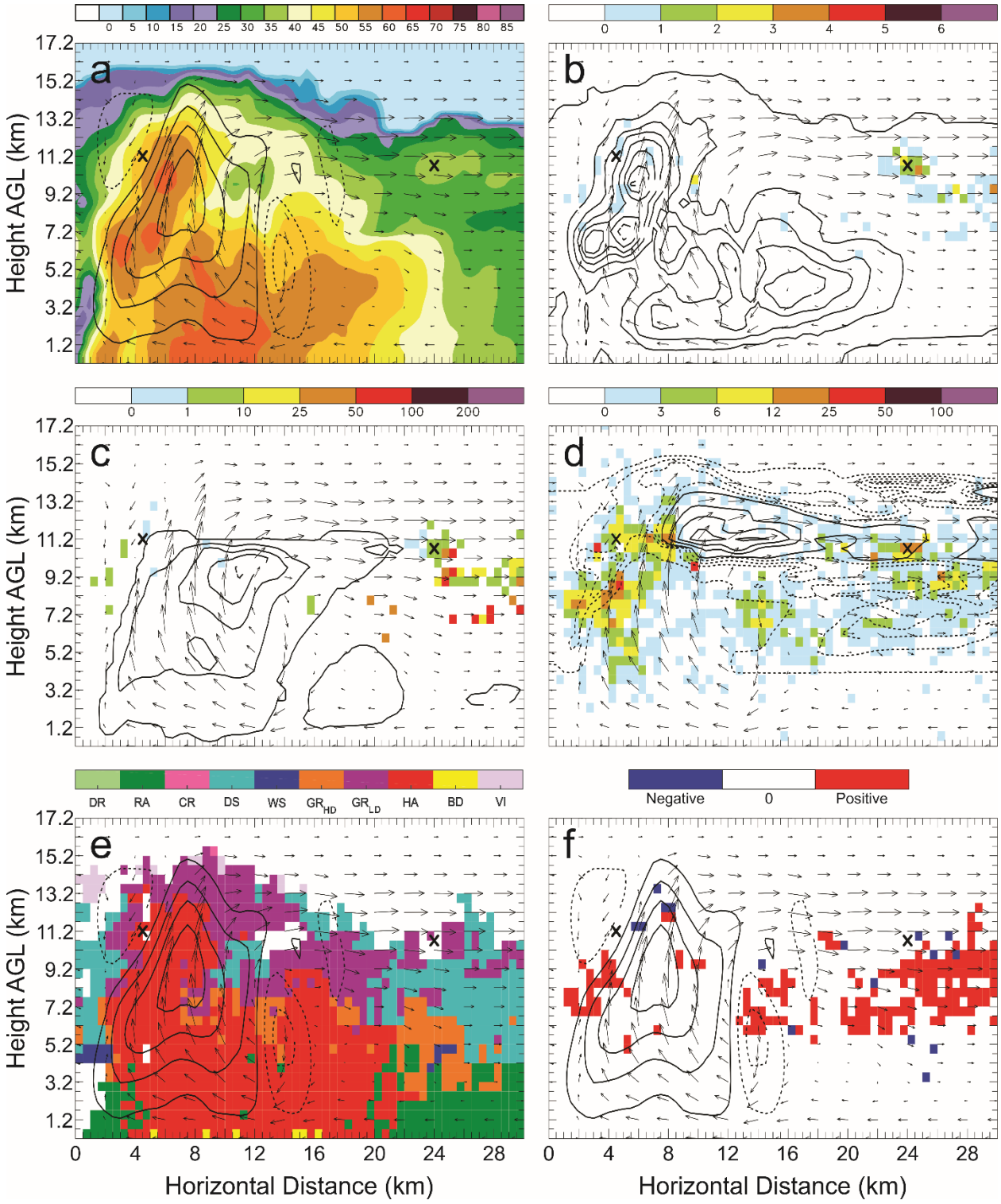

Figure 61: Vertical cross-sections for 29 May 00:00 UTC. As in Figure 59, but taken along the central line in Figure 3(f).

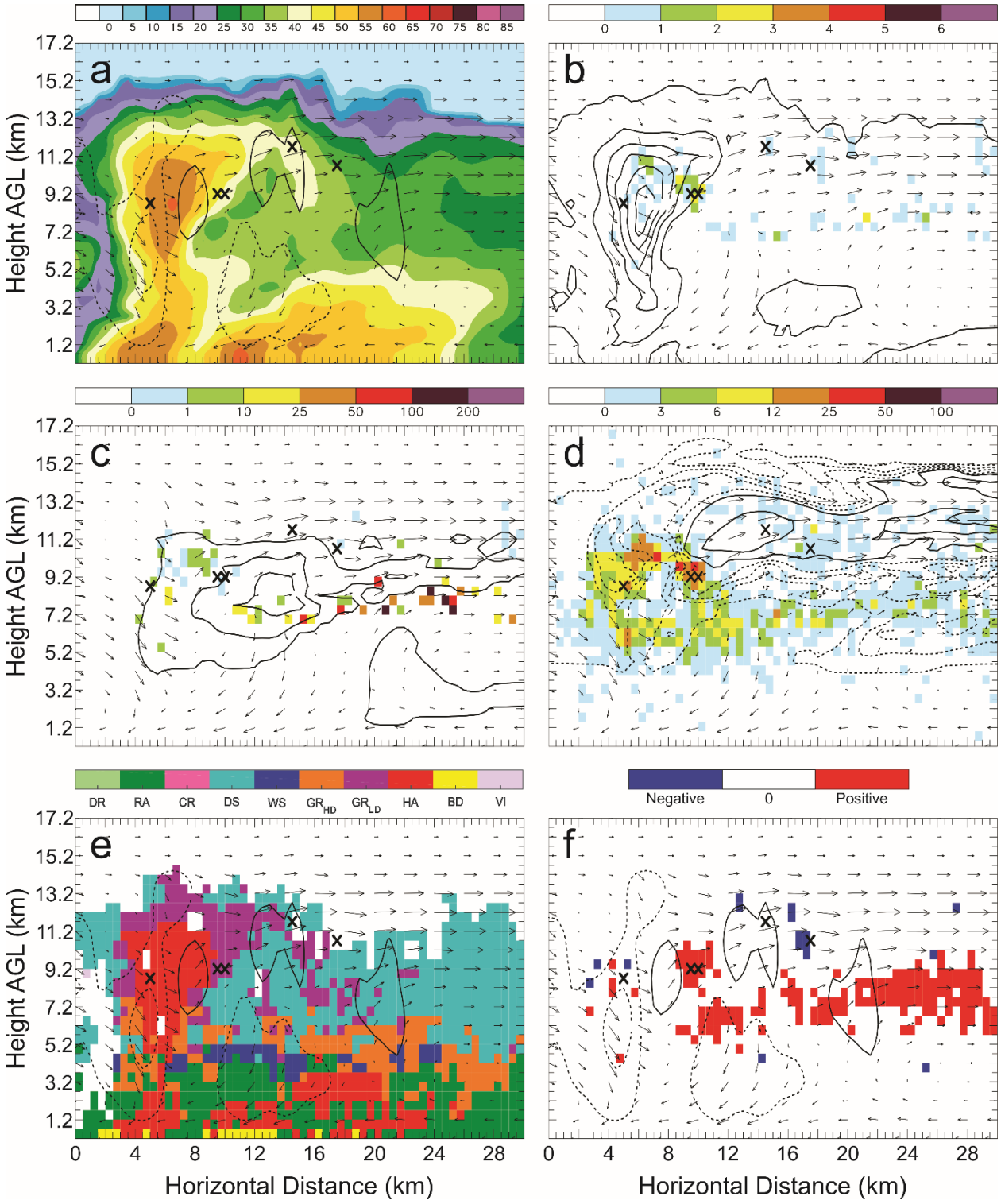

Figure 62: Vertical cross-sections for 29 May 00:00 UTC. As in Figure 59, but taken along the second line from the north in Figure 3(f).

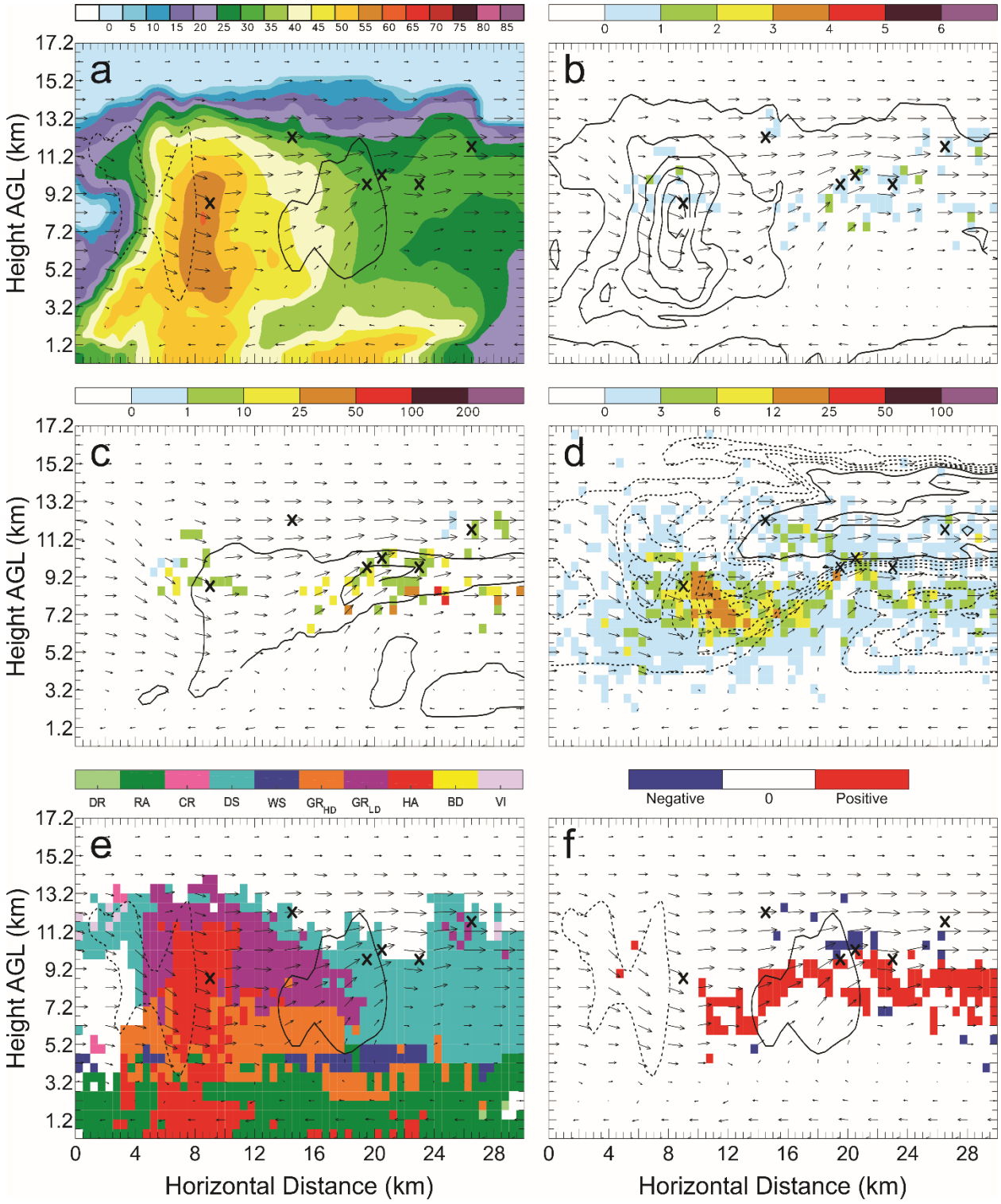

Figure 63: Vertical cross-sections for 29 May 00:00 UTC. As in Figure 59, but taken along the northernmost line in Figure 3(f).

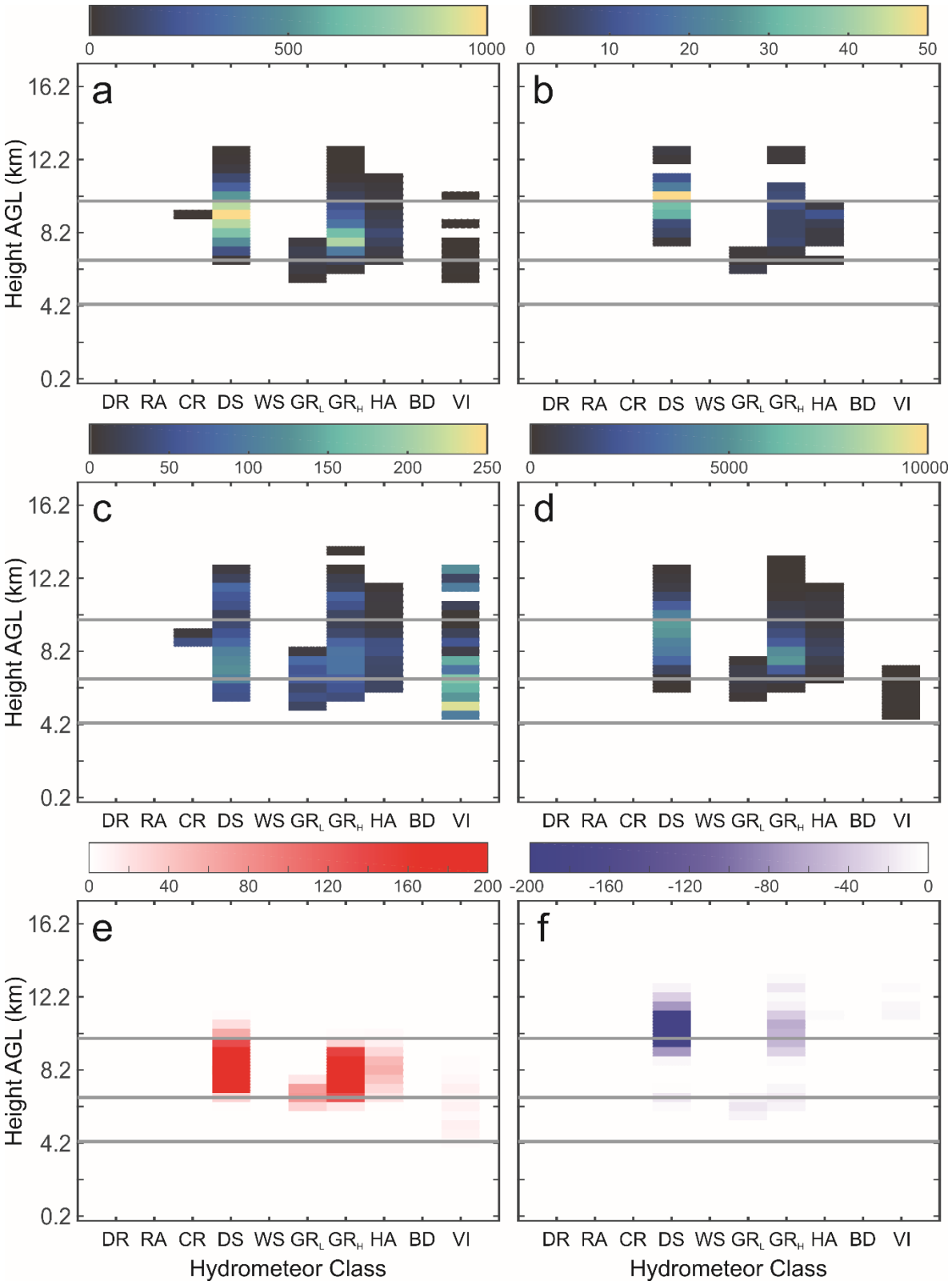

Figure 64: Lightning parameters that correspond with HCA classes in all grid cells at each horizontal level at 23:09 UTC: a) Total FED, b) total FID, c) mean FP, d) total SD, e) total points assigned positive charge, and f) total points assigned negative charge. The horizontal grey lines represent the 0ºC, -20ºC, and -40ºC levels.

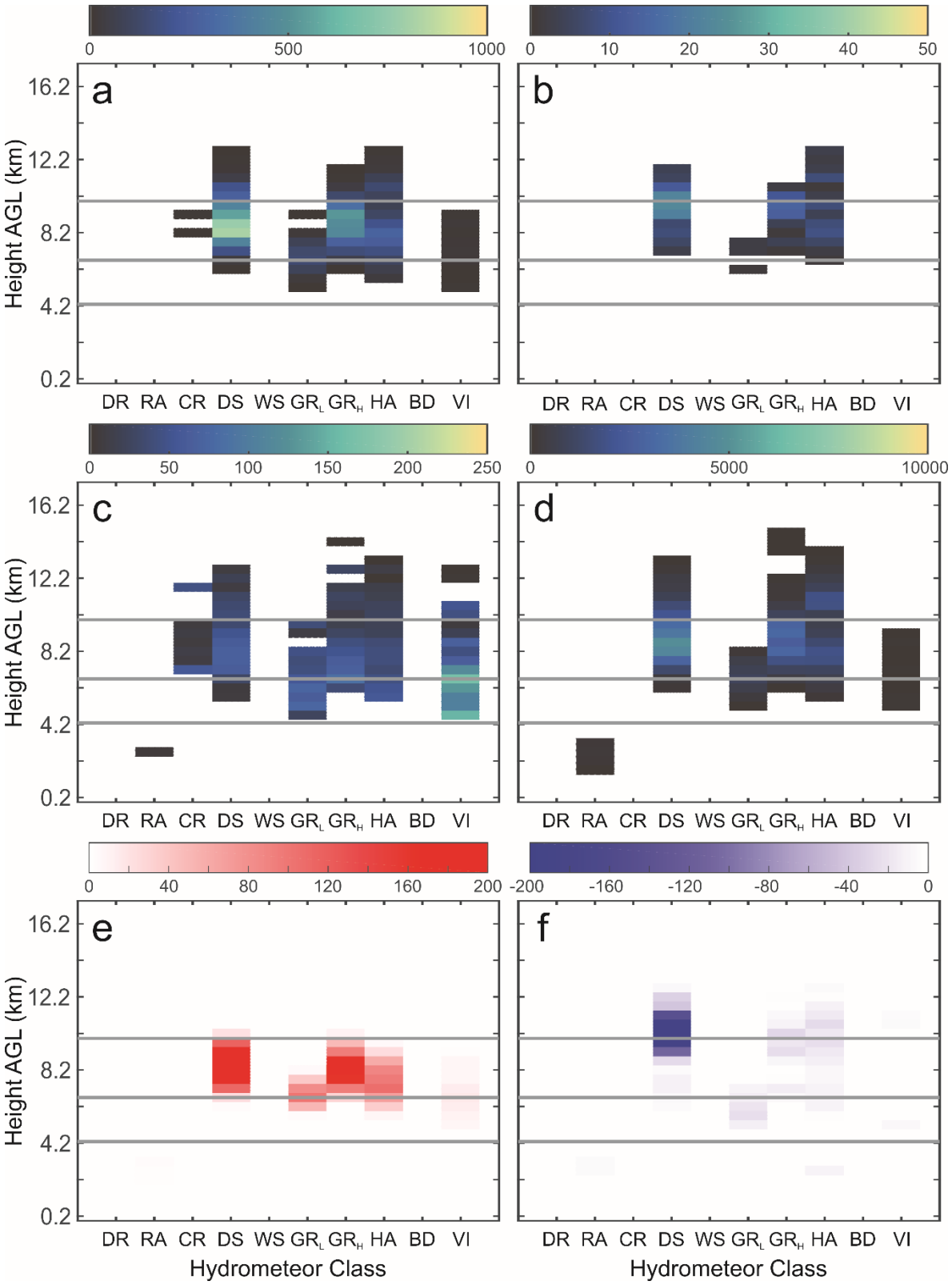

Figure 65: As in Figure 64, but for 23:21 UTC.

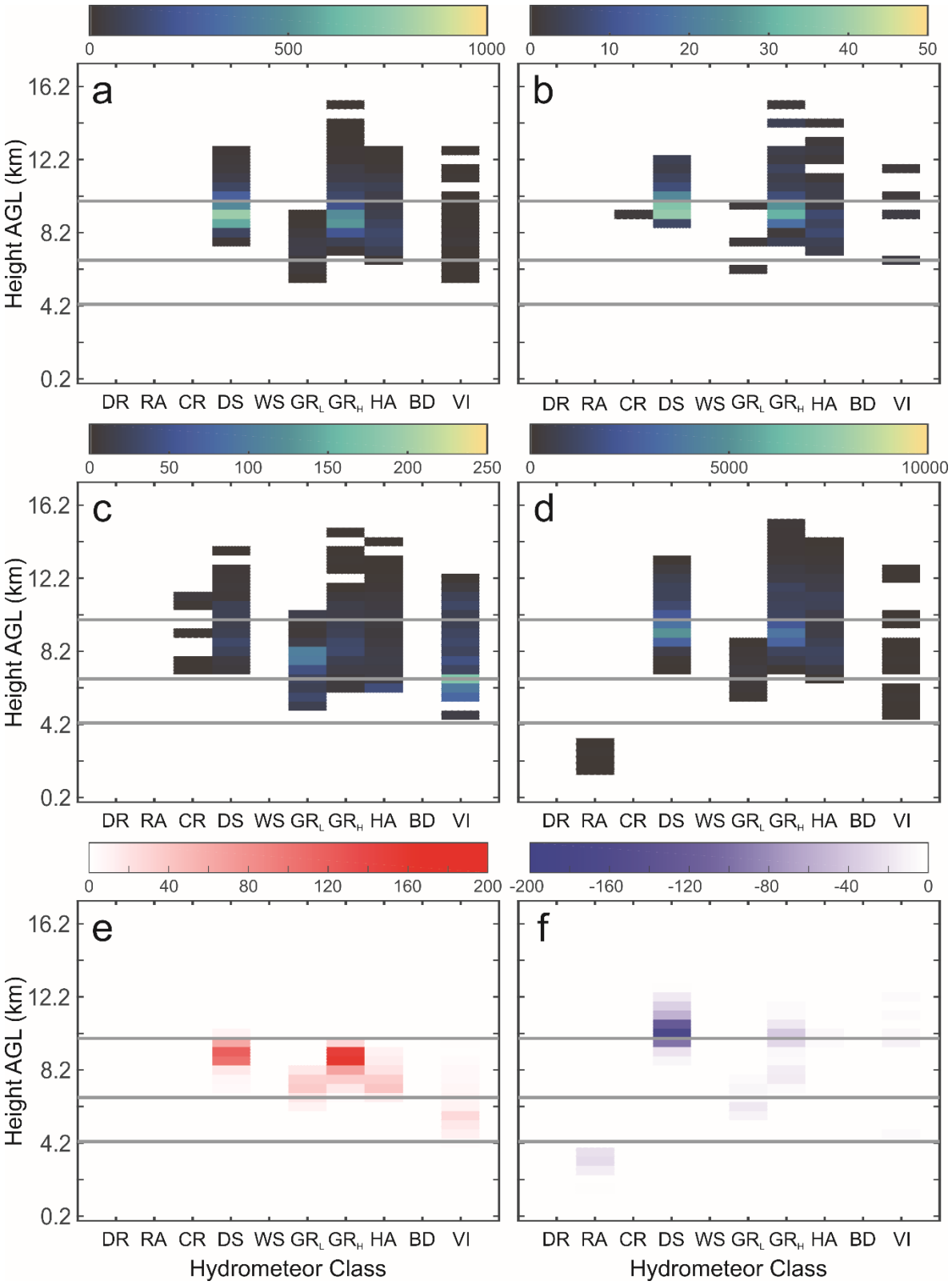

Figure 66: As in Figure 64, but for 23:33 UTC.

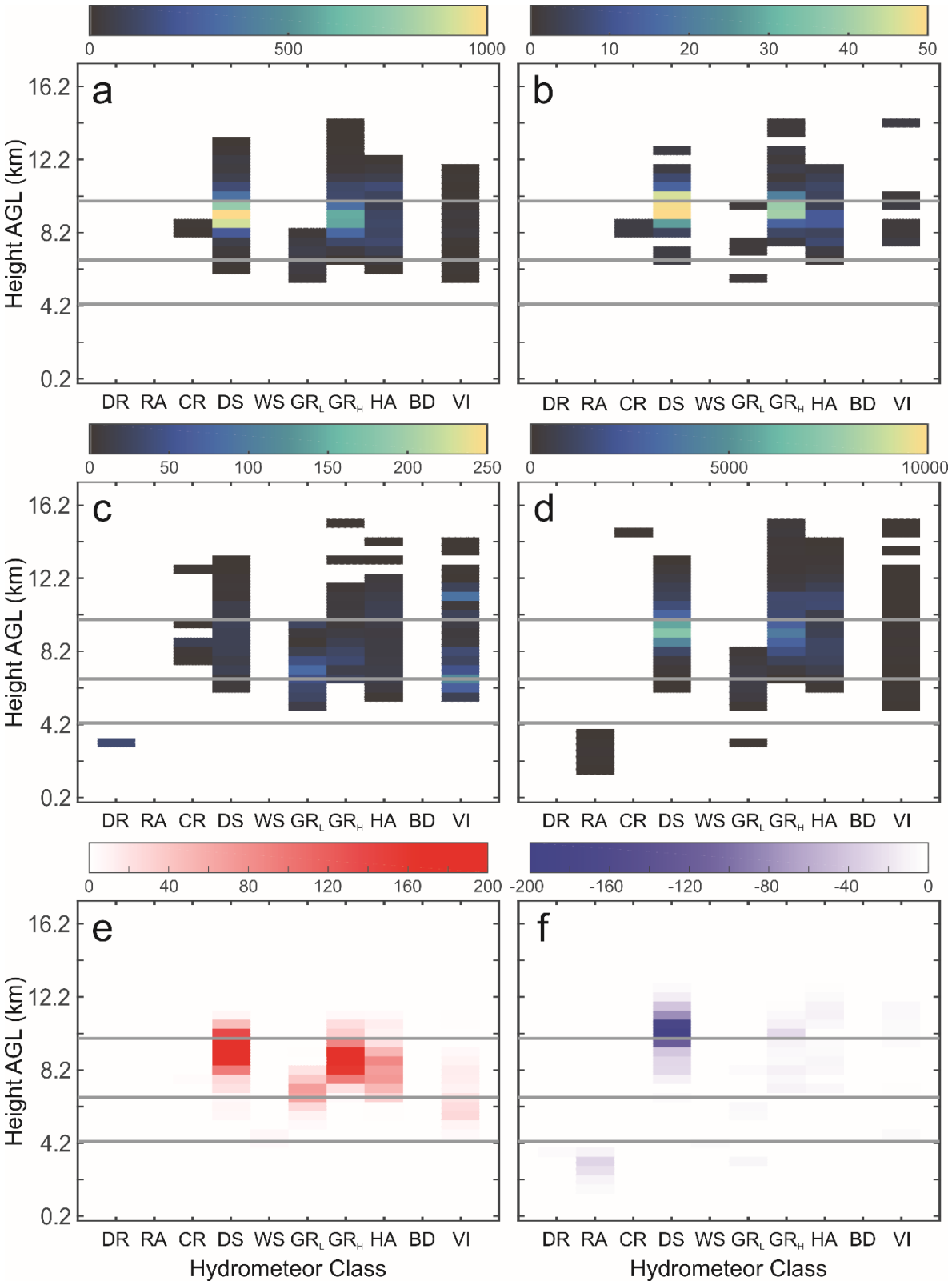

Figure 67: As in Figure 64, but for 23:42 UTC.

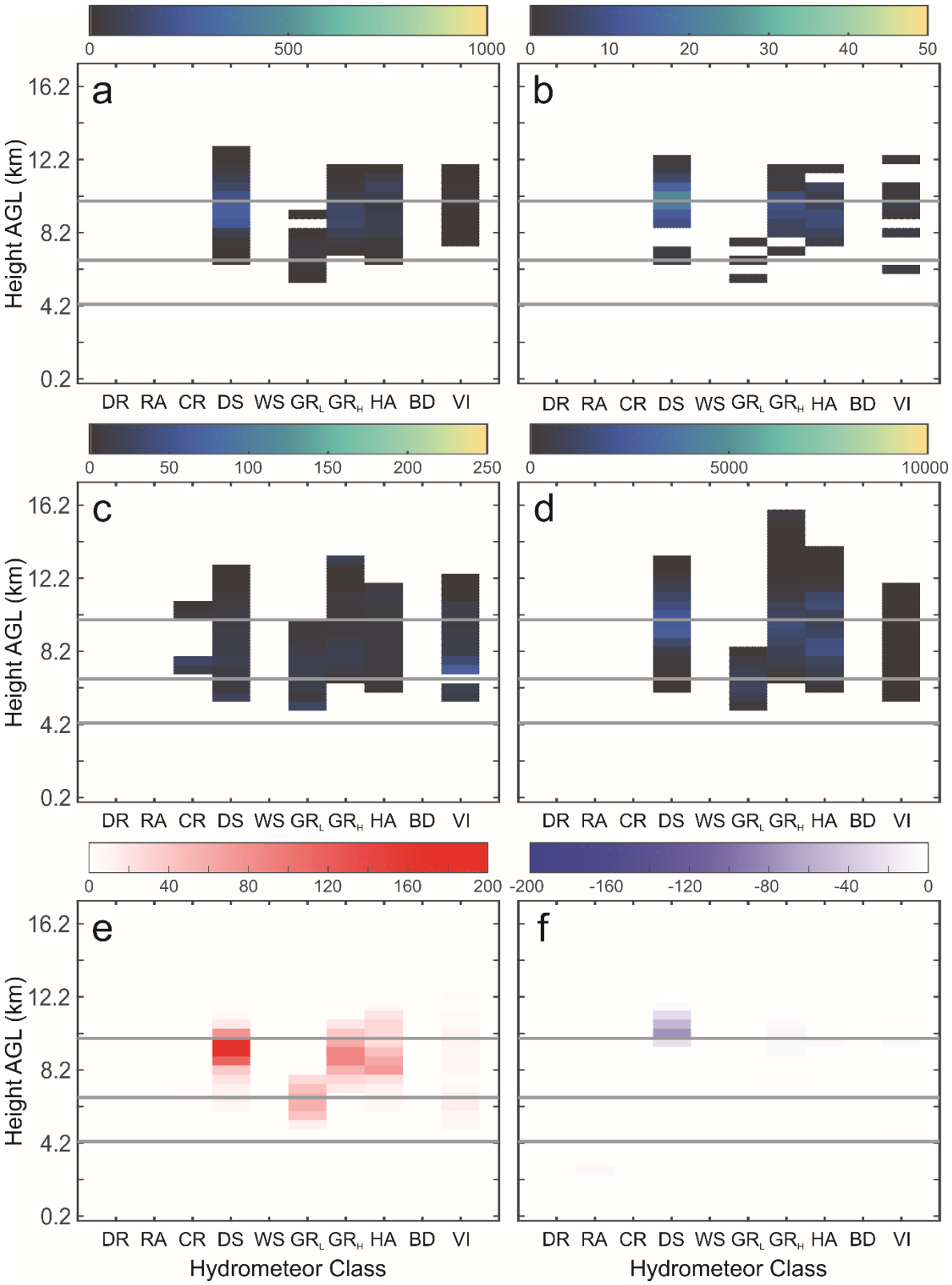

Figure 68: As in Figure 64, but for 23:51 UTC.

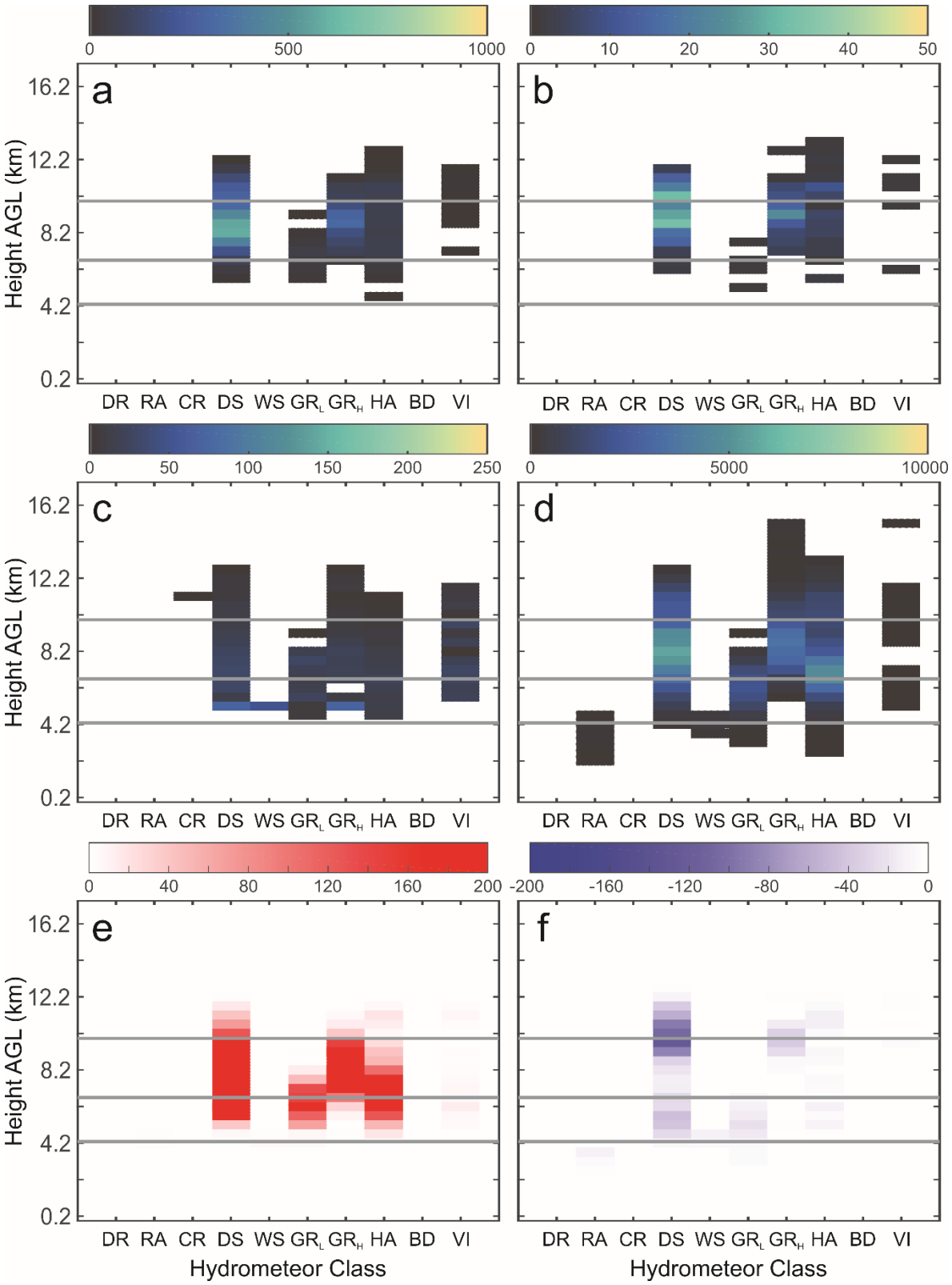

Figure 69: As in Figure 64, but for 00:00 UTC.

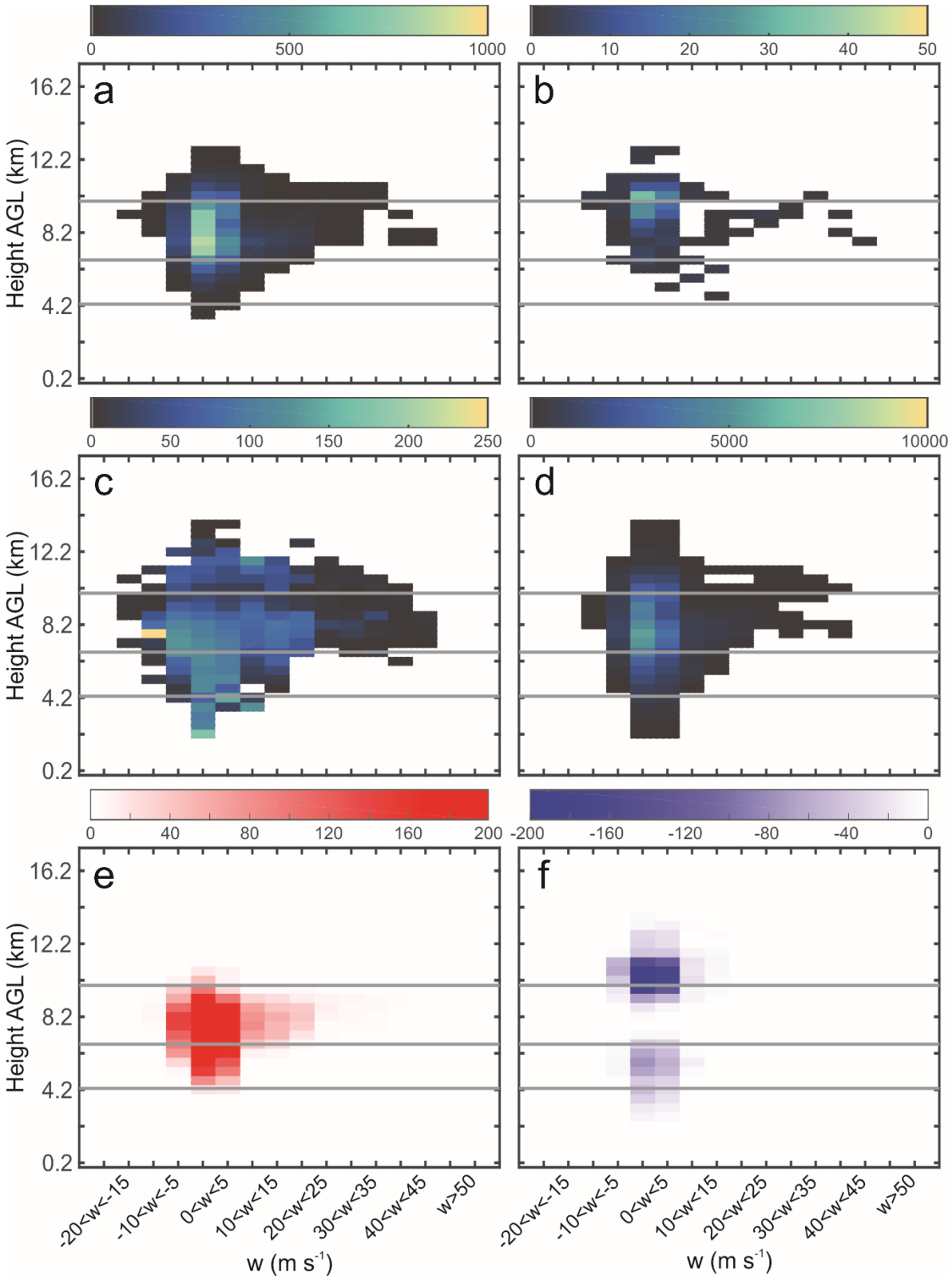

Figure 70: Lightning parameters that correspond with 5 m s^{-1} bins of w in all grid cells at each horizontal level at 23:09 UTC: a) Total FED, b) total FID, c) mean FP, d) total SD, e) total points assigned positive charge, and f) total points assigned negative charge. The horizontal grey lines represent the 0ºC, -20ºC, and -40ºC levels.

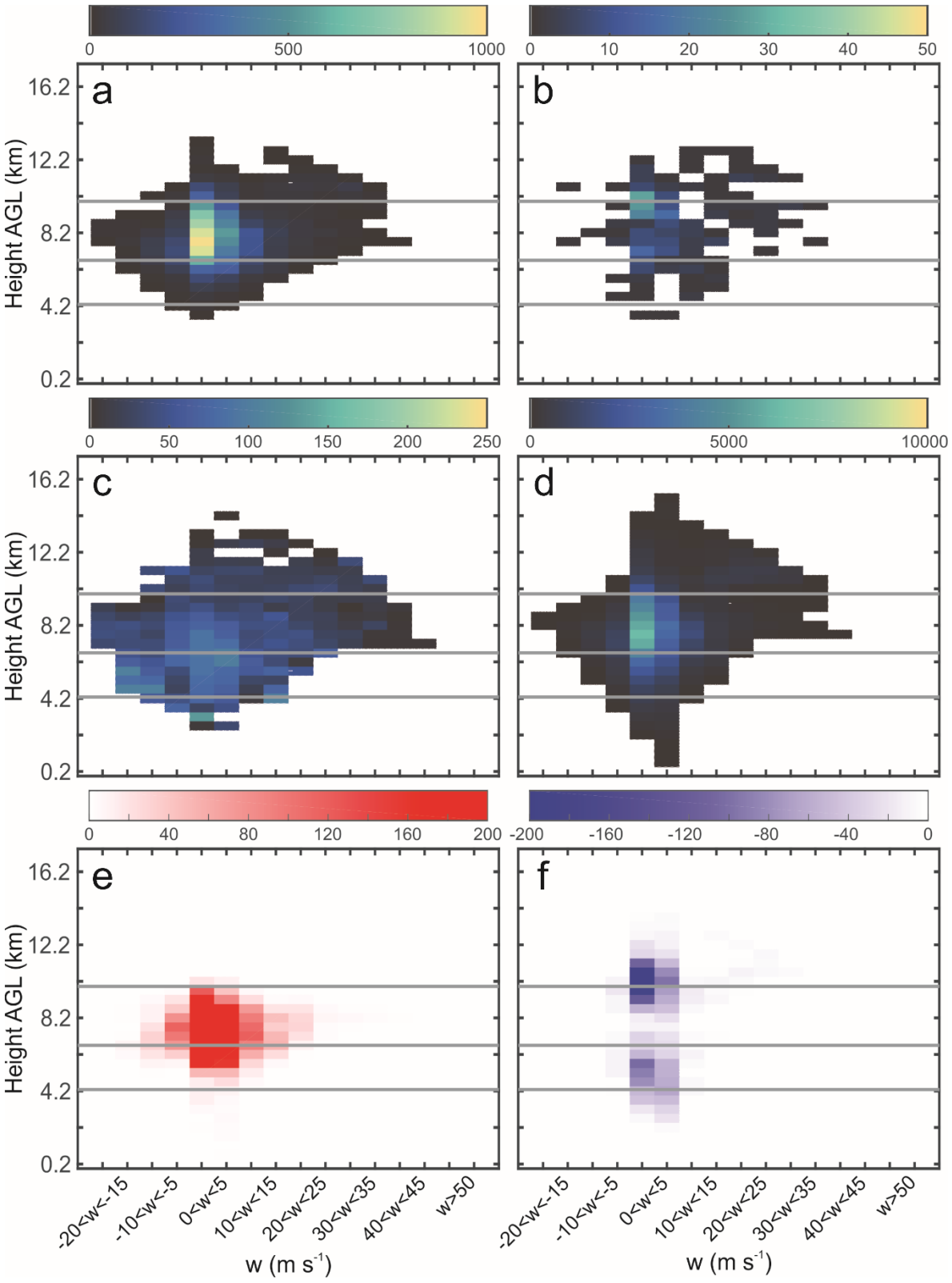

Figure 71: As in Figure 70, but for 23:21 UTC.

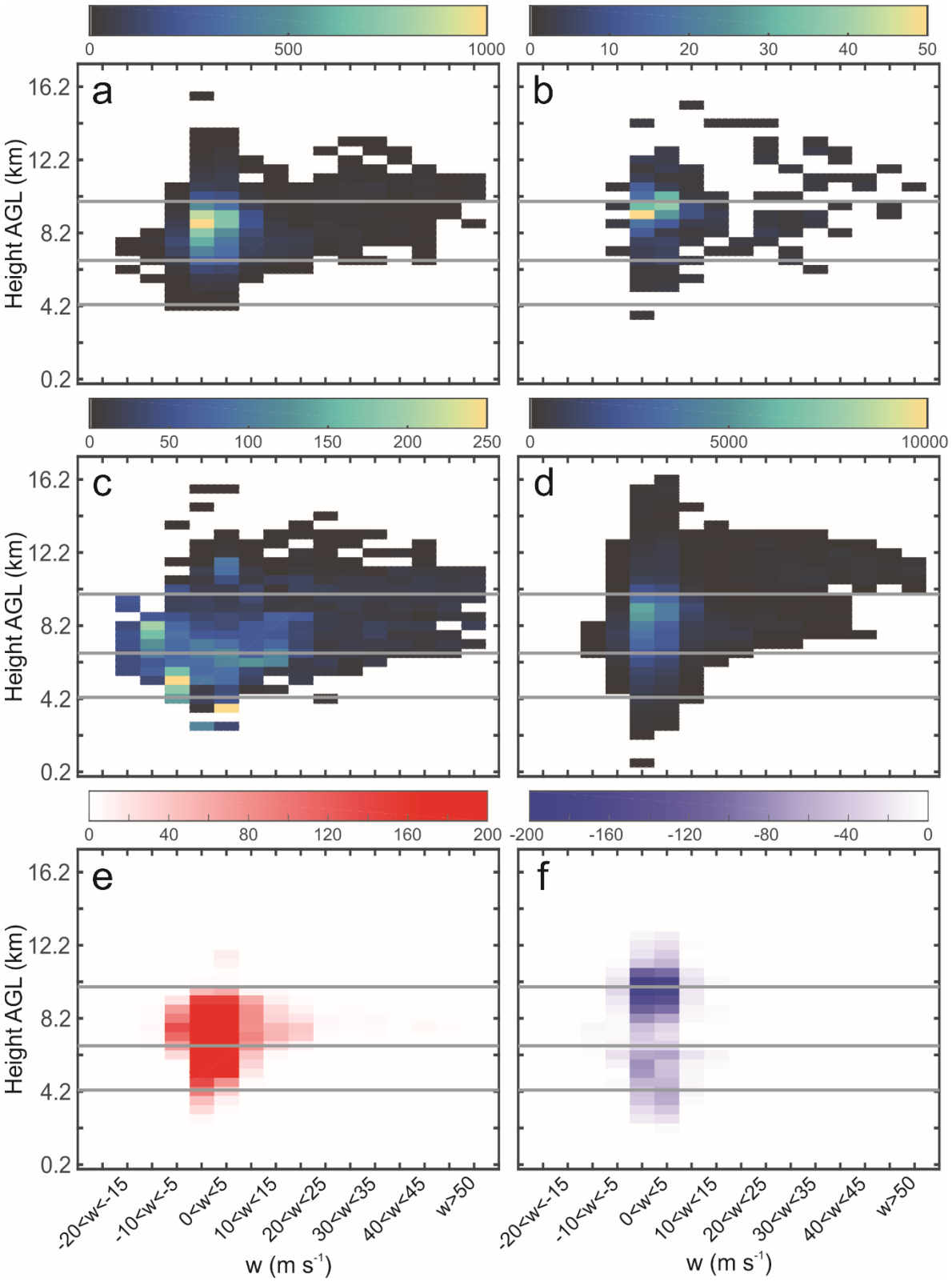

Figure 72: As in Figure 70, but for 23:33 UTC.

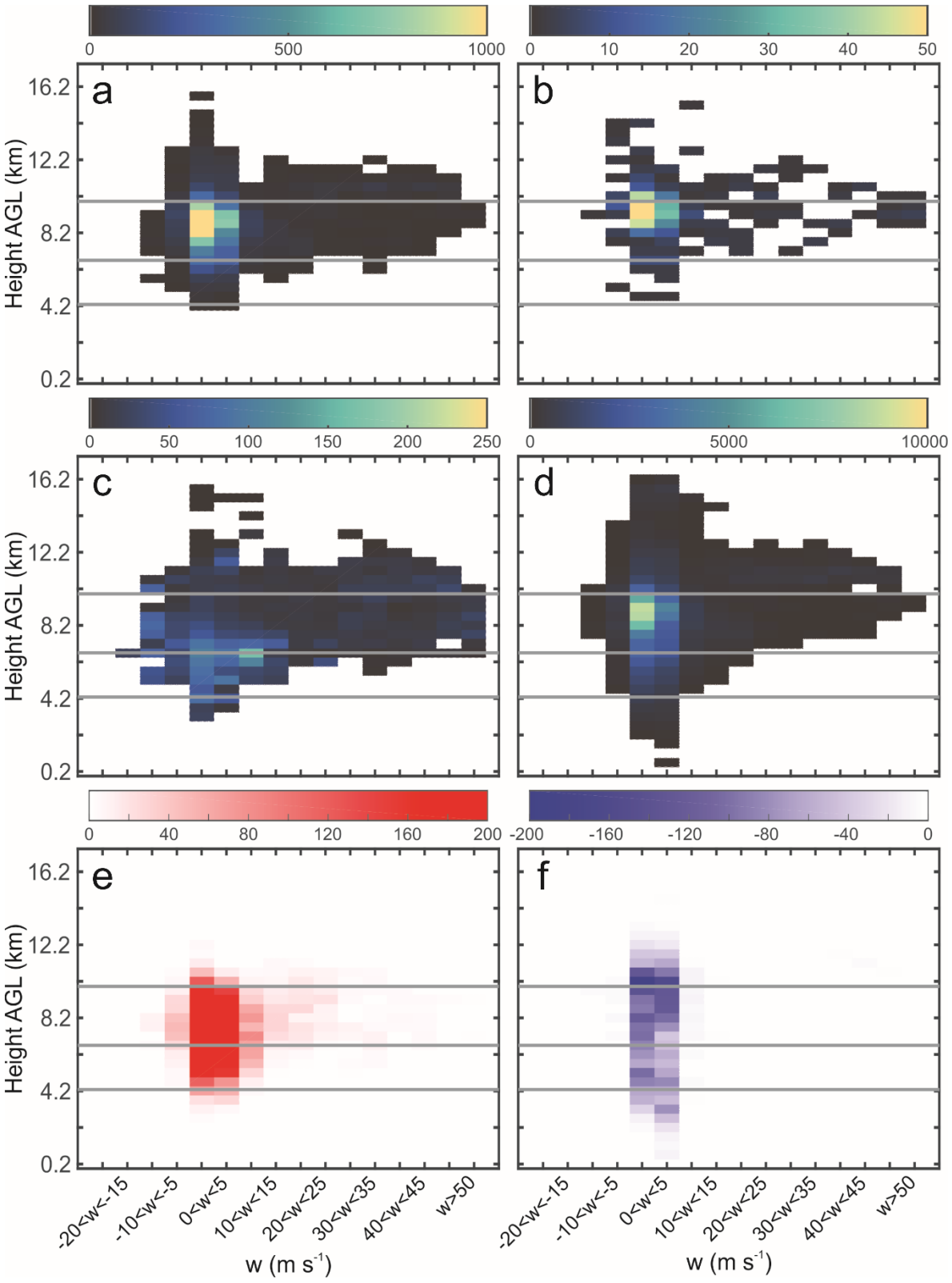

Figure 73: As in Figure 70, but for 23:42 UTC.

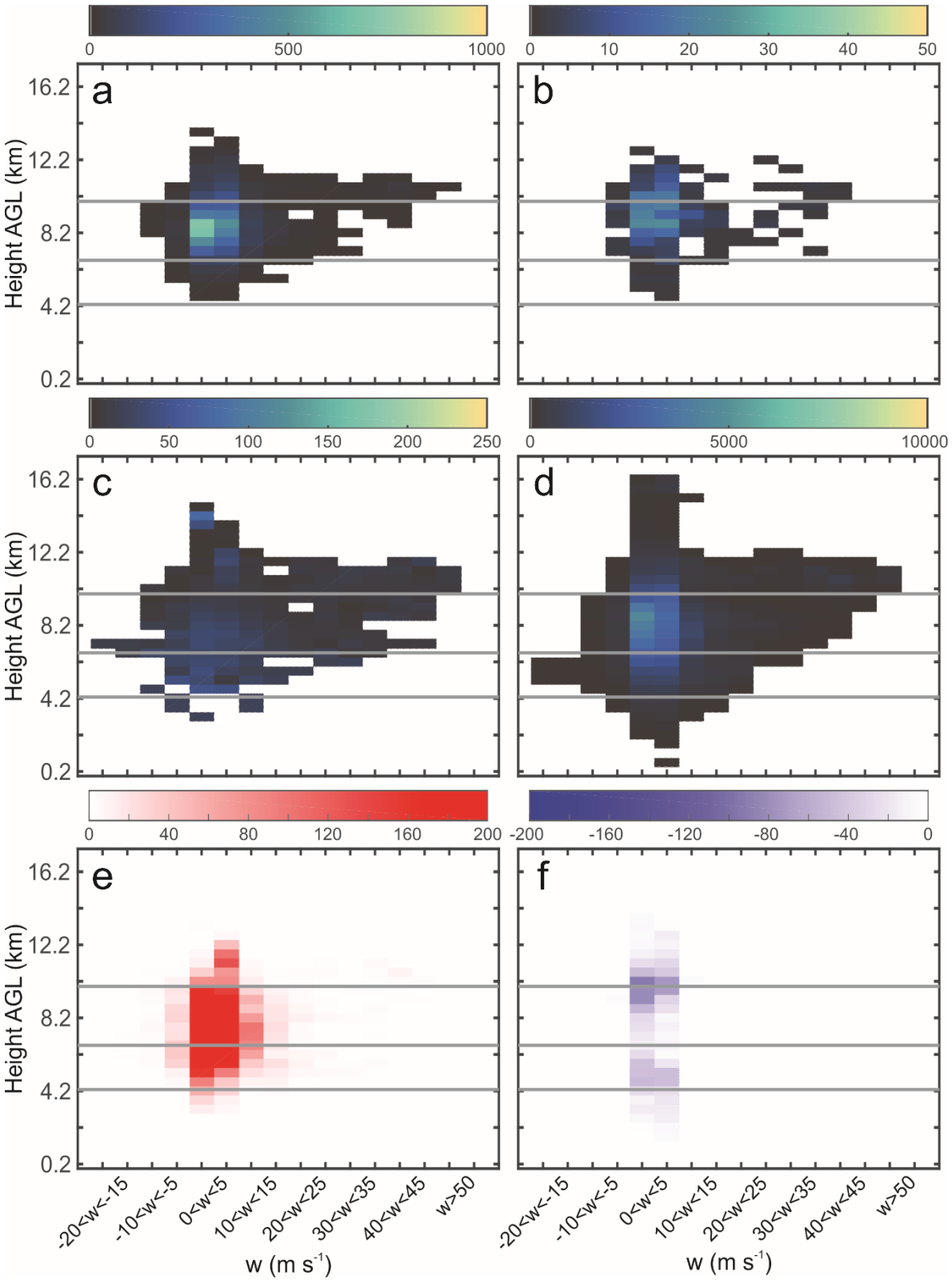

Figure 74: As in Figure 70, but for 23:51 UTC.

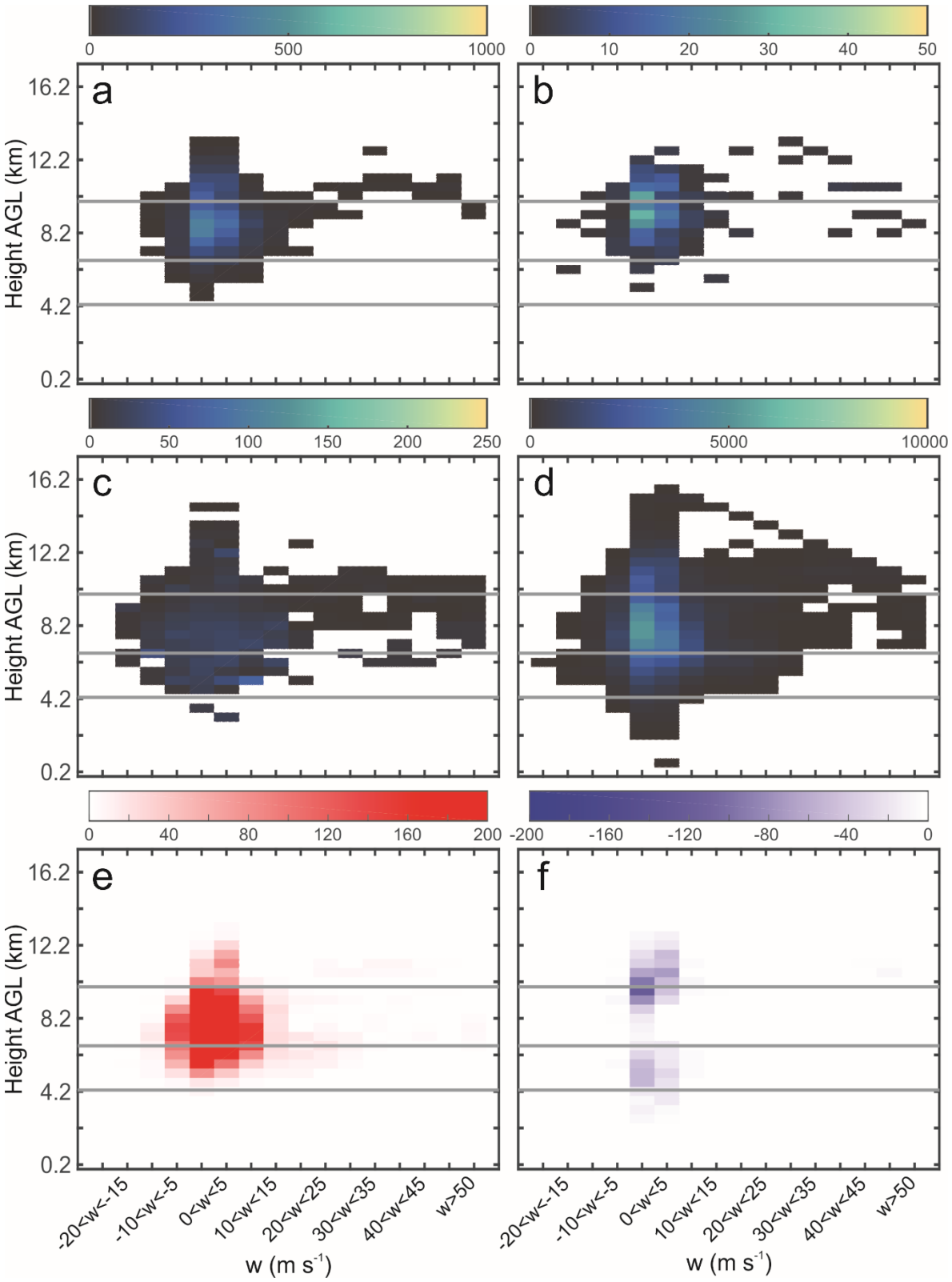

Figure 75: As in Figure 70, but for 00:00 UTC.

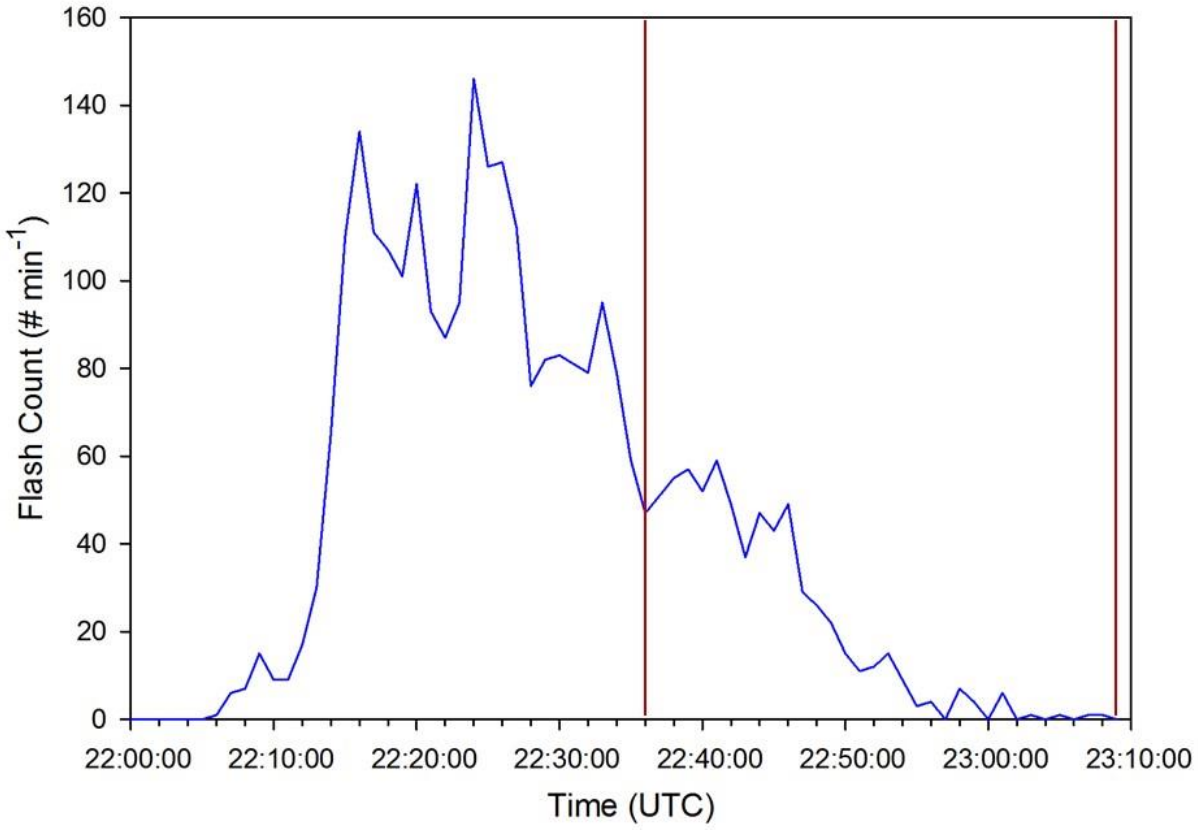

Figure 76: Total flash rate for the 16 June 2012 multicell.

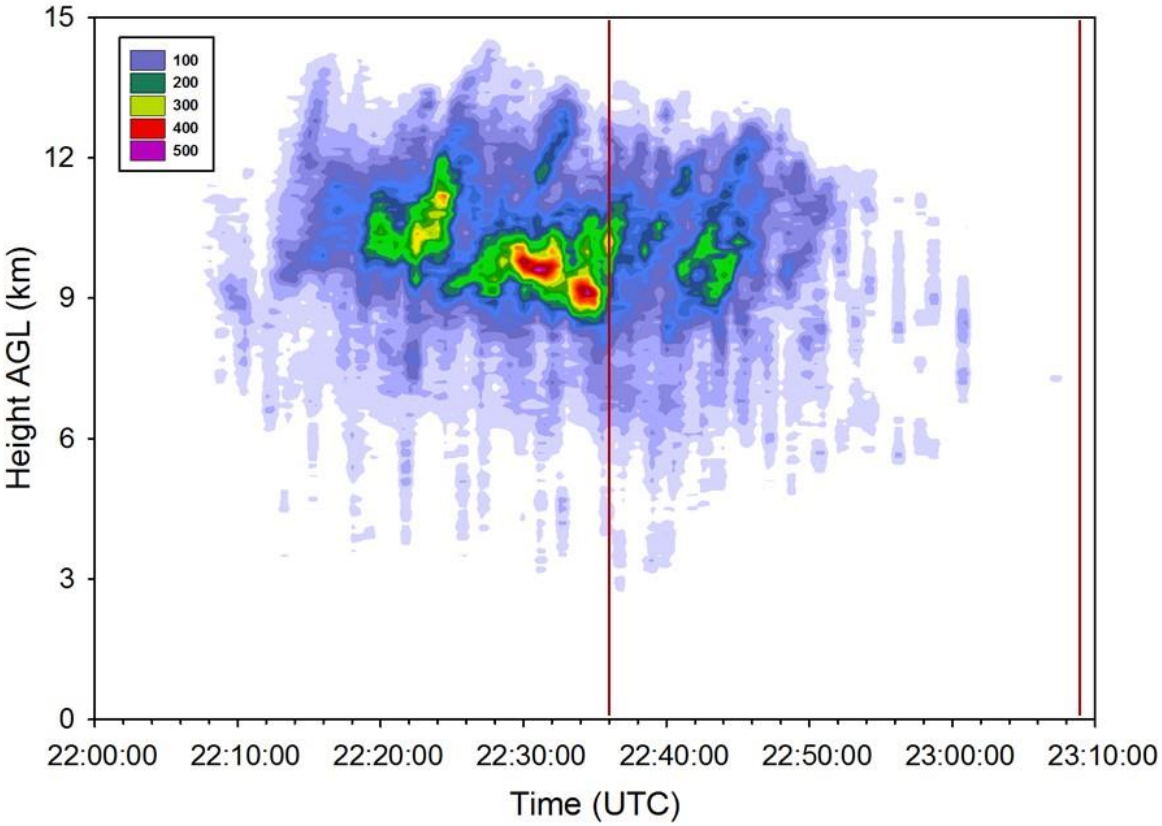

Figure 77: Vertical VHF source density for the 16 June 2012 multicell.

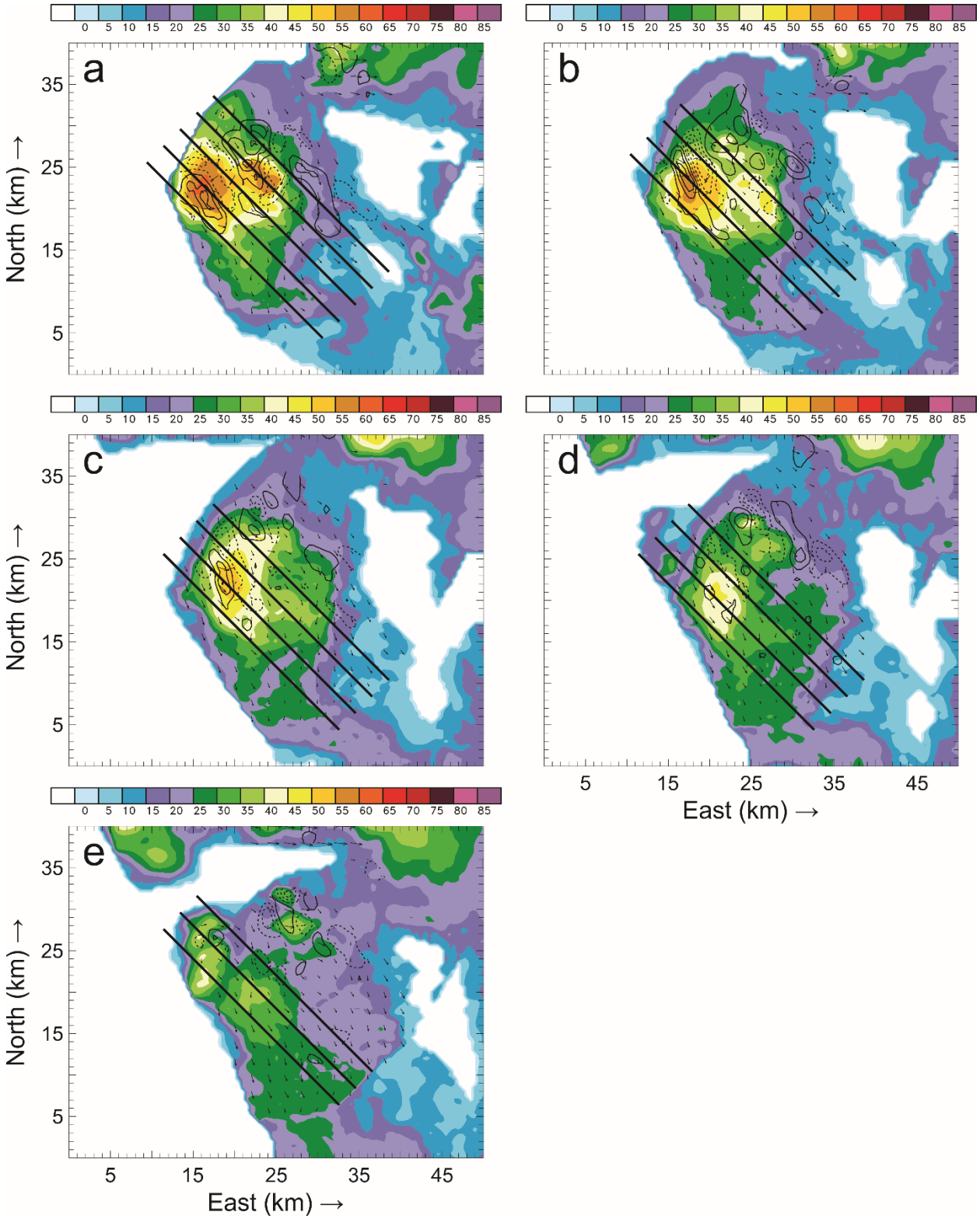

Figure 78: Horizontal cross-sections of color-filled Z, w contours (every 10 m s^{-1} starting at 5 m s^{-1}), and horizontal storm-relative wind vectors at 6.2 km AGL for a) 22:36 UTC, b) 22:42 UTC, c) 22:48 UTC, d) 22:54 UTC, e) 23:00 UTC, and f) 00:00 UTC. The diagonal black lines on each figure indicate the locations of the vertical cross sections generated for each analysis time.

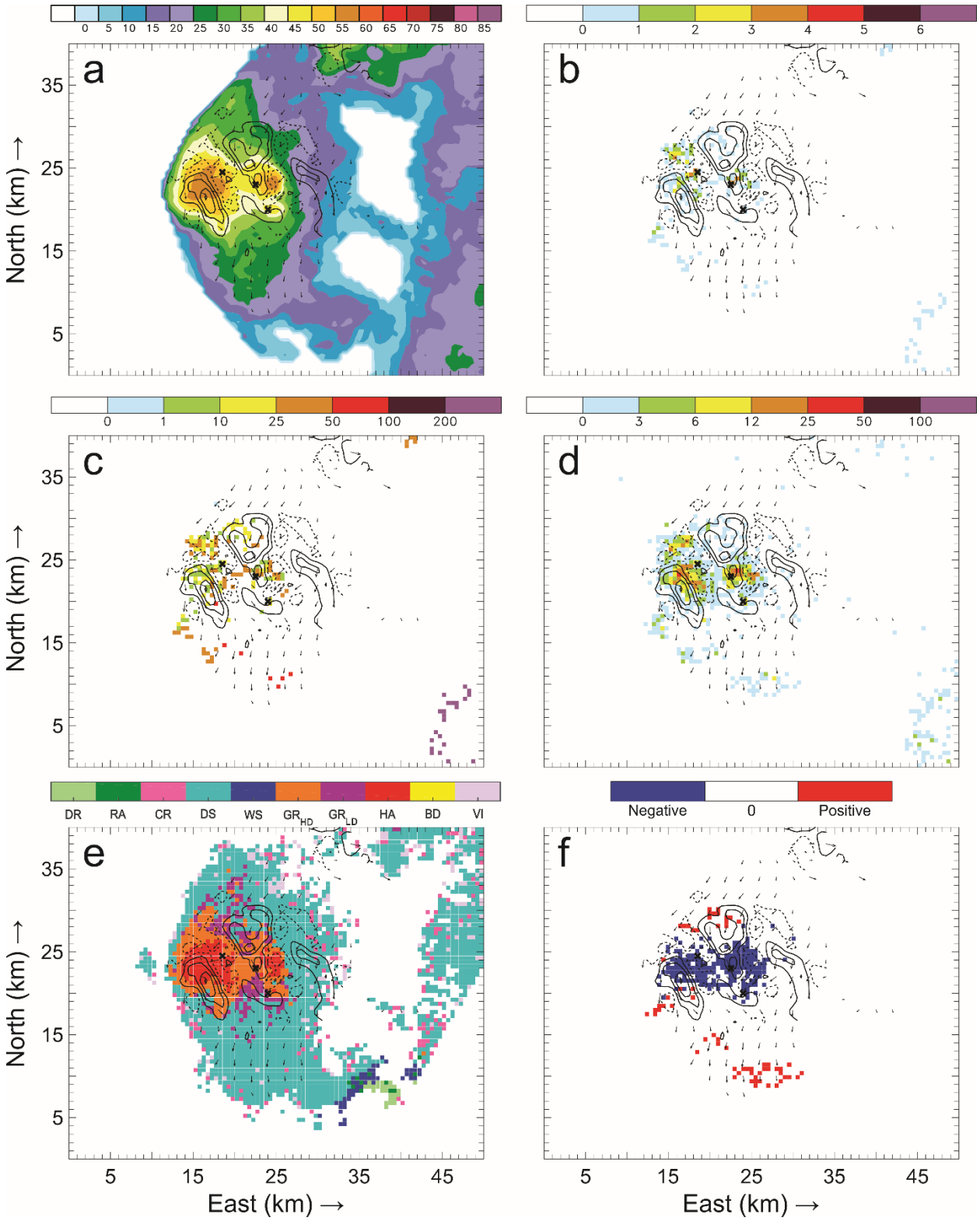

Figure 79: Horizontal cross-sections for 16 June 22:36 UTC taken at 7.2 km AGL of: a) color-filled Z and w contours (every 10 m s^{-1} starting at 5 m s^{-1}); b) color-filled FED and w contours; c) color-filled FP and w contours; d) color-filled SD and w contours; e) color-filled HCA and w contours; and f) color-filled net inferred space charge and w contours. All figures have the same horizontal storm-relative wind vectors, and black X's denote grid cells with FID > 0.

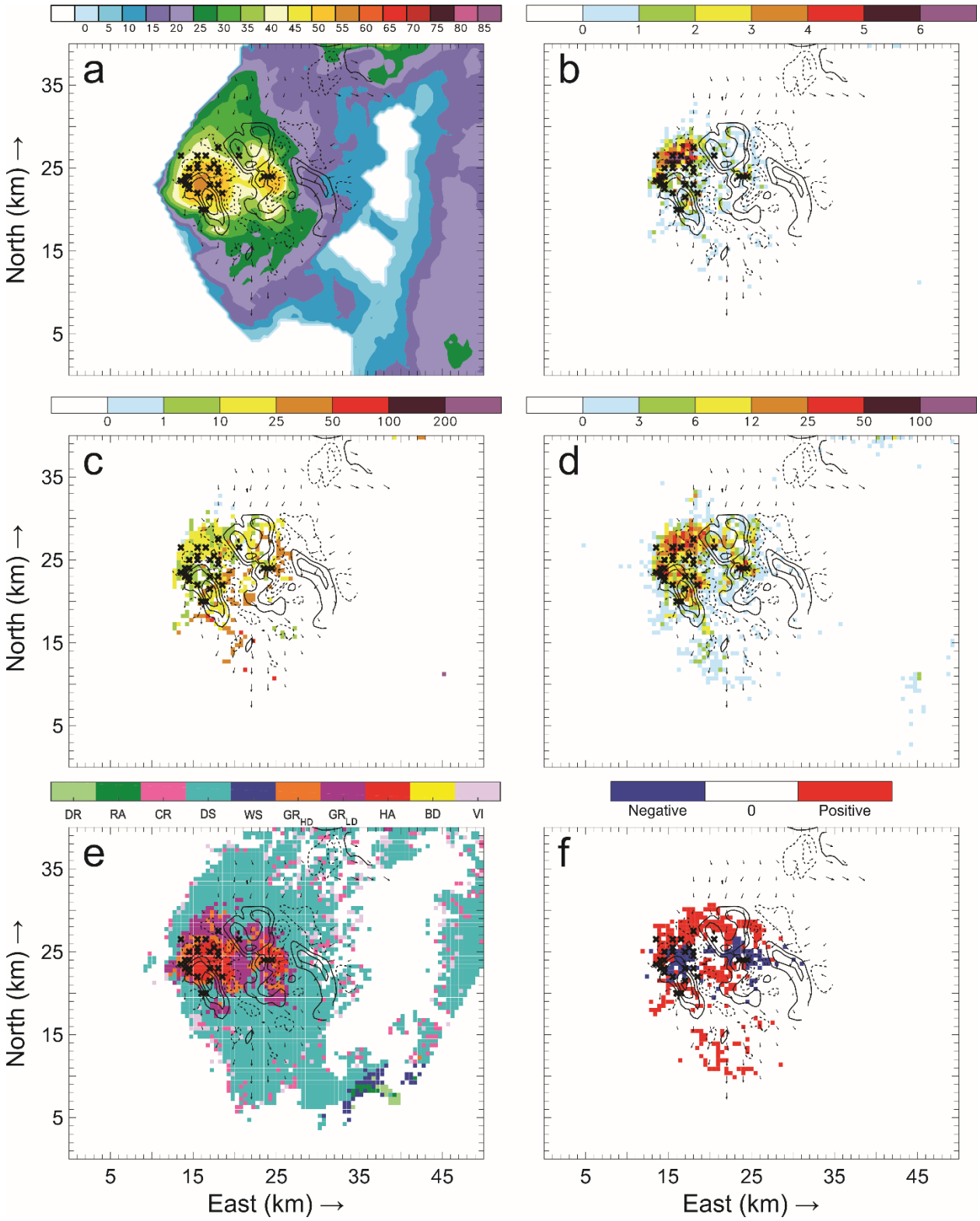

Figure 80: Horizontal cross-sections for 16 June 22:36 UTC. As in Figure 79, but taken at 8.2 km AGL.

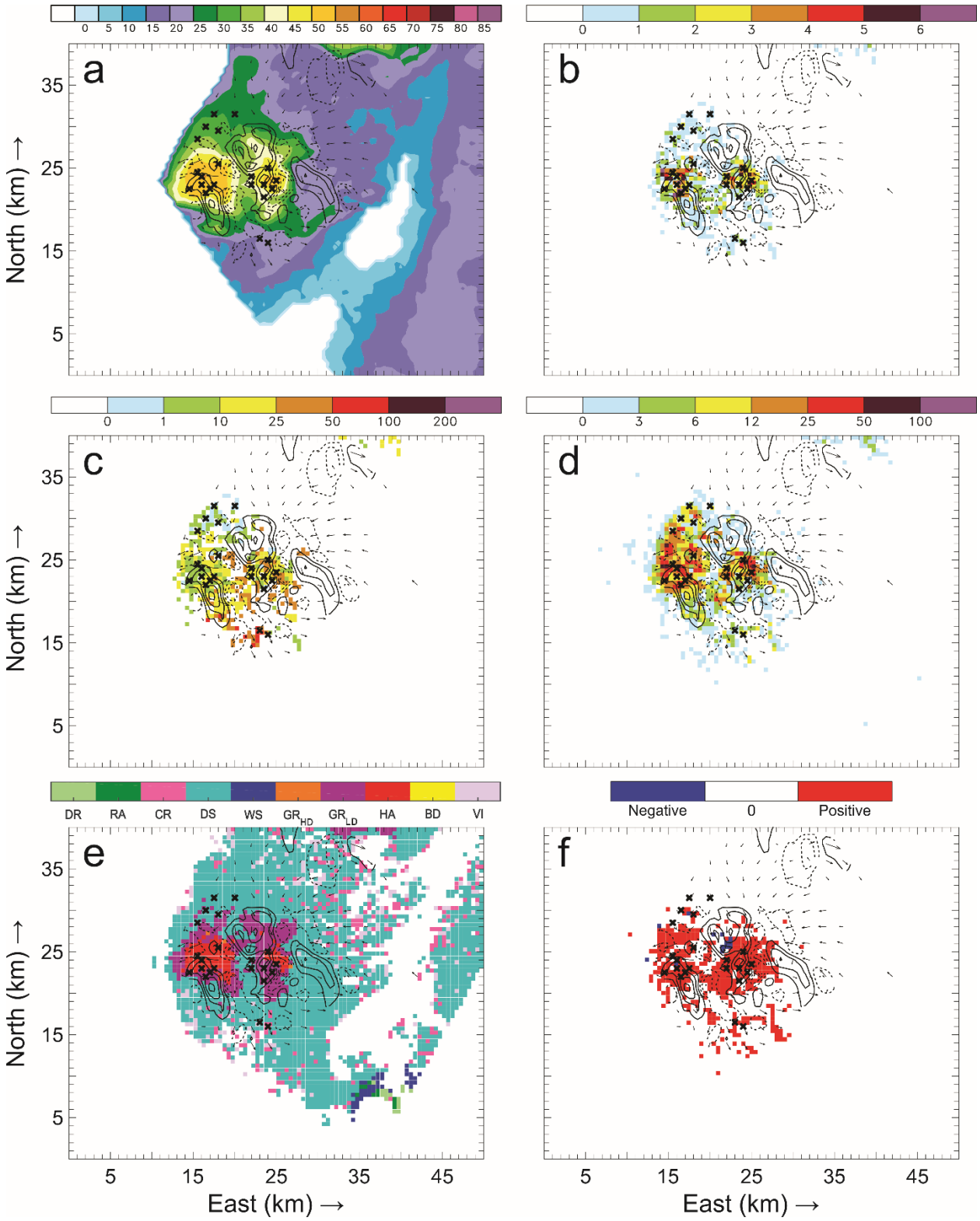

Figure 81: Horizontal cross-sections for 16 June 22:36 UTC. As in Figure 79, but taken at 9.2 km AGL.

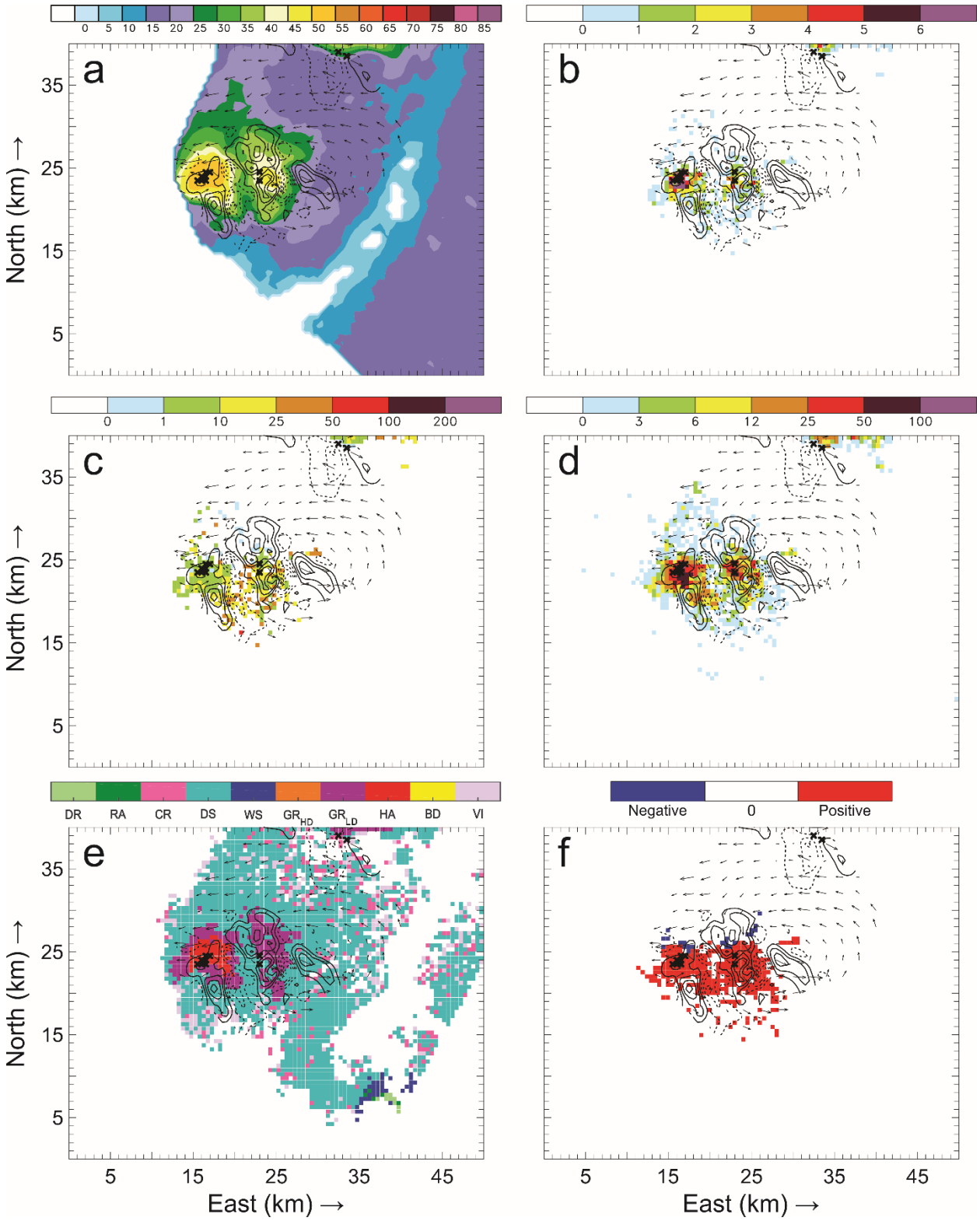

Figure 82: Horizontal cross-sections for 16 June 22:36 UTC. As in Figure 79, but taken at 10.2 km AGL.

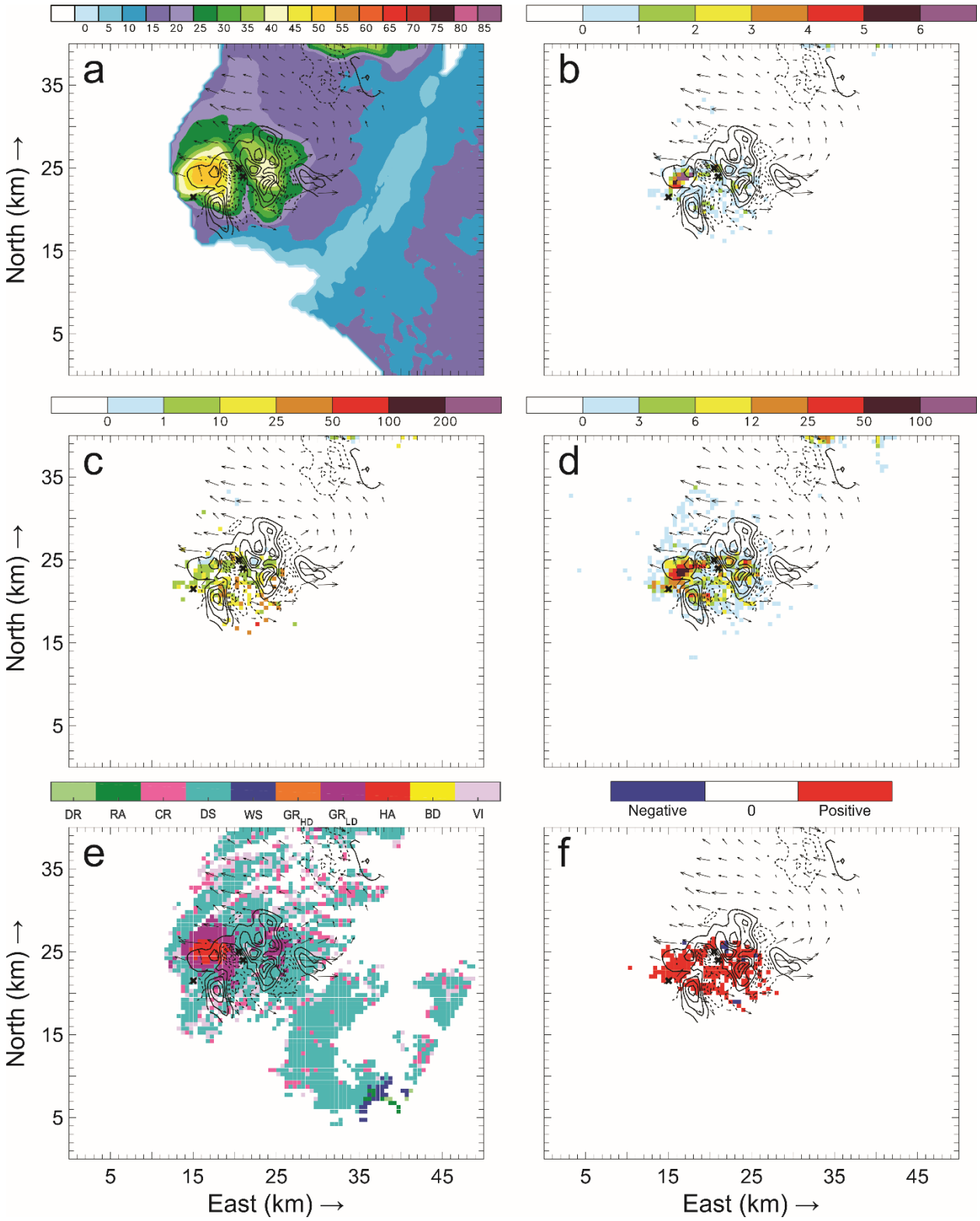

Figure 83: Horizontal cross-sections for 16 June 22:36 UTC. As in Figure 79, but taken at 11.2 km AGL.

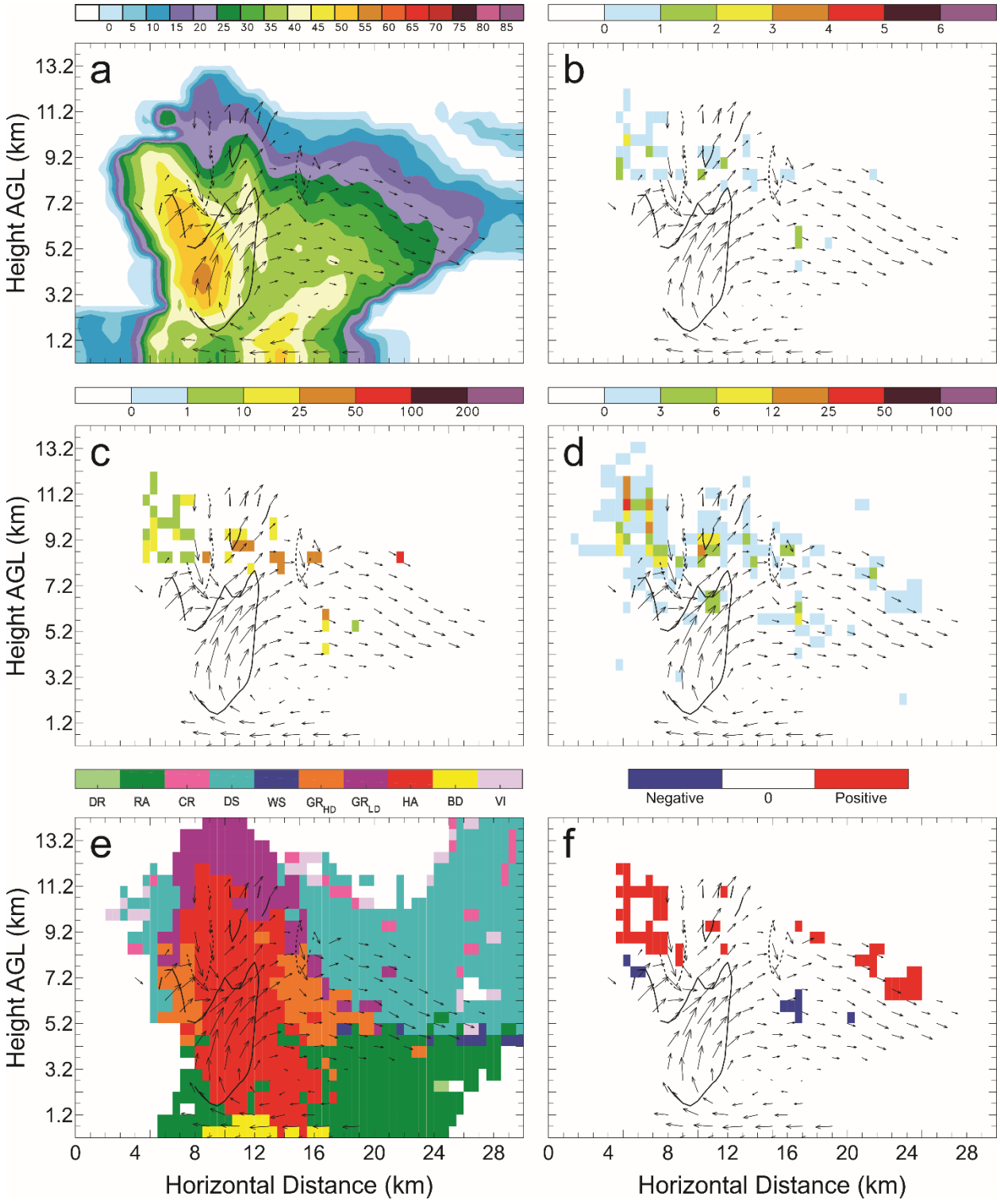

Figure 84: Vertical cross-sections for 16 June 22:36 UTC taken along the westernmost line in Figure 90(a) of: a) color-filled Z and w contours (every 10 m s^{-1} starting at 5 m s^{-1}); b) color-filled FED and w contours; c) color-filled FP and w contours; d) color-filled SD and w contours; e) color-filled HCA and w contours; and f) color-filled net inferred space charge and w contours. All figures have the same horizontal storm-relative wind vectors, and black X's denote grid cells with FID > 0.

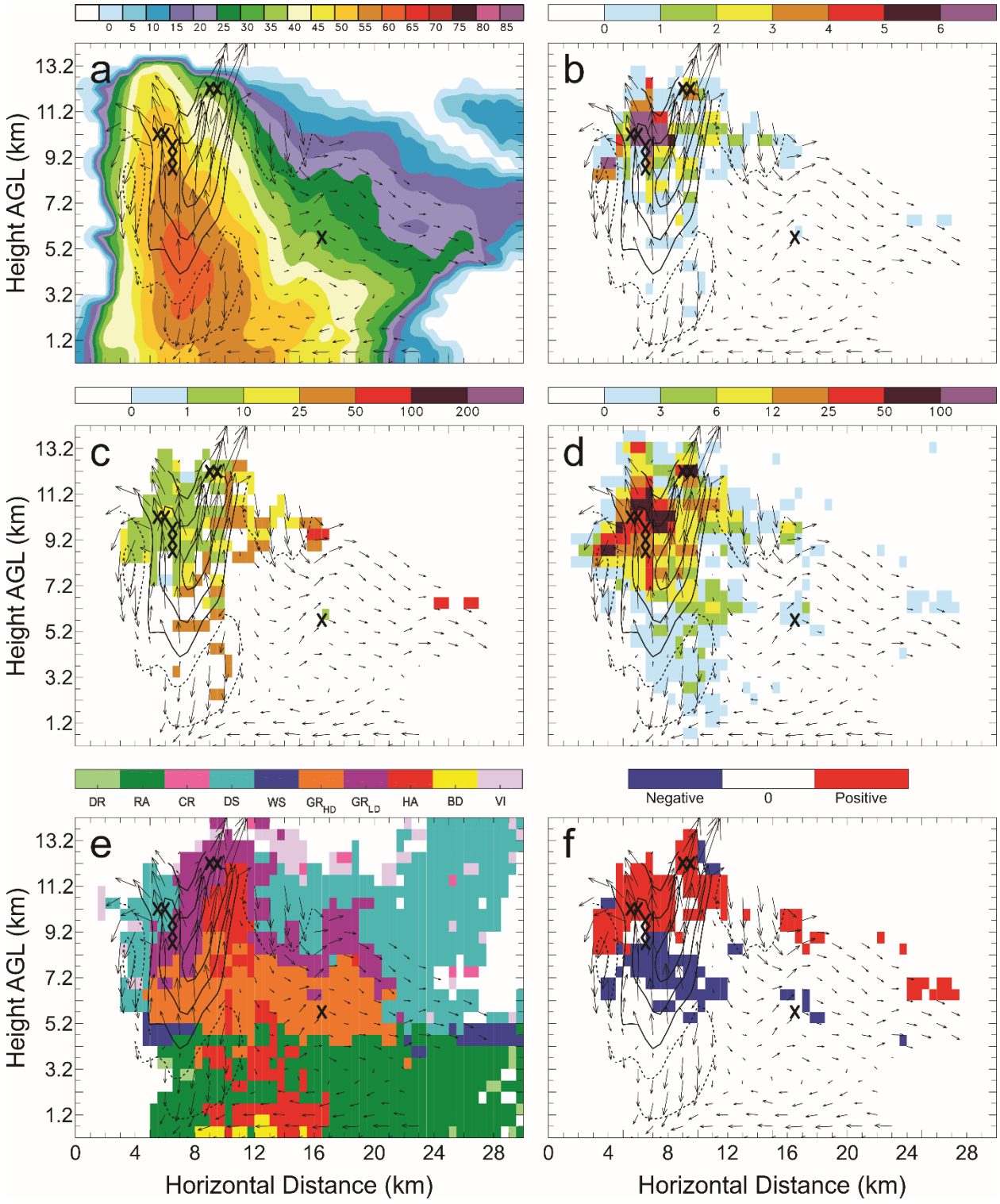

Figure 85: Vertical cross-sections for 16 June 22:36 UTC. As in Figure 84, but taken along the second line from the west in Figure 78(a).

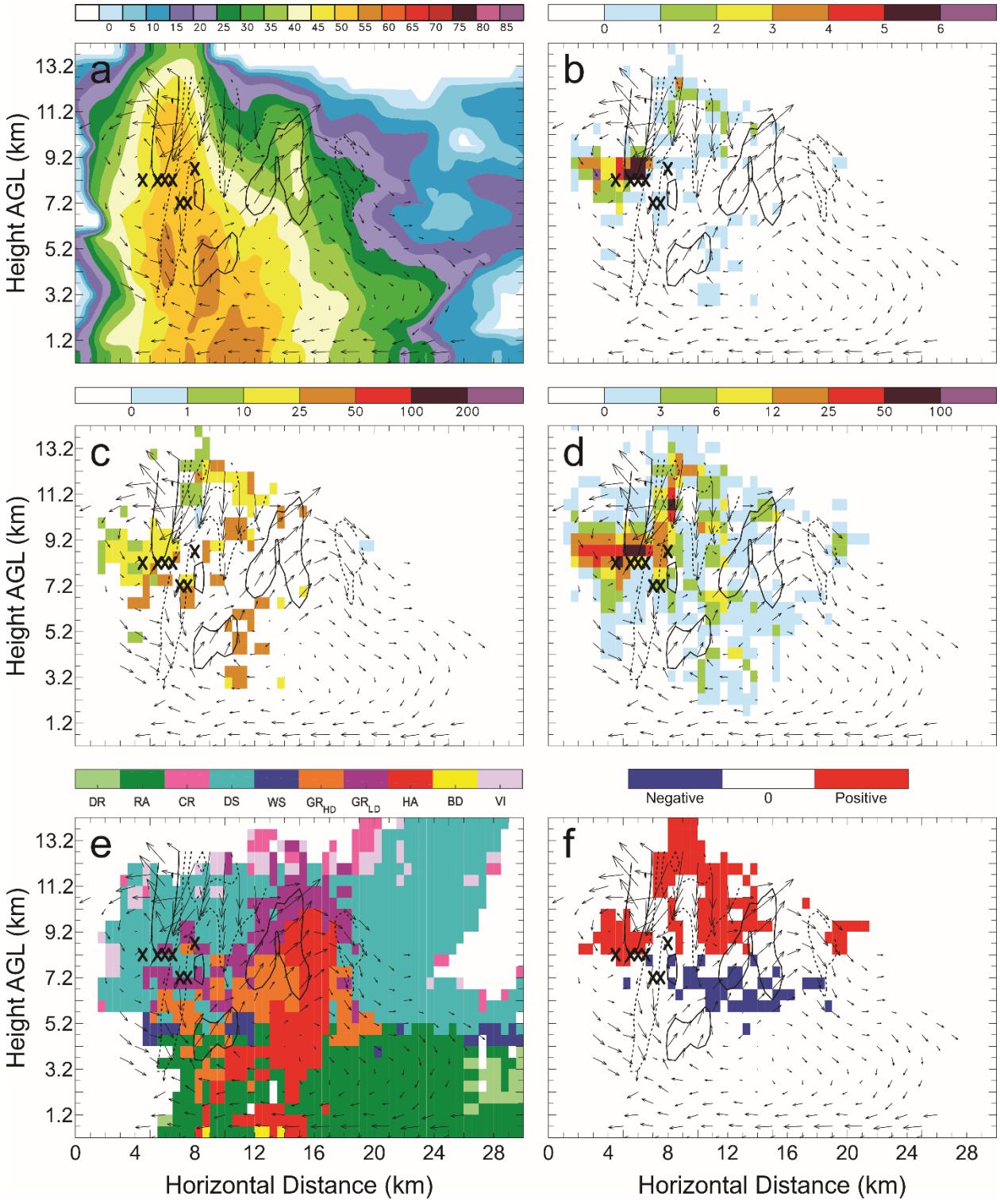

Figure 86: Vertical cross-sections for 16 June 22:36 UTC. As in Figure 84, but taken along the central line in Figure 78(a).

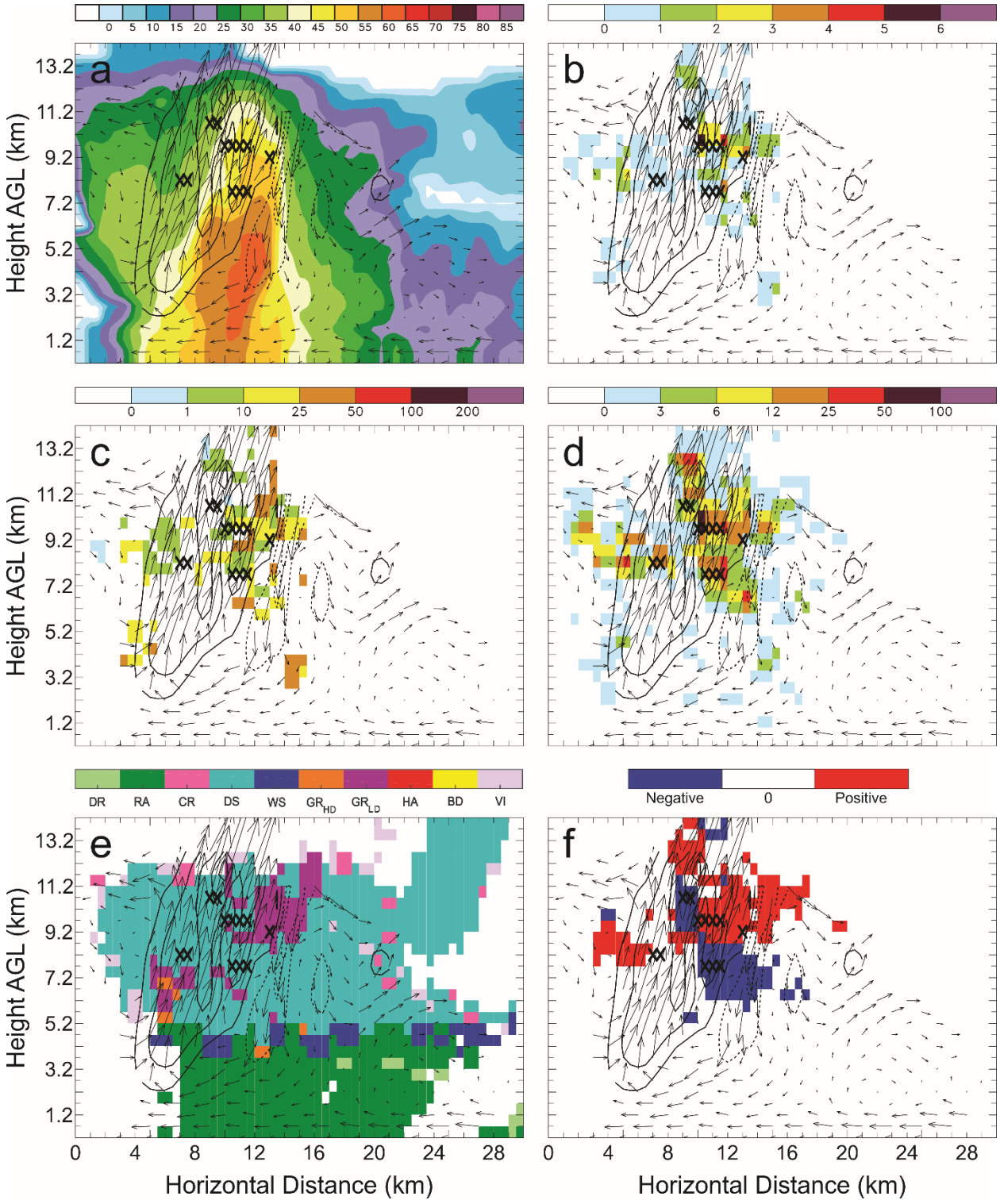

Figure 87: Vertical cross-sections for 16 June 22:36 UTC. As in Figure 84, but taken along the second line from the east in Figure 78(a).

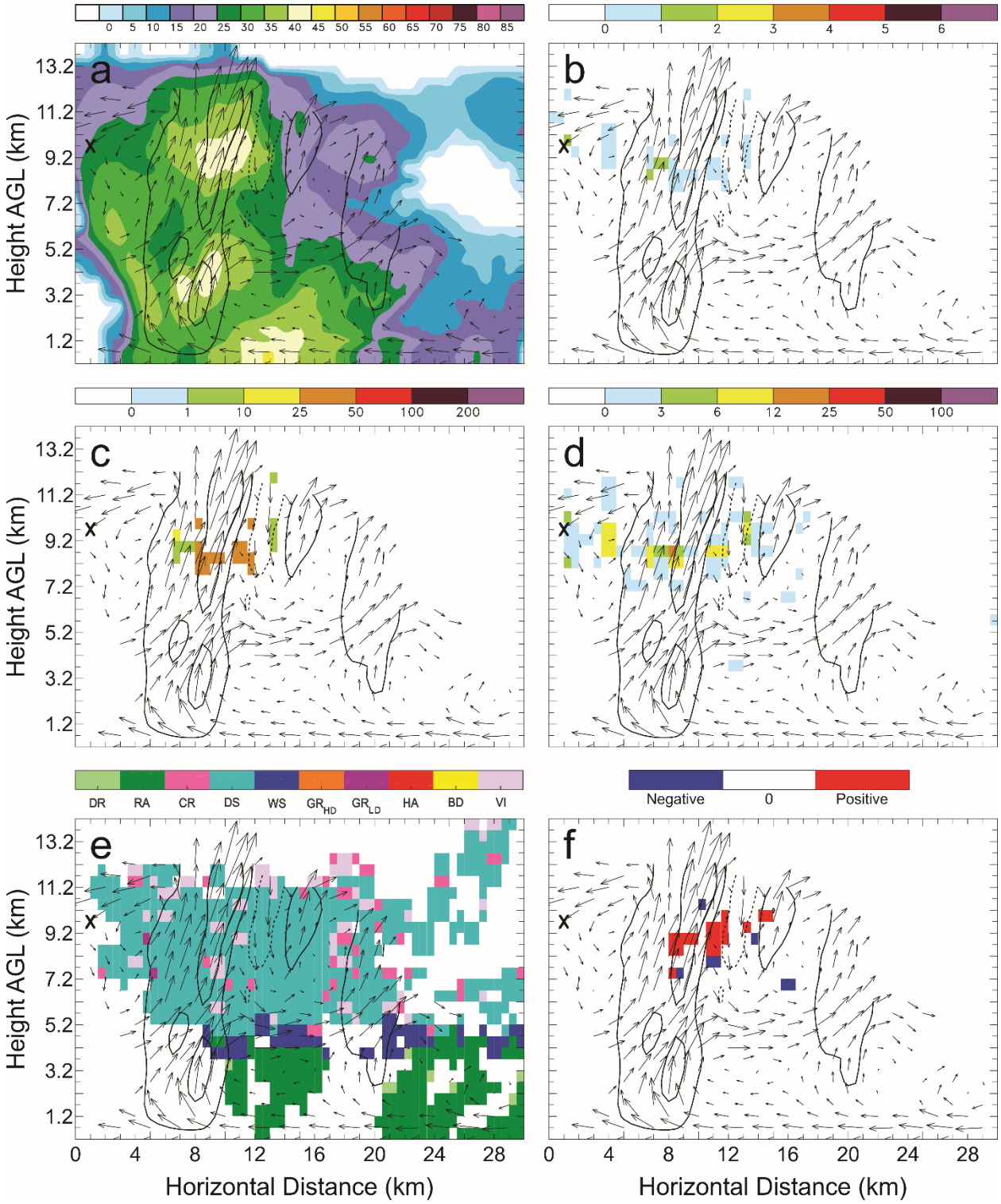

Figure 88: Vertical cross-sections for 16 June 22:36 UTC. As in Figure 84, but taken along the easternmost line in Figure 78(a).

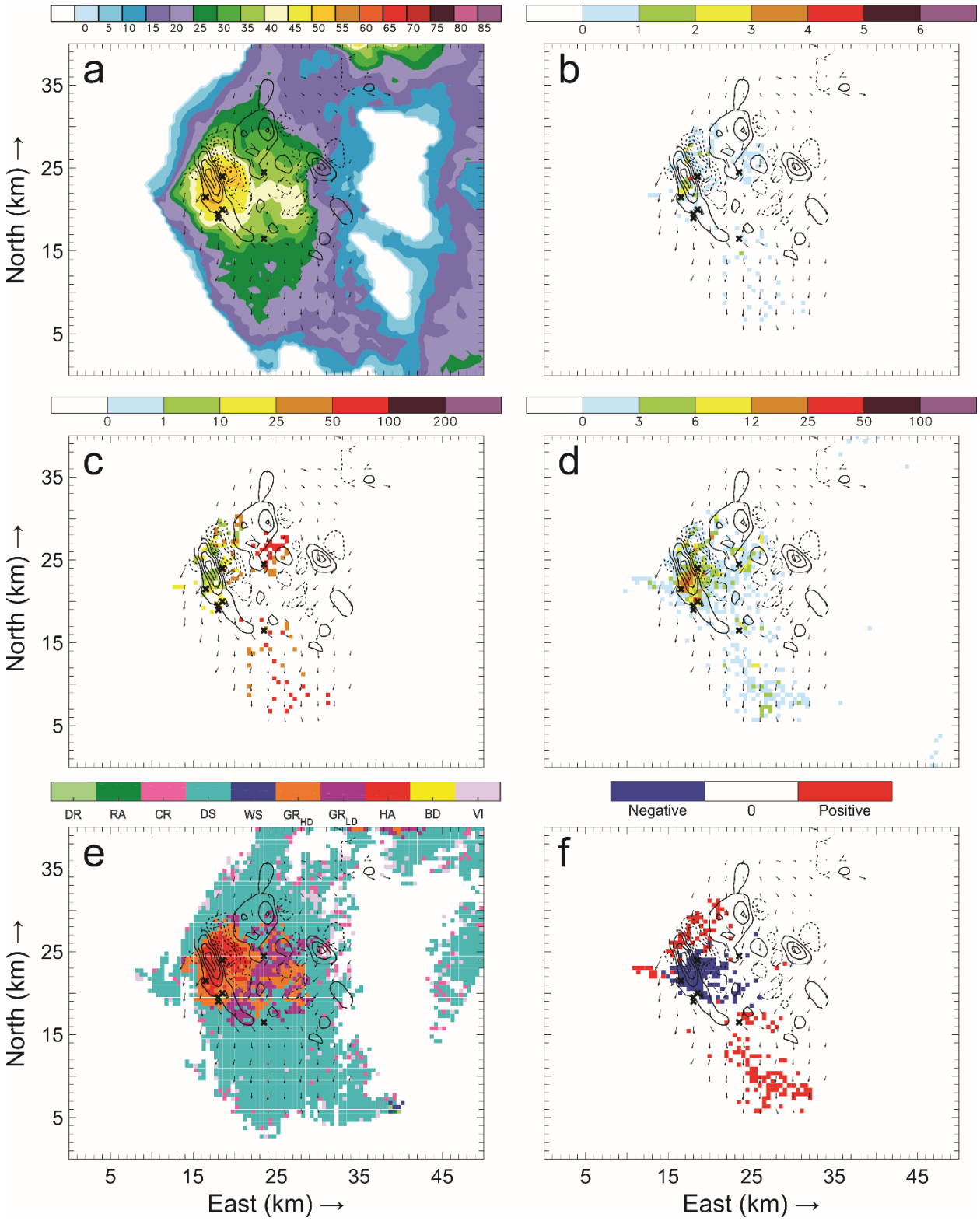

Figure 89: Horizontal cross-sections for 16 June 22:42 UTC taken at 7.2 km AGL of: a) color-filled Z and w contours (every 10 m s^{-1} starting at 5 m s^{-1}); b) color-filled FED and w contours; c) color-filled FP and w contours; d) color-filled SD and w contours; e) color-filled HCA and w contours; and f) color-filled net inferred space charge and w contours. All figures have the same horizontal storm-relative wind vectors, and black X's denote grid cells with FID > 0.

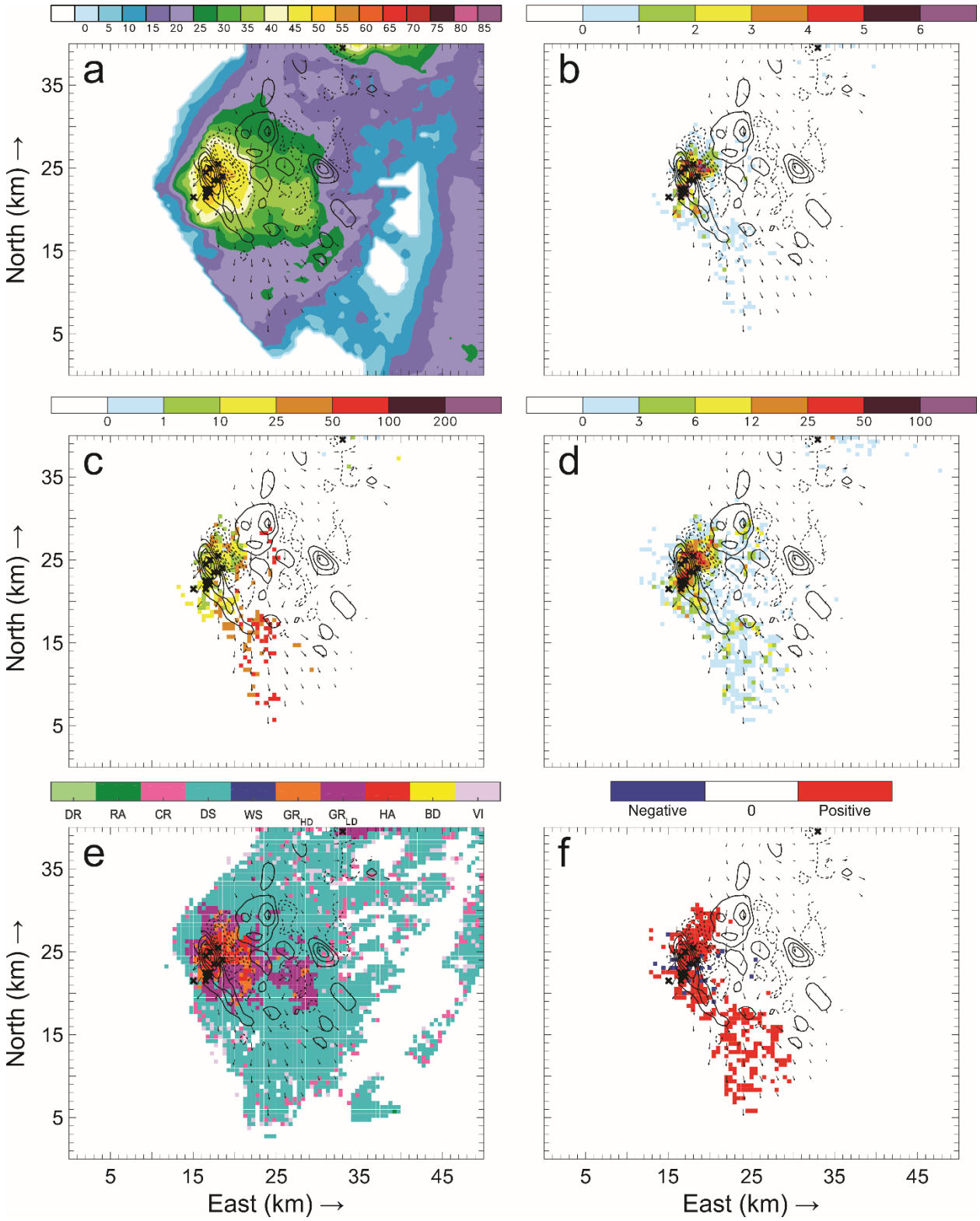

Figure 90: Horizontal cross-sections for 16 June 22:42 UTC. As in Figure 89, but taken at 8.2 km AGL.

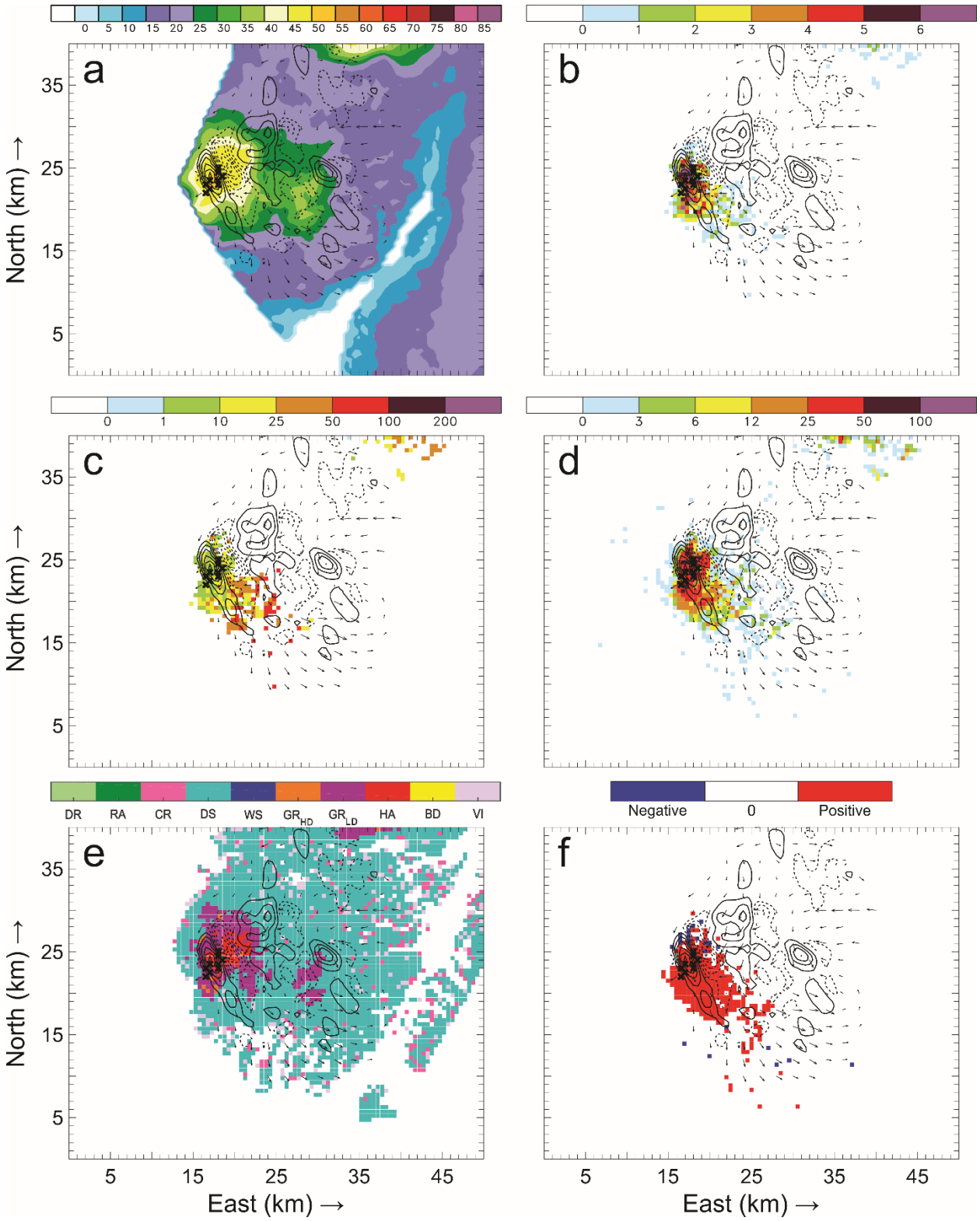

Figure 91: Horizontal cross-sections for 16 June 22:42 UTC. As in Figure 89, but taken at 9.2 km AGL.

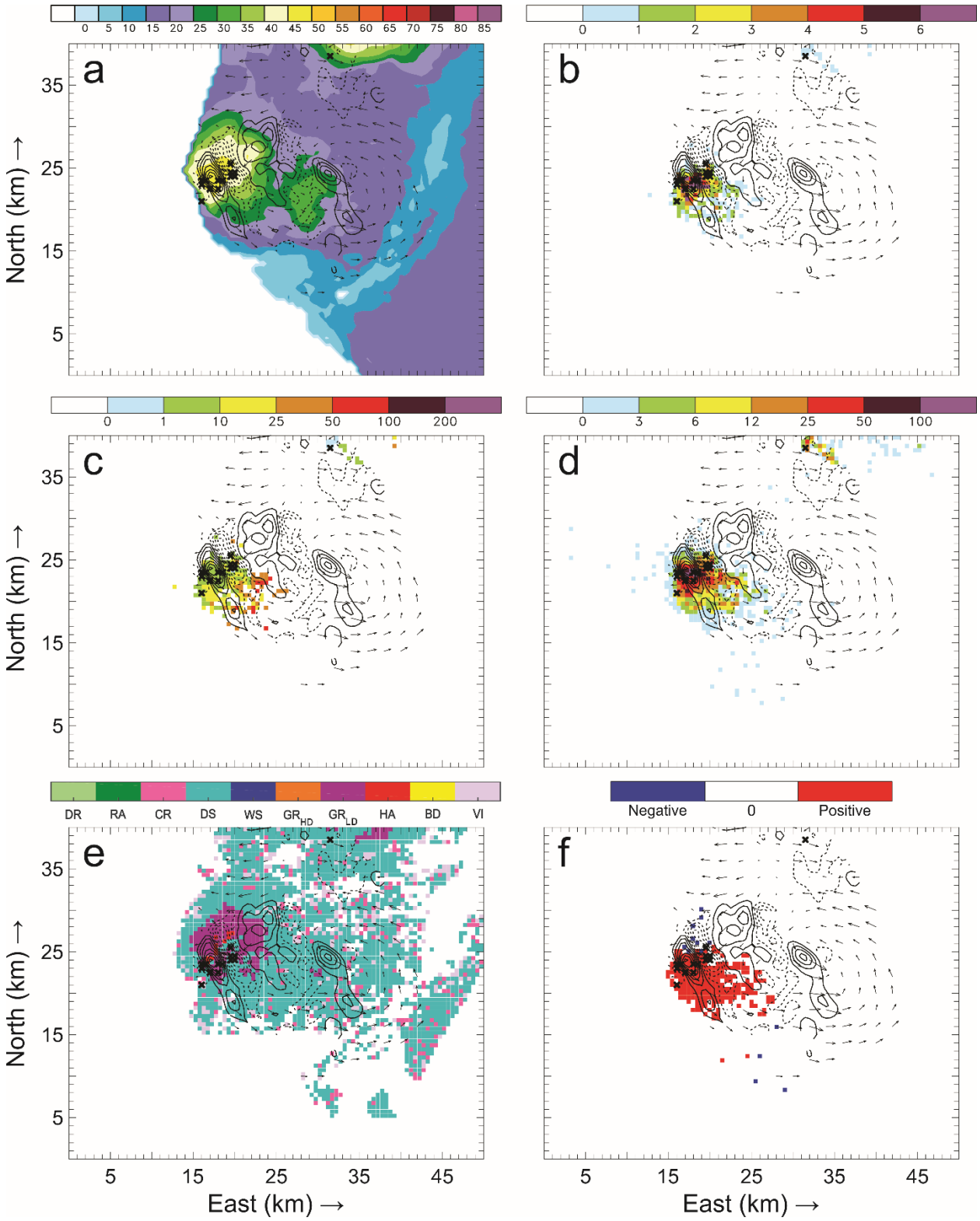

Figure 92: Horizontal cross-sections for 16 June 22:42 UTC. As in Figure 89, but taken at 10.2 km AGL.

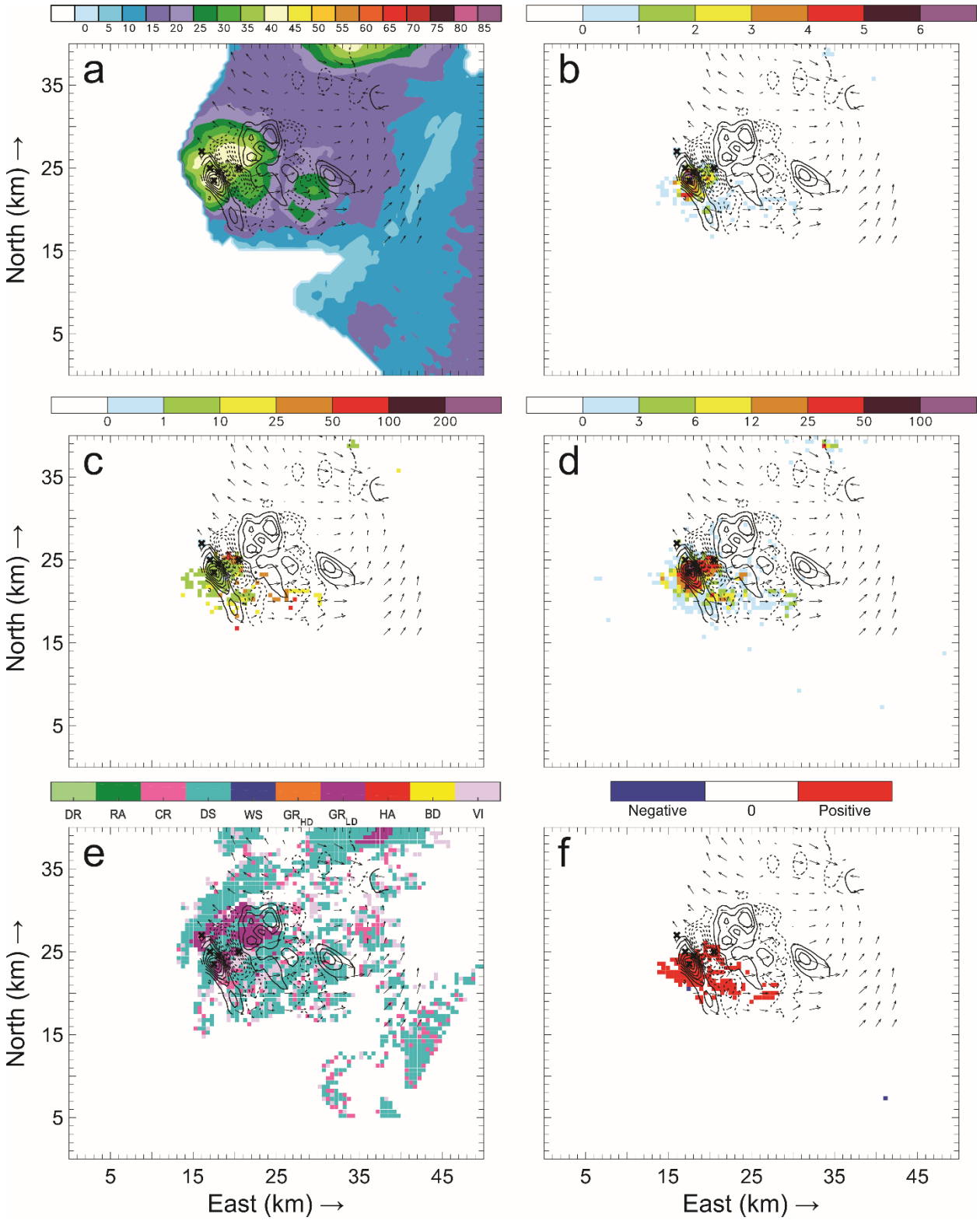

Figure 93: Horizontal cross-sections for 16 June 22:42 UTC. As in Figure 89, but taken at 11.2 km AGL.

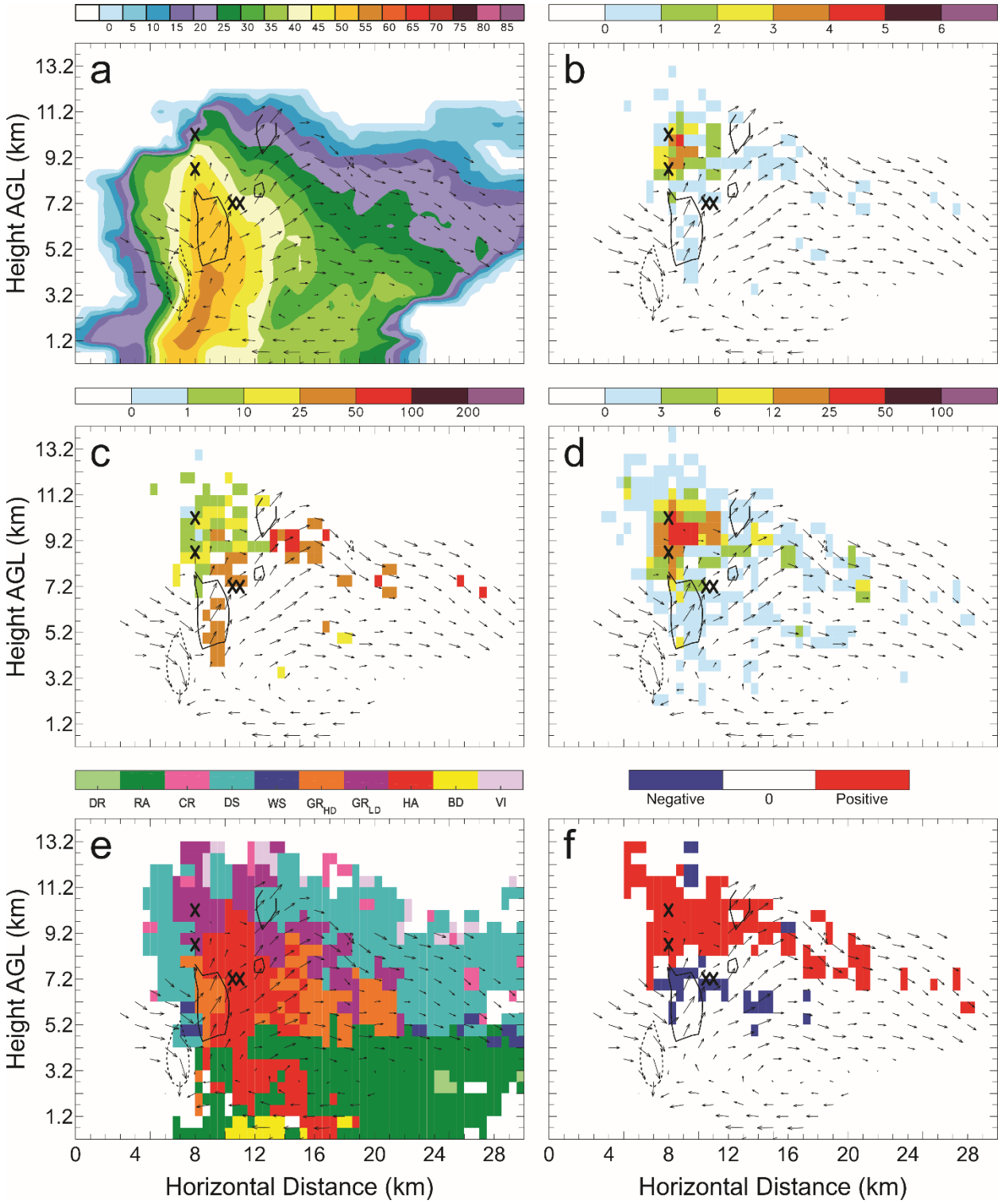

Figure 94: Vertical cross-sections for 16 June 22:42 UTC taken along the westernmost line in Figure 78(b) of: a) color-filled Z and w contours (every 10 m s^{-1} starting at 5 m s^{-1}); b) color-filled FED and w contours; c) color-filled FP and w contours; d) color-filled SD and w contours; e) color-filled HCA and w contours; and f) color-filled net inferred space charge and w contours. All figures have the same horizontal storm-relative wind vectors, and black X's denote grid cells with FID > 0.

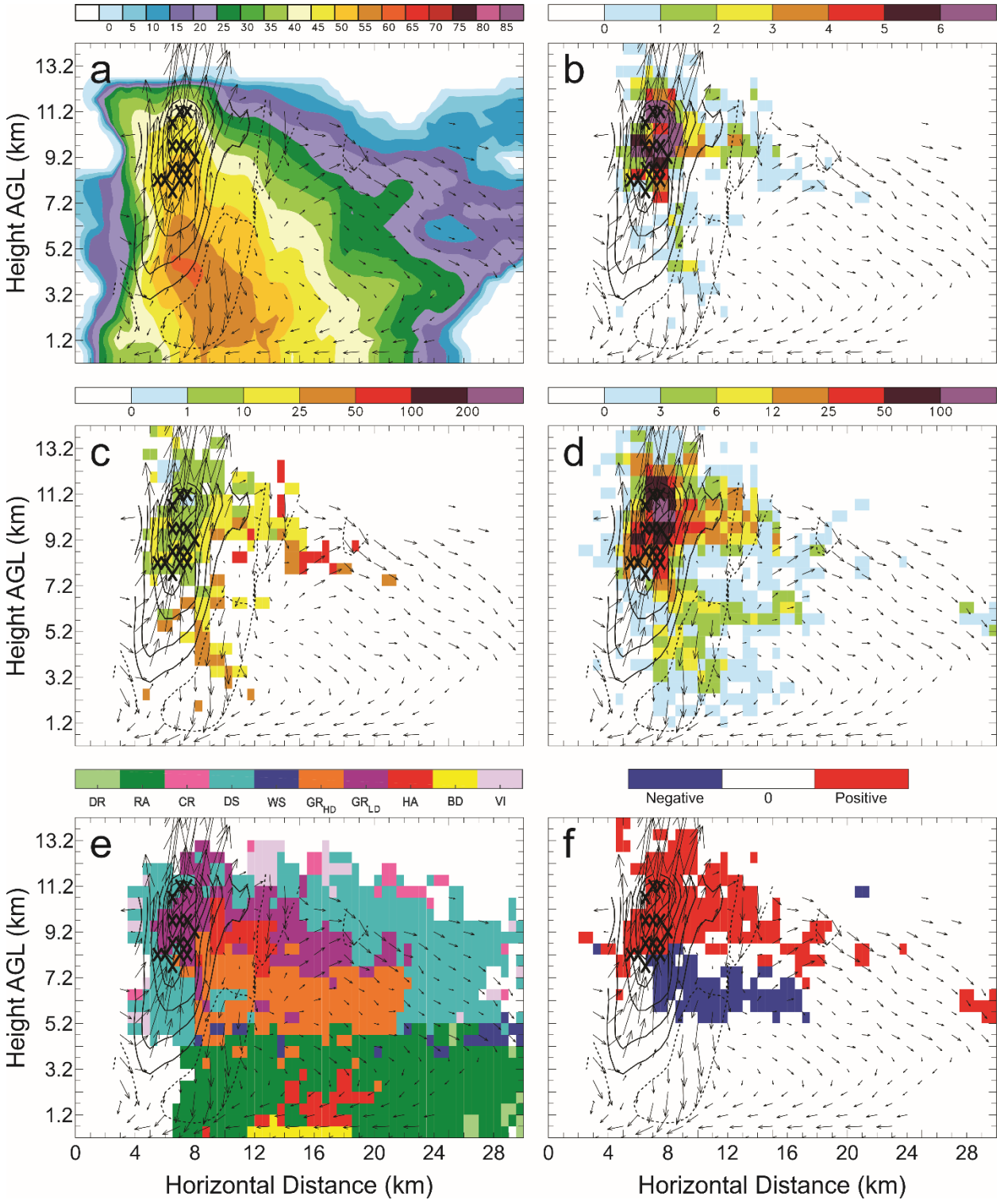

Figure 95: Vertical cross-sections for 16 June 22:42 UTC. As in Figure 94, but taken along the second line from the west in Figure 78(b).

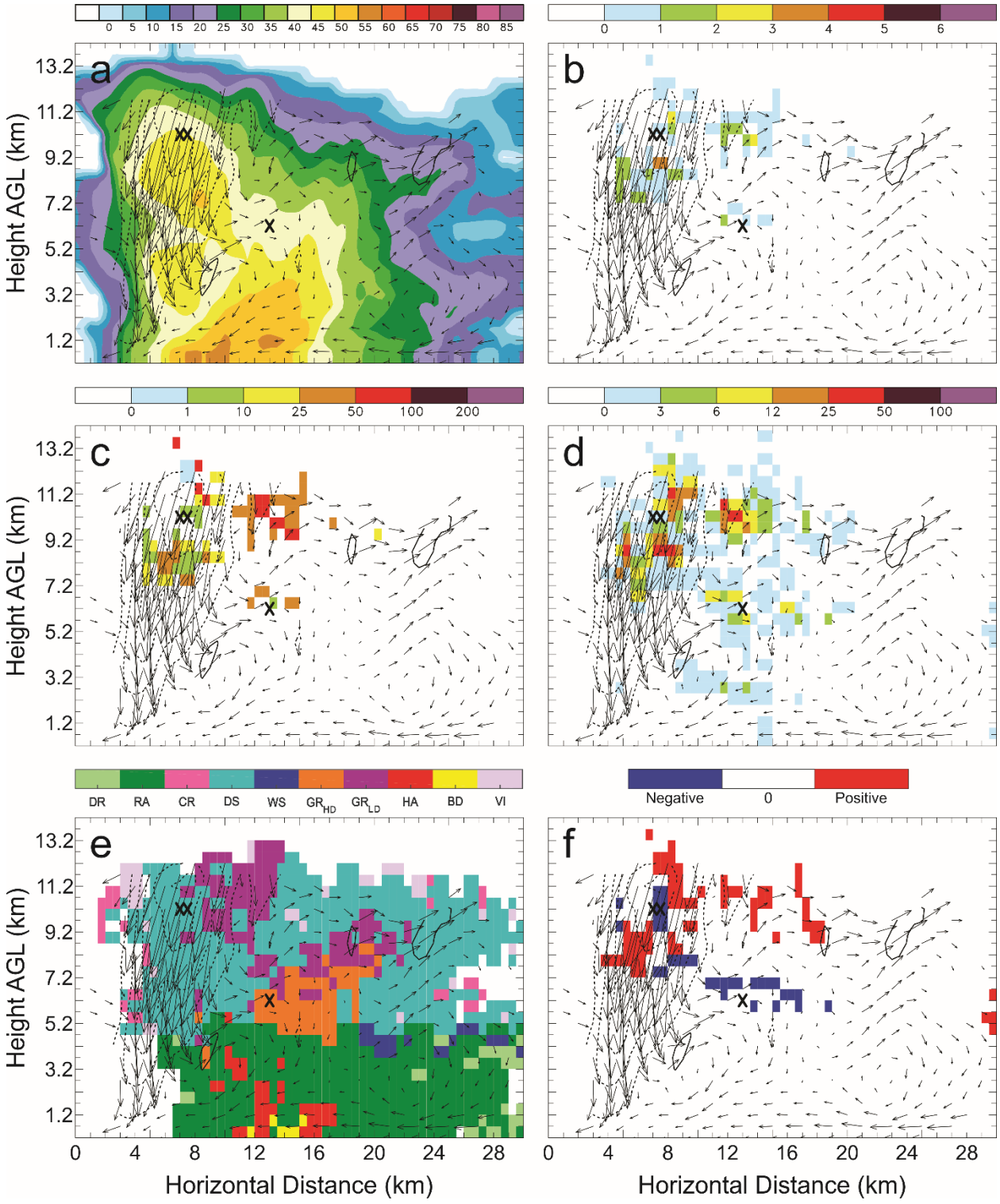

Figure 96: Vertical cross-sections for 16 June 22:42 UTC. As in Figure 94, but taken along the second line from the east in Figure 78(b).

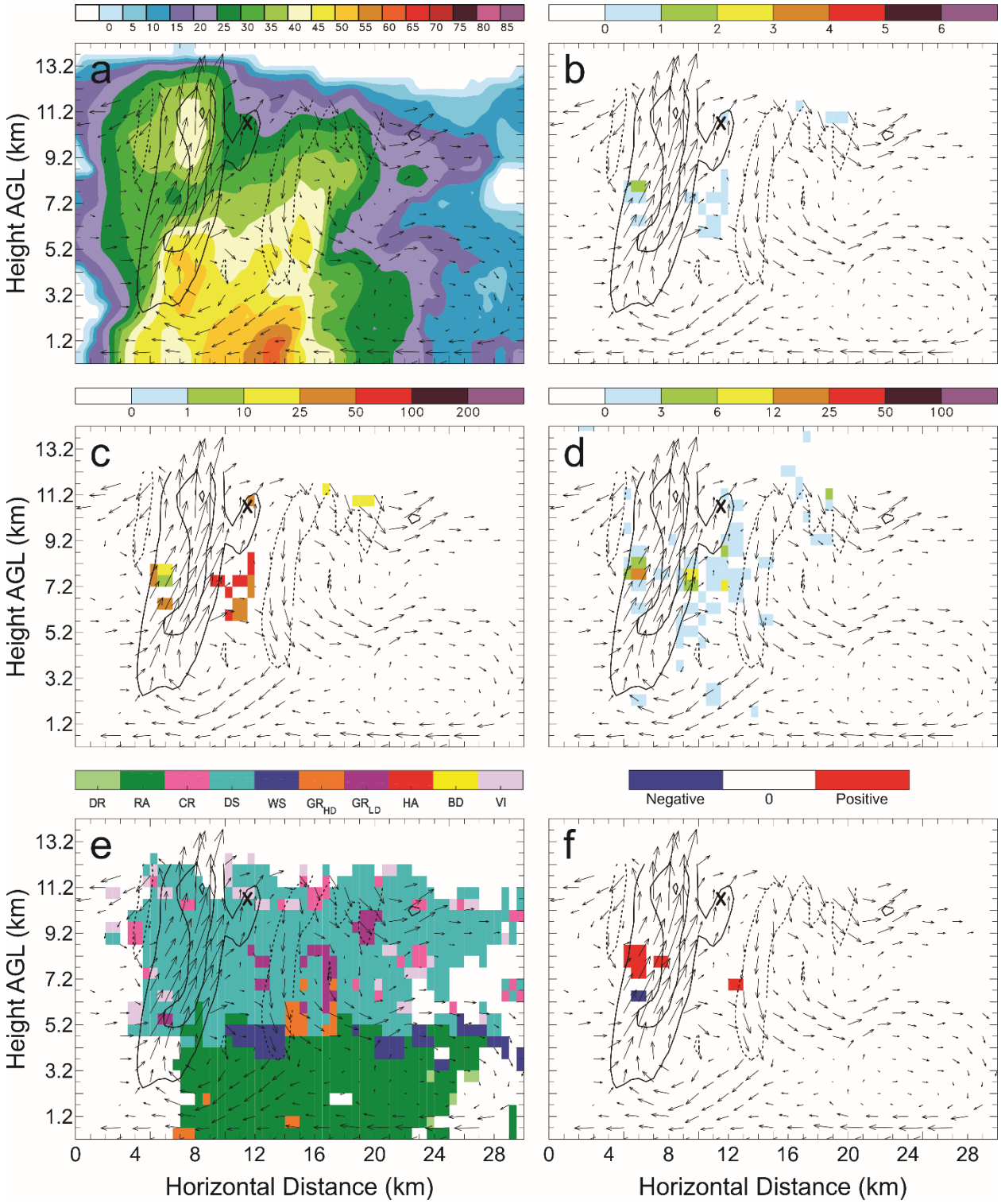

Figure 97: Vertical cross-sections for 16 June 22:42 UTC. As in Figure 94, but taken along the easternmost line in Figure 78(b).

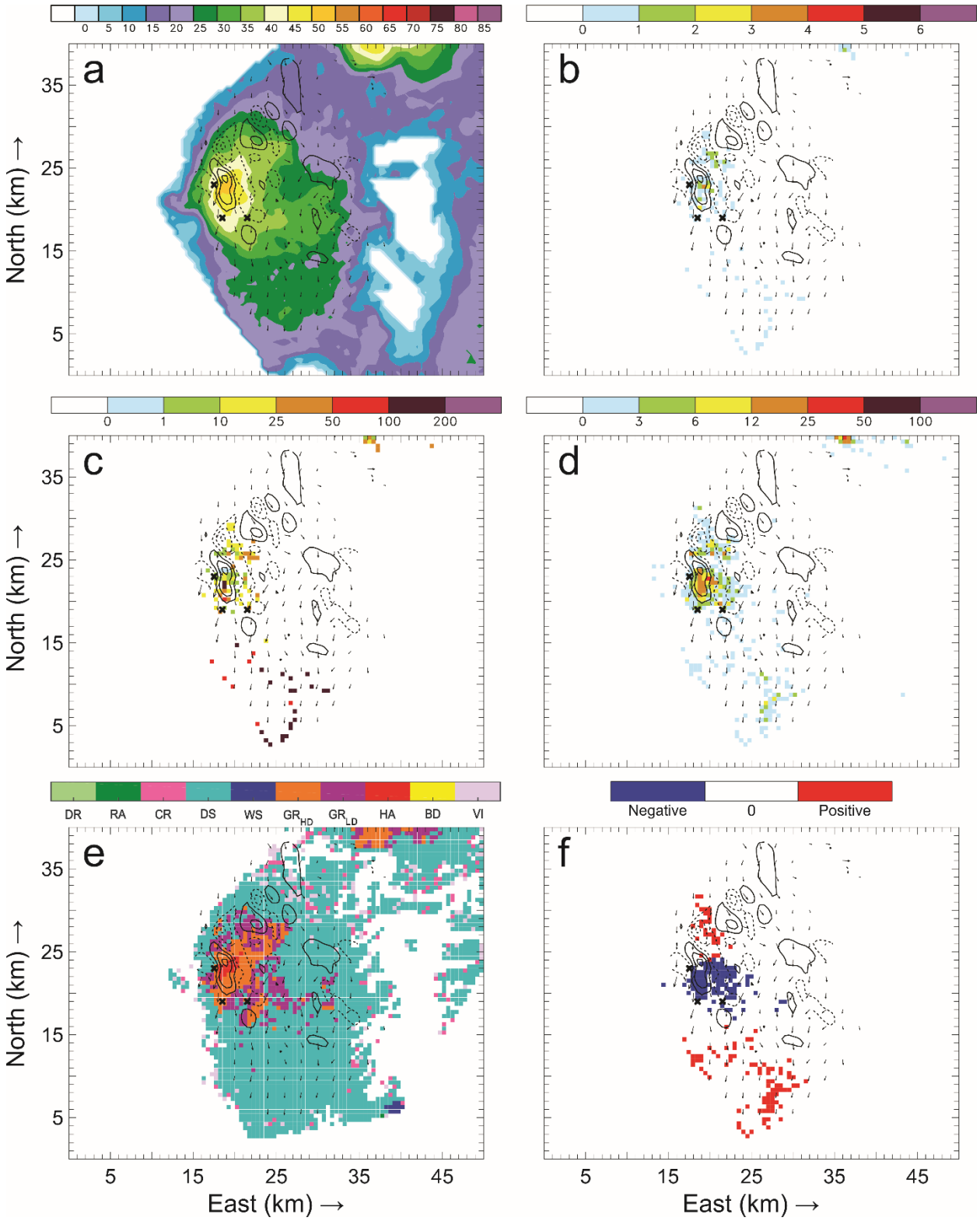

Figure 98: Horizontal cross-sections for 16 June 22:48 UTC taken at 7.2 km AGL of: a) color-filled Z and w contours (every 10 m s^{-1} starting at 5 m s^{-1}); b) color-filled FED and w contours; c) color-filled FP and w contours; d) color-filled SD and w contours; e) color-filled HCA and w contours; and f) color-filled net inferred space charge and w contours. All figures have the same horizontal storm-relative wind vectors, and black X's denote grid cells with FID > 0.

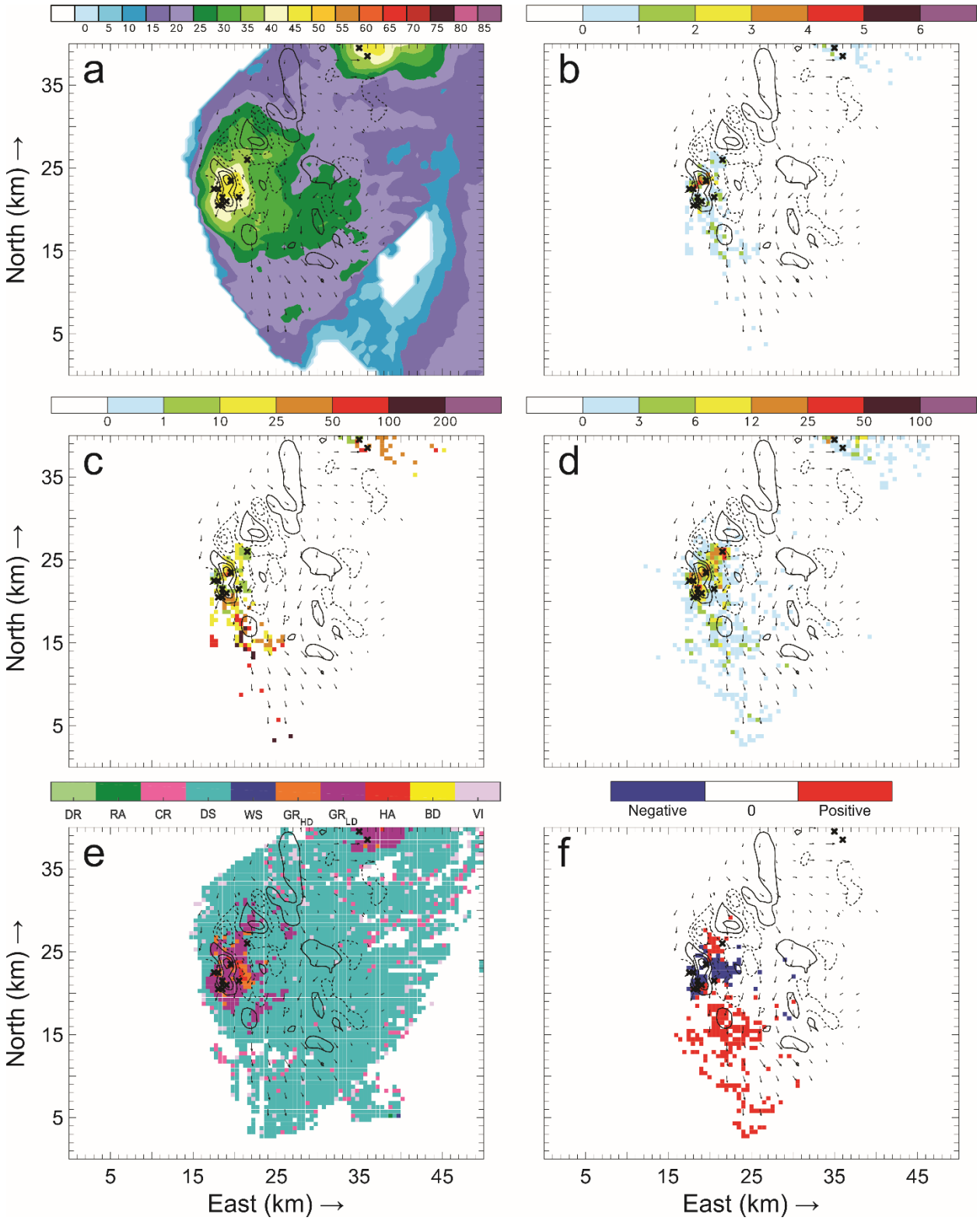

Figure 99: Horizontal cross-sections for 16 June 22:48 UTC. As in Figure 98, but taken at 8.2 km AGL.

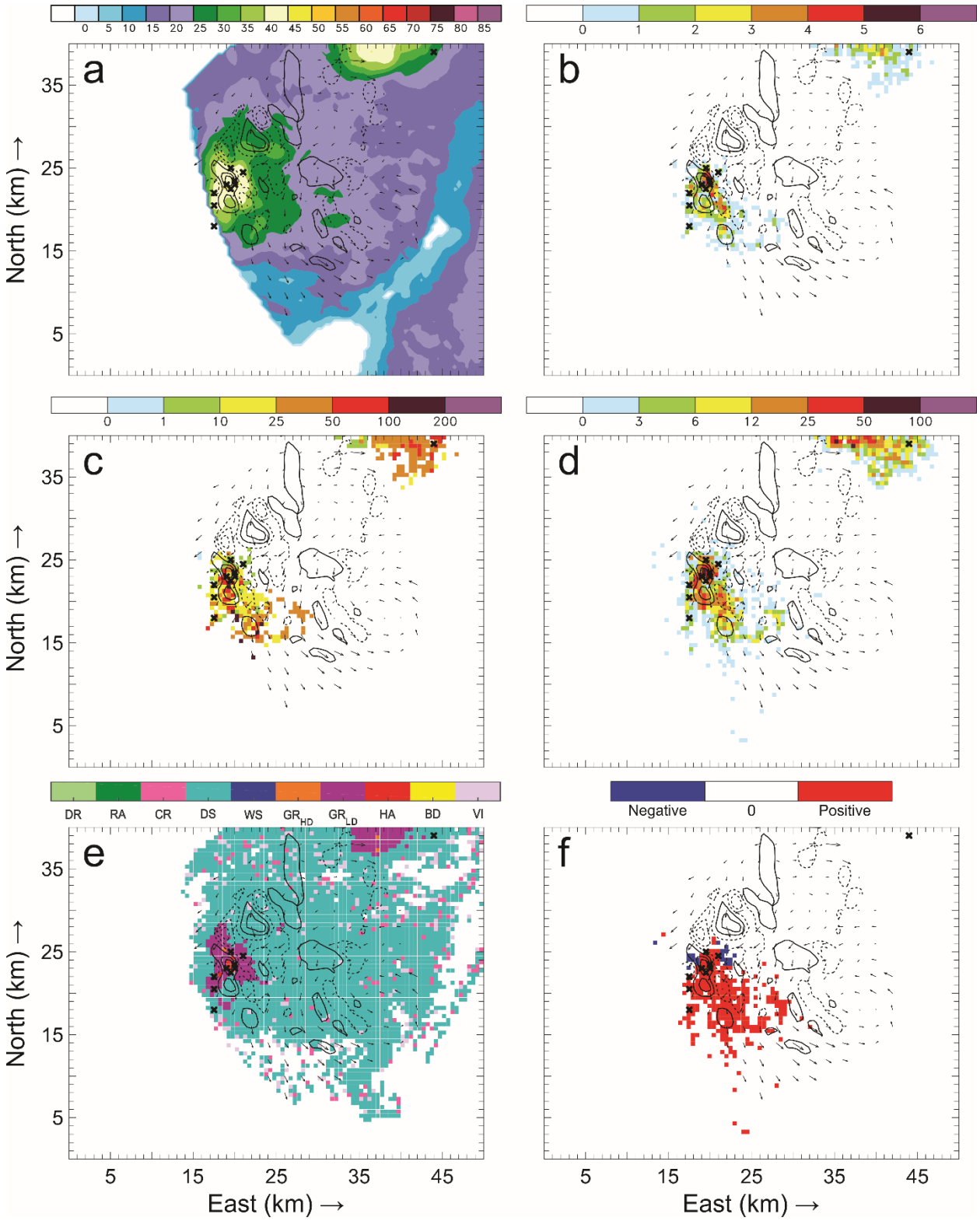

Figure 100: Horizontal cross-sections for 16 June 22:48 UTC. As in Figure 98, but taken at 9.2 km AGL.

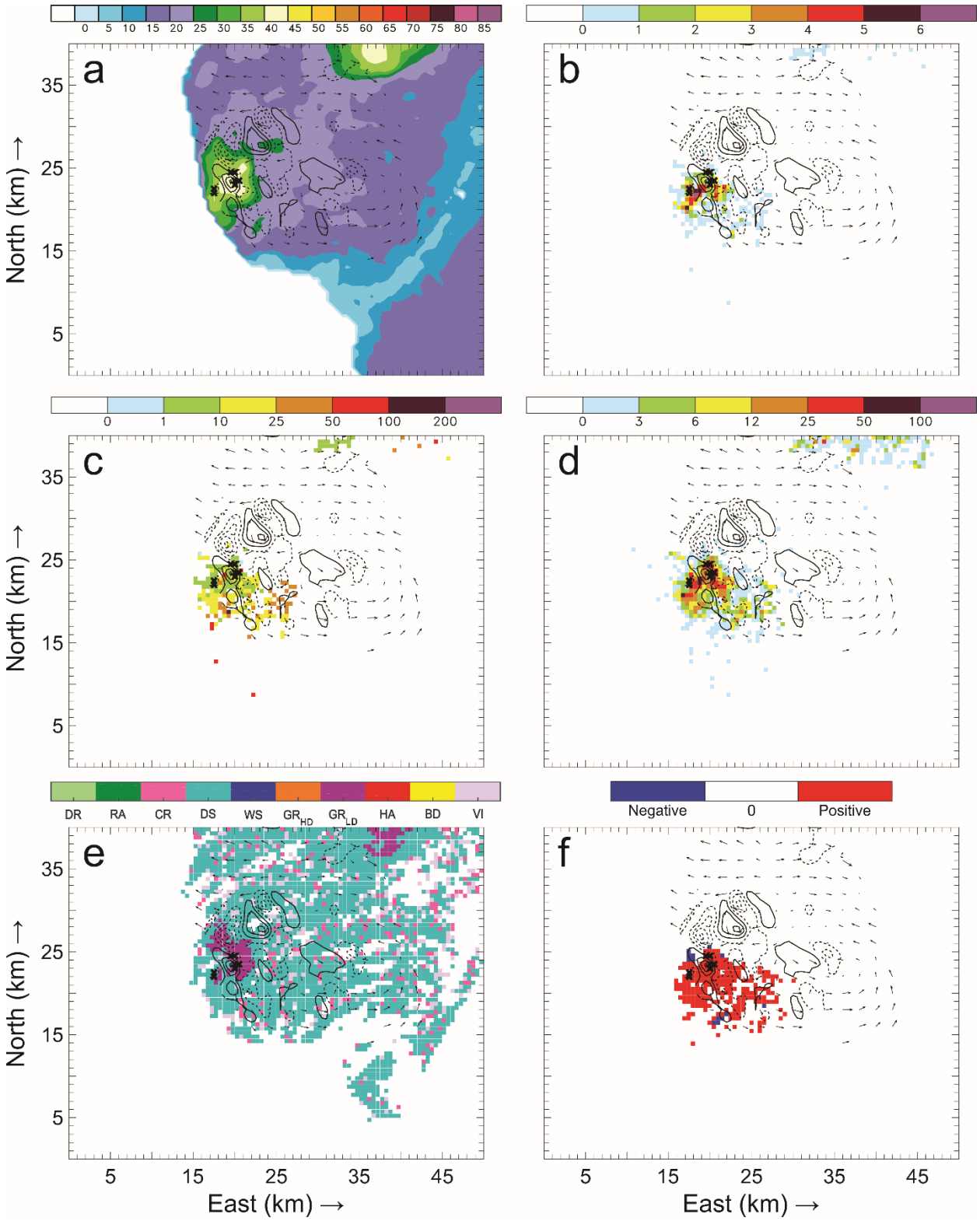

Figure 101: Horizontal cross-sections for 16 June 22:48 UTC. As in Figure 98, but taken at 10.2 km AGL.

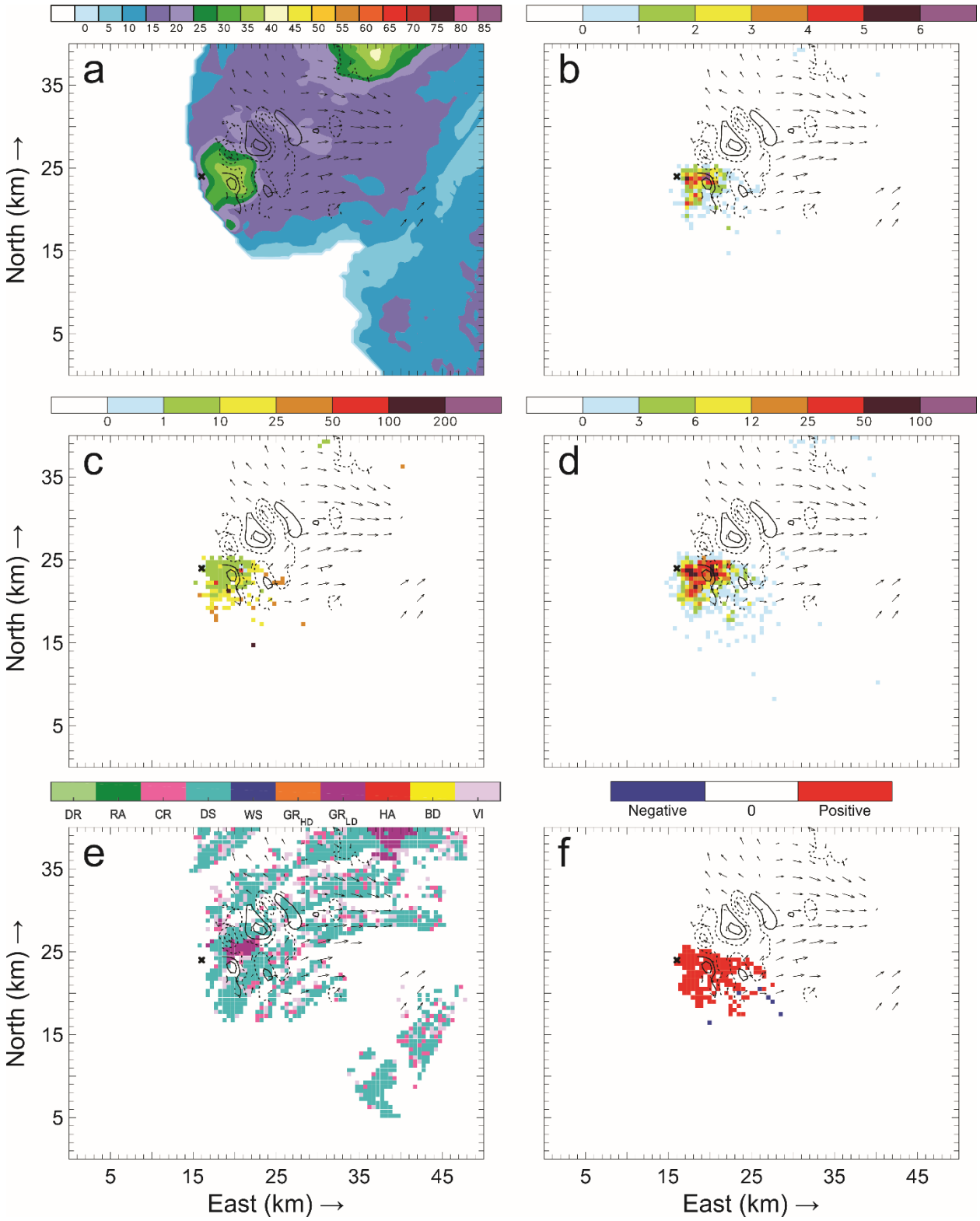

Figure 102: Horizontal cross-sections for 16 June 22:48 UTC. As in Figure 98, but taken at 11.2 km AGL.

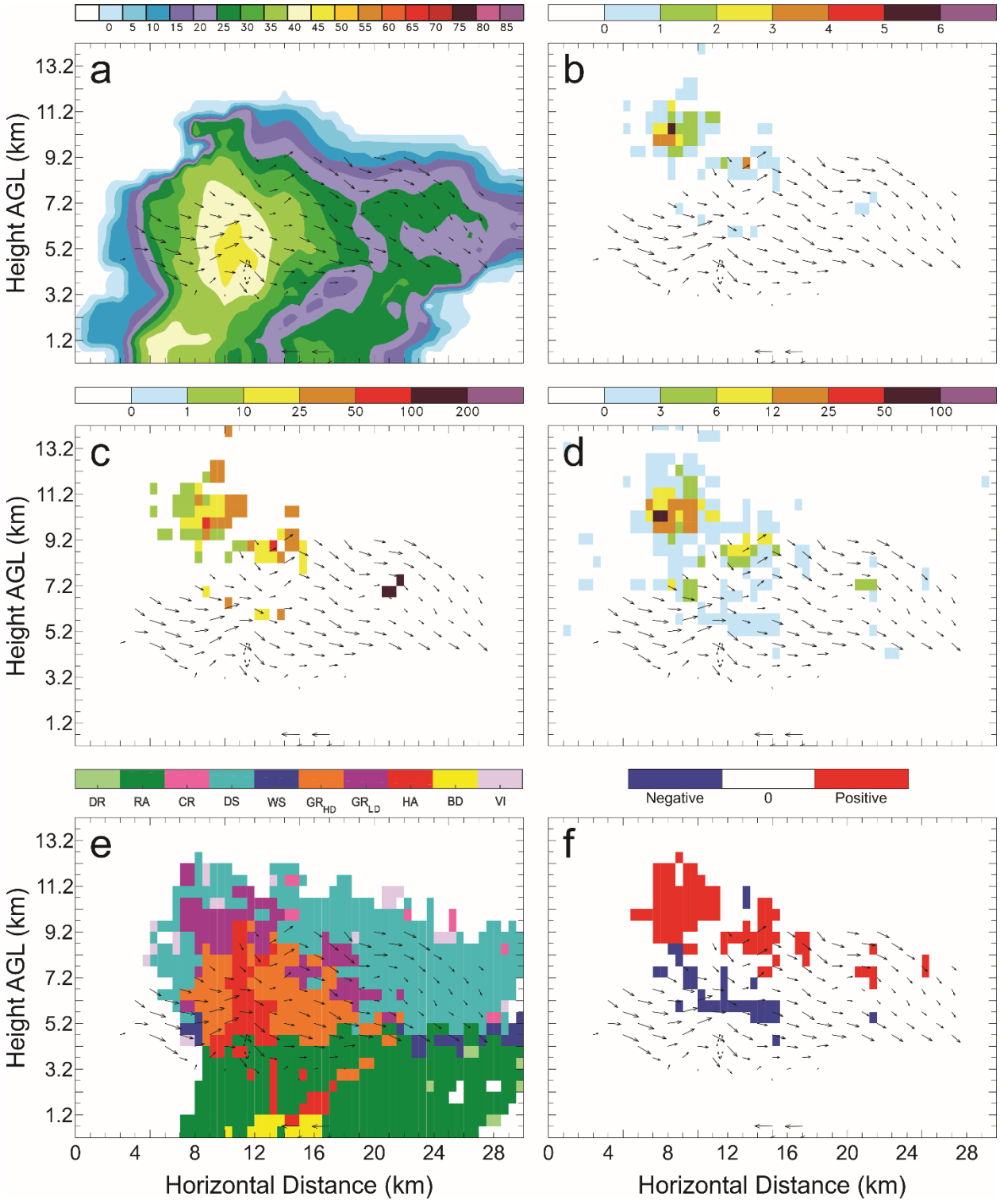

Figure 103: Vertical cross-sections for 16 June 22:48 UTC taken along the westernmost line in Figure 78(c) of: a) color-filled Z and w contours (every 10 m s^{-1} starting at 5 m s^{-1}); b) color-filled FED and w contours; c) color-filled FP and w contours; d) color-filled SD and w contours; e) color-filled HCA and w contours; and f) color-filled net inferred space charge and w contours. All figures have the same horizontal storm-relative wind vectors, and black X's denote grid cells with FID > 0.

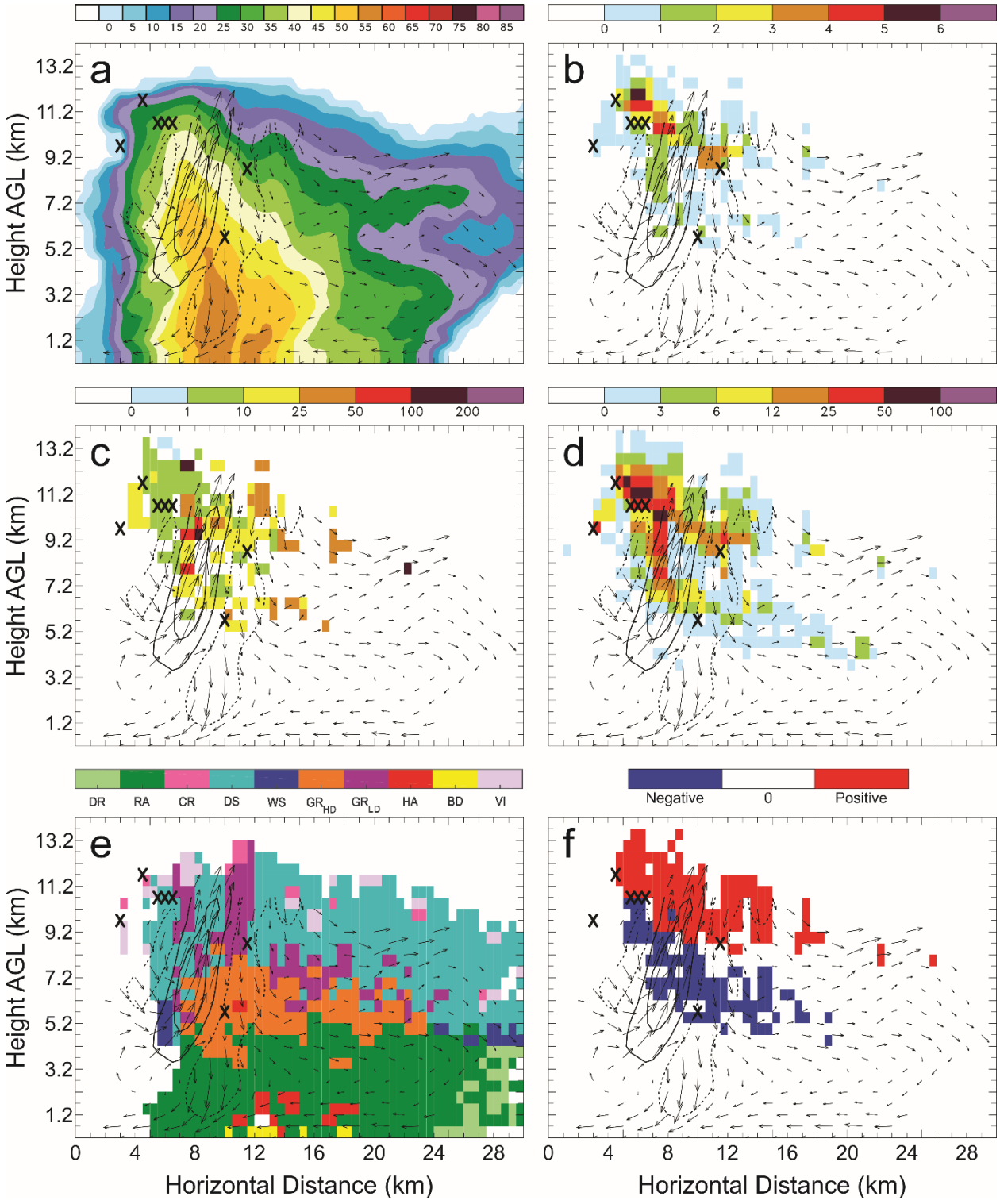

Figure 104: Vertical cross-sections for 16 June 22:48 UTC. As in Figure 103, but taken along the second line from the west in Figure 78(c).

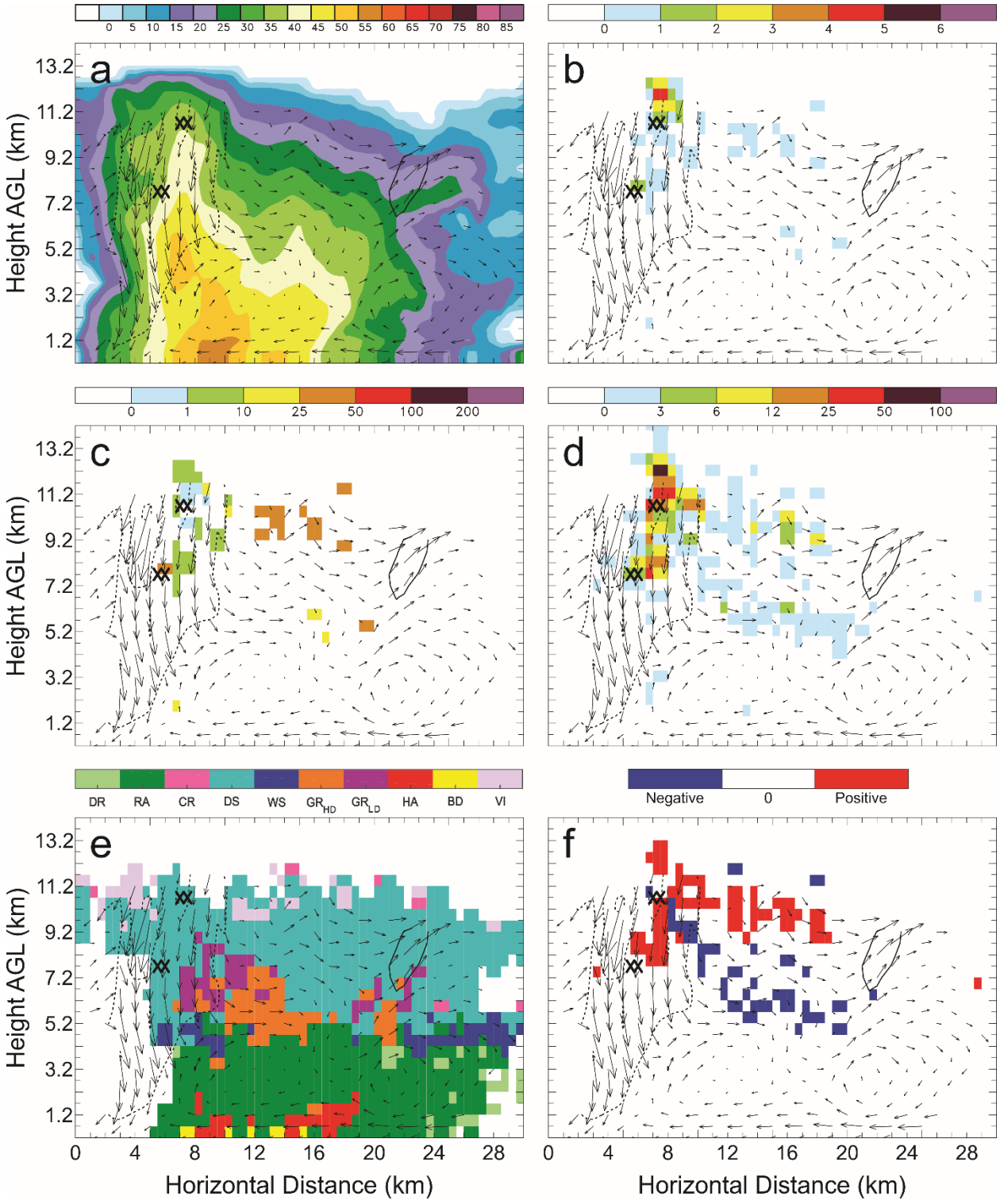

Figure 105: Vertical cross-sections for 16 June 22:48 UTC. As in Figure 103, but taken along the second line from the east in Figure 78(c).

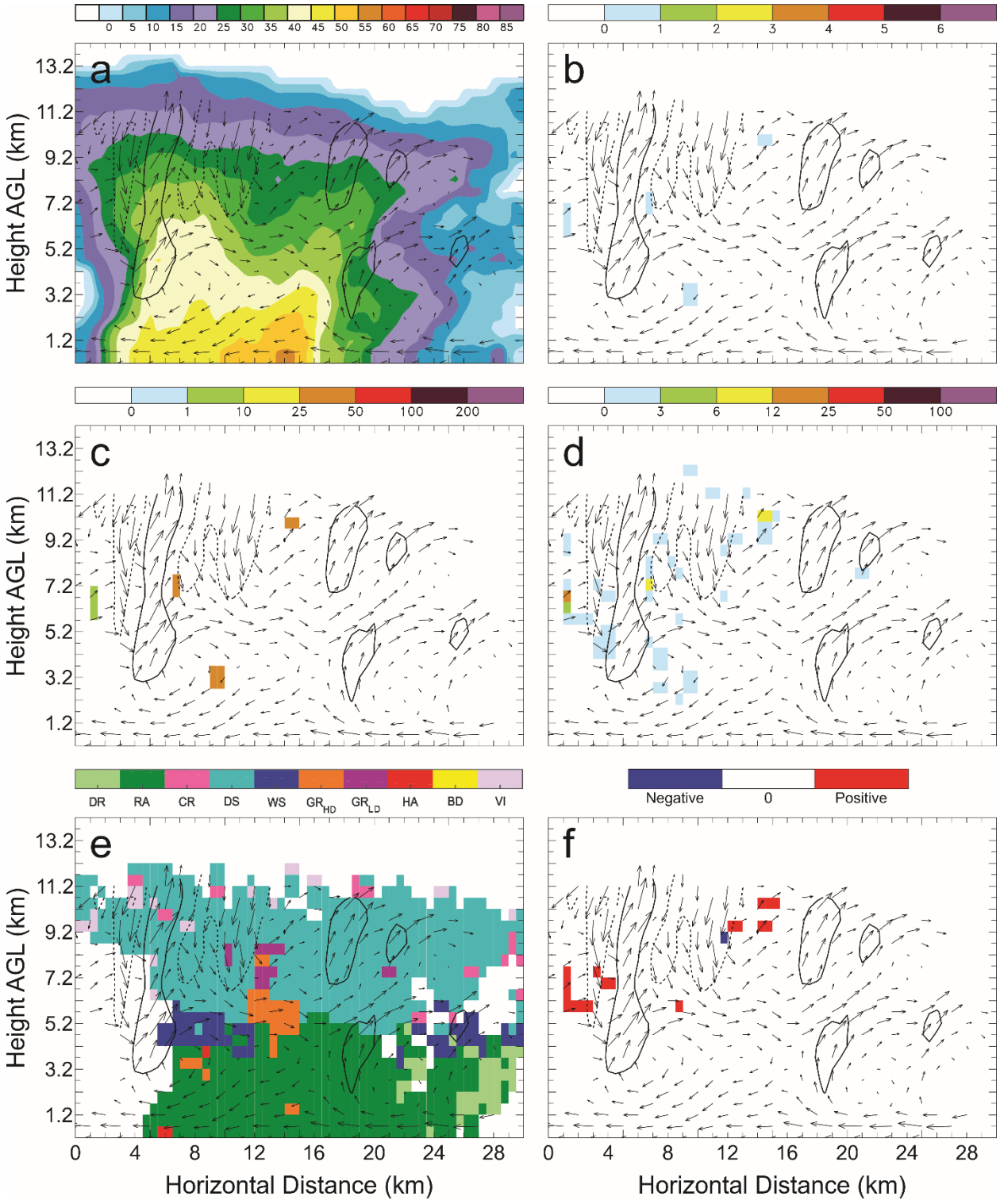

Figure 106: Vertical cross-sections for 16 June 22:48 UTC. As in Figure 103, but taken along the easternmost line in Figure 78(c).

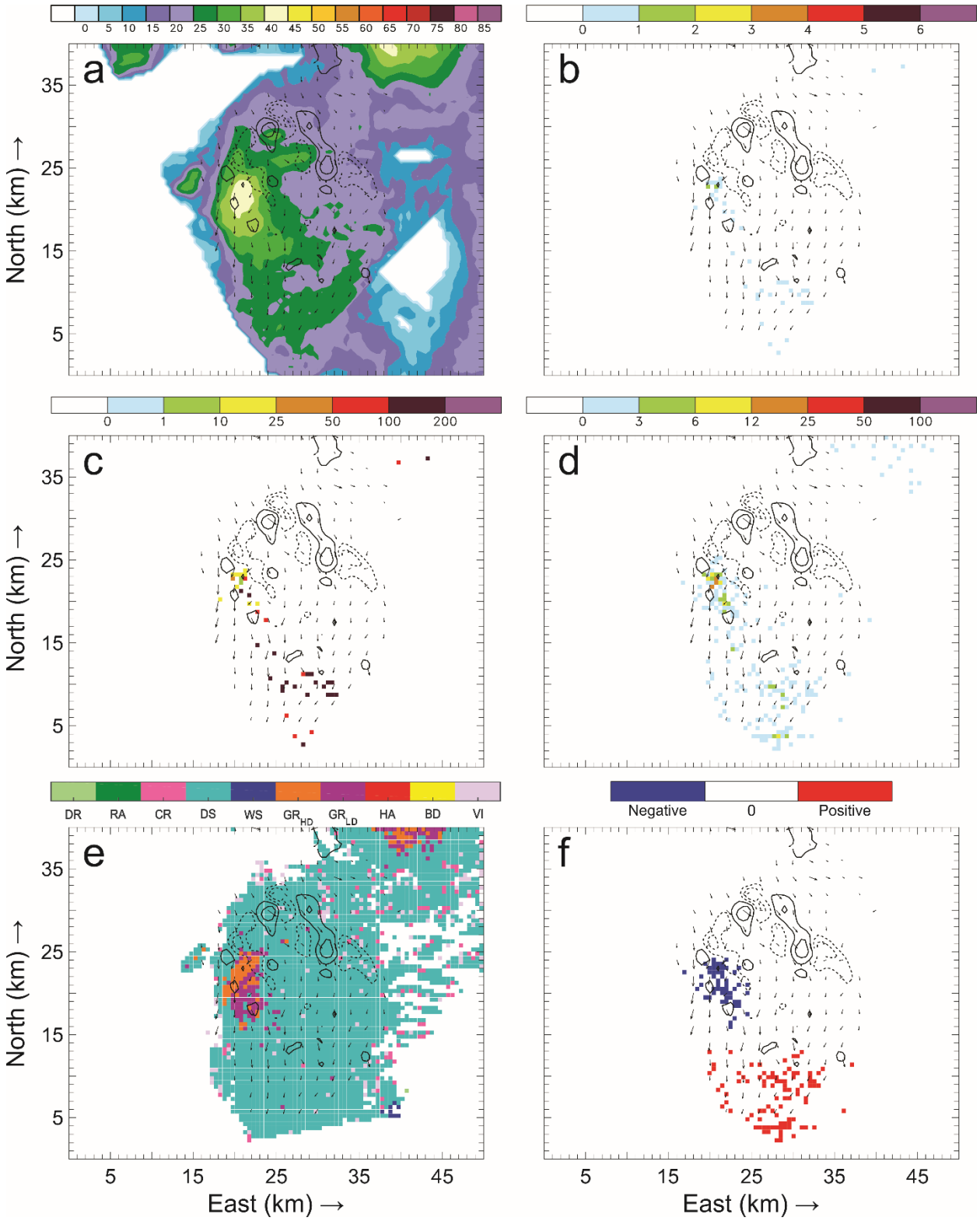

Figure 107: Horizontal cross-sections for 16 June 22:54 UTC taken at 7.2 km AGL of: a) color-filled Z and w contours (every 10 m s^{-1} starting at 5 m s^{-1}); b) color-filled FED and w contours; c) color-filled FP and w contours; d) color-filled SD and w contours; e) color-filled HCA and w contours; and f) color-filled net inferred space charge and w contours. All figures have the same horizontal storm-relative wind vectors, and black X's denote grid cells with FID > 0.

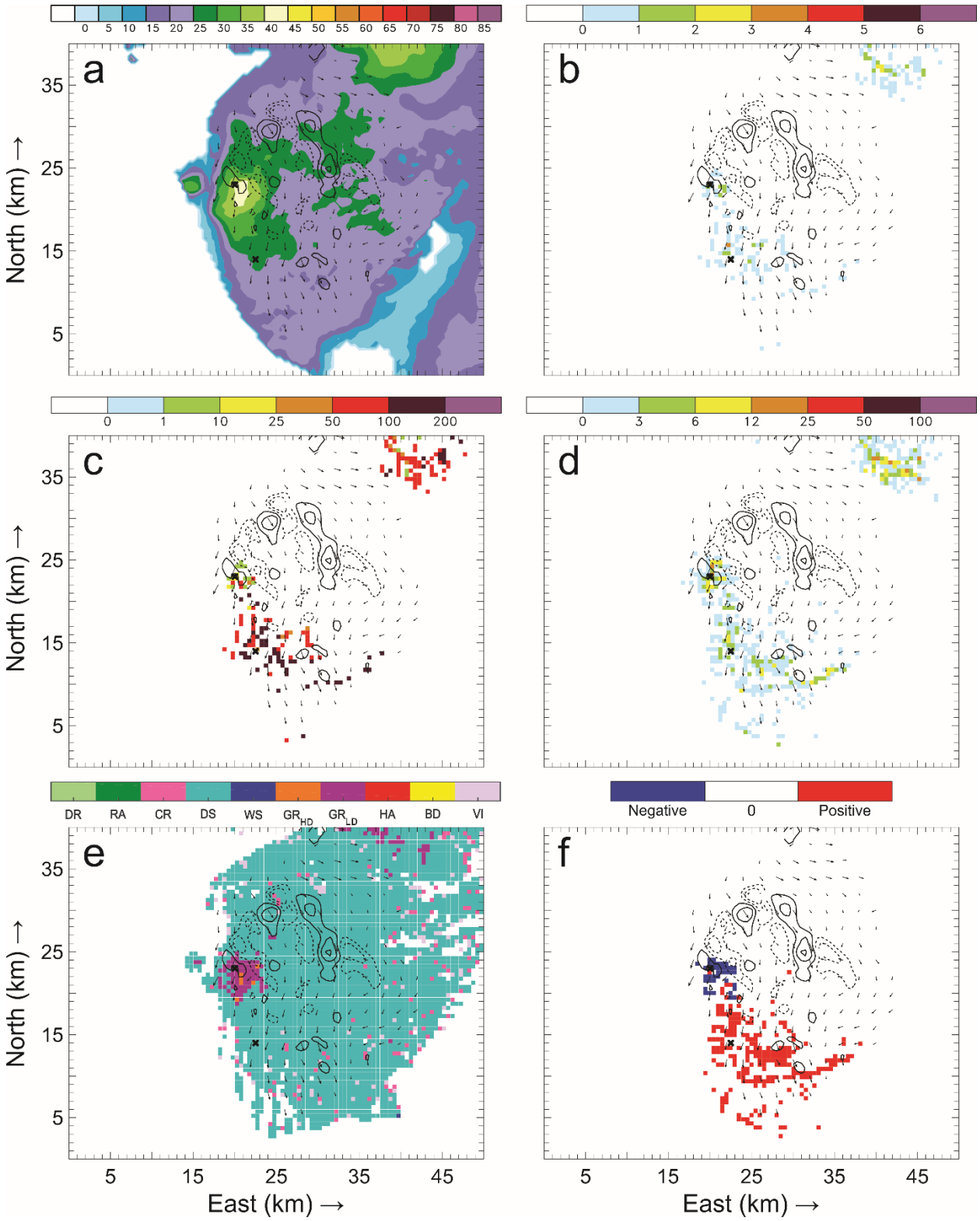

Figure 108: Horizontal cross-sections for 16 June 22:54 UTC. As in Figure 107, but taken at 8.2 km AGL.

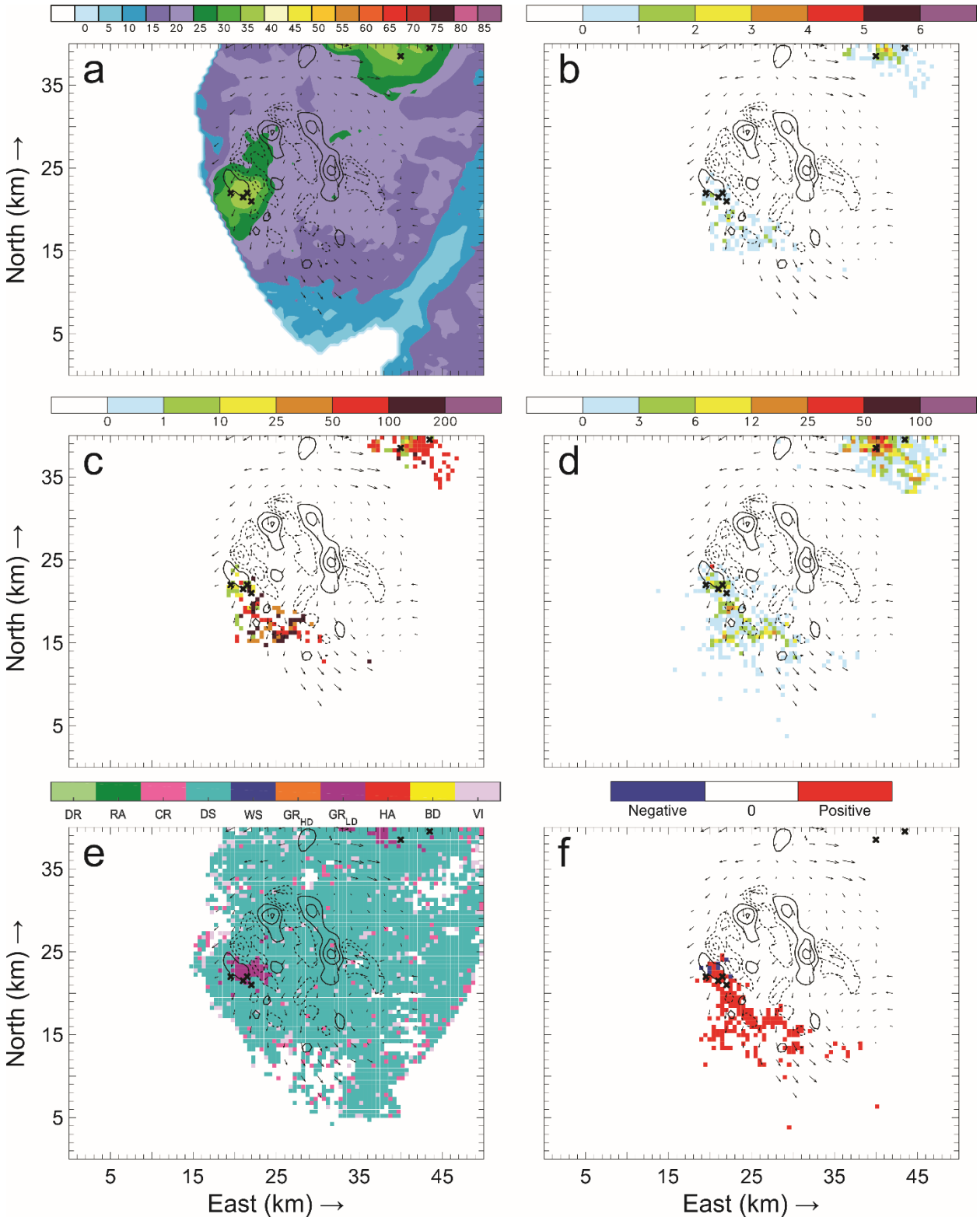

Figure 109: Horizontal cross-sections for 16 June 22:54 UTC. As in Figure 107, but taken at 9.2 km AGL.

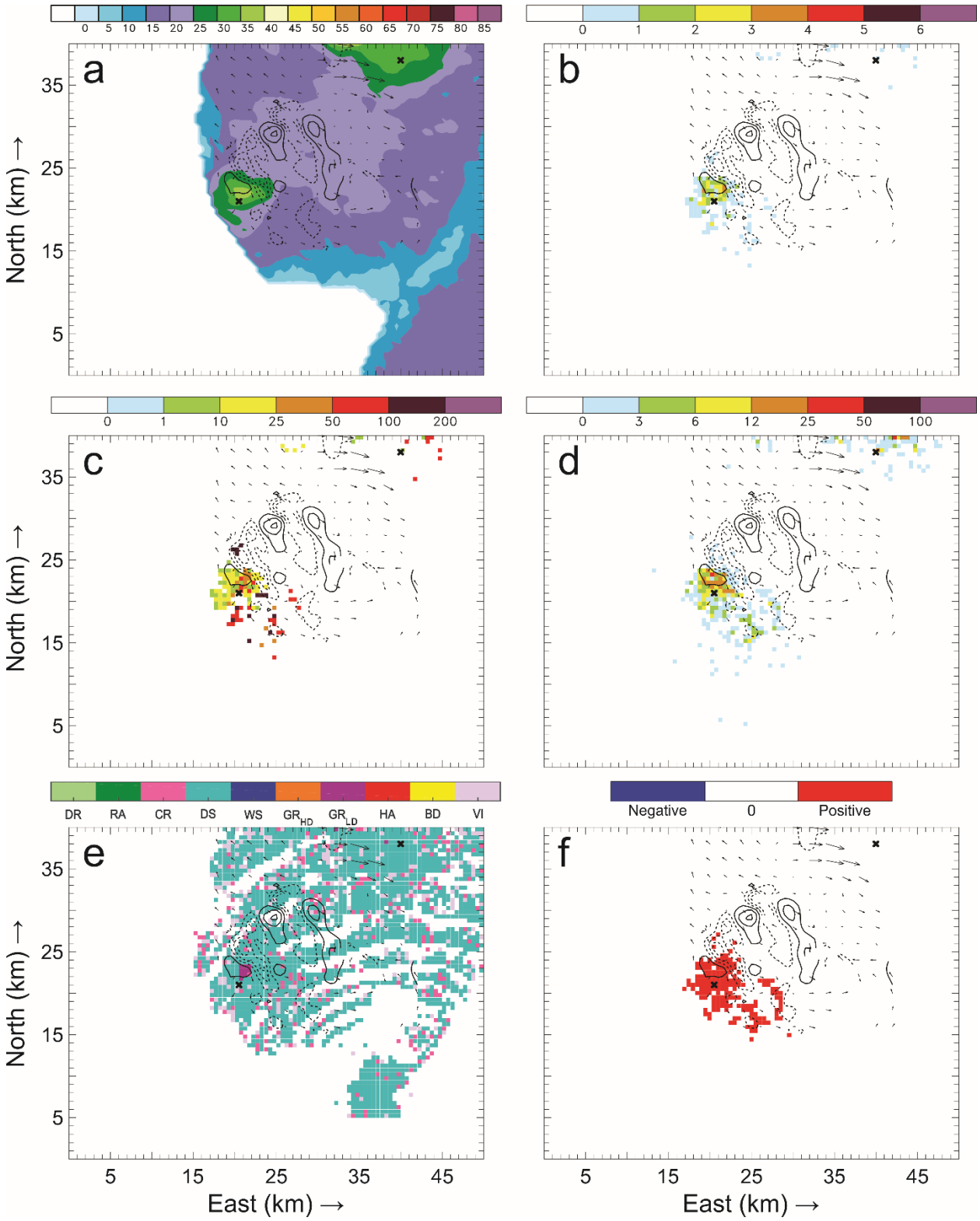

Figure 110: Horizontal cross-sections for 16 June 22:54 UTC. As in Figure 107, but taken at 10.2 km AGL.

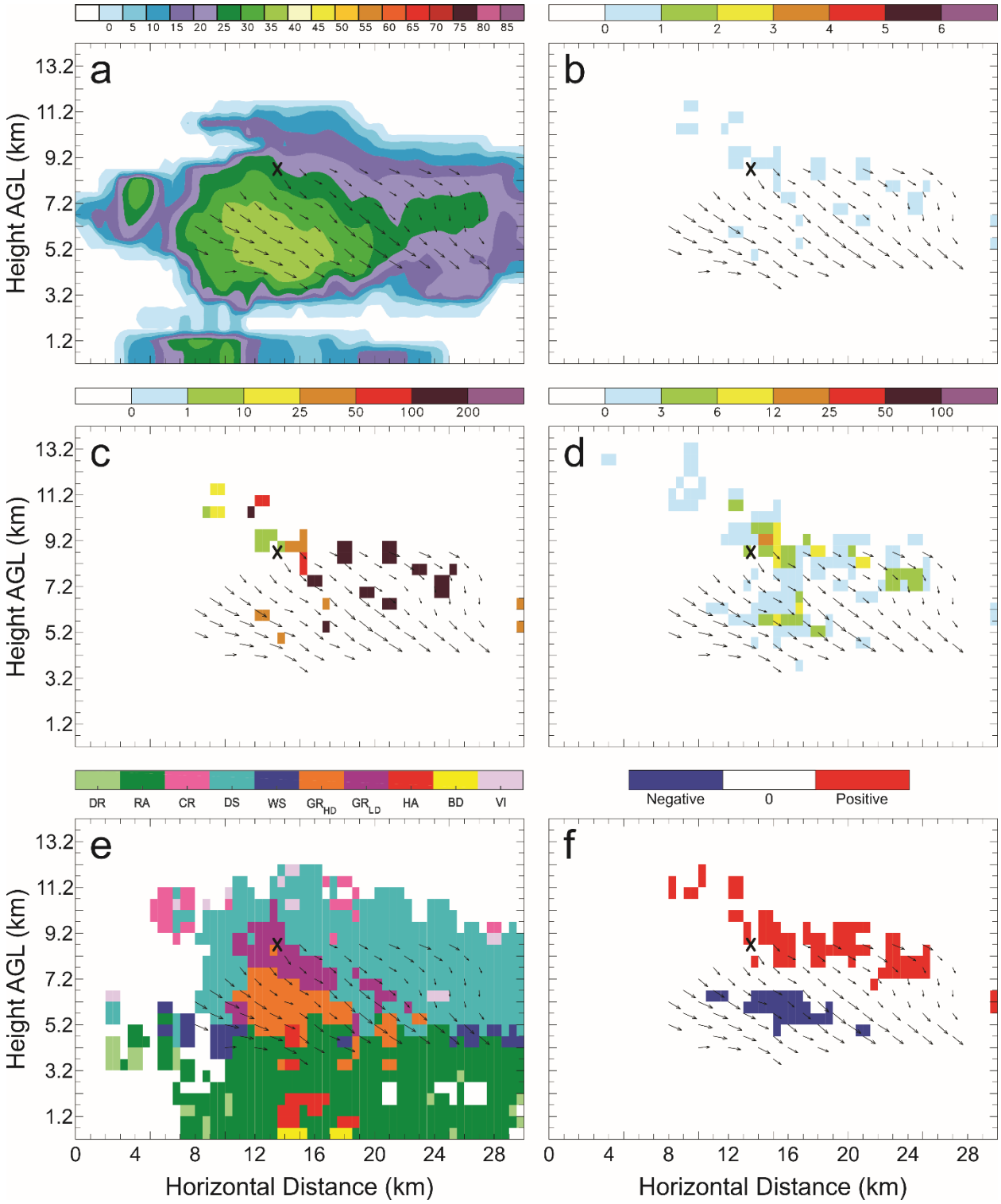

Figure 111: Vertical cross-sections for 16 June 22:54 UTC taken along the westernmost line in Figure 78(d) of: a) color-filled Z and w contours (every 10 m s^{-1} starting at 5 m s^{-1}); b) color-filled FED and w contours; c) color-filled FP and w contours; d) color-filled SD and w contours; e) color-filled HCA and w contours; and f) color-filled net inferred space charge and w contours. All figures have the same horizontal storm-relative wind vectors, and black X's denote grid cells with FID > 0.

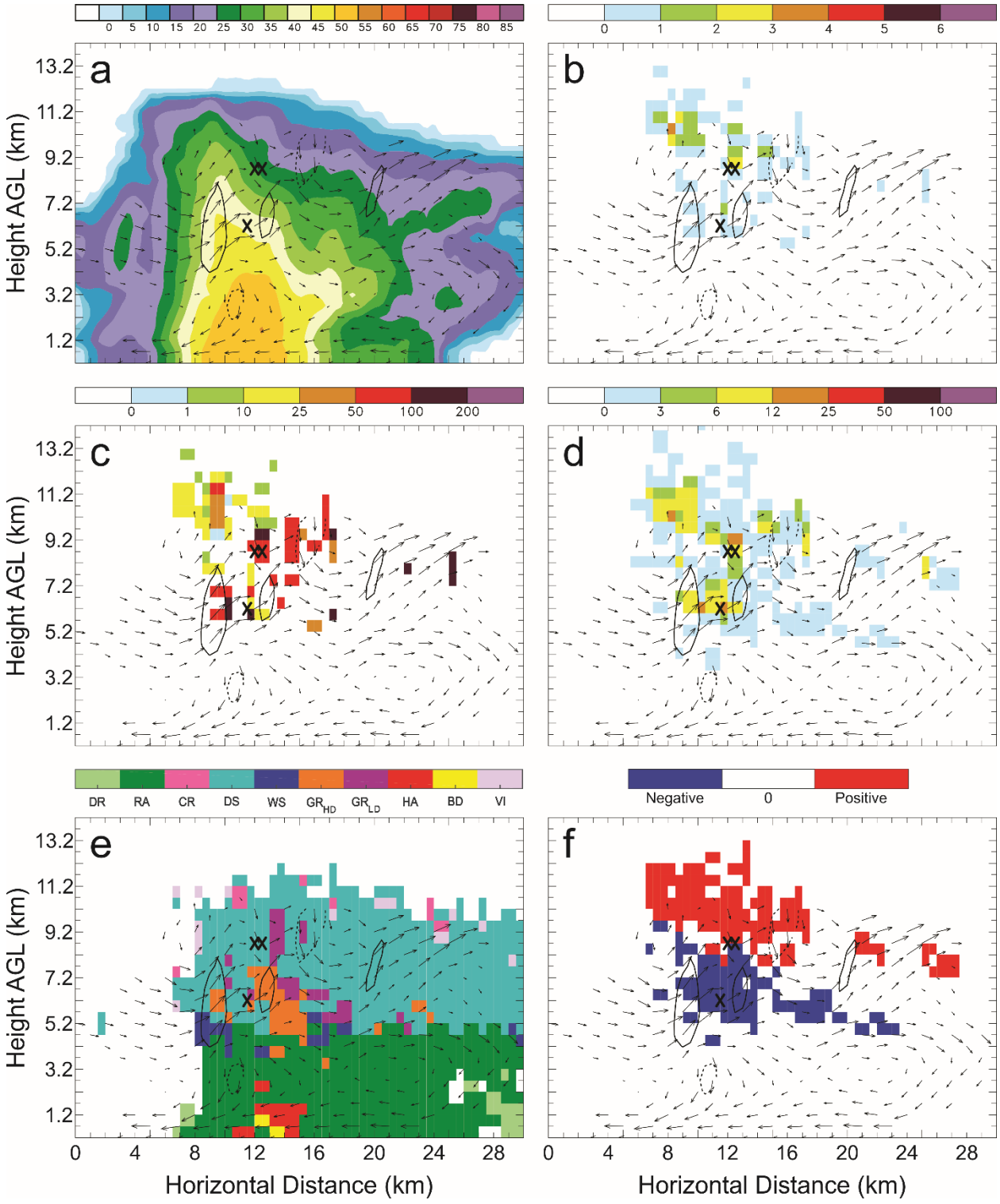

Figure 112: Vertical cross-sections for 16 June 22:54 UTC. As in Figure 111, but taken along the second line from the west in Figure 78(d).

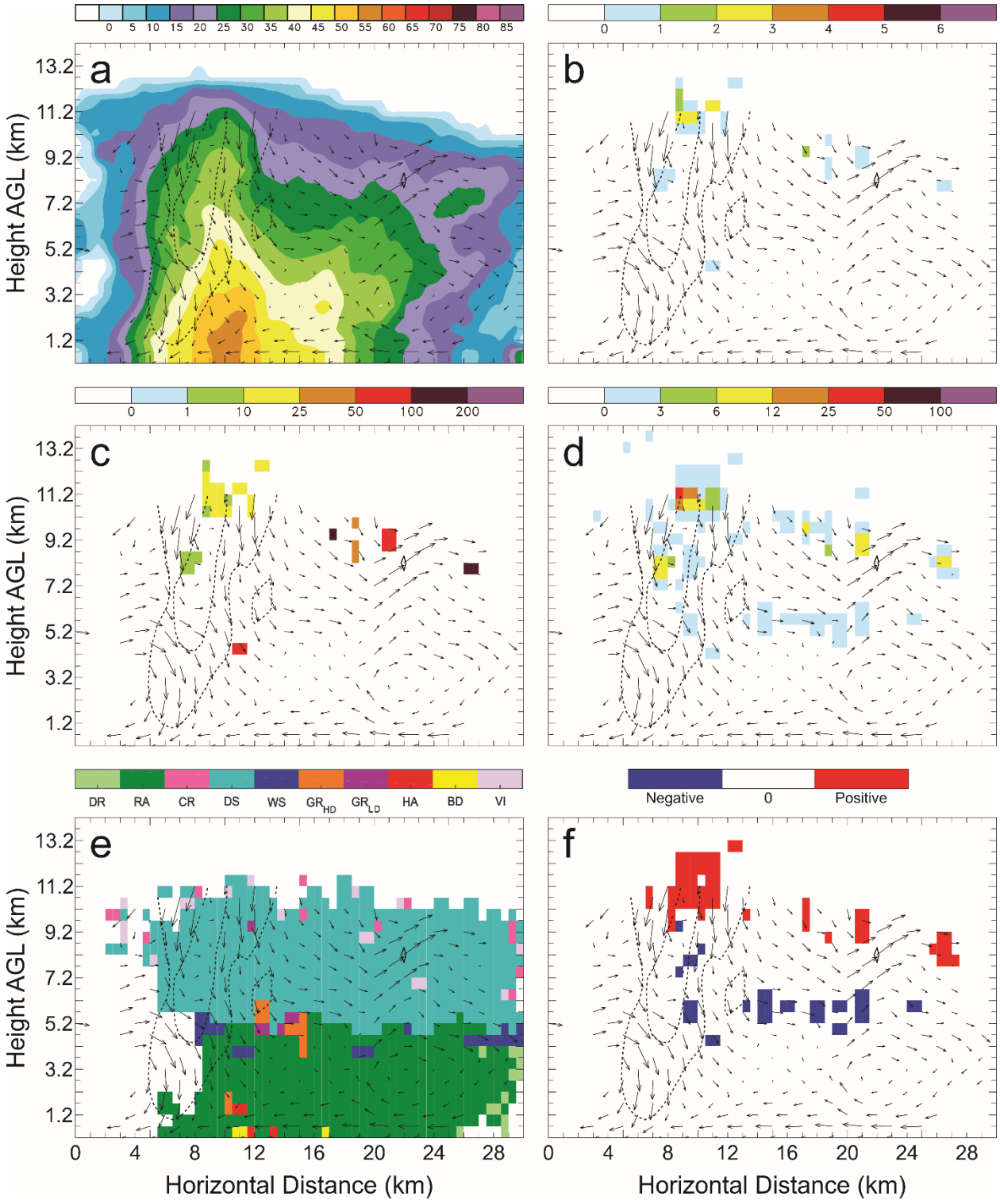

Figure 113: Vertical cross-sections for 16 June 22:54 UTC. As in Figure 111, but taken along the second line from the east in Figure 78(d).

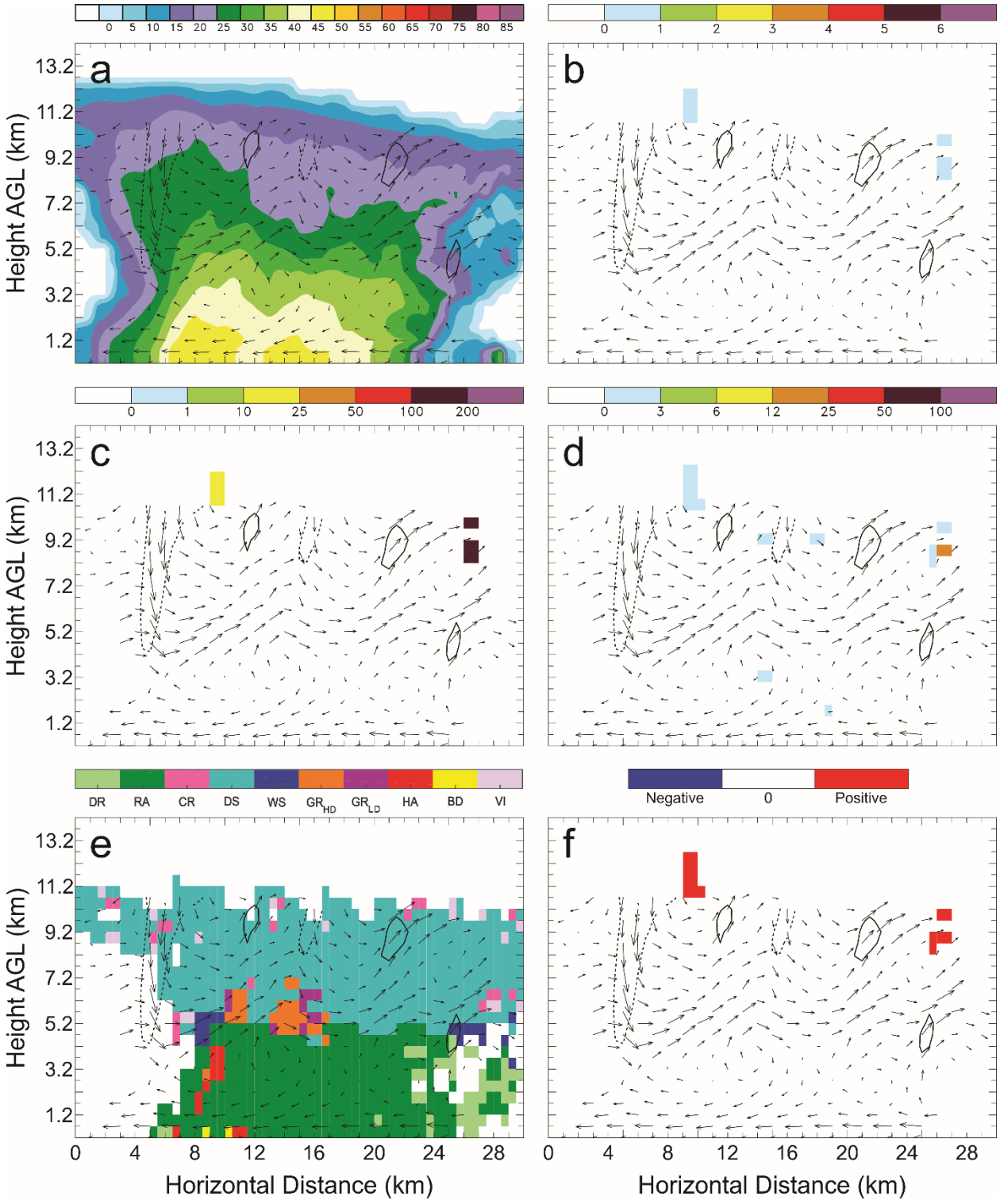

Figure 114: Vertical cross-sections for 16 June 22:54 UTC. As in Figure 111, but taken along the easternmost line in Figure 78(d).

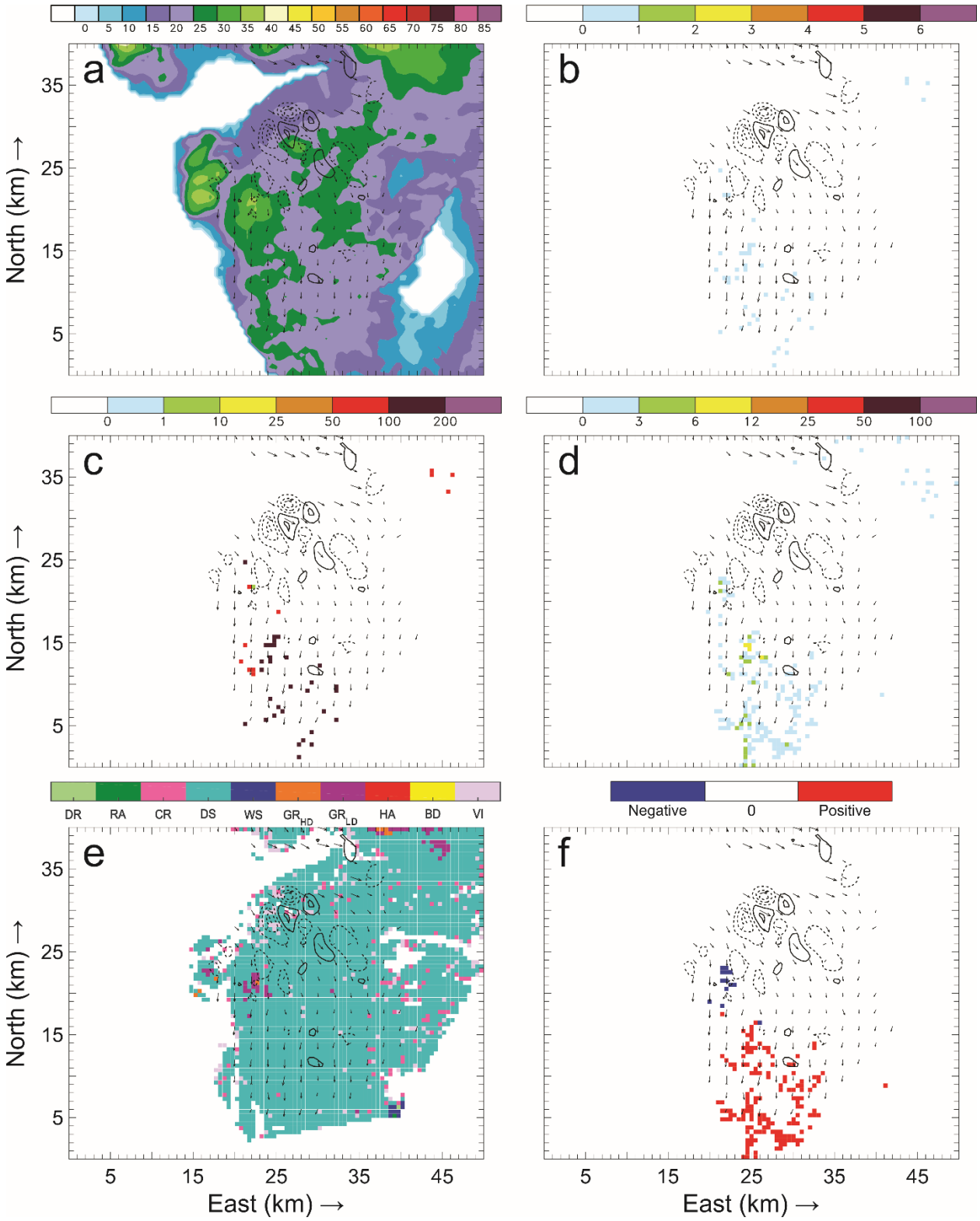

Figure 115: Horizontal cross-sections for 16 June 23:00 UTC taken at 7.2 km AGL of: a) color-filled Z and w contours (every 10 m s^{-1} starting at 5 m s^{-1}); b) color-filled FED and w contours; c) color-filled FP and w contours; d) color-filled SD and w contours; e) color-filled HCA and w contours; and f) color-filled net inferred space charge and w contours. All figures have the same horizontal storm-relative wind vectors, and black X's denote grid cells with FID > 0.

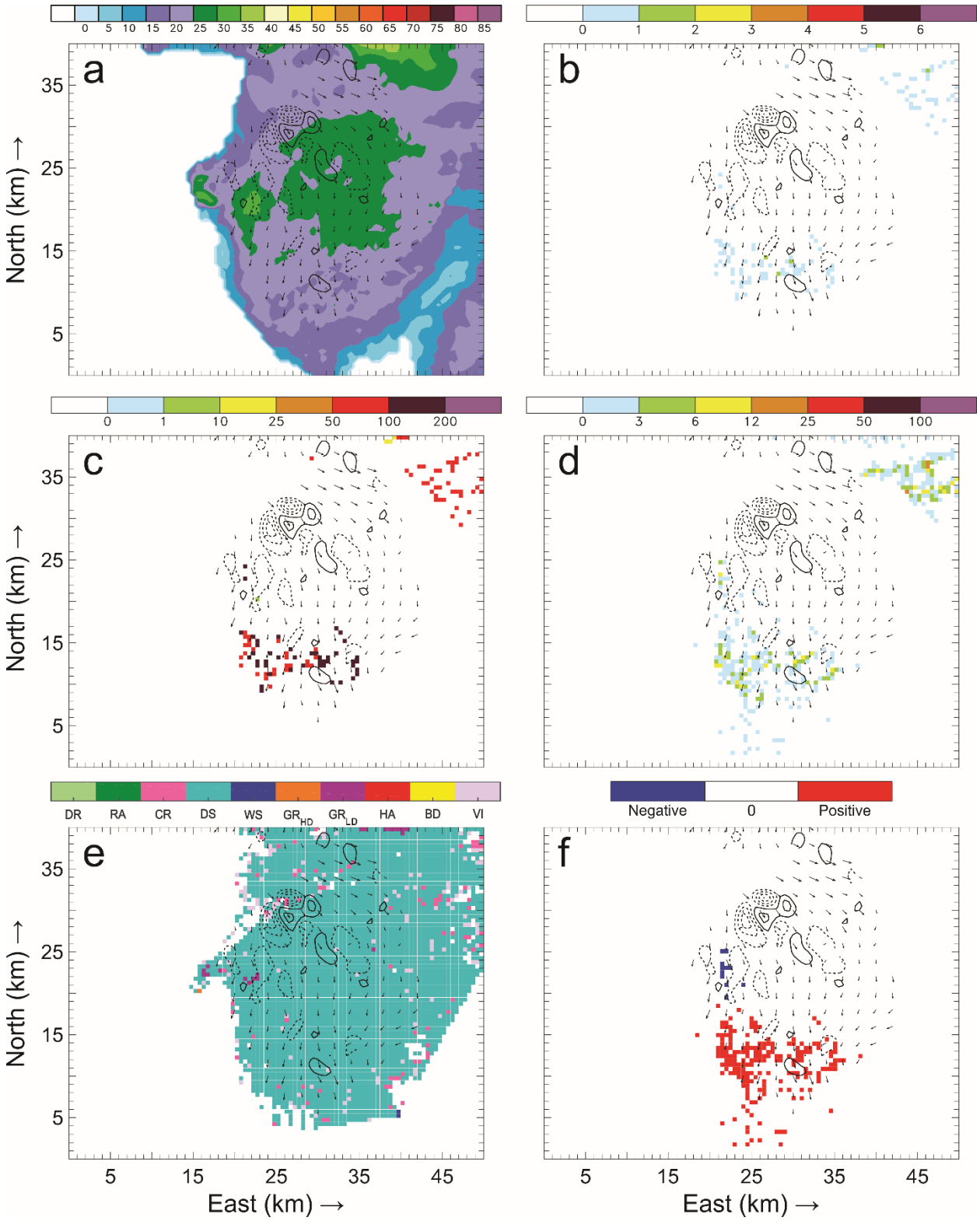

Figure 116: Horizontal cross-sections for 16 June 23:00 UTC. As in Figure 115, but taken at 8.2 km AGL.

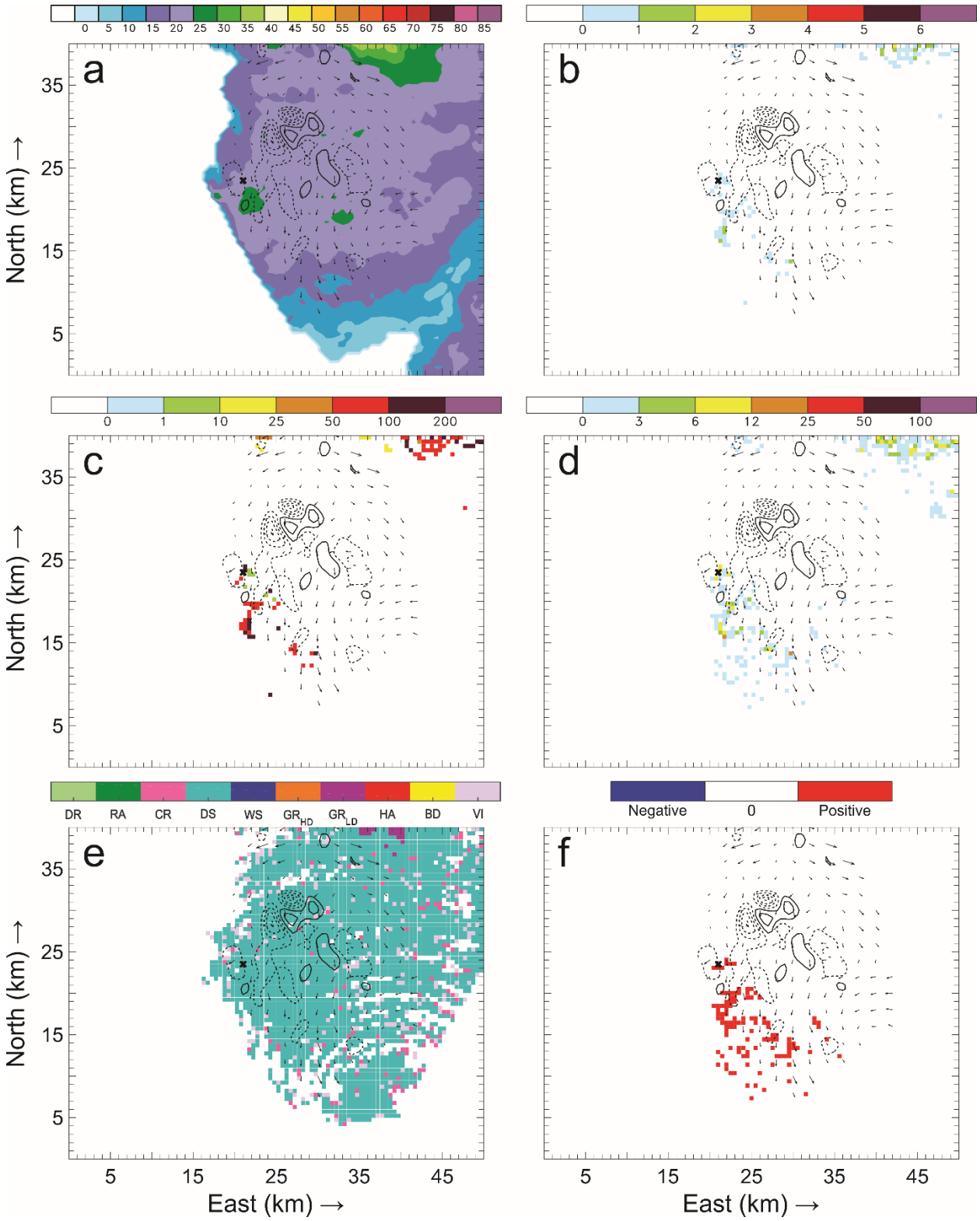

Figure 117: Horizontal cross-sections for 16 June 23:00 UTC. As in Figure 115, but taken at 9.2 km AGL.

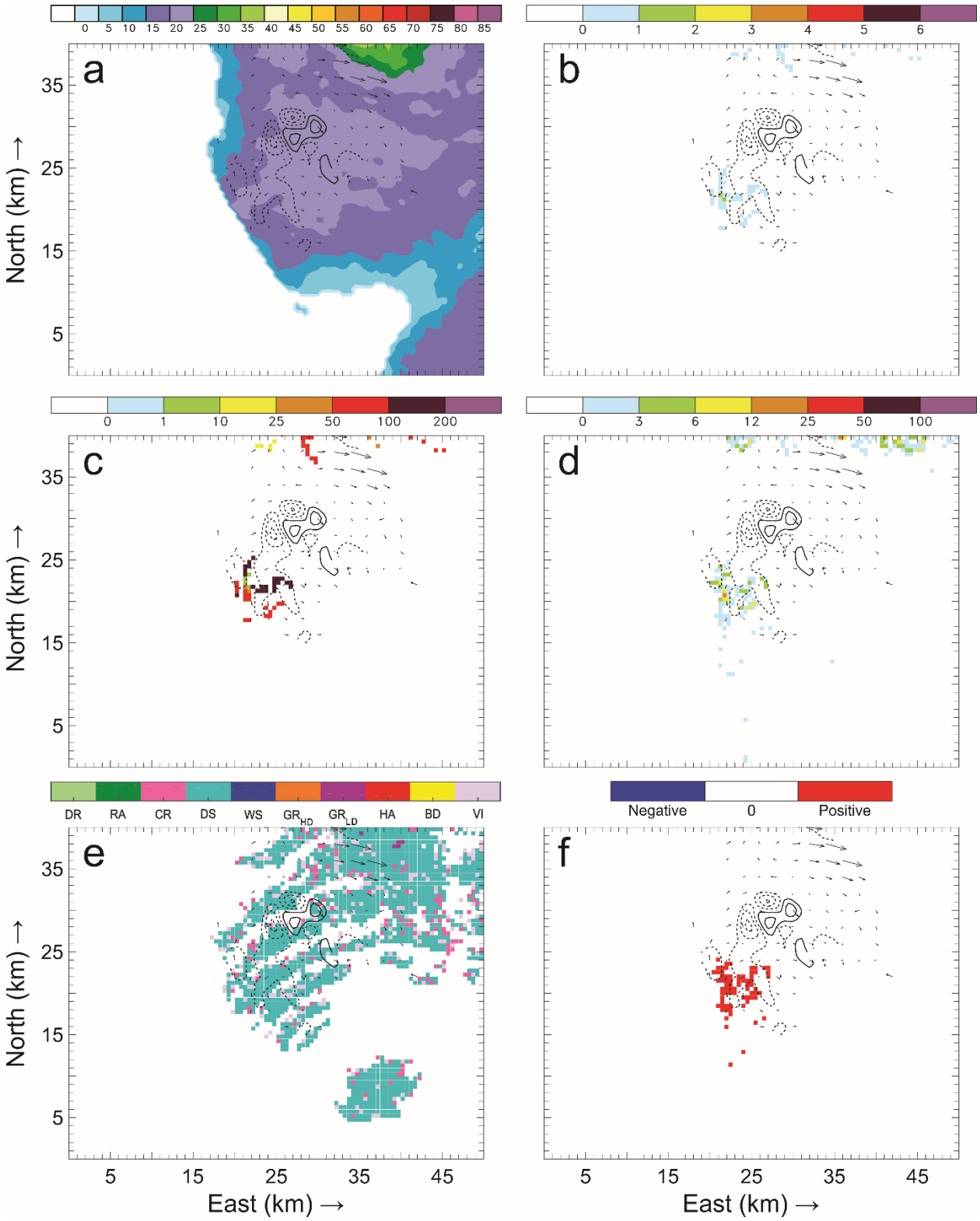

Figure 118: Horizontal cross-sections for 16 June 23:00 UTC. As in Figure 115, but taken at 10.2 km AGL.

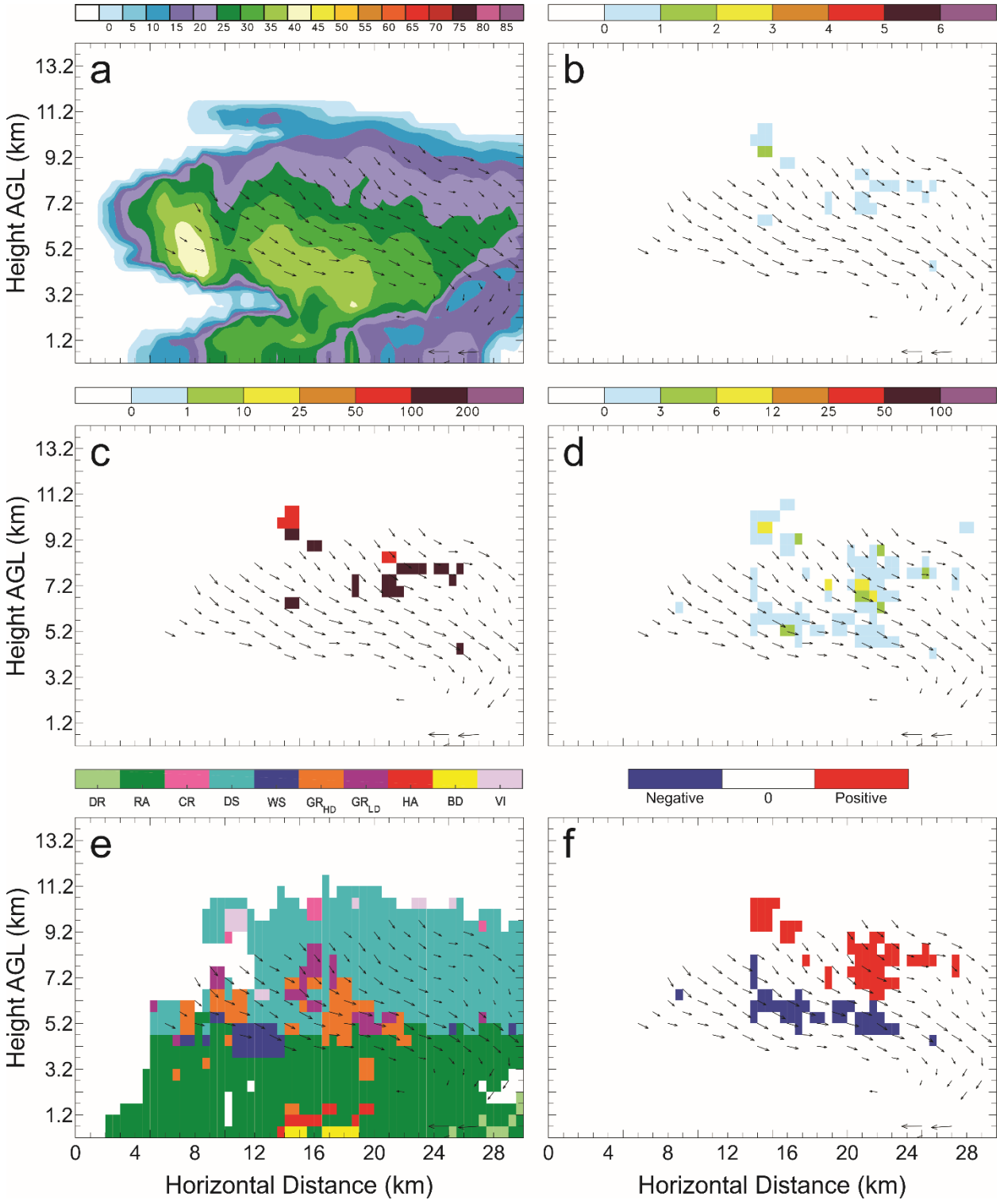

Figure 119: Vertical cross-sections or 16 June 23:00 UTC taken along the westernmost line in Figure 78(e) of: a) color-filled Z and w contours (every 10 m s^{-1} starting at 5 m s^{-1}); b) color-filled FED and w contours; c) color-filled FP and w contours; d) color-filled SD and w contours; e) color-filled HCA and w contours; and f) color-filled net inferred space charge and w contours. All figures have the same horizontal storm-relative wind vectors, and black X's denote grid cells with FID > 0.

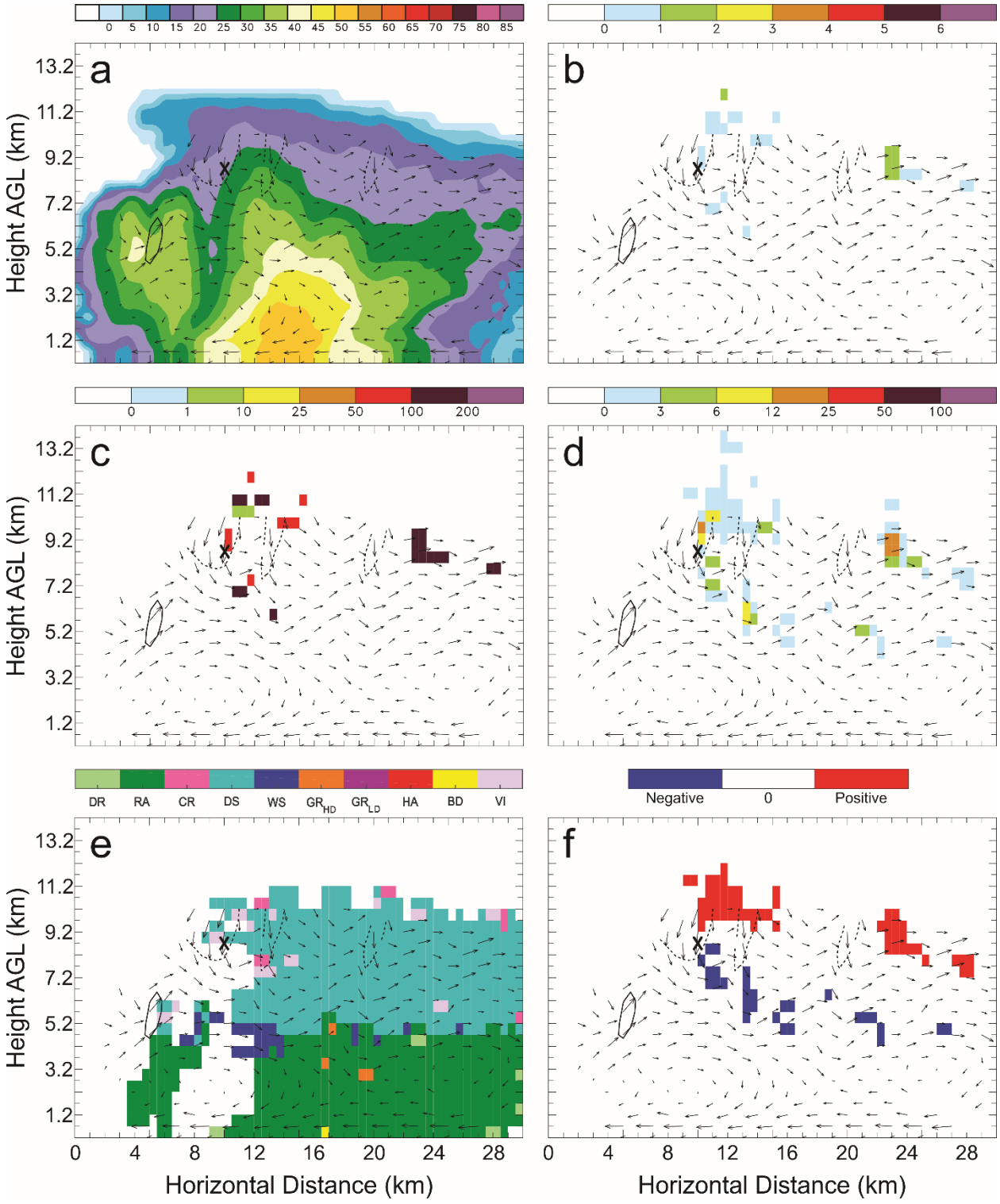

Figure 120: Vertical cross-sections or 16 June 23:00 UTC. As in Figure 119, but taken along the central line in Figure 78(e).

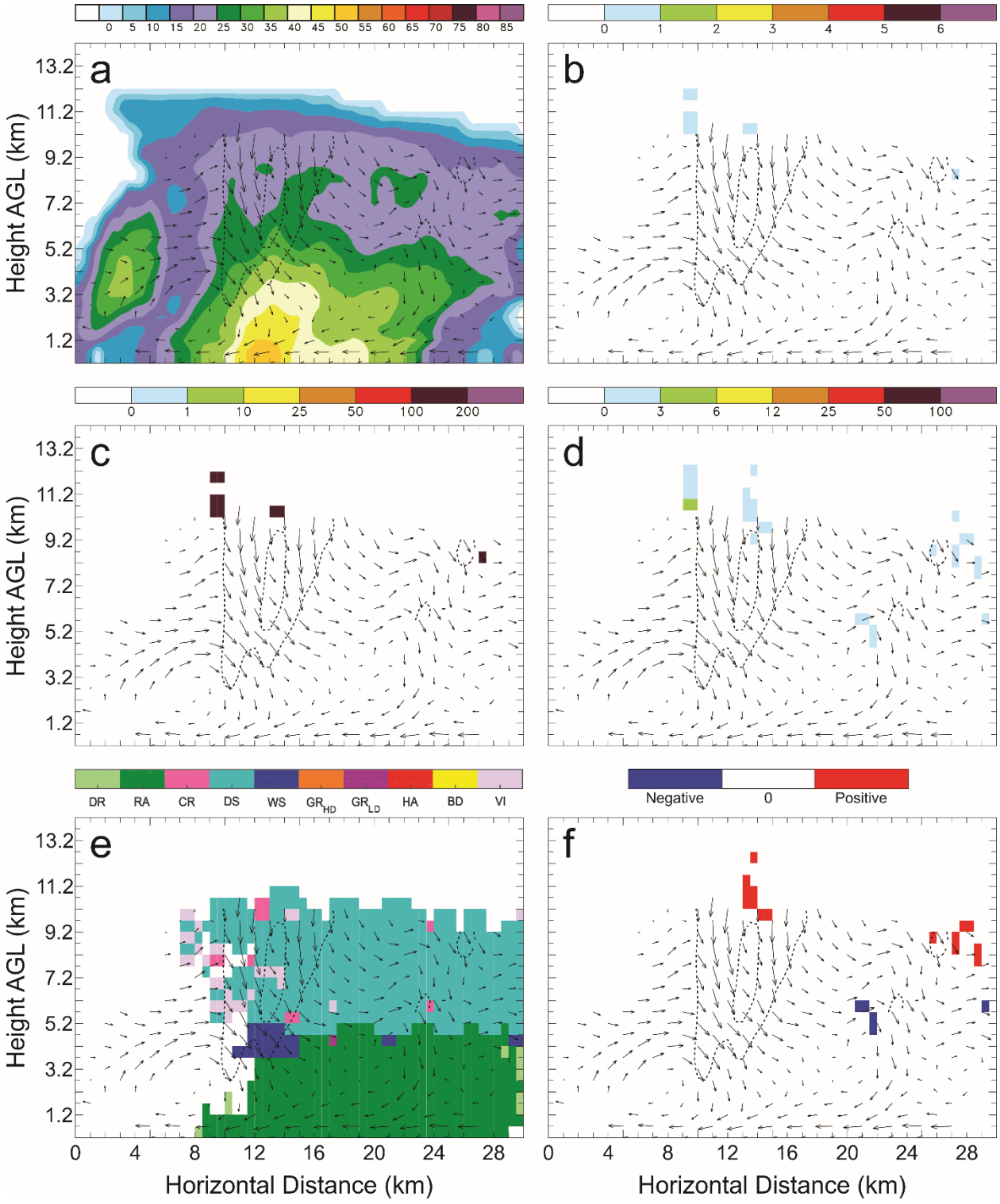

Figure 121: Vertical cross-sections or 16 June 23:00 UTC. As in Figure 119, but taken along the easternmost line in Figure 78(e).

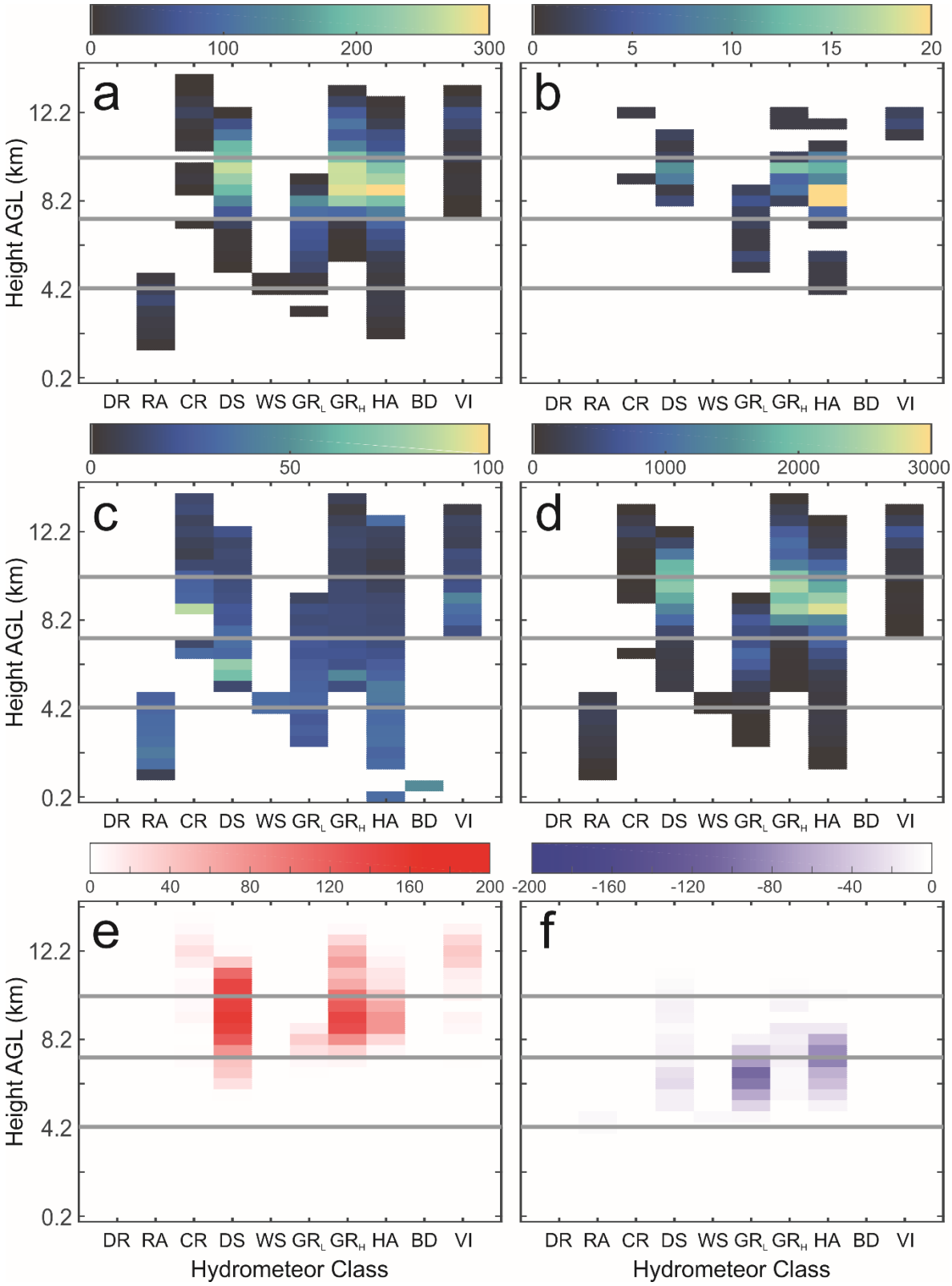

Figure 122: Lightning parameters that correspond with HCA classes in all grid cells at each horizontal level at 22:36 UTC: a) Total FED, b) total FID, c) mean FP, d) total SD, e) total points assigned positive charge, and f) total points assigned negative charge. The horizontal grey lines represent the 0ºC, -20ºC, and -40ºC levels.

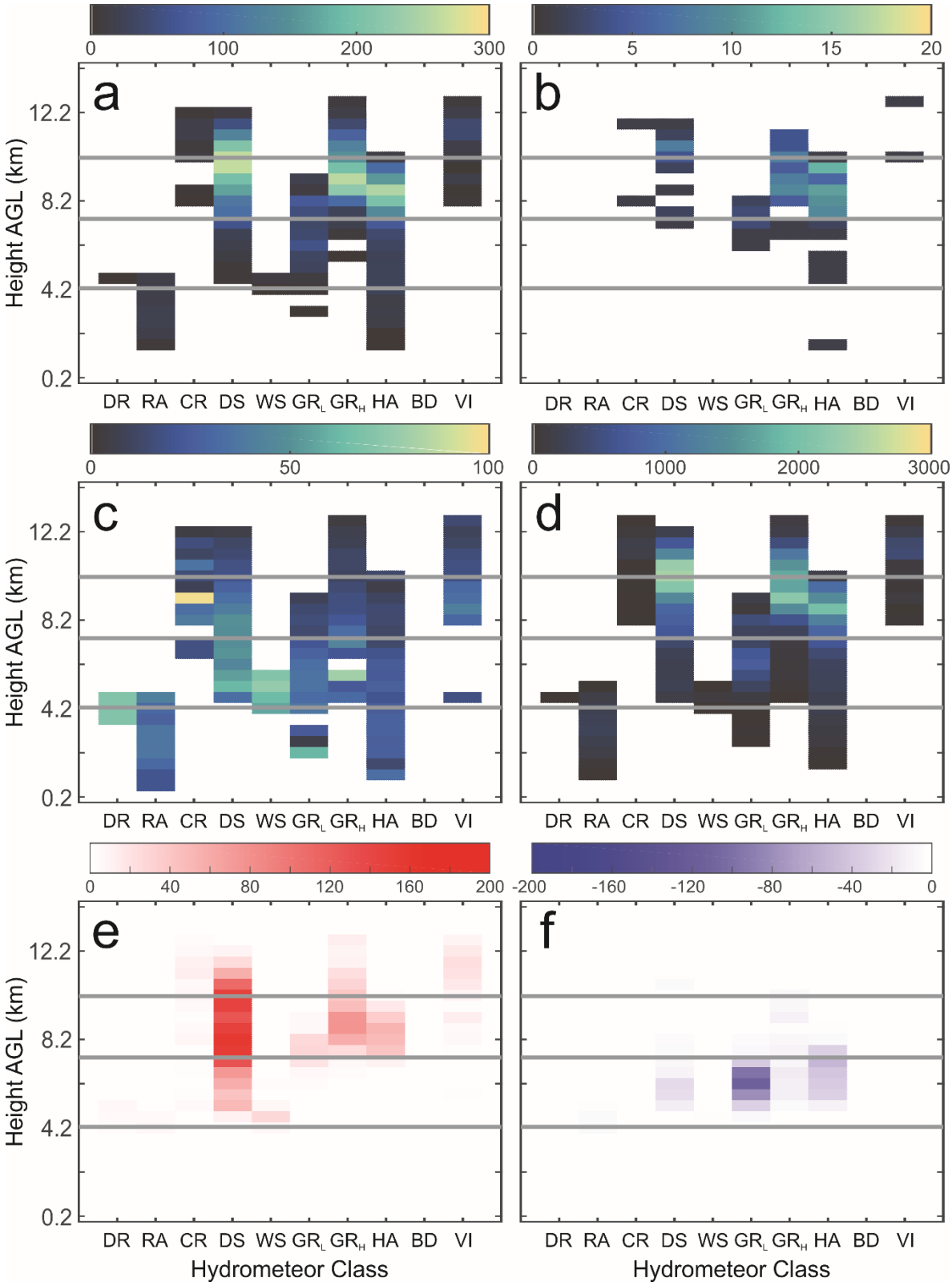

Figure 123: As in Figure 122, but for 22:42 UTC.

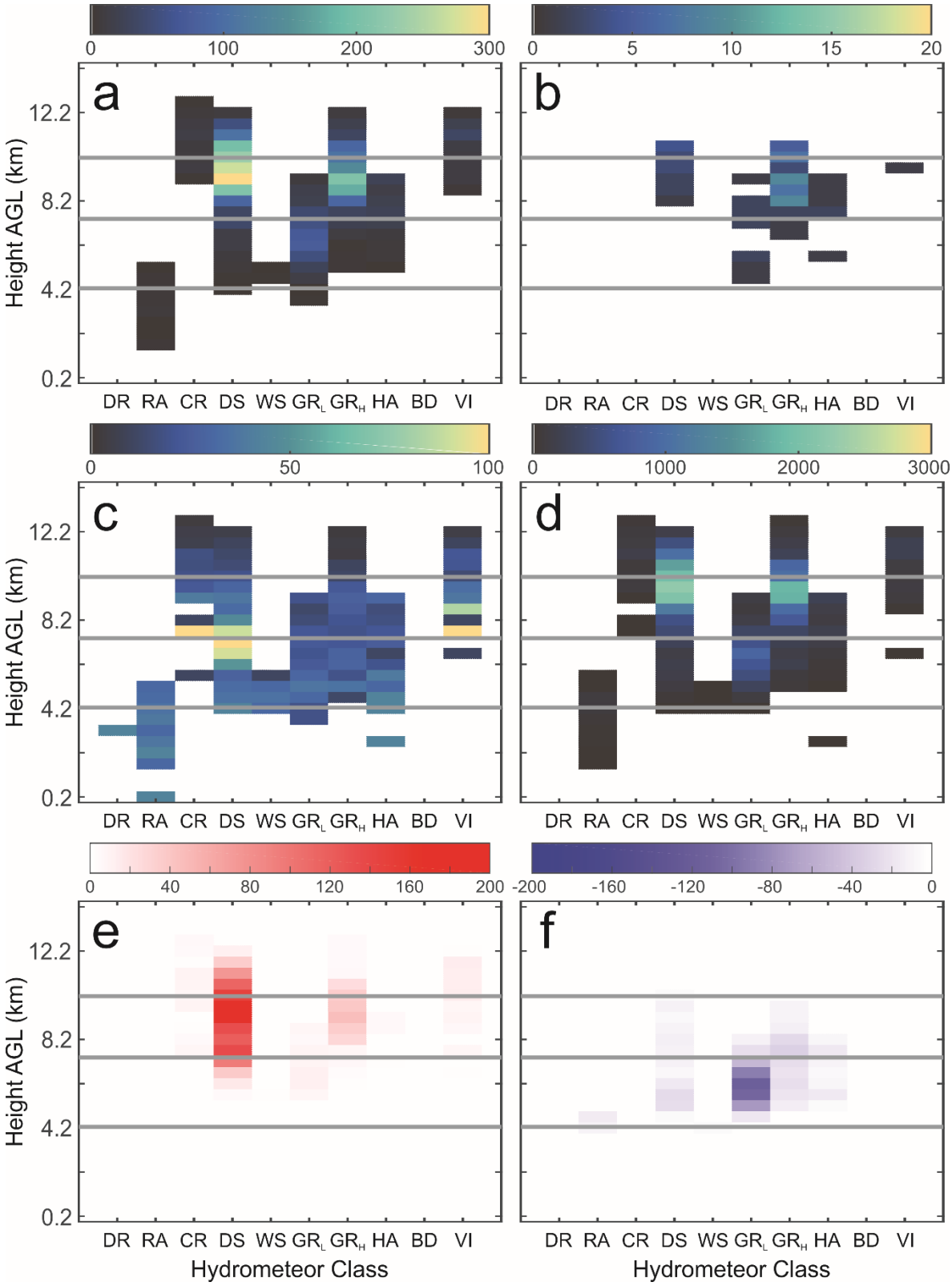

Figure 124: As in Figure 122, but for 22:48 UTC.

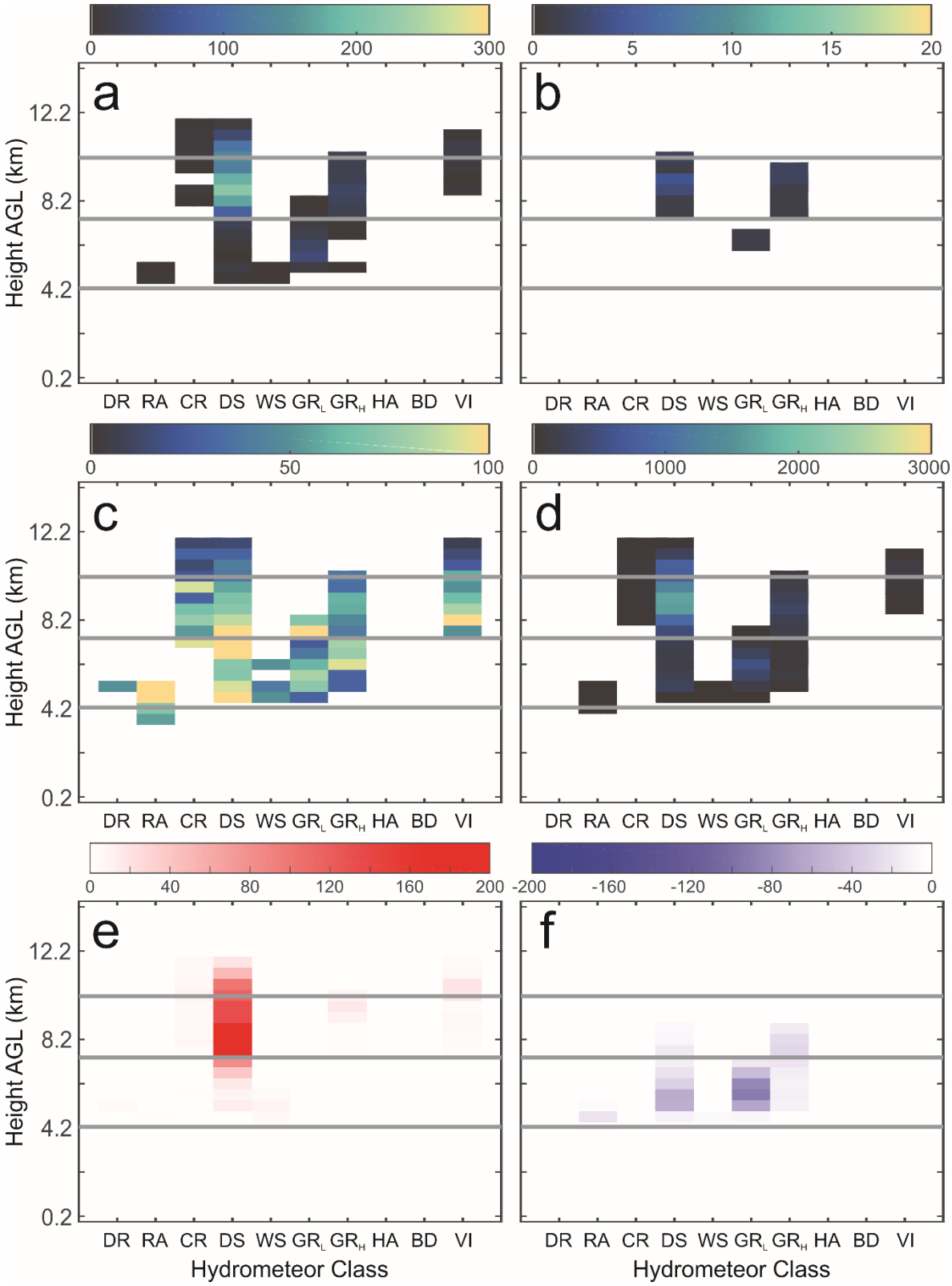

Figure 125: As in Figure 122, but for 22:54 UTC.

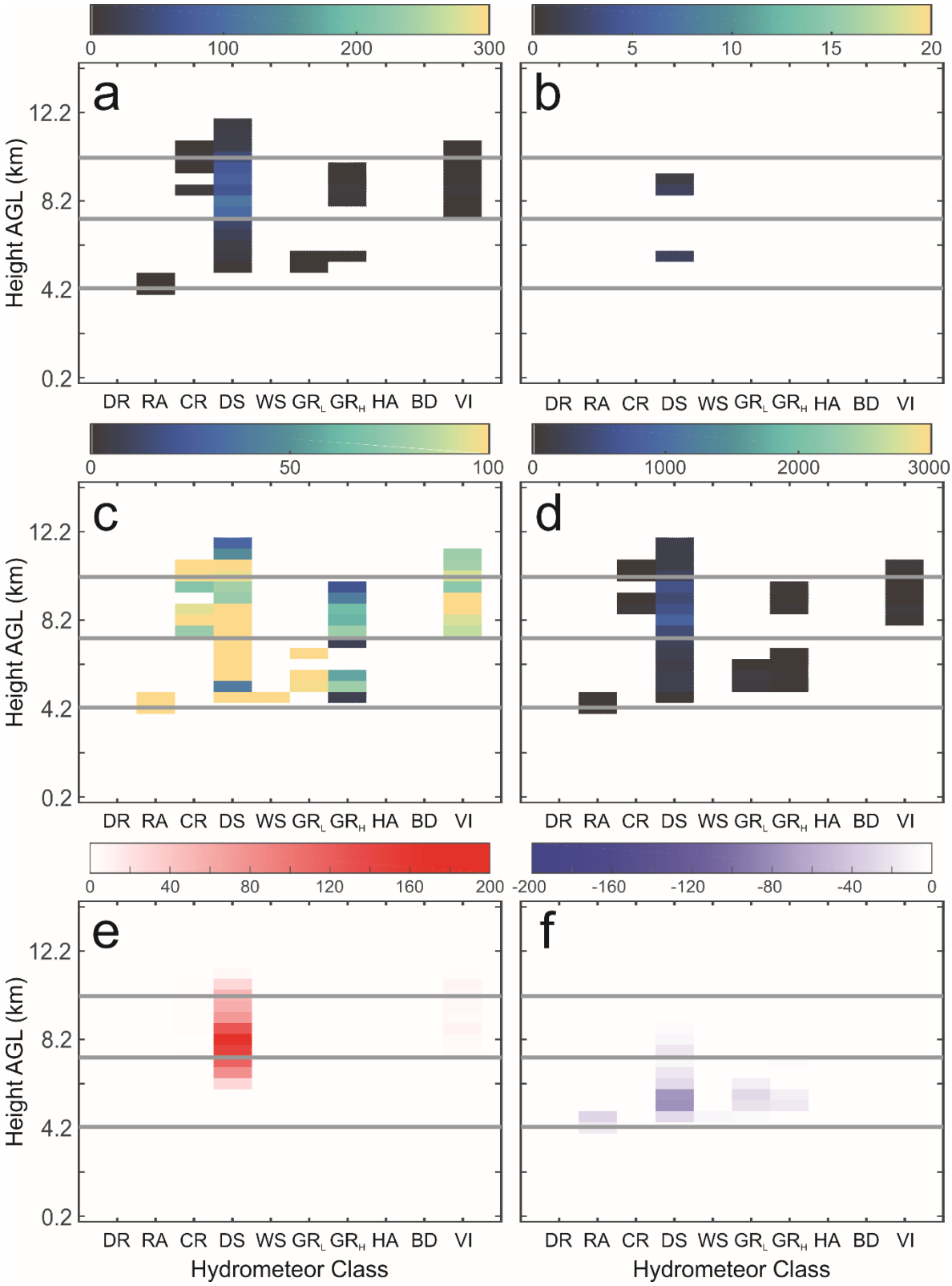

Figure 126: As in Figure 122, but for 23:00 UTC.

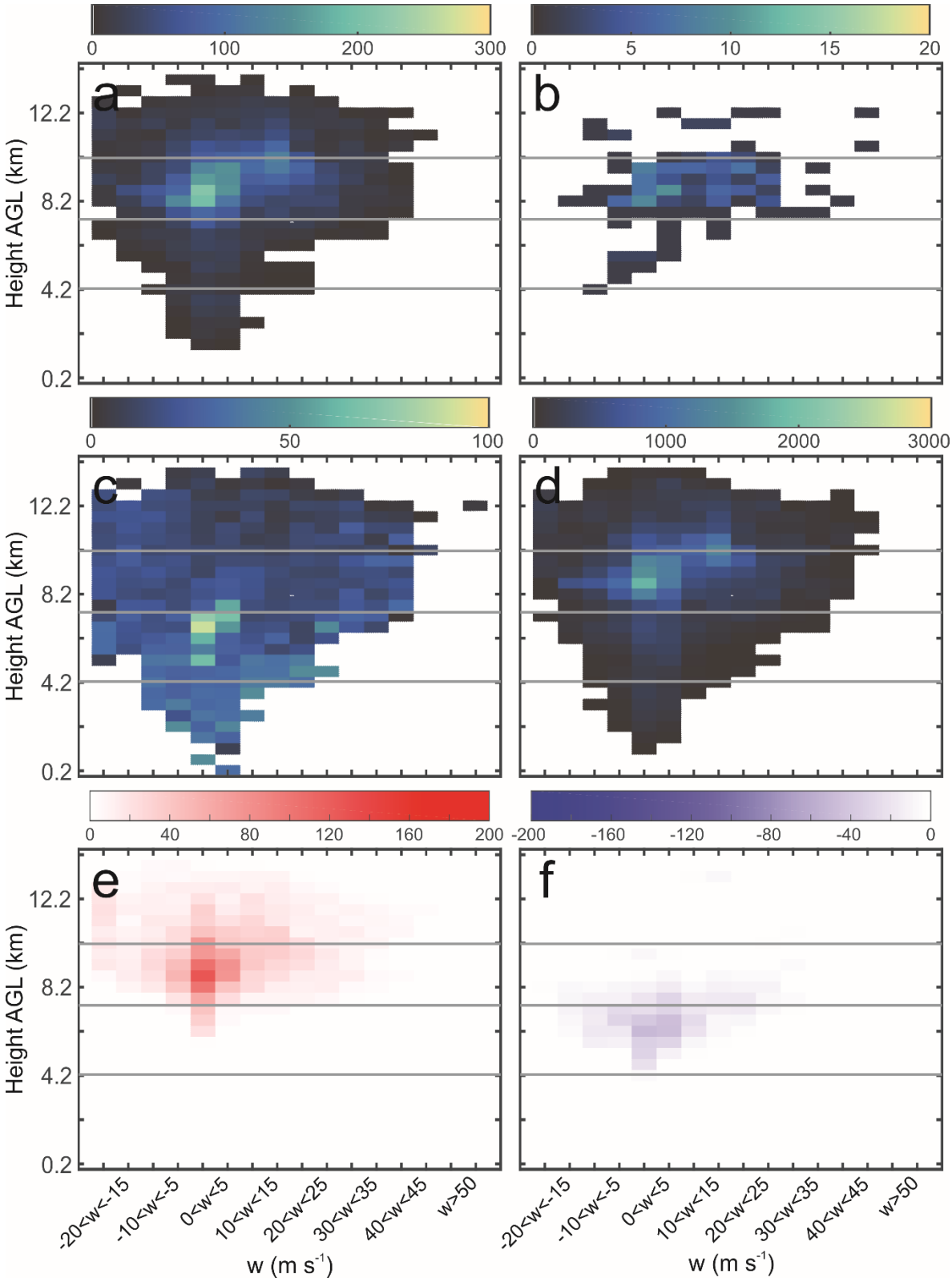

Figure 127: Lightning parameters that correspond with 5 m s^{-1} bins of w in all grid cells at each horizontal level at 22:36 UTC: a) Total FED, b) total FID, c) mean FP, d) total SD, e) total points assigned positive charge, and f) total points assigned negative charge. The horizontal grey lines represent the 0ºC, -20ºC, and -40ºC levels.

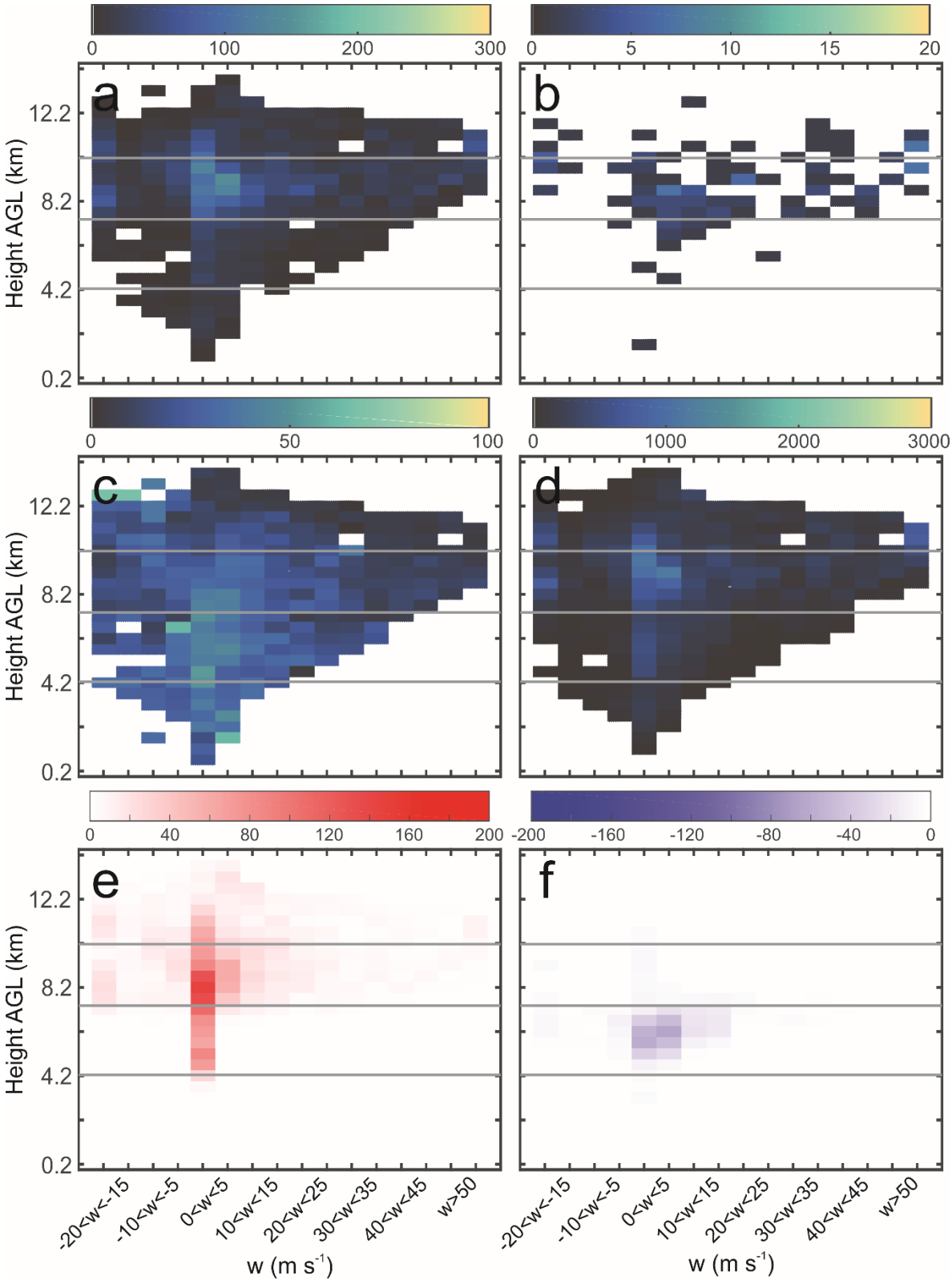

Figure 128: As in Figure 127, but for 22:42 UTC.

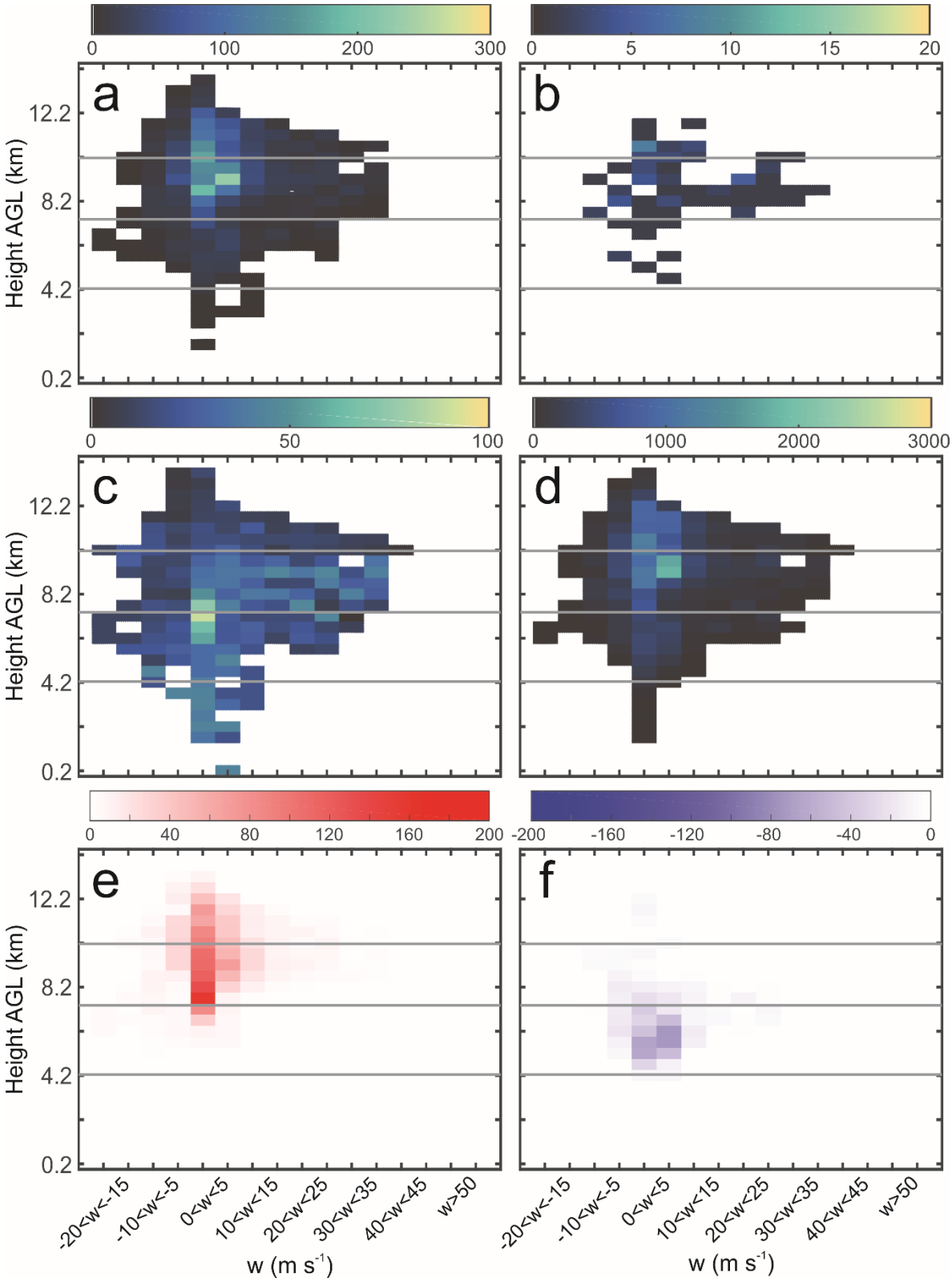

Figure 129: As in Figure 127, but for 22:48 UTC.

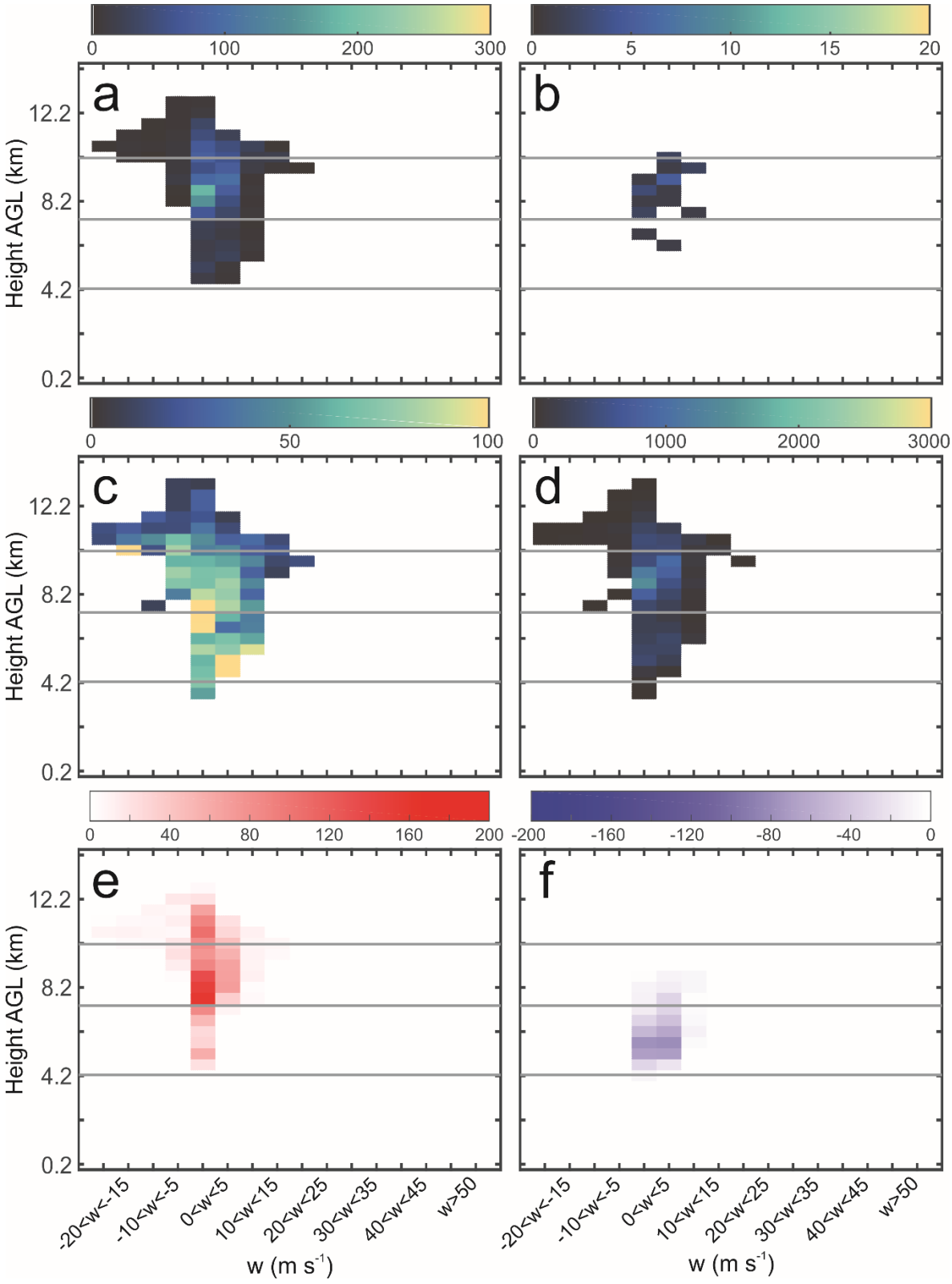

Figure 130: As in Figure 127, but for 22:54 UTC.

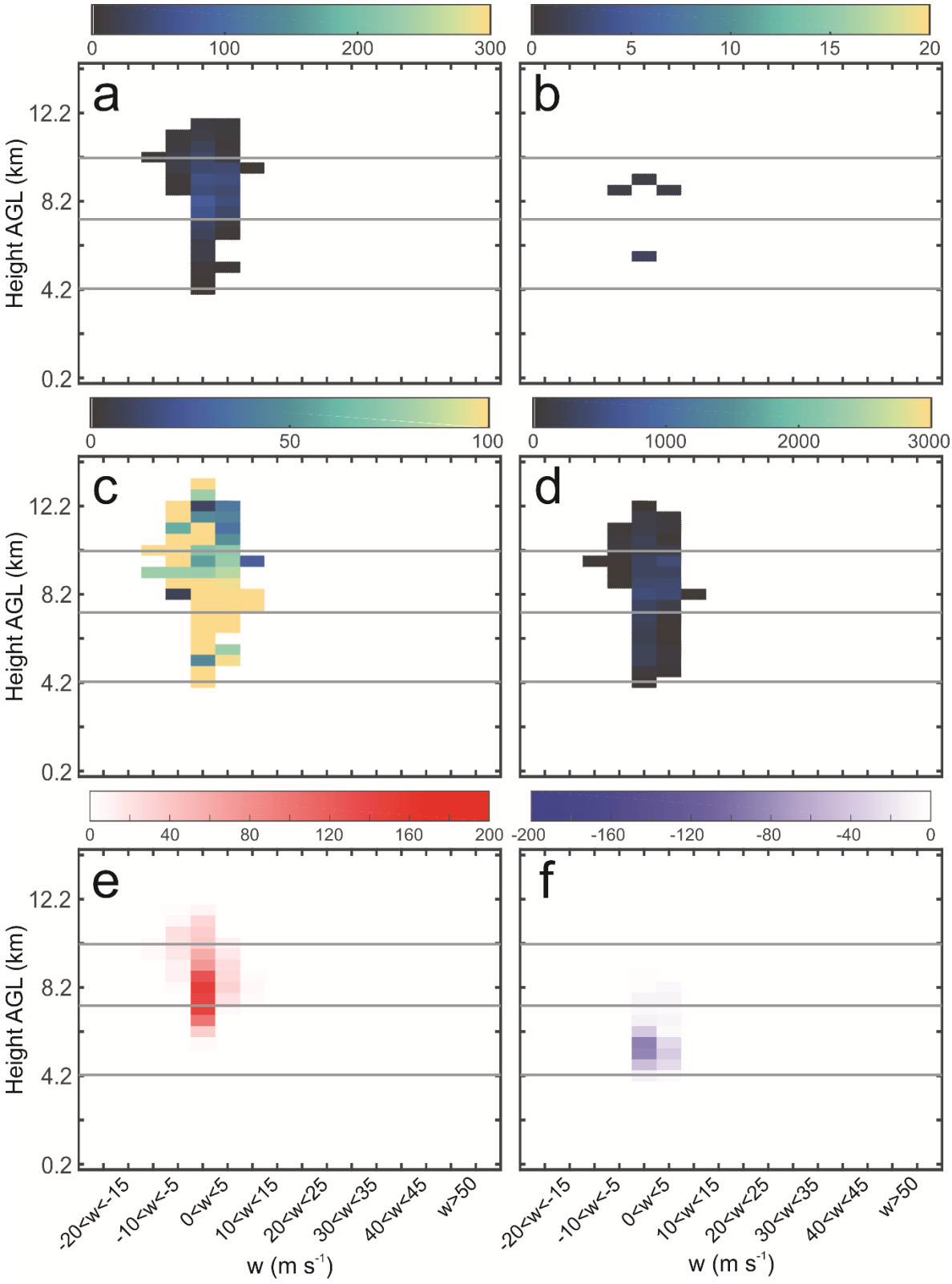

Figure 131: As in Figure 127, but for 23:00 UTC.

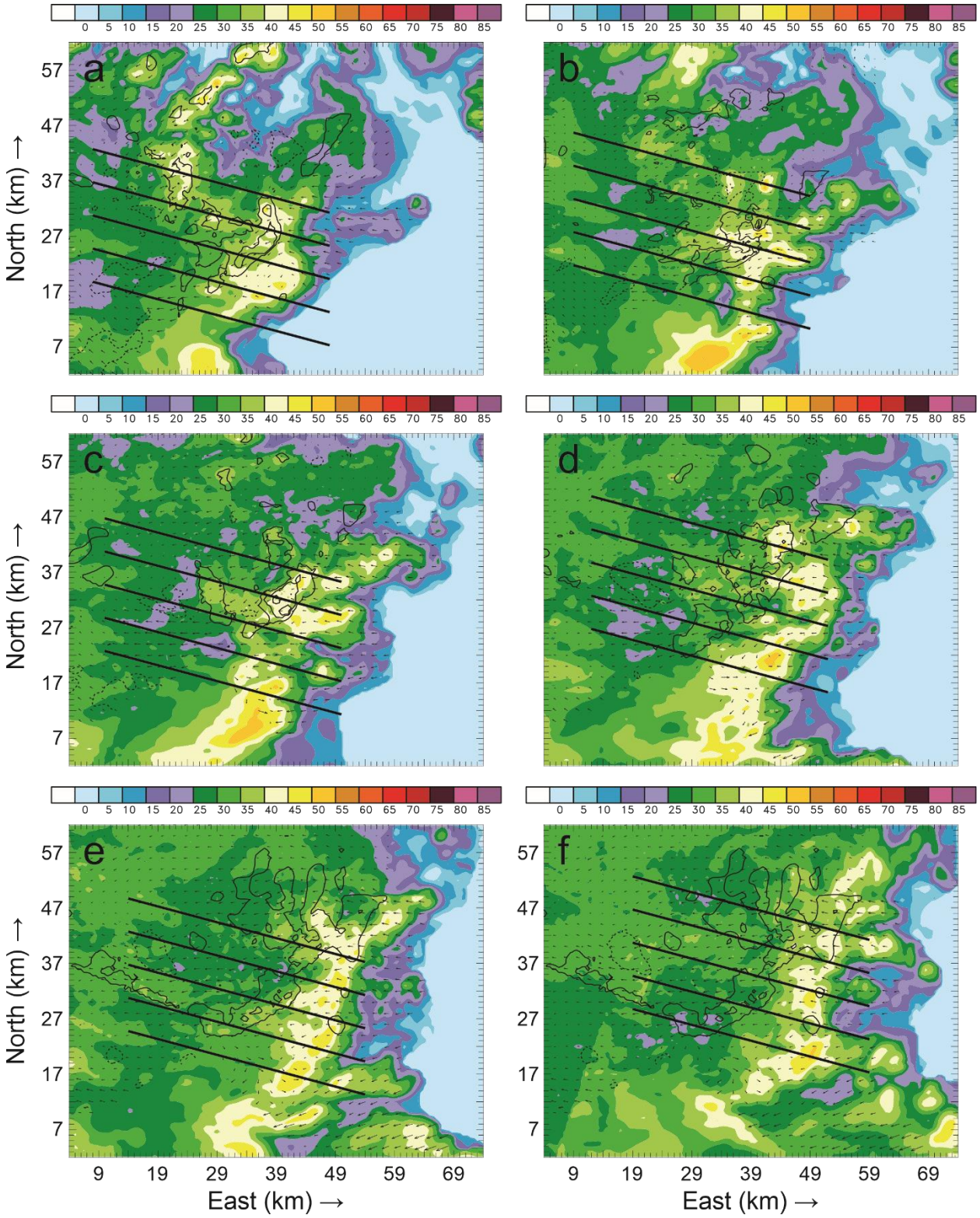

Figure 132: Horizontal cross-sections of color-filled Z, w contours (every 10 m s^{-1} starting at 5 m s^{-1}), and horizontal storm-relative wind vectors at 4.7 km AGL for a) 20:51 UTC, b) 21:03 UTC, c) 21:15 UTC, d) 21:27 UTC, e) 21:39 UTC, and f) 21:51 UTC. The diagonal black lines on each figure indicate the locations of the vertical cross sections generated for each analysis time.

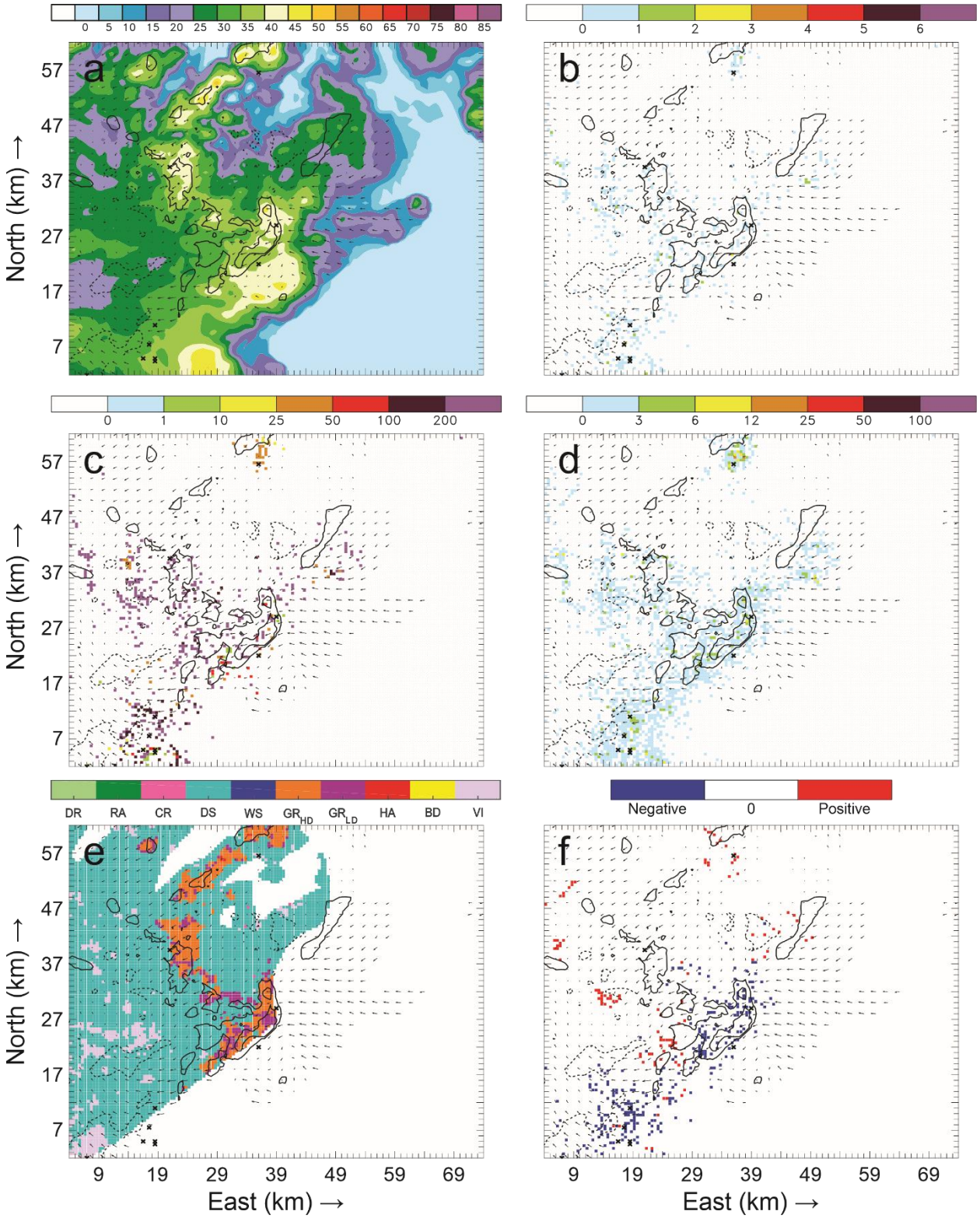

Figure 133: Horizontal cross-sections for 6 June 20:51 UTC taken at 4.7 km AGL of: a) color-filled Z and w contours (every 10 m s^{-1} starting at 5 m s^{-1}); b) color-filled FED and w contours; c) color-filled FP and w contours; d) color-filled SD and w contours; e) color-filled HCA and w contours; and f) color-filled net inferred space charge and w contours. All figures have the same horizontal storm-relative wind vectors, and black X's denote grid cells with FID > 0.

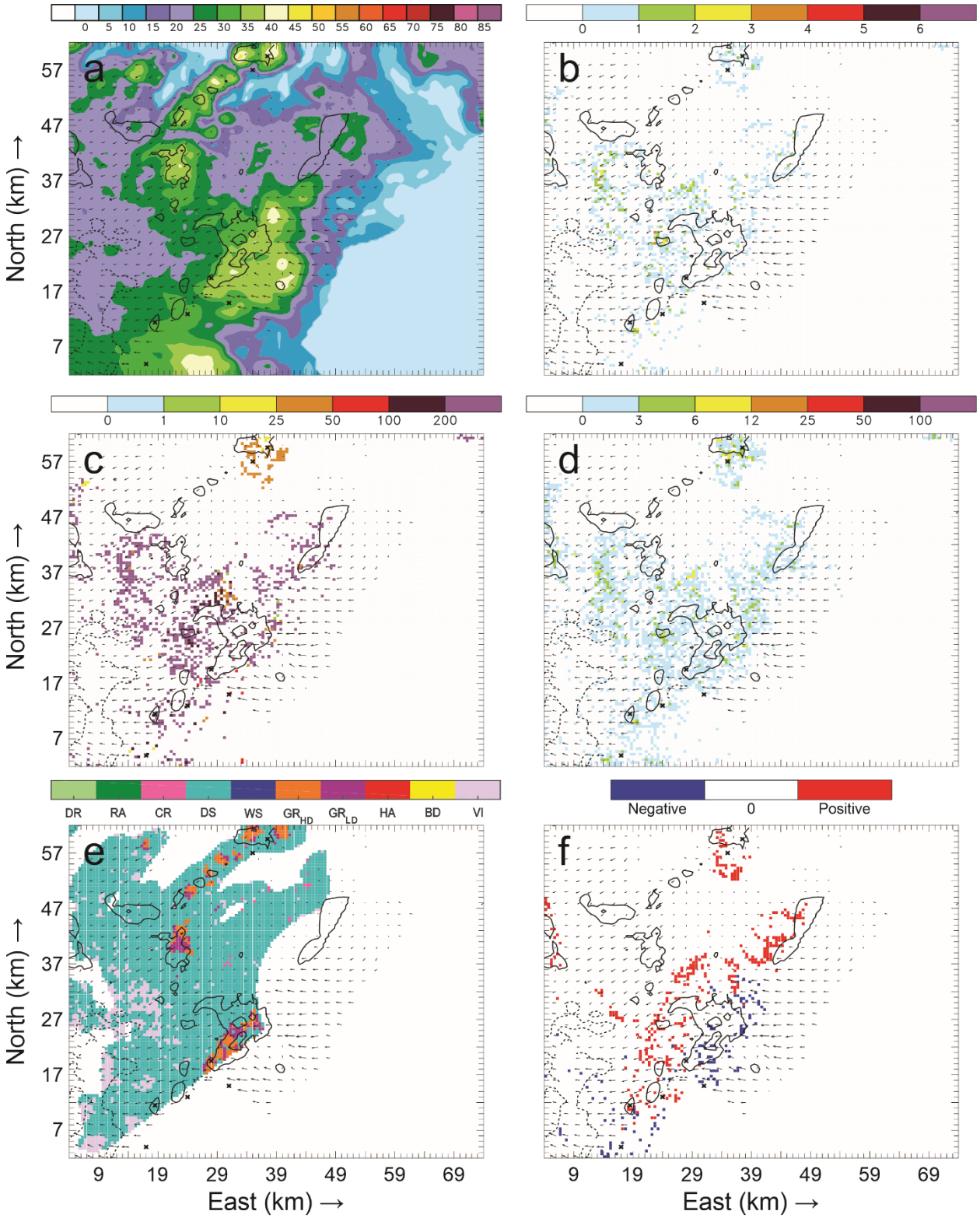

Figure 134: Horizontal cross-sections for 6 June 20:51 UTC. As in Figure 133, but taken at 5.7 km AGL.

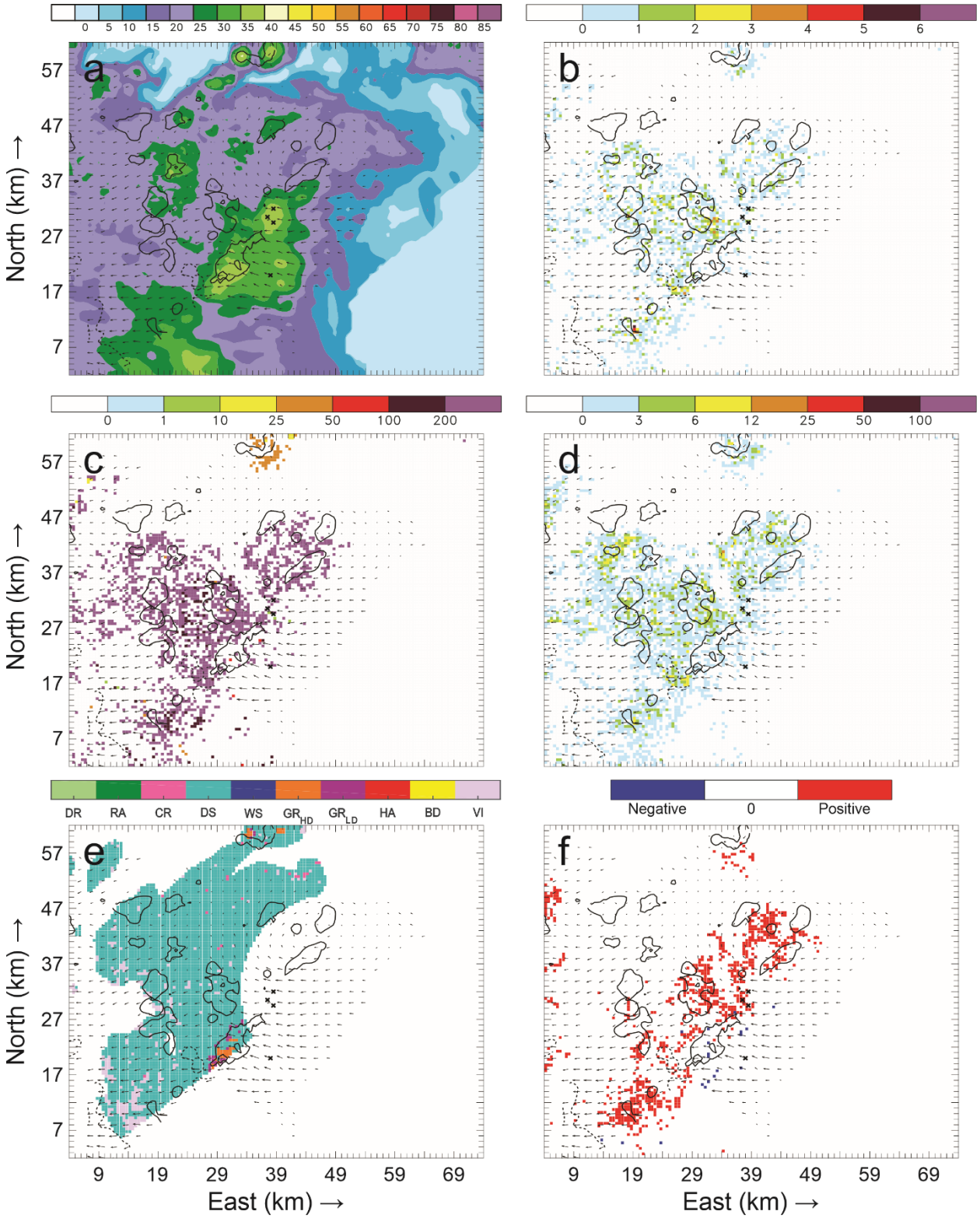

Figure 135: Horizontal cross-sections for 6 June 20:51 UTC. As in Figure 133, but taken at 6.7 km AGL.

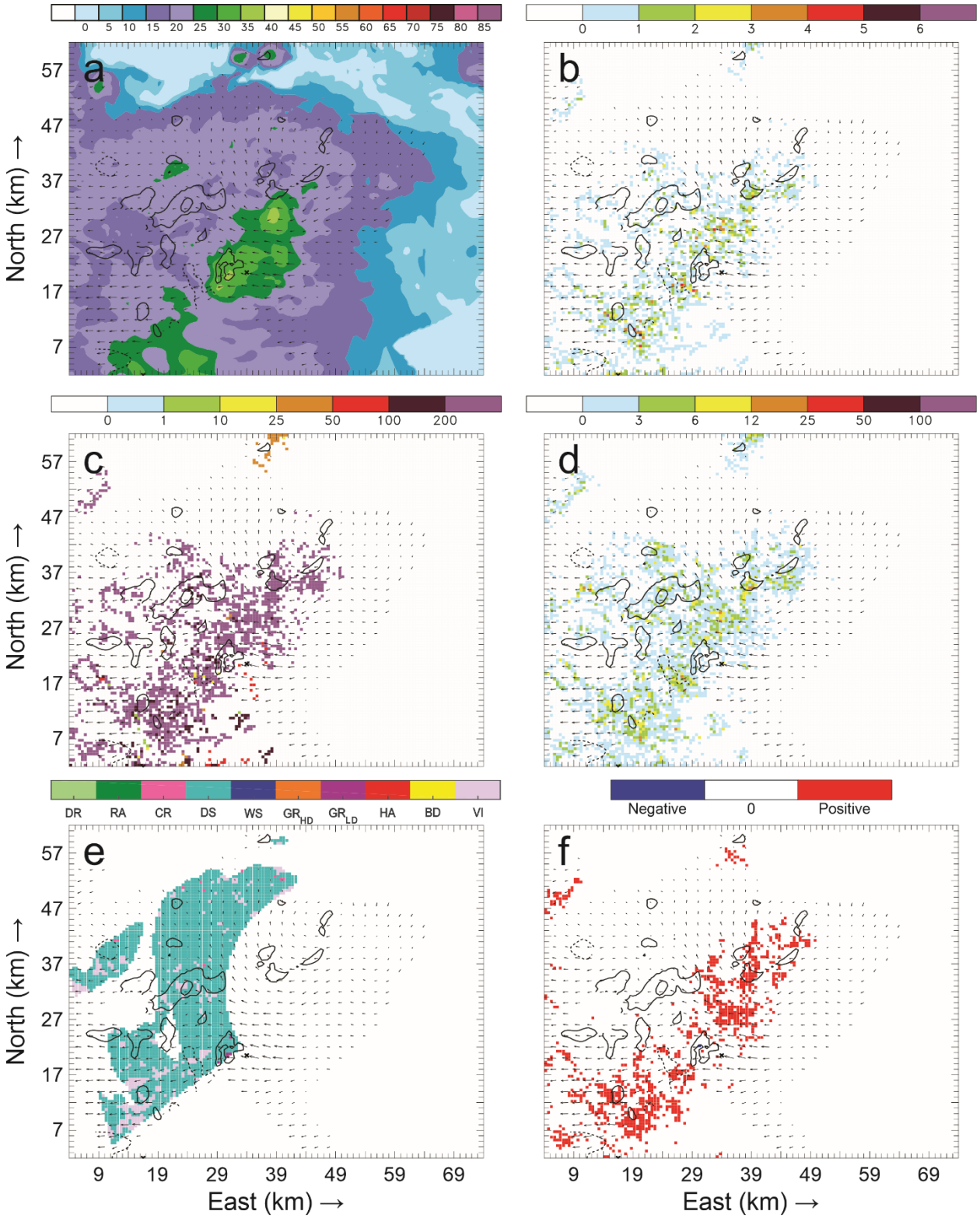

Figure 136: Horizontal cross-sections for 6 June 20:51 UTC. As in Figure 133, but taken at 7.7 km AGL.

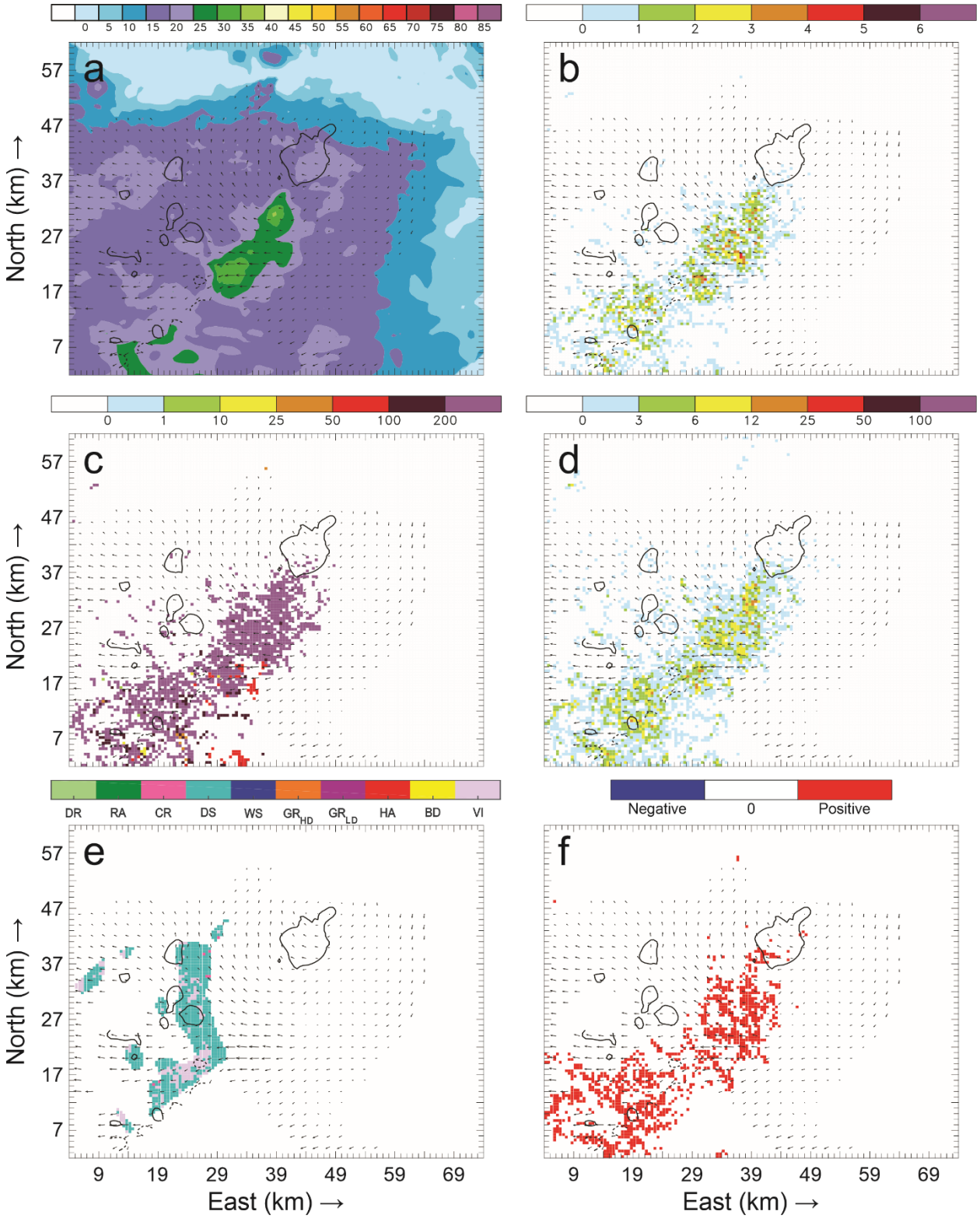

Figure 137: Horizontal cross-sections for 6 June 20:51 UTC. As in Figure 133, but taken at 8.7 km AGL.

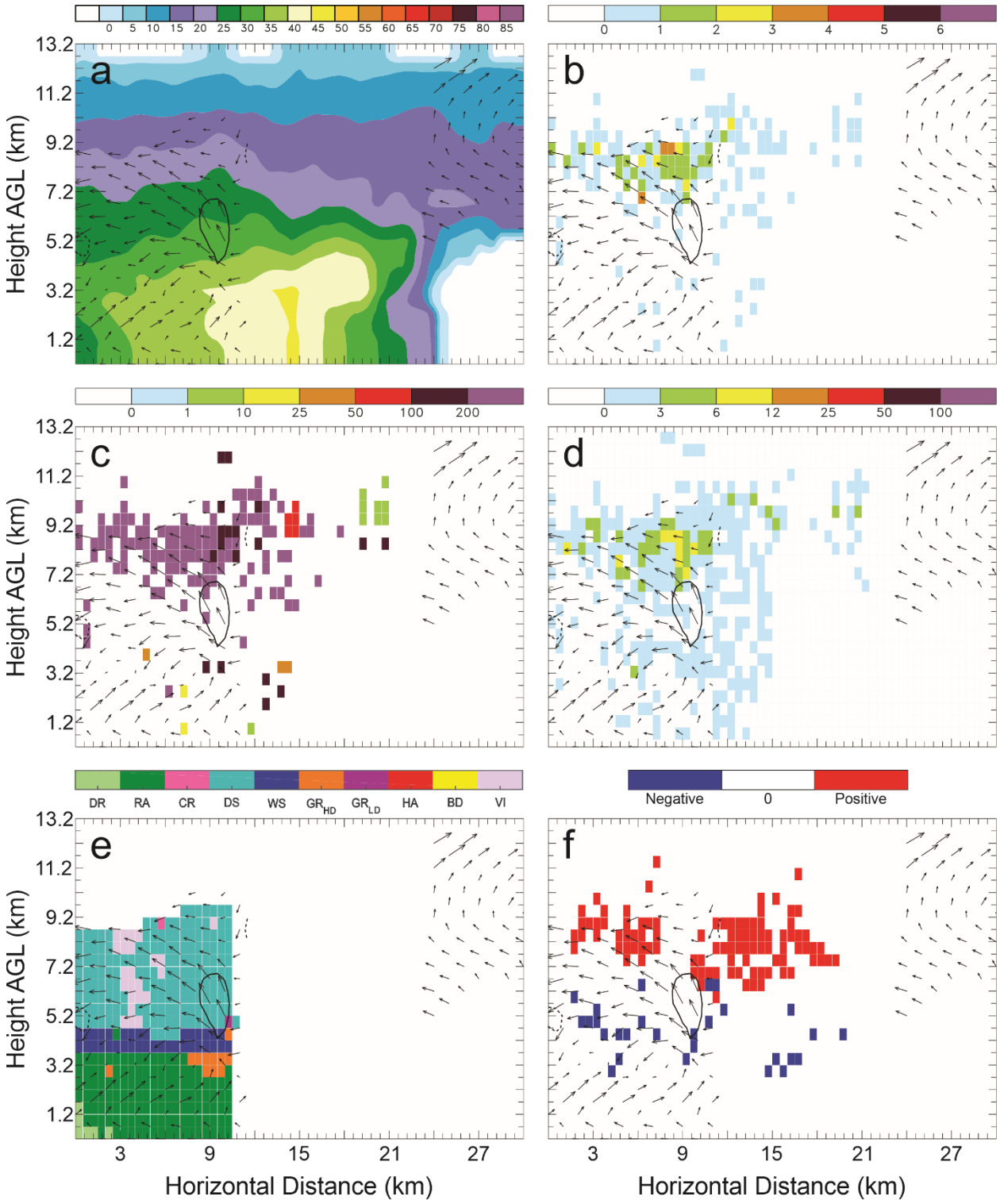

Figure 138: Vertical cross-sections for 6 June 20:51 UTC taken along the southernmost line in Figure 132(a) of: a) color-filled Z and w contours (every 10 m s^{-1} starting at 5 m s^{-1}); b) color-filled FED and w contours; c) color-filled FP and w contours; d) color-filled SD and w contours; e) color-filled HCA and w contours; and f) color-filled net inferred space charge and w contours. All figures have the same horizontal storm-relative wind vectors, and black X's denote grid cells with FID > 0.

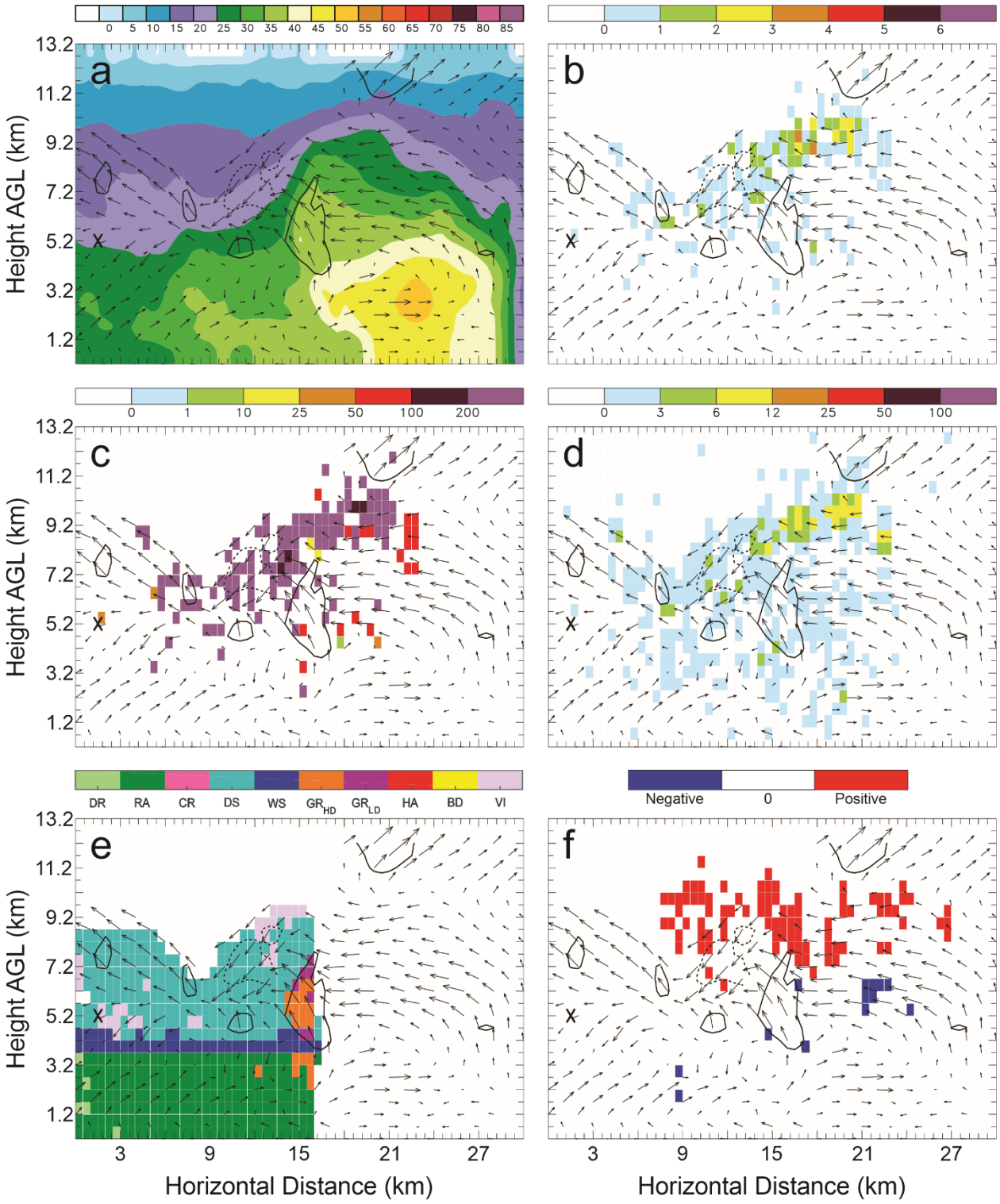

Figure 139: Vertical cross-sections for 6 June 20:51 UTC. As in Figure 138, but taken along the second line from the south in Figure 132(a).

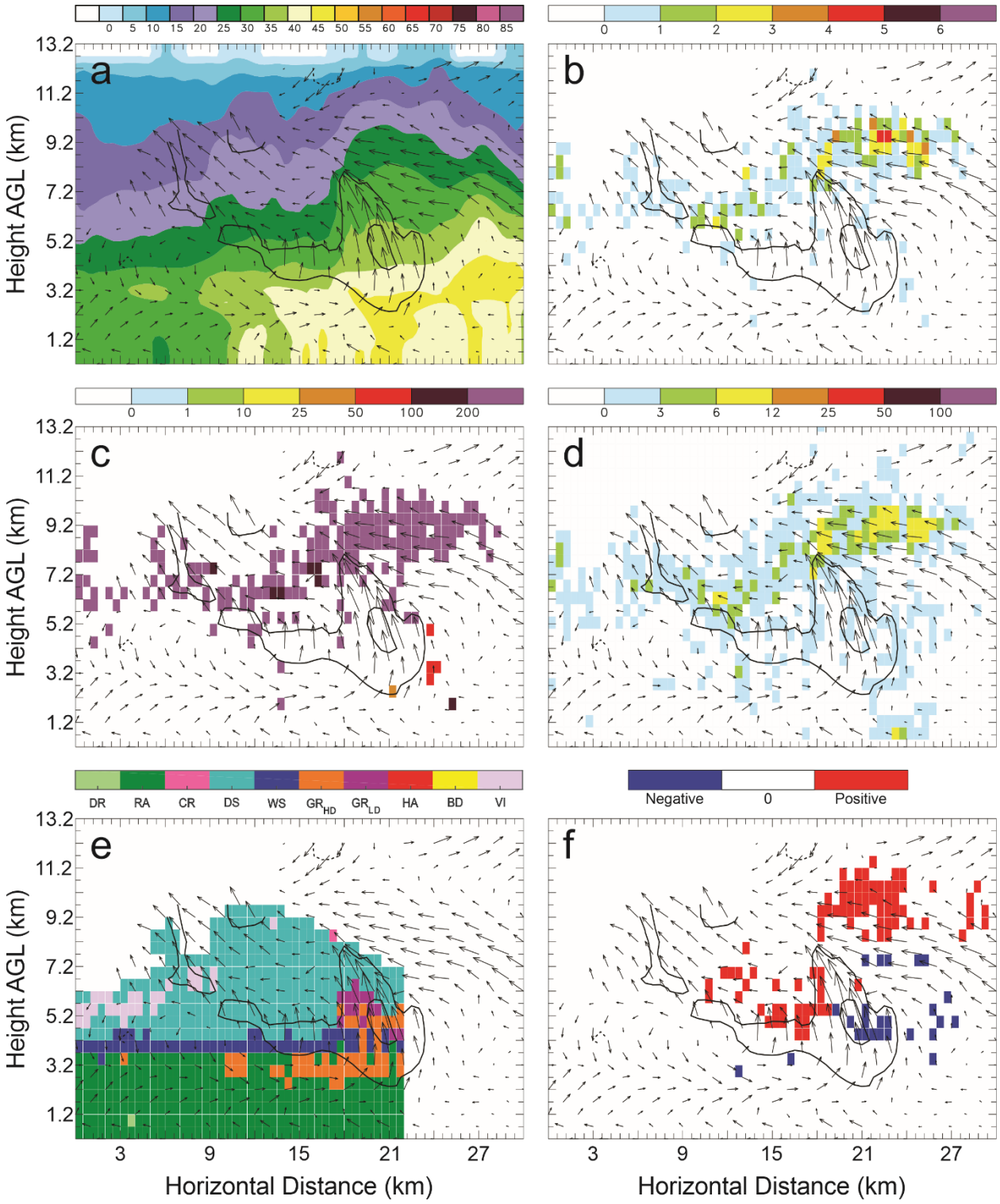

Figure 140: Vertical cross-sections for 6 June 20:51 UTC. As in Figure 138, but taken along the central line in Figure 132(a).

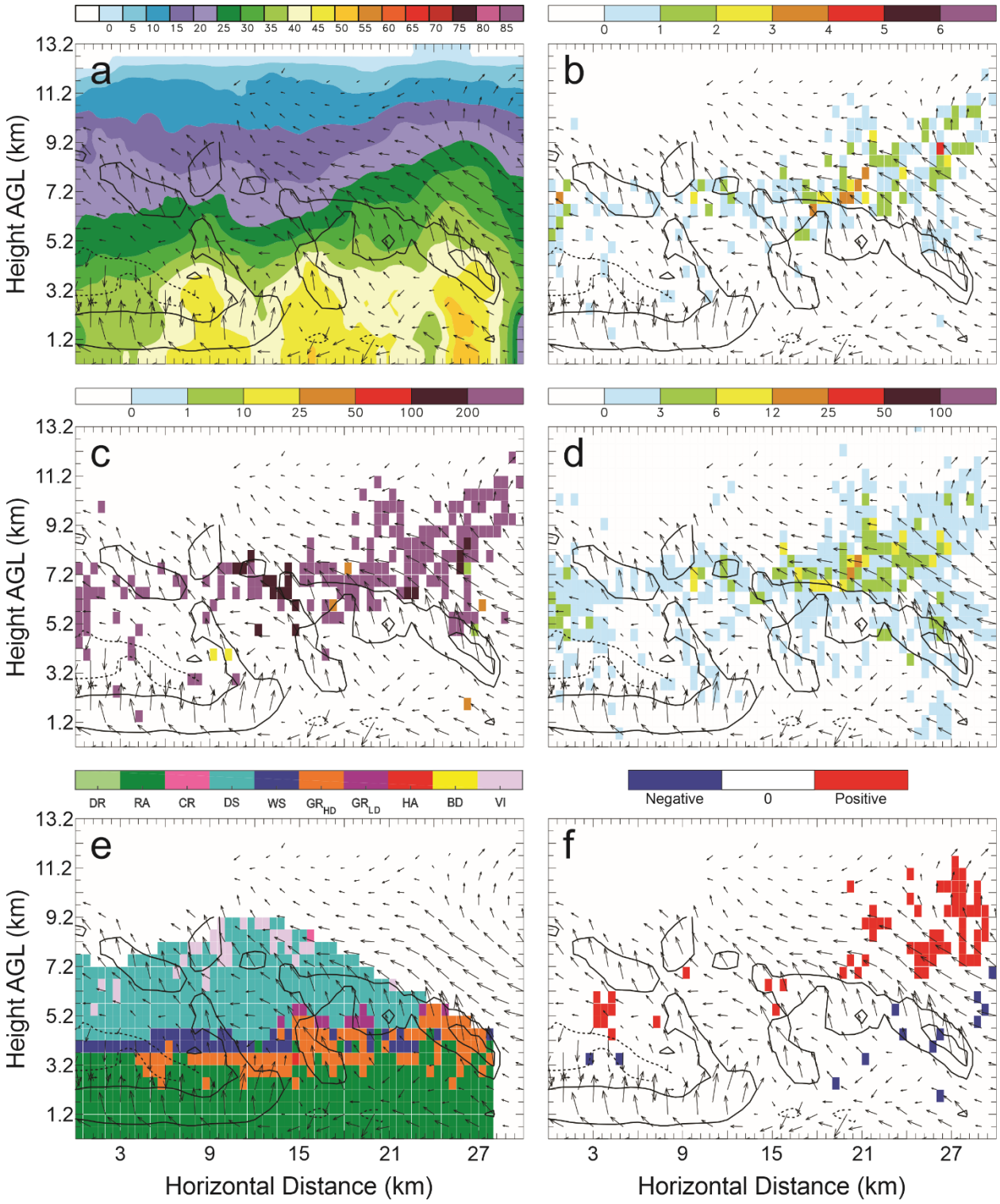

Figure 141: Vertical cross-sections for 6 June 20:51 UTC. As in Figure 138, but taken along the second line from the north in Figure 132(a).

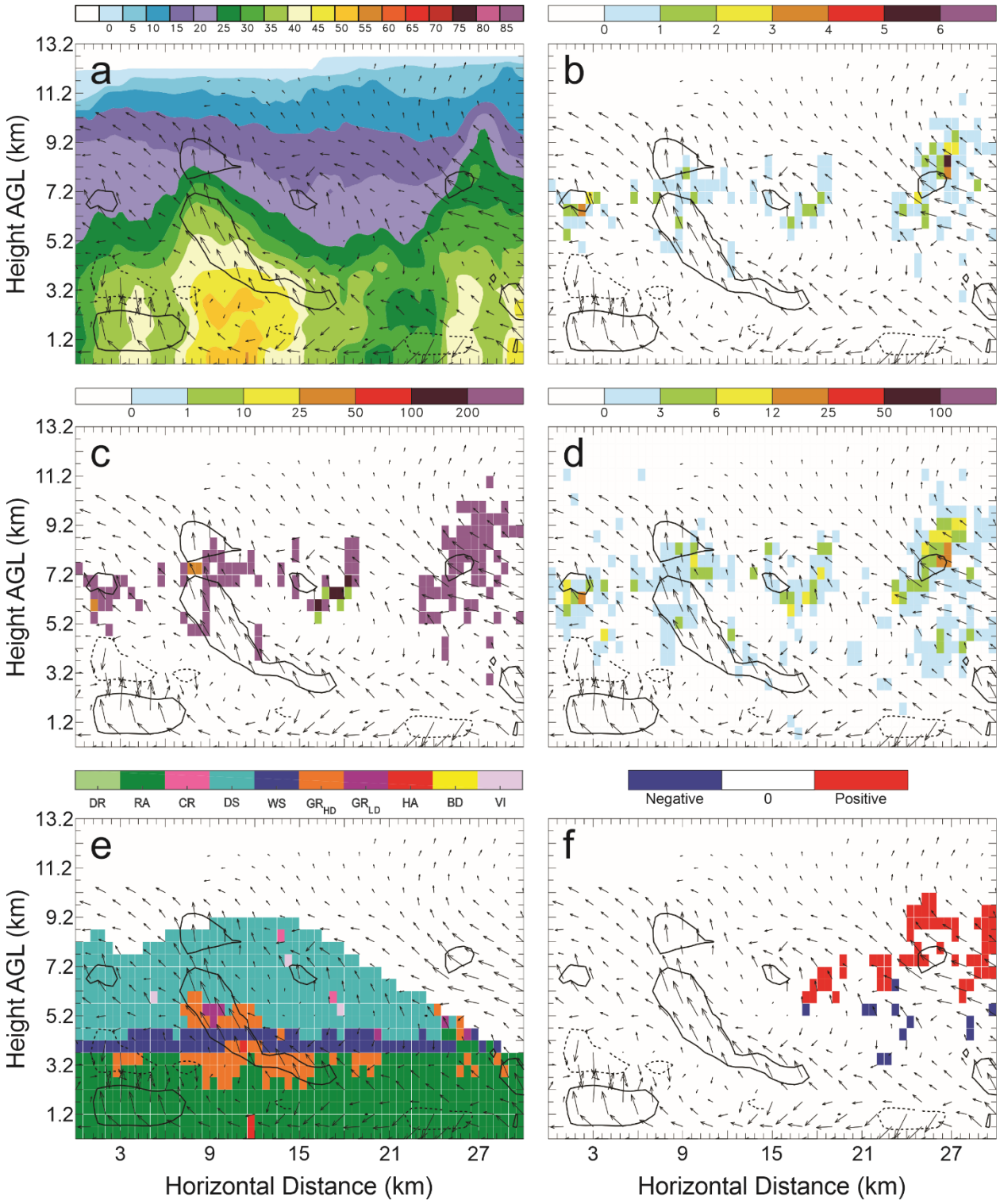

Figure 142: Vertical cross-sections for 6 June 20:51 UTC. As in Figure 138, but taken along the northernmost line in Figure 132(a).

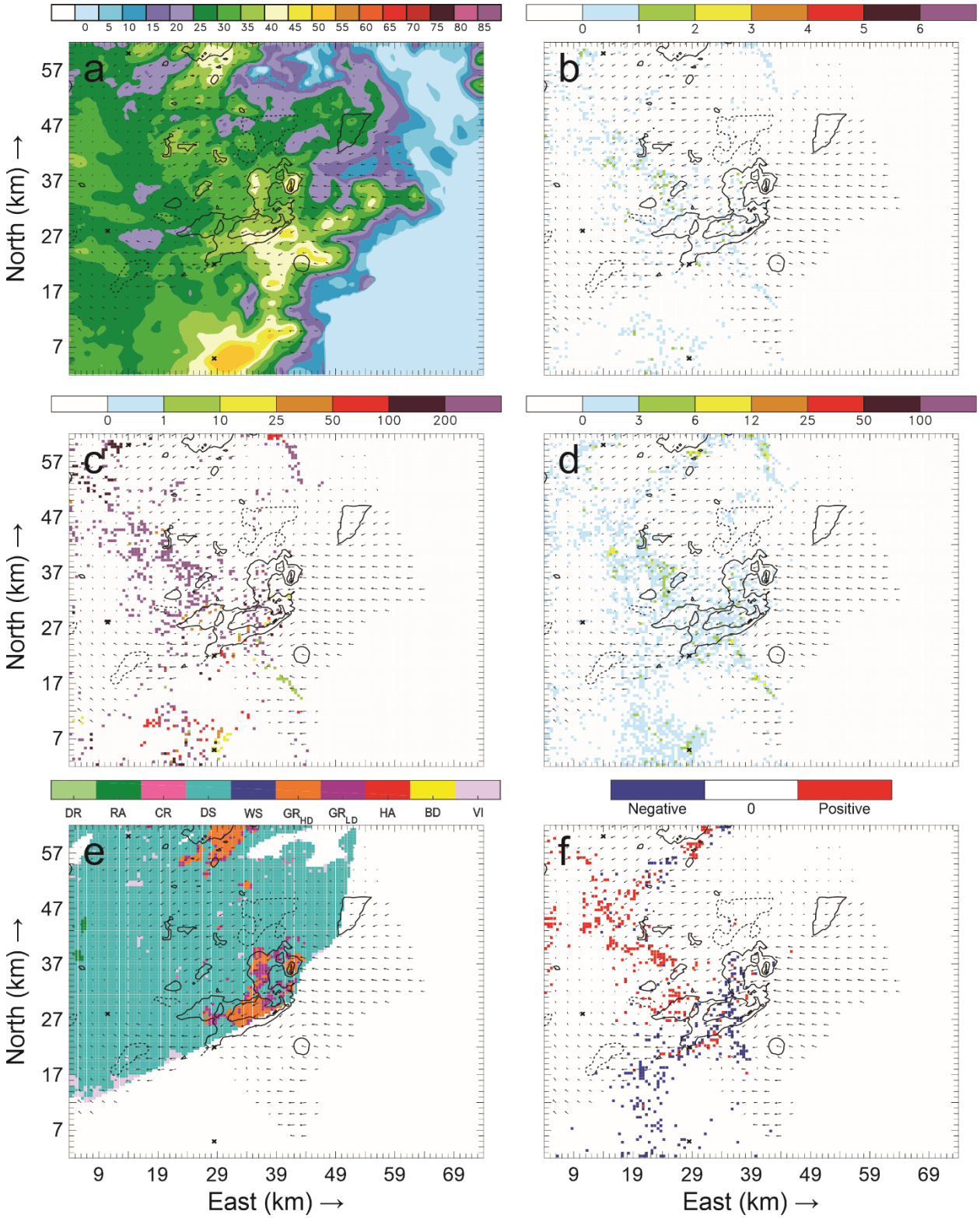

Figure 143: Horizontal cross-sections for 6 June 21:03 UTC taken at 4.7 km AGL of: a) color-filled Z and w contours (every 10 m s^{-1} starting at 5 m s^{-1}); b) color-filled FED and w contours; c) color-filled FP and w contours; d) color-filled SD and w contours; e) color-filled HCA and w contours; and f) color-filled net inferred space charge and w contours. All figures have the same horizontal storm-relative wind vectors, and black X's denote grid cells with FID > 0.

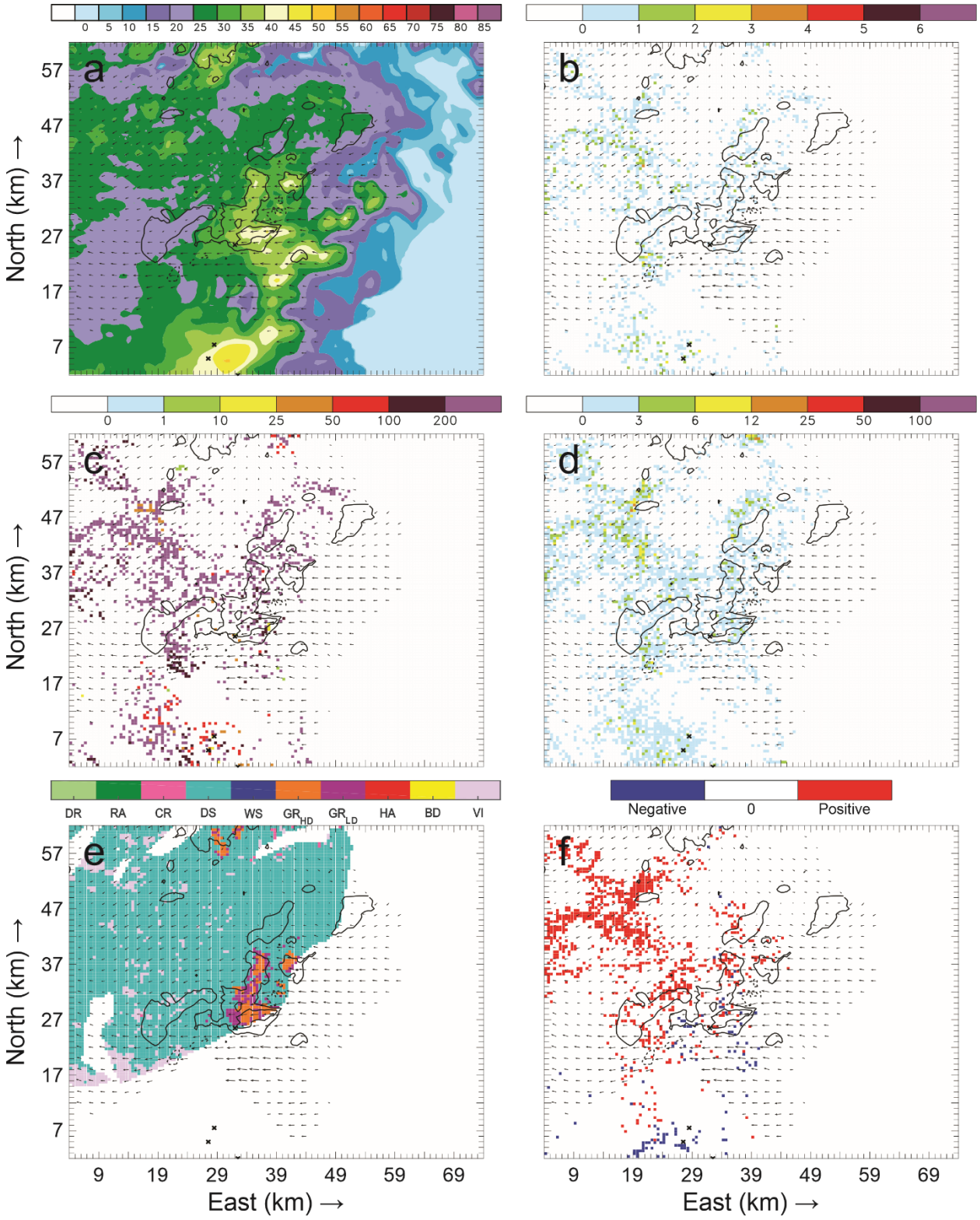

Figure 144: cross-sections for 6 June 21:03 UTC. As in Figure 143, but taken at 5.7 km AGL.

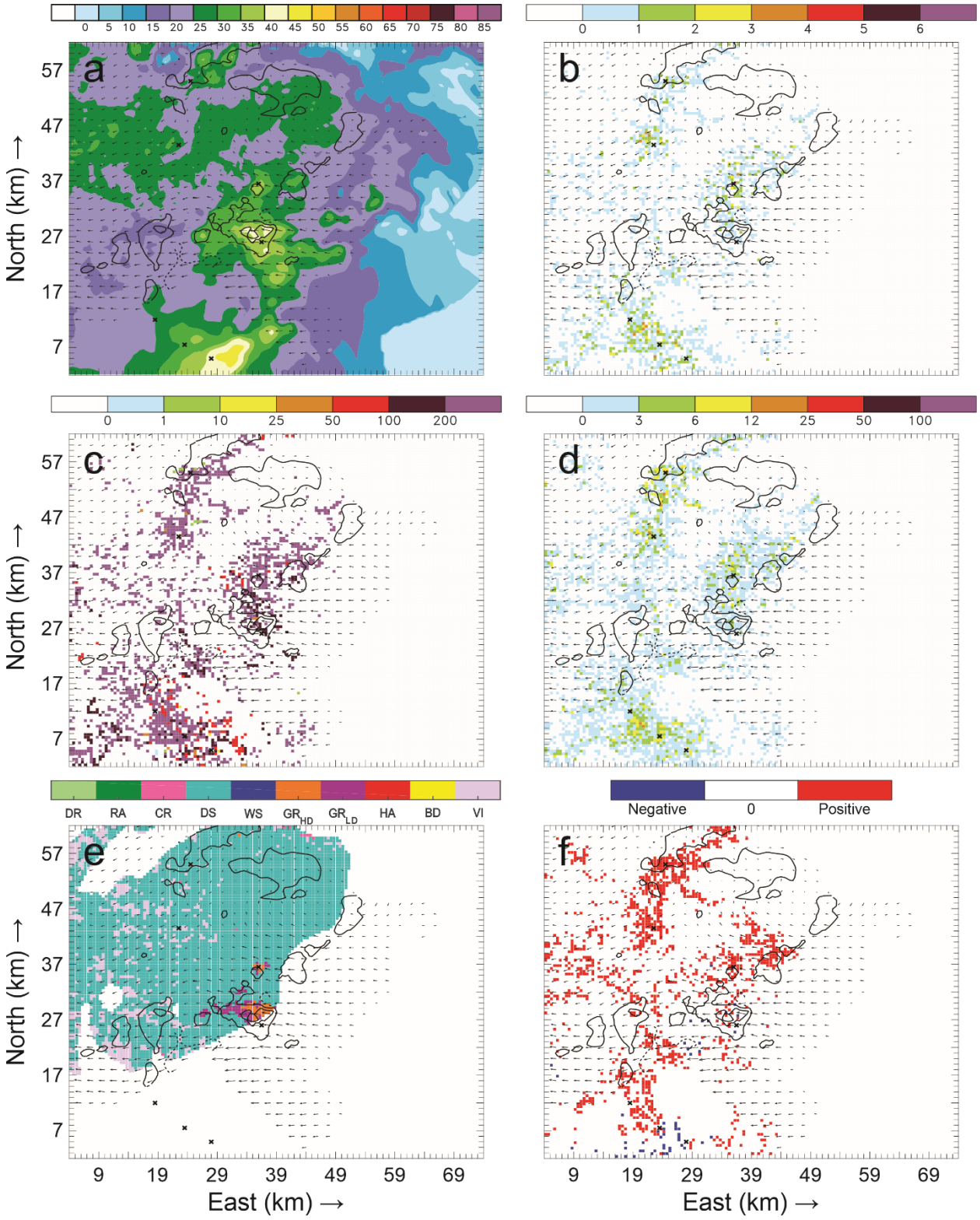

Figure 145: cross-sections for 6 June 21:03 UTC. As in Figure 143, but taken at 6.7 km AGL.

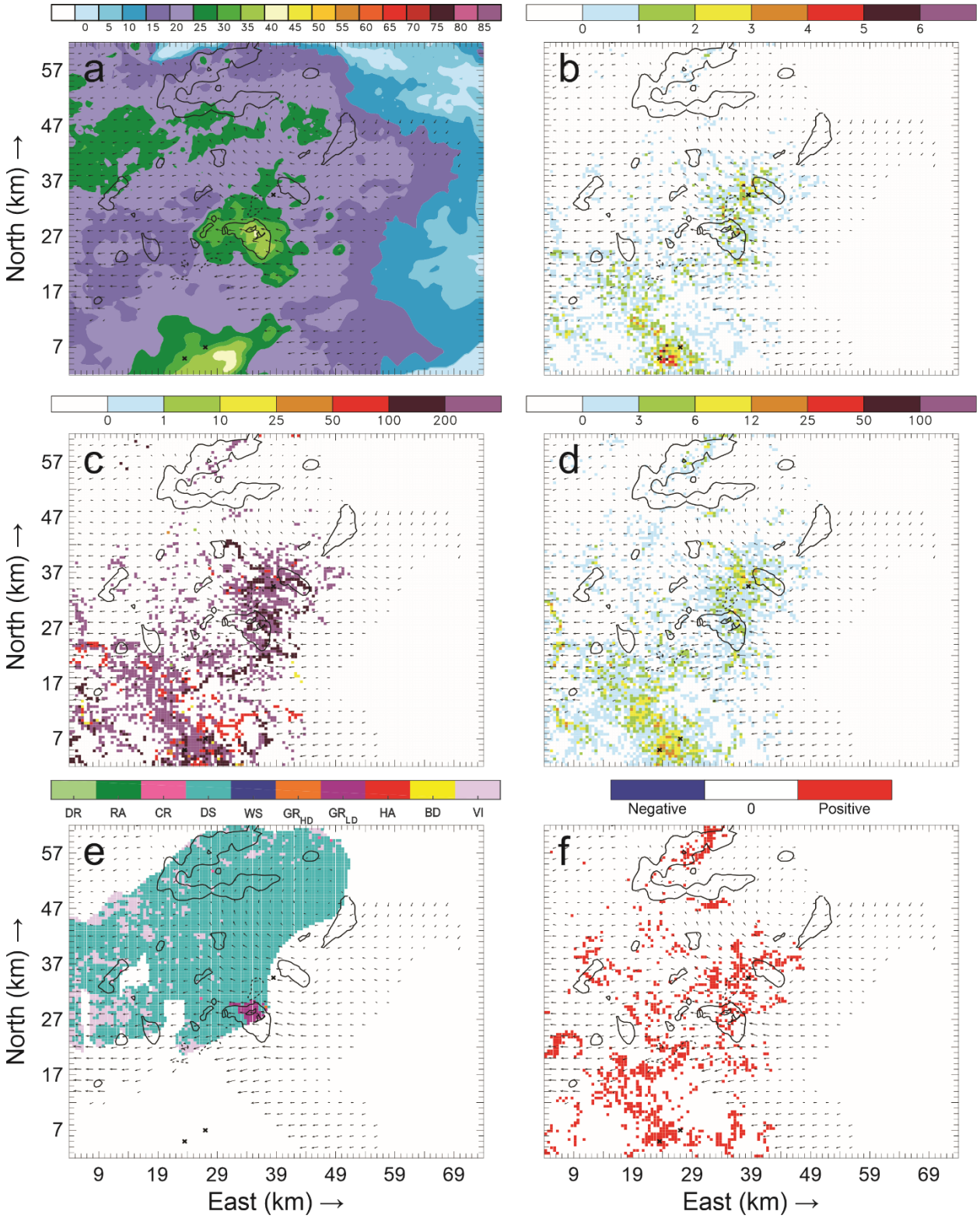

Figure 146: cross-sections for 6 June 21:03 UTC. As in Figure 143, but taken at 7.7 km AGL.

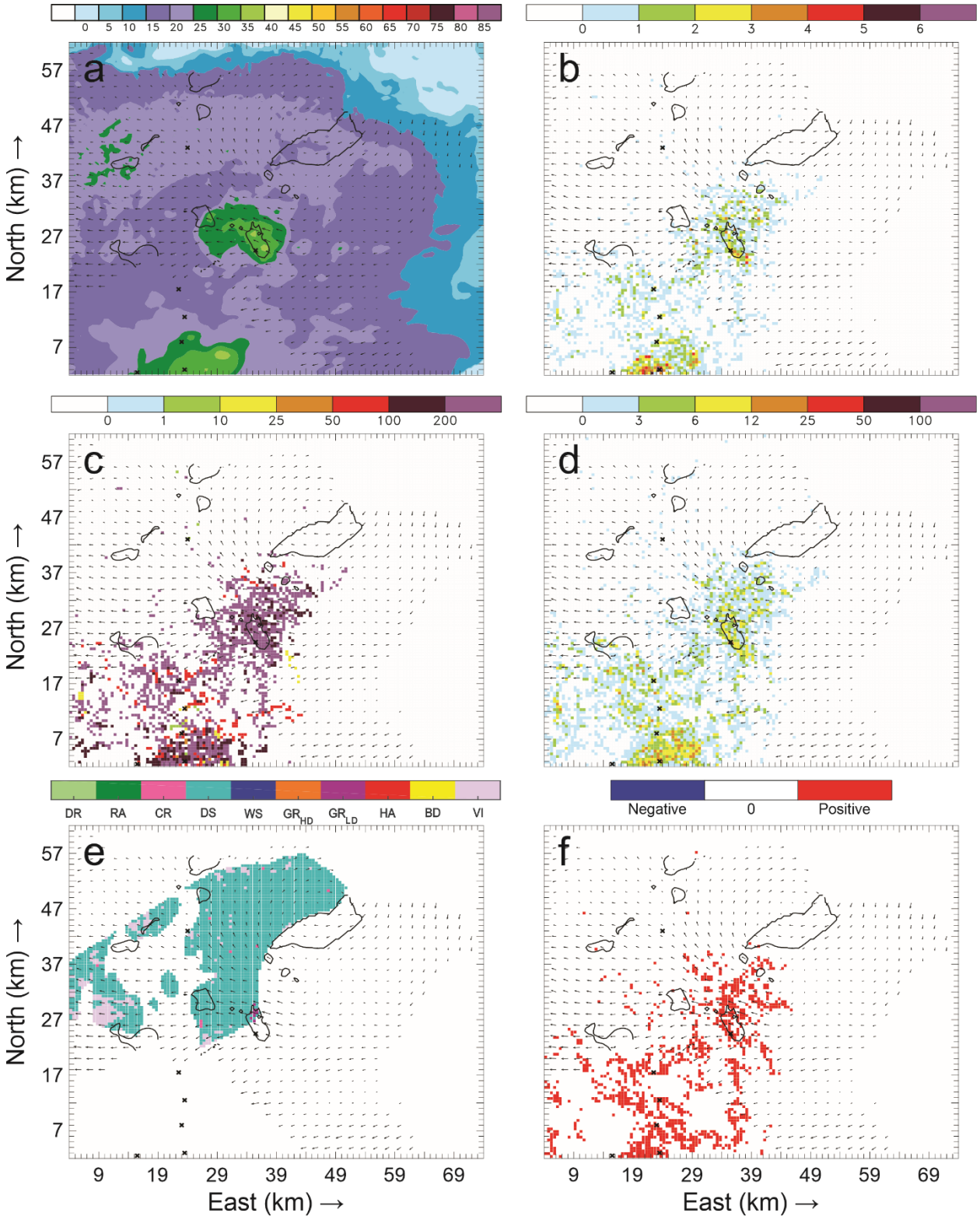

Figure 147: cross-sections for 6 June 21:03 UTC. As in Figure 143, but taken at 8.7 km AGL.

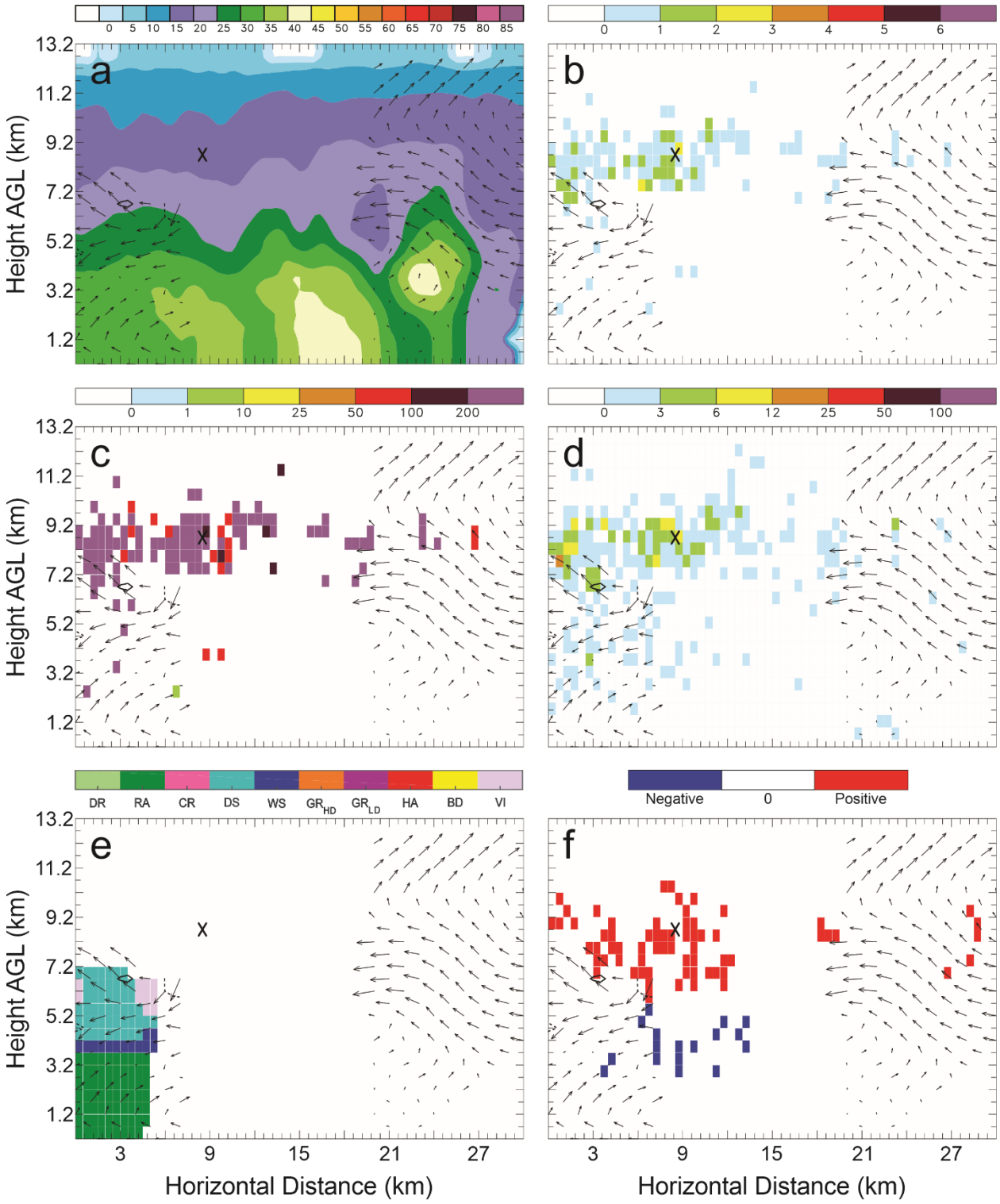

Figure 148: Vertical cross-sections for 6 June 21:03 UTC taken along the southernmost line in Figure 132(b) of: a) color-filled Z and w contours (every 10 m s^{-1} starting at 5 m s^{-1}); b) color-filled FED and w contours; c) color-filled FP and w contours; d) color-filled SD and w contours; e) color-filled HCA and w contours; and f) color-filled net inferred space charge and w contours. All figures have the same horizontal storm-relative wind vectors, and black X's denote grid cells with FID > 0.

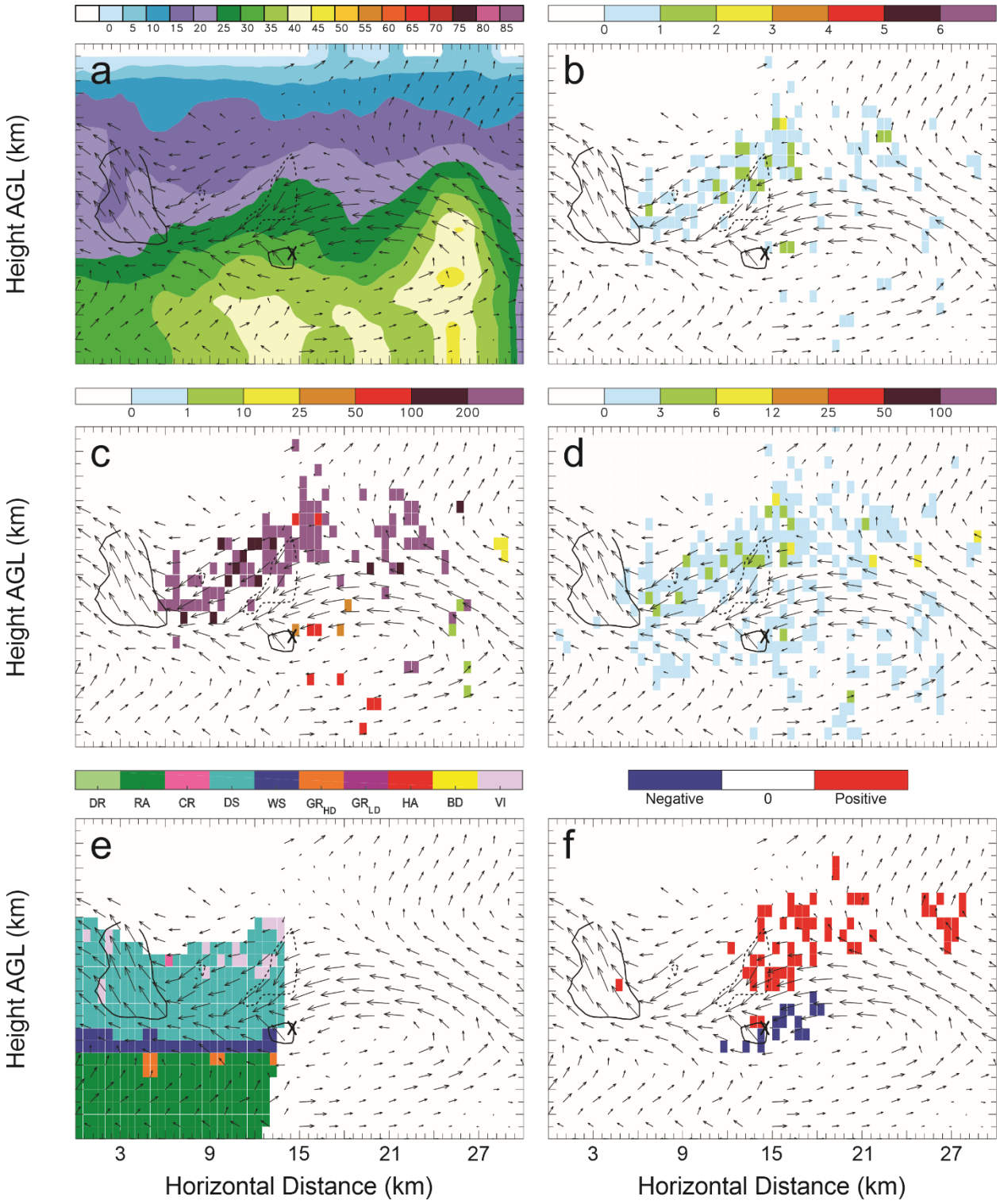

Figure 149: Vertical cross-sections for 6 June 21:03 UTC. As in Figure 148, but taken along the second line from the south in Figure 132(b).

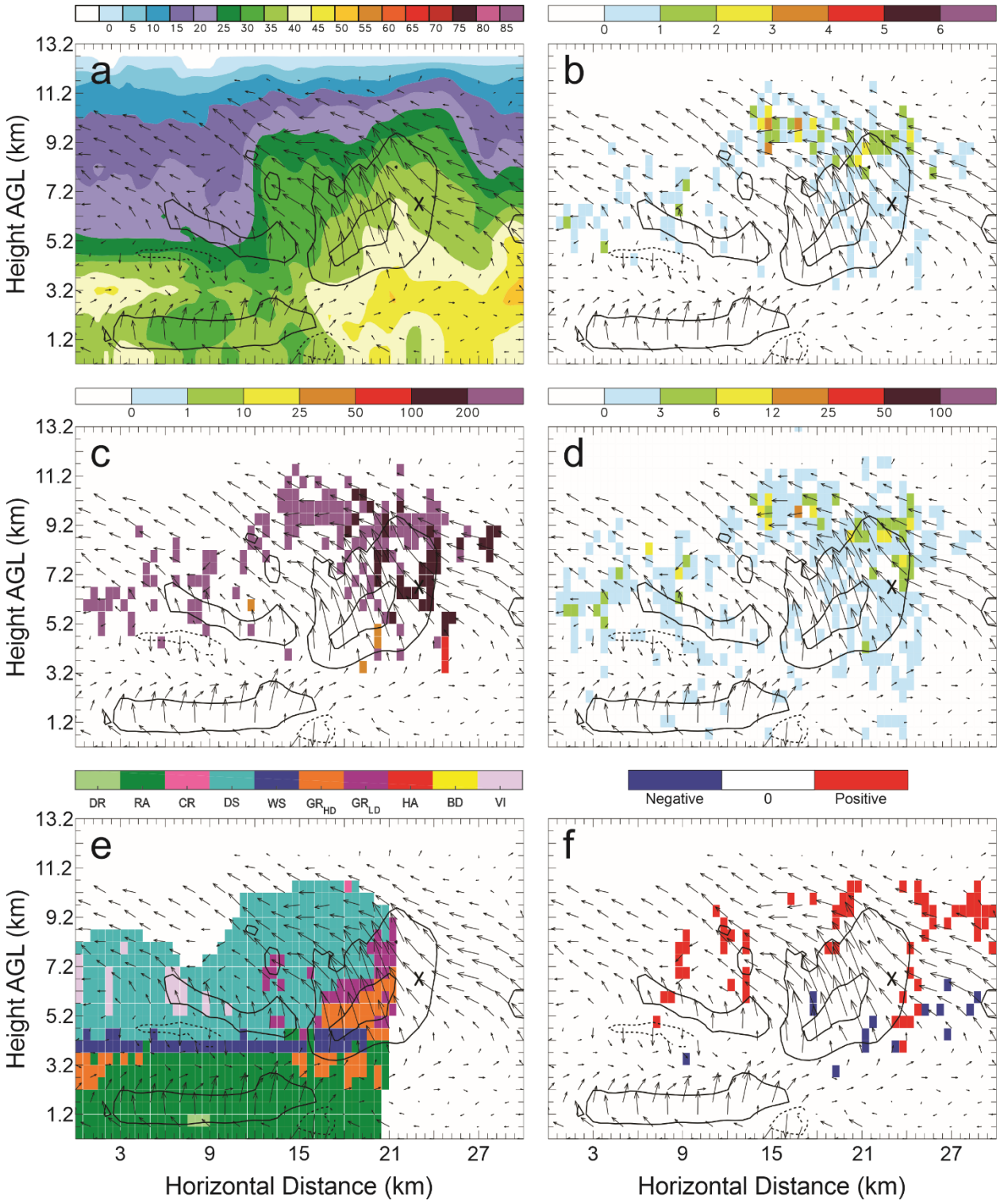

Figure 150: Vertical cross-sections for 6 June 21:03 UTC. As in Figure 148, but taken along the central line in Figure 132(b).

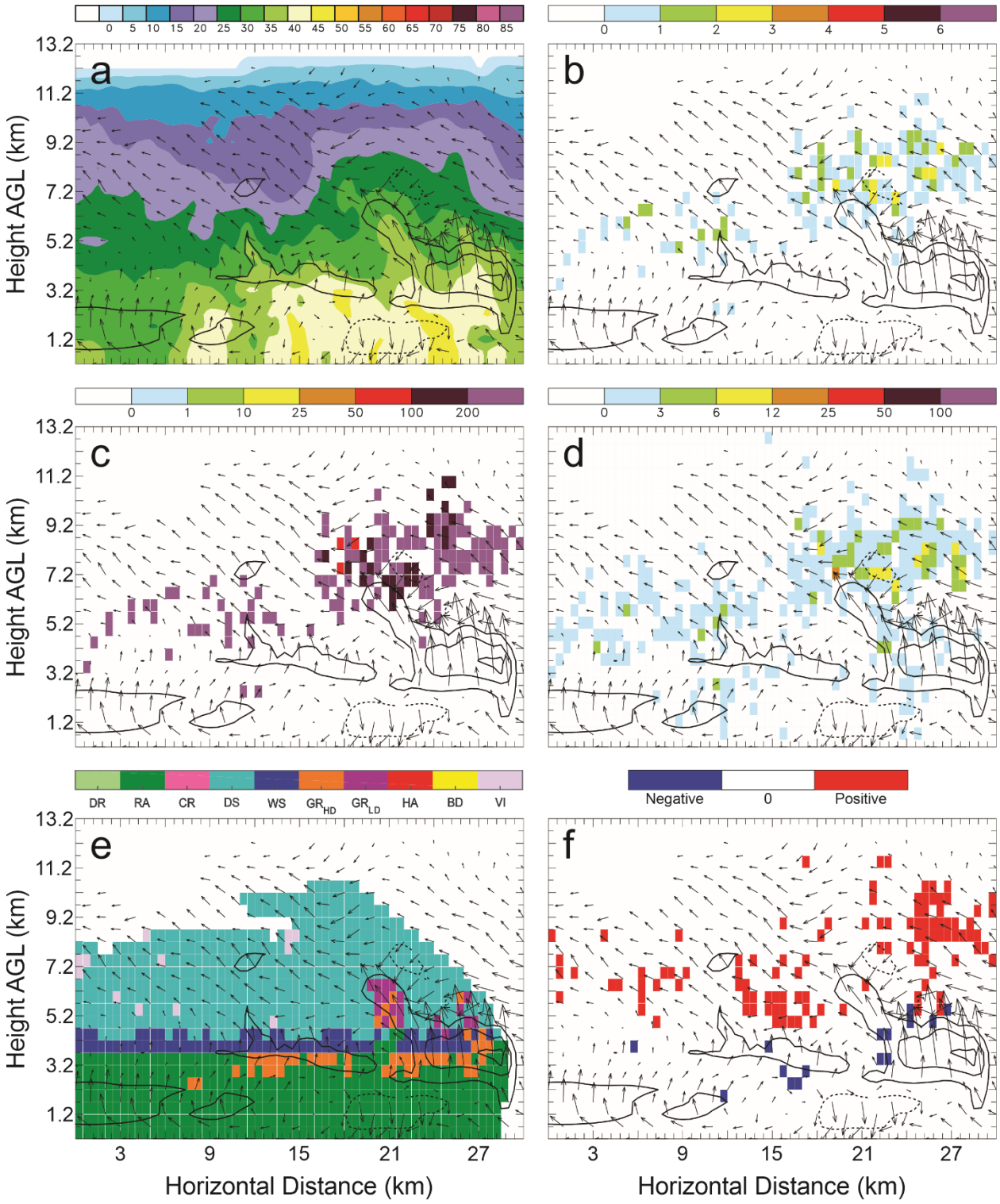

Figure 151: Vertical cross-sections for 6 June 21:03 UTC. As in Figure 148, but taken along the second line from the north in Figure 132(b).

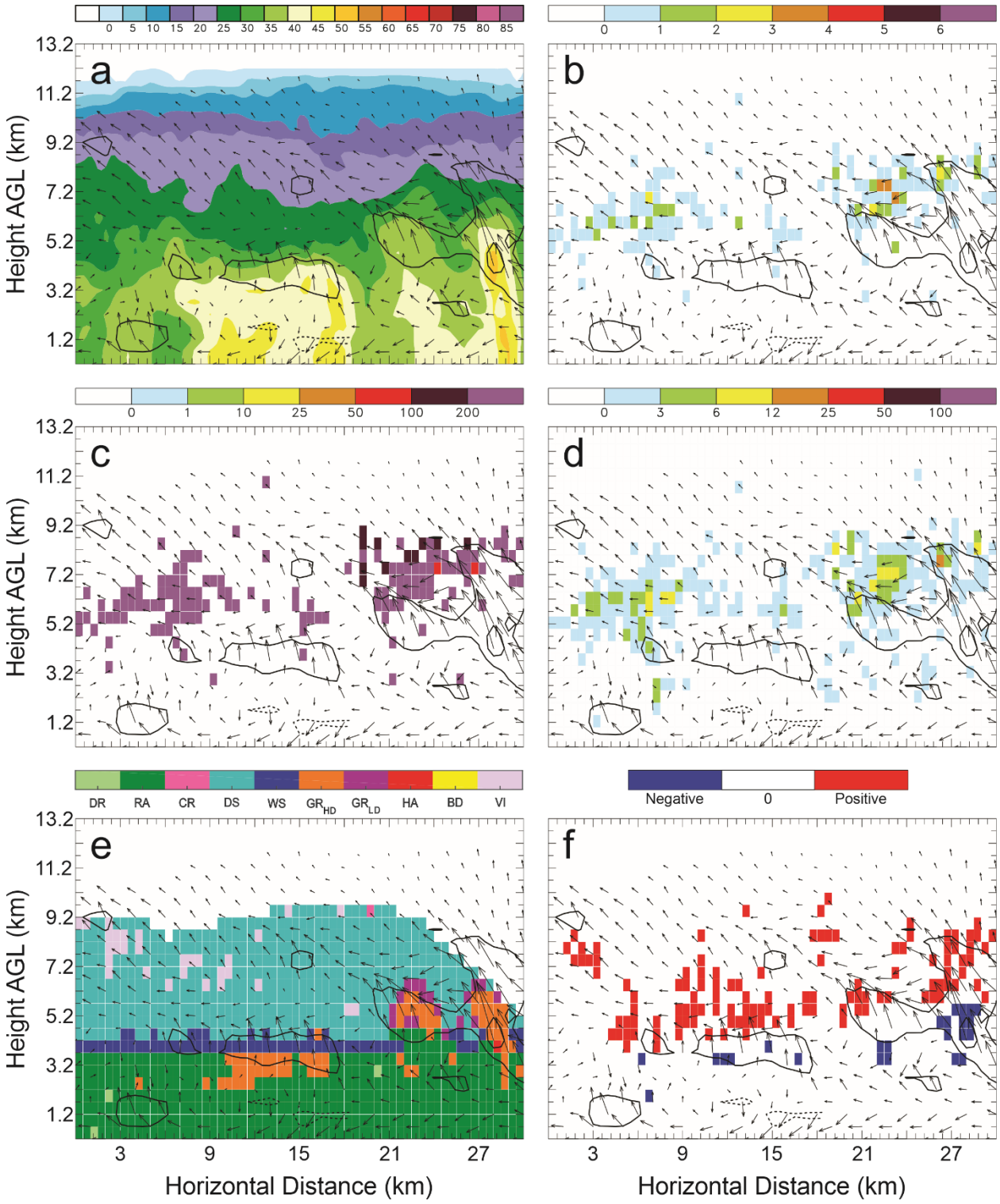

Figure 152: Vertical cross-sections for 6 June 21:03 UTC. As in Figure 148, but taken along the northernmost line in Figure 132(b).

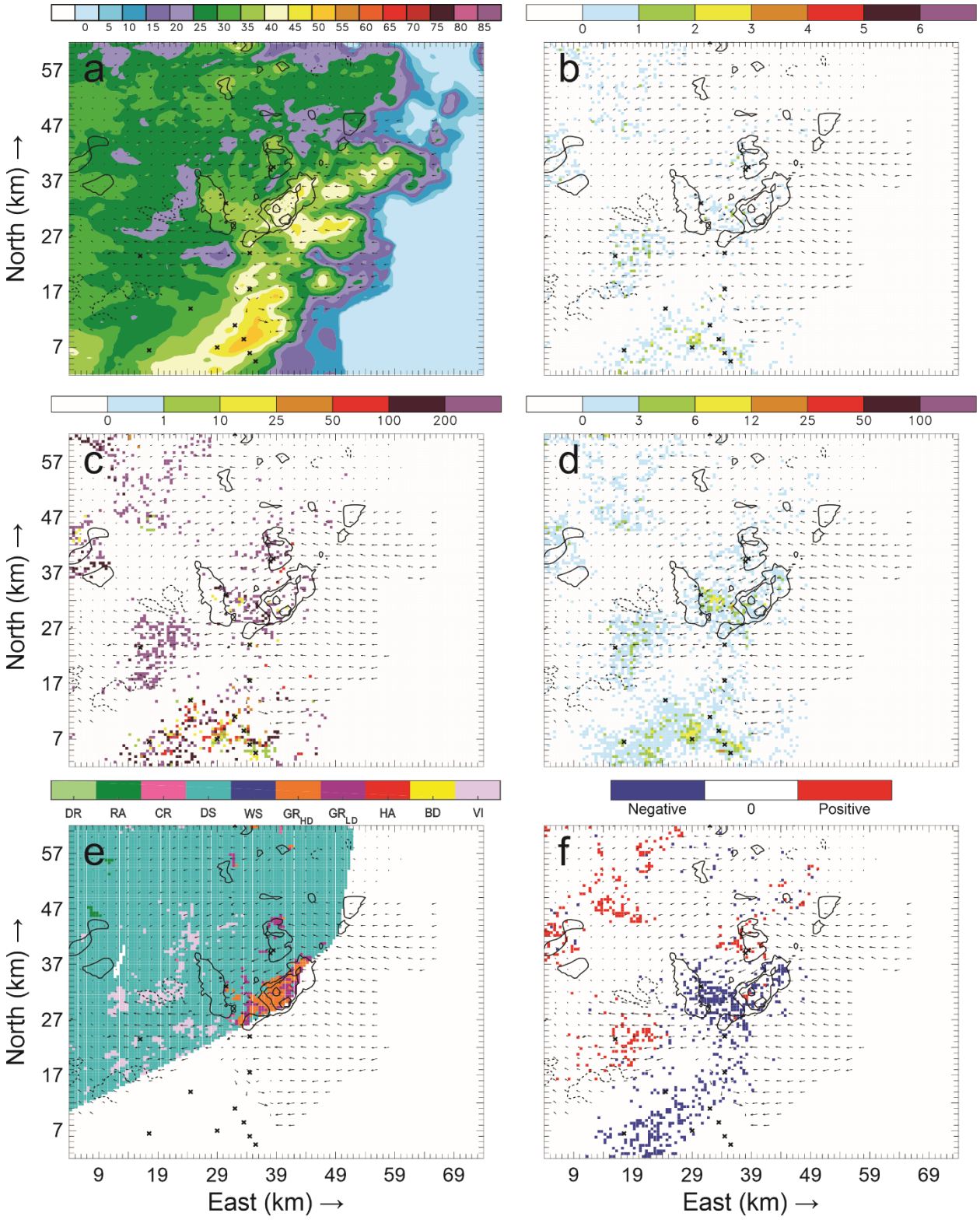

Figure 153: Horizontal cross-sections for 6 June 21:15 UTC taken at 4.7 km AGL of: a) color-filled Z and w contours (every 10 m s^{-1} starting at 5 m s^{-1}); b) color-filled FED and w contours; c) color-filled FP and w contours; d) color-filled SD and w contours; e) color-filled HCA and w contours; and f) color-filled net inferred space charge and w contours. All figures have the same horizontal storm-relative wind vectors, and black X's denote grid cells with FID > 0.

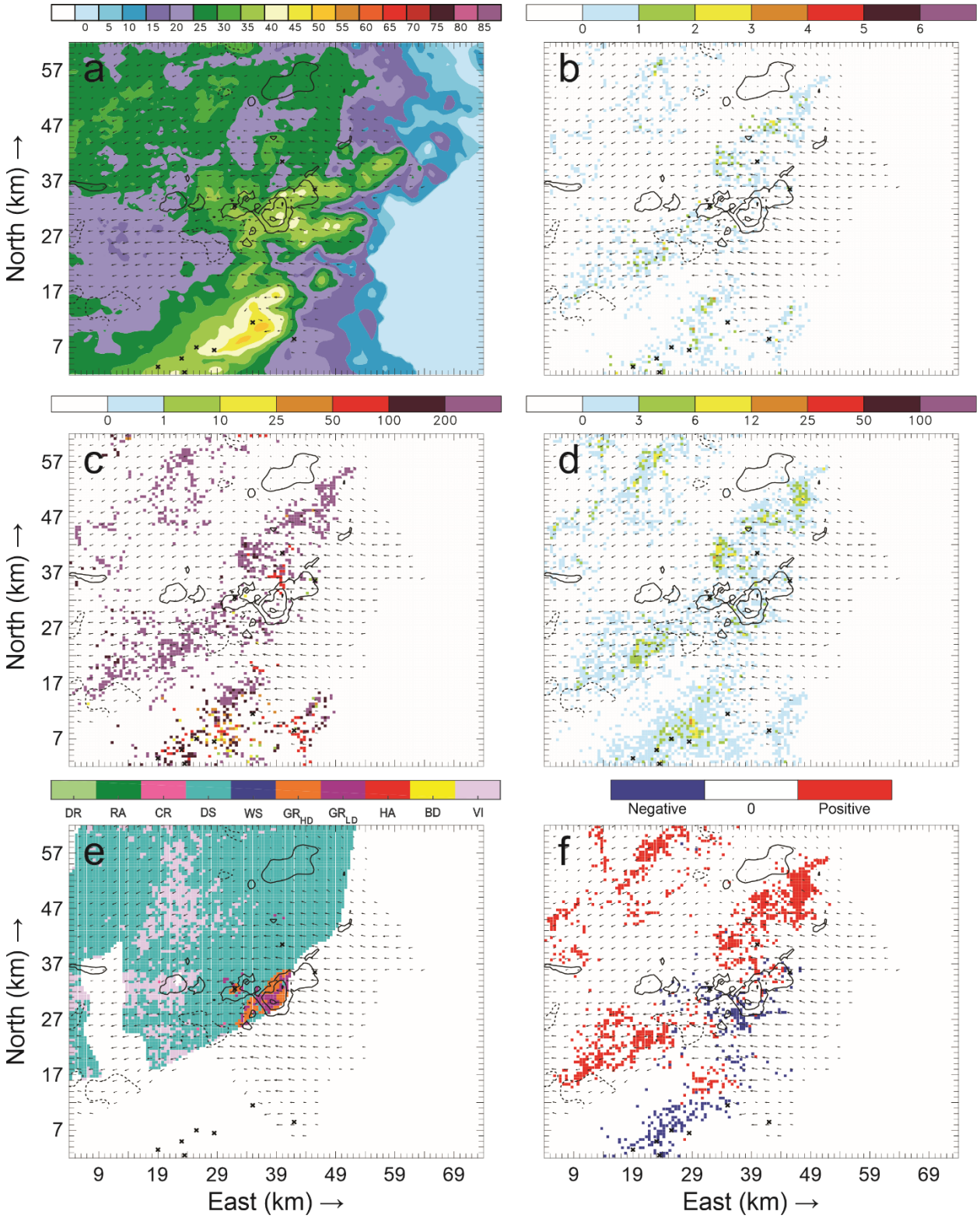

Figure 154: Horizontal cross-sections for 6 June 21:15 UTC. As in Figure 153, but taken at 5.7 km AGL.

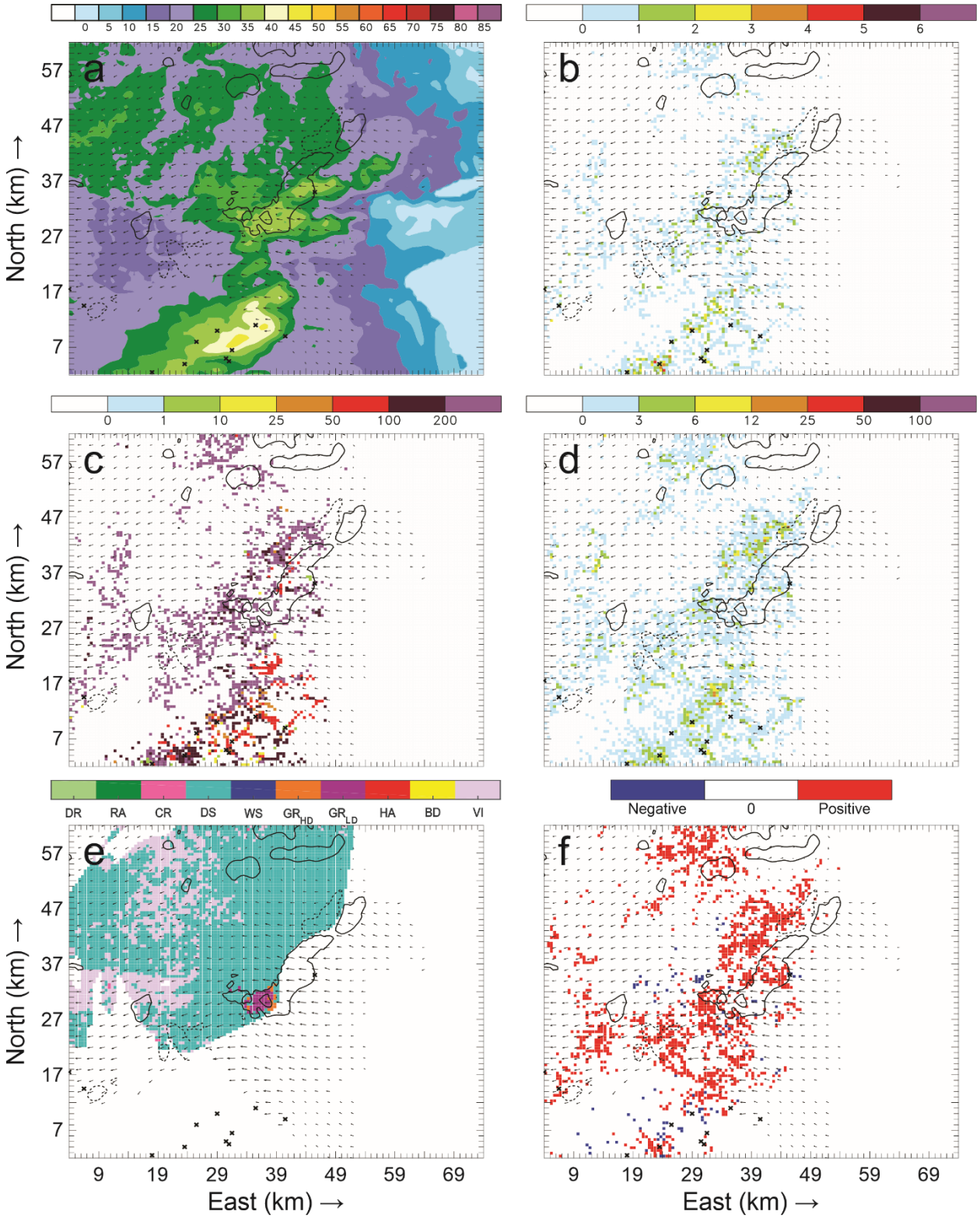

Figure 155: Horizontal cross-sections for 6 June 21:15 UTC. As in Figure 153, but taken at 6.7 km AGL.

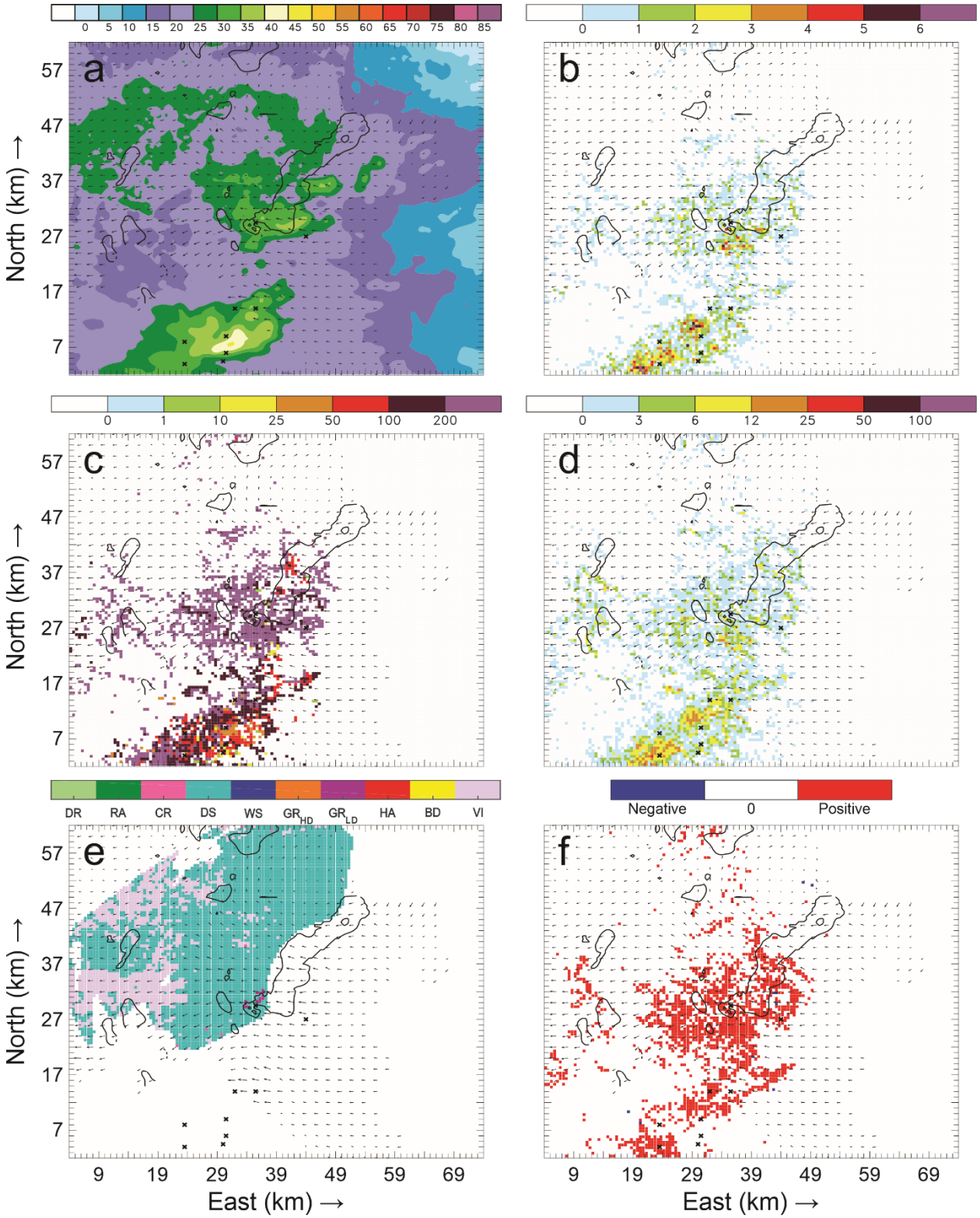

Figure 156: Horizontal cross-sections for 6 June 21:15 UTC. As in Figure 153, but taken at 7.7 km AGL.

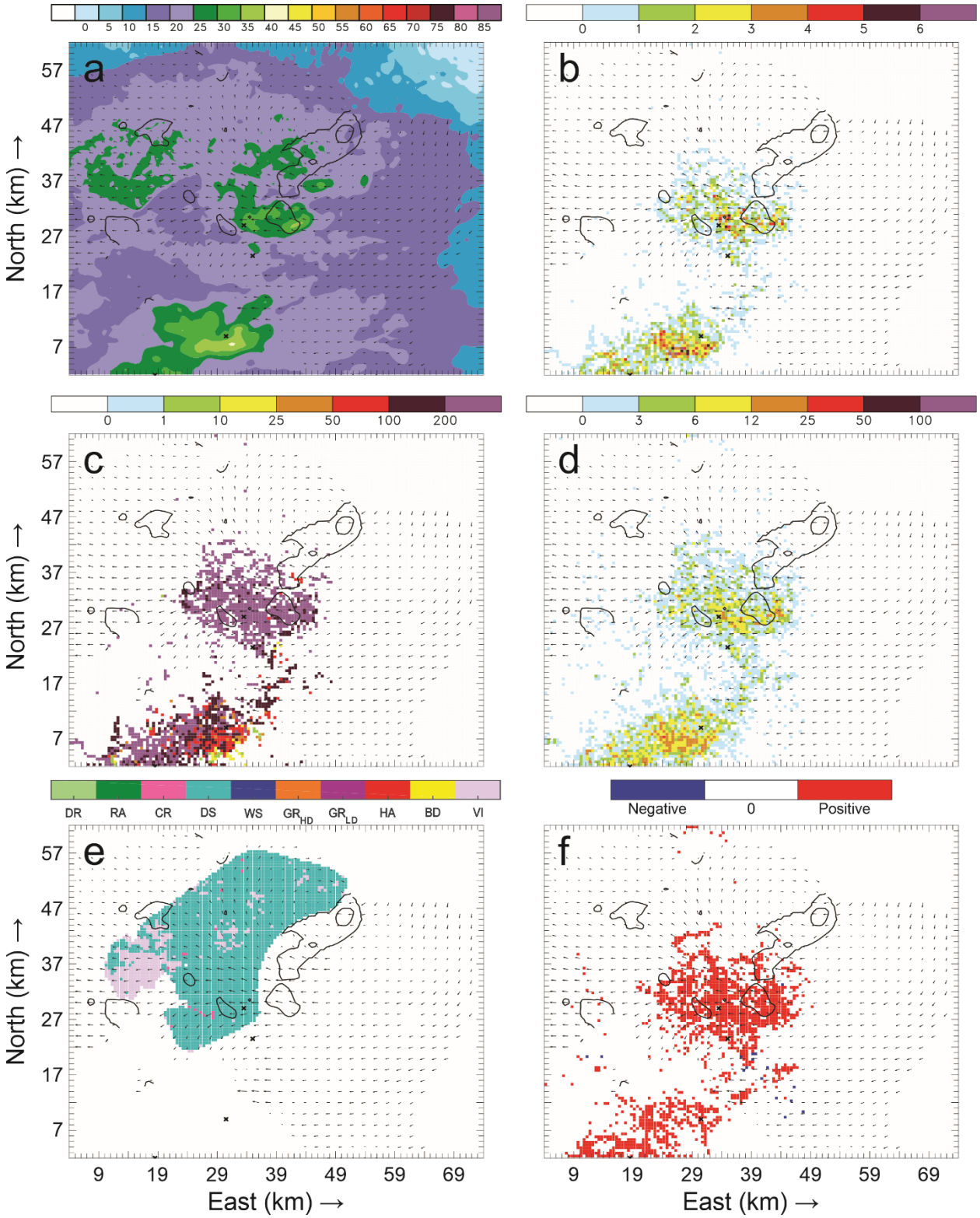

Figure 157: Horizontal cross-sections for 6 June 21:15 UTC. As in Figure 153, but taken at 8.7 km AGL.

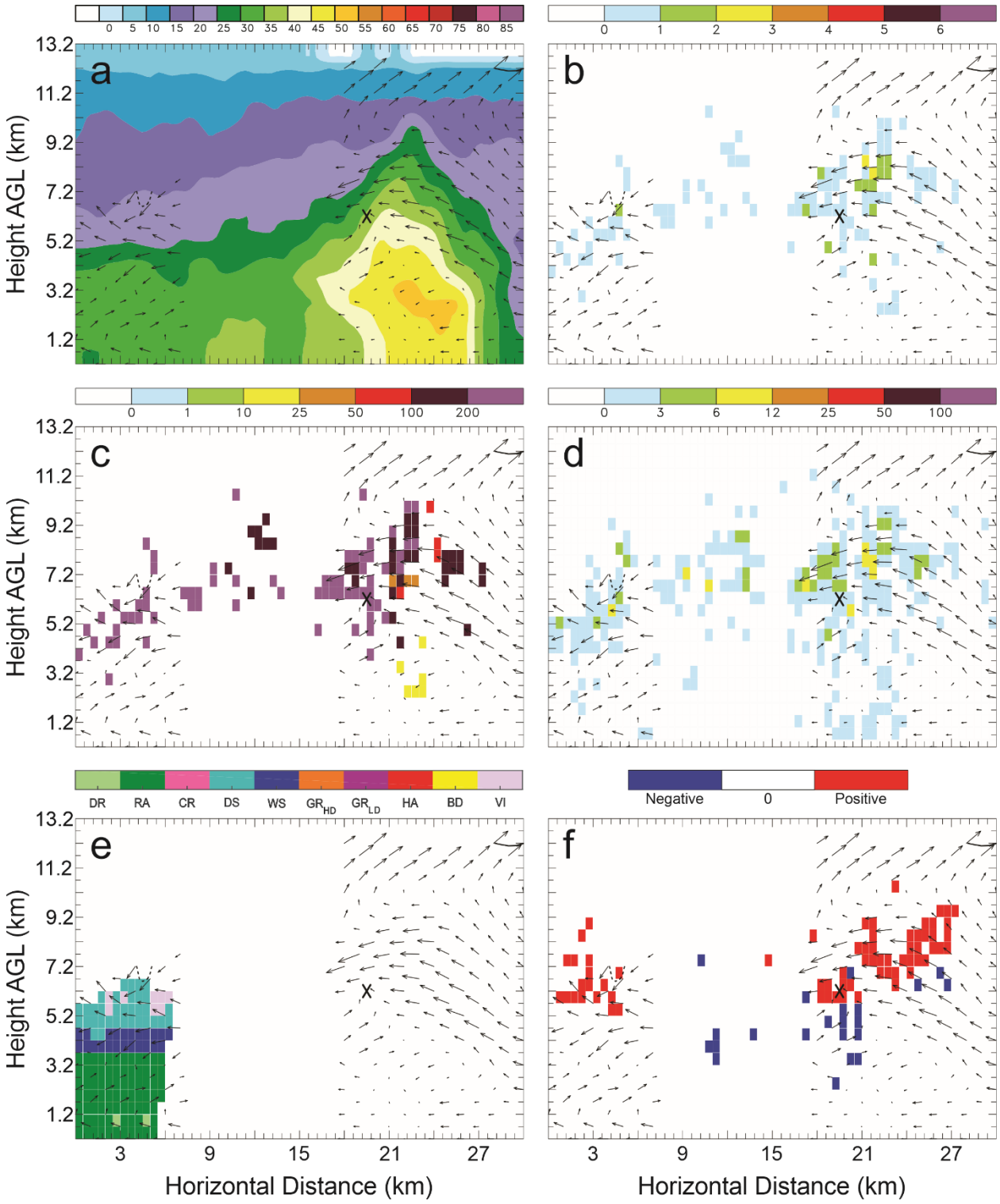

Figure 158: Vertical cross-sections for 6 June 21:15 UTC taken along the southernmost line in Figure 132(c) of: a) color-filled Z and w contours (every 10 m s^{-1} starting at 5 m s^{-1}); b) color-filled FED and w contours; c) color-filled FP and w contours; d) color-filled SD and w contours; e) color-filled HCA and w contours; and f) color-filled net inferred space charge and w contours. All figures have the same horizontal storm-relative wind vectors, and black X's denote grid cells with FID > 0.

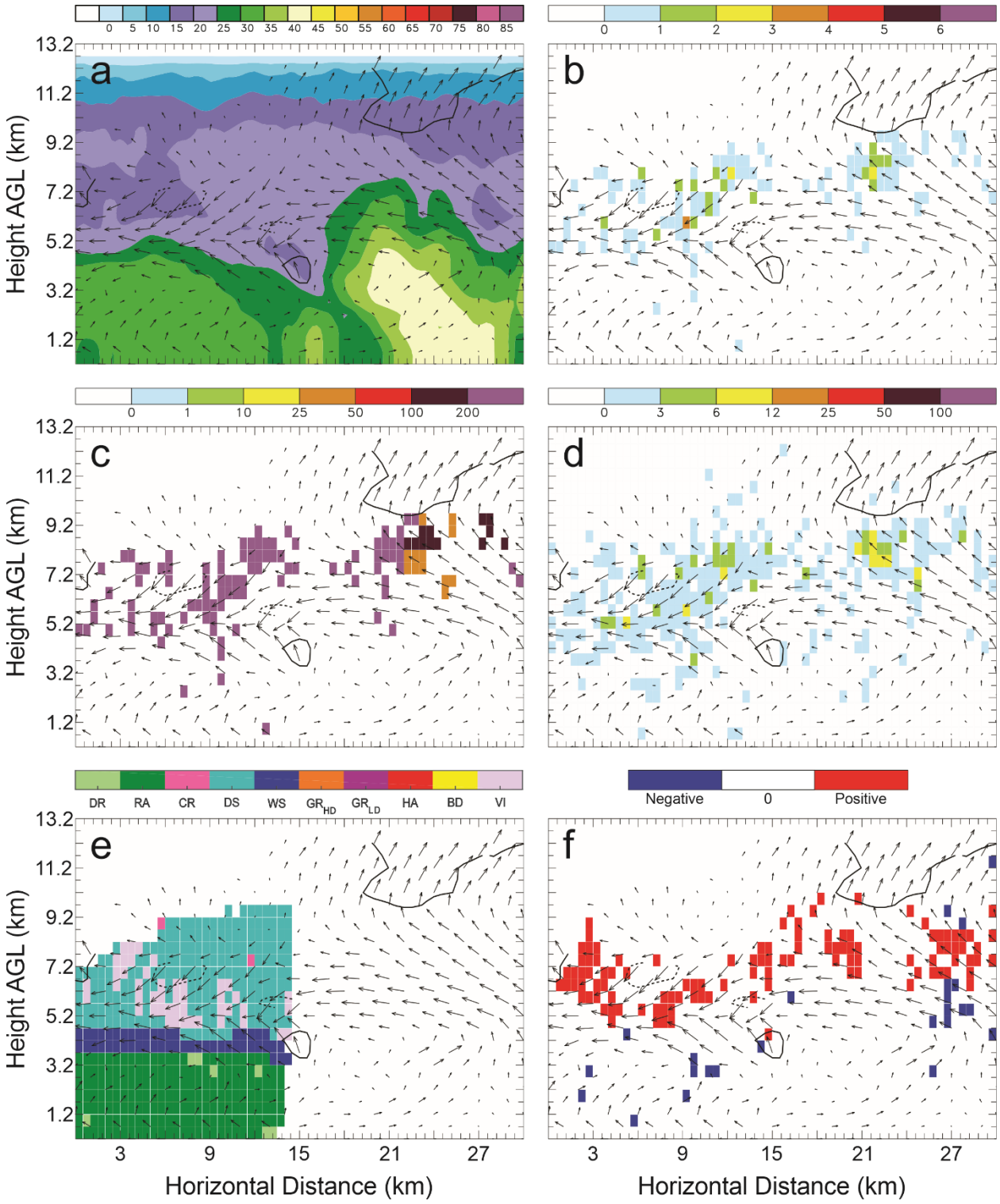

Figure 159: Vertical cross-sections for 6 June 21:15 UTC. As in Figure 158, but taken along the second line from the south in Figure 132(c).

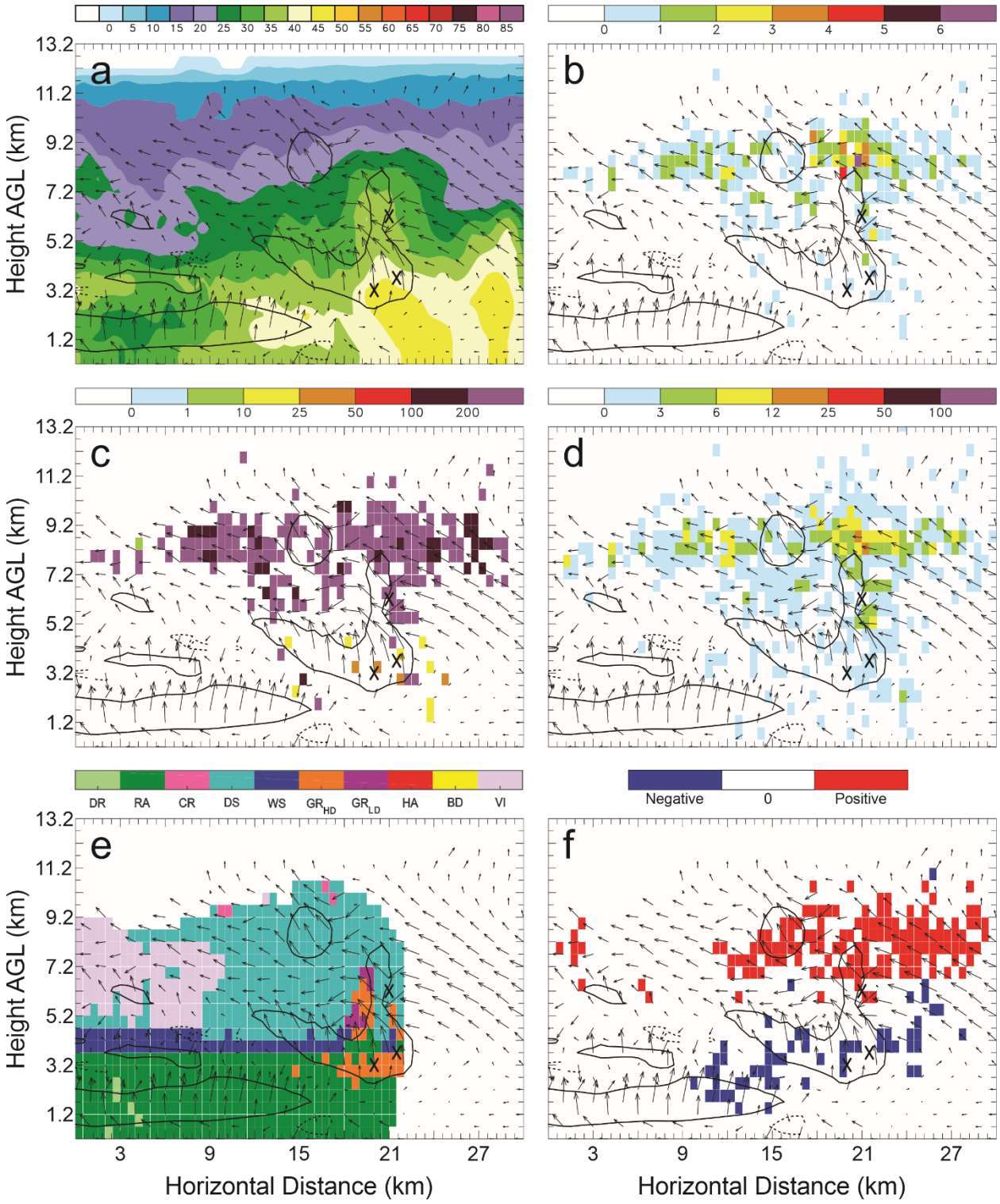

Figure 160: Vertical cross-sections for 6 June 21:15 UTC. As in Figure 158, but taken along the central line in Figure 132(c).

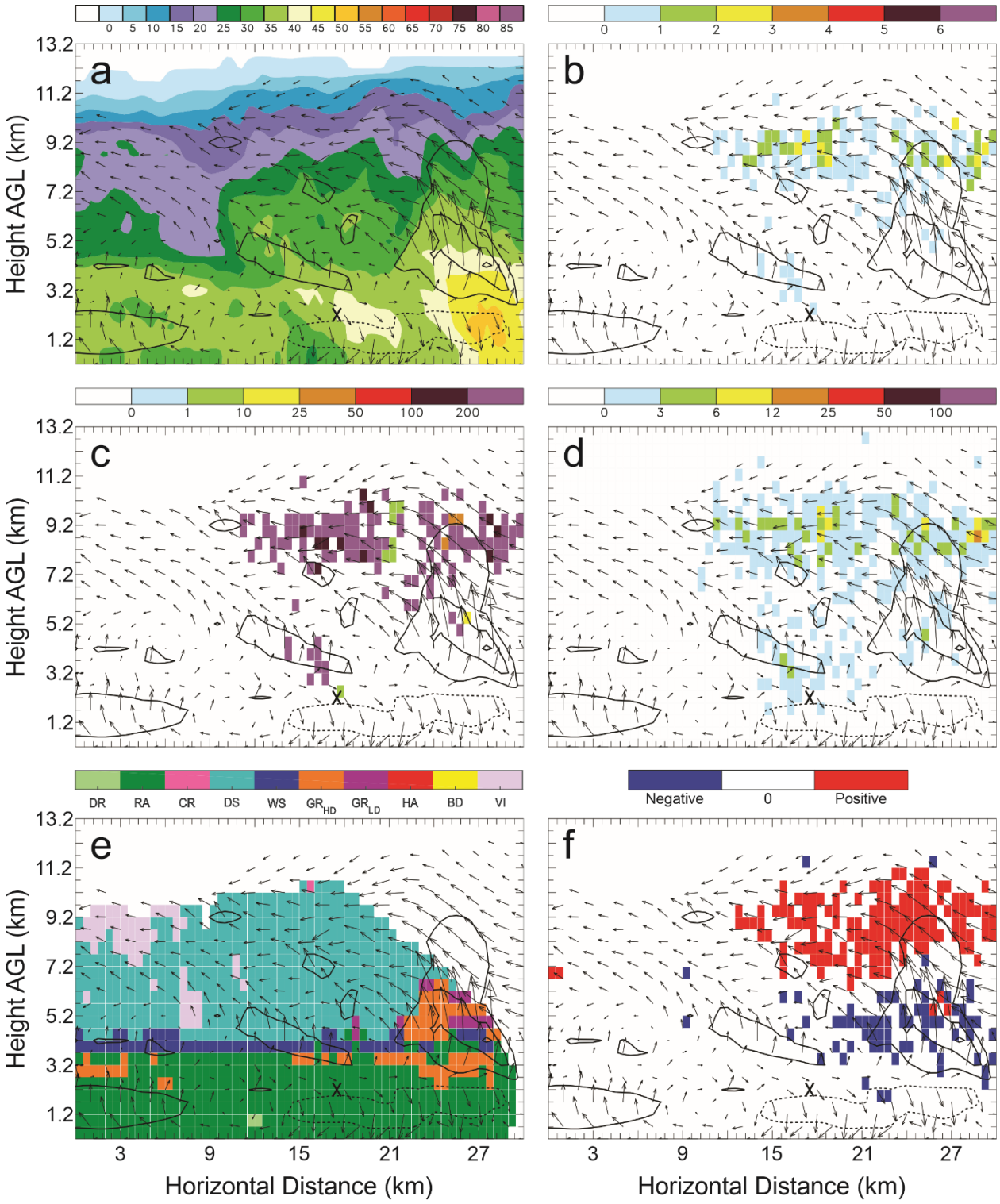

Figure 161: Vertical cross-sections for 6 June 21:15 UTC. As in Figure 158, but taken along the second line from the north in Figure 132(c).

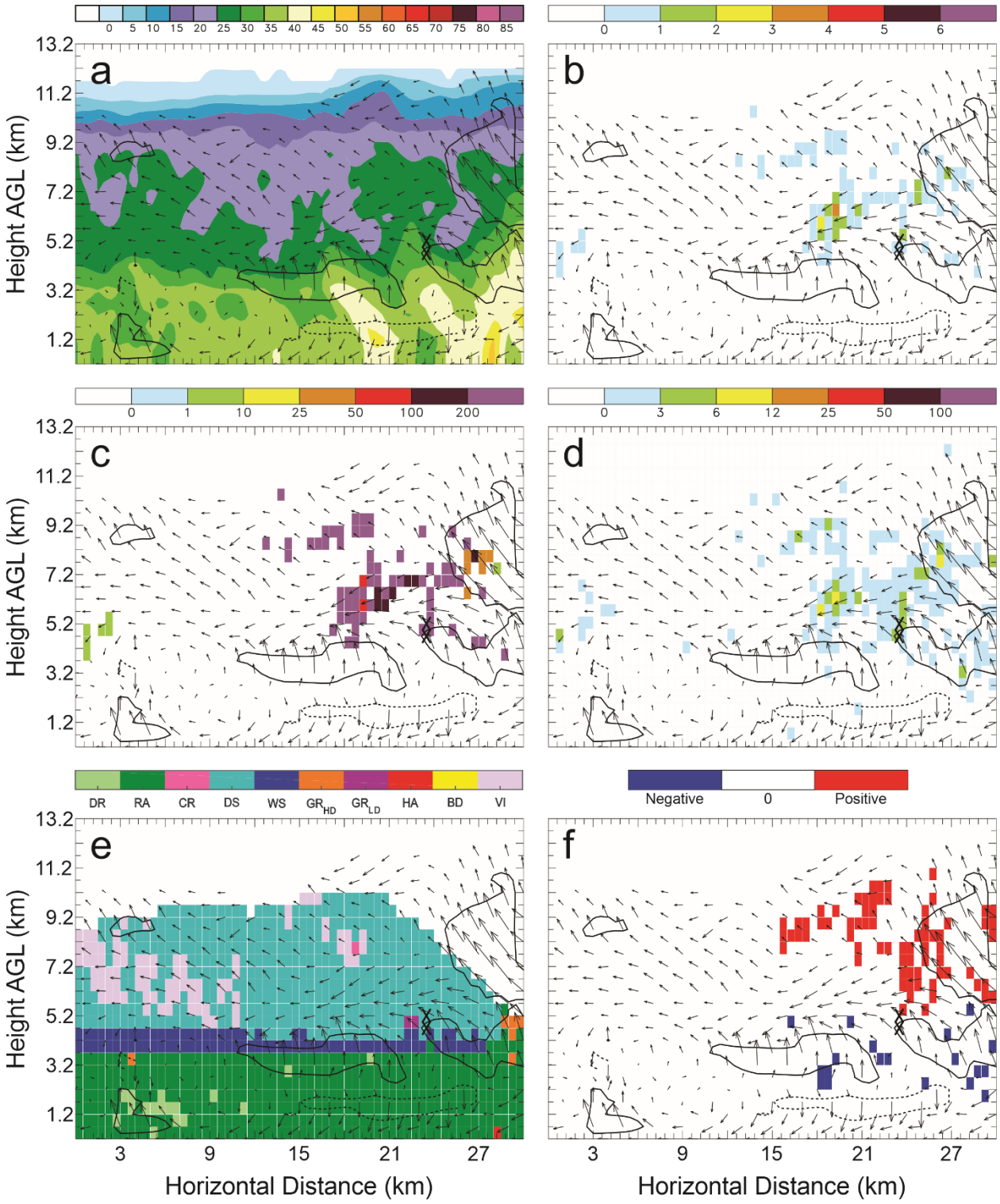

Figure 162: Vertical cross-sections for 6 June 21:15 UTC. As in Figure 158, but taken along the northernmost line in Figure 132(c).

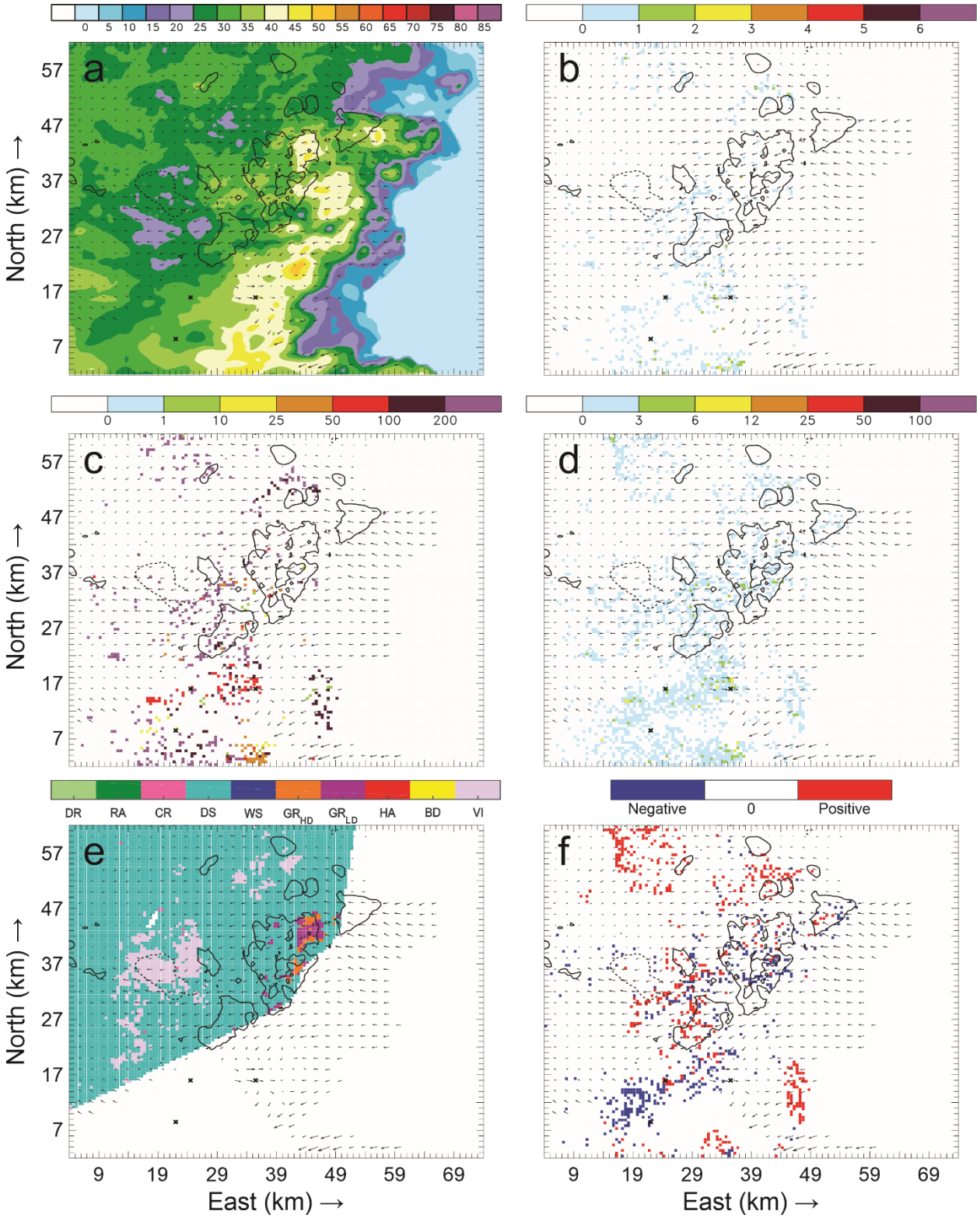

Figure 163: Horizontal cross-sections for 6 June 21:27 UTC taken at 4.7 km AGL of: a) color-filled Z and w contours (every 10 m s^{-1} starting at 5 m s^{-1}); b) color-filled FED and w contours; c) color-filled FP and w contours; d) color-filled SD and w contours; e) color-filled HCA and w contours; and f) color-filled net inferred space charge and w contours. All figures have the same horizontal storm-relative wind vectors, and black X's denote grid cells with FID > 0.

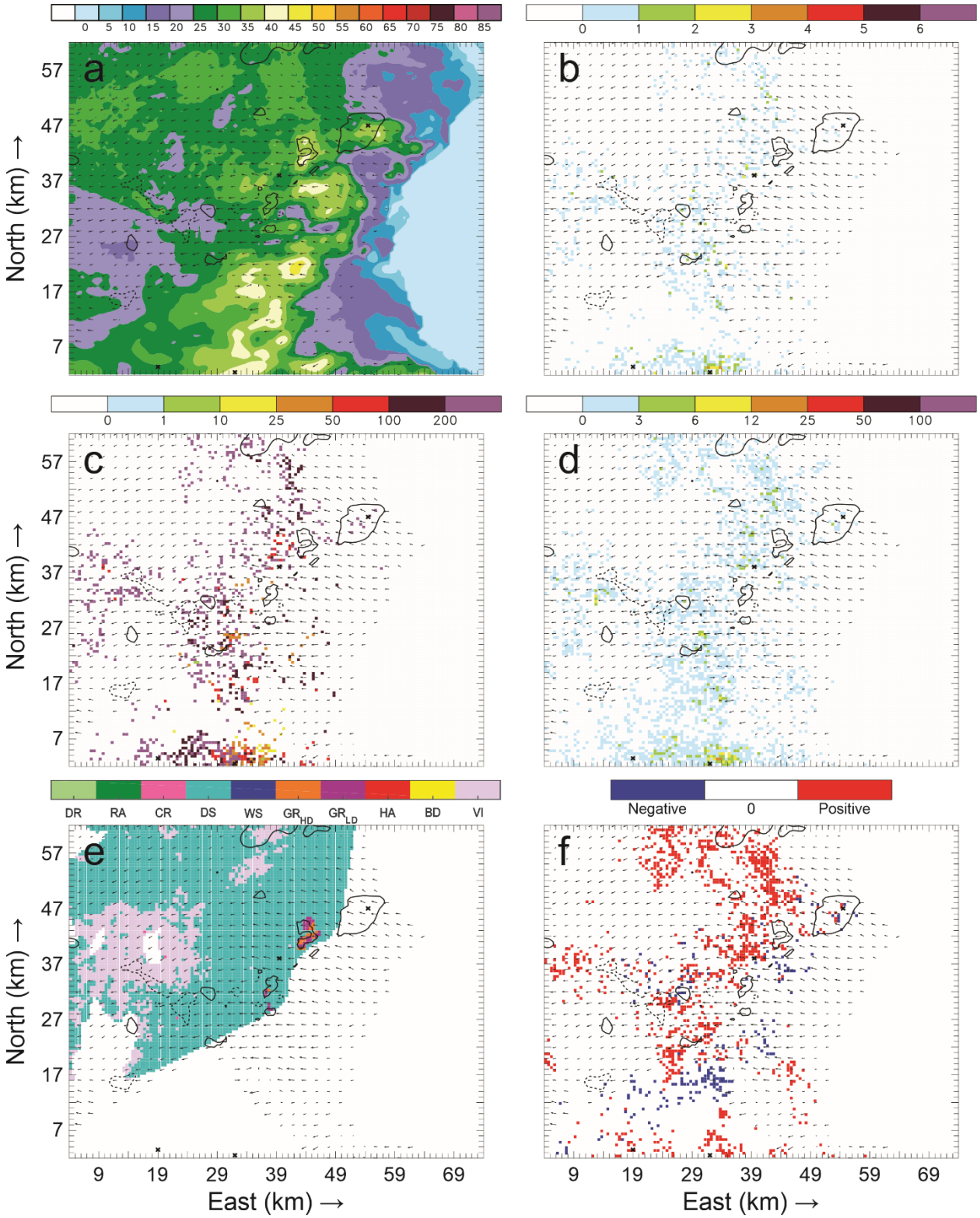

Figure 164: Horizontal cross-sections for 6 June 21:27 UTC. As in Figure 163, but taken at 5.7 km AGL.

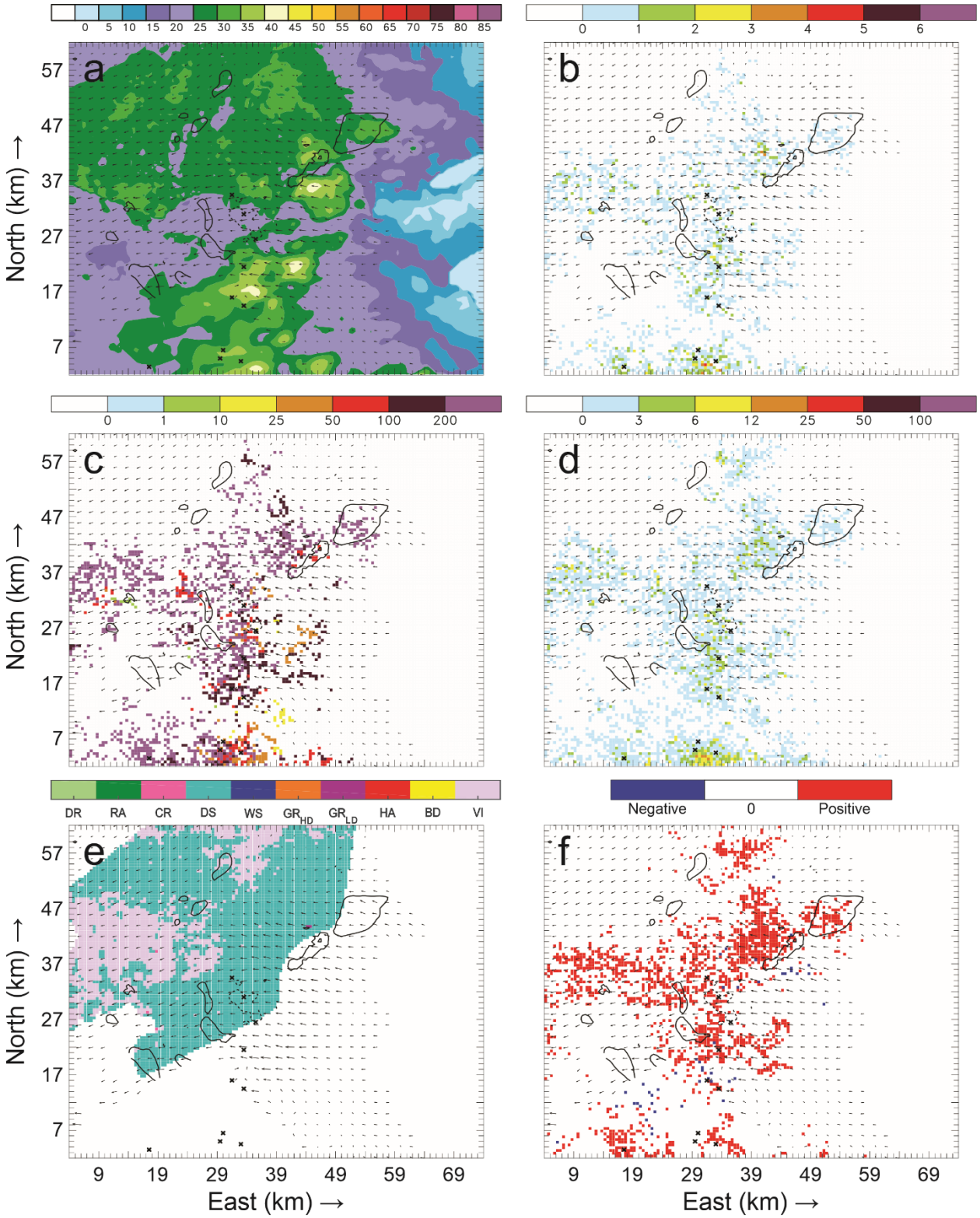

Figure 165: Horizontal cross-sections for 6 June 21:27 UTC. As in Figure 163, but taken at 6.7 km AGL.

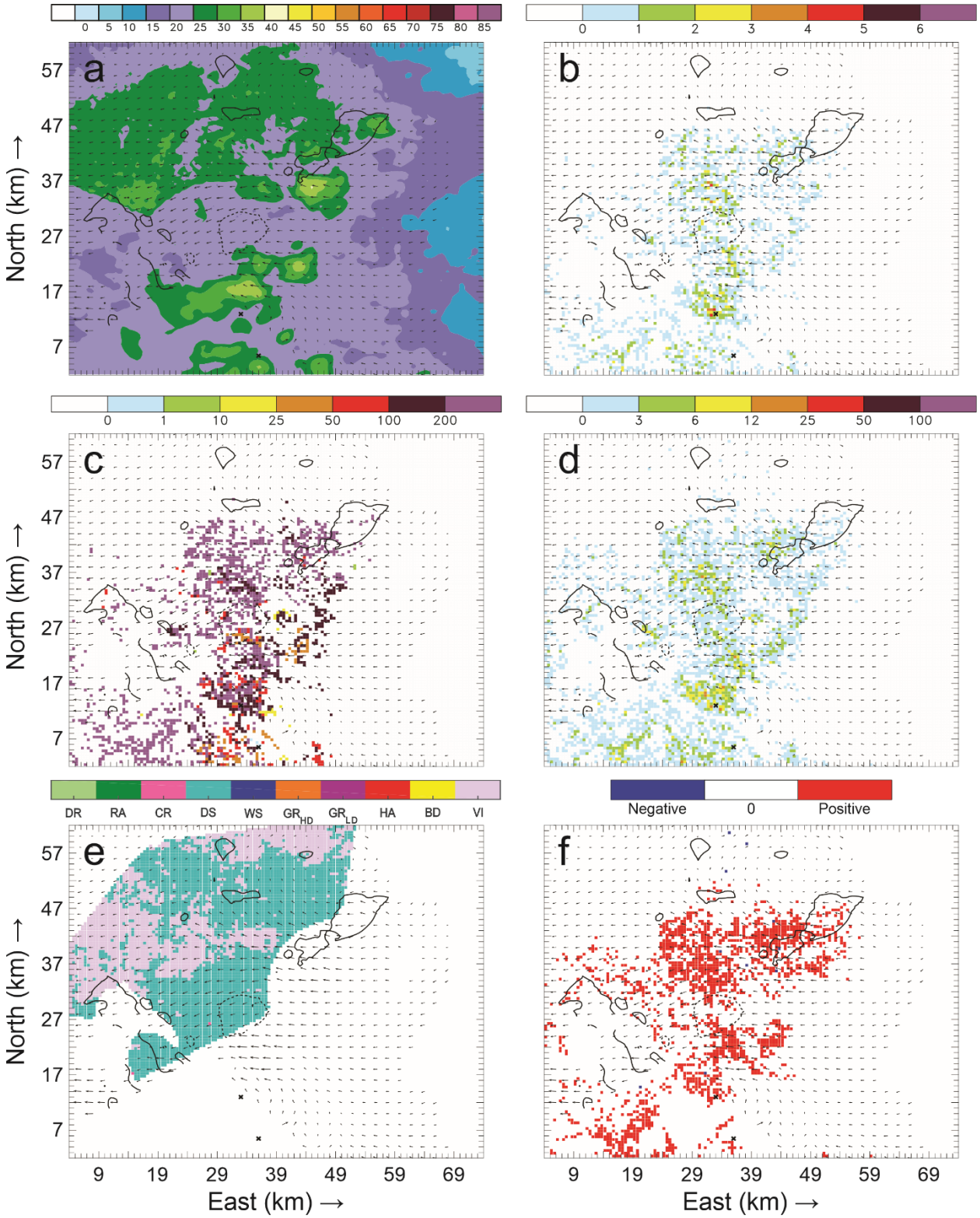

Figure 166: Horizontal cross-sections for 6 June 21:27 UTC. As in Figure 163, but taken at 7.7 km AGL.

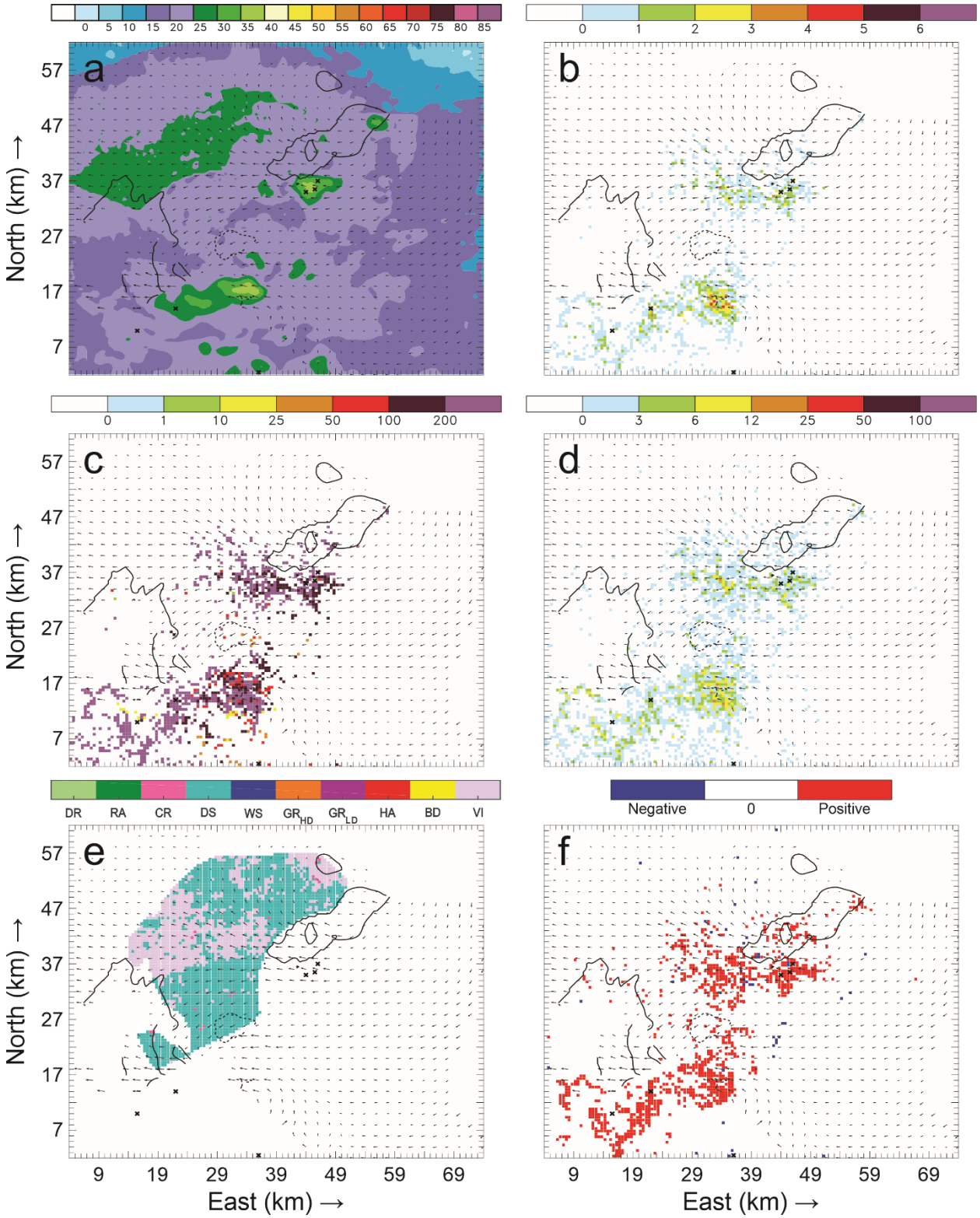

Figure 167: Horizontal cross-sections for 6 June 21:27 UTC. As in Figure 163, but taken at 8.7 km AGL.

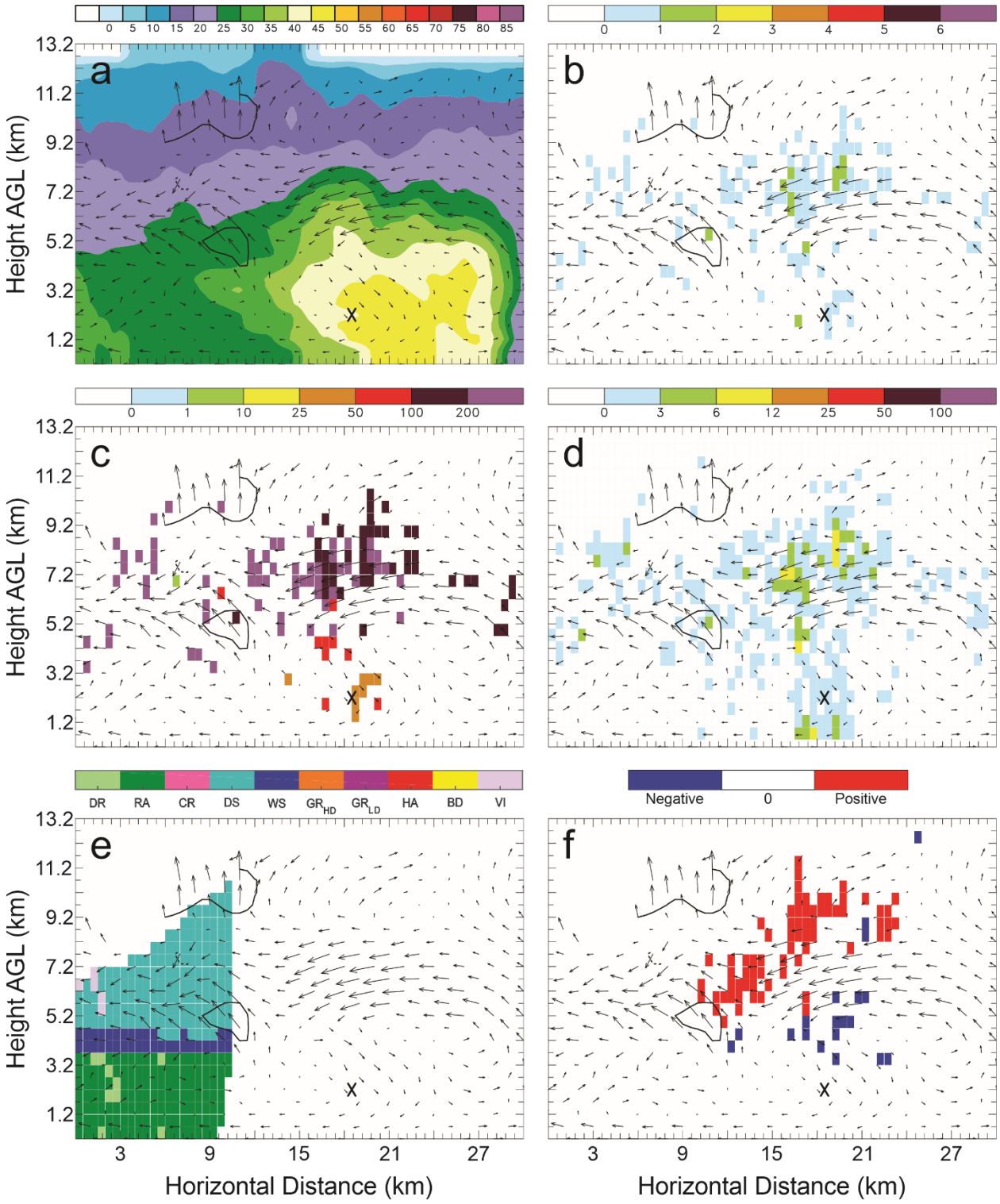

Figure 168: Vertical cross-sections for 6 June 21:27 UTC taken along the southernmost line in Figure 132(d) of: a) color-filled Z and w contours (every 10 m s^{-1} starting at 5 m s^{-1}); b) color-filled FED and w contours; c) color-filled FP and w contours; d) color-filled SD and w contours; e) color-filled HCA and w contours; and f) color-filled net inferred space charge and w contours. All figures have the same horizontal storm-relative wind vectors, and black X's denote grid cells with FID > 0.

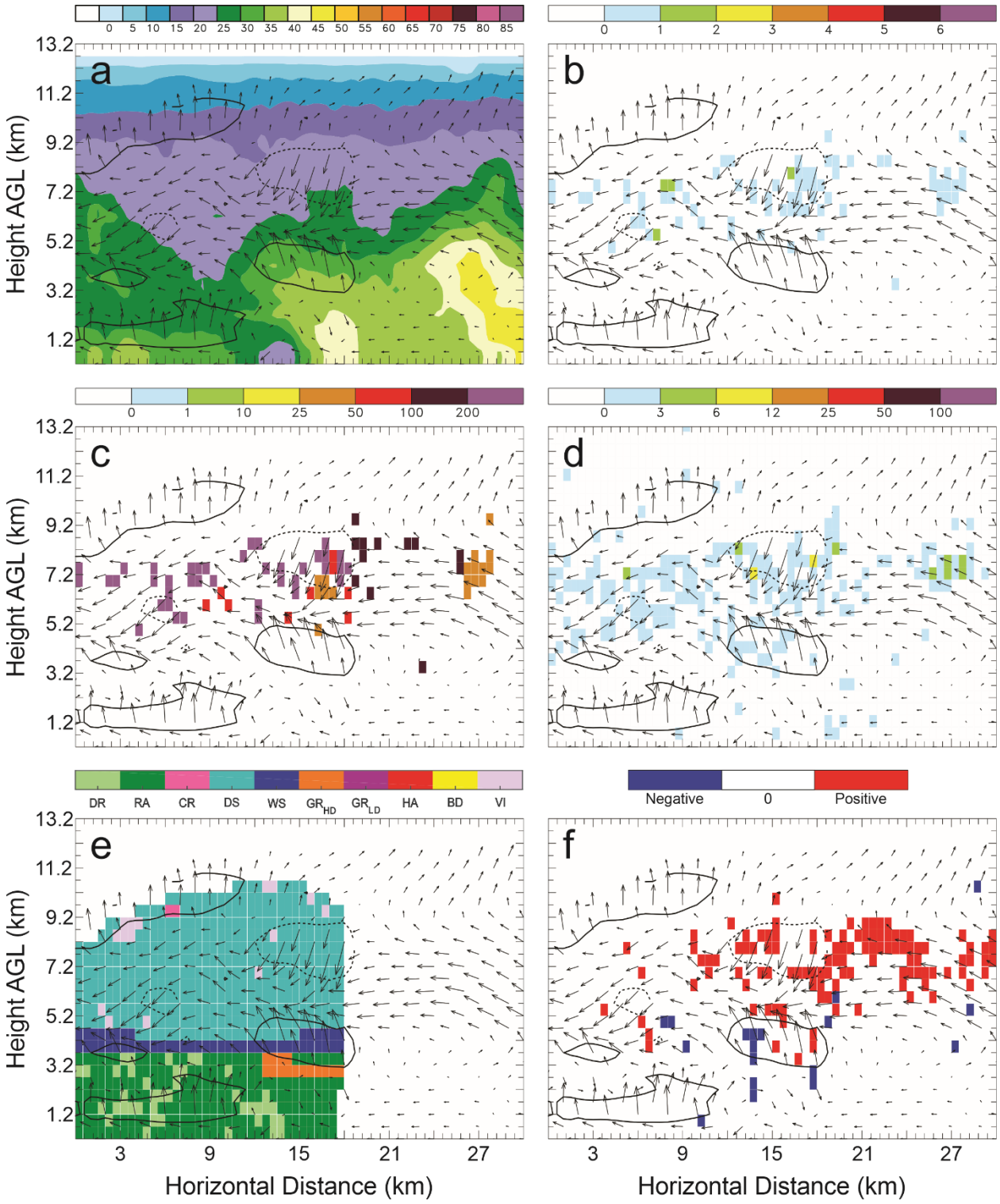

Figure 169: Vertical cross-sections for 6 June 21:27 UTC. As in Figure 168, but taken along the second line from the south in Figure 132(d).

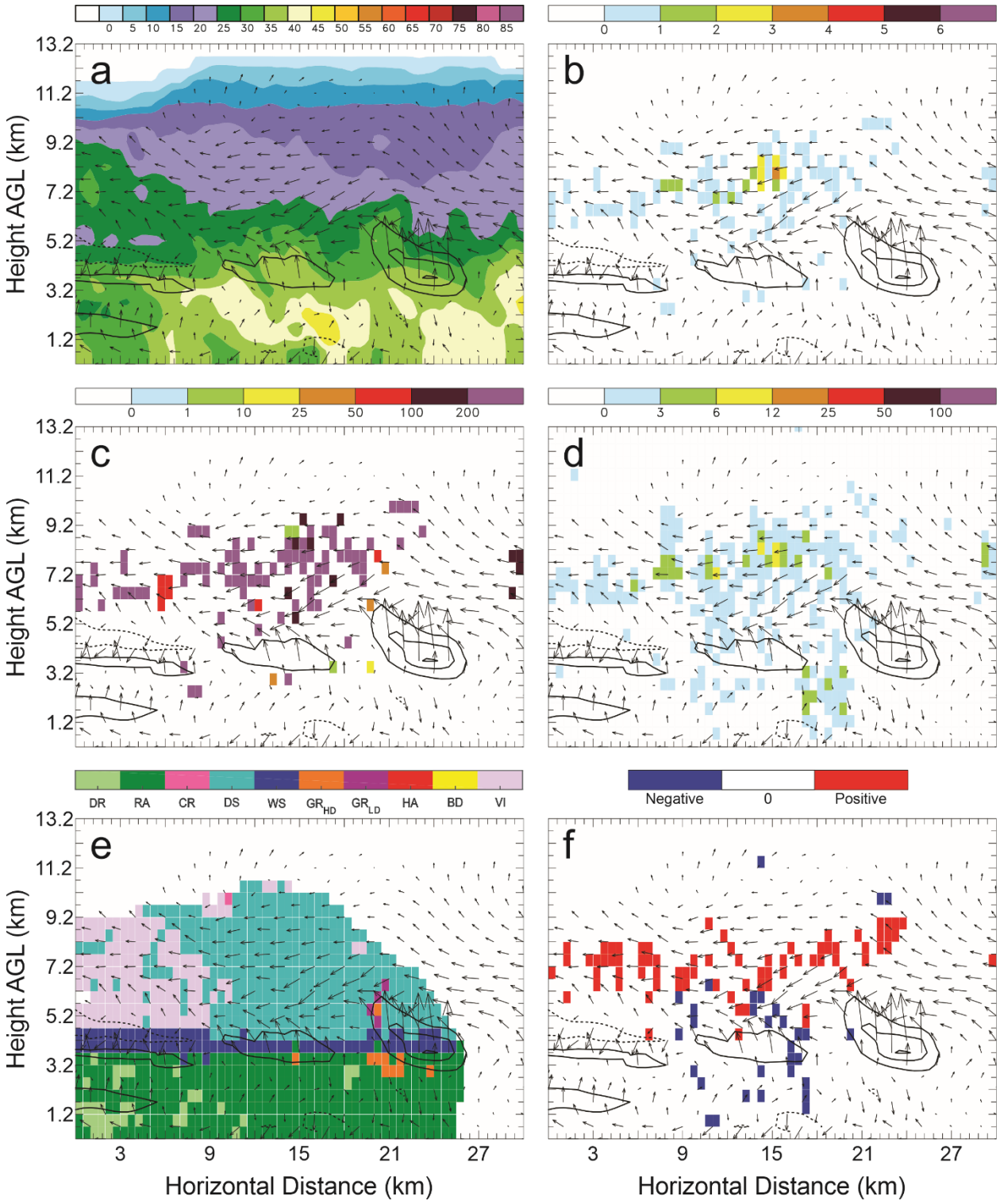

Figure 170: Vertical cross-sections for 6 June 21:27 UTC. As in Figure 168, but taken along the central line in Figure 132(d).

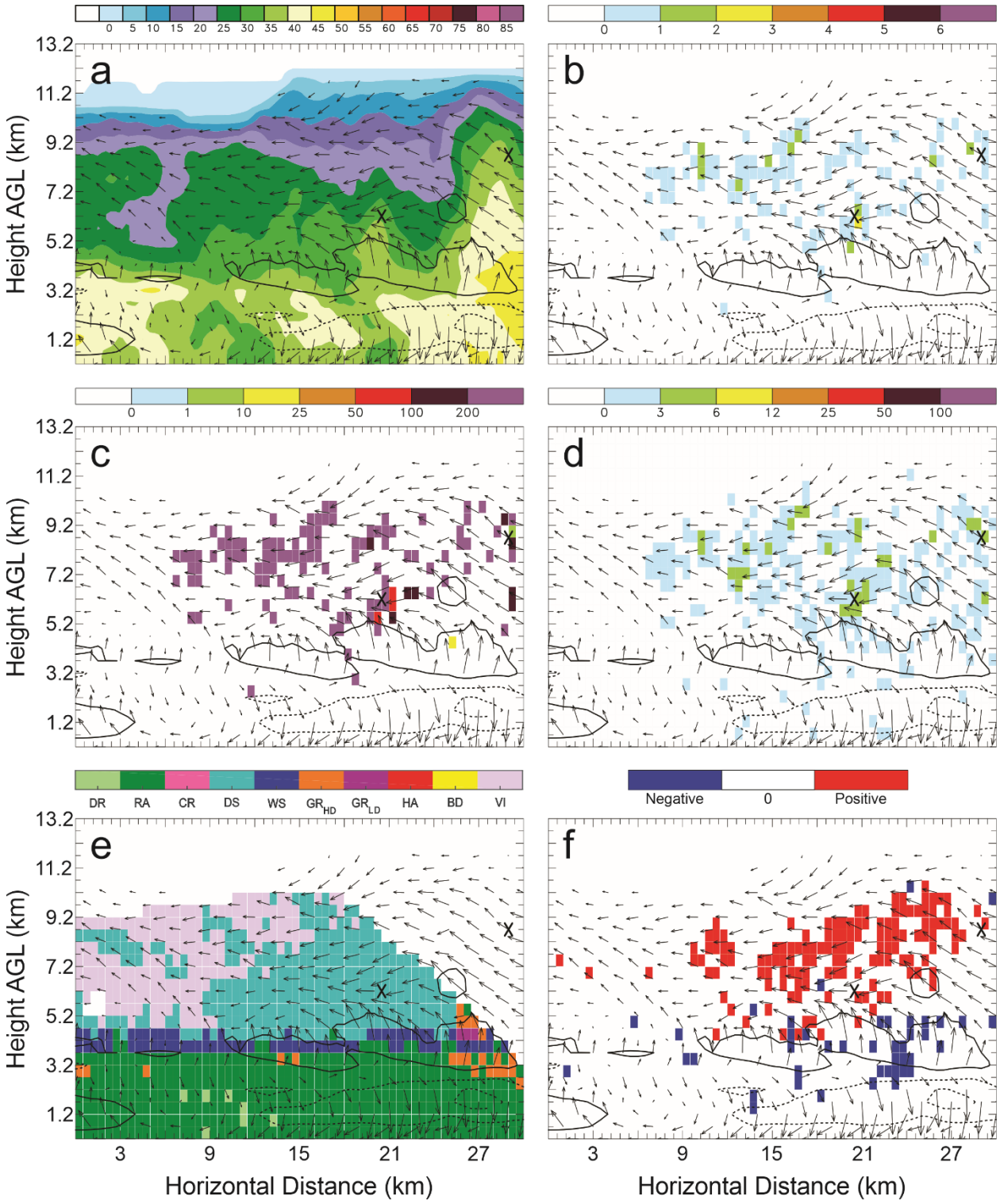

Figure 171: Vertical cross-sections for 6 June 21:27 UTC. As in Figure 168, but taken along the second line from the north in Figure 132(d).

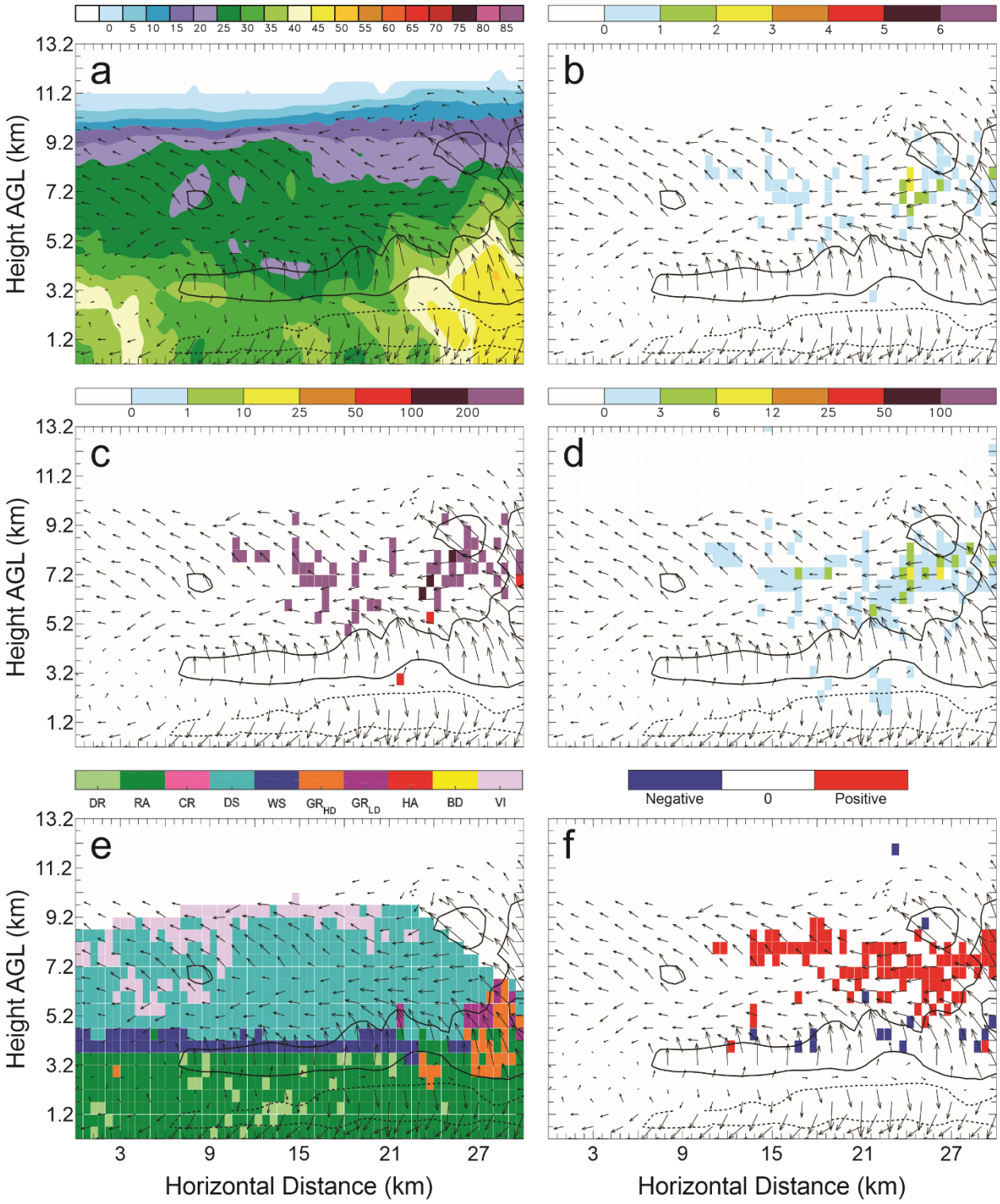

Figure 172: Vertical cross-sections for 6 June 21:27 UTC. As in Figure 168, but taken along the northernmost line in Figure 132(d).

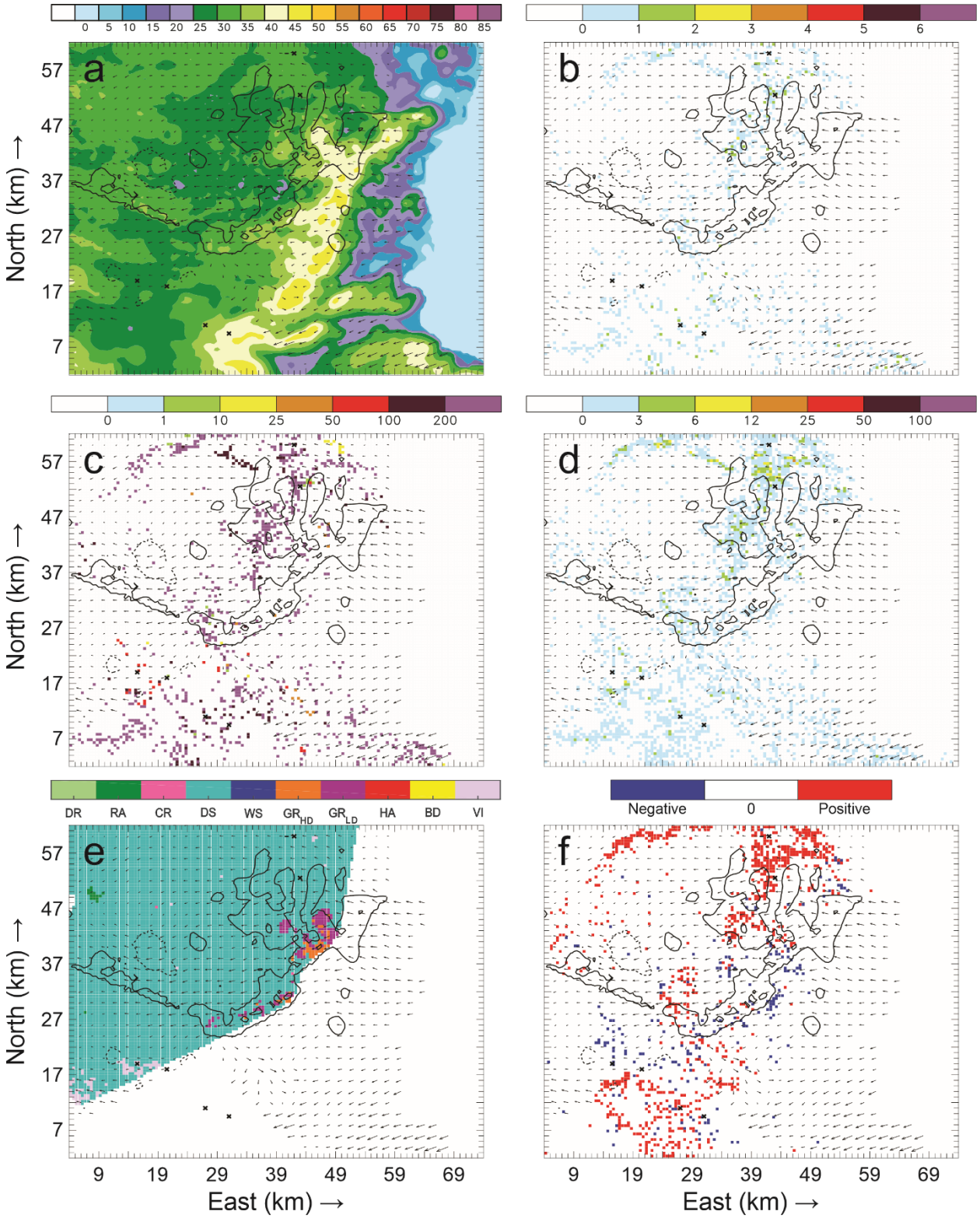

Figure 173: Horizontal cross-sections for 6 June 21:39 UTC taken at 4.7 km AGL of: a) color-filled Z and w contours (every 10 m s^{-1} starting at 5 m s^{-1}); b) color-filled FED and w contours; c) color-filled FP and w contours; d) color-filled SD and w contours; e) color-filled HCA and w contours; and f) color-filled net inferred space charge and w contours. All figures have the same horizontal storm-relative wind vectors, and black X's denote grid cells with FID > 0.

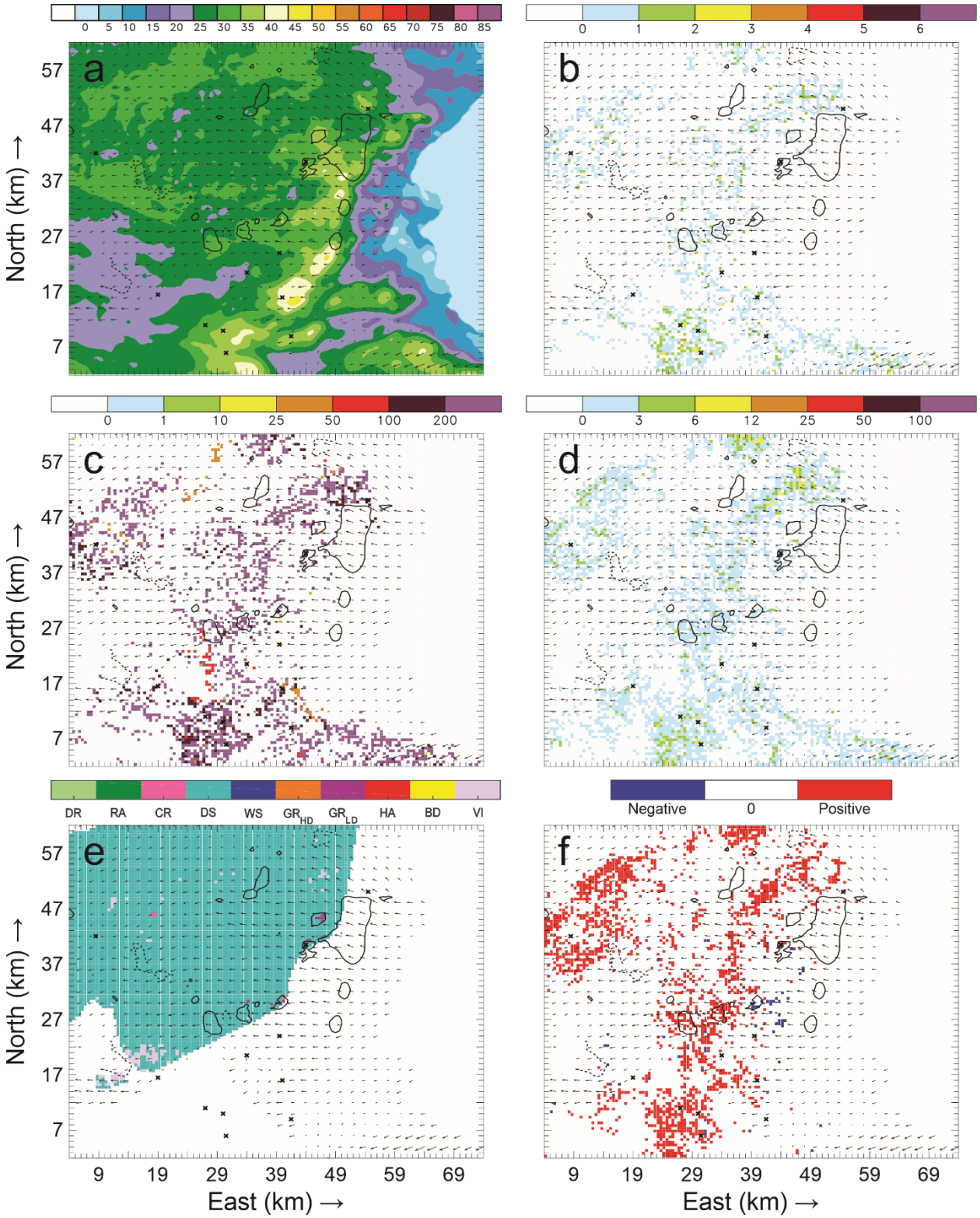

Figure 174: Horizontal cross-sections for 6 June 21:39 UTC. As in Figure 173, but taken at 5.7 km AGL.

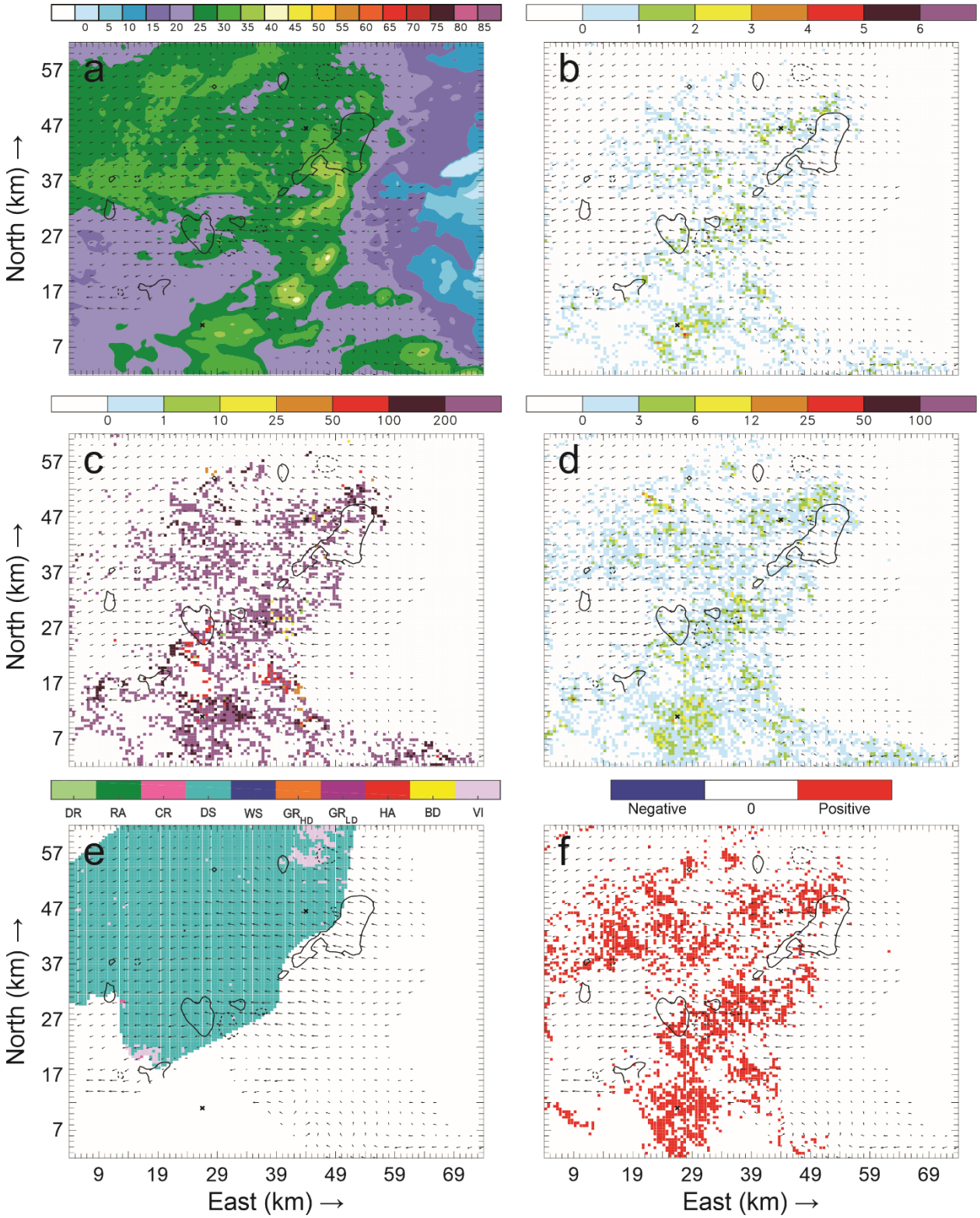

Figure 175: Horizontal cross-sections for 6 June 21:39 UTC. As in Figure 173, but taken at 6.7 km AGL.

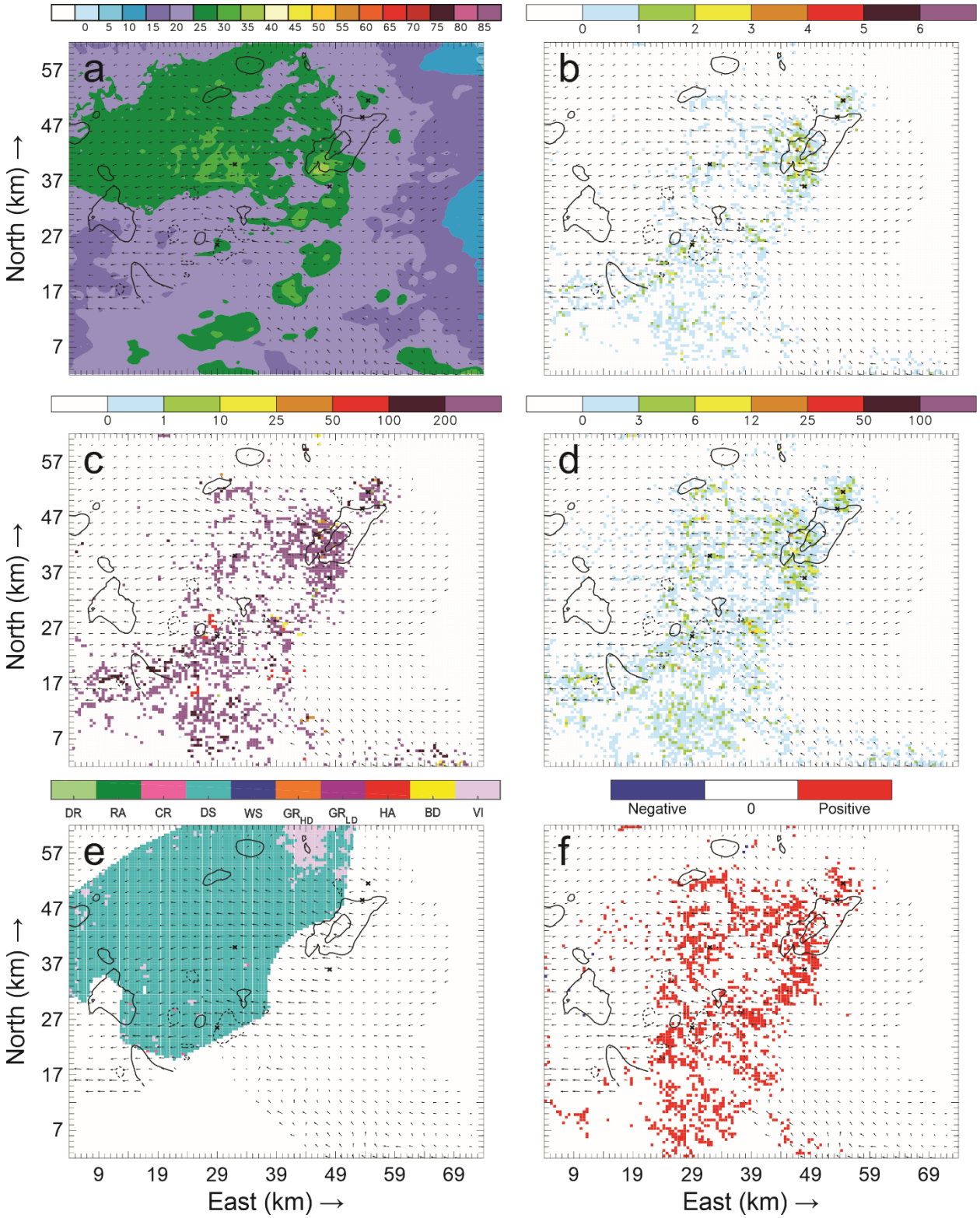

Figure 176: Horizontal cross-sections for 6 June 21:39 UTC. As in Figure 173, but taken at 7.7 km AGL.

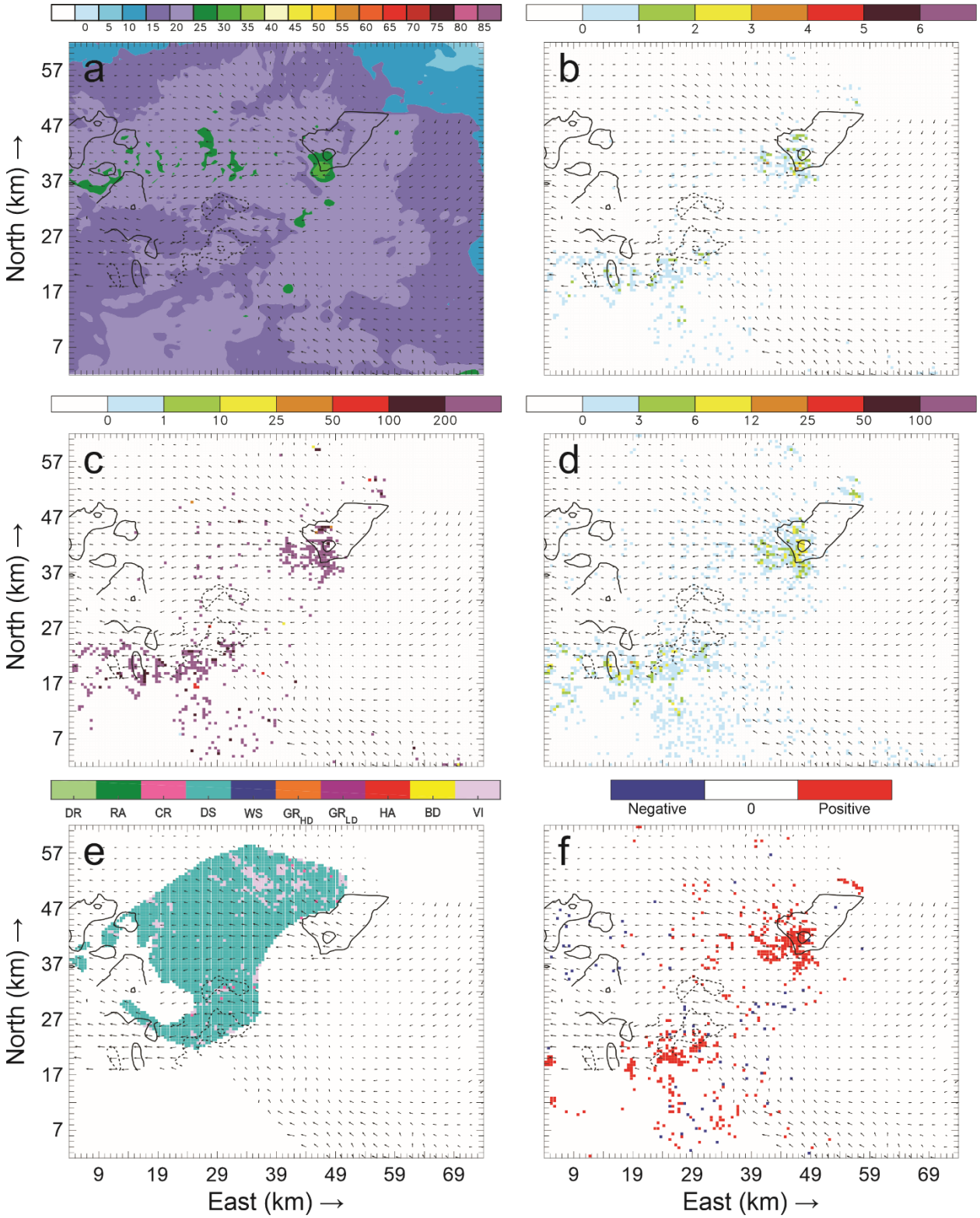

Figure 177: Horizontal cross-sections for 6 June 21:39 UTC. As in Figure 173, but taken at 8.7 km AGL.

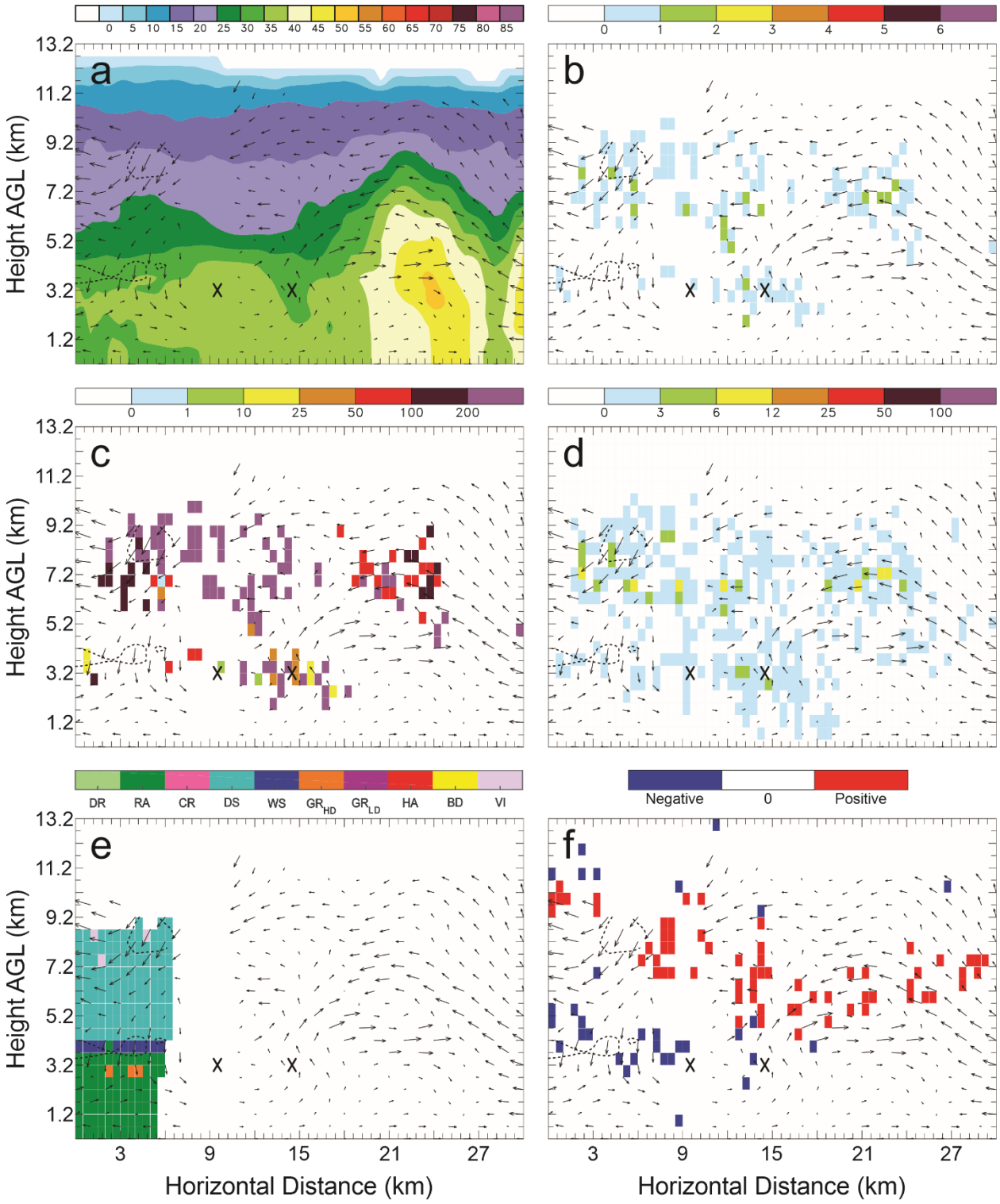

Figure 178: Vertical cross-sections for 6 June 21:39 UTC taken along the southernmost line in Figure 132(e) of: a) color-filled Z and w contours (every 10 m s^{-1} starting at 5 m s^{-1}); b) color-filled FED and w contours; c) color-filled FP and w contours; d) color-filled SD and w contours; e) color-filled HCA and w contours; and f) color-filled net inferred space charge and w contours. All figures have the same horizontal storm-relative wind vectors, and black X's denote grid cells with FID > 0.

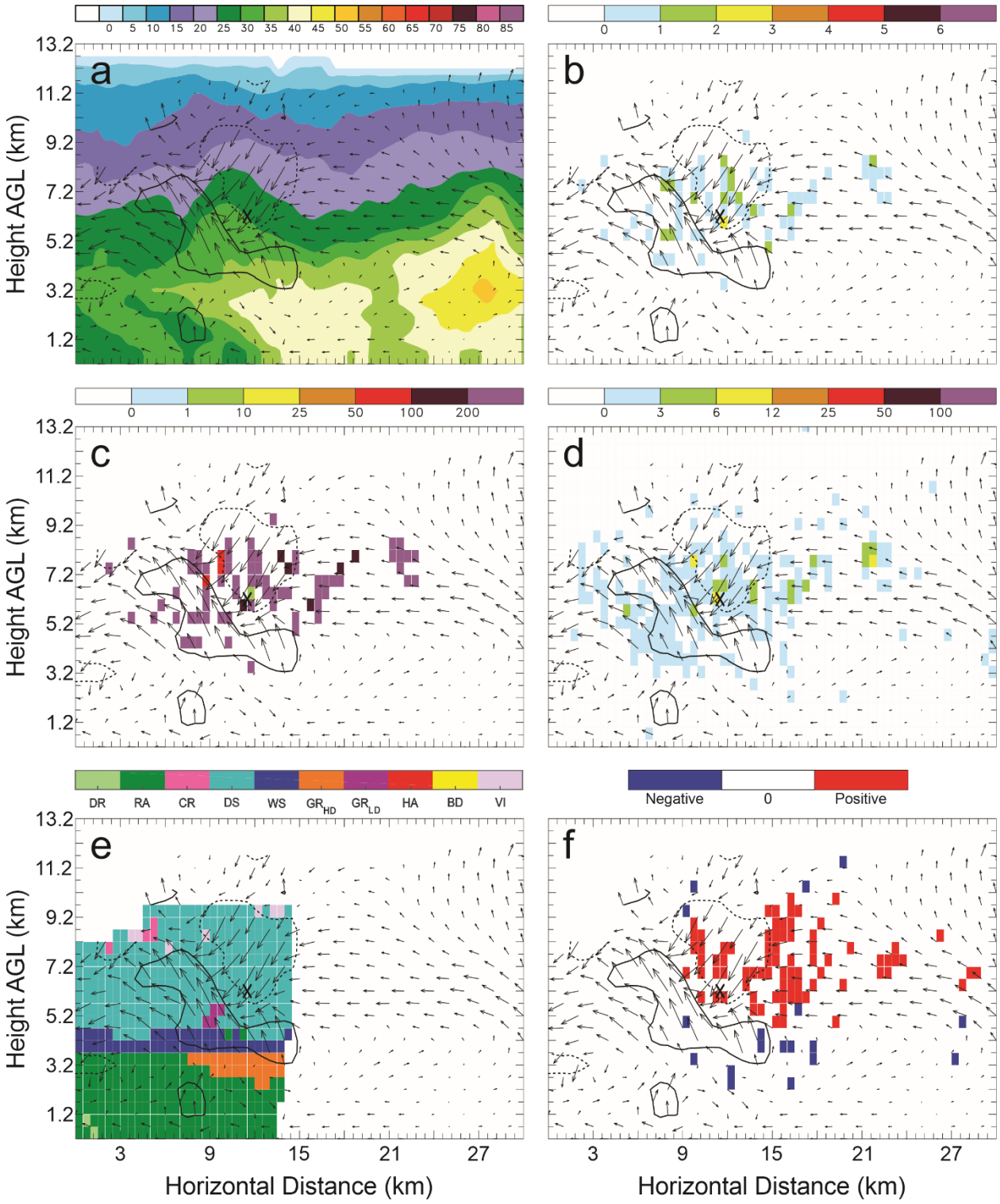

Figure 179: Vertical cross-sections for 6 June 21:39 UTC. As in Figure 178, but taken along the second line from the south in Figure 132(e).

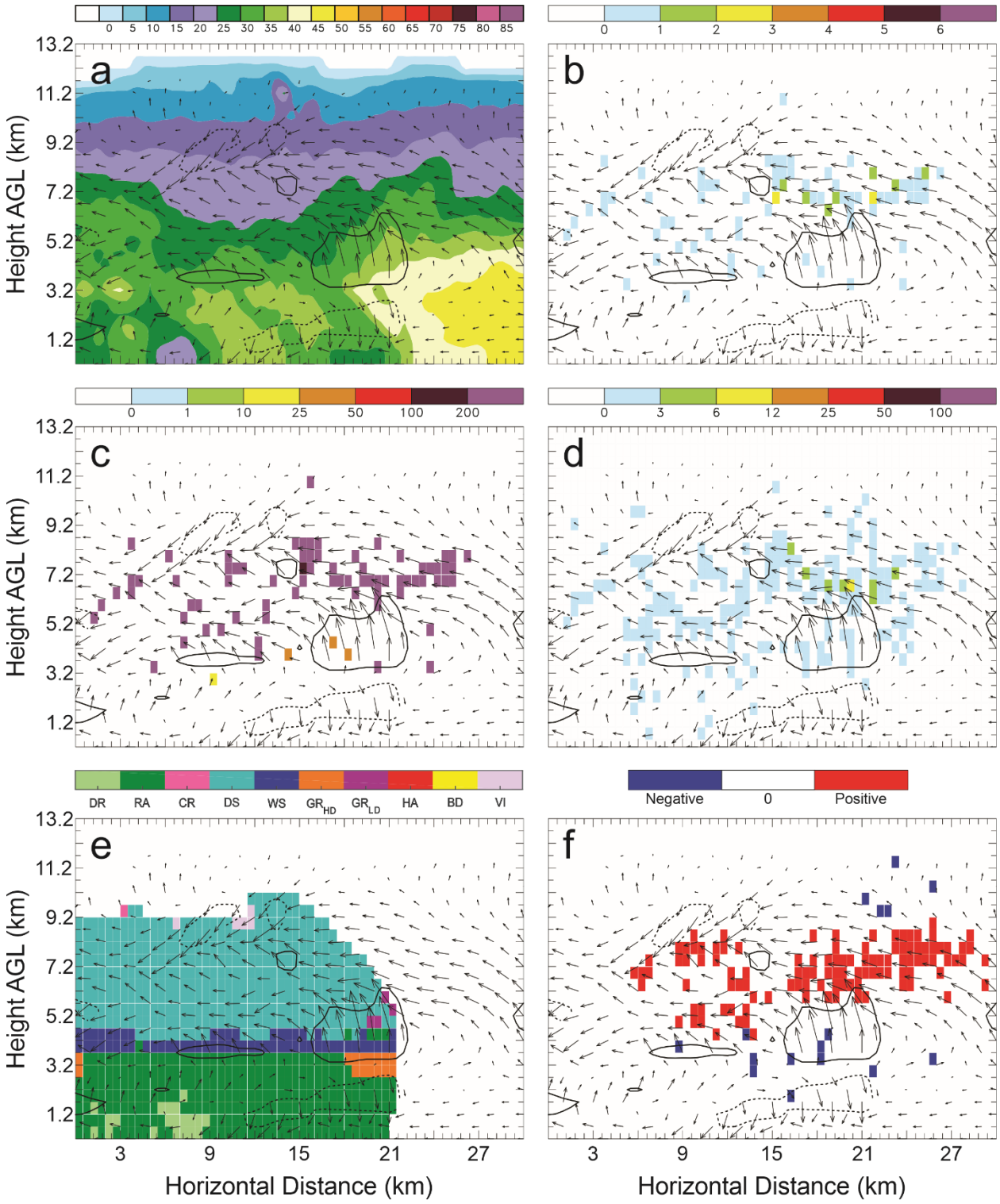

Figure 180: Vertical cross-sections for 6 June 21:39 UTC. As in Figure 178, but taken along the central line in Figure 132(e).

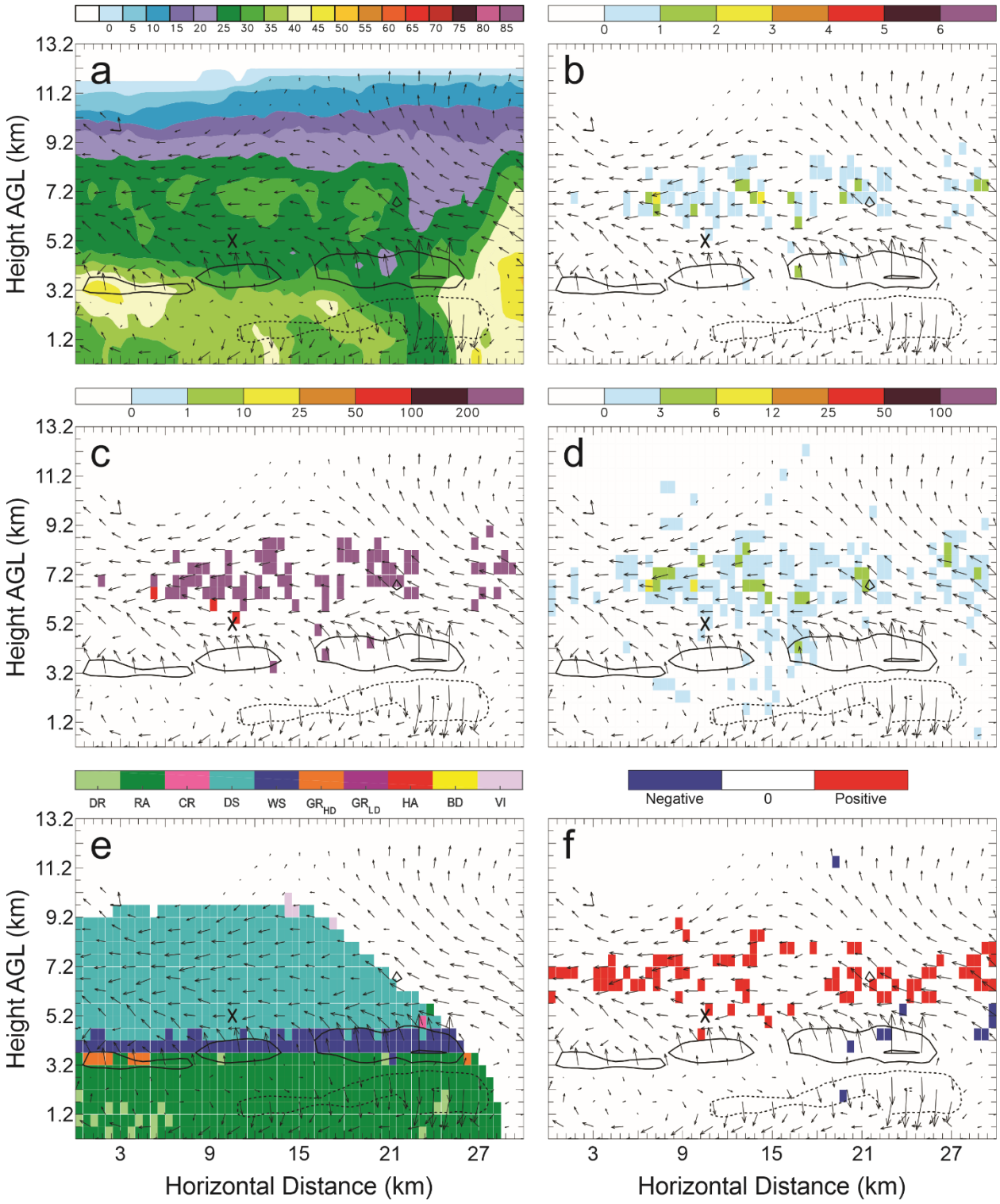

Figure 181: Vertical cross-sections for 6 June 21:39 UTC. As in Figure 178, but taken along the second line from the north in Figure 132(e).

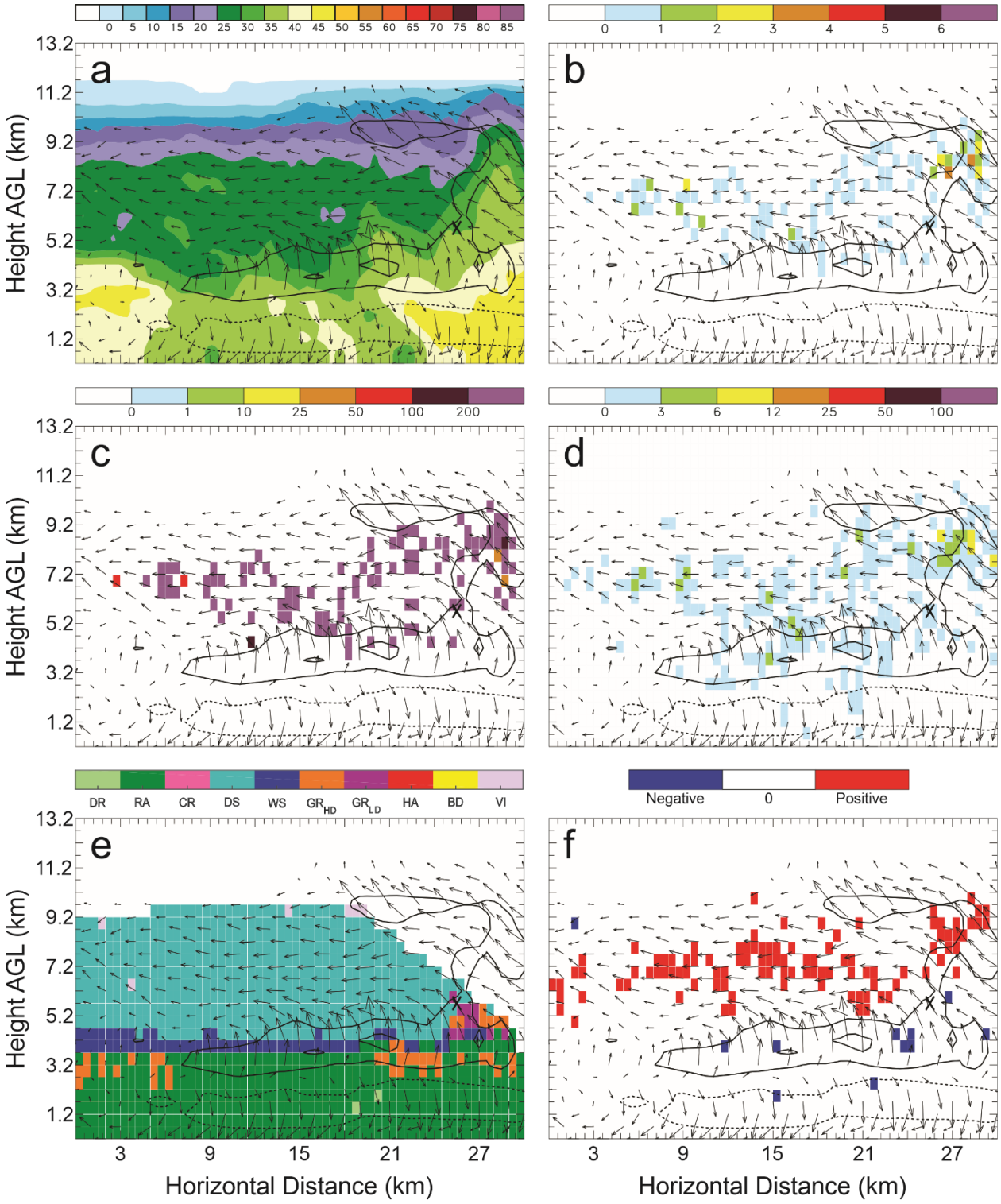

Figure 182: Vertical cross-sections for 6 June 21:39 UTC. As in Figure 178, but taken along the northernmost line in Figure 132(e).

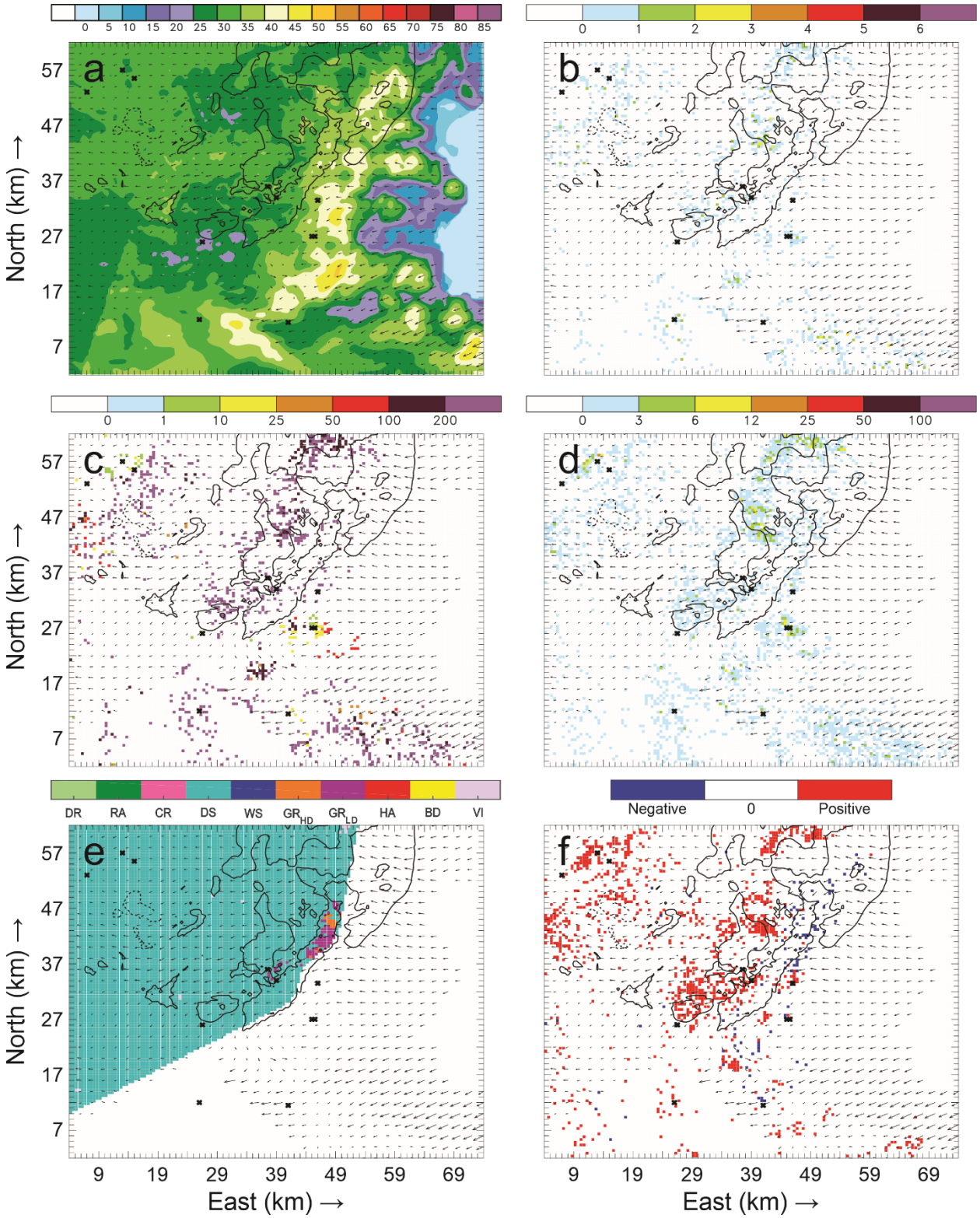

Figure 183: Horizontal cross-sections for 6 June 21:51 UTC taken at 4.7 km AGL of: a) color-filled Z and w contours (every 10 m s^{-1} starting at 5 m s^{-1}); b) color-filled FED and w contours; c) color-filled FP and w contours; d) color-filled SD and w contours; e) color-filled HCA and w contours; and f) color-filled net inferred space charge and w contours. All figures have the same horizontal storm-relative wind vectors, and black X's denote grid cells with FID > 0.

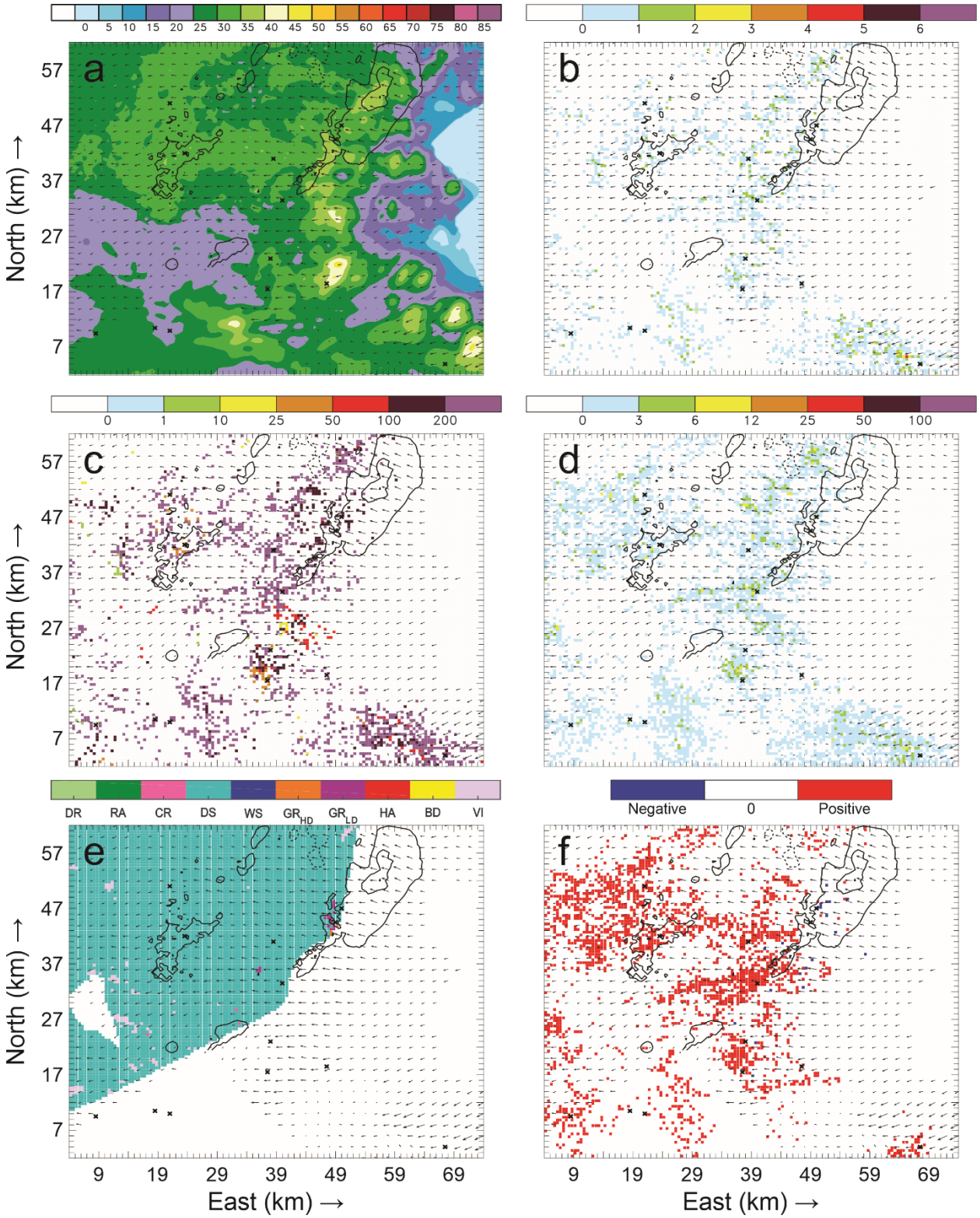

Figure 184: Horizontal cross-sections for 6 June 21:51 UTC. As in Figure 183, but taken at 5.7 km AGL.

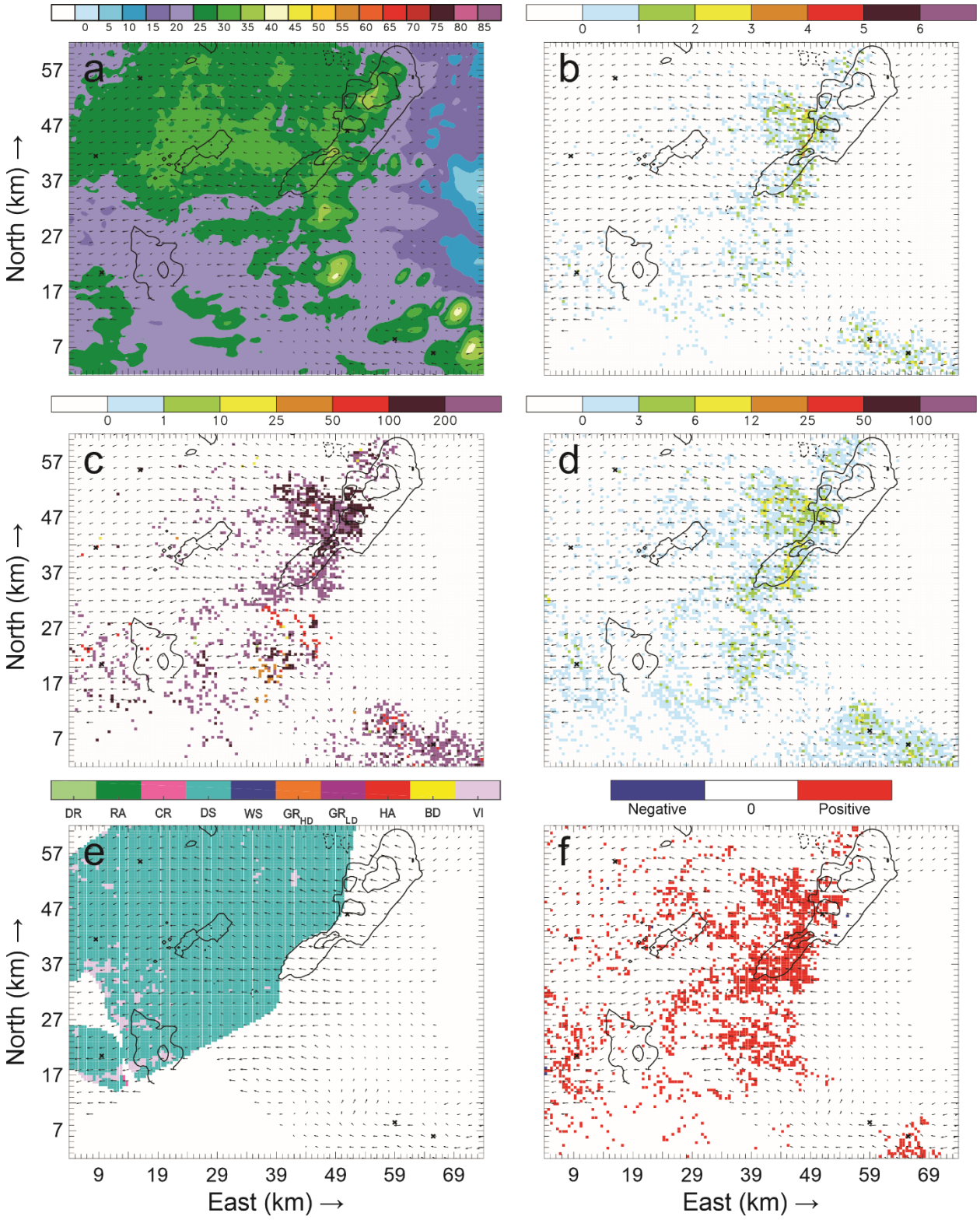

Figure 185: Horizontal cross-sections for 6 June 21:51 UTC. As in Figure 183, but taken at 6.7 km AGL.

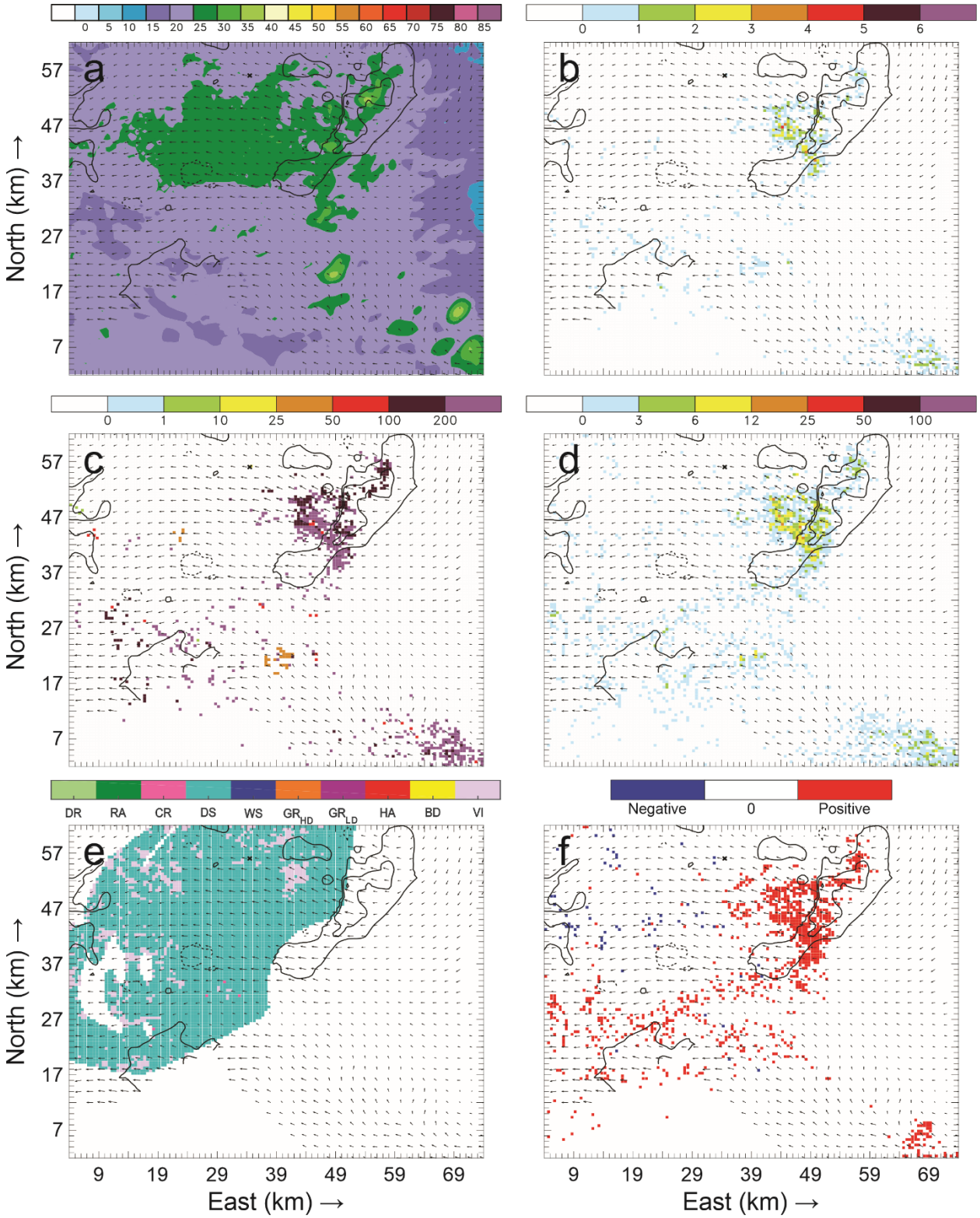

Figure 186: Horizontal cross-sections for 6 June 21:51 UTC. As in Figure 183, but taken at 7.7 km AGL.

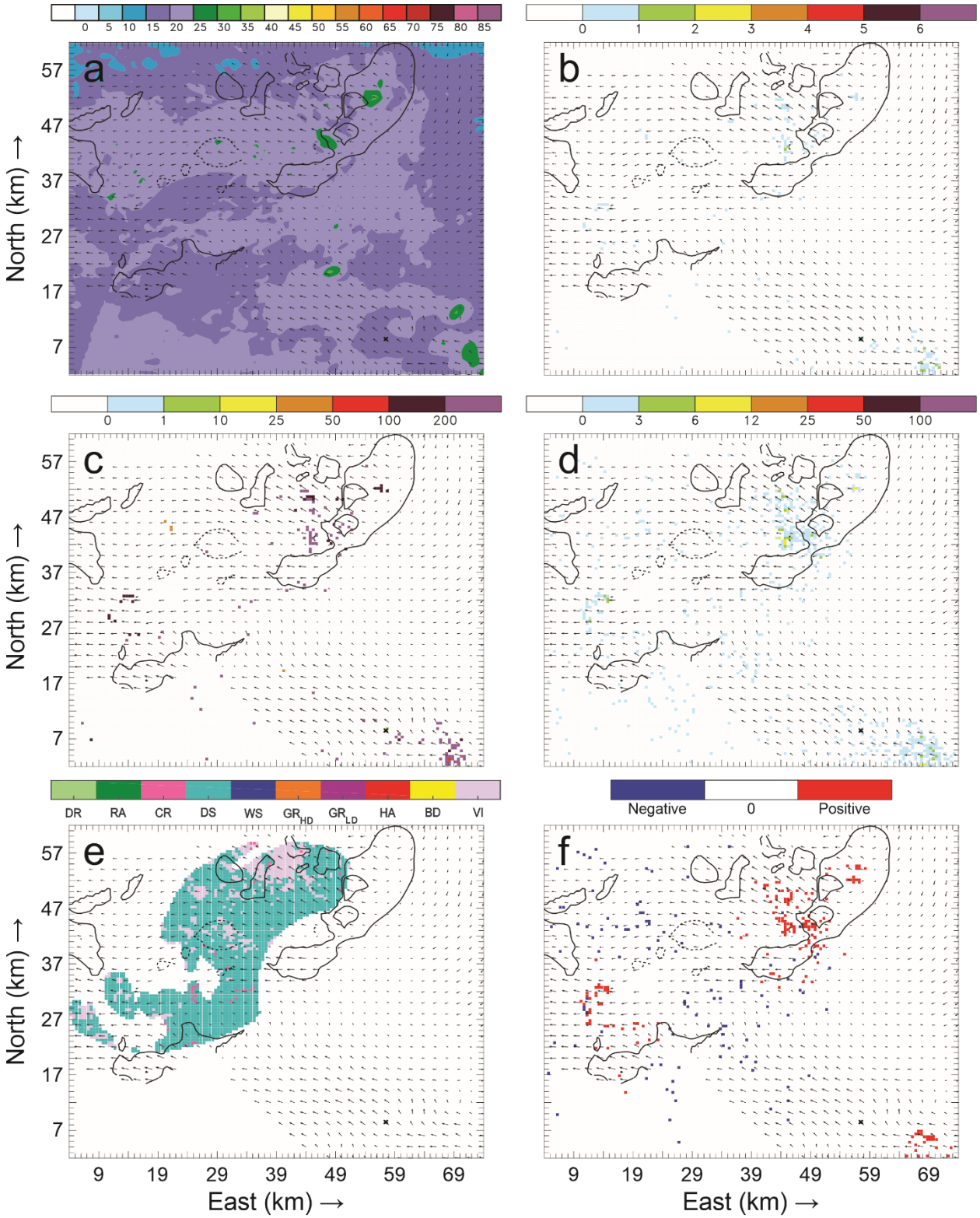

Figure 187: Horizontal cross-sections for 6 June 21:51 UTC. As in Figure 183, but taken at 8.7 km AGL.

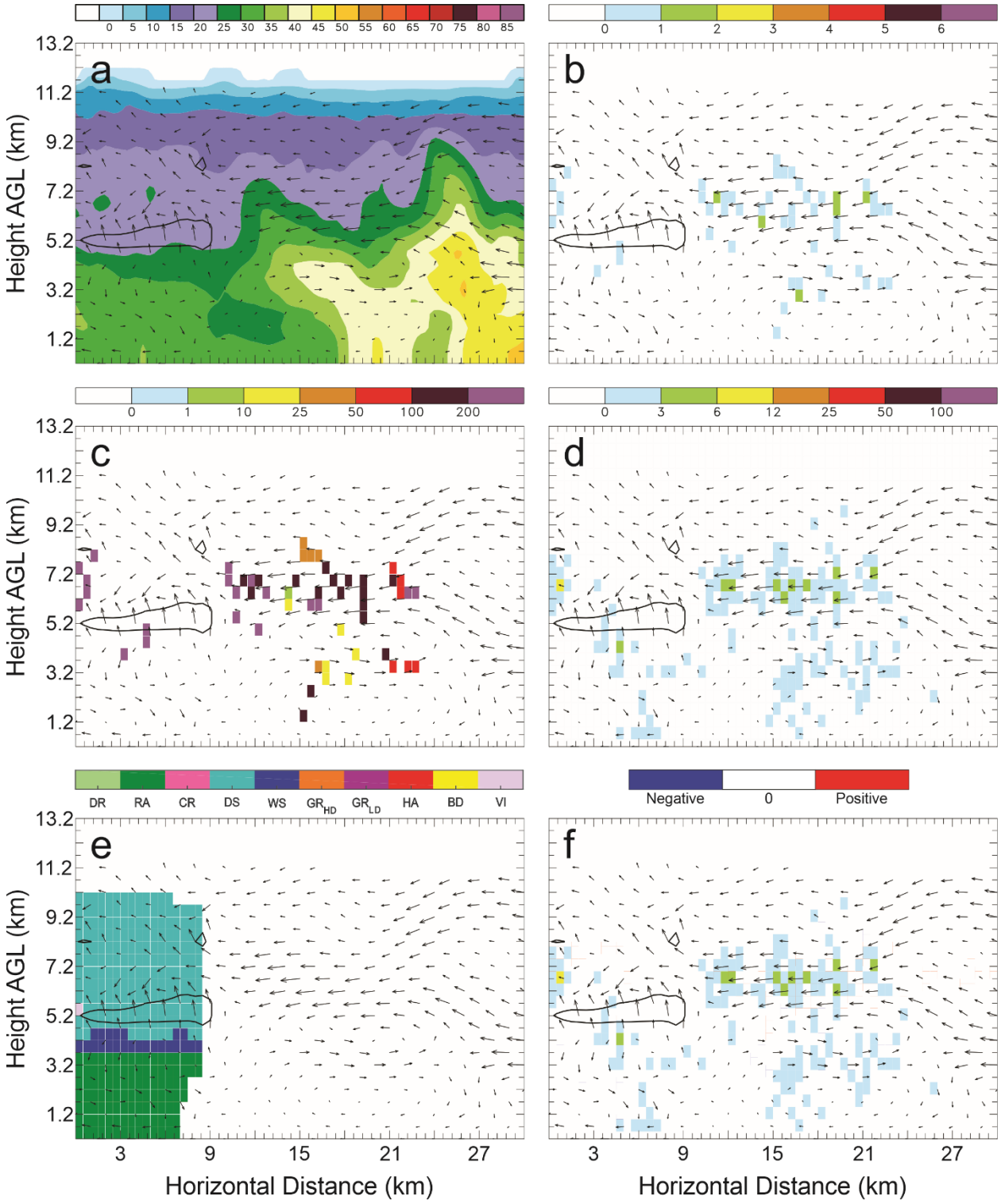

Figure 188: Vertical cross-sections for 6 June 21:51 UTC taken along the southernmost line in Figure 132(f) of: a) color-filled Z and w contours (every 10 m s^{-1} starting at 5 m s^{-1}); b) color-filled FED and w contours; c) color-filled FP and w contours; d) color-filled SD and w contours; e) color-filled HCA and w contours; and f) color-filled net inferred space charge and w contours. All figures have the same horizontal storm-relative wind vectors, and black X's denote grid cells with FID > 0.

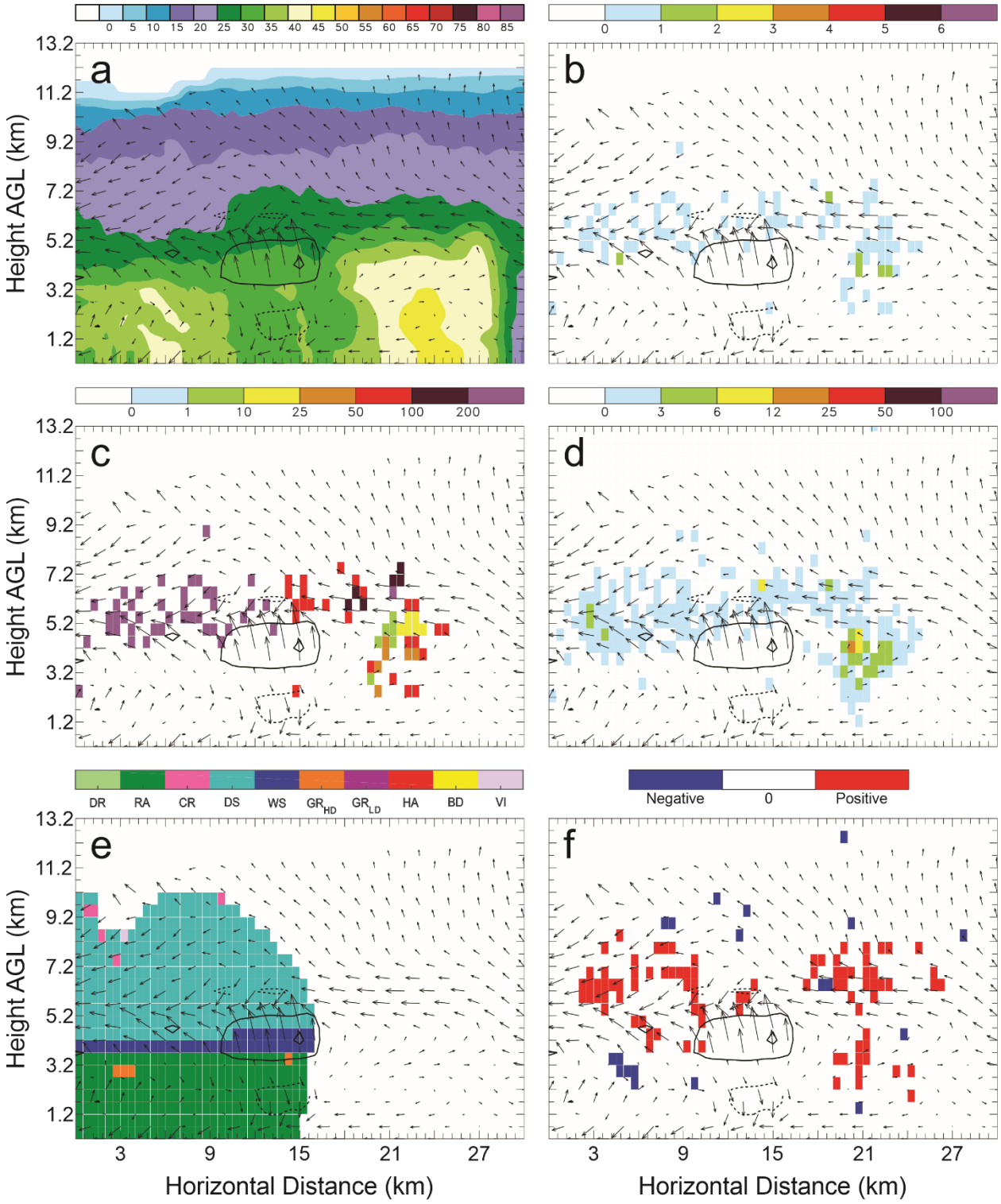

Figure 189: Vertical cross-sections for 6 June 21:51 UTC. As in Figure 188, but taken along the second line from the south in Figure 132(f).

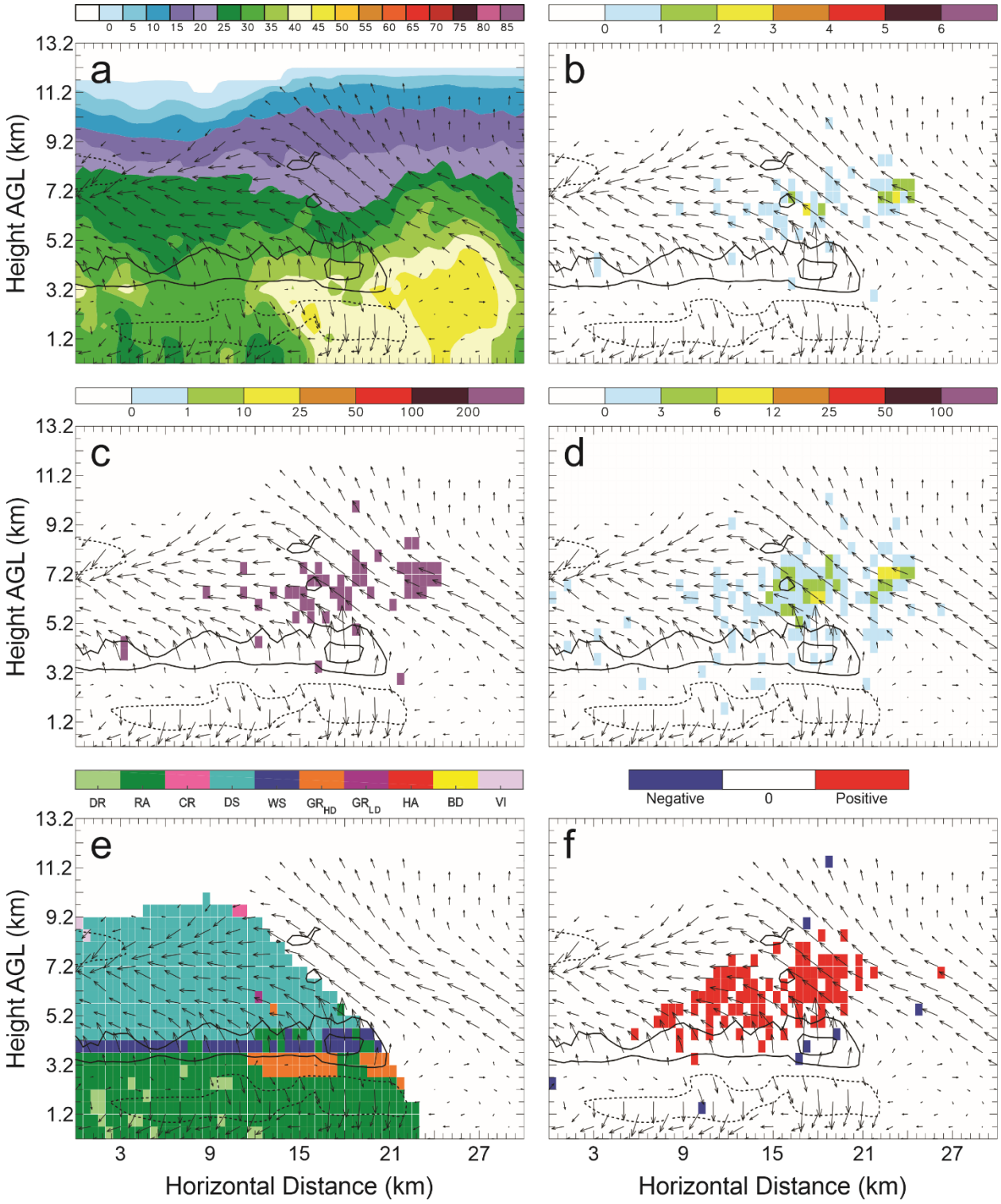

Figure 190: Vertical cross-sections for 6 June 21:51 UTC. As in Figure 188, but taken along the central line in Figure 132(f).

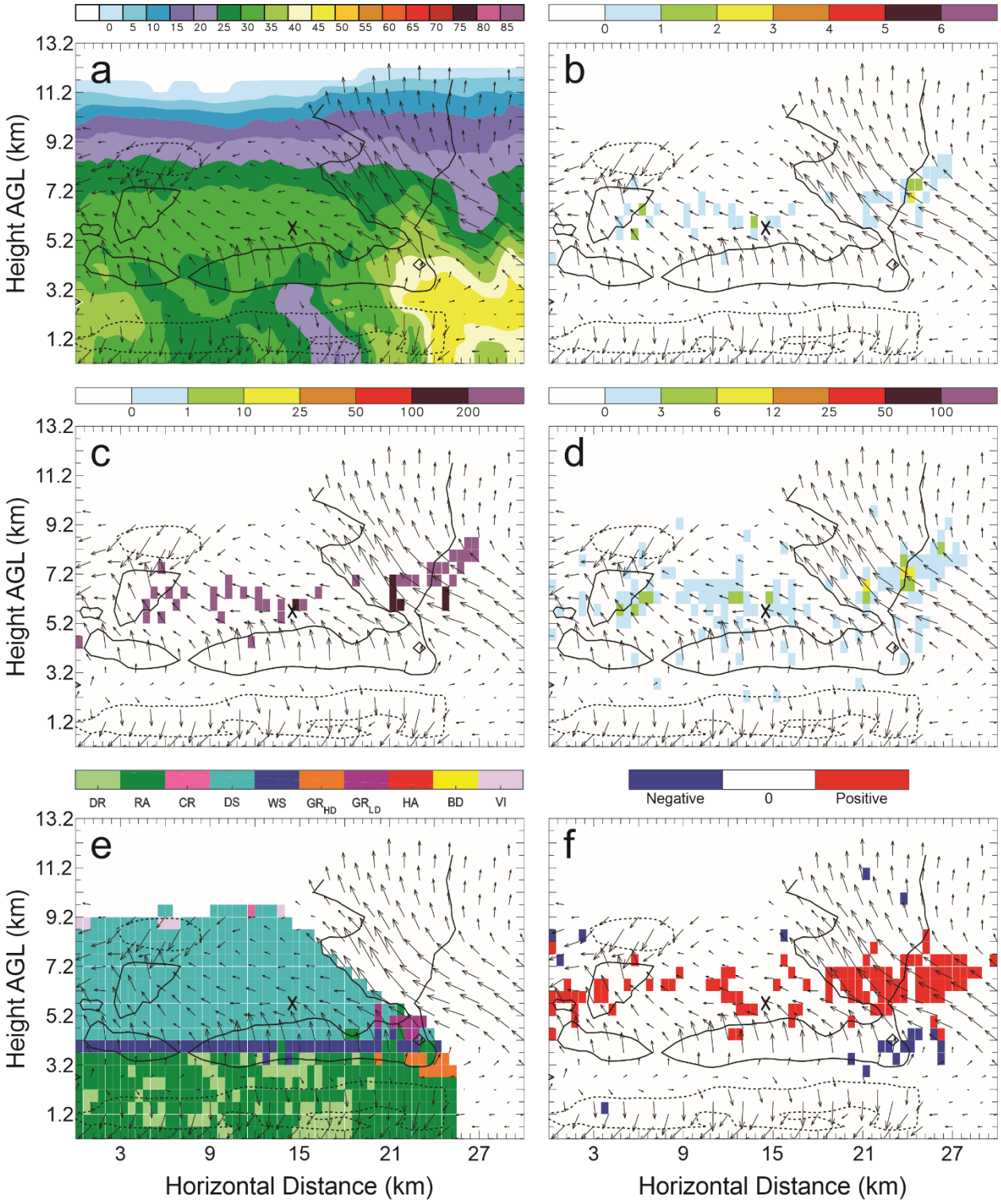

Figure 191: Vertical cross-sections for 6 June 21:51 UTC. As in Figure 188, but taken along the second line from the north in Figure 132(f).

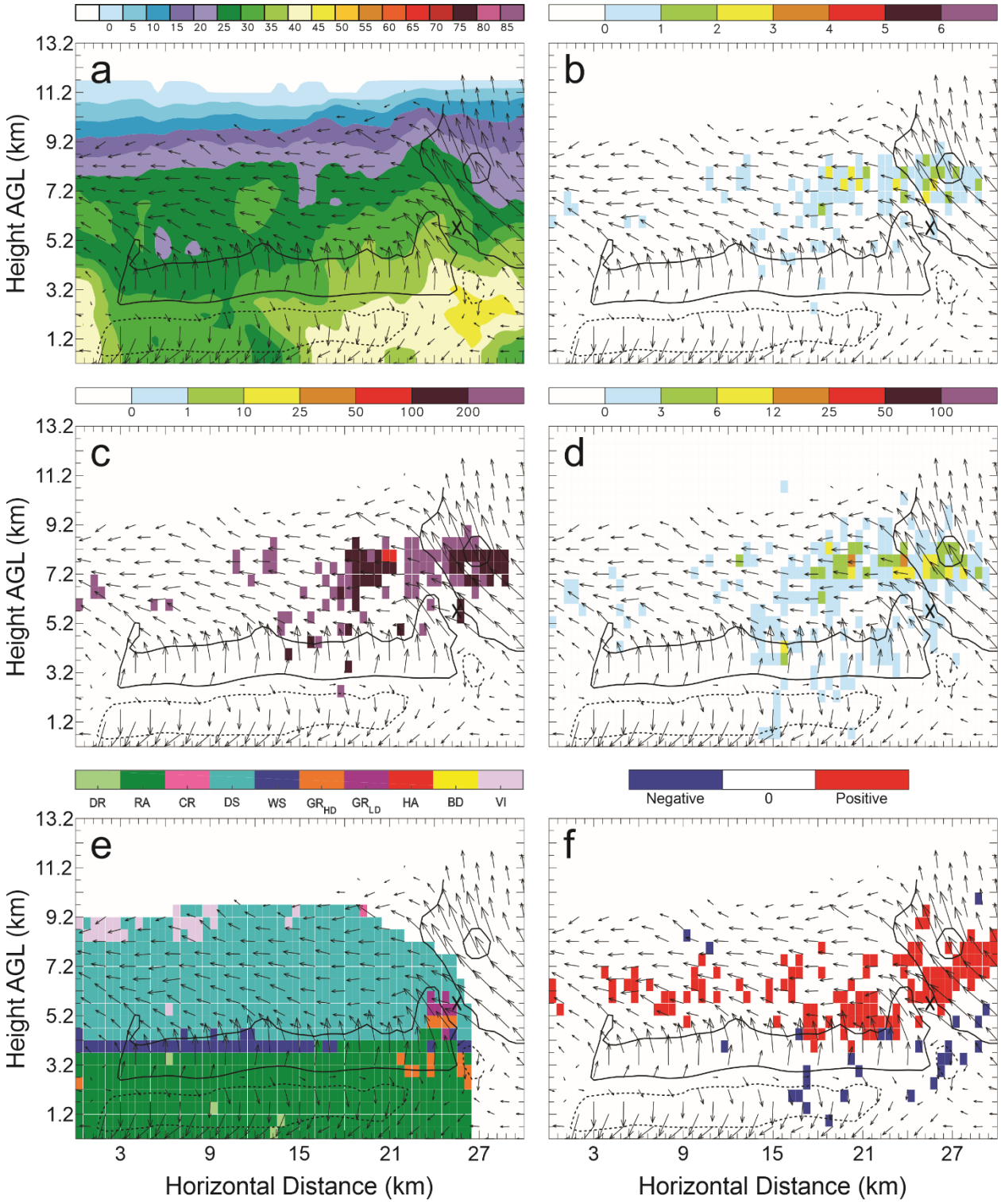

Figure 192: Vertical cross-sections for 6 June 21:51 UTC. As in Figure 188, but taken along the northernmost line in Figure 132(f).

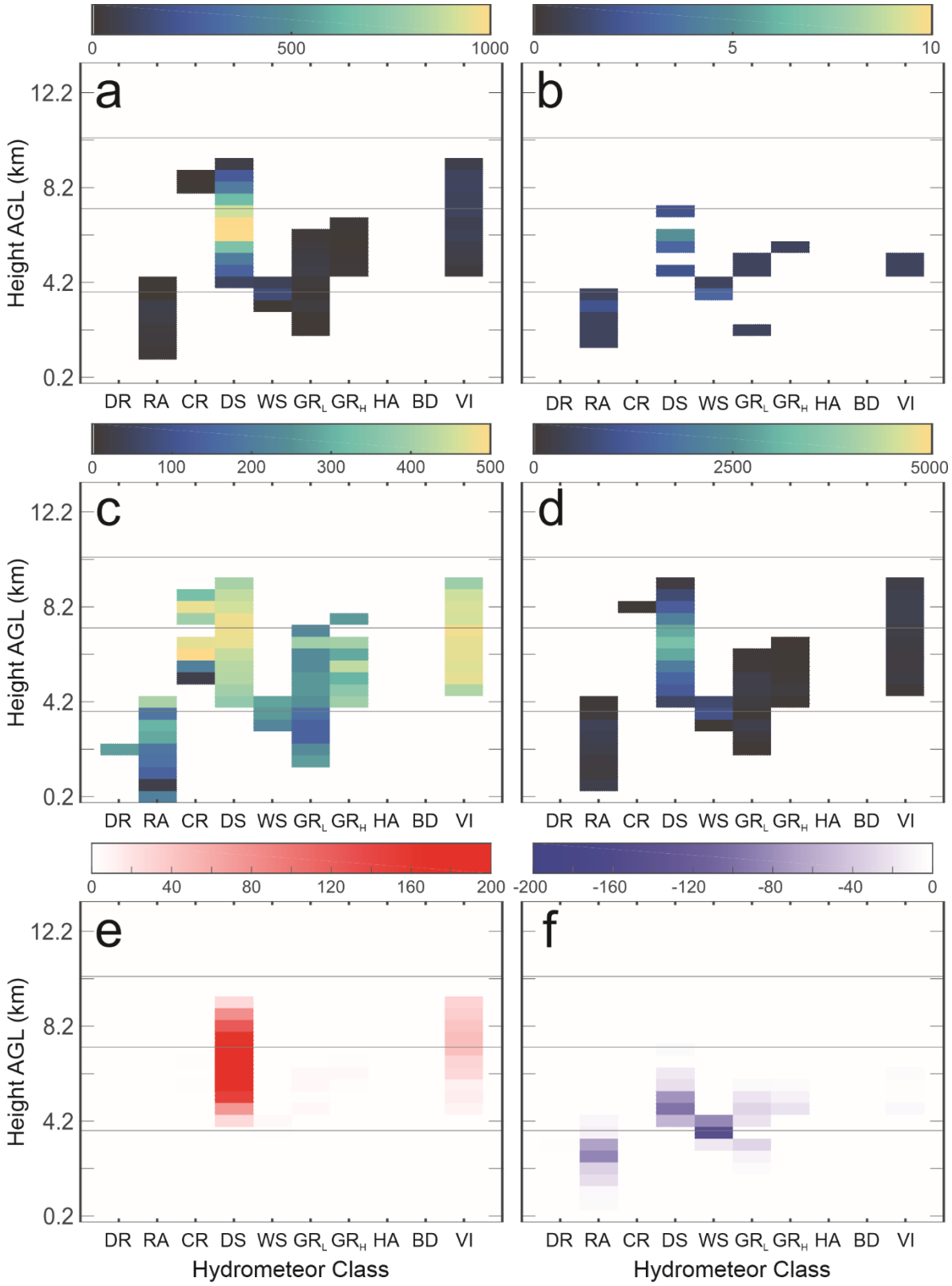

Figure 193: Lightning parameters that correspond with HCA classes in all grid cells at each horizontal level at 20:51 UTC: a) Total FED, b) total FID, c) mean FP, d) total SD, e) total points assigned positive charge, and f) total points assigned negative charge. The horizontal grey lines represent the 0ºC, -20ºC, and -40ºC levels.

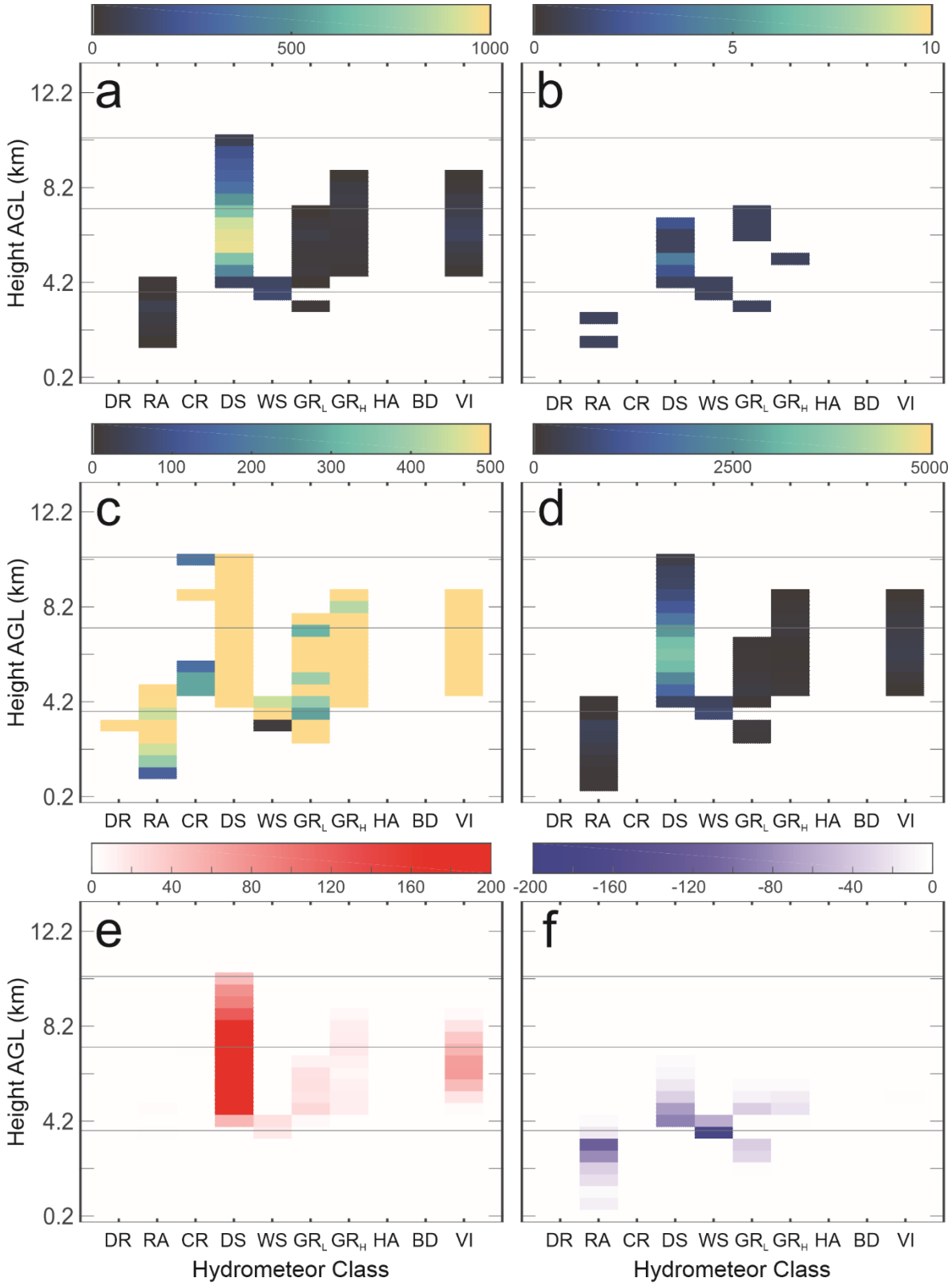

Figure 194: As in Figure 193, but for 21:03 UTC.

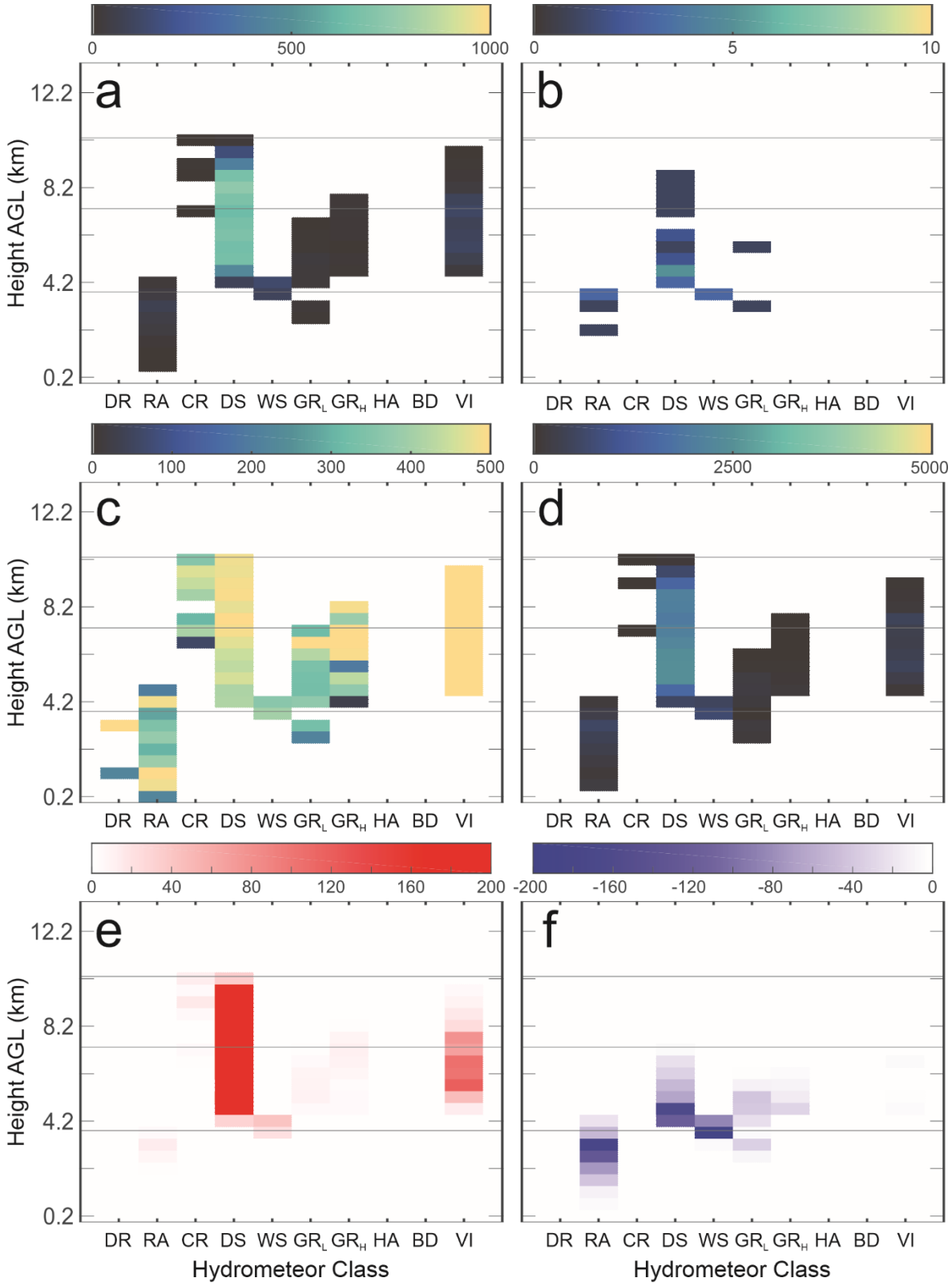

Figure 195: As in Figure 193, but for 21:15 UTC.

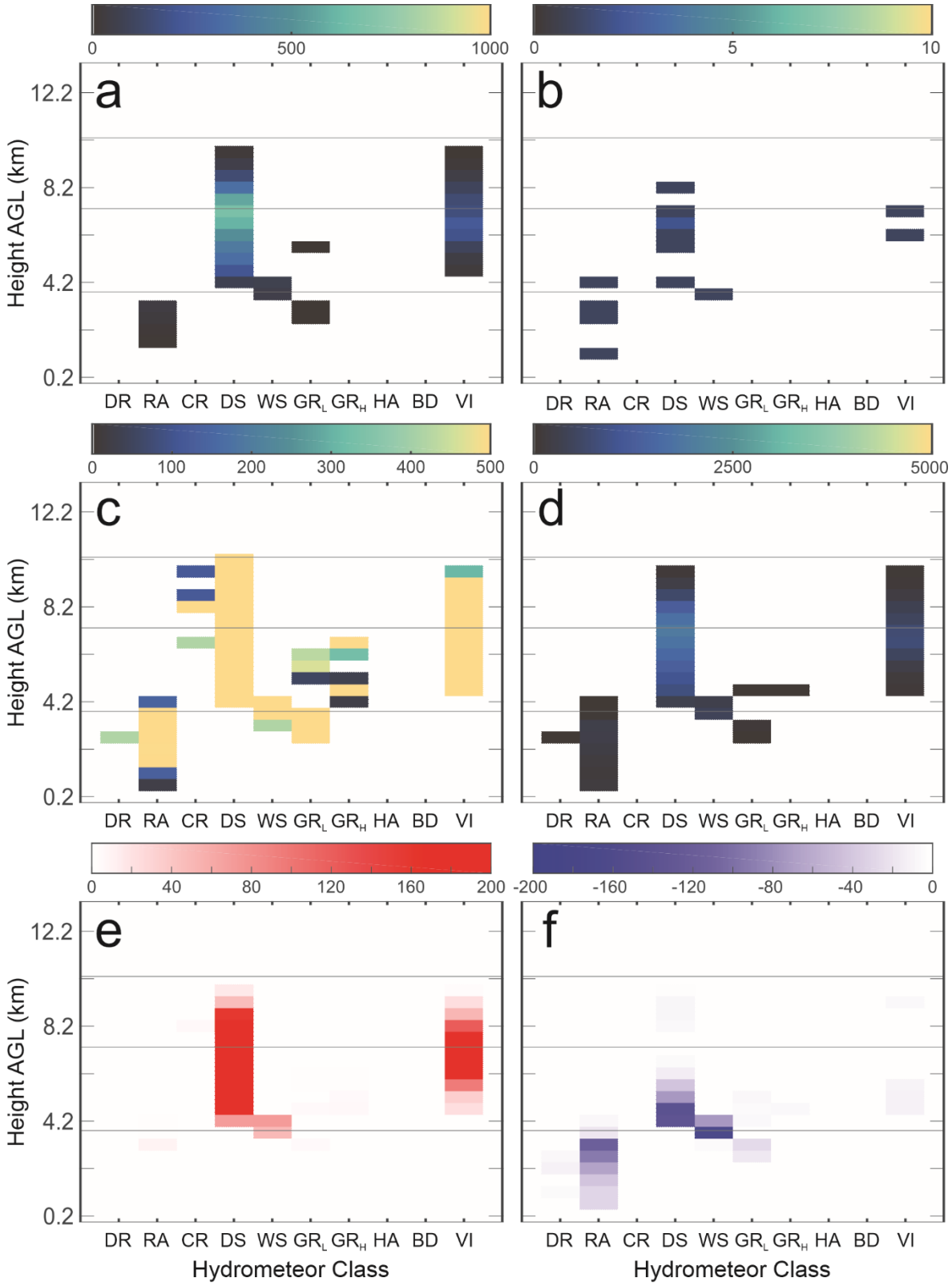

Figure 196: As in Figure 193, but for 21:27 UTC.

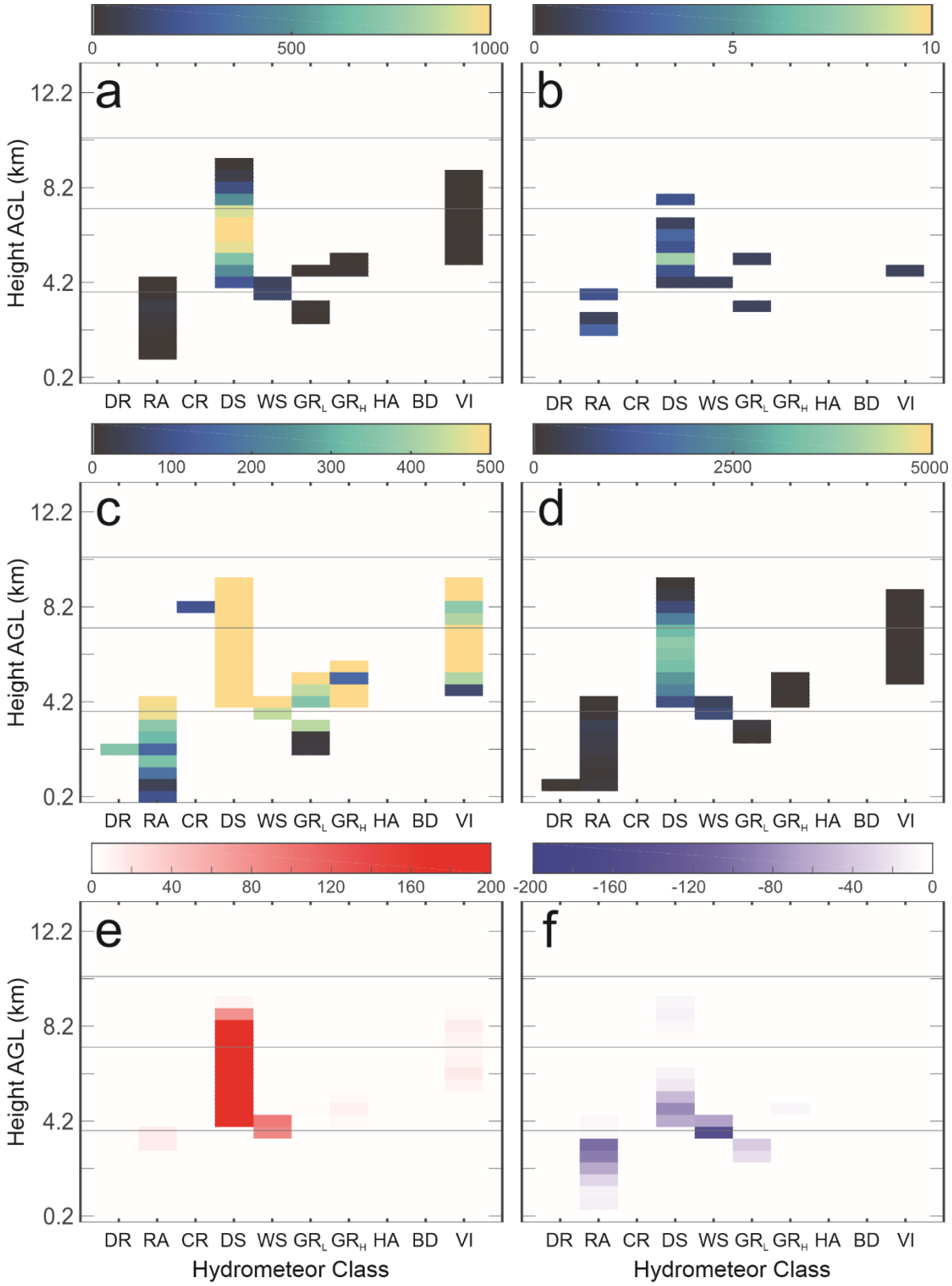

Figure 197: As in Figure 193, but for 21: 39 UTC.

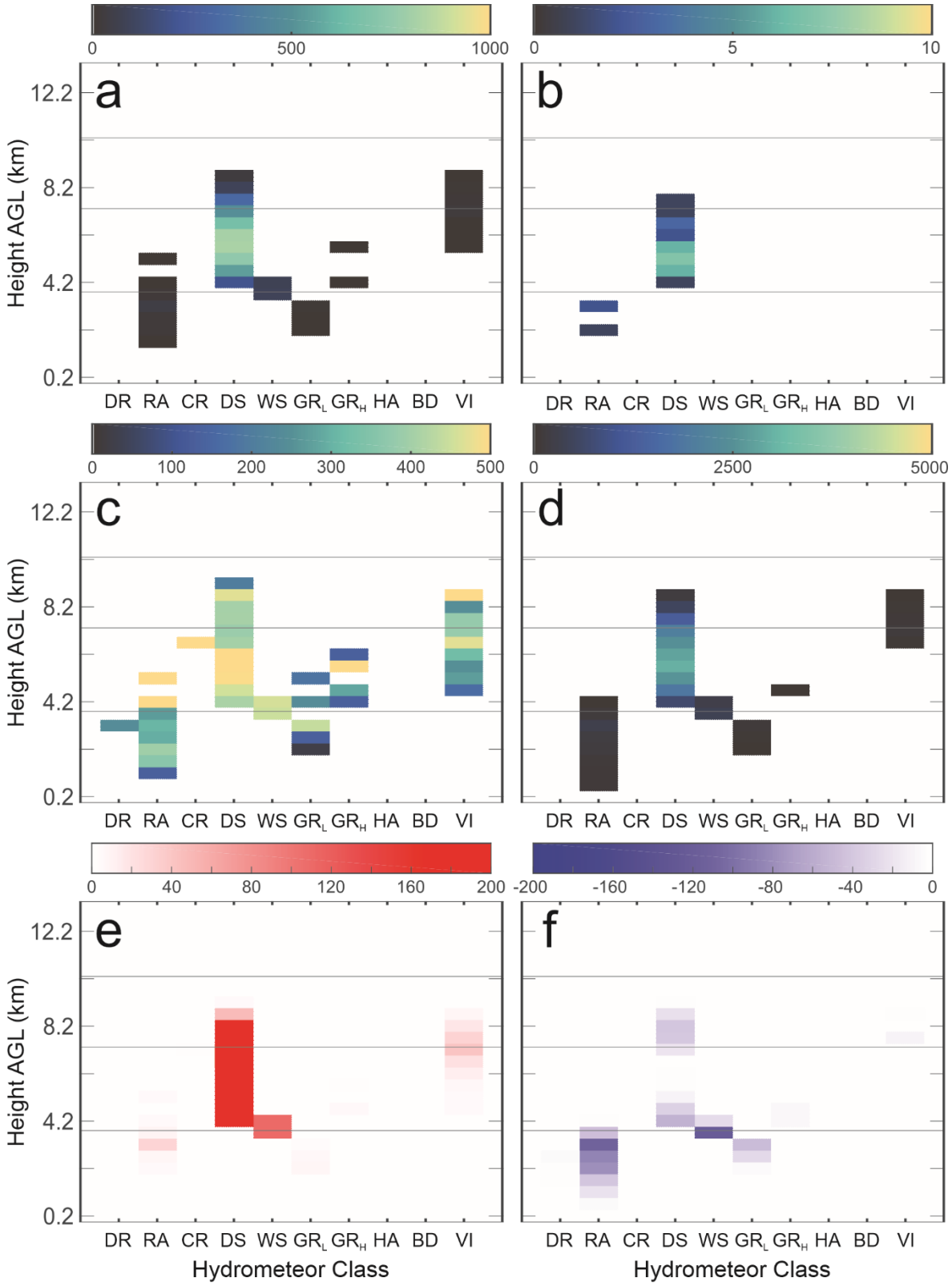

Figure 198: As in Figure 193, but for 21:51 UTC.

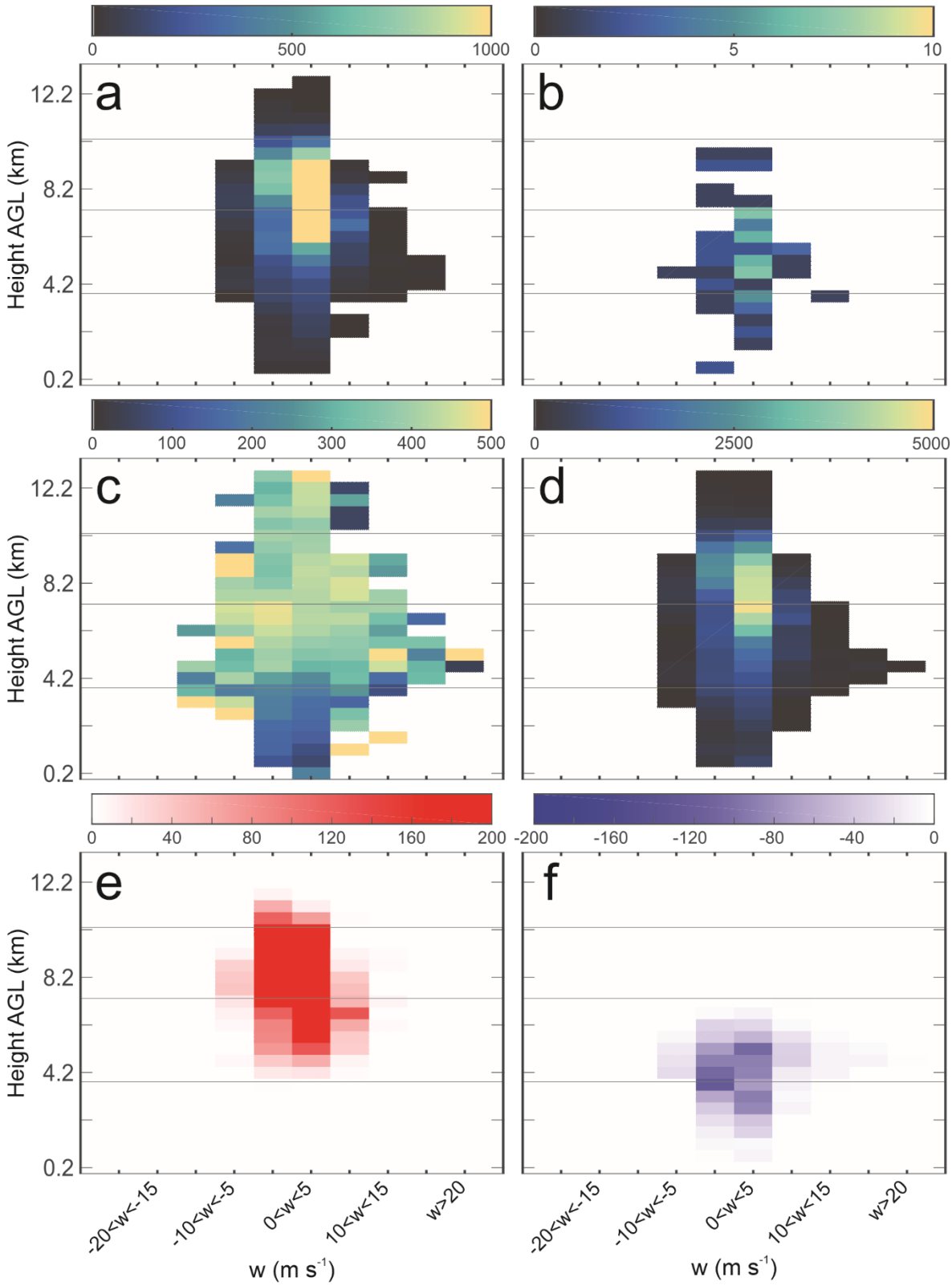

Figure 199: Lightning parameters that correspond with 5 m s^{-1} bins of w in all grid cells at each horizontal level at 20:51 UTC: a) Total FED, b) total FID, c) mean FP, d) total SD, e) total points assigned positive charge, and f) total points assigned negative charge. The horizontal grey lines represent the 0°C, -20°C, and -40°C levels.

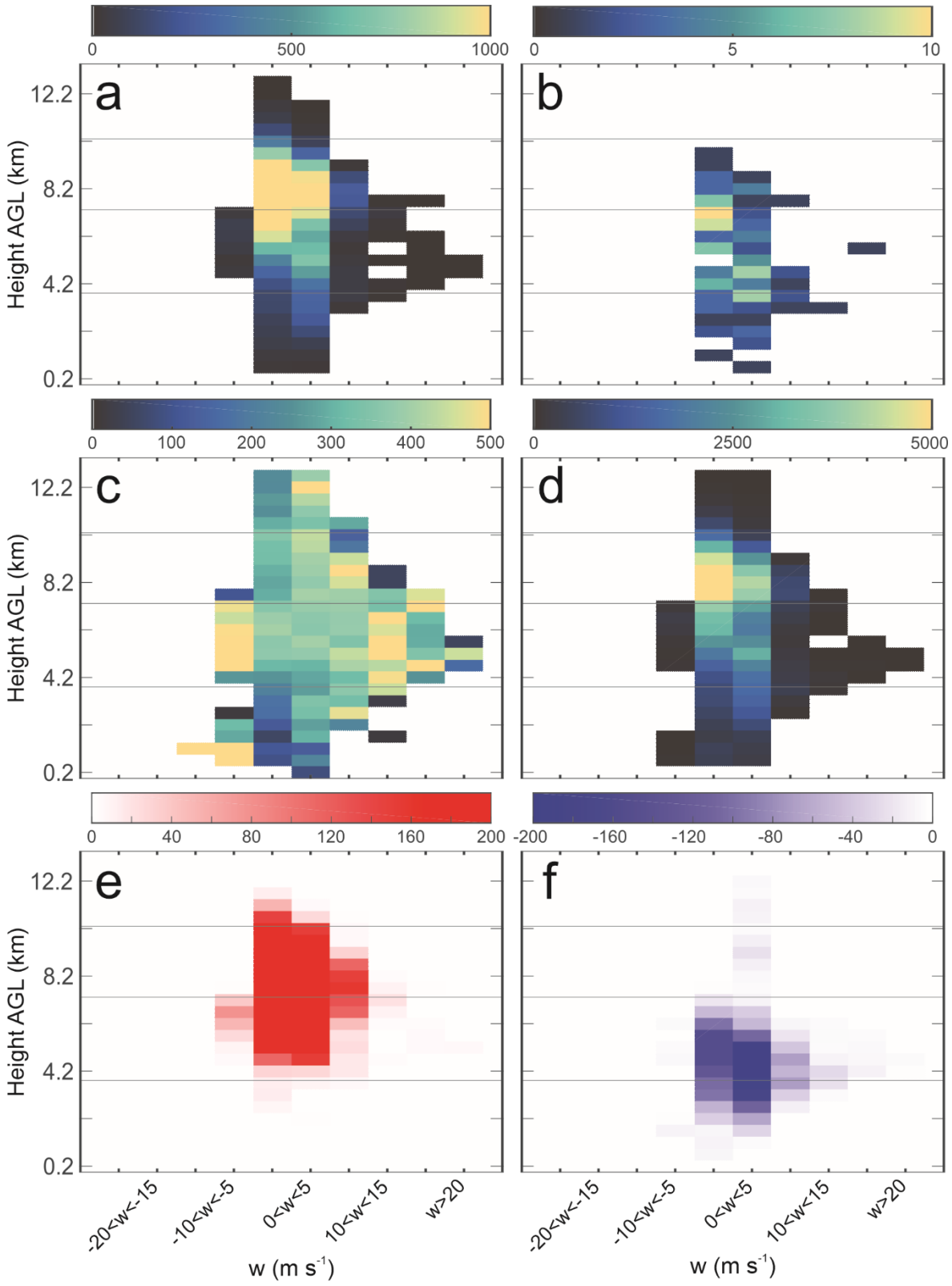

Figure 200: As in Figure 199, but for 21:03 UTC.

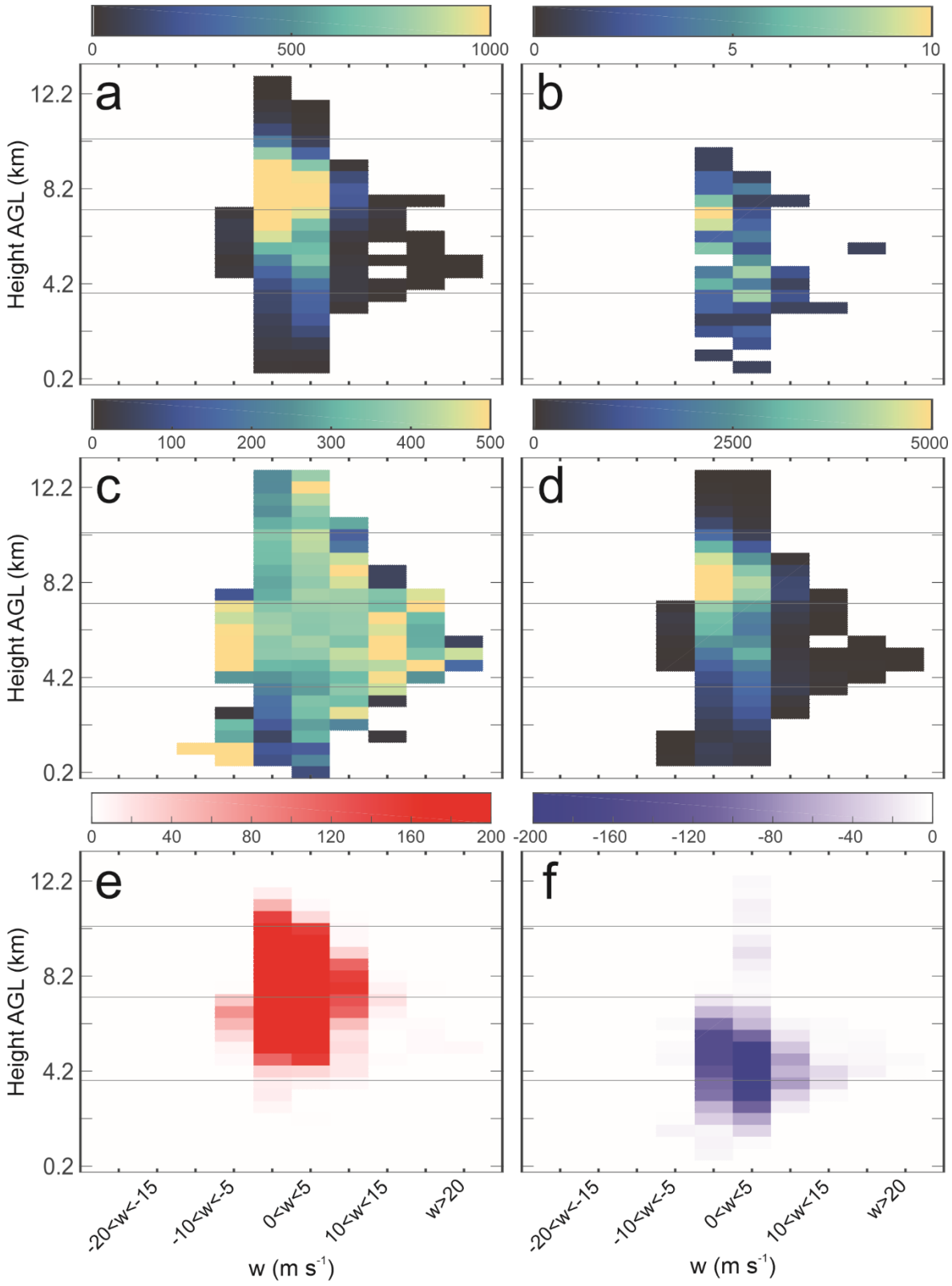

Figure 201: As in Figure 199, but for 21:15 UTC.

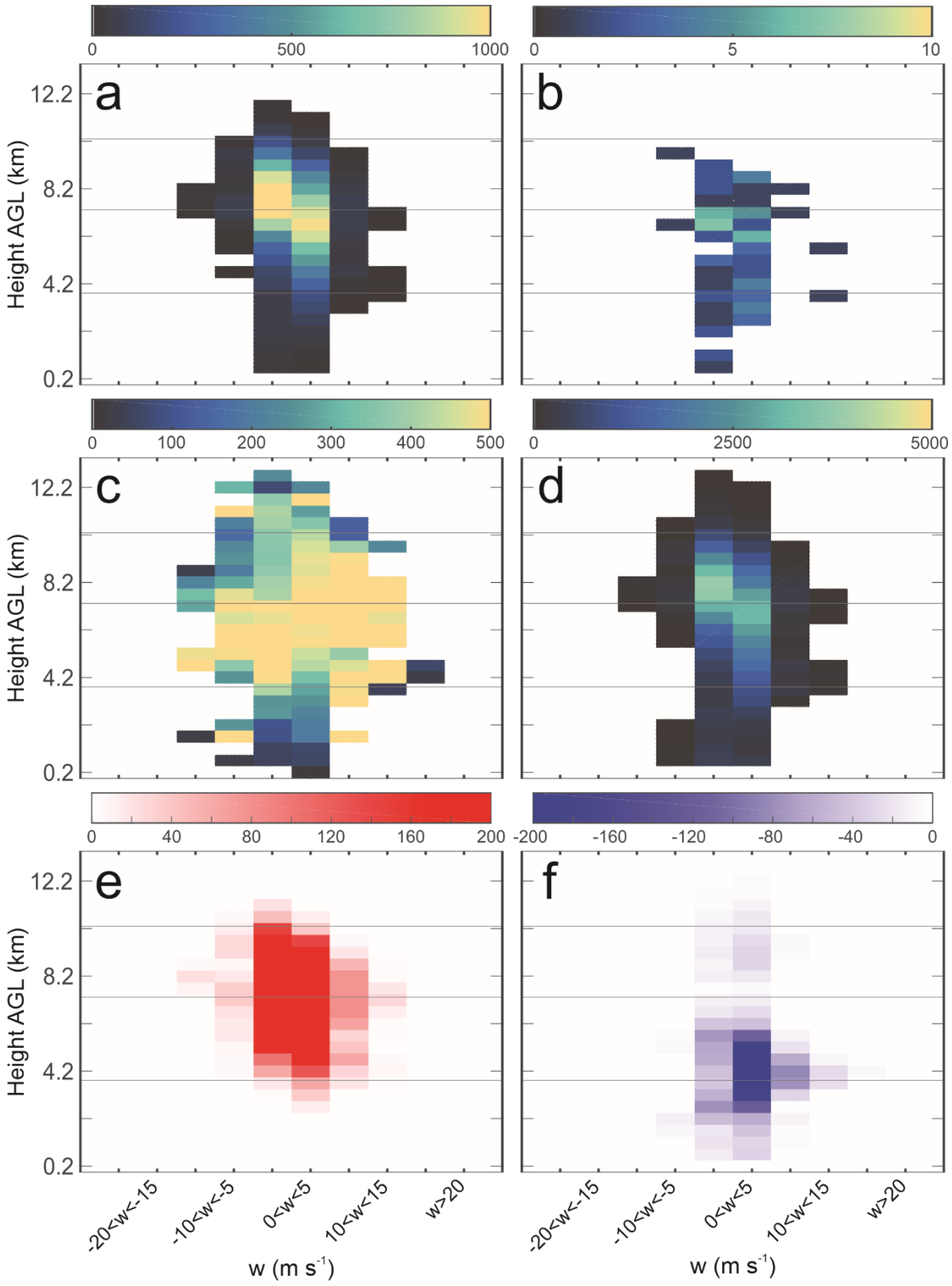

Figure 202: As in Figure 199, but for 21:27 UTC.

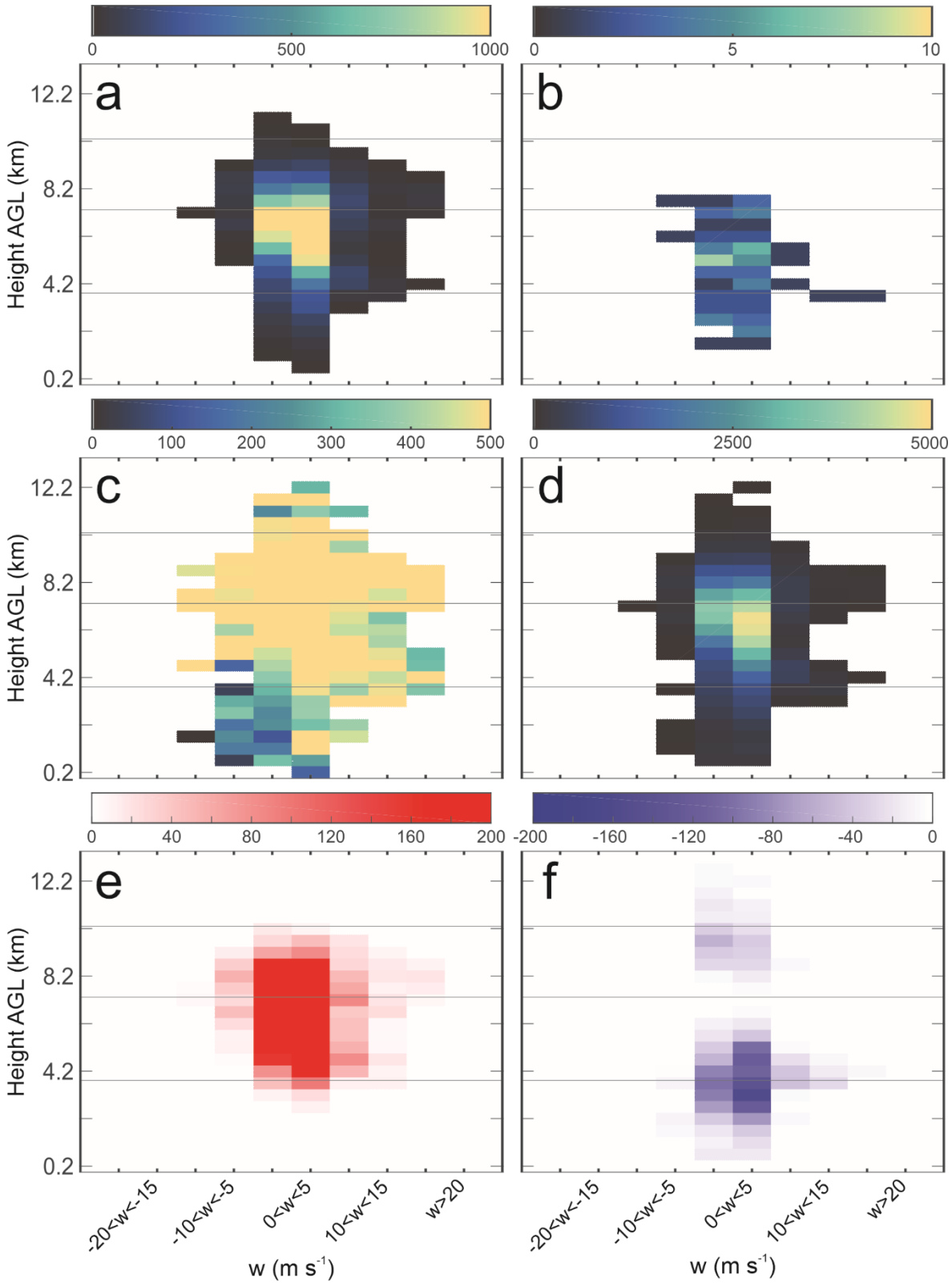

Figure 203: As in Figure 199, but for 21:39 UTC.

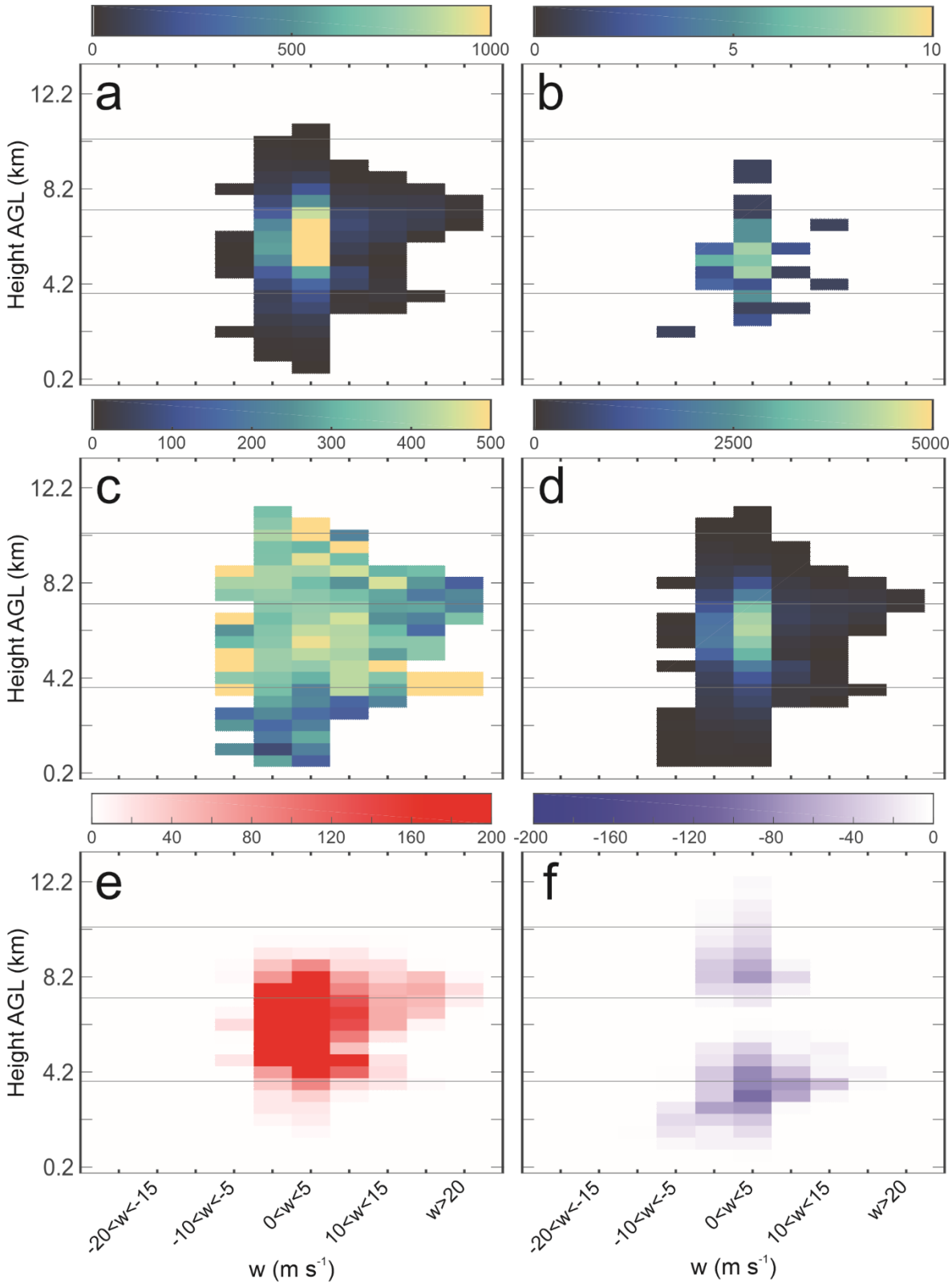

Figure 204: As in Figure 199, but for 21:51 UTC.

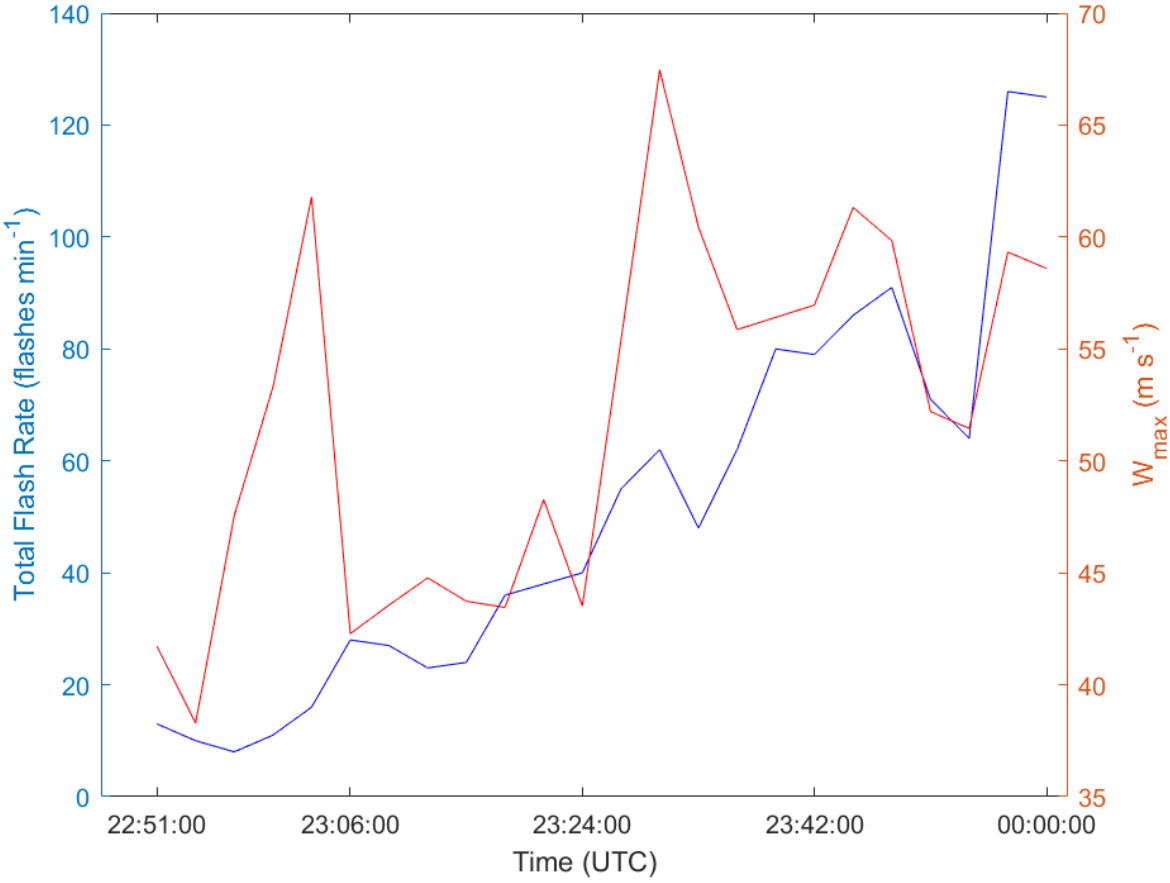

Figure 205: Time series of total flash rate (blue) and w_{max} (red) for the 29 May 2012 Kingfisher supercell.

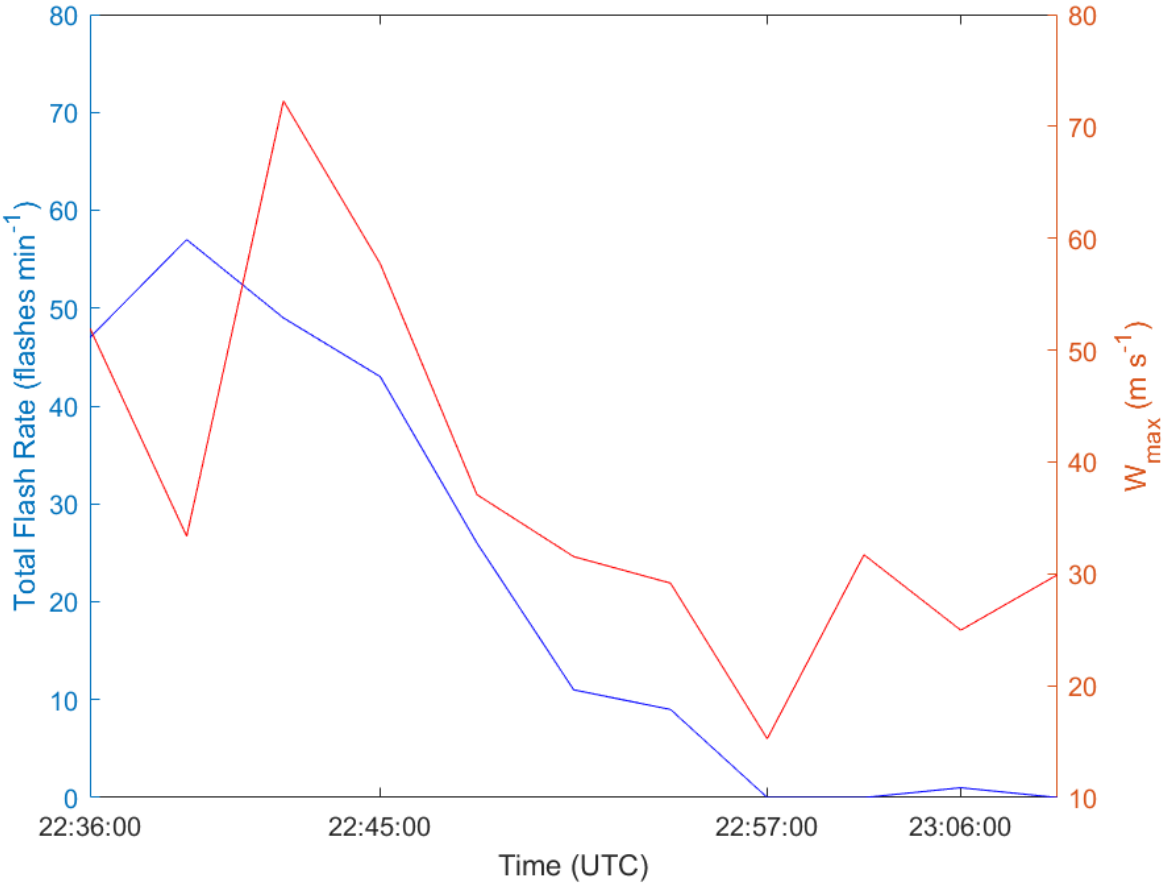

Figure 206: Time series of total flash rate (blue) and w_{max} (red) for the 16 June 2012 Eakly multicell.

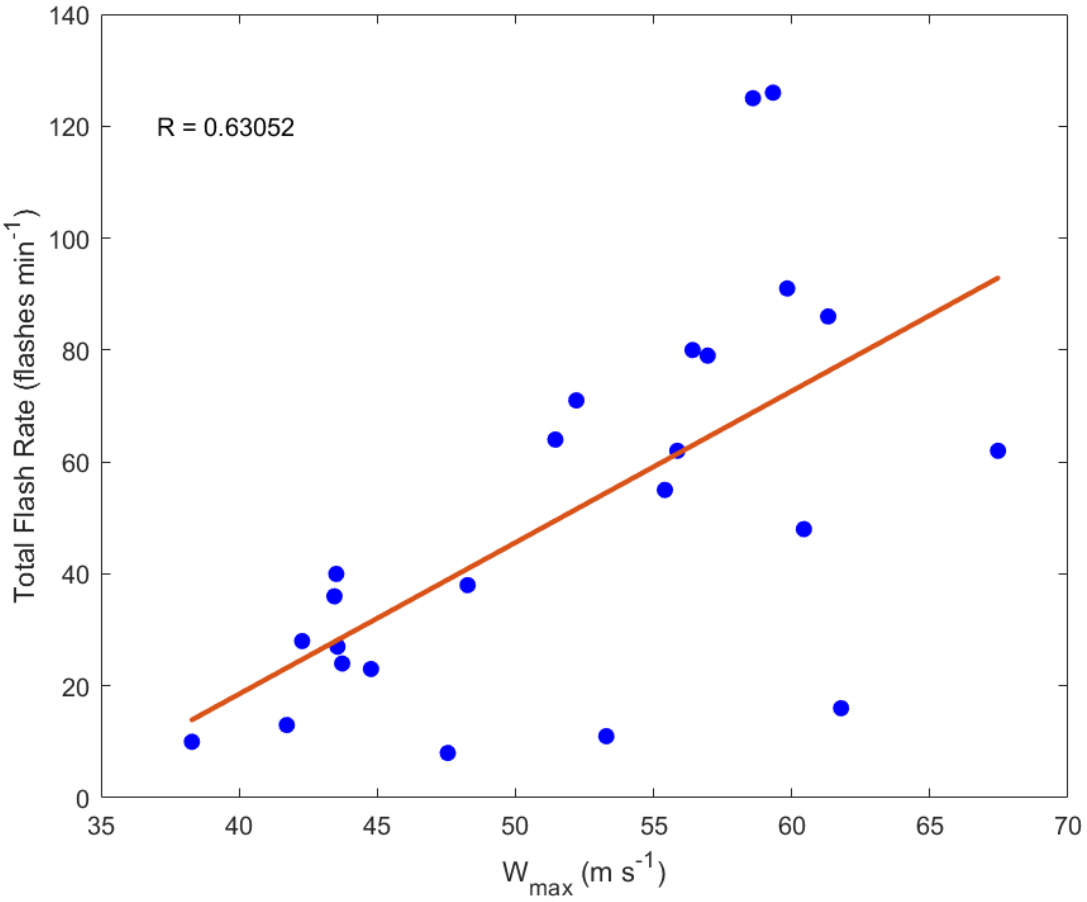

Figure 207: Total flash rate versus w_{max} with a best fit linear regression line and correlation coefficient for the 29 May 2012 Kingfisher supercell.

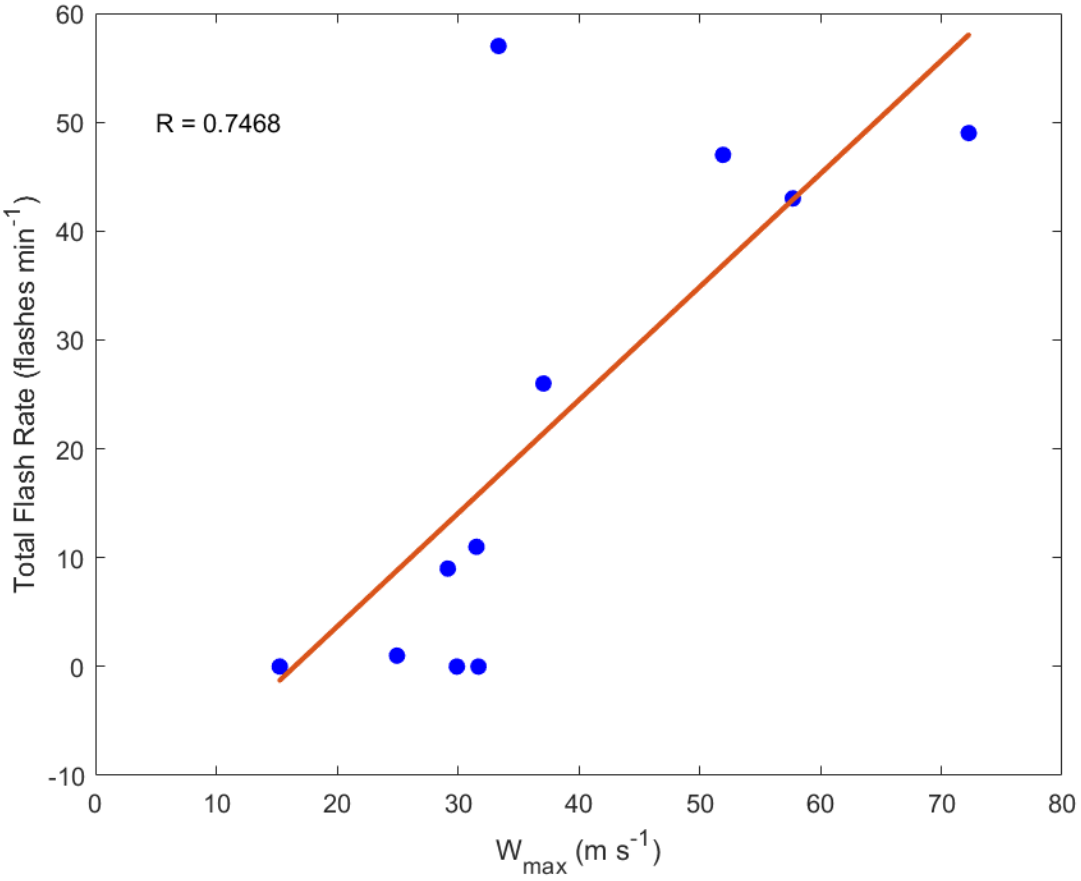

Figure 208: Total flash rate versus w_{max} with a best fit linear regression line and correlation coefficient for the 16 June 2012 Eakly multicell.